AEC RESEARCH AND DEVELOPMENT REPORT

HW-81746
1—
1963

HANFORD RADIOLOGICAL SCIENCES RESEARCH AND DEVELOPMENT ANNUAL REPORT FOR 1963

STAFF MEMBERS
OF PHYSICS AND INSTRUMENTS LABORATORY
CHEMICAL LABORATORY

JANUARY THROUGH DECEMBER 1963

EDITED BY
C. C. GAMERTSFELDER and J. K. GREEN

JANUARY 1964

HANFORD LABORATORIES

HANFORD ATOMIC PRODUCTS OPERATION
RICHLAND, WASHINGTON

GENERAL ELECTRIC

LEGAL NOTICE

HW-81746

UC-48, Biology and Medicine
(TID-4500, 32nd Ed.)

HANFORD RADIOLOGICAL SCIENCES RESEARCH AND DEVELOPMENT ANNUAL REPORT FOR 1963

By

Staff Members of
Physics and Instruments Laboratory
Chemical Laboratory
Hanford Laboratories

Edited by
C. C. Gamertsfelder and J. K. Green

January 1964

HANFORD ATOMIC PRODUCTS OPERATION
RICHLAND, WASHINGTON

Work performed under Contract No. AT(45-1)-1350 between the Atomic Energy Commission and General Electric Company

Printed by/for the U.S. Atomic Energy Commission

Printed in USA. Price $5.00 Available from the

Office of Technical Services
Department of Commerce
Washington 25, D. C.

TABLE OF CONTENTS

TABLE OF CONTENTS (Contd.)

TABLE OF CONTENTS (Contd.)

TABLE OF CONTENTS (Contd.)

TABLE OF CONTENTS (Contd.)

TABLE OF CONTENTS (Contd.)

TABLE OF CONTENTS (Contd.)

TABLE OF CONTENTS (Contd.)

HANFORD RADIOLOGICAL SCIENCES RESEARCH AND DEVELOPMENT ANNUAL REPORT FOR 1963

ATMOSPHERIC PHYSICS

Prediction of Environmental Exposures from Sources Near the Ground, Based on Hanford Experimental Data - J. J. Fuquay, C. L. Simpson, and W. T. Hinds

Values of peak exposure and standard deviations of exposure distributions downwind from a continuous point source are presented for 46 Hanford ground source diffusion experiments. Exposure data were found to order in terms of atmospheric stability when plotted as a function of the travel time. The crosswind variances of the exposure distributions were expressed in terms of the travel time and the product of the standard deviation of the wind direction distribution and the mean wind speed, $\sigma_\theta \bar{u}$, in an equation resulting from G. I. Taylor's work in 1921.

Prediction methods developed from these concepts permit extrapolation of the results obtained from short releases to much longer release periods. Good agreement between predicted and observed exposure distributions were obtained from these models, using independent data.

Introduction

In the summer of 1959, the Green Glow Program was initiated at Hanford to obtain diffusion data out to 25.6 km from a ground source in stable atmospheres. Details of the experimental design, method of zinc sulfide plume generation, supporting meteorological instrumentation, sampling techniques, and method of sample assay have been given by Barad and Fuquay.[1.1] Diffusion and meteorological data obtained in the test series have been summarized by Barad and Fuquay.[1.2]

From 1960 through 1962, experimentation continued at Hanford extending the testing to periods in which the atmosphere was neutral and unstable. These tests which collectively are called the Hanford 30 Series were conducted with essentially the same experimental techniques as those of the Green Glow program. The collection of diffusion data at the outermost distances was curtailed in the 30 Series program because of manpower shortages.

The data that were obtained afford the means for a comprehensive analysis directed toward relating diffusion parameters to the meteorological measurements which were made concurrently. At this time, several results have been obtained which suggest a profitable approach in the analysis and application of experimental diffusion data. The most significant departure from most of the other experimental studies is that atmospheric diffusion is viewed as a time-dependent process. Significant improvement in the ordering of data, such as the peak exposure (time integrated concentration), is evidenced when these values are plotted as a function of a calculated travel time compared to results obtained by considering arc distance as the independent variable. This concept has been the basis for further analysis of the Hanford data and has led to the development of a plume growth model in which the parameters depend only on meteorological variables. These results are pertinent to many of the applied problems of the day. Therefore, the objectives of this paper are:

- to make the Hanford data available to other investigators
- to present pertinent diffusion concepts which have been developed at this time
- to demonstrate how these concepts are applied in predicting diffusion.

The Data

Of the 66 field tests that were successfully completed in the Green Glow and Hanford 30 Series programs, 46 were selected for the analysis. Twenty tests were rejected primarily because the lateral dimensions of the

mean plume were not sufficiently contained within the sampling grid. Rejecting these tests eliminated the necessity for extrapolating data so that the final results are not affected by judgments of this kind. Ten of the twenty tests were set aside for later use as independent verification of prediction methods.

Tables 1.1, 1.2, and 1.3 summarize some of the meteorological and diffusion data of the 46 tests that comprise the reliable data.

Table 1.1 lists the test run number, data of the run and the times denoting the beginning and termination of the release. The Richardson's number calculated from wind and temperature measurements near the source is also given. These calculations were made by a method suggested by Lettau[1.3] using data collected at the 7 and 50 ft levels of the Hanford Meteorology Tower during the period of emission. The final columns contain the mean wind speed (mps), the computed standard deviation (deg) of the wind direction distribution for the emission period, and the product $\sigma_\theta \bar{u}$ (rad m/sec). The speed and direction data which apply to the 7 ft level were taken from strip chart records. The standard deviation, σ_θ, was computed from its statistical definition using 20 sec direction averages over the emission period.

Table 1.2 gives the values of the peak exposure, E_p, for each run and each arc on the Hanford grid. Exposure is often defined as the time-integrated concentration with units of g sec/m^3. The peak exposure is the largest exposure value on the arc and, therefore, defines the centerline of the mean plume. The total mass of zinc sulfide, Q(g), released for each test is also given.

The data presented in Table 1.3 are the standard deviation of the crosswind exposure distribution, σ_y(m). This statistic, which is a measure of the lateral spread of the plume, has been calculated with the basic are exposure data and is summarized for each run and arc distance.

TABLE 1.1

RELEASE TIME, RICHARDSON NUMBER AND $\sigma_\theta \bar{u}$
FOR THE HANFORD GROUND SOURCE DIFFUSION TESTS

Run Number	Date	Time Release Began	Time Release Ended	Ri	$\bar{u}_7$, m sec^{-1}	σ_θ, deg	$\sigma_\theta \bar{u}$, rad m/sec
5	7/8/59	2120	2150	0.097	1.7	3.6	0.107
6	7/10/59	2217	2247	0.049	3.8	8.0	0.532
7	7/13/59	2201	2231	0.119	0.9	5.6	0.104
8	7/15/59	2200	2230	0.083	2.3	4.2	0.168
9	7/18/59	2324	2354	0.112	2.5	9.5	0.415
10	7/19/59	2201	2231	0.037	5.6	4.7	0.459
13	7/24/59	2230	2300	0.078	3.3	7.7	0.442
15	7/31/59	0010	0040	0.247	1.5	18.3	0.478
17	8/7/59	2130	2200	0.032	3.8	4.2	0.277
18	8/9/59	2145	2215	0.031	3.9	5.7	0.386
19	8/11/59	2145	2215	0.011	5.0	7.9	0.690
21	8/14/59	2108	2138	0.067	3.8	4.5	0.296
22	8/17/59	2050	2120	0.031	4.6	5.7	0.455
23	8/18/59	2050	2120	0.018	4.8	4.3	0.360
25	8/25/59	2210	2240	0.028	4.4	7.9	0.607
26	8/28/59	2100	2130	0.036	3.7	5.1	0.329
30	2/18/60	0927	0947	- 0.176	2.5	11.0	0.480
31	3/11/60	0955	1025	- 0.027	3.4	8.5	0.503
32	3/15/60	0955	1025	- 0.023	7.2	6.8	0.857
33	4/22/60	0604	0634	0.005	1.8	5.1	0.160
34	5/11/60	0522	0552	0.309	1.1	18.3	0.351
35	7/19/60	0432	0502	0.044	3.8	9.4	0.623
38	8/12/60	0510	0540	0.389	1.4	15.5	0.378
40	8/31/60	1405	1505	- 0.117	4.1	10.5	0.750
41	9/1/60	1657	1727	- 0.015	6.7	4.6	0.536
42	9/7/60	0344	0444	0.083	2.1	11.2	0.410
43	9/13/60	0522	0552	0.070	1.9	7.1	0.236
44	9/27/60	0457	0557	0.057	2.1	11.7	0.428
45	10/12/60	1248	1317	- 0.076	6.3	12.7	1.399
46	10/18/60	0523	0614	0.086	1.6	9.5	0.266
50	4/11/61	0515	0545	0.051	3.5	8.0	0.490
51	5/1/61	1002	1032	- 0.229	4.8	11.3	0.948
52	5/12/61	0545	0615	- 0.026	4.1	10.0	0.713
53	6/27/61	0550	0611	0.021	3.2	5.7	0.317
54	7/12/61	0307	0337	0.151	2.0	7.0	0.244
55	7/18/61	0356	0426	0.084	2.3	5.4	0.216
56	8/3/61	0545	0615	0.108	0.7	10.6	0.130
57	8/9/61	0359	0429	0.089	2.6	4.4	0.200
60	2/9/61	0949	1019	- 0.010	3.0	7.9	0.414
61	2/28/62	1115	1146	- 0.085	4.2	8.2	0.601
65	7/24/62	2150	2305	0.054	4.1	10.9	0.779
66	7/25/62	2213	2313	0.074	3.0	17.4	0.912
67	7/29/62	2227	2312	0.130	1.6	8.2	0.229
68	7/30/62	2107	2152	0.048	3.9	5.5	0.374
69	7/31/62	2130	2230	0.053	4.5	13.6	1.066
70	8/1/62	2141	2356	0.083	2.6	8.9	0.403

TABLE 1.2

VALUES OF PEAK EXPOSURE, $E_p \times 10^3$, FOR ARCS OF THE HANFORD GRID, AND Q_t

Run Number	Arc Distance, m						
	200	800	1600	3200	12,800	25,600	Q_t, #
5	1067	233.7	79.26	20.38	1.144	0.1495	1728
6	283	19.36	4.206	1.435	0.4599	-	1699
7	1399	214	67	7.629	0.2671	-	1699
8	1123	119.4	36.05	8.610	0.7350	-	1699
9	547.1	90.66	7.189	0.2072	0.07257	-	1215
10	462.5	34.93	10.84	2.593	0.8479	0.1869	1357
13	556.7	41.23	3.747	0.5742	-	-	2360
15	118.6	12.61	1.684	0.1909	-	-	3173
17	1171	90.64	6.198	0.5440	0.2835	-	3146
18	1042	83.62	14.79	1.846	0.7428	0.3305	3631
19	566	51.75	10.71	3.343	0.5315	0.1158	3569
21	1521	140.4	35.19	5.854	0.5523	0.5578	3600
22	1151	102	26.95	7.475	1.047	0.2892	3569
23	1096	105.1	27.15	5.135	0.4557	0.3133	3690
25	935	71.01	19.16	4.376	0.2935	0.09671	3569
26	881.8	110.1	29.73	7.387	0.5854	0.2092	3569
30	230	11.39	1.089	0.2800	-	-	728
31	308.2	16.93	4.448	1.250	-	-	1286
32	280.9	16.84	4.038	0.676	-	-	1084
33	1070	102.2	32.47	14.50	-	-	1042
34	387.2	55.44	-	7.231	-	-	986
35	143.8	11.80	4.508	1.430	-	-	279
38	396	31.10	-	1.772	-	-	471
40	581.3	21.52	4.074	0.732	-	-	1210
41	459.2	40.93	12.390	2.646	-	-	1161
42	397	38.75	11.290	2.967	-	-	643
43	209.2	42.34	-	2.639	-	-	283
44	309.6	27.16	11.03	2.460	-	-	748
45	144.8	8.735	1.754	0.3837	-	-	1240
46	838.2	124.2	31.48	8.682	-	-	972
50	478	53.15	11.390	1.976	-	-	1150
51	341.8	12.29	1.682	0.335	-	-	2015
52	647.8	47.71	10.860	3.413	-	-	2485
53	160.7	16.96	4.017	1.252	-	-	446
54	855.6	104.10	24.150	6.153	-	-	686
55	719.6	80.95	24.550	5.505	-	-	1340
56	1612	291.5	40.30	5.758	-	-	1310
57	1247.01	167.80	50.220	9.114	-	-	1410
60	725.5	67.24	13.350	6.531	-	-	1946
61	589.4	10.17	3.448	1.393	-	-	2518
65	189.3	18.60	4.749	0.895	0.1194	-	740
66	361	33.82	8.589	2.387	0.1863	-	1426
67	303.8	29.94	9.277	2.649	-	-	467
68	237.6	24.08	7.557	1.914	-	-	455
69	305	22.47	6.156	2.104	0.2557	-	1241
70	390.7	39.03	12.760	3.968	0.2068	-	911

TABLE 1.3

OBSERVED VALUES OF σ_y (METERS) FOR ARCS OF THE HANFORD GRID

Run Number	Arc Distance, m					
	200	800	1600	3200	12,800	25,600
5	12	34	64	159	715	1907
6(a)	34	127	202	274	527	-
7	37	146	215	301	618	-
8	15	70	161	244	460	-
9	29	108	-	312	1503	1657
10	18	56	94	166	250	1019
13	29	85	-	226	782	-
15(a)	-	186	-	474	603	1434
17	17	56	-	261	505	862
18	15	61	146	345	380	2100
19	28	98	182	310	594	1600
21	16	44	89	217	413	996
22	17	51	90	145	281	1054
23	17	47	86	171	860	-
25(a)	31	88	136	175	891	1827
26	16	41	70	122	451	1523
30	26	76	-	257	-	-
31	22	81	144	410	-	-
32	25	85	147	240	-	-
33	14	43	64	89	-	-
34(a)	55	201	-	326	-	-
35(a)	26	100	154	186	-	-
36(a)	43	191	-	973	-	-
40	27	84	163	325	-	-
41	16	46	80	151	-	-
42(a)	34	138	285	625	-	-
43	21	71	-	211	-	-
44(a)	46	167	300	518	-	-
45	36	146	268	427	-	-
46	27	80	-	278	-	-
50	24	88	186	460	-	-
51	35	137	187	534	-	-
52	28	75	111	178	-	-
53	17	46	90	160	-	-
54(a)	21	77	144	330	-	-
55	18	61	121	209	-	-
56(a)	36	126	295	742	-	-
57	13	32	54	111	-	-
60	19	58	90	135	-	-
61	25	87	134	503	-	-
65	40	158	314	588	1001	-
66(a)	55	232	453	835	1832	-
67	34	-	268	381	-	-
68	21	65	102	127	-	-
69	41	157	278	446	923	-
70	28	99	171	229	1280	-

(a) Bimodal or multimodal

Travel Time

For this analysis, the diffusion was considered to depend on the time of plume travel. Values of the peak exposures and standard deviations of the observed distributions were plotted against time rather than distance. The travel time concept is not new. Many of the classical studies of atmospheric diffusion have led to models with time as the independent variable. Sutton,[1.4] in his book, reviewed the works of G. I. Taylor and O. F. T. Roberts, which are examples of this approach. These models were derived from Lagrangian considerations. There is thus a problem introduced in defining the travel time for experiments with measurements made in a fixed reference frame. In this study, t was determined simply by dividing the distance at which the sample was obtained by the mean wind speed at the source at the height of release, $x/\bar{u}$.

The dependence of diffusion on stability is more marked when the data are plotted against time than when the data are plotted against distance. Both time and distance relationships have been investigated.

Peak exposure values which have been normalized for the wind speed and source strength stratify well in terms of meteorological parameters by using the time concept. Much of the order is lost when these data are plotted against travel distance making it difficult to evaluate the effects of meteorological variations. The differences that can result from these two approaches are emphasized with an example. Data from three of the runs are plotted against distance in Figure 1.1 and against the calculated travel time in Figure 1.2. Represented on the ordinates is the normalized peak exposure, $E_p\bar{u}/Q_t$ (m^{-2}). Because the most significant difference in the runs is the stability of the atmosphere associated with them, it is essential that this effect be evident in the analysis if useful prediction models are to be derived. The relationships shown in Figure 1.1 do not order with stability. Contrary to accepted fundamentals the exposure data for the very stable run are less at all distances than those for the slightly stable run. Furthermore, at 200 and 3200 m, the stable data lie below those associated with instability.

In contrast, Figure 1.2 shows the same data plotted as a function of the travel time. For any given travel time, the very stable curve yields a higher exposure value than that of the slightly stable curve, which in turn is higher than that of the unstable curve. These data were selected from the sample to demonstrate as dramatically as possible the differences in the time and distance concepts. In most cases, the effects are not so pronounced as shown, but are still evident, and there is no doubt that the stability dependence can best be identified for all of the data when travel time is taken as the independent variable.

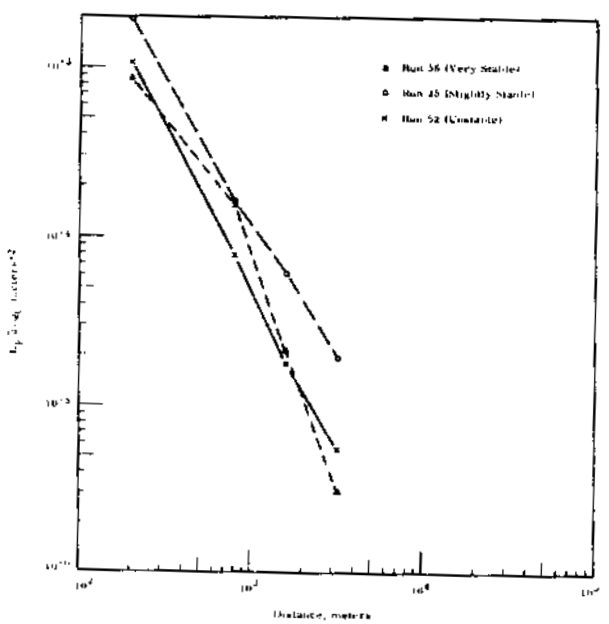

FIGURE 1.1

Normalized Peak Exposure, $E_p\bar{u}/Q_t$, Versus Distance for Three Diffusion Tests with Differing Conditions of Atmospheric Stability

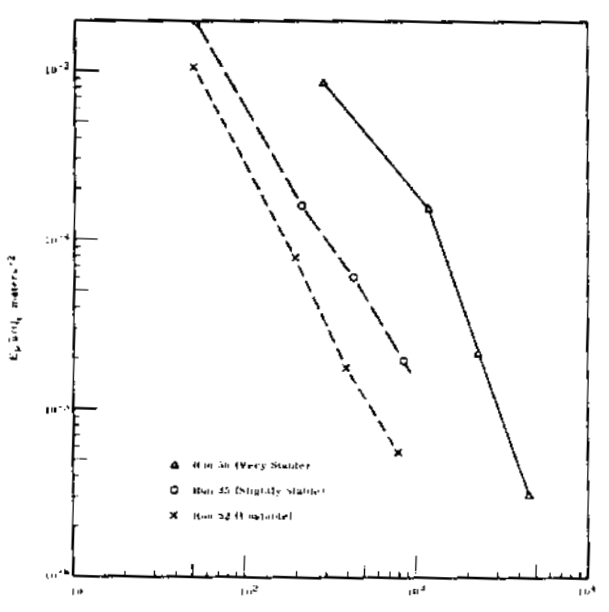

FIGURE 1.2

Normalized Peak Exposure, $E_p\bar{u}/Q_t$, Versus Time for Three Diffusion Tests with Differing Conditions of Atmospheric Stability

Lateral Growth, σ_y

Taylor[1.5] identified the mean turbulent eddy energy as the significant meteorological parameter determining dispersion in the atmosphere. Assuming that the autocorrelation of eddy motions decreased exponentially with time, Taylor showed that the variance of the diffusing matter was expressed as

$$\sigma^2 = At - A\alpha + A\alpha e^{-t/\alpha} . \quad (1)$$

The distribution variance is σ^2, t is the travel time, and A and α are parameters that determine the shape of the autocorrelation function. For lateral growth, the ratio A/α is equivalent to twice the mean eddy energy, $2\overline{v'^2}$. The evaluation of $\overline{v'^2}$ would thus permit the solution of Equation 1. A problem arises, though, in that $\overline{v'^2}$ is a Lagrangian statistic whereas the meteorological measurements were made at fixed locations. It thus was necessary to approximate $\overline{v'^2}$ with the wind data which were available.

The square of the product of mean wind speed and the standard deviation of the wind direction distribution, $(\sigma_\theta \bar{u})^2$, approximates the quantity $\overline{v'^2}$. This can be shown by assuming that the eddy fluctuation at any instant normal to the mean flow is

$$v' = u \tan \theta' . \quad (2)$$

The component of the wind speed in the direction of the mean flow is u, and θ' is the angular deviation of the direction from the mean at any instant. In this reference system, $\bar{v}$ and $\bar{\theta}$ are zero. One can substitute θ' for the $\tan \theta'$ without serious error for deviations from the mean up to 30°.

Replacing u with $\bar{u} + u'$ and squaring the equation produces

$$v'^2 = (\bar{u}^2 + 2\bar{u}u' + u'^2)\theta'^2 . \quad (3)$$

In determining the average value of v'^2 the long term contribution due to $2\bar{u}u'$ is zero because u' can have both positive and negative values. Ignoring u'^2 as being small with respect to $\bar{u}^2$, the average is given approximately by

$$\overline{v'^2} \simeq \bar{u}^2 \overline{\theta'^2} = \bar{u}^2 \sigma_\theta^2 . \quad (4)$$

Equation 3 shows that the parameter of interest for determining σ_y is $\sigma_\theta \bar{u}$, not σ_θ alone. The results obtained in comparing the two parameters using the experimental data leave no doubt that $\sigma_\theta \bar{u}$ is superior to σ_θ as a predictor. In Figure 1.3, the ratio σ_y/σ_θ is plotted against the travel time. Figure 1.4 shows the ratio $\sigma_y/\sigma_\theta \bar{u}$ as a function of the travel time.

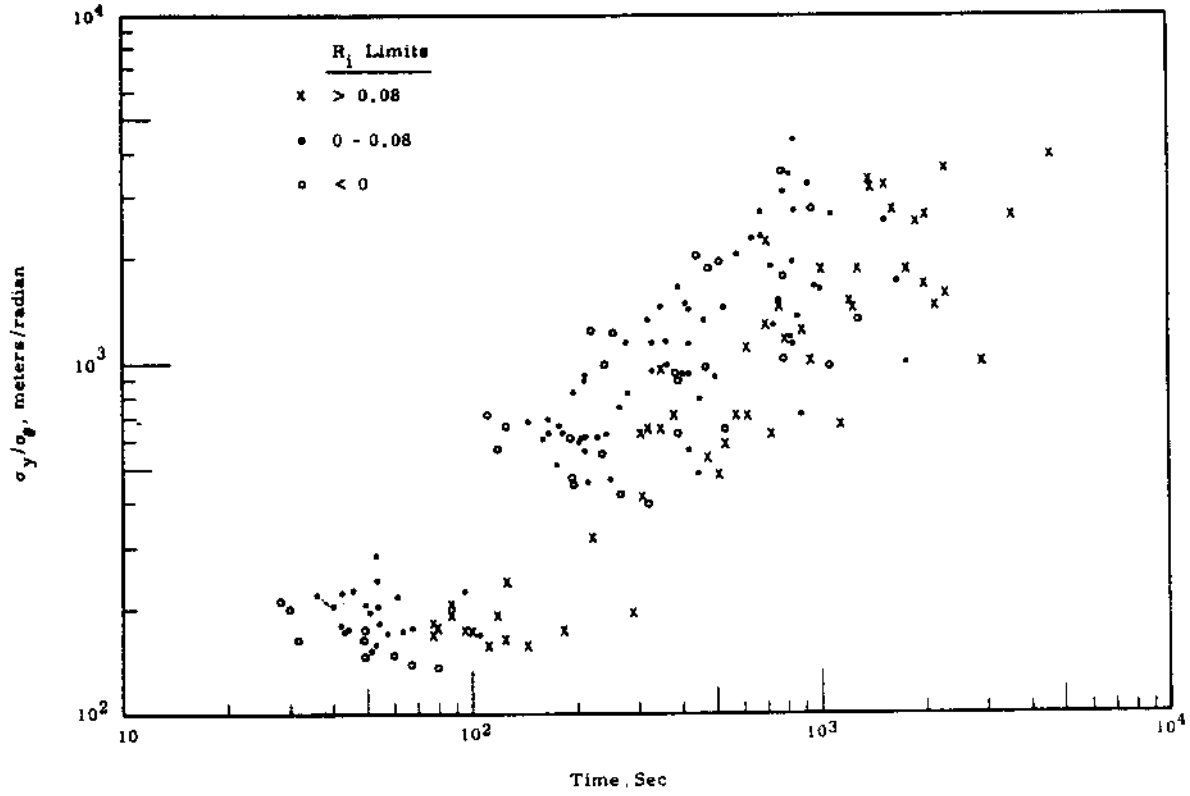

FIGURE 1.3

Ratio of Plume Standard Deviation to Wind Azimuth Standard Deviation, σ_y/σ_θ, Versus Time

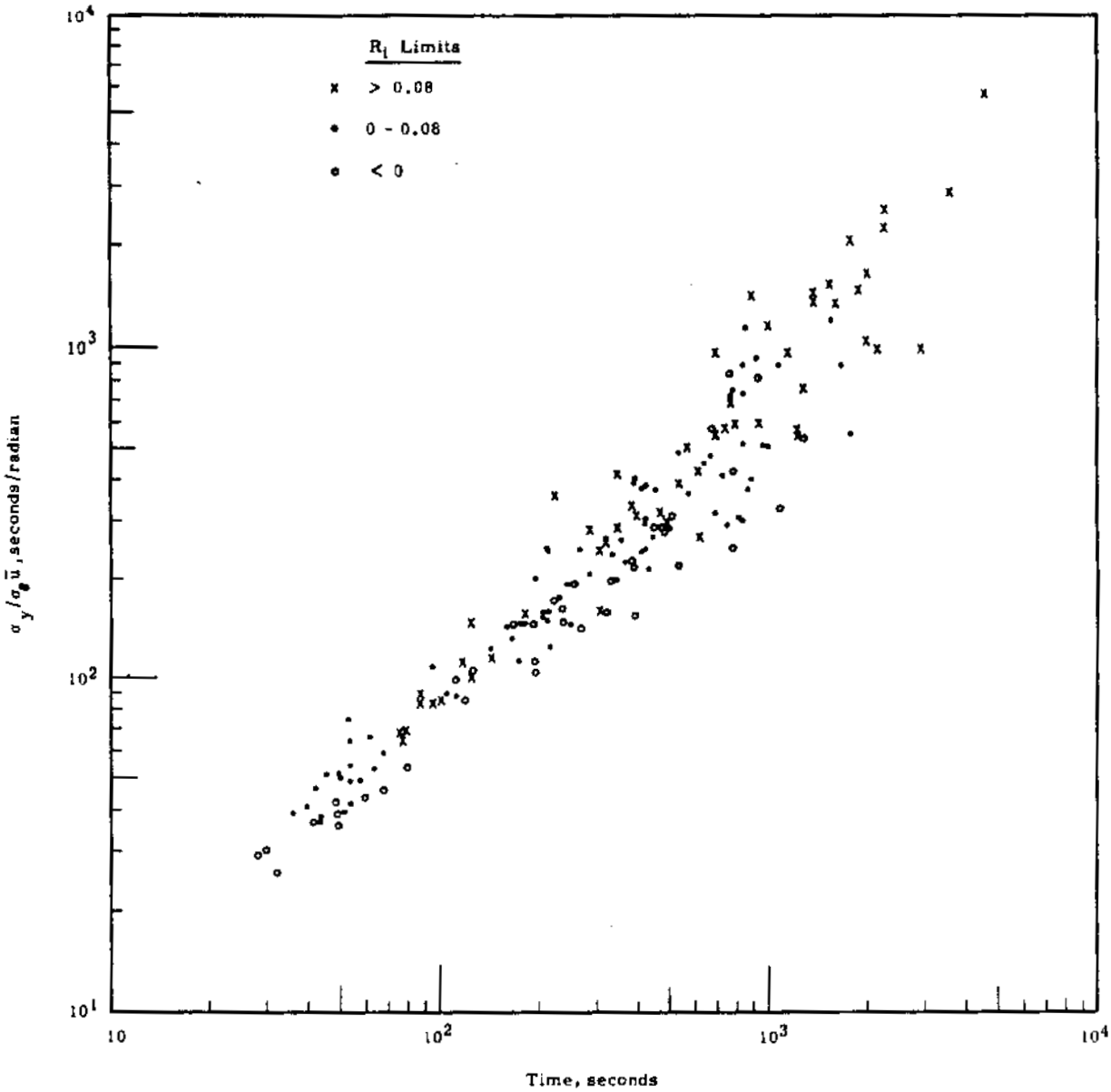

FIGURE 1.4

Ratio of Plume Standard Deviation to the Product Wind Speed Times Wind Azimuth Standard Deviation, $\sigma_y/\sigma_\theta \bar{u}$, Versus Time

The scatter of the data in Figure 1.3 has been significantly reduced in Figure 1.4 by simply accounting for the mean wind speed. The data points are further identified according to the atmospheric stability as

measured by the Richardson's number. The legends are included in the figures. The effect of stability on lateral growth of the plume appears to be small.

That Taylor's model was appropriate for representing the experimental data was initially suggested from the results shown in Figure 1.5. The σ_y data in the plot are from only those runs in which the crosswind exposure distribution was bell-shaped. The runs which are not used are identified in Table 1.3 by (a). The data were subdivided into groups specified by intervals of $\sigma_\theta \bar{u}$ and averaged. The data points in Figure 1.5 are, therefore, the average σ_y values for the interval of $\sigma_\theta \bar{u}$ shown. The lines drawn through the data have a slope near unity at small t and appear to approach a slope of one-half at large values of t. These are the limiting values for Equation (1).

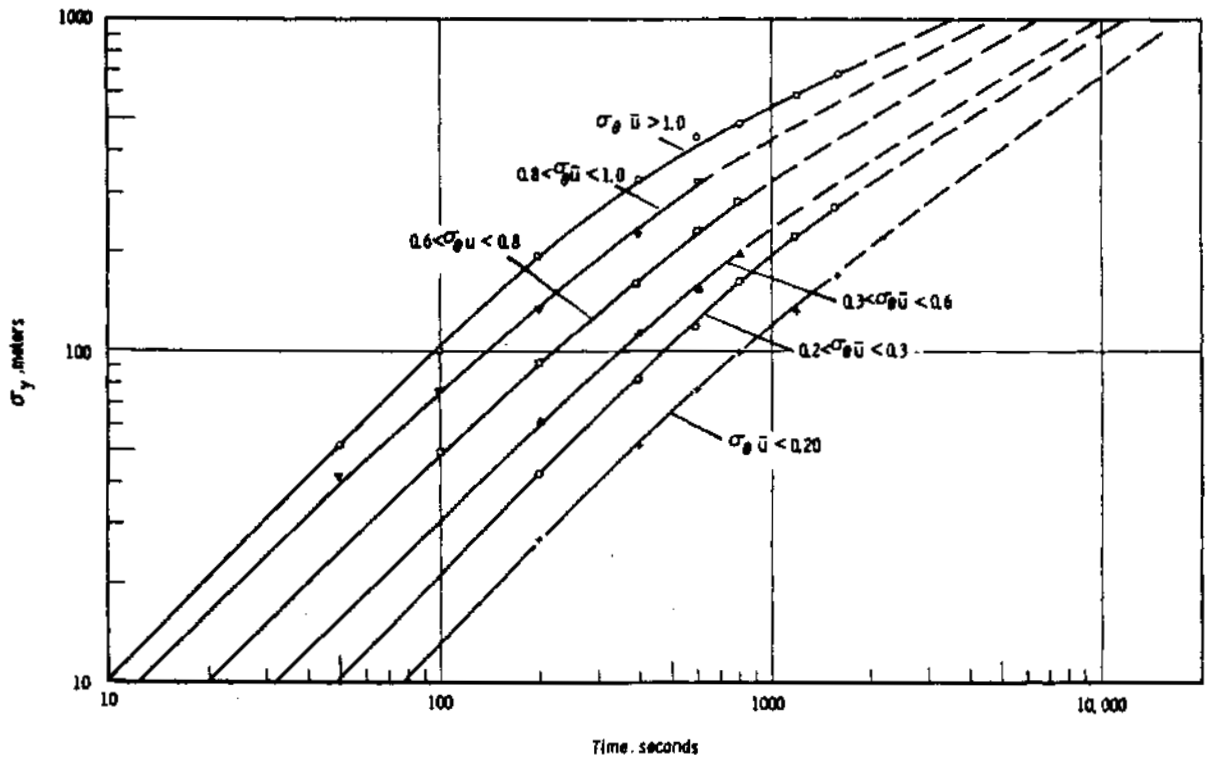

FIGURE 1.5

Standard Deviation of Plume Width
as a Function of Travel Time and Wind Variability

The solution of Equation (1) is shown in Figure 1.6 where the parameters A and α have been determined from the experimental data. A rough estimate of A was readily obtained by solving the equation at large t where the constant and exponential terms are small relative to the first term. The ratio $A/2(\sigma_\theta \bar{u})^2$ was then used to estimate α. From these rough estimates, adjustments were made to obtain a good fit to the test data by trial and error attempts, which resulted in the following relations:

$$A = 13 + 232.5\ \sigma_\theta \bar{u}$$

$$\alpha = \frac{A}{2(\sigma_\theta \bar{u})^2} \quad . \tag{5}$$

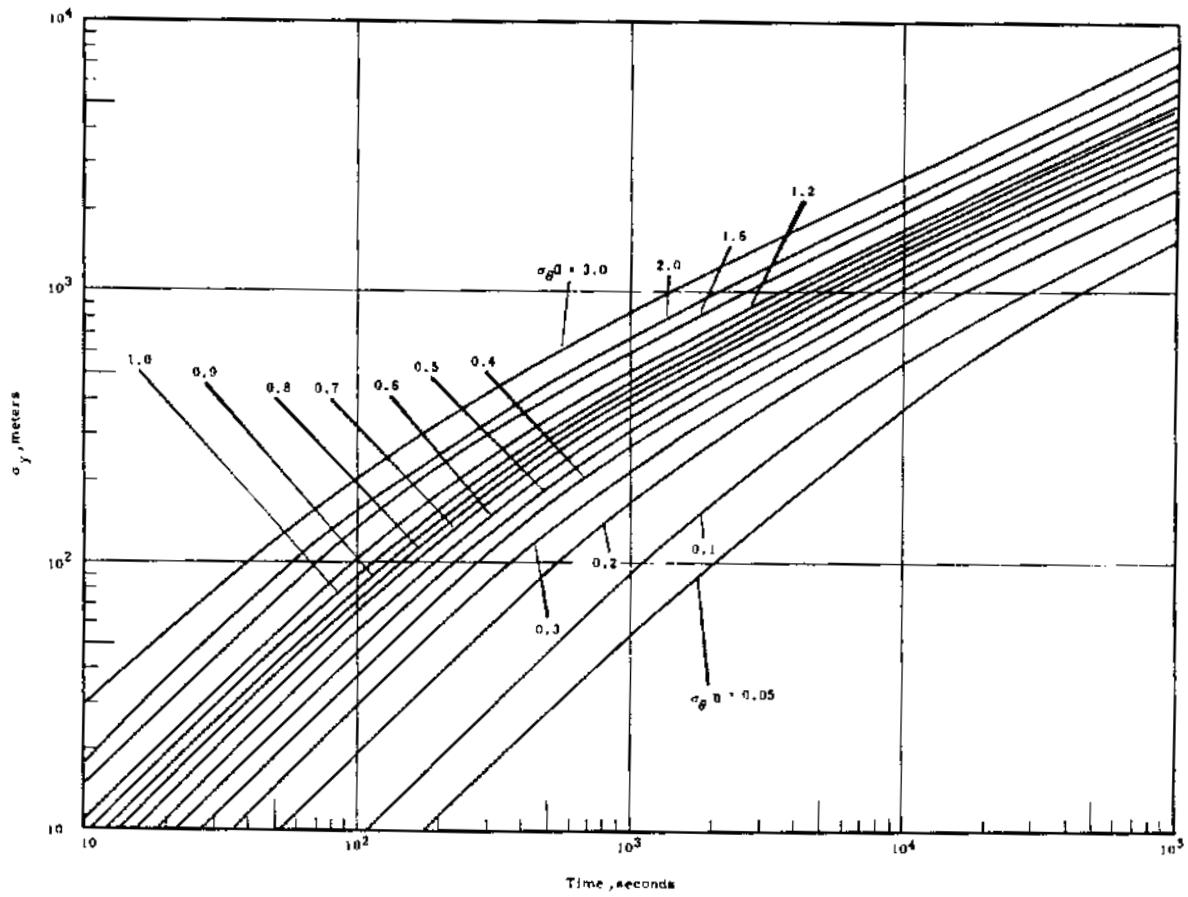

FIGURE 1.6

Standard Deviation of Plume Width
as a Function of Travel Time and Wind Variability

Exposure

The travel time dependence of the peak exposure normalized to the source strength and the wind speed is shown in Figure 1.7. The experimental data have again been divided into groups which have been jointly specified by the Richardson's number, Ri, and the wind variability, $\sigma_\theta \bar{u}$. The solid lines are the average exposures for the groups. The hatched areas define the limits and include all the data from which the averages were derived. The intervals of Ri and $\sigma_\theta \bar{u}$ that apply to these areas are noted.

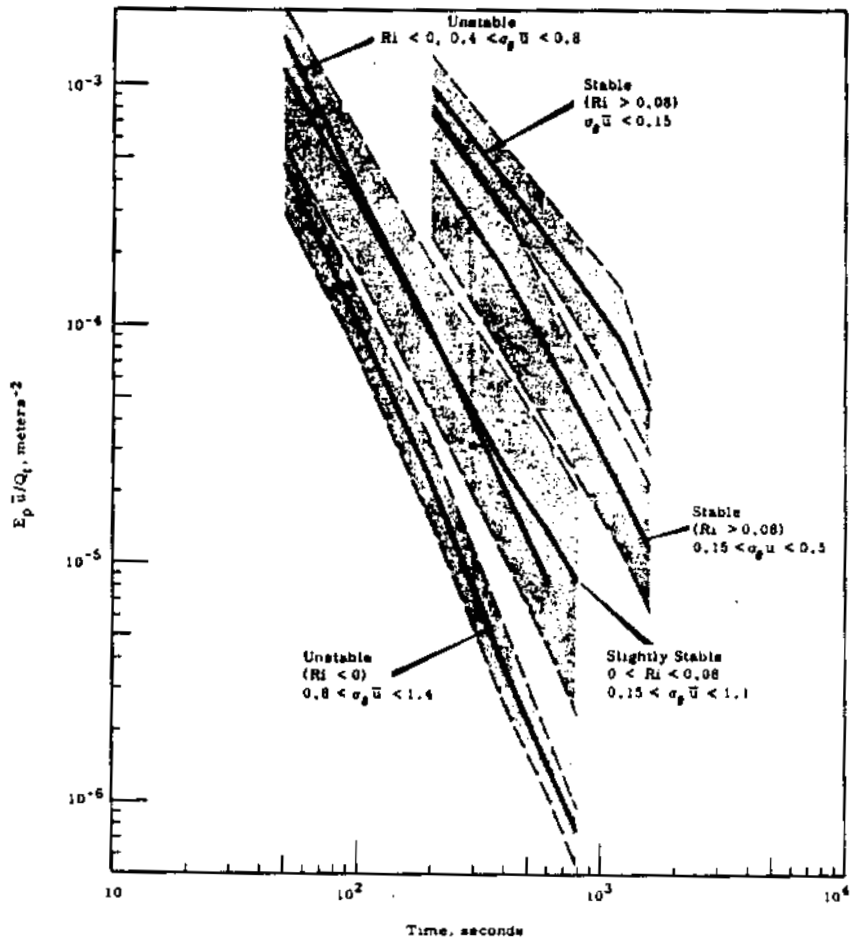

FIGURE 1.7
Normalized Peak Exposure, $E_p \bar{u}/Q_t$, Versus Time

Stratification of exposure data in terms of stability parameters is a common procedure in the analysis of experimental data. Although the identification of the stability effect has led to the development of useful prediction schemes, the range of exposures, which are observed for a given stability category, is still quite large. This range has been reduced by further stratification of the data with the parameter $\sigma_\theta \bar{u}$. Thus, in a given stability category, the wide and narrow plumes have been separated. This effect is evident in the stable curves in Figure 1.7. The averages and limits which are shown were derived from data obtained in very stable atmospheres. The limits would necessarily be much larger if Ri was the only criterion for stratification. This effect is evident also in the unstable curves.

Prediction

The means for predicting exposure distributions have been presented. One can calculate σ_y from Equation (1) or determine it directly from Figures 1.5 or 1.6, if $\sigma_\theta \bar{u}$ is known. The normalized peak exposure is obtained from Figure 1.7 by selecting the curve appropriate for the values of Ri and $\sigma_\theta \bar{u}$, which have been calculated. The exposure distribution for any travel time can be readily calculated with the additional assumption that distribution within the plume is normal.

In applied problems, the assumption that crosswind exposures are normally distributed is often not valid. Trends and shifts in wind direction during the period of emission will result in skewed and multimodal exposure distributions downwind. A simple method for handling these situations has been successfully tested at Hanford.

When trends and shifts in wind direction are observed during the emission period, it is necessary to subdivide that period so that the frequency distribution of the wind directions within each interval is bell-shaped. A long release may thus be considered as two or more successive shorter releases, each apportioned its share of the source strength, Q, and each centered on its mean wind direction, $\bar{\theta}$. Because the intervals are chosen

so that the wind distribution is bell-shaped, there is reasonable assurance that assuming the resulting exposure distribution to be normal is valid. One can calculate $\sigma_\theta \bar{u}$, Ri, and $\bar{\theta}$ for each interval and the exposure distribution for each is determined from the graphs that have been presented. The final result is obtained by summing the individual solutions for the intervals. The composite is the exposure distribution which resulted from the actual release. This distribution may take any shape even though it was formed by summing curves which were normal.

Independent Verification

Figures 1.8, 1.9, and 1.10 show predicted exposure distributions for a stable run which was not used in developing the methods. The exposure is represented on the ordinate. The azimuth is given on the abscissa, the zero value selected to lie near the center of the distribution. The solid line connects the observed data. The dashed line is the predicted distribution that was derived through the summing of nine normal curves. The emission period for this run was 3 1/2 hr, much longer than any of the tests used to derive Fgiures 1.5 or 1.7. Considering these complexities, the predictions of the positions and magnitudes of the major peaks are, indeed, encouraging, even at a distance of 8 mi.

Figure 1.11 compares predicted and observed values of the normalized exposures for 11 runs not included in developing the prediction methods. The comparison was made at 3200 m from the source. Good verification has been obtained even though many of the runs were characterized by complex distributions. The circled datum point represents a planned 40 min run in which a trace quantity of elemental I^{131} was released near the ground. Prediction of the distribution began during the release and was completed shortly after its termination to test the adaptability of the procedures for applied problems.

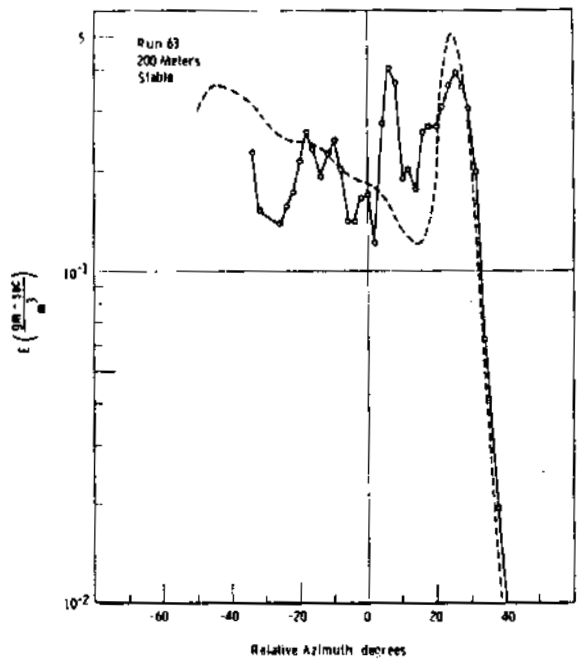

FIGURE 1.8

Comparison of Predicted and Observed Exposures

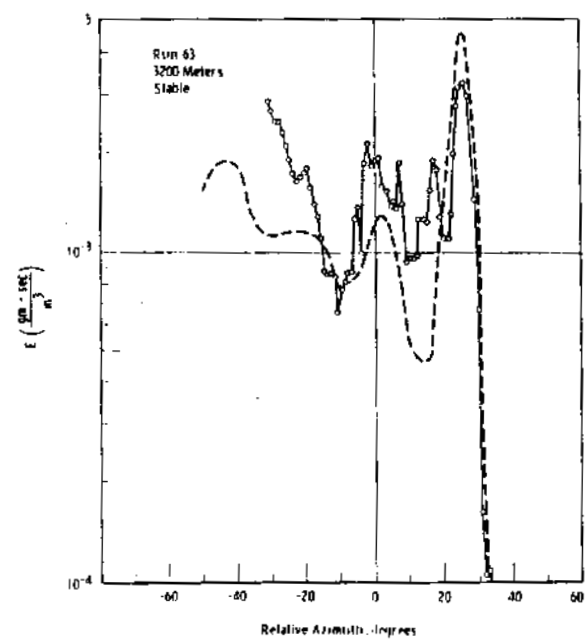

FIGURE 1.9

Comparison of Predicted and Observed Exposures

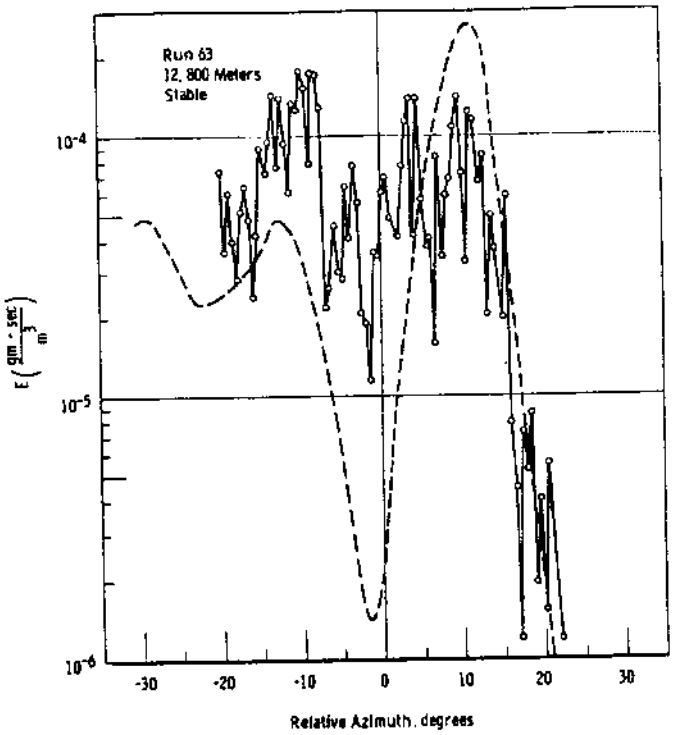

FIGURE 1.10

Comparison of Predicted and Observed Exposures

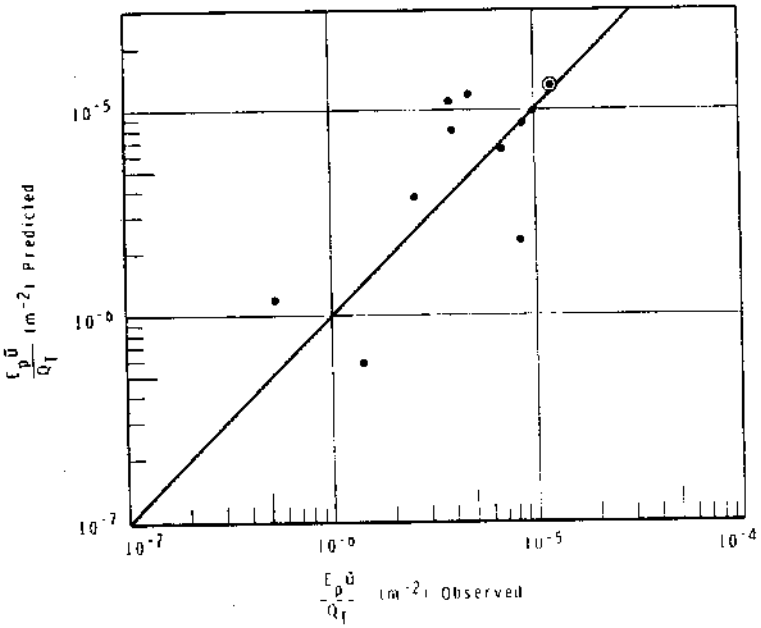

FIGURE 1.11

Comparison of Predicted and Observed Maximum Exposures at a distance of 3200 m for 11 Experiments

Conclusions

The data definitely indicate that the crosswind variance of a plume is not a straightforward power function of time (or distance), but is proportional to the square of the travel time for times on the order of a few hundred seconds and proportional to the first power of time for times on the order of thousands of seconds. In addition, there is every indication that the standard deviation of wind direction, σ_θ, is not a parameter to use for discussion of diffusion results; rather, the product, $\sigma_\theta \bar{u}$, the Eulerian approximation to Lagrangian crosswind turbulent velocity, is to be used. These two results plus the concept of diffusion as a time dependent process, not distance dependent, yield a method for comparatively precise predictions of exposure distributions from sources near the ground.

Comparison of Results of Atmospheric Diffusion Experiments with Calculations from Prediction Models - J. J. Fuquay and C. L. Simpson

Results of 340 diffusion experiments utilizing a ground source and encompassing a wide range of atmospheric stabilities are summarized. Peak exposures normalized for wind speed and source strength when plotted against the travel-time show stratification when stability and growth parameters are factored into the analysis. Differences in the results between sites are greatly reduced when diffusion is considered time dependent from those which result from the distance from source concept. In general, exposure limits for unstable, neutral, moderately stable, and stable meteorological conditions are established, which are compared with the predictions from some of the diffusion models currently being applied. Whereas, the agreement between predicted and observed exposure values are good for diffusion in neutral and unstable atmospheres, there are significant differences noted in the stable case. These differences point to the need to investigate atmosphere mechanisms which have not been factored into the models. Results of the Hanford model, which attempts to account for depletion of the plume through deposition, are presented.

Introduction

In the last 10 yr, there has been a large amount of experimental data obtained from diffusion programs in the United States. The emphasis

has been on studying the environmental contamination resulting from a continuous release of material near the ground. This appears to be as logical a starting point as any since the results of such experimentation serve to satisfy many of the demands of the atomic, chemical, and space industries while at the same time present much fewer difficulties in the experimental design, requiring less equipment and expense than studies with an elevated source.

Major experimental programs which have contributed to the understanding of diffusion resulting from releases near the ground include Prairie Grass (O'Neill, Nebraska, 1956),[1.6] Green Glow (Hanford, Washington, 1959),[1.7] 30 Series (Hanford, Washington, 1960-1963), Ocean Breeze (Cape Kennedy, Florida, 1961-1962)[1.8] Dry Gulch (Vanderberg Air Force Base, California, 1961-1962),[1.8] National Reactor Testing Station Series (Arco, Idaho, 1960-1962)[1.9] and the FRT-2 Series (Dugway, Utah, 1960)[1.10] The total number of experiments has reached 340, all of which either have been documented or are presently being prepared for publication. There is now the opportunity to examine these data as a whole and to gain insight into any differences that there might be between them. In addition, these results can be compared with those obtained from prediction models which are now popularly employed.

A priori, differences might be expected between results at the various sites primarily because of differences in the tracers used, the physical characteristics of the surfaces, and the climatological regimes. The first two considerations bear directly on the depletion of the cloud through deposition of material on the surface which it contacts, causing lower air dosages than would be expected if deposition were not occurring. The complexities of these interactions are not fully understood; and, at the present time, the models that attempt to account for them have not been adequately subjected to tests.

Consolidation of Data from Major U.S. Dispersion Programs

The data from the U.S. diffusion programs which represent a wide range of atmospheric stabilities where ground exposures were measured in some cases to distances of 20 mi from the source deserve further investigation in order that

- Evaluation of general diffusion models can be made or new models developed
- Future experimental programs can be designed to provide definitive data based on inadequacies of past programs.

Table 1.4 summarizes those field programs with respect to tracer material and nature of the terrain which are discussed in this paper.

TABLE 1.4

SUMMARY OF TEST SERIES CHARACTERISTICS

Test Series	Tracer	Terrain	Vegetation	Location
Prairie Grass (PG)	Sulfur Dioxide	Flat	Mowed Grass	O'Neill, Nebraska
Hanford (H)	Zinc Sulfide	Gently Rolling	Sage, 1 meter high	Richland, Washington
Ocean Breeze (OB)	Zinc Sulfide	Flat	Palmetto, 1/2 meter high	Cape Kennedy, Florida
Dry Gulch[a] (B) (DG-B)	Zinc Sulfide	Flat	Brush, 1/2 meter high	Vandenberg, California
Dry Gulch (D) (DG-D)	Zinc Sulfide	Rough Terrain	Brush, 1/2 meter high	Vandenberg, California
Fission Products Release I (FRT-1)	Zinc Sulfide and Fission Products	Gently Rolling	Desert Sage, 3/4 meter high	Arco, Idaho
National Reactor Test Station Series (NRTS)	Fluorescein	Gently Rolling	Desert Sage, 3/4 meter high	Arco, Idaho
Fission Products Release II (FRT-2)	Iodine -131	Flat	Salt Flats	Dugway, Utah

(a) Two grids were used at Vandenberg. The brush was generally sparse, but was characterized by rough terrain. A few trees were located on both the B and D courses.

Figures 1.12, 1.13, and 1.14 summarize the results of these test series averaged in terms of the stability and the horizontal growth of the plume. The normalized peak exposure is plotted on a logarithmic scale (ordinate) having units of meters^{-2} and time of travel in seconds on the abscissa. Identification of the test series is designated by letters corresponding to those given in Table 1.4, and curves associated with stable conditions are given as solid lines; whereas, those conducted when the atmosphere was unstable are dashed. The number of experiments included in each curve is given in parenthesis. The very dark lines on each of the three figures are the Hanford curves characterizing diffusion in very stable and very unstable conditions, and serve here to identify the relative positions of the curves in the separate figures. The Hanford curves have been further delineated to point up the degrees of stability (i.e., very stable to slightly stable , etc.) thus accounting for six curves on Figure 1.12 with the most stable conditions on the right and greatest instability represented by the dashed curve on the extreme left. Delineation of the curves was made on the basis of the stability (Richardson number) and surface wind direction variability ($\sigma_\theta \bar{u}$).

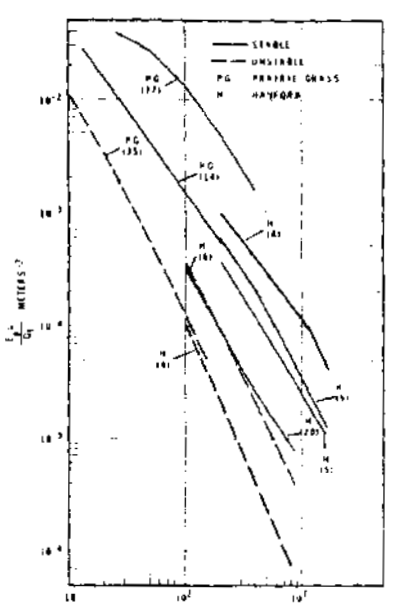

FIGURE 1.12

Variation of Normalized Exposure
with Time for Prairie Grass and Hanford

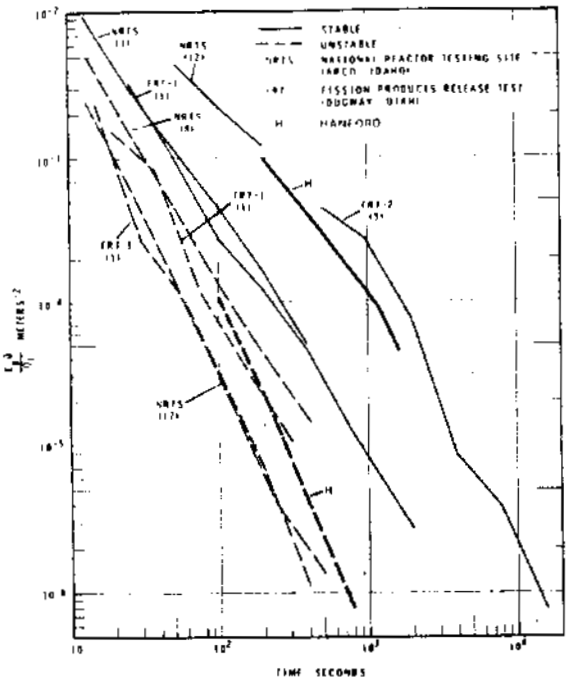

FIGURE 1.13

Variation of Normalized Exposure with Time for NRTS and Dugway, Utah

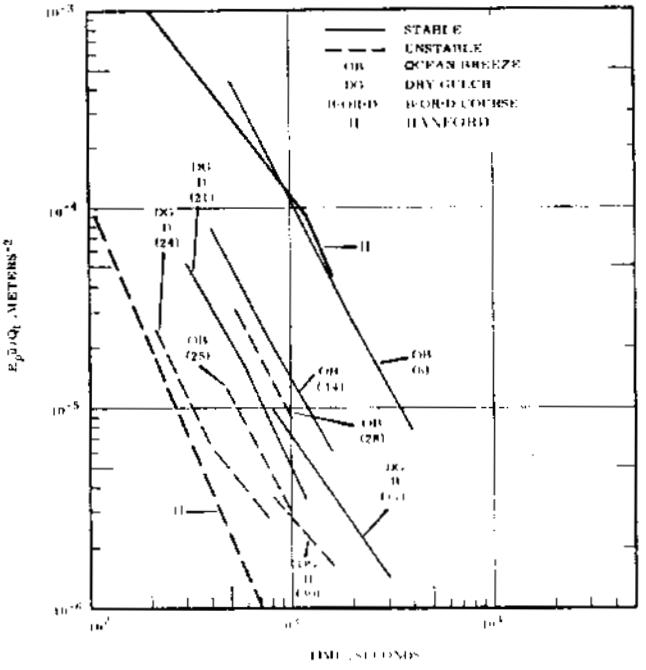

FIGURE 1.14

Variation of Normalized Exposure with Time for Cape Kennedy and Vandenberg Air Force Base

AEC-GE RICHLAND, WASH.

An attempt has been made to treat the data from other sites in the same manner and thus reduce the variance considerably. These curves should be viewed, however, with the knowledge that all the available data were not consistent; that is where Richardson numbers were available at some sites, stability ratios were available at others and, also, the parameter $\sigma_\theta \bar{u}$ was available (at the time of writing) only for the Hanford, NRTS, and Prairie Grass data. Thus the generalizations inferred from the figures should be valid, but modification using a consistent set of data for all series might eventually enhance these results. The data presently available support this premise and independent verification for the NRTS data has been made by Slade.[1.11] Before proceeding with the relative comparisons, two important features inherent here require further amplification.

First, it will be noted that diffusion here is considered to be dependent on the time of travel, and not the distance from the source at which the sample was obtained. The travel time, t, was computed here from the ratio of the distance and the mean wind speed at the release height. This concept is consistent with the basic developments of G. I. Taylor and improves significantly the intersite comparisons. A good example of this point can be made by examining the average very stable curves for Prairie Grass and Hanford. Using the distance-concept, Prairie Grass data indicate an order of magnitude higher exposure than Hanford at 200 m; yet, if the time-dependency is assumed, the difference is reduced to a factor of four with indications that the curves are converging as the travel-time increases.

The second significant feature of this summary, which has been briefly referred to, is that of classifying the curves with respect to the parameter $\sigma_\theta \bar{u}$, as well as some measure of the thermal stability. Here, σ_θ is the standard deviation of the wind directions observed over the period of emission, and $\bar{u}$ is the mean wind speed in that period. This is an Eulerian parameter which is analogous to the Lagrangian quantity $\overline{(v'^2)}^{1/2}$. Fuquay, Simpson, and Hinds,[1.12] using Hanford data, have shown that the horizontal growth, σ_y, is proportional to $(\sigma_\theta \bar{u})t^p$, where p is near unity

for small t and approaches 1/2 for t in the vicinity of 1000 sec - a result analogous to the theoretical development by Taylor. The classification of the Hanford curves presented here with respect to $\sigma_\theta \bar{u}$ is given in this paper.

If diffusion is considered to be time-dependent and if $\sigma_\theta \bar{u}$ as well as a stability parameter is used to classify the data, the exposure differences that are observed between test sites are considerably reduced from those inferred by other analyses. The agreement shown in Figures 1.12, 1.13, and 1.14 is generally good for data from tests obtained under diversified conditions and involving differences in experimental technique. The very stable curves at all sites compare reasonably well as do the unstable, and if a finer resolution of data can be achieved by growth factors such as $(\sigma_\theta \bar{u})$, which is suggested here, the indications are that these empirical results are consistent. This is not to claim that the problems of general diffusion from ground sources have been empirically solved, for this is clearly not the case. Channelled flow, for example, will yield results which deviate greatly from these averaged curves, making it clear that each problem should be analyzed with respect to its peculiarities. The studies at Vandenberg clearly demonstrate this. Diffusion data, however, that are presented here indicate that the differences that might be expected at these sites are on the average not great, giving some hope to developing models which are not severely contradicted by the experimental data presently available.

Comparison of Experimental Data with Prediction Models

Figure 1.15 further summarizes the data into groups that may be referred to as very stable, moderately stable, quasi-neutral, and unstable. The limits of each of these classes correspond to the range of the data from the three preceding figures. The other curves given in Figure 1.15 are the predictions of several of the models which are commonly applied at the present time. Of these, the Sutton diffusion model is best known. Cramer's curve, based on the Prairie Grass data, was one of the first to be developed from ground source experimental data, and is of interest particularly in the

prediction of diffusion in stable atmospheres. Recently, Pasquill has presented a system for prediction based on a summary of experimental data and designed for ready application for those dealing with applied problems. Two of his curves characteristic of stable and unstable conditions are shown. Finally, the Hanford curves are calculated from a model used at Hanford for several years that attempts to account for the depletion of the cloud brought about by deposition on the surface. Obviously, these represent only some of the models presently available. Other models compare reasonably well with these and there is no major difference in the exposure values for short travel-times.

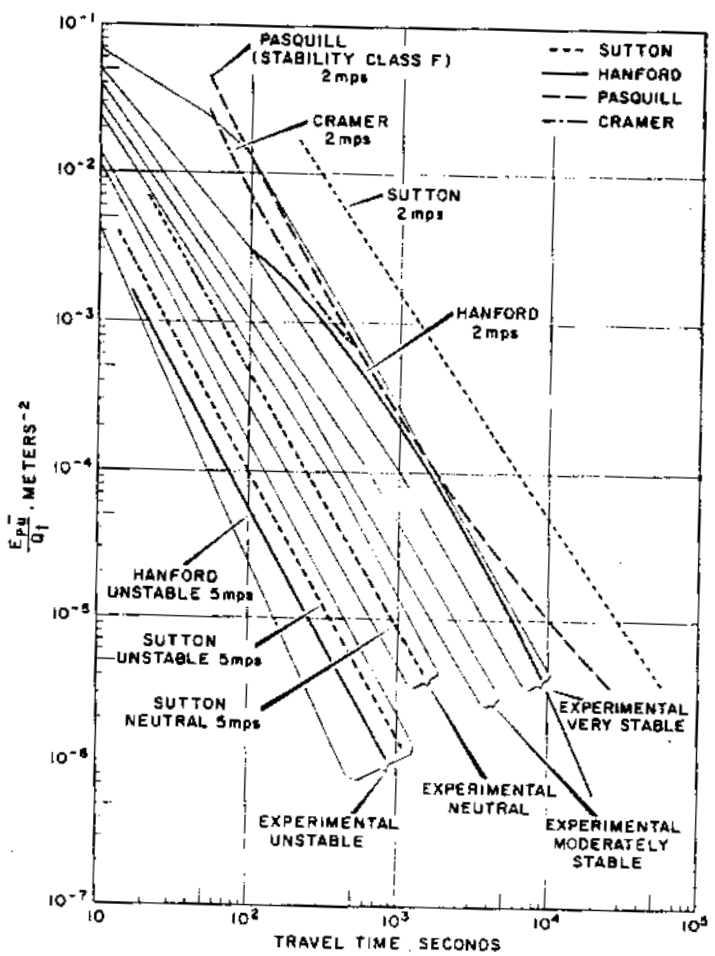

FIGURE 1.15

Comparison of Experimental Exposure Data with Predictions from Several Models

Figure 1.15 shows excellent agreement between the predictions of Sutton and Hanford for ground releases during neutral and unstable atmospheres. This is quite appropriate since the Hanford model for these conditions is Sutton's model with A.C. Chamberlain's modification [1.13] to account for deposition and a Hanford innovation to extend the results to the unstable case.

It is in the prediction of ground source diffusion in stable cases that large differences between the models, the predictions resulting from them, and the experimental data occur.

The models generally yield predictions of exposure higher than those which are observed during stable atmospheric conditions. For any travel-time, there is, at least, an order of magnitude difference between exposures observed and calculated. This differential appears to result primarily from the horizontal growth of the plume, so that the two experimental zones in Figures 1.15 represent narrow plumes (high exposures) and wide plumes (low exposures). Diffusion models yield predictions which more closely approximate the higher values. Better agreement between the observed and predicted values can be obtained by using higher values of the wind speed in the model. For example, the Sutton predictions agree with the stable experimental data when the wind speed at the height of release is 5 m/sec. There is contradiction in such manipulation, however, for the atmosphere is rarely stable when the wind speed is this high near the ground. Wind data for the 2 m height obtained during the Prairie Grass and Hanford tests show that speeds of 2-3 m/sec are expected in moderately stable and very stable atmospheres and speeds in excess of 4 m/sec are quite rare.

Summary and Conclusions

The differences between observed and predicted exposures become very important at travel-times beyond 10^4 sec. This corresponds to distances beyond 10 mi, which is the region in which greater demands for

prediction are being made. Extrapolation of the Cramer, Sutton, and Pasquill curves yield an order of magnitude difference at 10^4 sec; and, because of their relative curvatures, this difference becomes greater as the travel-time increases. It is, therefore, important to exercise care in the extrapolation of any data which points up the need to reevaluate these models that are generally applicable for short travel-times and determine whether extrapolation can be justified in light of the experimental data presently available. The Hanford curve results from a model that attempts to account for deposition. Although the agreement at short travel-times between the Hanford model on the one hand and the Cramer and Pasquill models on the other is good, the differences in curvature bring about great differences beyond 10 mi. From the evidence at hand, the Hanford model appears to predict the exposures at the larger distances reasonably well although exhibiting the same conservative characteristic of all the other models.

Demands are increasing today for predictions to distances 10 to 100 mi from the point of release. To meet such demands, it is attractive to rely on those models which have proved reliable for the short range estimates. However, particularly in the stable case, it appears that the extrapolation may not be justified, and it is suspected that atmospheric mechanisms that are not fully understood must be studied and their effects accounted for. The effect of depletion of the cloud due to deposition is accounted for as if the cloud were depleted at all heights. Yet, deposition is a boundary layer phenomenon, depleting the lower layers of the cloud and, perhaps, not altering the dosage distribution at higher levels. One must appraise the applicability of the dispersion model in relation to the needs of the applied problem to be solved to stay within the bounds of scientific knowledge.

Dispersion from Elevated Sources - C. E. Elderkin, W. T. Hinds, and N. E. Nutley

Surface measurements of the atmospheric diffusion from continuous point source releases at 56.4 m have continued at Hanford with 14 tests performed during 1963. Analyses of eight earlier tests compared well with results anticipated from a bivariate normal model, but consistent deviations from the model are noted.

Experiments were resumed at Hanford to determine the dispersion of airborne tracer material released from an elevated source at 56.4 m. Continuous releases have been made ranging from 15 min to 1 hr during neutral or unstable vertical density gradients with wind speeds ranging from about 4 to 13 m/sec. Air samples at 1.5 m above the surface were taken along 9 arcs at 4° intervals extending over more than 120° of azimuth centered on the meteorology tower. The arc distances were 100, 200, 300, 400, 500, 600, 800, 1200, and 1600 m from the source.

During 1963, the second series of elevated source tests, comprised of 14 releases, was conducted over this diffusion grid, and the data are being reduced for analysis. An analysis of the eight best tests of the first series (1962) provided the anticipated as well as some unexpected results, and a more detailed study of these tests is continuing.

For the eight tests, the standard deviation of the crosswind distribution of the plume, σ_y, as determined from the surface measurements of exposure is shown in Figure 1.16 as a function of distance, x. Except for the three widest plumes, the data agree well with the results obtained from ground source data at Hanford. The average "Green Glow" σ_y power function regression formula reported in 1960 ($\sigma_y = 0.28\ x^{0.86}$), and σ_y results obtained for daytime releases from a ground source during the 30 Series program, both compare well with these results.

Following the lead of Simpson, Fuquay, and Hinds in their analysis and organization of diffusion data as a function of time rather than distance,

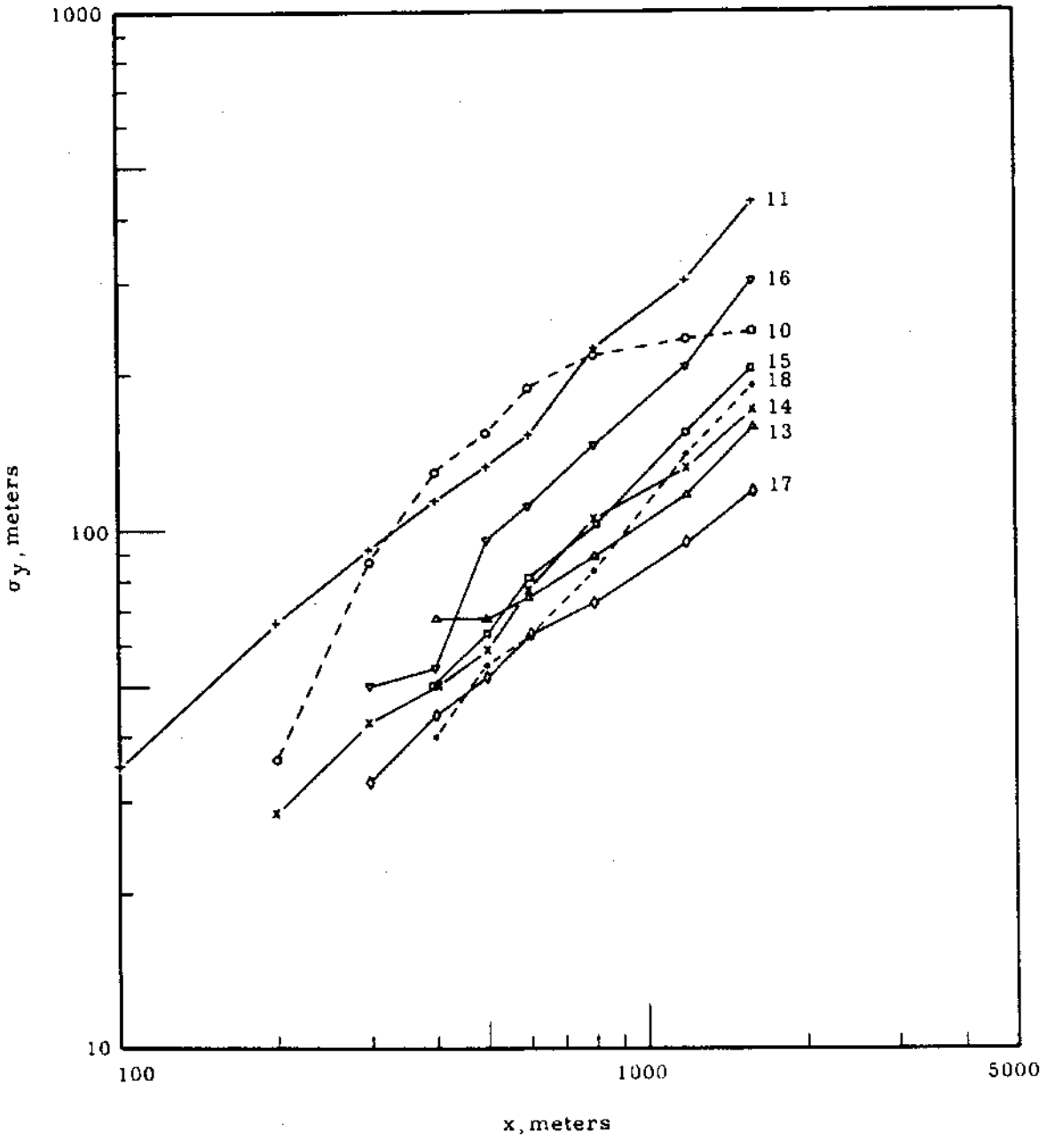

FIGURE 1.16

Standard Deviation of Crosswind Exposure Distributions
Versus Distance for Elevated Source Releases

Figure 1.17 shows σ_y as a function of travel time determined from the source height wind speed. These data show a definite dependence on $\sigma_\theta \bar{u}$, used as an estimate of $\sqrt{\overline{v'^2}}$, where σ_θ is the standard deviation of wind direction fluctuations in radians. They are in excellent agreement with ground source σ_y data similarly analyzed. Values of $\sigma_\theta \bar{u}$ are listed in Table 1.5 along with source height wind speeds and bulk Richardson numbers for each of the eight tests. The σ_y versus time curves demonstrate wider plumes with increasing $\sigma_\theta \bar{u}$ as expected from G. I. Taylor's theory of diffusion by continuous movements.

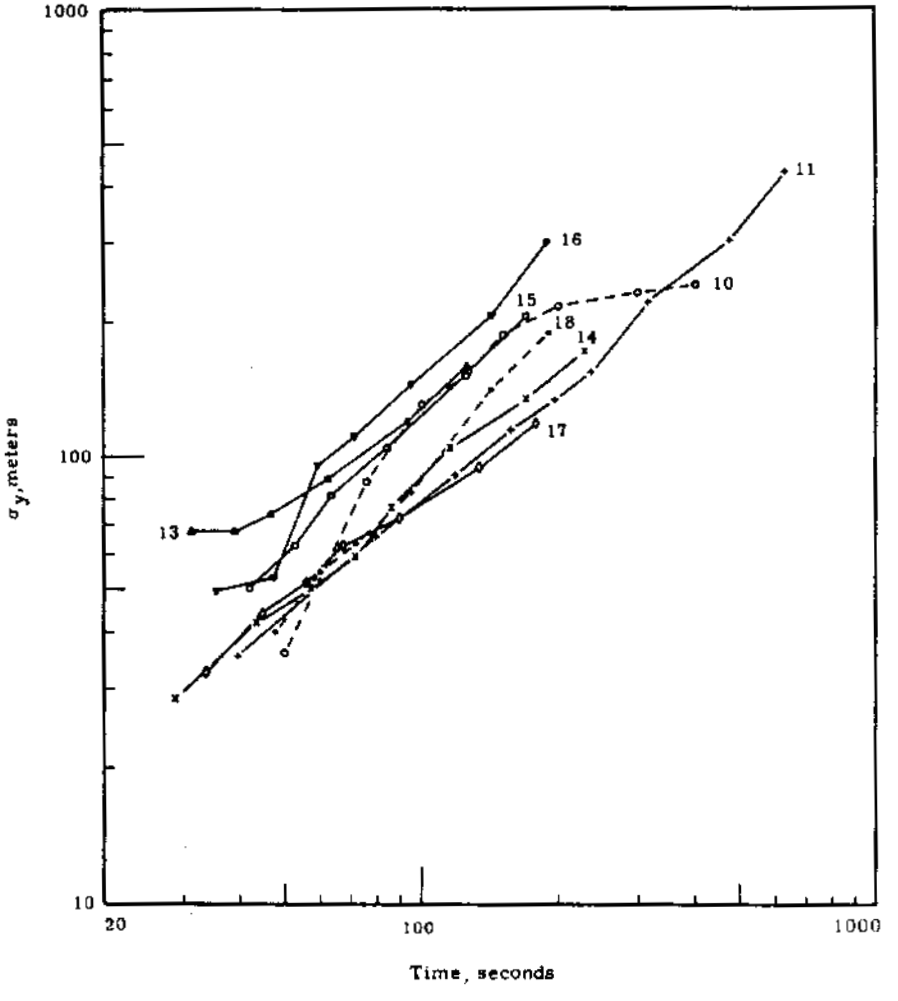

FIGURE 1.17

Standard Deviation of Crosswind Exposure Distributions Versus Travel Time for Elevated Source Releases

TABLE 1.5

METEOROLOGICAL PARAMETERS
FOR EIGHT DISPERSION EXPERIMENTS

Test Number	Ri 250'-50'	$\bar{u}_{200'}$, m/sec	$\sigma_\theta \bar{u}$, radian-m/sec
10	- 0.66	4.0	1.46
11	- 0.78	2.5	0.86
13	- 0.23	13.0	1.40
14	- 0.30	7.0	1.06
15	- 0.04	9.5	1.24
16	- 0.07	8.4	1.48
17	- 0.55	8.9	0.91
18	- 0.38	8.4	1.07

A plot of the normalized peak exposure, $E_p \bar{u}/Q_t$, as a function of time in Figure 1.18 was found to organize the data very well. Beyond the maxima, these curves embrace a narrow range, and the limited data in this region indicated the decrease of exposure with time is proportional to about $(t)^{-2.0}$ to $(t)^{-2.5}$. This decrease with distances is comparable to results from Hanford unstable ground source tests. It is indicated that beyond about 3 min travel time after release, ground source diffusion data might be used to estimate the surface exposure from a 56.4 m release in unstable conditions with reasonable accuracy.

The maximum value of the axial or peak exposure curves in Figure 1.18 is shown to consistently decrease in value as the maximum occurs at longer travel times. This might be expected from the form of the bivariate normal model, which gives at the point of maximum exposure at the surface, $\sigma_z = H/\sqrt{2}$, and estimates for a 56.4 m release, $(E_p \bar{u}/Q_t)_{max} = 7.34 \times 10^{-5} (\sigma_z/\sigma_y)$; where the ratio, (σ_z/σ_y); is assumed constant for all travel times in a given test. Thus the value of $(E_p \bar{u}/Q_t)_{max}$ would be expected to decrease as it occurred at longer travel times when σ_y becomes larger.

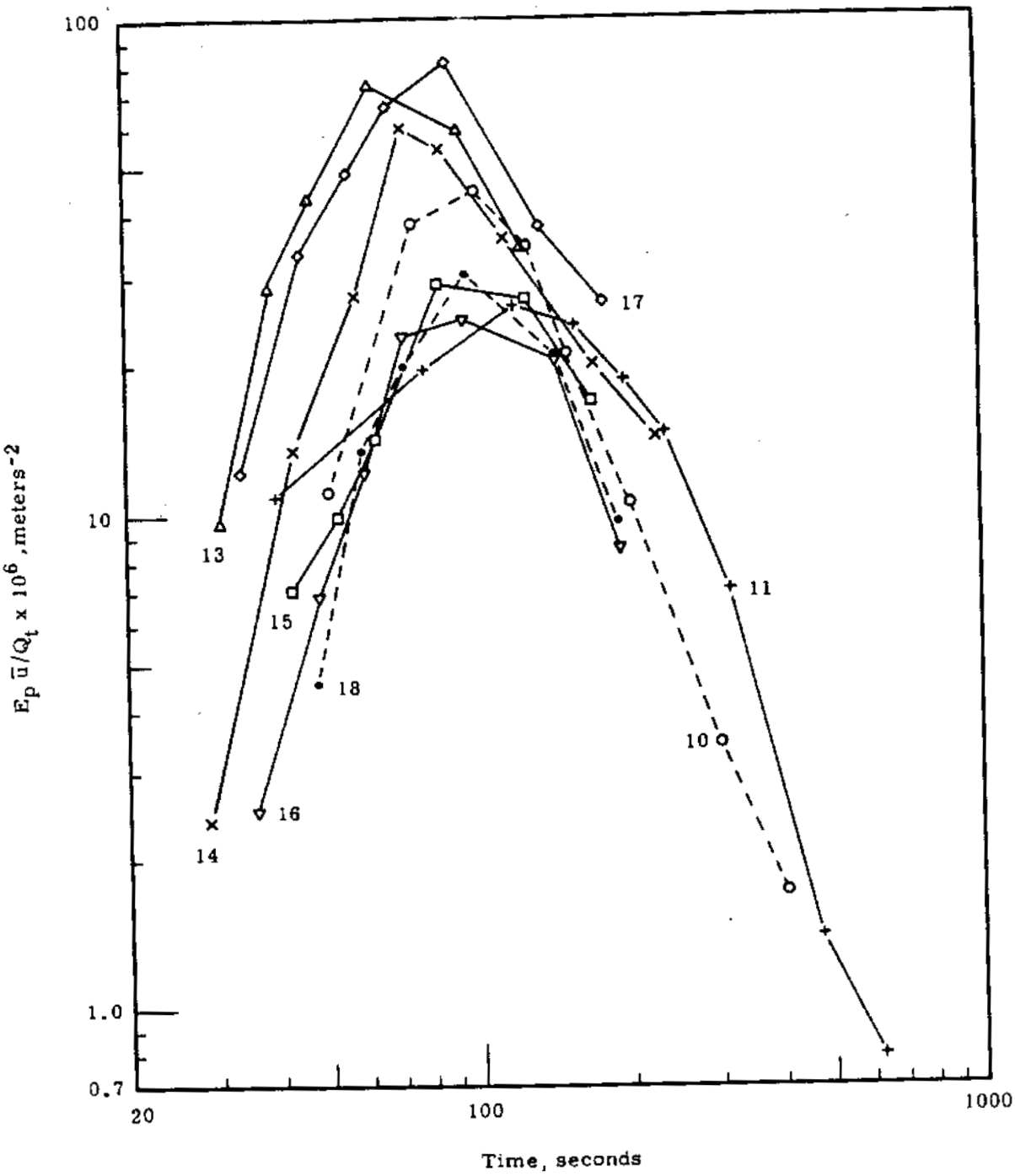

FIGURE 1.18

Normalized Peak Exposure Versus Travel Time
for Elevated Source Releases

The bivariate normal model also predicts at the point on the surface where the crosswind integrated exposure reaches a maximum, $\sigma_z = H$, and the constant value $(CIE\ \bar{u}/Q_t)_{max} = 8.57 \times 10^{-3}$. However, Figure 1.19 shows the experimental maximum values decreasing consistently as the maximum occurs at increasingly longer travel times. It can be seen in Table 1.6 that all experimental values deviate from the bivariate normal value of 8.57×10^{-3} by less than a factor of 2. However, the organized deviations indicated in Figure 1.19 suggest a physical mechanism, rather than statistical variation, as the cause of the deviations. It should be mentioned that normalized crosswind integrated exposures plotted as a function of distance lacked the degree of organization seen in Figure 1.19.

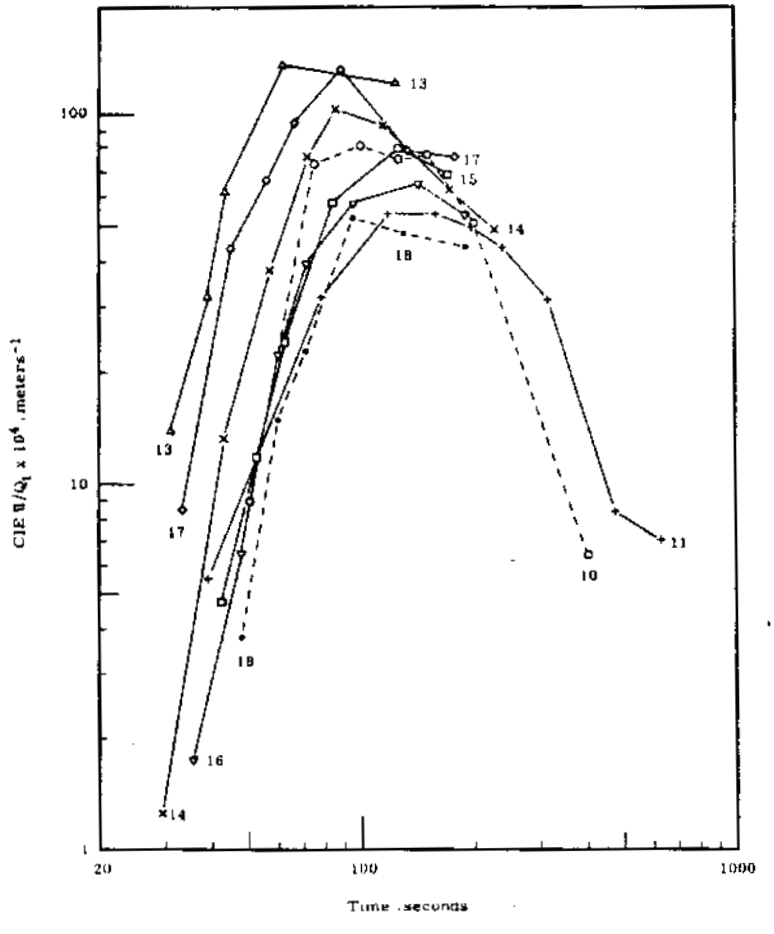

FIGURE 1.19

Normalized Crosswind Integrated Exposure
Versus Travel Time for Elevated Source Releases

TABLE 1.6

COMPARISON OF MEASURED AND COMPUTED EXPOSURE VALUES

Test Number	t_{CIE} Maximum, sec	(CIE $\bar{u}/Q_t$) Maximum, meters^{-1}	(σ_y) CIE Maximum, meters	σ_z/σ_y	Calculated $(E_p\ \bar{u}/Q_t)$ Maximum, meters^{-2}	Measured $(E_p\ \bar{u}/Q_t)$ Maximum, meters^{-2}
10	92	8.5×10^{-3}	115	0.49	3.6×10^{-5}	4.5×10^{-5}
11	130	5.6×10^{-3}	98	0.58	4.2×10^{-5}	2.6×10^{-5}
13	72	15.0×10^{-3}	99	0.57	4.2×10^{-5}	7.4×10^{-5}
14	93	10.5×10^{-3}	83	0.68	5.0×10^{-5}	6.0×10^{-5}
15	110	8.4×10^{-3}	135	0.42	3.1×10^{-5}	2.9×10^{-5}
16	112	6.9×10^{-3}	165	0.34	2.5×10^{-5}	2.5×10^{-5}
17	87	13.5×10^{-3}	72	0.78	5.8×10^{-5}	8.1×10^{-5}
18	112	6.1×10^{-3}	103	0.55	4.0×10^{-5}	3.0×10^{-5}

Using the height of release as an estimate of σ_z at the time when CIE $\bar{u}/Q_t$ reaches a maximum, and taking corresponding values of σ_y from Figure 1.17, the ratio (σ_z/σ_y) was calculated for each test and is listed in Table 1.6. These values were then used in the bivariate normal expression $(E_p\ \bar{u}/Q_t)_{max} = 7.34 \times 10^{-5}\ (\sigma_z/\sigma_y)$ to estimate the normalized peak exposures shown in Table 1.6 along with measured maximum normalized peak exposures. Again, the measured values are within a factor of 2 of the estimates, but the tests that were most widely over- and under-estimated were the same ones that deviated most in the crosswind integrated exposure estimate.

Surface isopleths of exposure were drawn for the tests analyzed thus far. These provide a detailed view of the diffusion pattern at the surface from which more accurate estimates of the diffusion parameters can be obtained. The features of the axial and crosswind distributions of exposure discussed above can be determined more completely with a dense sampling of the isopleth patterns than with the rather widely spaced field measurements used in the first analysis.

Plans for future tests include more dense field sampling. An additional three arcs will be added within the present grid and a limited arc at 3200 m, which has been used in a few tests but has yielded no definitive results, will be extended. A sampler, measuring instantaneous concentrations at a point, has been used in a number of the most recent elevated source tests. Its use has been limited primarily to instrument operational checks, but, in the coming year, it should be fully integrated into the diffusion testing program. Plans are also being formulated for sampling from an aircraft. Such measurements should provide a new dimension in understanding the diffusion from elevated source releases.

Precipitation Scavenging Processes - R. J. Engelmann

Rain scavenging efficiencies measured using zinc sulfide particles are presented. These are compatible with the air flow patterns thought to exist about raindrops. The efficiencies are combined with Hanford raindrop spectra to yield washout coefficients in light rains.

In previous submissions of this report, a method was described for measuring precipitation scavenging efficiencies in the outdoors. Details of the method, and of the current scavenging research and results, may be found in Reference (1.14).

The experimental method, briefly, consists of the release of a fluorescent particulate tracer into the atmosphere, the sampling of its concentration in the air using special filters, and the sampling of its concentration in raindrops that have fallen through the plume. The raindrop samplers are described in References (1.14) and (1.15). The air-sampling system possesses an anisokinetic sampling error which is significant for at least the larger particulates.

Wind tunnel work produced a preliminary evaluation of this anisokinetic error, [1.14] and thereby allowed determinations of scavenging efficiencies. The scavenging efficiency is defined as the proportion of material in the path of a raindrop that is collected and retained. (Since the proportion contacting the drop is called the target efficiency, and the

proportion of these sticking is called the retention or coalescence efficiency, the scavenging efficiency is the product of the two.)

Analysis of the variables involved in the scavenging process produces several dimensionless parameters, which are expected to determine the target efficiency. For small particles, the most important of these is the impaction parameter. Both predicted target efficiencies and measured collected efficiencies are conventionally correlated to this parameter, which is the abscissa in Figure 1.20. The impaction parameter,

$$K = \left(\frac{2}{9\mu}\right)\left(\frac{U}{S}\right)(a^2\rho),$$

is a relationship of the viscosity of the air, the ratio of the raindrop velocity and radius, and the product of the square of the particle radius with the particle density.

In Figure 1.20, as Curves 3 and 5, are given Langmuir's [1.16, 1.17] predictions for potential and viscous flows. These curves represent the theoretical limits of target efficiencies for small particles and uncharged raindrops.

Also entered are the Hanford measurements as Curves 2, 4, and 6. These measurements were made in the outdoors with zinc sulfide particulate tracers.

For comparison, McCully et al's., [1.18] results for zinc sulfide tracers 2330 and 2210 are also given as Curves 1 and 7. McCully attributed the difference in these curves to a difference in wettability of the two tracers. These data were taken in natural rain, and represent some sort of average, over drop size. McCully's data could be interpreted as showing a rapid increase of efficiency in the vicinity of K = 10. There are very few 10 μ particles in Tracer 2210, and error is more likely in this region.

Because each drop size has a single value of terminal velocity, and the air viscosity is relatively constant, it is possible to plot the efficiency

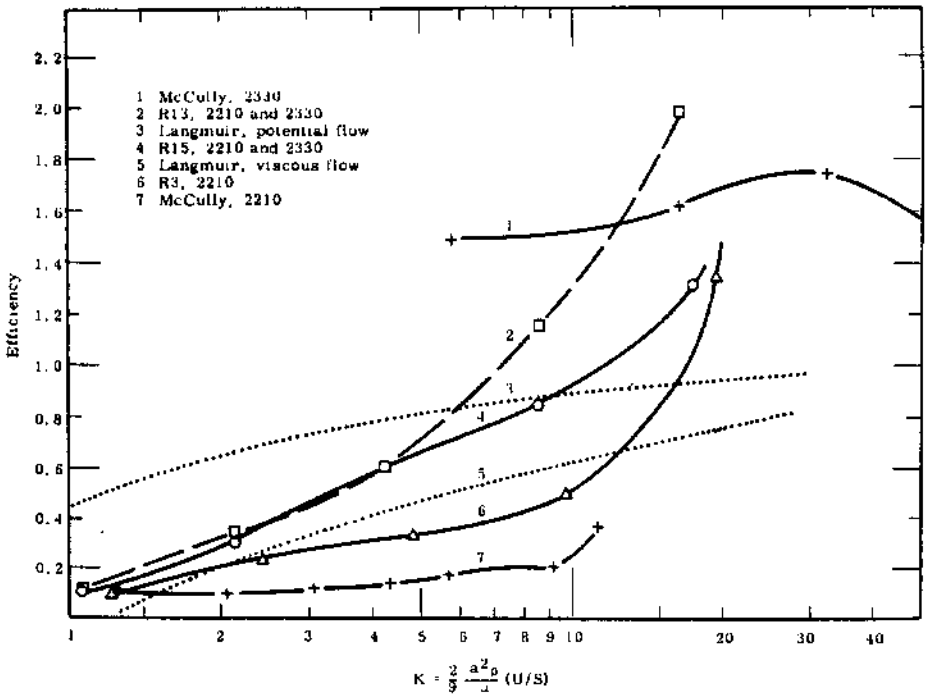

FIGURE 1.20

Scavenging Efficiencies for Zinc Sulfide Versus K

as a function of the parameter, $a^2\rho$, as is done in Figure 1.21. Each of the efficiency versus drop diameter curves is labelled with a value of $a^2\rho$ in units of microns squared, grams per cubic centimeter.

The efficiencies for drop sizes of 0.99 and 1.56 mm were directly measured in two field tests. Efficiencies for other drop sizes were determined by comparison of the collections of different sized drops from several other tests.

The laboratory measurements of Kinzer and Cobb [1.19] are shown as the dashed, peaked curve in Figure 1.21. Their experiments were conducted with water droplets of 13 μ diameter, or $a^2\rho = 42$. Langmuir's prediction for $a^2\rho = 42$ appears as a dashed curve for comparison. Also plotted are two measurements by Walton and Woolcock [1.20] with small waterdrops falling through clouds of methylene blue particles, with $a^2\rho = 49$ and 789.

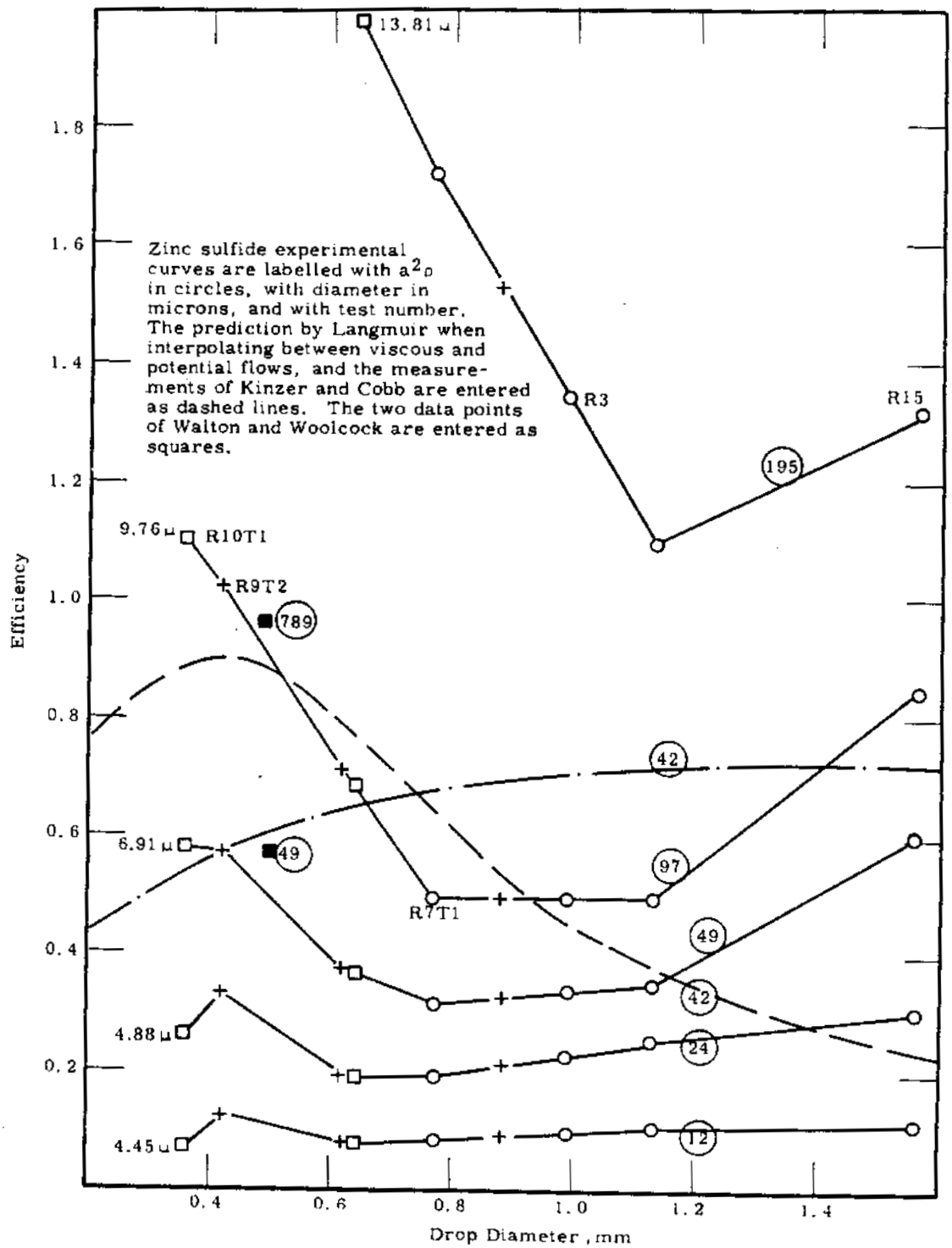

FIGURE 1.21

Scavenging Efficiencies Versus Drop Diameter and $\alpha^2\rho$

AEC-GE RICHLAND, WASH.

The predominant features of the zinc sulfide scavenging efficiencies are

- The higher efficiencies for the 0.4 mm diameter drop
- Efficiencies greater than 1.0 with all drops for particles larger than 13 μ
- A rapid increase in efficiency with particle size in the general region of 10 μ diameter
- A minimum in efficiency for all particle sizes with drop sizes of about 0.8 mm diameter.

The author proposes that these features can be adequately explained with the classical inertial impaction of particles on the leading side of the drops, in addition to wake effects and electrostatic and gravitational forces, as follows.

The flow about a sphere at very small Reynold's numbers has only a thin boundary layer, and closes on the downstream side to be effectively without a wake.[1.21] As the Reynold's number increases, however, the boundary layer thickens, and a ring vortex forms in the wake. With further increases in the Reynold's number, the vortex gains in size and speed. Eventually, vorticity is being introduced to the wake more rapidly than it can diffuse, and the vortex breaks off from the obstacle and is carried off downstream.

Those particles which nearly reach the raindrop as it passes gain another opportunity for contact when fluid convergence and electrical attraction carry them into this wake vortex. For the smaller raindrops, this vortex remains attached to the drop as it falls, and provides a large time interval for collection of the particles on the trailing or upper side of the drop. For larger drops, the vortex may be shed before the particles can impact on the trailing side, and the particles have less chance of collection. While the ring vortex is attached, particles therein fall with respect to the drop, and are attracted toward the drop by electrostatic forces. The collection of the heavier and larger particles is favored.

The number of particles subjected to collection is increased when the raindrop carries an electrical charge, since all particles are then subjected to an attractive force regardless of the fluid flow. Even very weak charges may be effective in drawing into the wake those particles that have narrowly missed the drop.

The 1.5 efficiency observed by McCully may be that efficiency that can be obtained with inertial and wake effects coupled with the weak electrical charges that occur in natural rainfalls.

It is not necessary to invoke differences in tracers to explain these results, since the increase in efficiency toward 1.5 is observed with Tracer 2210, alone, as well as with 2210 and 2330 in combination. Of course, this does not exclude the possibility that the retention efficiency may be less than 1.0, and the target efficiency correspondingly greater than the observed efficiencies.

The wake effect argument has further support in that the data for zinc sulfide agree with that taken with water particles by Kinzer and Cobb, at least in the high efficiency with the 0.4 mm drop. Then, too, a contribution in the wake has been mathematically demonstrated by Pearcey and Hill[1.22] for smaller drops, and actually observed by Telford, et al.,[1.23, 1.24] Rosinski and Nagamoto,[1.25] Magarvey and Geldart,[1.26] and, perhaps, even by Walton and Woolcock.[1.20]

Moller's[1.27] research on larger spheres in water has shown separation or shedding of the wake vortices at a Reynold's number of 450, corresponding to a raindrop diameter of 1.35 mm. There was some elevation of the number by the trough in his experiments. The Reynold's number where shedding occurs from a cylinder is about 75, as inferred from photographs.[1.21, 1.28] This corresponds to a raindrop of 0.5 or 0.6 mm diameter. These diameters do not conflict with the location of the apparent minimum effcicency.

The efficiencies in Figure 1.21 have been used with Hanford raindrop spectra[1.15] to calculate washout coefficients for very light rains. These

are reported below in Table 1.7. The washout coefficient for a particular storm and pollutant is the proportion of the material washed out per unit time.

TABLE 1.7

WASHOUT COEFFICIENTS, Λ,
USING VARIOUS SCAVENGING EFFICIENCIES
IN RAINS OF 0.04 AND 0.55 mm/hr

Efficiency Source	$a^2\rho$, μ^2 g/cm	Λ 0.04 mm/hr, sec^{-1}	Λ 0.55 mm/hr, sec^{-1}
Langmuir	42	1.4×10^{-5}	1.9×10^{-4}
Kinzer and Cobb, Water	42	2.2×10^{-5}	1.8×10^{-4}
Hanford, Zinc Sulfide	49	1.3×10^{-5}	1.2×10^{-4}
Hanford, Zinc Sulfide	97	2.5×10^{-5}	2.0×10^{-4}

The research conducted with zinc sulfide treated only a portion of the scavenging problem. The data come from only a few tests in artificial rain, and it would be well to obtain data in natural rainfalls using additional tracers. There may be significant changes in target efficiencies with small changes in electrical charge, and there may exist differences in retention efficiency dependent upon particle "wettability" or upon drop size. Although greater accuracy and proof of theory may come from laboratory measurement, measurement made in the field in natural rain removes much doubts as to the applicability of the test results to later prediction.

Testing in natural rain requires improvement in plume generation techniques. With improved equipment and experimental designs, dry deposition of tracer on the rain sample can be reduced, and errors introduced by the anisokinetic sampling of the plume in some tests can be reduced or eliminated.

Particularly advantageous would be a portable testing system, which could be taken to sites with rain or snow, and easily oriented with the wind direction.

The scavenging power of snow appears to have been overlooked in the literature, and this may be a serious omission. The measurements of efficiencies for the variety of individual crystals should, perhaps, be preceded by measurements of the bulk washout coefficient, Λ, for various snow classifications and precipitation rates.

Atmospheric Tracer Technology - P. W. Nickola and M. F. Scoggins

The Rankin technique for assay of bulk field samples of airborne fluorescent tracer continued to yield good results. Recent recounts were in good agreement with counts made in 1959. The possibility of replacing water with trichloroethane as the carrier for particulate tracers during generation is promising. Larger tracer emission rates would be possible. Tests disclose that the effects of extreme heat and of solar radiation on Fluorescent Tracer 2210 were negligible. Field models of the zinc sulfide real time sampler disclose an improvement of approximately four in sensitivity over the prototype model. Results from two field experiments involving tracers other than the standard 2210 are presented.

Assay and Control of Routine Field Samples

This was the fifth consecutive year in which the "Rankin Counter" provided a simple, reliable and accurate assaying procedure for thousands of bulk field samples of the fluorescent airborne tracer used by Hanford's Atmospheric Physics Operation. This automated assaying device permits the examination of more than 300 samples per man day.

Periodic checks of the stability of this counter continue. Recently, 20 filters which had been counted in routine fashion in 1959 were recounted. The mean value of the 20 recounts was 100.6% of the 1959 count. Of the 20 filters recounted, 10 were within the standard deviation computed in 1959 for recounts of the same filter.

Generation Technique

Most users of the fluorescent particulate tracer technique have claimed success in their efforts to disperse the powders in dry form. However,

Hanford experienced considerable difficulty in generating an agglomerate-free tracer at a consistent generation rate by the "standard" dry generating techniques. As a consequence, the Hanford technique has employed a wet generating procedure since the 1953 startup.

Briefly, the generating technique which solved the dry powder problems entails the suspension of the fluorescent particles in a large container of water, and subsequent regulated dispersal of the atomized particle-tracer slurry by means of a conventional insecticide spraying apparatus.

It is assumed that these tiny water droplets evaporate to leave individual tracer particles suspended in the atmosphere. To assist in this evaporation, hot gases from a combustion chamber are mixed with the water droplets at release.

However, to some degree, there will be inadequate evaporation in the cases of • high relative humidity of the air, • release of larger water droplets, and • high release rates of water.[1.14] The seriousness of this problem is difficult to determine and will depend upon the type of field test conducted. To provide more versatility and range of safe operation, slurries other than with water are considered. The solvent, trichloroethane 1-1-1, has the desirable characteristics of high density and vapor pressure which are required for good evaporation and high release rates. Yet it is nonflammable and does not appear to affect tracer fluorescence. Computations and tests show that it can be safely used in field programs. Tests are continuing.

The hot gases into which the atomized generation slurry is injected at the instant of generation reach about 300 F. Although no conjecture on the possible effect of the heat on the fluorescent properties of the pigment has been raised in print, investigators have verbally questioned the technique. As a consequence, a test was derived to evaluate the heating effect.

Six stainless steel discs were fabricated. These discs had dimensions such that when inserted in the Rankin counter, a face of the disc was in the

routine counting position. Several drops of a dilute water suspension of Tracer 2210 were placed on five of the six discs and allowed to dry at room temperature. The sixth disc was retained as a blank. Each disc was counted five times in the Rankin counter to determine its expected count rate. The discs were then strongly heated in a laboratory oven and recounted, as is outlined in Table 1.8. The sixth disc was heated exactly as discs A, B, C, and D, but the count rate remained at the background rate of 0 to 5 counts/min.

For ease in comparison, the postheating counts in Table 1.8 have been normalized with the preheating count rate being considered 100%. Each percentage in the table is the result of several Rankin counts.

The results can be considered as two separate tests. In the first test procedure, heating of Discs A through D to 500 F for 4 min gave no deleterious effect (98.7% of preheat count rate compared to 96.6% for the unheated control). Subsequent heatings to 1100 F and 1800 F did reduce the Rankin count by about 20%. However, these temperatures and durations were significantly greater than those to which the tracer would be exposed in routine generation.

The second test involved Disc E, the previous control, which was heated to about 1800 F for approximately 20 sec. The heating resulted in no decrease from the previous control counts. This, again, was a much more severe treatment than would be experienced in routine field procedure.

The results of thes tests would strongly indicate that no loss of mass due to tracer heating during generation would be indicated by the Rankin counting method.

Effect of Solar Radiation on Fluorescent Tracer

Although the generation and assay procedures used in the Hanford fluorescent tracer technique are unique, the use of various fluorescent particulates in investigations of atmospheric motions is not. Some doubt has been cast on the use of such techniques by Eggleton and Thompson[1.29] and others. One of the chief criticisms has been that the particles are likely

to lose considerable fluorescence as they are exposed to solar radiation during their airborne flight. An experiment was designed to test this hypothesis for Tracer 2210 and the Rankin fluorescent particle counter.

Filters were selected from a field run in which the tracer generation, field sampling, and filter pickup all occurred during hours of darkness. The filters were stored inside an opaque box until they were assayed on the Rankin counter. Subsequently, the filters were exposed to bright sunlight and recounted several times. Table 1.9 indicates the solar exposure times and the change in counts after two extended periods of bright solar radiation. For ease in comparison, the postradiation counts have been normalized with the preradiation count rate considered as 100%. Each percentage is the result of three Rankin counts.

TABLE 1.8

EFFECT OF EXTREME HEAT ON TRACER 2210 IN THE RANKIN COUNTER

	Disc A	Disc B	Disc C	Disc D	Mean Discs A-D	Disc E
Preheat Count Rates, counts/min	8079	6846	3911	17,256		20,591
(Normalized to %)	100.0%	100.0%	100.0%	100.0%	100.0%	100.0%
Discs A, B, C and D heated to 500 F for approximately 4 min. Disc E not heated.						
Recounts	99.7%	96.5%	100.7%	97.9%	98.7%	96.6% (Control)
Discs A, B, C and D heated to 1100 F for approximately 4 min. Disc E not heated.						
Recounts	75.4%	72.4%	88.9%	81.1%	79.4%	95.4% (Control)
Discs A, B, C and D heated to 1800 F for approximately 10 sec. Disc E heated (for first time) to 1800 F for approximately 20 sec.						
Recounts	72.6%	70.6%	90.6%	81.8%	80.2%	95.7%

TABLE 1.9

EFFECT OF SOLAR RADIATION ON TRACER 2210 IN THE RANKIN COUNTER

	Filter 1	Filter 2	Filter 3	Filter 4	Filter 5
Preradiation Count Rates, counts/min	6658	16,065	35,542	35,083	79,308
(Normalized to %)	100.0%	100.0%	100.0%	100.0%	100.0%
Filters exposed to bright sunlight for 4.1 hr					
First Recount	103.4%	102.7%	105.8%	103.8%	100.0%
Filters stored in opaque boxes for 11 days					
Second Recount	99.5%	99.7%	103.3%	101.8%	100.8%
Filters exposed to bright sunlight for 3.1 hr					
Third Recount	101.6%	100.7%	103.7%	103.0%	100.6%

On the basis of this evidence, one may conclude that the Rankin counting technique does not indicate less tracer after exposure of the filters to sunlight. There is even a suggestion that a slightly greater mass is indicated by the recount of filters shortly after exposure to sunlight. But the mixture of positive and negative changes after filters were stored implies that the filters eventually return to their presunlight counts. With the knowledge that the Rankin counting system is considered under control when the drift about a standard counting rate is 3%, then the preceding conjectures can best be replaced by the statement that the effect of sunlight on the count rate of Tracer 2210 is negligible. Since the calibration of the Rankin counter is nearly linear when relating mass to count rate, the same statement can be made for indicated mass.

Real Time Sampler

The prototype of a device capable of monitoring concentration of fluorescent pigment on a real time scale has been reported.[1.30] Three field models of this sampler were fabricated in 1963. Although the process of calibration on these devices was still underway at year's end, it appears that the detection limit of the field model is approximately 4×10^{-7} g/m^3—a concentration 1/5 of that estimated possible with the prototype model.

Although not enough data have been amassed from use of these samplers to report in the form of a study, they have been operated successfully during five field diffusion experiments. Table 1.10 presents the percent of time the ratio of "instantaneous" concentration (C) to the mean concentration ($\overline{C}$) equalled or exceeded a given value during a field release of tracer from an elevation of 200 ft. The data were collected at two distances (600 and 1600 m) from the source, and near the maximum $\overline{C}$ for each distance. The data are presented as an example of the type of information that can be generated with the aid of these devices. A minimum of data specifying the real time history of concentration resulting from a continuously emitting source are presently available in the annals of diffusion meteorology.

TABLE 1.10

PERCENT OF TIME $C/\bar{C}$ EQUALS OR EXCEEDS THE INDICATED RATIO

Ratio	Percent of Time	
	600 m	1600 m
0	100.0	100.0
1	15.8	22.0
2	10.9	14.2
3	8.2	10.4
5	5.2	6.3
10	2.1	2.1
20	0.14	0.32
30	0.039	0.053
34.6	0 (Peak C)	0.041
40	0	0.022
50	0	0.006
58.5	0	0 (Peak)

Multitracer Technique

Progress toward field capability with a dual atmospheric tracer system was minimal in 1963. The emphasis of effort in the other problem areas, the uncovering of new problems on the way to complete field capability with a dual system, and the plain fact that development and demonstration of such a system is a formidable task, all contributed to the slow pace.

Primary effort in new tracer development during 1963 was devoted to investigation of the differentiation of two fluorescent pigments in the conventional Rankin counter. Differentiation was attempted by pulse height. Problems in sensitivity arose due to variation in pulse height from a given pigment from run to run. To a smaller degree, pulse height seems to depend on flow rate through the sampling filter and/or distance from the tracer source. Success of this type of multitracer technique depends to a considerable extent on being able to relate

these pulse height variations to a measurable parameter and thus predict them. This work is continuing.

Despite the obvious limitations of the technique, an experiment was carried out in which two fluorescent tracers (2210 and 2267) were emitted at different times for separate field collection. Tracer 2267 was emitted from a ground level source; the 2210 was emitted from a source at an elevation of 200 ft. By assaying the filters separately on the Rankin counter, the true areal distribution of each tracer could be ascertained. The Rankin counts from the individual field runs were then combined and reseparated by the pulse height analysis technique. The results are shown in Figures 1.22 and 1.23. Isopleths were drawn to equal Rankin count rates.

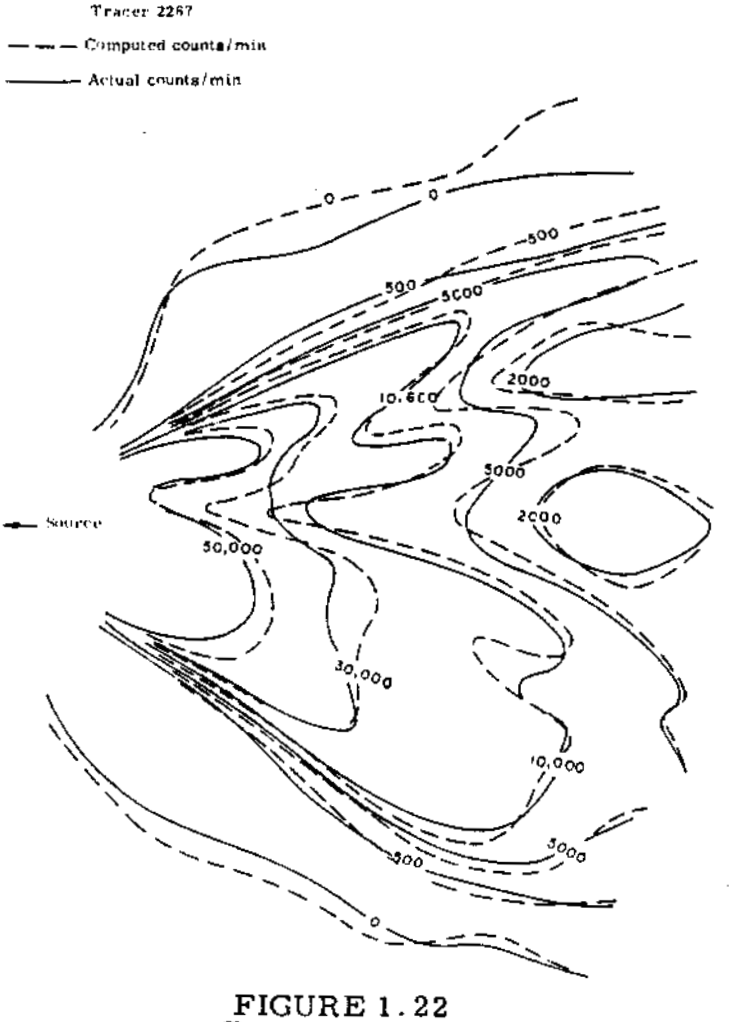

FIGURE 1.22
Computed and Actual Distribution of Tracer 2267

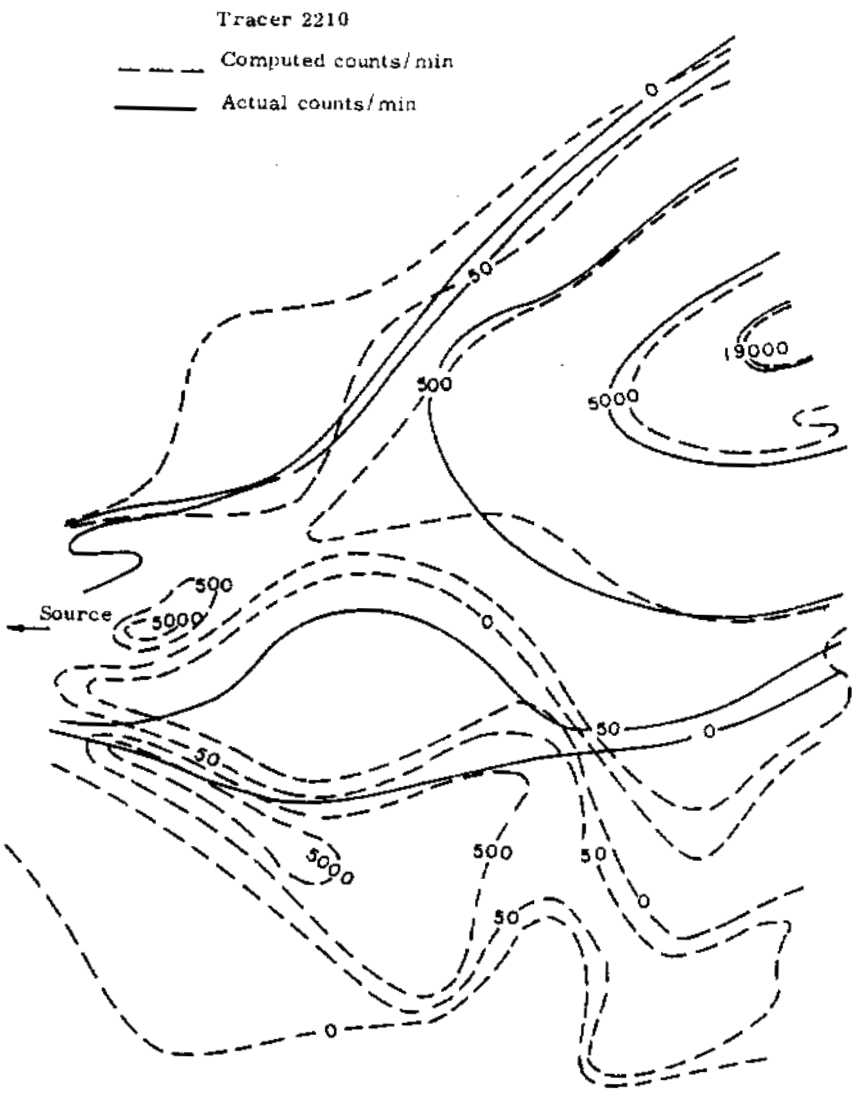

FIGURE 1.23
Computed and Actual Distribution of Tracer 2210

The computed areal distribution for Tracer 2267 is in acceptable agreement with the actual distribution. However, there is much poorer agreement in computed versus actual distribution for Tracer 2210. As could be anticipated, the areas of maximum disagreement can and did occur where there is a significant mass of one tracer (2267, in this instance) coupled with minimal mass of the other (2210). For Tracer 2210, a secondary maximum with count rates higher than 5000 counts/min was indicated for an area in which, in fact, there was no Tracer 2210.

I^{131} Release

On July 25, 1963, 120 mcuries of I^{131} were released from the routine generation site of the Hanford stable diffusion course. Although this release had other primary experimental objectives and the release was of a minimal amount for purposes of atmospheric diffusion studies, the air samples taken at routine field sampling positions did serve a useful purpose insofar as tracer technology is concerned. They presented an opportunity for a rough appraisal of the compatability of a gaseous tracer technique with the existing fluorescent particle technique.

The peak exposures of I^{131} observed at the four routine sampling distances were in excellent agreement with peak exposures experienced with Tracer 2210 under similar atmosphere conditions. Also, on the basis of a method for forecasting exposures derived from Hanford fluorescent tracer data,[1.31] a prediction of crosswind distributions of exposure for the I^{131} experiment was made. Figure 1.24 gives, for 200 m, observed and predicted exposure for the 120 mcuries of I^{131} emitted. Agreement is reasonably good. Agreement between predicted and observed is considerably less satisfactory at 3200 m from the source (Figure 1.25). However, the quantity of I^{131} collected on a sampler at the 3200 m distance was approaching the detection limit of the samplers used. Also, it should be kept in mind that the dotted line is a prediction, and, therefore, undoubtedly, does not represent the exact distribution of fluorescent tracer that would have been observed had it truly been emitted.

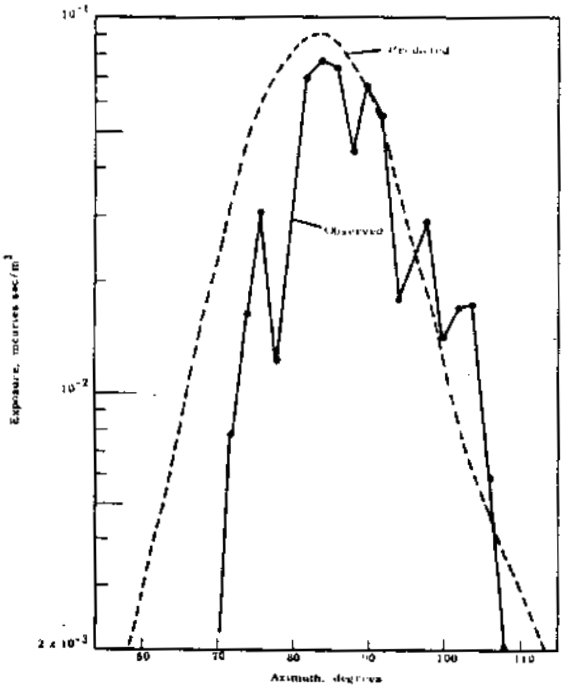

FIGURE 1.24

Crosswind Exposure of I^{131} at 200 m from Source

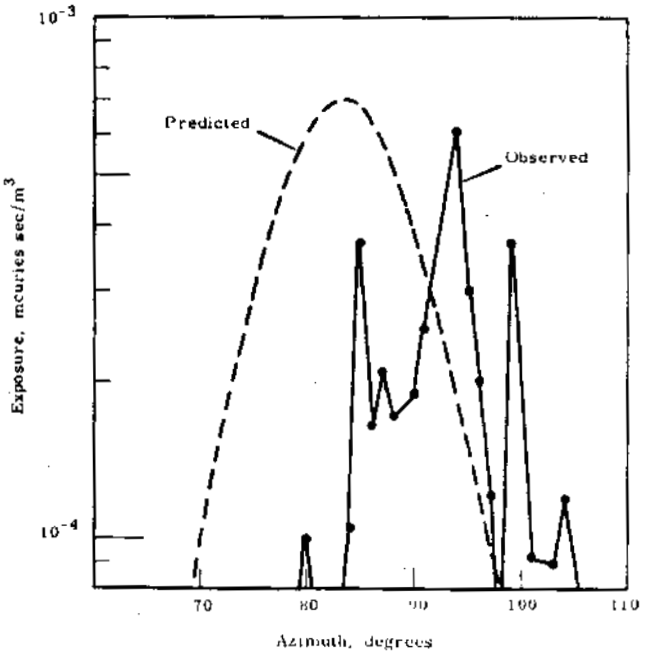

FIGURE 1.25

Crosswind Exposure of I^{131} at 3200 m from Source

REFERENCES

1.1 M. L. Barad and J. J. Fuquay (eds.) "The Green Glow Diffusion Program," Geophysical Research Papers No. 73. Air Force Cambridge Research Laboratories, Geophysics Research Directorate, Mass. Also HW-71400 Vol. I. 1962.

1.2 M. L. Barad and J. J. Fuquay (eds.) "The Green Glow Diffusion Program," Geophysical Research Papers No. 73. Air Force Cambridge Research Laboratories, Geophysics Research Directorate, Mass. Also HW-71400 Vol. II. 1962.

1.3 H. H. Lettau. "Computation of Richardson Numbers, Classification of Wind Profiles and Determination of Roughness Parameters," Exploring the Atmosphere's First Mile, Vol. I. H. H. Lettau and B. Davidson (eds.) Pergamon Press, New York.

1.4 O. G. Sutton. Micrometeorology. McGraw Hill, New York. 1953.

1.5 G. I. Taylor. "Diffusion by Continuous Movements," Proceedings of the London Mathematical Society, series 2, vol. 20, pp. 196-211.

1.6 M. L. Barad (ed.) "Project Prairie Grass," Geophysical Research Paper No. 59. Air Force Cambridge Research Laboratories, Geophysics Research Directorate, Mass. Vol. I - AD-152 572, Vol. II - AD-152 573. 1958. (See also AFCRC-TR-58-235, Vol. I and Vol. II.)

1.7 M. L. Barad and J. J. Fuquay (eds.) "The Green Glow Diffusion Program," Geophysics Research Paper No. 73. Air Force Cambridge Research Laboratories, Geophysics Research Directorate, Mass. HW-71400 Vol. II. 1962.

1.8 D. A. Haugen and J. J. Fuquay. The Ocean Breeze and Dry Gulch Diffusion Programs - Volume I. HW-78435. November 1963.

1.9 N. F. Islitzer. Unpublished Data. 1963. (Personal Communication)

REFERENCES (Contd.)

1.10 Convair, Division of General Dynamics Corporation. Fission Products Field Release Test - II, FZK-9-149(NARF-60-10T). September 1960.

1.11 D. H. Slade. Unpublished Data. 1963. (Personal Communication)

1.12 J. J. Fuquay, C. L. Simpson and W. T. Hinds. Prediction of Environmental Exposures from Sources Near the Ground, Based on Hanford Experimental Data, HW-SA-3229. September 1963.

1.13 A. C. Chamberlain. Aspects of Travel and Deposition of Aerosol and Vapor Clouds, AERE-HP-R-1261. September 1953.

1.14 R. J. Engelmann. Rain Scavenging of Particulates, HW-79382. December 1963.

1.15 R. J. Engelmann. The Hanford Raindrop Sampler and Selected Spectra, HW-73119. March 21, 1962.

1.16 I. Langmuir. "The Production of Rain by a Chain Reaction in Cumulus Clouds at Temperature Above Freezing," J. Met., vol. 5, pp. 175-192. 1948.

1.17 I. Langmuir and K. B. Blodgett., General Electric Research Laboratory. Mathematical Investigation of Water Droplet Trajectories, RL-225. 1945.

1.18 C. R. McCully, M. Fisher, G. Langer, J. Rosinski, H. Glaess and D. Werle. "Scavenging Action of Rain on Air-borne Particulate Matter," Ind. Eng. Chem., vol. 48, pp. 1512-1516. 1956.

1.19 G. D. Kinzer and W. E. Cobb. "Laboratory Measurements and Analysis of the Growth and Collection Efficiency of Cloud Droplets," J. Met., vol. 15, pp. 138-148. 1958.

REFERENCES (Contd.)

1.20 W. H. Walton and A. Woolcock. "The Suppression of Airborne Dust by Water Spray," Aerodynamic Capture of Particles, E. G. Richardson (ed.) pp 129-153. Pergamon Press, New York. 1960.

1.21 S. Goldstein. Modern Developments in Fluid Dynamics. Oxford University Press., London. 1938.

1.22 T. Pearcey and G. W. Hill. "A Theoretical Estimate of the Collection Efficiencies of Small Droplets," Q. J. Roy. Met. Soc. vol. 83, pp. 77-92. 1957.

1.23 J. W. Telford, N. S. Throndike and E. G. Bowen. "The Coalescence Between Small Water Drops," Q. J. Roy. Met. Soc. vol. 81, pp 241-250. 1955.

1.24 J. W. Telford and N. S. Thorndike. "Observations of Small Drop Collisions," J. Met. vol. 18, pp. 382-387. 1961.

1.25 J. Rosinski and C. Nagamoto. "Particle Trajectories and Adherence to Cylindrical Sticky Surfaces," Koll. Z. vol. 175, pp. 29-33. 1961.

1.26 R. H. Magarvey and J. W. Geldart. "Drop Collisions Under Conditions of Free Fall," J. of the Atmospheric Sciences. vol. 19, pp. 107-113. 1962.

1.27 W. Möller. "Experimentelle Untersuchungen zur Hydrodynamik der Kugel," Phy. Z. vol. 39, pp. 57-80. 1938.

1.28 O. K. G. Tietjens. Applied Hydro- and Aeromechanics. McGraw-Hill, New York. 1934.

1.29 A. E. J. Eggleton and N. Thompson. "Loss of Fluorescent Particles in Atmospheric Diffusion Experiments by Comparison with Radio-xenon Tracer, Nature. vol. 192, pp. 935-936. December 9, 1961.

REFERENCES (Contd.)

1.30 P. W. Nickola and J. J. Fuquay. "Advances in Atmospheric Tracer Technology," Hanford Radiological Sciences Research and Development Annual Report for 1962, HW-77609, pp. 1.30-1.34. 1963.

1.31 C. L. Simpson, J. J. Fuquay, and W. T. Hinds. Forecasting Dispersion from a Source Near Ground Level, HW-SA-3192. January 29, 1964.

RADIOLOGICAL PHYSICS

Radioactivity in Alaskan Eskimos in 1963

H. E. Palmer, W. C. Hanson*, B. I. Griffin, and D. M. Fleming

During the summer of 1963 people at five villages above the Arctic Circle in Alaska were measured for radioactivity with a transportable whole body counter. The adult people of the interior village of Anaktuvuk Pass showed the highest average Cs^{137} burden, 628 nanocuries. This is an increase of nearly 50% over the summer before. The maximum burden found was 1.24 microcuries.

Measurements with a portable whole body counter during the summer of 1962 showed that Eskimos in northern Alaska had accumulated more fallout Cs^{137} in their bodies than people in the rest of the United States.[2.1] These high levels resulted primarily from the food chain lichen-to-caribou-to-man.[2.2] Lichens contain more Cs^{137} than most food chain components because their long lifetime permits more accumulation. New measurements made during the summer of 1963 show continued high and generally increased accumulations of Cs^{137}. The increases were probably associated with new fallout resulting from resumption of weapon testing in 1961.

Table 2.1 compares results obtained during 1962 and 1963. The same counter was used both years; during 1963 the counter was also calibrated for Cs^{137} in children (4 through 14 yr) so more young people were measured. Measurements were made at Fort Yukon was well as at the villages visited in 1962.

The adult Eskimos (15 yr and older) at Anaktuvuk Pass showed nearly a 50% increase in average body burden of Cs^{137} over 1962. Everyone counted both years had increased with the increases ranging from 5 to 112%. The average percent increase was less than that shown by people counted at Richland, Washington who contained an average of 6 nanocuries in 1962 and 12 nanocuries in 1963. The food chains controlling

---

* Biology Laboratory, Hanford Laboratories

the Cs^{137} in the people of Washington are, of course, much different than those for the Eskimos. A man from Anaktuvuk Pass had the highest amount of Cs^{137} found: 1.24 microcuries.

TABLE 2.1

Cs^{137} IN PERMANENT ESKIMO RESIDENTS OF ALASKAN ESKIMO VILLAGES, nanocuries

	Average for Adults 15 yr and Older		Maximum		Average for Children 5 to 14 yr
	1962	1963	1962	1963	1963
Anaktuvuk Pass	421	628	790	1240	217
Kotzebue	138	140	518	732	42
Barrow	52	60	166	177	19
Point Hope	17	39	119	88	17
Fort Yukon		34		181	13

The International Committee on Radiological Protection recommends that the maximum permissible body burden of Cs^{137} be set at 3.0 microcuries for individuals in the population at large who are not exposed in the course of their occupation. No recommendation was made concerning average levels of Cs^{137} for groups such as the Alaskan Eskimos.

Cs^{134} was again present in the Eskimos.(2.3) In the 10 Eskimos containing the most Cs^{137}, the Cs^{134}:Cs^{137} activity ratio decreased from 0.012 in 1962 to 0.0067 in 1963; the actual amount of Cs^{134} decreased by 22%. These figures indicate that the composition of the fallout was changing, presumably due to the arrival of new material from tests that started in 1961. If the new material contained no Cs^{134} and if the Eskimos were in equilibrium with the old fallout, the amounts of Cs^{134} in the Eskimos would have decreased by 28%, nearly the percentage observed. The fact that Cs^{134} was picked up on an air filter at Richland, Washington in January, 1963, with a Cs^{134}:Cs^{137} ratio of 0.016 may indicate that the fallout in Alaska and in Washington came from different tests.

The change in the Cs^{134}:Cs^{137} ratio indicates that the increases found at Anaktuvuk Pass were associated with new fallout material. It is improbable that any significant part of the increases was due to more caribou being eaten. Caribou is a principal item in their diet and it is relatively available at all times of the year because of storage of carcasses in permafrost pits. Furthermore, those people counted indicated that they had eaten about the same amount of caribou in 1962-63 as in 1961-62. The large increase in the Cs^{137} in the people at Point Hope resulted largely from a poor harvest of caribou in 1962 and a good one in 1963. The people at Kotzebue were counted about 2 mo later than in 1962. Since their diet contains less caribou meat in the summer, they had a chance to eliminate some of the Cs^{137} they contained; earlier counting might have shown a significant increase.

Urine samples obtained during the winter of 1962-63 through the U.S. Public Health Service hospital at Fort Yukon were counted for Cs^{137}. The results indicated an average body burden of about 120 nanocuries. This was of particular interest because the main meat in their diet came from moose, which indicated another food chain of interest. For these reasons the Athapascan Indians at Fort Yukon were counted in 1963. A period of approximately 4 mo, months in which there was little caribou or moose meat in their diet, is presumed to be the cause of the difference between the 34 nanocuries observed by counting and the 120 by urinalysis.

Acknowledgements

We thank Kasume Kasugi of the U.S. Public Health Service for use of the hospital facilities at Kotzebue and Barrow and M. G. Brewer, Director of the Arctic Research Laboratory, for invaluable support in transporting equipment at Barrow and Anaktuvuk Pass and the use of the laboratory facilities.

Human Uptake of Cs^{137} from Reindeer Meat - H. E. Palmer

Humans who eat reindeer meat absorb most of the Cs^{137} it contains. Cooking may remove half or more of the Cs^{137} from the meat.

Since Laplanders and Alaskan natives have acquired high body burdens of Cs^{137} from eating reindeer, caribou, and moose meat,[2.1, 2.4] it is desirable to know what fraction of the Cs^{137} in the meat they eat is taken up by their bodies. This paper reports some measurements of uptake and of the loss of Cs^{137} from the meat during cooking. The study was made with reindeer meat purchased at Kotzebue, Alaska that contained about 7.3 nanocuries of Cs^{137} per pound of meat.

The Cs^{137} content of the meat was measured with the shadow shield whole body counter before and after the cooking. The loss of Cs^{137} from the meat depended on the manner of cooking. Boiling of round steaks removed about 60% of the activity. Roasting of steaks in aluminum removed 30 to 50%. Meyer et al.[2.5] found similar losses for Cs^{134} in beef. Studies at the University of Tennessee[2.6] showed that in boiling meat the percentage of Cs^{134} removed varied with the surface exposed and that 90% could be removed from ground beef. Apparently Eskimos use the juices that contain the Cs^{137} lost from the meat in their cooking so that the losses are not effective in reducing their body burdens. The results indicate how their body burdens might be reduced significantly by not using the juices.

Five people ate two meals each of the cooked meat after it had been measured for Cs^{137}. All excreta were collected from the male subjects for 4 days and measured for Cs^{137}. The uptake was the ratio of the amount retained in the body (the difference between the intake and the excess over a normal excretion pattern) to the intake. The subjects received whole body counts before and 4 days after eating the meat. The amount retained was determined this way for the female subject. Otherwise, the whole body counts were used just to confirm the amount of uptake. The results are given in Table 2.2. They show that most of the Cs^{137} in the meat was retained by

the body. These uptake values for Cs^{137} in meat are similar to those obtained for Cs^{137} in other types of food. The values are higher than those obtained by Naversten;[2.7] however, his values were based on measurements taken 27 days rather than 4 days after ingestion.

TABLE 2.2

UPTAKE OF Cs^{137} FROM MEAT

Subject	Sex	Cs^{137} Ingested, nanocuries	Cs^{137} Excreted Over Normal, nanocuries	Uptake, %	Increase in Body Burden by Whole Body Counting, nanocuries
1	M	8.38 (roasted meat)	0.40	96	7
2	M	8.16 (roasted meat)	0.27	97	8
3	M	8.20 (roasted meat)	0.64	92	7
4	M	6.40 (boiled meat and broth)	0.90	86	5
5	F	8.27 (roasted meat)		> 90	8

Determination of the Average Cs^{137} Body Burden of a Population by Urinalysis - H. E. Palmer

The correlation between the cesium and potassium excreted in the urine must be due to a constant daily ingestion and excretion of potassium together with a slow and constant elimination of cesium rather than to any similarity in metabolism. Three Alaskan villages and Richland, Washington were studied by urinalysis.

Last year the existence of a good correlation between the ratio of the Cs^{137} to the K^{40} excreted in the urine by Alaskan Eskimos and their whole body burden of Cs^{137} was reported.[2.8] The correlation is not good enough to permit reliable estimation of the body burden from urine measurements for a single individual. However, urine measurements should be a good way of determining the average burden of a large group of people. This paper discusses the probable reasons for the correlation and describes further tests of the correlation, measurements by urinalysis

in three Alaskan villages, and measurements at Richland, Washington that show a similar correlation probably exists in the rest of the United States.

Although cesium and potassium are chemically similar, their metabolism by the body is similar only up to a certain point. Rasoff et al.[2.9] found that cesium, like potassium, disappears rapidly from the bloodstream and accumulates in the soft tissue of the body with the bulk of it going to the muscle tissue. After this initial deposition, the metabolic similarity seems to end. The body has a certain potassium capacity which is directly proportional to the muscle mass.[2.10] If the potassium capacity is exceeded by the intake of excess potassium in the body, this excess potassium is excreted within a few hours. However, since most of the potassium in the body is exchangeable,[2.11] any ingested potassium will exchange with the potassium in the cell mass. Cesium is present in the diet and the body in only trace amounts, and its deposition in the body is different from potassium. Relman[2.12] showed that cesium accumulates in preference to potassium in muscle tissue, and that in rats up to 2/3 of the intramuscular potassium can be replaced by cesium. Once the cesium has been deposited within the muscle tissue cells it very strongly resists exchange with the other alkali metals. Mraz et al[2.13] suggested that the only way cesium is released from tissue is through catabolism. Attempts to enhance cesium excretion have met with very little success.[2.8] The very slow release of cesium from tissue is confirmed by the relatively long biological half-life of about 100 days compared to about 25 days for potassium.

Since the cesium in the muscle tissue exchanges very slowly and the potassium exchanges quite rapidly, the correlation between the ratio of cesium and potassium in the urine to the body burden of Cs^{137} must be due to constant daily ingestion and excretion of potassium together with elimination of cesium proportional to the amount in the body rather than to any similarity in the metabolism of the two elements. Taylor et al[2.14] found

that the average daily urinary excretion of potassium was 2.2 ± 0.5 g. Twenty-four hour urine samples collected from a subject at Hanford for 10 days gave an average of 3.3 ± 0.9 g of potassium per day. Nearly constant ingestion of potassium is to be expected in view of the nearly constant potassium content of our main foods. The potassium content of most meats, vegetables, fruits, and cereals does not vary by more than a factor of two.[2.15] The daily urinary excretion of Cs^{137} for an individual is a constant fraction of the total body burden.[2.9, 2.14, 2.16] However, this constant fraction (which is related to the biological half-life) is not the same for each individual, so the urinalysis method is not a generally useful method for estimating individual body burdens of Cs^{137}. The average body burden of a group of people can be determined by measuring urine samples or a pooled sample from the group and using the potassium content to eliminate the need for 24 hr urine samples.

Five additional urine samples were collected from Eskimos during the summer of 1963. The results are shown together with the 1962 results in Figure 2.1. The new results show the same correlation as the old.

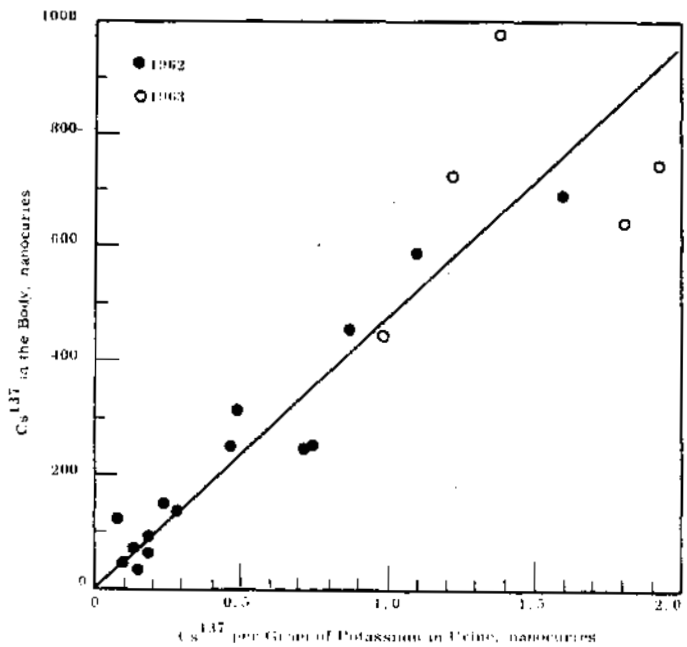

FIGURE 2.1

Correlation of Urinalysis and Whole Body Counting

The Alaskan whole body counting studies in the summer of 1962 were made in northern Alaska above the Arctic Circle. The body burdens of Cs^{137} in the more southern area were not known. During the winter of 1962-63 urine samples were collected from the U.S. Public Health Service hospitals at Fort Yukon, Tanana, and Bethel. From the Cs^{137}:K ratios in the urine samples, the average body burden of the people in these areas was found to be 118, 40, and 65 nanocuries for the regions of Fort Yukon, Tanana, and Bethel. A check on one of these results was made later when a whole body counter was taken to Fort Yukon. The average burden determined in July, 1963, was 34 nanocuries. However, the people had not been eating caribou meat since February, and about 4 mo elapsed between the urinalysis and the whole body counts (about two biological half-lives) during which the burdens could be expected to decrease to this level.

The International Committee on Radiological Protection recommends that the maximum permissible body burden of Cs^{137} be set at 3.0 microcuries for individuals in the population at large who are not exposed in the course of their occupation. No recommendation was made concerning average levels of Cs^{137} for groups such as the Alaskan Eskimos.

As a test of the urinalysis method for groups of people of a different race and living habits and having low level body burdens of Cs^{137} (about 10 nanocuries), combined urine samples from 450 people living in Richland, Washington, were measured and gave a value of 11.5 nanocuries for the average body burden. The samples were collected in three groups of 150 people each; the values from the groups were 11.7, 11.3, and 11.5 nanocuries. The average burden of 60 Richland people measured at the Hanford whole body counter at the same time was 12.5 nanocuries.

These results show that the average Cs^{137} burden can be estimated from the combined urine samples from a group of people. This method should find use in determining the amount of Cs^{137} in populations which are not near a whole body counting facility. The estimates can be obtained

without any inconvenience to the people in the groups, since the samples can be easily obtained from hospitals, schools, or universities.

A Scintillation Counter for In Vivo Detection of Plutonium - B. I. Griffin and W. C. Roesch

A scintillation counter was constructed for in vivo study of plutonium deposited in the lung. The counter detects the X-rays and gamma rays from plutonium's uranium and americium daughters. The sensitivity is in the range 10 to 100 nanocuries.

Studies were reported last year of scintillation counters for use in the detection of the X-rays emitted following the decay of plutonium.(2.17) It was concluded that it is possible to build a large counter suitable for in vivo detection of plutonium deposited deep in the body, particularly in the lungs. This paper describes such a counter that was built and some of its characteristics. The counter is not yet in its final form; work is still being done on reduction of its background.

The counter consists of four 6 by 7 by 12 in. boxes suspended to permit horizontal and vertical movement and rotation about a horizontal axis. Each box contains 13 EMI/US-9514-S photomultiplier tubes. On each tube is a NaI(Tl) scintillator 1 mm thick by 1.75 in. in diameter. The scintillators are cleaved crystals mounted on quartz and covered with 0.001 in. aluminum foil. In addition, each scintillator is fastened to the phototube and covered with a layer of rubber cut from the finger of a surgeon's glove. Each box is covered with a thin layer of Mylar for protection and with black paper to prevent light from reaching the phototubes. Magnetic shielding is provided by two layers of 0.01 in. Co-Nettic A foil on each phototube. The anodes of the 52 phototubes are connected. High voltage to each tube is individually adjustable. The counter is housed in a general purpose, 4 in. thick, lead shield. An angle iron framework 3 by 3 by 10 ft supports the ceiling and doors (3 by 4 ft opening). The roof is laid on 20 gage mild sheet steel bolted to the frame. This shield is large enough to permit counting of people.

Noise from the dark current in photomultiplier tubes and radioactivity in surrounding objects are important sources of background in X-ray scintillation counting. Last year's report describes the basis for the choice of the low noise, high gain EMI/US-9514-S phototube and of the materials surrounding the scintillator. It also describes the use of a Thoraeus filter as a liner for a lead shield. The present shield is lined with 0.025 in. of cadmium plus, on the inner surface, 0.01 in. of copper. It was predicted that the completed counter would have a background counting rate in the X-ray channels less than 1.5 counts/min per tube. The measured background in the empty shield is 1.1 counts/min per tube or a total of 56 counts/min.

When phantoms made of sugar or water are counted, the background is higher because radiation is scattered into the counter. The increase is only about 5%. People are both sources and scatterers of radiation. They increase the background between 60 and 180%.

The sensitivity of the counter, the minimum detectable amount of plutonium that can be detected, depends on the position of the plutonium in the lung, the isotopic composition of the plutonium and the time since the last removal of the daughter products, and the choice of the channels used on the multichannel analyzer. Both Pu^{239} and Pu^{240} lead to the emission of uranium L X-rays. Pu^{241} is a beta emitter with 13 yr half-life that leads to Am^{241}. The decay of Am^{241} produces 27 and 60 kev gamma rays and the L X-rays of neptunium; the latter have energies similar to those of the uranium daughters of Pu^{239} and Pu^{240}. There is also an iodine escape peak from the 60 kev gamma ray at 27 kev in the pulse height spectrum of NaI scintillators. The presence of these radiations helps in the detection of the plutonium because they may as much as double the number of X- and gamma rays per alpha particle emitted. They make interpretation difficult, however, because one cannot infer the alpha particle rate from the X- and gamma ray counts unless he knows the isotopic composition (seldom the case in health physics applications).

To get some idea of the counter sensitivity some plutonium placed in the lung cavity of a Remab phantom was counted. The body of the phantom was filled with distilled water and the lung cavity with chipped styrofoam. The minimum detectable amount was then estimated with the formula

$$MDA = (k/S)\,(b/t)^{\frac{1}{2}} \qquad (1)$$

where b is the background counting rate, t is the counting time, S is the counting rate per unit activity, and k is a statistical factor conservatively taken to be 3 (see Nicholson [2.18]) for a more rigorous discussion of such problems). Values of $b^{\frac{1}{2}} / S$ for different ranges of pulse height were compared on the multichannel analyzer. Figure 2.2 shows the background spectrum. It is not obvious what selection of channels will minimize the minimum detectable amount. The best choice was the pulse height range 13.6 to 66.4 kev (Channels 17 to 83 at 0.8 kev per channel). It was found that S = 0.23 counts/nanocurie-min for these channels for plutonium recently separated from its daughters but of unknown isotopic composition. The background was 330 counts/min for an empty counter; in the worst case it might be 2.8 times this for a man in the counter. For 20 min counting time, Equation (1) gives MDA = 70 nanocuries. For an old plutonium source, the minimum detectable amount was 8 nanocuries. Neither of these results is more than indicative because of the lack of knowledge of the isotopic composition. Actually, of course, the real problem at present is that Equation (1) does not apply because the sensitivity is not limited by statistics on background but by variations in background from one individual to the next.

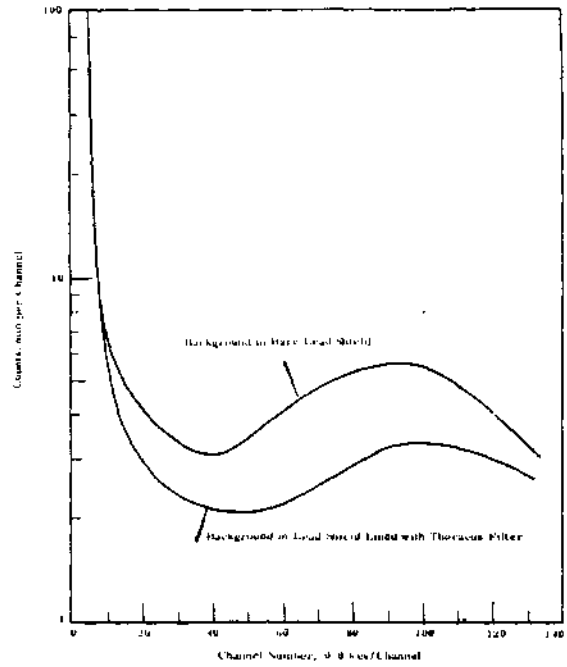

FIGURE 2.2

Background Counting Rate of Plutonium Scintillation Counter

Determination of P^{32} In Vivo - H. E. Palmer

A transmission proportional counter and a NaI(Tl) scintillator operated in coincidence for detection of P^{32} beta rays emitted from the head is better for in vivo measurements than a bremsstrahlung counter. The background is lower and is much less variable from person to person. Relatively little shielding is required.

Several reports have described the determination of P^{32} in the human body by detection of bremsstrahlung.[2.19, 2.20, 2.21] The bremsstrahlung counter is a 4 1/2 in. diameter by 3 mm thick NaI(Tl) scintillator with a 0.001 in. thick aluminum window. Body burdens as low as 200 nanocuries can be detected with it. A typical spectrum obtained with this counter placed at the head of a subject containing about 1 microcurie of P^{32} is shown in Curve A of Figure 2.3. Some of this spectrum, however, is not due to bremsstrahlung. An absorber that absorbs beta particles but does not significantly absorb the bremsstrahlung produces Curve B when placed between the counter and the subject's head. Curve B is the true bremsstrahlung spectrum. Curve C, the difference between Curves A and B, is the spectrum due to beta rays emitted from the surface

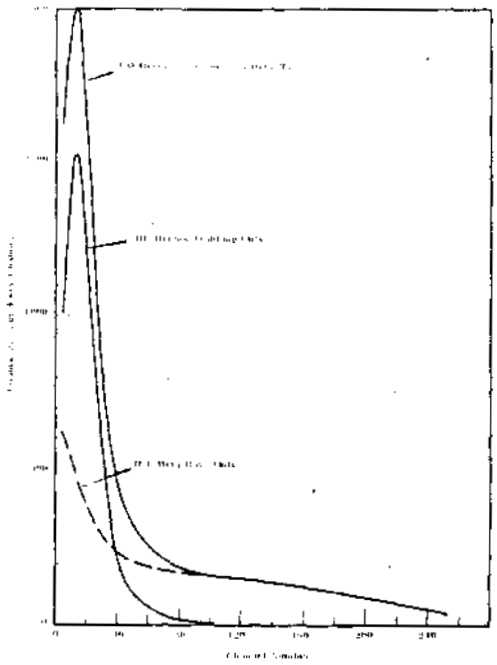

FIGURE 2.3
Bremsstrahlung Counter Spectra

the head. The areas under Curves B and C are nearly equal, that is, about the same number of counts are obtained from beta particles as from bremsstrahlung. This indicated that counting of only the beta particles should be investigated. If the background could be reduced sufficiently, the minimum detectable amount of P^{32} might be even lower than for bremsstrahlung counting.

Counting of beta rays emitted through the skin may not work for other pure beta ray emitters which are metabolized differently than phosphorus. Although phosphorus, like calcium is associated with bone growth, it is also an essential component of all cells. The blood contains several different compounds of phosphorus. Much of the P^{32} in the body is circulated in the blood stream and reaches the surface of the body. An isotope such as Sr^{90} which rapidly deposits in bone probably would not emit many beta rays from the surface of the body.

To reduce the background during the detection of beta rays a transmission type proportional counter was placed in front of the bremsstrahlung counter. This proportional counter was 1 by 6 by 6 in. and

was divided by ground wire into six small counters, each having a cross section of 1 inch^2 and a length of 6 in. The thin windows were 0.008 in. Mylar. The counter was operated as a flow counter using 90% argon-10% methane. The six anodes were connected together and in coincidence with the NaI scintillator. Coincident pulses in the NaI were pulse-height analyzed. Inside a good lead shield a large share of the background in the bremsstrahlung counter alone is due to relatively high energy gamma rays that scatter so as to leave only a little energy in the scintillator. The coincidence requirement eliminates this kind of background. Beta rays from the skin can go through the proportional counter with little trouble and are counted nearly as well as before.

The background of this coincidence counter, for 40 to 1000 kev pulses in the NaI, was 12 counts/min when operated in the Hanford iron room with a phantom head made of sugar. With the coincidence circuit turned off it was 130 counts/min. Typically, the coincidence rate was 20 counts/min when counting a subject containing only normal amounts of K^{40} and Cs^{137}. A pressed wood beta absorber placed between the head and the counter reduced the rate to 15 counts/min. This indicates that normal beta background from the head is about 5 counts/min, probably from K^{40} beta rays. The other 3 counts/min are probably due to Compton recoil electrons produced by gamma rays emitted from the body. The background due to higher than normal gamma radiation in a subject can be determined with the beta ray absorber over the counter. All normal subjects counted so far have had about the same beta ray rate, 4 to 5 counts/min.

The counter was calibrated with five subjects containing known amounts of P^{32}. The average counting rate at the side of the head is 1.0 count per 20 min per nanocurie of P^{32} in the body. The range of rates was ± 15% for the five subjects. Figure 2.4 shows the counts obtained on two of the subjects who were studied for several weeks; one of the subjects

was reinjected after 28 days. Their effective half-life for P^{32} was 10 days. This agrees with previous results obtained with the bremmstrahlung counter at higher activity levels of P^{32}.

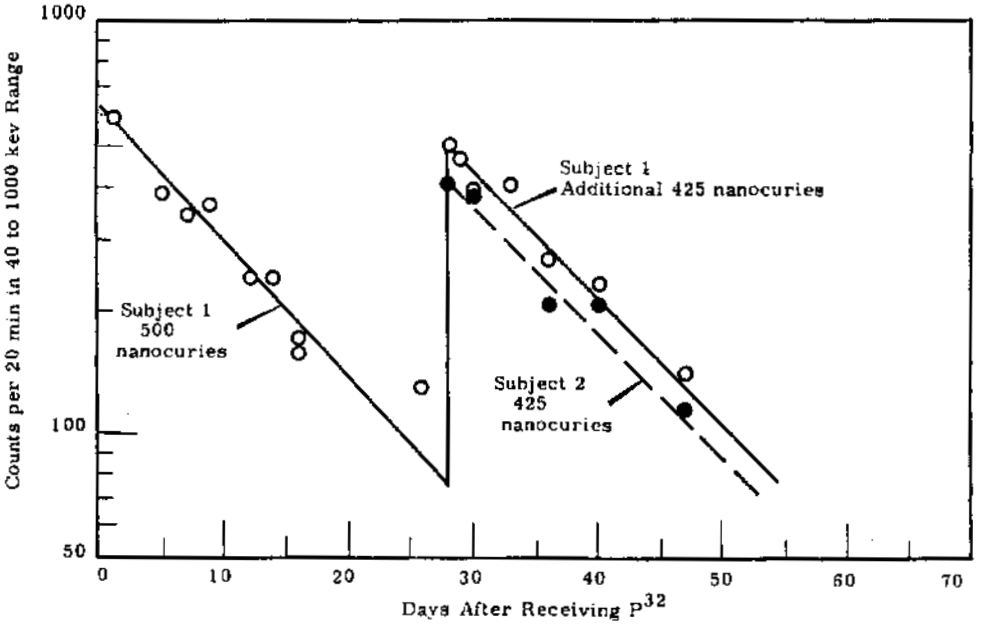

FIGURE 2.4
Retention of Low Level Burdens of P^{32}

The detection limit for the counter is about 40 or 50 nanocuries of P^{32} at the 95% confidence level. This is much better than for the bremsstrahlung counter because the background is lower and shows much less variation from person to person.

The coincidence counter has a higher counting rate over the head than over any other body extremity. It is not used over the torso because organs such as the liver concentrate potential interfering isotopes such as Zn^{65}. Another advantage of using an extremity such as the head is that only that extremity and the counter need be shielded; an iron room is not needed. The counting rate with the head and counter shielded with lead 2 in. thick (total weight 1000 lb) was the same as in the iron room. Such small and lightweight shielding requirements make it feasible to add such a counter to the Hanford Mobile Whole Body Counter facility.

One reason for developing a sensitive, in vivo counter for P^{32} was to measure people who eat Columbia River fish. Whitefish contain the most P^{32}, and during the fall often reach 2 nanocuries/g, wet weight.[2.22] A person eating 1/2 lb of such whitefish and absorbing 75% of the P^{32} would acquire a body burden of 350 nanocuries. Two subjects ate 3/4 lb each of whitefish caught in the Columbia River during December, 1963. After allowing 1 day for absorption of the P^{32}, the subjects were measured with the coincidence counter and showed body burdens of 70 and 110 nanocuries.

Acknowledgements

The people with known body burdens of P^{32} were provided by the University of Oregon Medical School and by Swedish Hospital.

Shadow Shield Whole Body Counter - H. E. Palmer

New calibrations for Na^{24}, I^{132}, and Cs^{137} were made. The discrepancy in measurements of potassium losses of kidney patients was resolved. Differential scanning results for Cs^{132} are presented.

Previous reports have described the development and calibration of a shadow shield whole body counter.[2.23, 2.24] This paper describes further studies of interest.

The counter was calibrated for Na^{24} so that it could be used to determine neutron dose in the event of a criticality accident. The result was 5.1 counts/min/nanocurie. It was also calibrated for I^{132} in the thyroid. If fission products are released in a criticality accident, the I^{132} activity in the air may be many times that of I^{131} in the hours immediately following. When the thyroid is stationary and centered under the scintillator of the counter, the sensitivity is 112 counts/min/nanocurie.

A new polyethylene phantom body was obtained and tested for use in calibration work. When it was filled with KCl solution and counted in the shadow shield, it gave 0.504 counts/min per g of potassium. The calibration of the counter is 0.502 counts/min/g. However, when a known amount of

Cs^{137} was placed in the phantom, it gave 20% more counts than the calibration would indicate. This renews our conviction that the use of phantoms for calibration is not justified.

In a cooperative study with Swedish Hospital, Cs^{137} calibration factors were obtained for people of different body sizes. There seems to be a linear relationship between the weight:height ratio and the calibration factor for ratios in the range 0.9 to 2.9 lb/in.

The counting of patients before and after treatment with an artificial kidney was reported last year.[2.24] Measurements showed a typical decrease in potassium of 15 g in a treatment. The analysis of the potassium lost to the artificial kidney solution showed only one half this amount. The difference is probably due to the lost potassium having a counting calibration different from most of the potassium in the body. The cell mass of the body has a definite potassium capacity. When the body content exceeds this capacity, the excess is excreted except in the case of kidney failure when it remains in the extracellular fluid. The potassium in the extracellular fluid is probably distributed differently and therefore counted with a different efficiency than that in the muscle cells. A potassium solution placed in the position of the heart in a phantom had a counting efficiency about twice that for the normal potassium in the body.

The use of the shadow shield counter in differential scanning to study tumor localization and potassium distribution was described last year.[2.24] A study of the distribution of Cs^{132} in subjects for 8 days following ingestion was made using just the natural collimation of the shadow shield counter. Figure 2.5 shows how the counting rates varied with time at four different positions along the body. These counts have been corrected for radioactive decay and the amount excreted from the body. After ingestion, the C^{132} activity decreased in the abdomen and upper chest areas and increased in the region of the legs. It appears that an equilibrium distribution was not reached unitl about 6 days after ingestion.

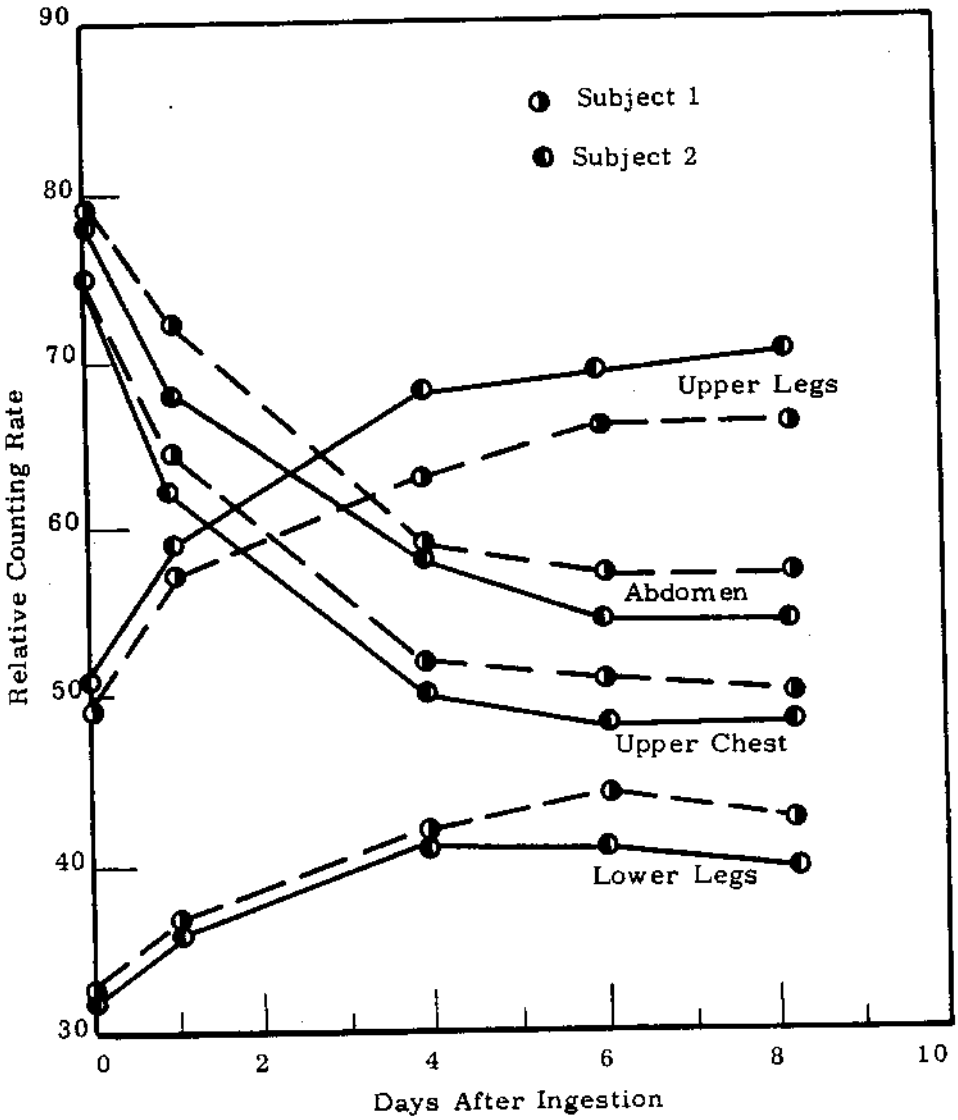

FIGURE 2.5

Changes in Distribution of Cs^{132}

Measurement of Uranium Ore Particle Inhalation by Radon Daughter Counting* - R. W. Perkins,** H. E. Palmer, and B. O. Stuart†

---

* This paper is presented on page 3.95

** Radiological Chemistry

† Biology Laboratory

Pulse Shape Discrimination in Fast Neutron Dosimetry - L. L. Nichols and W. C. Roesch

Most of the light energy liberated by neutrons in an organic scintillator can be detected and distinguished from that produced by gamma rays, but the ratio of the light emitted to the neutron dose is not independent of neutron energy. Methods of correcting for this are discussed.

Last year's report [2.25] discussed the start of studies of the application of pulse shape discrimination to fast neutron dosimetry. It was found later that neutrons from the C(d, n) reaction from carbon contamination of the Van de Graaff system were distorting the neutron spectra being used. After reduction of the contamination, many of the pulse height spectra were remeasured. Figure 2.6 shows the results. Each spectrum is of the counts due to 1 mrad of neutrons. The spectra were obtained with a 1 1/2 in. diameter by 1/2 in. thick stilbene crystal mounted on an RCA 7265 photomultiplier using space charge effects for the pulse shape discrimination. The output of the shape circuit gated a multichannel analyzer that analyzed linear pulses from an earlier dynode of the phototube. The shape circuit was adjusted so that the rejection ration for Co^{60} gamma rays was approximately 1000 to 1. Under these conditions the shape circuit will not pass recoil proton pulses for protons of less than approximately 0.5 Mev.

In the ideal case of perfect linearity between the energy of the recoil particles and the resulting light and perfect discrimination between protons and electrons without rejection of any protons, the rate of light emission would be proportional to the neutron dose rate. If n_i were the counting rate of Channel i, this would be proportional to

$$I_1 = \sum_i i\, n_i . \qquad (1)$$

The ideal conditions do not hold. Light emitted is not proportional to energy absorbed, and recoil protons below some energy are not recorded. Nevertheless I_1 was computed and is shown in Figure 2.7. It is reasonably independent of energy above 2.5 Mev.

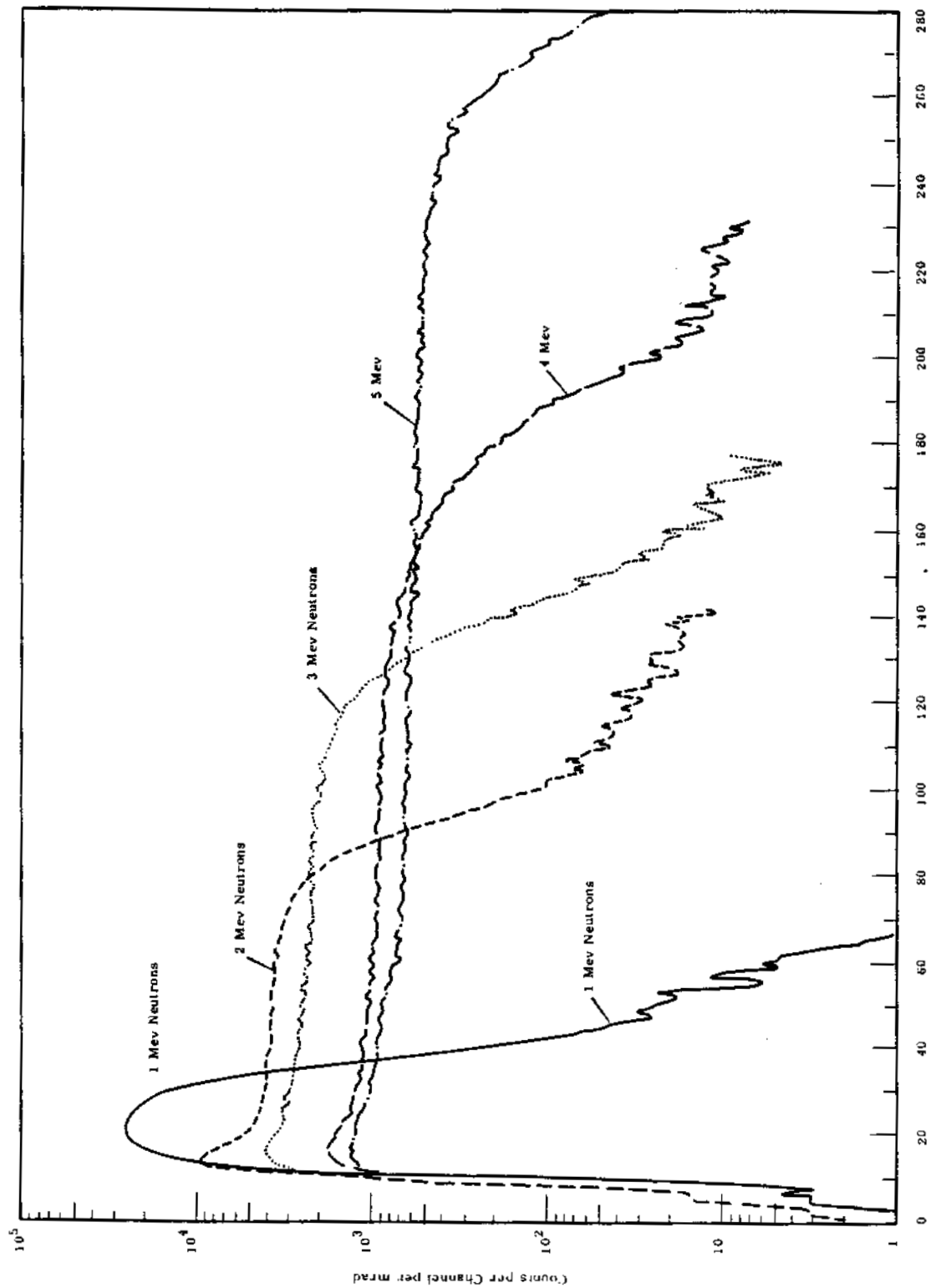

FIGURE 2.6

Pulse Height Spectra from Stilbene Detector with Pulse Shape Discrimination

AEC-GE RICHLAND, WASH.

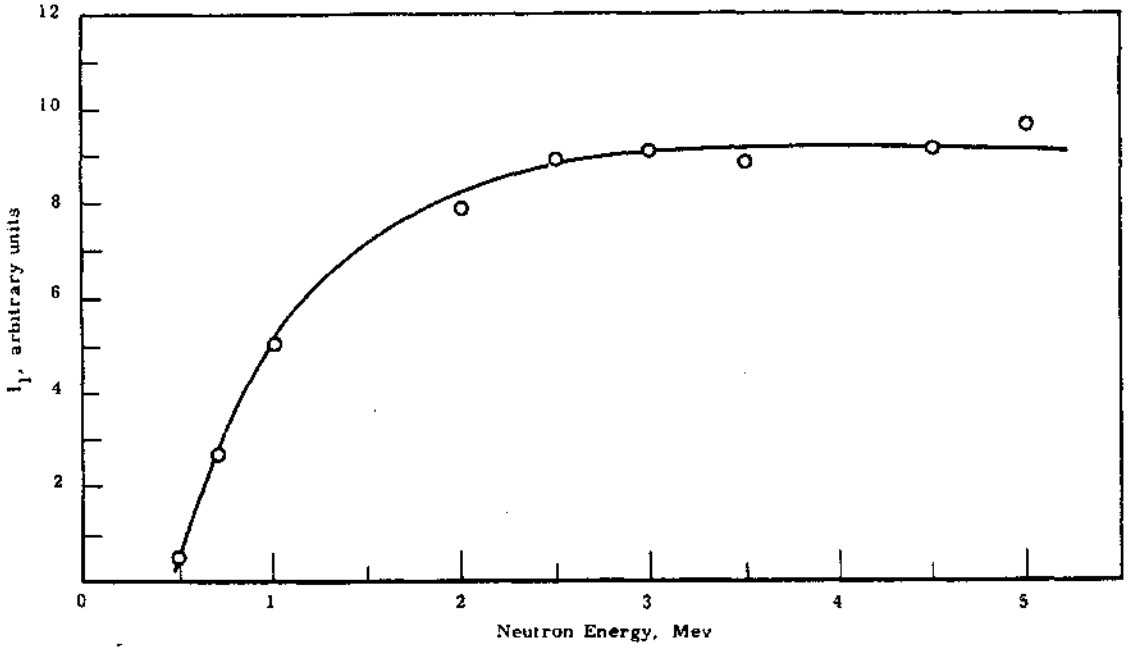

FIGURE 2.7

I_1, the "Integrated Light Output," of the Pulse Shape Discriminator System

The low sensitivity at low energy must be compensated for if pulse shape discrimination is to be used in instruments for measurements of neutron dose rate. Of course, it will never be possible to compensate by manipulation of the shape circuit data for those energies where the response is zero. One way of compensating would be to weight the pulse heights differently. Figure 2.8 shows $I_{\frac{1}{2}}$ defined by

$$I_{\frac{1}{2}} = \sum_i (i)^{\frac{1}{2}} n_i. \qquad (2)$$

It is evident that this does increase the response to low energies, but it also results in a decreasing response at high energies. Another way of weighting the pulses to improve the low energy response is

$$I_c = i_o \sum_{i=1}^{i_o} n_i + \sum_{i=i_o+1}^{\infty} i\, n_i. \qquad (3)$$

that is, to weight all small pulses by the number of some higher channel; this is equivalent to simply counting the low energy pulses and integrating the larger ones. The result is shown in Figure 2.8 for $i_o = 40$ for the

data of Figure 2.6. It extends the flat response down to about 1 Mev. The curves for I_1, $I_{\frac{1}{2}}$, and I_c in Figure 2.8 are each normalized differently; the purpose is just to compare their shapes.

Since the response cannot be improved where it is zero, it suggests that some other sort of detector with appreciable response only at low energy be combined with the pulse shape discrimination device. The response of a 4 by 4 mm Li^6I scintillator moderated with spherical polyethylene or boron-loaded polyethylene shields was investigated. The best results were obtained with a 2 in. diameter boron-loaded polyethylene sphere. Figure 2.9 shows the response of this device, arbitrarily normalized, and its combination with I_1. The resulting sensitivity is constant to within about ± 17% from at least 1/4 Mev on up. The ability to respond to the low energies is important.*

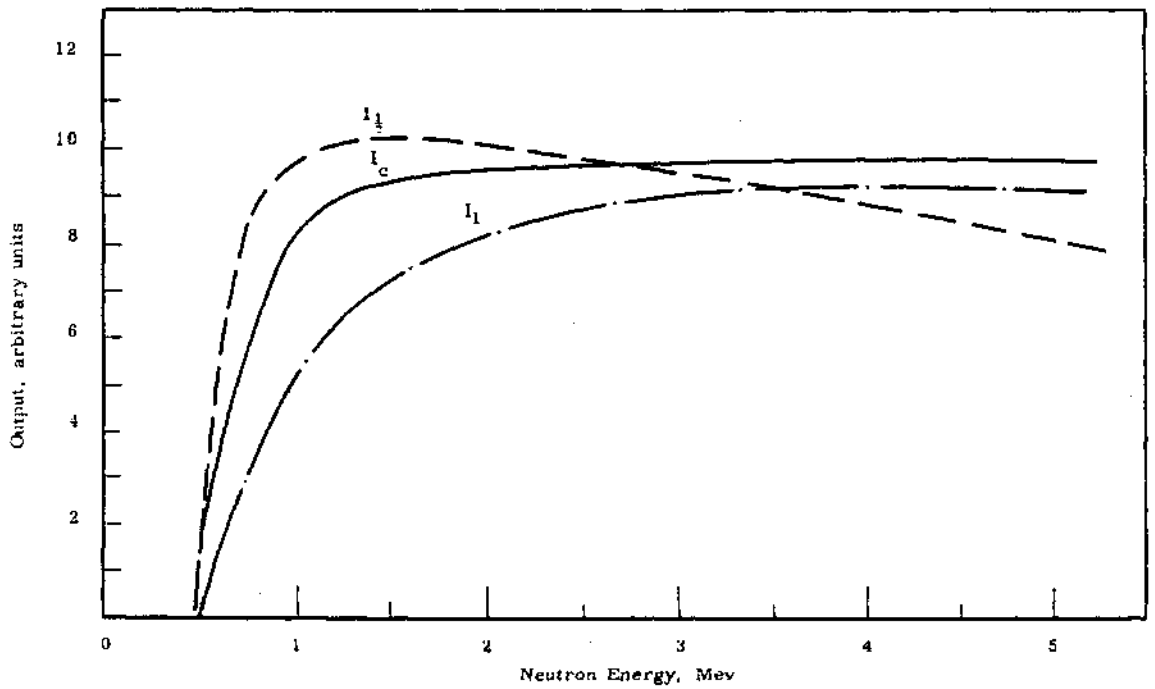

FIGURE 2.8

Modified Outputs of the Pulse Shape Discriminator System

* See, for example, "Low Energy Fast Neutrons," on page 2.29.

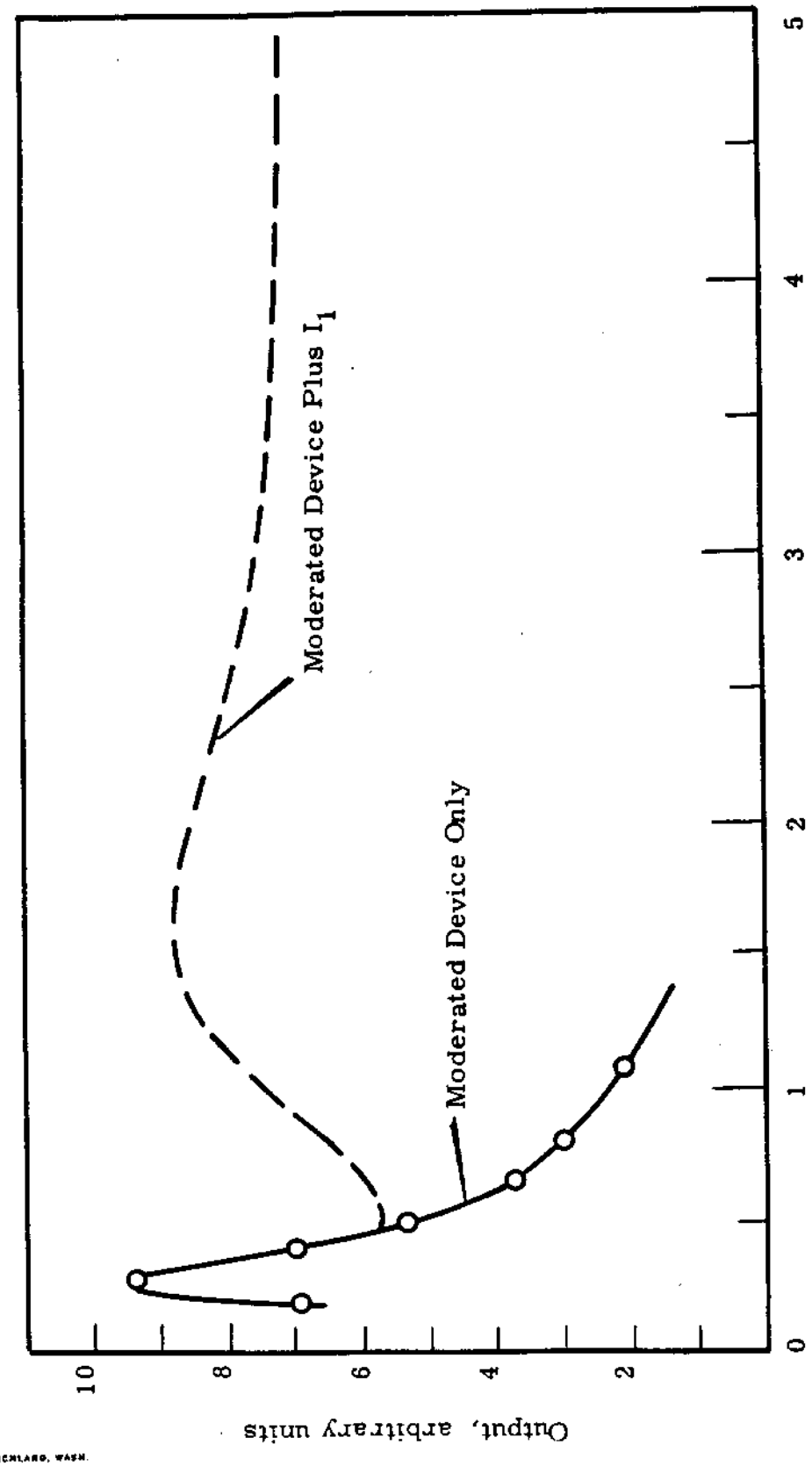

FIGURE 2.9

Use of a Moderated Detector to Supplement the Pulse Shape Discriminator System

Response of Paired Ion Chambers as a Function of Energy - R. A. R. Kent

Paired ion chambers, tissue-equivalent and tissue-equivalent minus hydrogen and nitrogen, possess responses as functions of energy for neutrons and photons which make them suitable for personnel dosimeters in plutonium production facilities.

Both photon and neutron radiations are expected in plutonium processing plants.[2.26] For unshielded plutonium, the photon dose rate considerably exceeds that from neutrons and is due mostly to low energy photons. Quite light shielding, however, results in nearly equal dose rates. Under these conditions a pair of ion chambers,[2.27] one tissue-equivalent and one similar in composition but containing no hydrogen or nitrogen, is expected to function satisfactorily and to make a good personnel dosimeter. This paper reports measurements of the sensitivity of such a chamber pair as a function of energy made to judge its usefulness in such plants.

The chambers were identically shaped 560 cm^3 cylinders. One was made of tissue-equivalent conducting plastic and filled with tissue-equivalent gas. The other was made of tissue-equivalent plastic but lined with a 1/16 in thick conducting Teflon liner and filled with CO_2. This construction was expected to provide very nearly equal scattering in both chamber walls and still make the second chamber relatively neutron insensitive. The chambers were read on a modified Townsend balance circuit;[2.28] the readings given in Figures 2.10 and 2.11 are the balance voltages required in this circuit.

For the neutron measurements, the chambers were exposed simultaneously at equal and opposite angles with respect to the beam of the Van de graaff. At the same time the neutrons were measured with a precision long counter. Fluxes measured with this counter were converted to dose rates by calculation. The difference in the chamber readings was taken to eliminate the effects of the gamma rays that were present. For the photon measurements, the chambers were exposed to the K-Fluorescent X-Ray Source.[2.29] Comparison was to the free air chamber calibration of the source.

Figure 2.10 shows the results for neutrons. The sensitivity is fairly constant above 1 Mev. The neutrons in a plutonium plant are expected to have energies in the range 0.1 to 10 Mev. For this range, a single calibration constant could be chosen that would give results accurate to at least ±18%. The decrease in sensitivity at low energies is much less than that exhibited by nuclear track film badges.

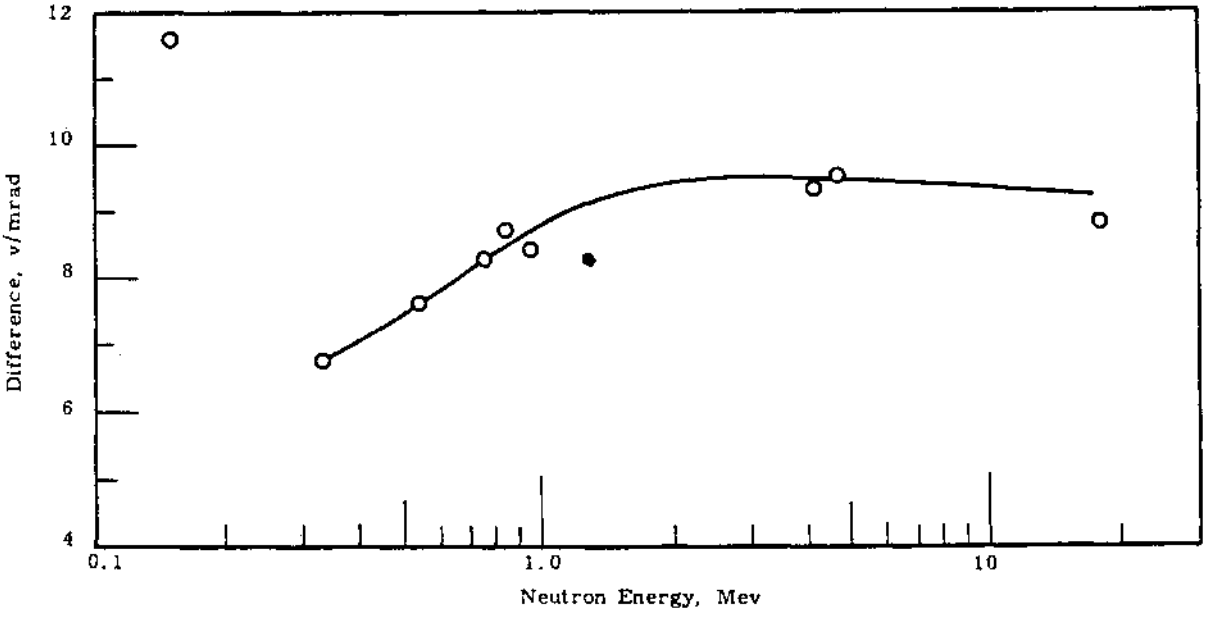

FIGURE 2.10

Sensitivity of Chamber Difference to Neutron Energy

Figure 2.11 shows the results for photons. Not shown are the results for radium gamma rays; they are essentially the same as for the highest energy shown. The decrease in sensitivity at low energy is due to absorption in the chamber walls. (The walls were made thick to withstand atmospheric pressure during cleaning and filling.) The range of energies measured covers the main energies expected in plutonium plants. Figure 2.11 shows no unexpected behavior. The decrease in response at the very low energies would be a help in discriminating against some of the X-rays found near plutonium.

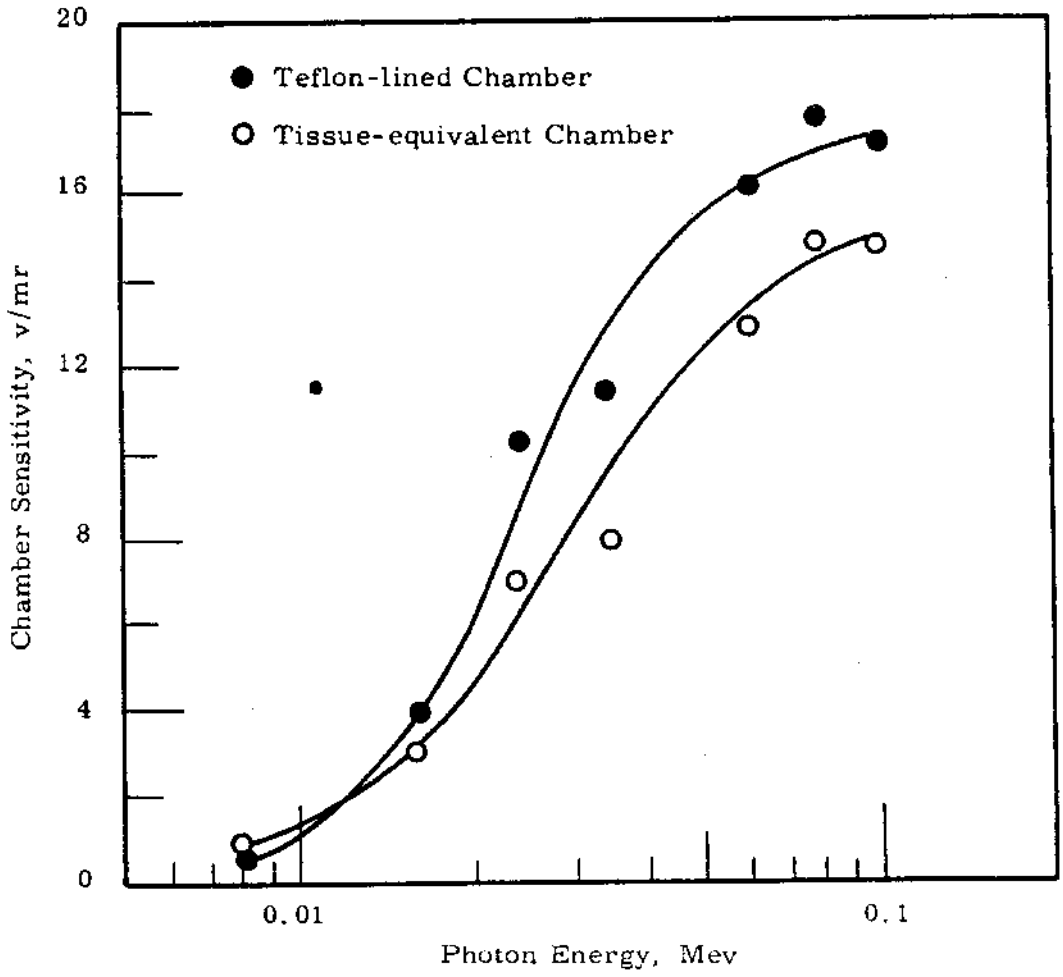

FIGURE 2.11

Sensitivity of the Chambers as a Function of Photon Energy

Precision Long Counter Intercomparisons - J. DePangher* and L. L. Nichols

Comparisons of eight different precision long counters show they can be built to have sensitivities within about 0.5% of each other. One counter suffered a small change in sensitivity.

The precision long counter is a device developed at Hanford (2.30) to be accurate and reproducible counter for the measurement of fast neutron fluxes. Several precision long counters were compared to verify reproducibility.

The following quantities were measured.

$$1(X)\ \frac{\text{count rate of PLC-X for an external source}}{\text{count rate of PLC-H-1 for same external source and with same } BF_3 \text{ tube}} \qquad (1)$$

$$r(X)\ \frac{\text{count rate of PLC-X for an internal source}}{\text{count rate of PLC-H-1 for same internal source and with same } BF_3 \text{ tube}} \qquad (2)$$

The symbol PLC-X specified the counter denoted by X. Counter H-1 is one built at Hanford and chosen to be the standard counter. These two quantities and the ratio 1(X):r(X) should all have the value unity if the counters are truly reproducible. It is felt that the ratio 1(X):r(X) is the best test for reproducibility.

Table 2.3 gives the values of 1(X), r(X), and 1(X)/r(X). The data for ML-1 (Mound Laboratory) and ANL-1 (Argonne National Laboratory) were obtained by comparing them at the respective laboratories with H-3. Counter H-3 is another one built at Hanford and used where the counter must be shipped any distance. The remainder of the data were obtained at Hanford by direct comparison with H-1.

---

* Lockheed Missiles and Space Company

TABLE 2.3

COMPARISON OF PRECISION LONG COUNTERS

X	1(X)	r(X)	1(X)/r(X)	Date*	Institution
H-1	1.000	1.000	1.000	--	Hanford
NBS-1	0.997	0.998	0.999	10-24-60	NBS
H-2	1.004	0.997	1.007	10-24-60	Hanford
H-3	0.990	0.997	0.993	3-9-62	Hanford
H-4	0.991	0.998	0.993	3-9-62	Hanford
L-1	0.984	0.992	0.993	3-9-62	Livermore
ML-1	0.987	0.990	0.997	10-8-62	Mound Lab.
ANL-1	0.984	0.988	0.996	12-23-62	Argonne
H-3	0.996	0.995	1.001	3-12-63	Hanford
H-2	1.003	0.998	1.005	3-21-63	Hanford

Counter H-3 originally gave 1(H-3)/r(H-3) = 0.993. It was then shipped to Mound Laboratory and to Argonne National Laboratory for comparisons. When the counter was returned to Hanford, the ratio had increased by 0.8% to 1.001. To make sure that H-1 had not changed, we compared H-2 with it again. Counter H-2 is another Hanford counter, one that had not been out of the laboratory. The comparison of H-2 with H-1 was within 0.2% of its earlier value indicating that H-1 was unlikely to have changed. No reason for the change in H-3 is known. It is quite possible that the change resulted from deformations produced by exposure to low temperatures during shipping between laboratories.

The first eight values of 1(X)/r(X) in Table 2.3 have a standard deviation of 0.5%. This means that the counters are quite reproducible. The change in H-3 is, of course, disturbing because it means that changes can take place and because the effect it had on the results for ML-1 and ANL-1 is not known. If the change occurred before or during the tests at Mound and Argonne, the standard deviation would be increased slightly.

---

* Chosen at about the middle of the period over which the comparison was made.

Low Energy Fast Neutrons - L. L. Nichols, W. C. Roesch, and J. G. Pengra*

This paper reports the start of a study to assess the importance of neutrons in the approximate energy range 0.1 to 1.0 Mev in health physics.

Most neutron sources of interest emit neutrons whose energies are higher than about 1 Mev. However, these neutrons are scattered and slowed down before they are captured so that there will always be lower energy neutrons present. Some neutron detectors do not respond to neutrons with energies less than some value. The efficiency of the nuclear track film badge personnel dosimeter, for example, decreases with decreasing energy below about 1 Mev and is zero below about 0.5 Mev. This study began as an attempt to estimate the fraction of the neutron dose that different neutron instruments might be missing.

Figures 2.12 and 2.13 give an appreciation of the problem. They show the flux density spectra calculated by Ritchie et al [2.31] for a slightly moderated neutron source, Figure 2.12 (the ORNL criticality accident), and for a well moderated source, Figure 2.13 (the Vinca accident). These spectra were converted to dose spectra. For Figure 2.12, 2% of the dose comes from neutrons with less than 0.1 Mev energy, 11% less than 0.5 Mev, and 23% less than 1 Mev. For Figure 2.13 the corresponding numbers are 10, 39, and 57%. In both cases, a significant part of the dose comes from neutrons of less than 1 Mev, and if one measured all neutrons above 0.1 Mev, not much would be missed.

Bramblett et al [2.32] and then Hankins [2.33] used a set of five different polyethylene spheres to moderate a Li^6I scintillator to obtain information about neutron spectra. An identical device was built at Hanford and calibrated at five different energies. The results are shown in Figure 2.14 with the calibration curves of Bramblett et al. The agreement

* Whitman College, Summer Professor at the Hanford Laboratories, 1963.

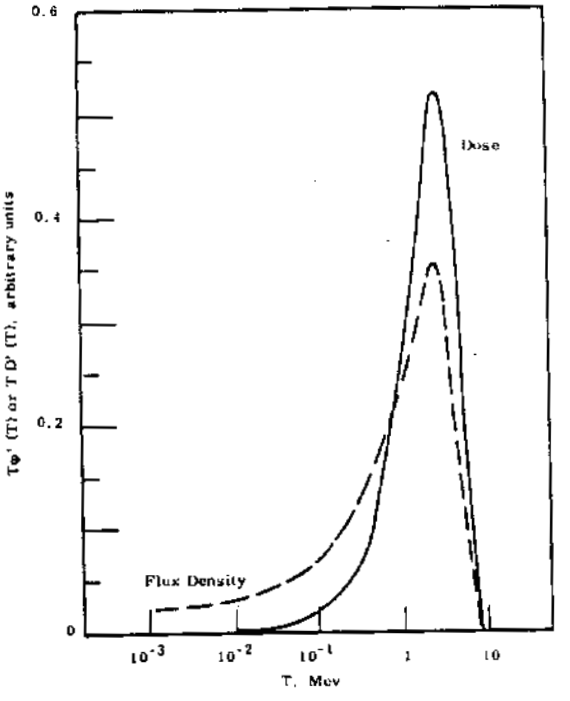

FIGURE 2.12

Dose and Flux Density Spectra ORNL Accident

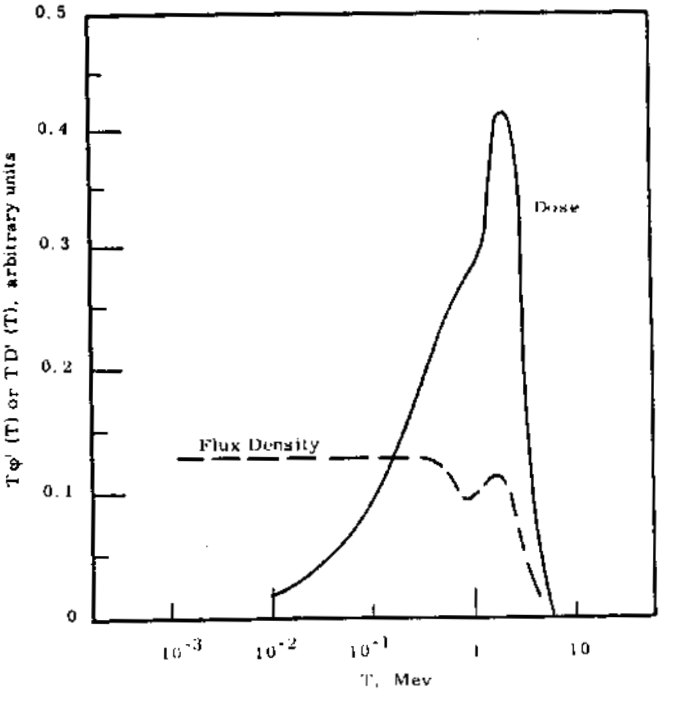

FIGURE 2.13

Dose and Flux Density Spectra Vinca Accident

AEC-GE RICHLAND, WASH.

is not very good. A good part of the original curves were interpolated. It is felt that the lack of agreement where comparisons can be made makes it undesirable to make a similar interpolation. It is felt that to assess the contribution of the low energy neutrons requires a spectrometer that will unambiguously display and evaluate the flux density of such neutrons in typical locations. After considerable study, it is concluded that this can be done with a suitable proportional counter spectrometer. . Such a spectrometer is now being built.

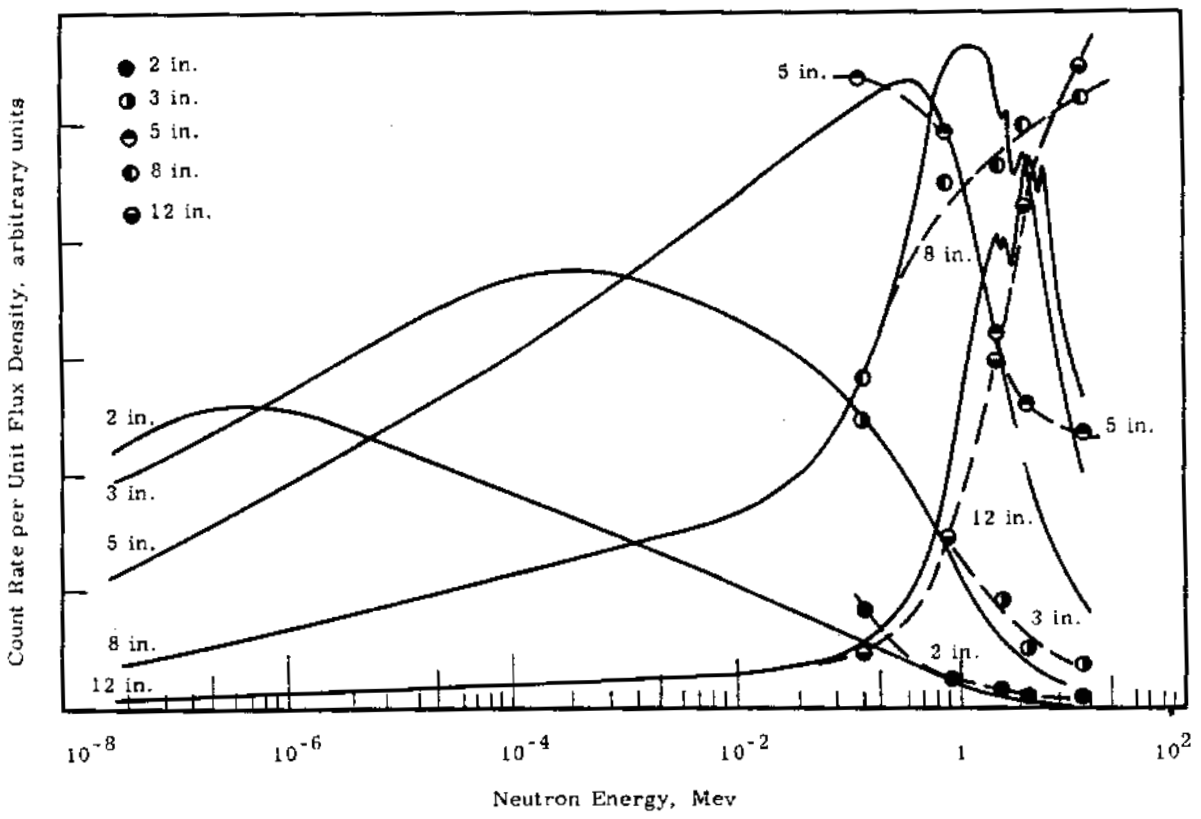

FIGURE 2.14

Calibration of the Sphere Spectrometer
(Solid Lines: Bramblett et al.[2.32] Points and Dashed Lines: Hanford)

Fast Neutron Medical Research Facility - W. C. Roesch, K. L. Swinth,* and L. L. Nichols

A fast neutron medical research facility employing a 14 Mev neutron generator such as used for activation analysis is being prepared for use by the University of Washington.

C. A. Paulsen of the University of Washington Medical school is engaged in research using fast neutrons. It was arranged that Hanford's Radiological Physics group would secure the components for and assemble an exposure facility that employed a neutron generator such as that used in neutron activation analysis. Hanford will also do the dosimetry and assemble the system. When completed, it will be moved to the University laboratory.

During the summer of 1963 three AEC Radiological Physics Fellowship students** made studies preliminary to the design of the neutron exposure facility for this project. They used the Hanford Van de Graaff to produce neutrons for their study. The resulting neutrons had very nearly the same energy that those from the neutron generator for the project will have (14 Mev). There was more gamma radiation than the neutron generator will produce because the higher energy Van de Graaff beam produced more nuclear reactions. The students studied the shielding properties of some nonhydrogeneous materials (copper, beryllium, etc). Ordinarily the hydrogen in the shield is what slows the neutrons down till they can be captured. It was thought that, at the high energy (14 Mev) of the generator neutrons, direct capture reactions might be more efficient. The results were not very accurate, but they were conclusive in showing that only hydrogeneous materials need be considered.

The students then measured the degree of gamma-ray contamination that could be expected. Neutrons produce gamma rays when captured in the hydrogen of the shield. The measurements indicated that an attempt

---

* University of Washington graduate student

** P. C. Nosler, T. J. Powell, and K. L. Swinth

should be made to reduce the number of gamma rays. The final shield design included lithium stearate close to the neutron target. The lithium captures neutrons in competition with the hydrogen but does not emit gamma rays. Lithium enriched in Li^6 would capture a greater proportion of the neutrons without gamma emission, but it was not felt that the extra expense of enrichment was justified because other reactions (inelastic scattering of high energy neutrons and capture of slow neutrons in the hydrogen of the body) give an irreducible minimum of gamma radiation.

Finally, the students measured the neutron spectrum under conditions similar to those that will exist in the exposure facility. They used pulse height analysis of the scintillations from stilbene to get the spectrum; scintillations produced by gamma rays were rejected by pulse shape discrimination. Figure 2.15 shows the results. The spectra are the pulse height spectra. The energy spectra would be slightly different because of the nonlinear energy-pulse height relation in stilbene. The peaks are at 14 Mev. The spectra contain fewer low energy neutrons than calculations indicated. The calculations were made for a uniform, infinite medium. In the exposure facility there is an empty tube from the neutron source to the subject. Evidently the fact that neutrons can proceed down this tube without scattering enhances their importance relative to those that are scattered in the surrounding shielding.

Specifications were drawn up for a neutron generator which was then purchased by the University. The one obtained was a Texas Nuclear, Model 9700. A shield and exposure facility were designed, the materials needed for it were obtained, the necessary structures were fabricated, the material is now being assembled at Hanford. Figure 2.16 is a sketch of approximately what the facility will look like. The neutron generator sits at the end of a shielding cave; it can be rolled out for adjustment and maintenance. The subject lies on stands that are also part

of the shielding. The stands roll in and out. They can be reversed and interchanged to change the orientation of the subject. The entrance to the cave is closed by a rolling door.

Preliminary studies have been made of the dosimetry. The neutrons apparently will be produced in a thin circular region of the target of the generator. It is assumed that they will be produced equally throughout this disk and calculations aimed at finding the most promising way of exposing the subject have been made. There is no problem for doses up to about 10 rad because the irradiated tissue can be placed far enough from the target to eliminate significant inverse square variations. For doses up to ten times that, however, the source must be put closer to the subject, and then different orientations used to compensate for inverse square variations. Completion of this work must await tests on the neutron generator to see if the neutrons do come from a uniform, circular disk. This cannot be done till the shield is completed. In the meantime, exposures of thermoluminescent dosimeters are being made with the Van de Graaff to have the technique under control when required for measurements in the facility.

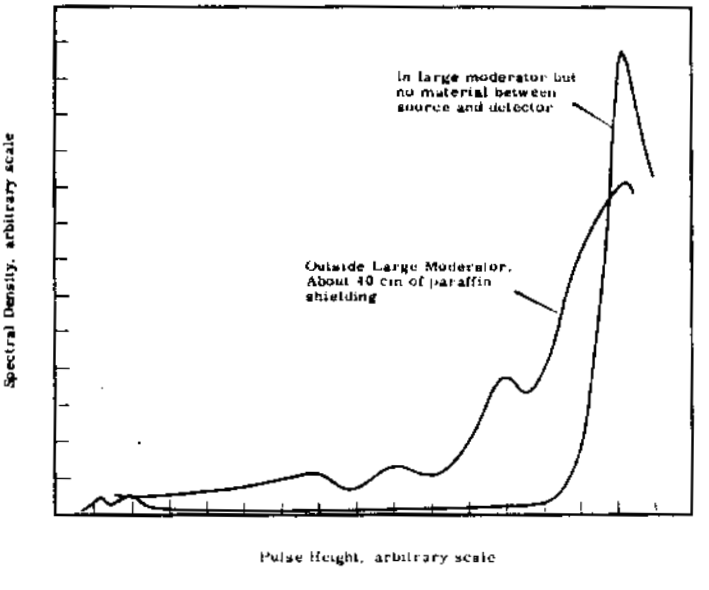

FIGURE 2.15

Neutron Pulse Height Spectrum from Stilbene Detector

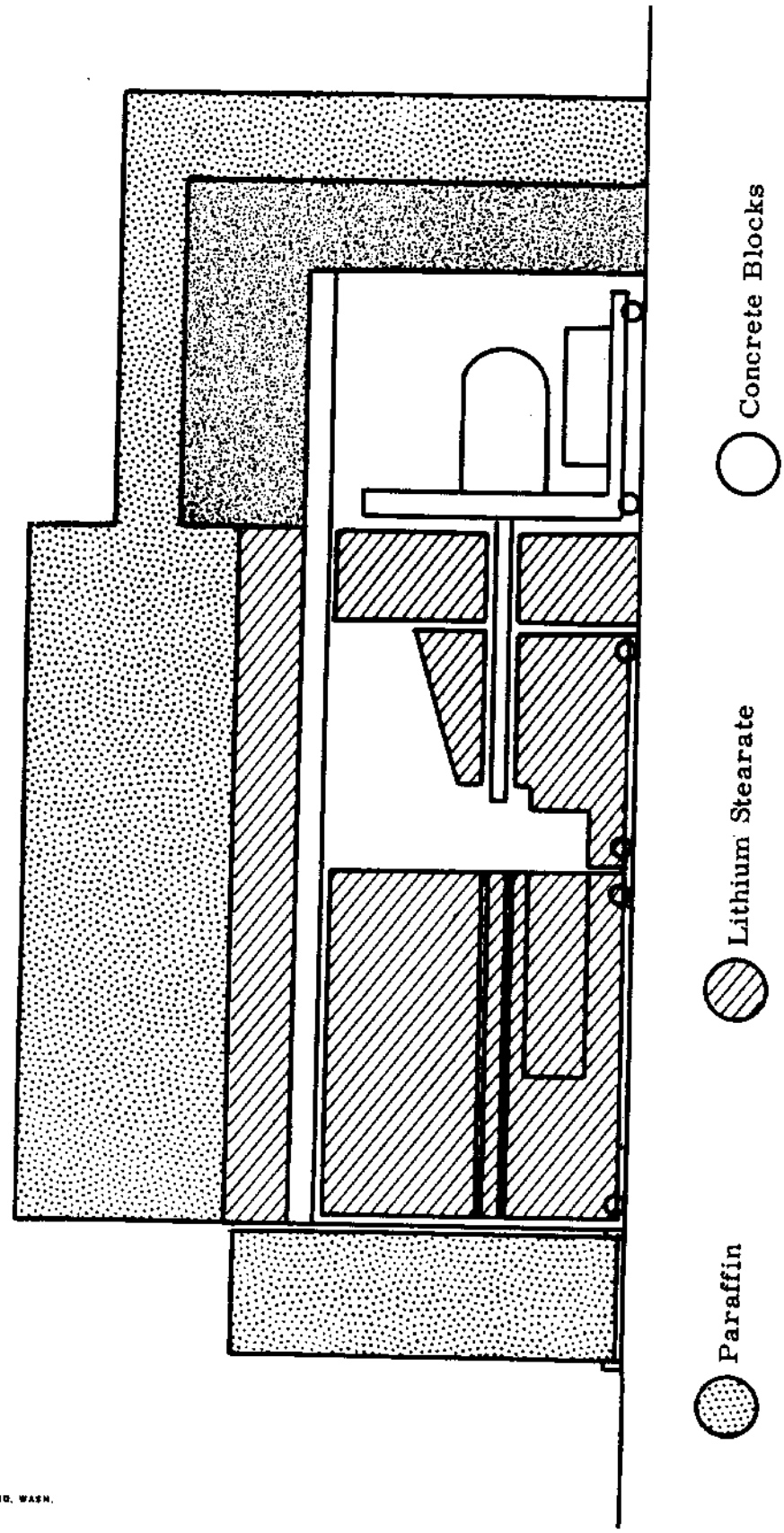

FIGURE 2.16
Fast Neutron Medical Research Facility

Fast Neutron Shielding - K. L. Swinth*

This paper reports measurements of the asymptotic transmission, Be^{-Lt}, of small shields of parafin, concrete bricks, and wood for 4.5 and 14.5 Mev neutrons.

In response to continued requests for information about small neutron shields, Hanford's Radiological Physics group is gathering experimental data on the shielding properties of common materials. Measurements are made as the need and opportunity arise. The transmission of paraffin, concrete bricks, and wood were measured to provide information needed in the design of the medical research facility for the University of Washington.

The Van de Graaff provided 14.5 Mev neutrons from the T(d, n) reaction and 4.5 Mev neutrons from the D(d, n) reaction. A precision long counter measured the neutrons that penetrated the shield. The counts obtained were divided by the integrated beam current to compensate for changes in Van de Graaff output.

In the first set of measurements the shields were about 4 ft^2 walls with the Van de Graaff target and the counter on the center line of the wall. The shields were wood (Douglas fir) and paraffin. Figure 2.17 shows the transmission curves for 14.5 Mev neutrons. Additional wood stacked around the target increased the neutron transmission for small, but not for large, shield thicknesses. For thicknesses of wood greater than 40 cm, the ratio of the counting rates with and without the shield was $2.2\ e^{-0.026t}$ (t is the thickness in cm). For more than 10 cm of paraffin, it was $1.8\ e^{-0.054t}$. The apparent decreased absorption at large thicknesses was due to neutrons that were scattered around the shield and counted.

In the second set of measurements paraffin and concrete bricks were used and an attempt was made to reduce the amount of shielding material needed. Figure 2.18a shows the transmission curves for 4.5 and

---

* University of Washington graduate student

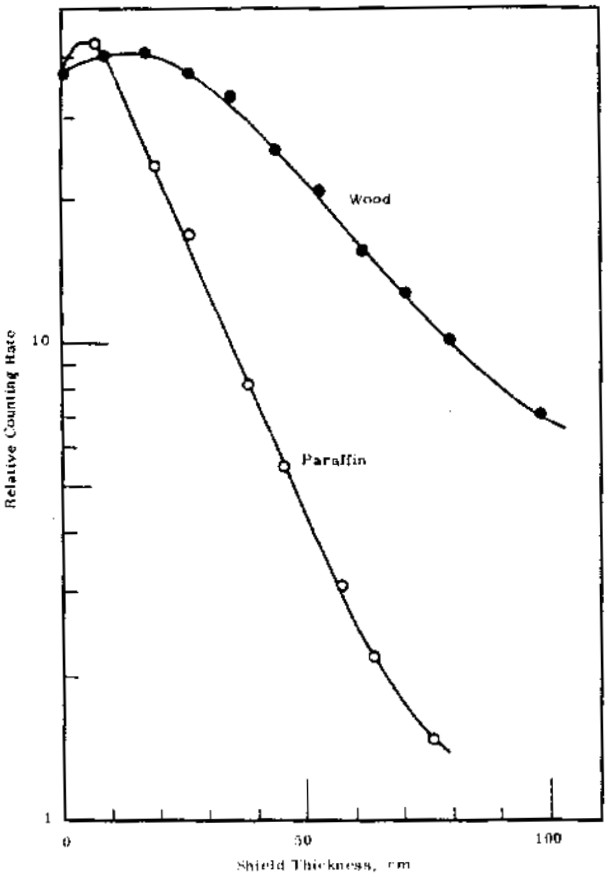

FIGURE 2.17
Fast Neutron Transmission

and 14.5 Mev neutrons for one cross sectional area of the shield. Figure 2.18b shows the transmission for two thicknesses of bricks and one of paraffin plotted against the inverse of the cross sectional area of the shield. When the asymptotic forms of the curves of Figure 2.18a are multiplied by the ratio, from Figure 2.18b, of the (extrapolated)

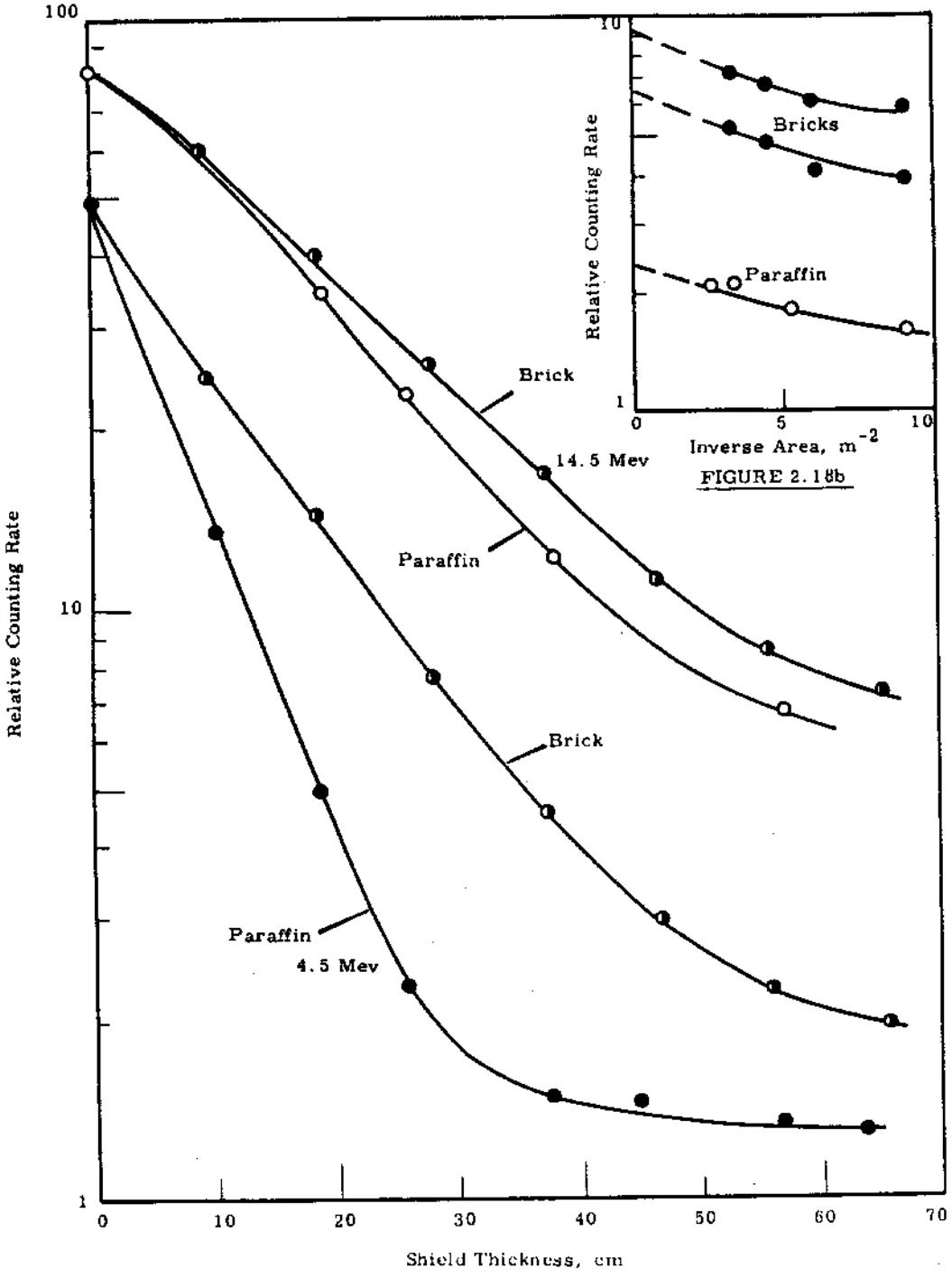

FIGURE 2.18b

FIGURE 2.18

a. Fast Neutron Transmission
b. Influence of Shield Area on Neutron Transmission

Half-Life of Sb^{124} - D. M. Fleming

The half-life of Sb^{124} reported last year (2.34) required correction for the presence of Sb^{125} in the sample. After sufficient time for radioactive decay, the percentage activity of the longer lived Sb^{125} was large enough to be measured by counting methods. The correction did not change the half-life from the original value of 60.20 ± 0.01 days.

The Heat Amplifier - D. M. Fleming and D. O. Allred

> The highest heat gain obtained from the heat amplifier, along with satisfactorily stable operation, was only about three.

In 1962 Myers and Fleming described (2.35) a heat amplifier that might be used to increase the sensitivity of calorimeters. They showed that amplification was possible but had not achieved successful stable operation. This paper describes a determination of the maximum gain that it appears possible to achieve with stable operation.

Figure 2.19 shows the gains determined as a function of the applied voltage for different values of the series resistance, R_s. What was actually measured were the thermistor currents with and without a heating coil operating in the calorimeter. The gains were determined from "load lines" much as in vacuum tube circuit analysis. A few actual measurements were made with series resistors to confirm the results. The steeper the gain curve , the more difficult it is to maintain a stable gain. When a gain curve does not exhibit a maximum, the instability results in a run-away behavior. The maximum stable amplification achieved was 3.35 with a 10 ohm series resistor.

In another experiment the heat amplifier was placed in dry ice to take advantage of more sensitive thermistor operation at lower temperatures. The results were similar to those shown in Figure 2.19.

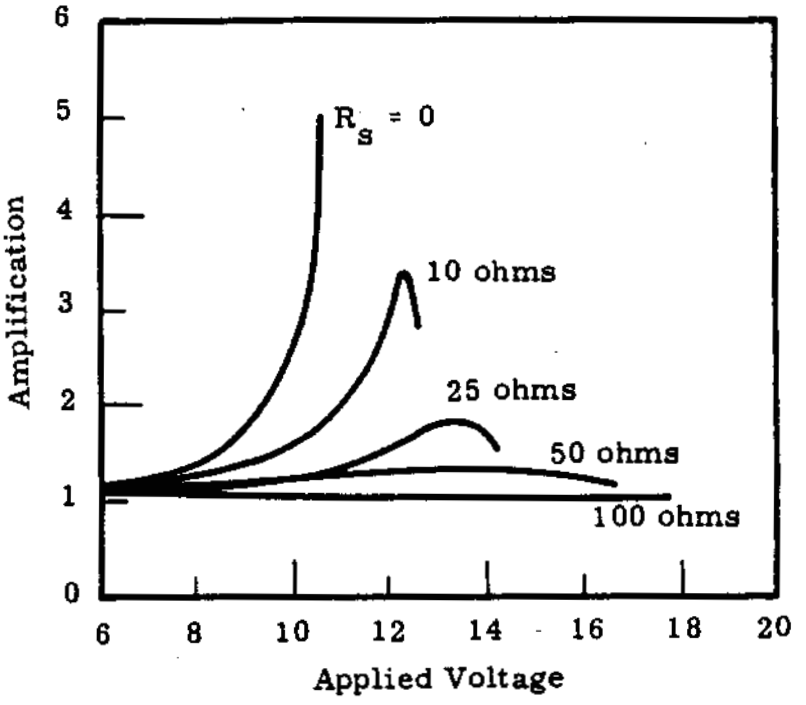

FIGURE 2.19
Heat Amplifier Characteristics

The Specific Power and the Half-Life of Pm^{147} - D. M. Fleming

The specific power of Pm^{147} is 0.330 ± 0.0007 w/g.
A preliminary value for its half-life is 2.68 yr.

Relatively large quantities of Pm^{147} became available by separation from Hanford wastes. Advantage was taken of this opportunity to make an accurate calorimetric determination of the power produced per unit mass by radioactive decay, the specific power, and of the half-life.

Two independently prepared samples were supplied by Hanford's Chemical Laboratory. Each was nominally 1000 curies. They were in the form of Pm_2O_3. Each specimen had been prepared by loading the oxide into an aluminum container which was sealed, decontaminated, and placed in a larger aluminum container which was welded shut.

A radiation calorimeter [2.36] was used for the measurements. It was operated isothermally. Temperature of the water bath was kept constant to within 10^{-4} C. The calorimeter was calibrated electrically with a heating coil in the place of the Pm^{147}. Small corrections were made for the nonlinearity of the thermistor when comparing the calibrating power with the power from the Pm^{147}.

The total powers for the two samples were 0.454 and 0.379 w. Dividing by the sample weight and correcting for the radioactive decay since the samples were prepared gave for the specific powers 0.331 and 0.330 w/g with an uncertainty of 0.0007 in both cases.

The samples have now decayed for approximately 1 yr and are being remeasured to provide a determination of the half-life. Preliminary data for one sample give a value of 2.68 yr.

Theory of Measurement in Beams - W. C. Roesch

> The average dose* rate in a beam of radiation smaller than an instrument equals the integral of the readings of the instrument in a plane perpendicular to the beam divided by the cross sectional area of the beam.

No matter how small a detector of radiation is made it seems there always comes a time when one wished to use it in a radiation field that is smaller than it is. Typically the field is a beam emerging from a hole in a shield. This paper gives a method for making such a measurement.

Figure 2.20 shows the profile of an instrument. The radiation is incident perpendicular to the X-Y plane. The reading of the instrument, R, is due to contributions from each part of the detector. Each contribution is proportional to the intensity of the radiation at that part, I(x, y). If the constant of proportionality, which may be different for each part of the instrument, is denoted by G(x, y), then

$$R = \int\int G(x, y)\, I(x, y)\, dx\, dy. \qquad (1)$$

---

* "Dose" here means exposure, kerma, or (absorbed) dose for equilibrium conditions.

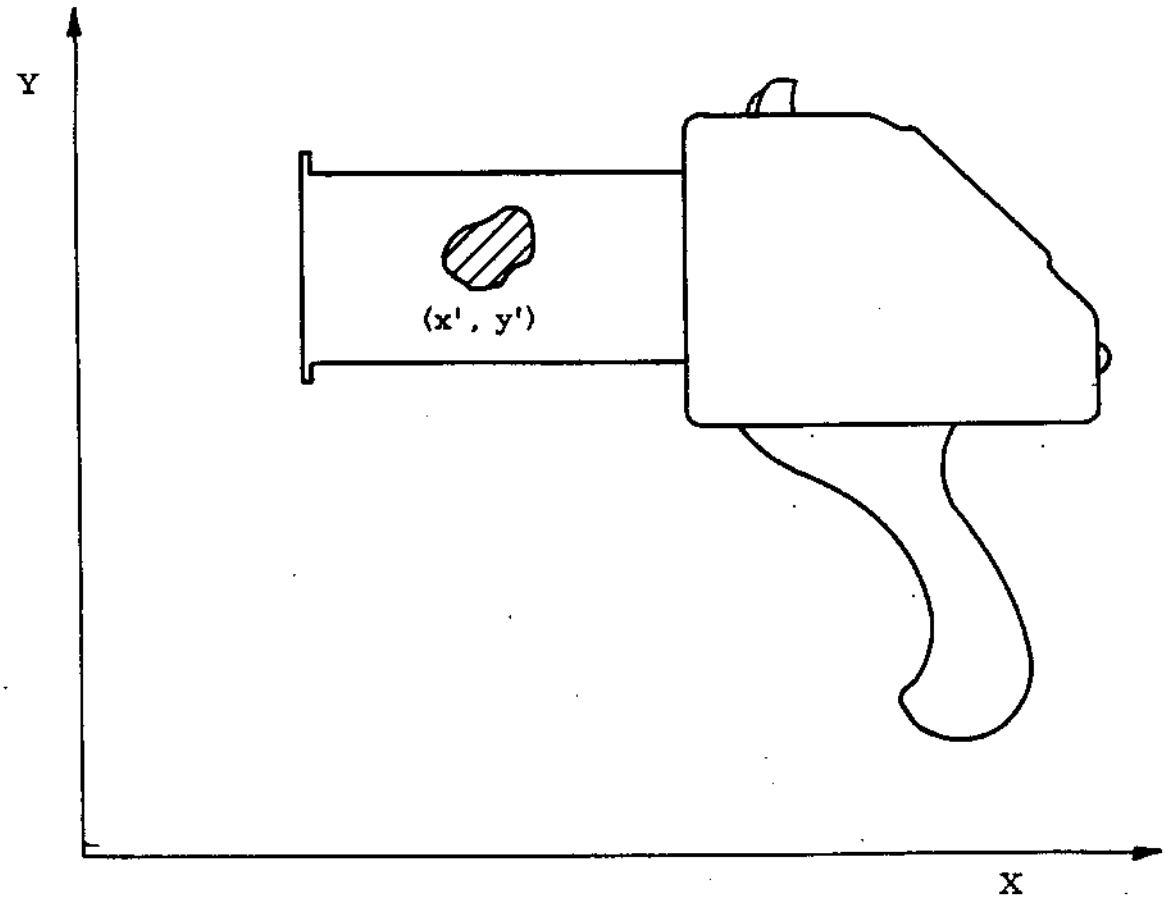

FIGURE 2.20

Coordinates Used in Theory of Measurement in Beams

AEC-GE RICHLAND, WASH.

The instrument is calibrated in a broad beam of uniform intensity, I_o, in which the dose rate is X_o. The reading of the instrument is made to equal X_o.

$$X_o = I_o \int\int G(x, y)\ dx\ dy. \tag{2}$$

The position of a beam of radiation is specified by giving the coordinates, (x', y'), of a particular point in the beam. The reading of the instrument depends on where the beam strikes it.

$$R(x',\ y') = \int\int G(x, y)\ I(x, y;\ x', y')\ dx\ dy. \tag{3}$$

When the readings are integrated over the values of (x', y') for which they are not zero,

$$\int\int R(x', y')\ dx'\ dy' = \int\int G(x, y)\ dx\ dy \int\int I(x, y;\ x', y')\ dx'\ dy'. \tag{4}$$

The integrals on the right can be separated because the first is X_o/I_o because of Equation (2), and the second is the average intensity in the beam, $\bar{I}$, times the area of the beam, A. Now, $X_o\ (\bar{I}/I_o)$ is the average dose rate, $\bar{X}$, in the beam, so

$$\bar{X} = (1/A) \int\int R(x',\ y')\ dx'\ dy'. \tag{5}$$

The measurement of the average dose rate is made by preparing suitable graphs of the readings of the instrument in a plane perpendicular to the beam, integrating these readings, and dividing the integral by the area of the beam. If the area of the beam is unknown, all that can be obtained from Equation (5) is the product of the average dose rate and the area; this may be all the information the experimenter really needs.

REFERENCES

2.1 H. E. Palmer, W. C. Hanson, B. I. Griffin, and W. C. Roesch. "Cesium-137 in Alaskan Eskimos," Science, vol. 142, pp. 64-66. 1963.

2.2 W. C. Hanson, H. E. Palmer, and B. I. Griffin. To be published in Health Physics.

2.3 H. E. Palmer and R. W. Perkins. "Cesium-134 in Alaskan Eskimos and in Fallout," Science, vol. 142, pp. 66-67. 1963.

2.4 K. Liden. "Cesium-137 Burdens in Swedish Laplanders and Reindeer," Acta Radiologica, vol. 56, pp. 237-240. 1961.

2.5 B. Meyer, J. Forrester, and M. C. Bell. "Effects of Three Cooking Methods on Cesium-134 Content of Beef from Orally Dosed Steers," Food Technology, vol. 16, pp. 110-112. 1962.

2.6 UT-AEC, Agricultural Research Laboratory. Semiannual Progress Report, July 1 - December 31, 1962. ORO-605, p. 61. 1962

2.7 Y. Naversten. "An Experimental Study on Human Uptake of Cs-137 from Meat," presented at Second Northern Meeting on Radioactive Food Chains, Helsinki, April 2-3, 1962.

2.8 H. E. Palmer, W. C. Hanson, and B. I. Griffin. "Cs^{137} Urinary Excretion by Alaskan Eskimos," Hanford Radiological Sciences Research and Development Annual Report for 1962, HW-77609. January 1963.

2.9 R. Rosoff, S. H. Cohn, and H. Spencer. "Cesium-137 Metabolism in Man," Radiation Research, vol. 19, pp. 643-654. 1963.

2.10 B. H. Scribner, J. M. Burnell, and A. L. Skinner. Syllabus for the Course on Fluid and Electrolyte Balance, University of Washington School of Medicine. 1960.

REFERENCES (Contd.)

2.11 C. E. Miller. Radiological Physics Division Semiannual Report, January - June, 1957, ANL-5755, p. 57. July 1957.

2.12 A. S. Relman. "The Physiological Behavior of Rubidium and Cesium in Relation to that of Potassium," Yale J. Biol. Med., vol. 29, pp. 248-262. 1956.

2.13 F. R. Mraz, M. LeNoir, J. J. Pinajian, and H. Patrick. "Influence of Potassium and Sodium on Uptake and Retention of Cesium-134 in Rats," Arch. Biochem. Biophys., vol. 66, pp. 177-182. 1957.

2.14 M. P. Taylor, J. Vennart, and D. M. Taylor. "Retention and Excretion of Cesium-137 by Man," Physics in Medicine and Biology, vol. 7, pp. 157-165. 1962.

2.15 H. C. Sherman. Chemistry of Food and Nutrition, Macmillan Co., New York, N.Y., 1946. 7th ed. pp. 626-630.

2.16 H. E. Palmer. "Retention of Isotopes," Research and Development Activities in the Radiological Sciences - 1961, p. 42. HW-73337, 1962.

2.17 B. I. Griffin and W. C. Roesch. "Plutonium X-ray Scintillation Counters," Hanford Radiological Sciences Research and Development Annual Report for 1962, HW-77609. January 1963.

2.18 W. L. Nicholson. Fixed Time Estimation of Counting Rates with Background Corrections, HW-76279. September 1963.

2.19 H. E. Palmer. "Detection of P^{32} In Vivo," Radiology, vol. 78, p. 115. 1962.

2.20 K. Liden and N. Starfelt. "Internal and External Bremsstrahlung Accompanying the Beta Rays of P^{32}," Phys. Rev., vol. 97, pp. 419-427. 1955.

REFERENCES (Contd.)

2.21 H. E. Palmer. "Determination of P^{32} in Vivo," Hanford Radiological Sciences Research and Development Annual Report for 1962, HW-77609. January 1963.

2.22 R. F. Foster. Evaluation of Radiological Conditions in the Vicinity of Hanford, January - March, 1962, HW-73366, p. 8. April 23, 1962.

2.23 H. E. Palmer. "The Shadow Shield Whole Body Counter," Research and Development Activities in the Radiological Sciences - 1961, HW-73337. 1962.

2.24 H. E. Palmer. "Shadow Shield Whole Body Counter," Hanford Radiological Sciences Research and Development Annual Report for 1962, HW-77609. January 1963.

2.25 L. L. Nichols and W. C. Roesch. "Pulse Shape Discrimination in Fast Neutron Dosimetry," Hanford Radiological Sciences Research and Development Annual Report for 1962, HW-77609. January 1963.

2.26 W. C. Roesch. "Surface Dose from Plutonium," Proceedings of the Second United Nations International Conference on the Peaceful Uses of Atomic Energy, vol. 23, pp. 339-345. United Nations, Geneva, 1958.

2.27 National Bureau of Standards, Handbook 75, Measurement of Absorbed Dose of Neutrons, and of Mixtures of Neutrons and Gamma Rays, U. S. Department of Commerce, Washington, D.C. 1961.

2.28 H. V. Larson. "A Sensitive Pocket Dosimeter Reader," Health Physics, vol. 4, pp. 233-235. 1961.

2.29 H. V. Larson, I. T. Myers, and W. C. Roesch. "Wide-Beam Fluorescent X-Ray Source," Nucleonics, vol. 13, no. 11, pp. 100-102. 1955.

REFERENCES (Contd.)

2.30 J. DePangher. "A Reproducible Precision Polyethylene Long Counter for Measuring Fast Neutron Flux," Research and Development Activities in the Radiological Sciences - 1960, HW-70050. January 16, 1961.

2.31 R. H. Ritchie, H. B. Eldridge, and V. E. Anderson. "Calculation of the Radiation Yield from Fission Assemblies and Comparisons with Experiments," In Selected Topics in Radiation Dosimetry, International Atomic Energy Agency, Vienna, Austria. pp. 657-666. 1961.

2.32 R. L. Bramblett, R. I. Ewing, and T. W. Bonner. "A New Type of Neutron Spectrometer," Nucl. Inst. Meth., vol. 9, 1-12. 1960.

2.33 D. E. Hankins. A Method of Determining the Intermediate Energy Neutron Dose, IDO-16655. March 10, 1961.

2.34 D. M. Fleming. "Calorimetric Determination of the Half-Life of Sb^{124}," Hanford Radiological Sciences Research and Development Annual Report for 1962, HW-77609. January 1963.

2.35 I. T. Myers and D. M. Fleming. "The Heat Amplifier - A New Technique in Calorimetry," Radiology, vol. 78, p. 111. 1962.

2.36 I. T. Myers, W. H. LeBlanc, and D. M. Fleming. "Precision Adiabatic Gamma-Ray Calorimeter Using Thermistor Thermometry," Rev. Sci. Inst., vol. 32, pp. 1013-1015. 1961.

RADIOLOGICAL CHEMISTRY

Radioanalytical Methods

Application of Multidimensional Gamma Ray Spectrometry -

R. W. Perkins

A multidimensional gamma ray spectrometry system has been devised that uses the coincidence gamma ray decay characteristic of radionuclides along with anti-coincidence shielding to provide extremely high sensitivity and selectivity. Its application in the measurement of reactor effluent water, fallout, and bioassay samples is discussed.

In the normal application of gamma ray spectrometry a single detector views a radioactive source. The amount of energy which each gamma ray loses in the detector is recorded by the spectrometer which provides an energy loss, or gamma energy spectrum of these interactions. Gamma rays which lose less than their full energy in the detector are, of course, recorded in the less than full energy portion (Compton continuum) of the gamma energy spectrum. In the quantitative measurement of radionuclides in a complex radionuclide mixture, the Compton events drastically reduce both the precision and sensitivity of the measurement of many radionuclides. Much of this Compton interference can be removed by anti-coincidence shielding techniques.(3.1)

Radionuclides which emit two or more gamma rays per disintegration can often be measured with much better precision and sensitivity by coincidence counting techniques. The counting arrangements normally involve placing the sample between two detectors and with appropriate coincidence equipment measuring the conicidence counting rate of the characteristic photon energies. This technique is routinely applied to the direct measurement of trace amounts of Cu^{64}, Sc^{46}, and Co^{60} (3.2) in Hanford waste streams; however, its selectivity is limited, and it is necessary that the sample composition be reasonably well known since other coincidence events may cause interference.

The recent availability of multidimensional pulse height analyzers with a large memory capcity have made multidimensional gamma ray

spectrometry practical. The spectrometry system used in this study was a Nuclear Data 4096 channel analyzer used in a 64 by 64 channel grouping arrangement in conjunction with two, anticoincidence shielded, 4 in. thick by 6 in. diameter, NaI(Tl) detectors (Figure 3.1). The analyzer unit is supplied with an Optikon unit which permits a very rapid readout of the entire memory.

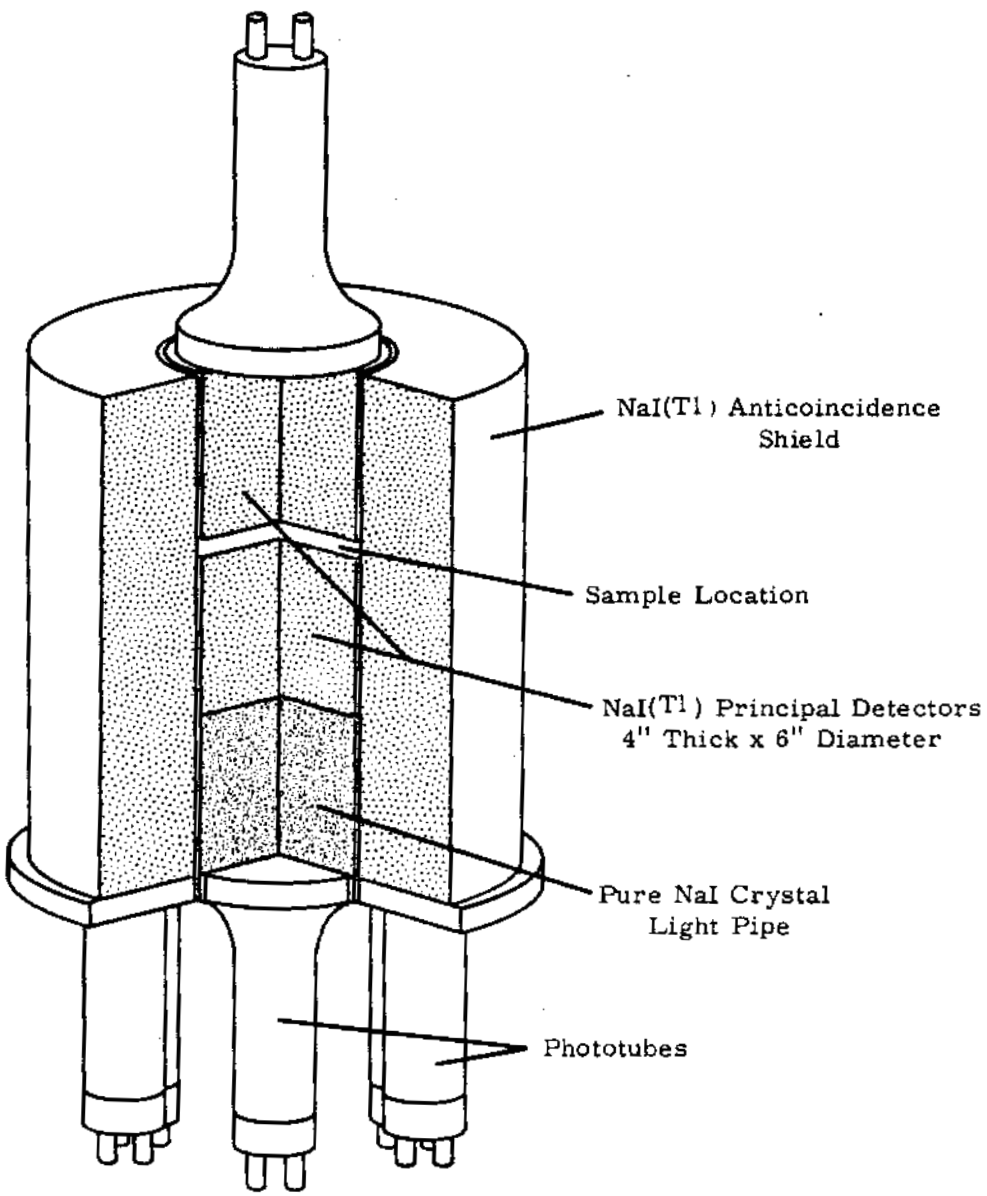

FIGURE 3.1
Detector System for Multidimensional Gamma Ray Spectrometer

A Tally paper tape readout is used as a readout for computer calculation. The sample to be measured is sandwiched between the 6 in. diameter detectors. The signals from the two detectors are fed to the separate analog-to-digital converters of the analyzer for energy analysis and from there to the memory storage unit. When a single photon interacts with one of the detectors, the event is stored on either the X or the Y axis of the memory. When two photons are emitted simultaneously, each interacting with a separate detector, the event is stored in an energy-energy plane at a point uniquely characteristic of the two energies. The spectra in Figures 3.2, 3.3, and 3.4 illustrate the manner of storage. With a detection system of this type the unique decay characteristic of many radionuclides are readily resolvable thus permitting a far greater sensitivity for detection and direct measurement of many minor radioactive constituents.

In addition to the much greater selectivity provided by this multidimensional analysis, a much lower background (100 to 1000 fold lower) is obtained.

It is difficult to present in three dimensions, a pictorial illustration of the applications; however, the measurement of Cu^{64} in Hanford reactor effluent water provides a reasonable example. In Figure 3.5 the normal spectrum of effluent water is compared with the multidimensional spectra. It is evident that where Cu^{64} cannot be measured from the normal spectrum it is easily measured from the multidimensional spectrum. The other prominent peaks are due to Na^{24}, As^{76}, Ga^{72}, La^{140}, Sc^{46}, Co^{60}, Sb^{124}, and Ba^{140} cannot be precisely measured directly from the normal gamma ray spectra of effluent water but are readily measured from the multidimensional spectra. As^{76} is measured from its 0.55 and 0.65 Mev photon cascade. Ga^{72} is measured from its 0.84 and 2.20 or 2.51 Mev cascade. La^{140} is measured from its 1.60 and 0.486 or 0.815 Mev cascade (Figure 3.3). Ba^{140} is measured from these same peaks after the excess 40 hr La^{140} has decayed. Sb^{124} is measured from its 0.603 and 1.69 Mev cascade. Sc^{46} is measured from its 0.892 and 1.118 Mev cascade (Figure 3.4), and Co^{60} from its 1.17 and 1.33 Mev cascade. The measurement of much of the natural

radioactivity in soils is easily accomplished with the multidimensional analyzer. The Th^{232} series back through Th^{228} can be directly measured from 2.61 and 0.583 Mev cascade of Tl^{208} (Figure 3.6). The uranium series back through Ra^{226} is readily measured from 0.607 Mev and 0.77 or 1.12 Mev cascade (Figure 3.7).

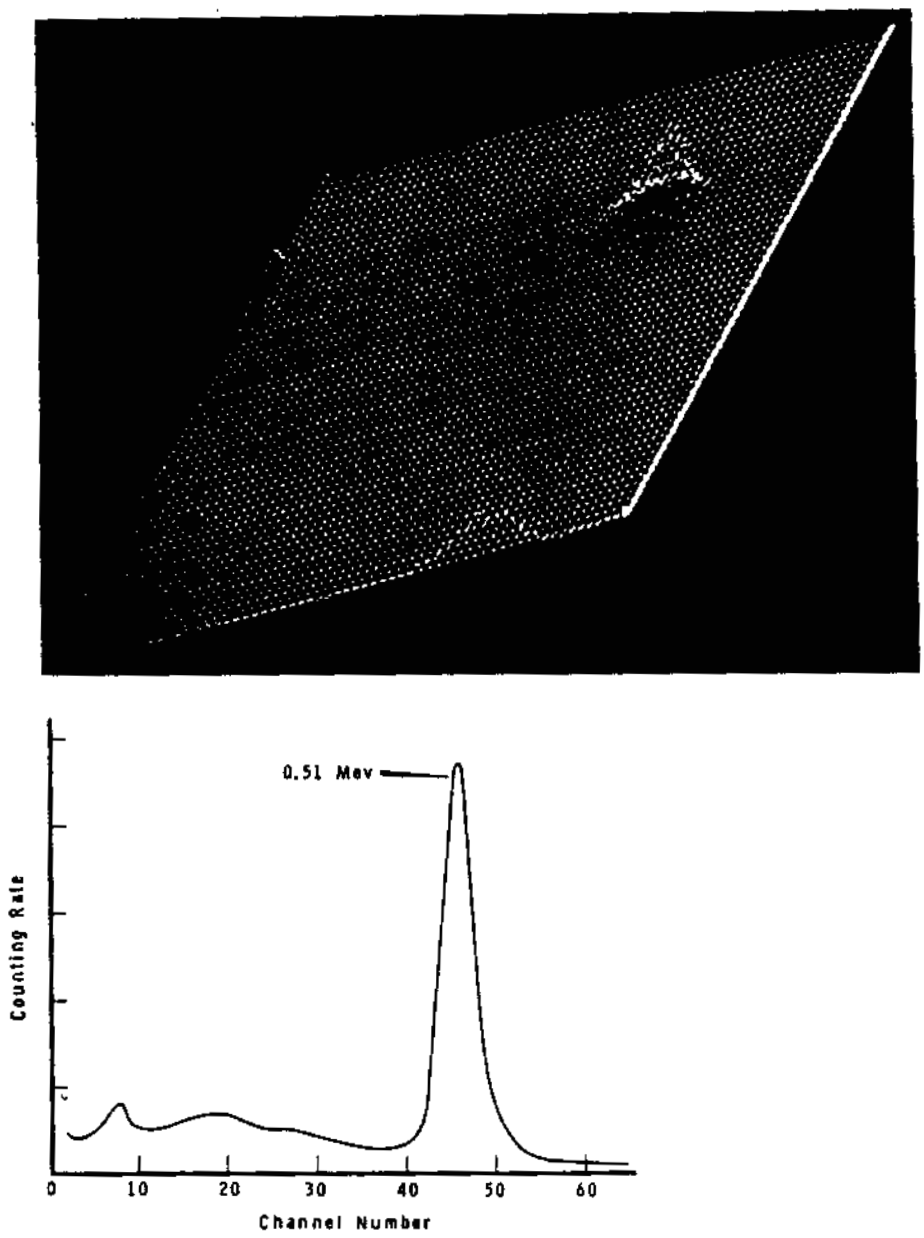

FIGURE 3.2

Cu^{64} Spectra

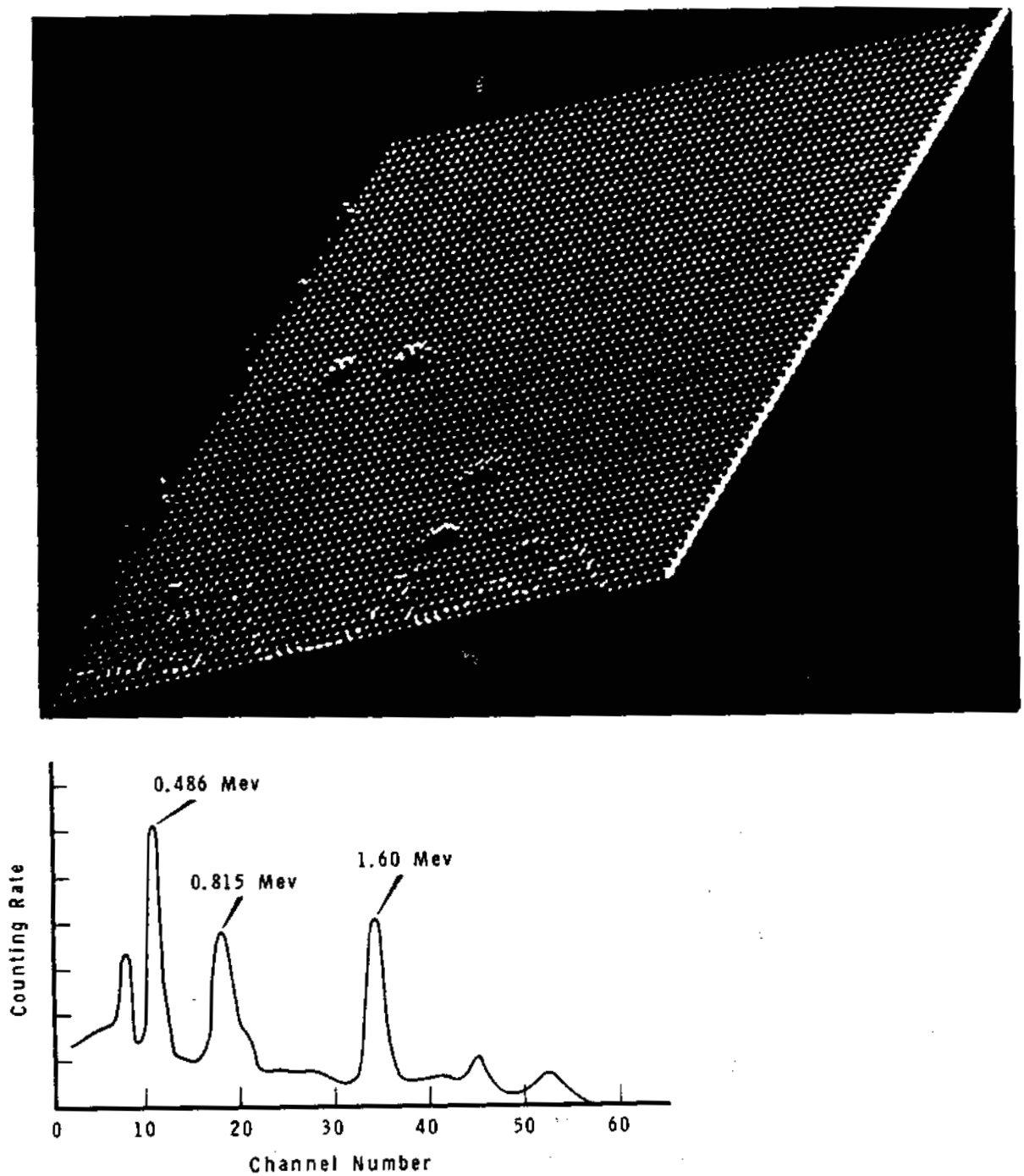

FIGURE 3.3

La^{140} Spectra

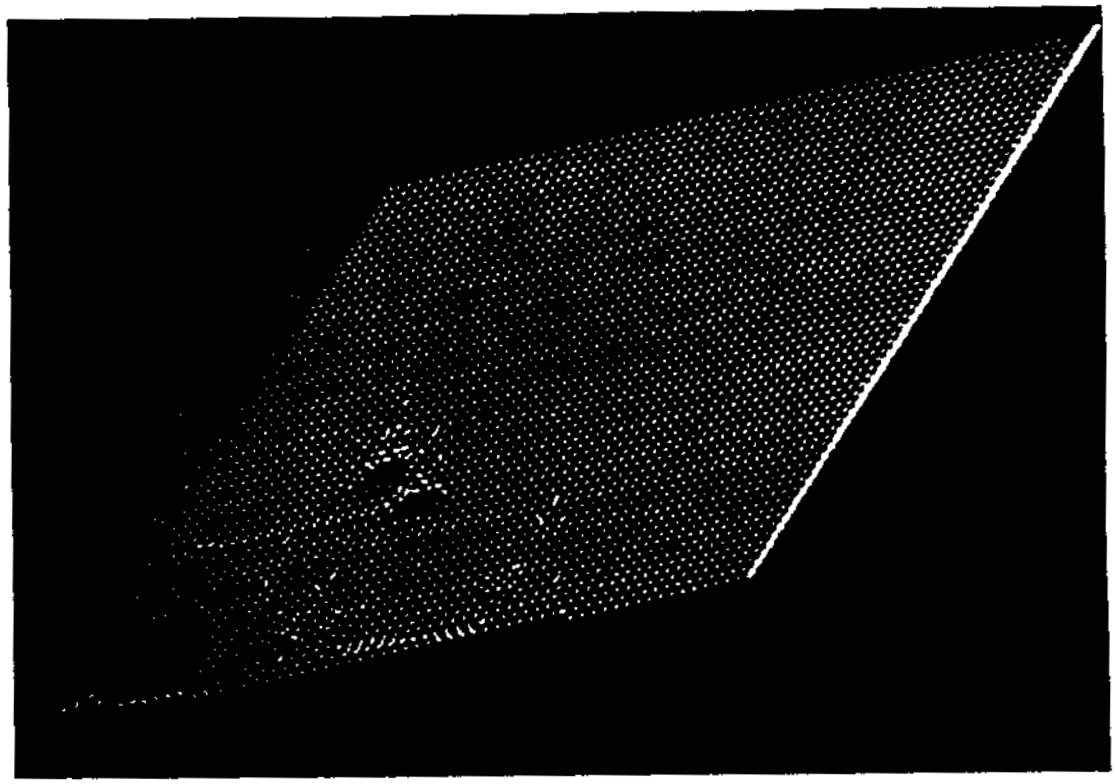

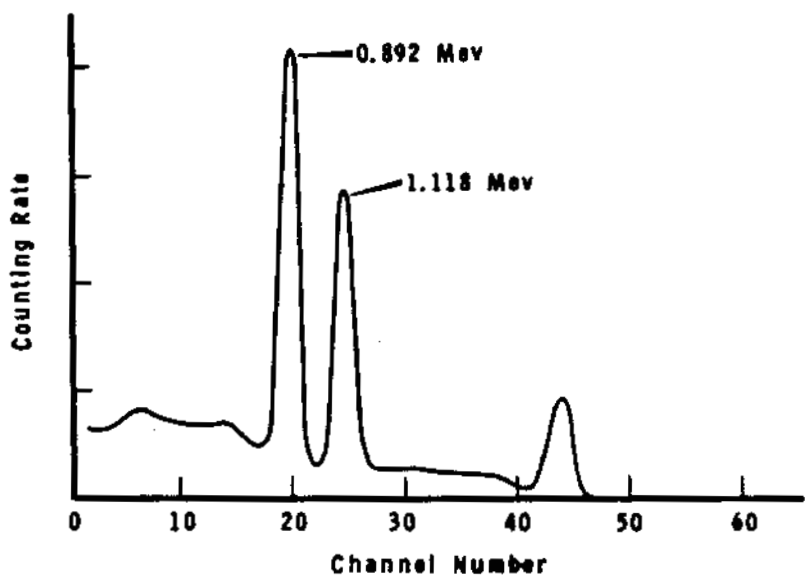

FIGURE 3.4

Sc^{46} Spectra

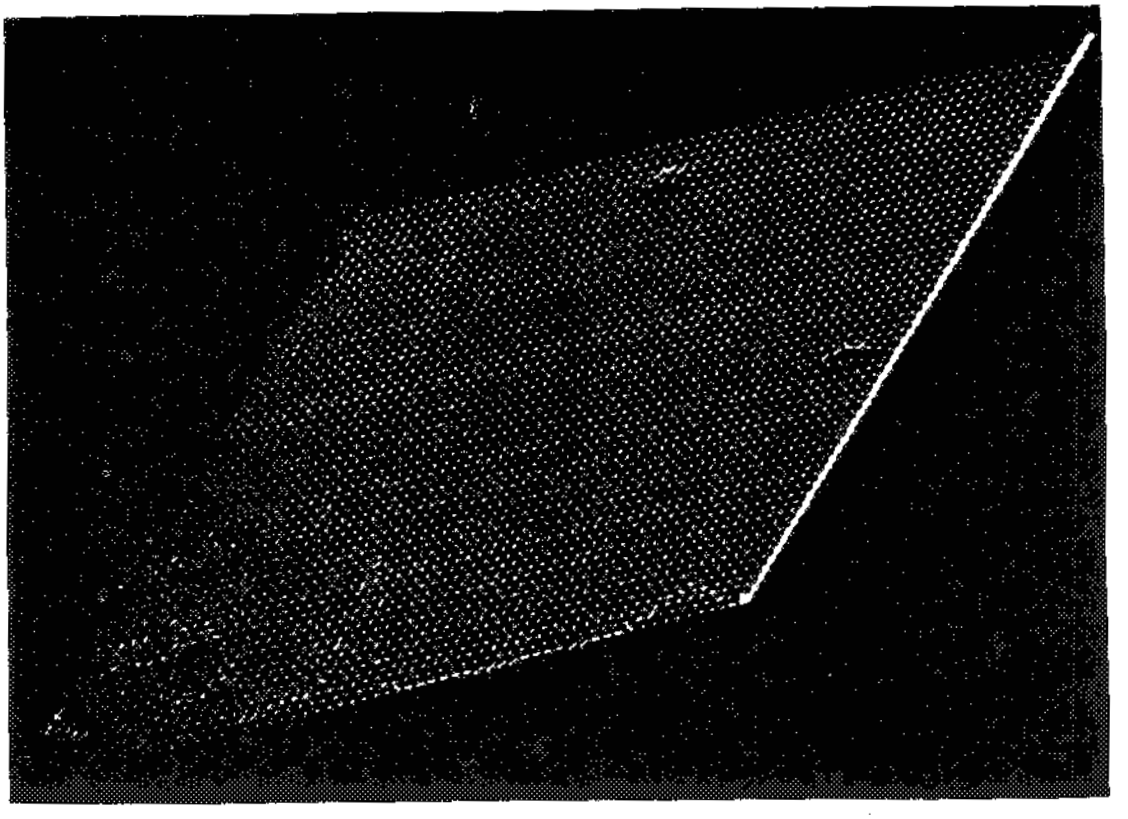

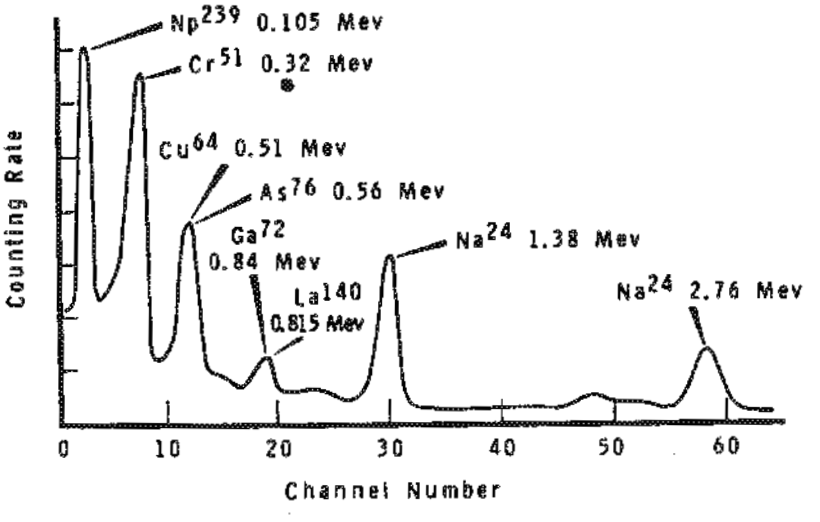

FIGURE 3.5

Reactor Cooling Water Gamma Ray Spectra

AEC-GE RICHLAND, WASH.

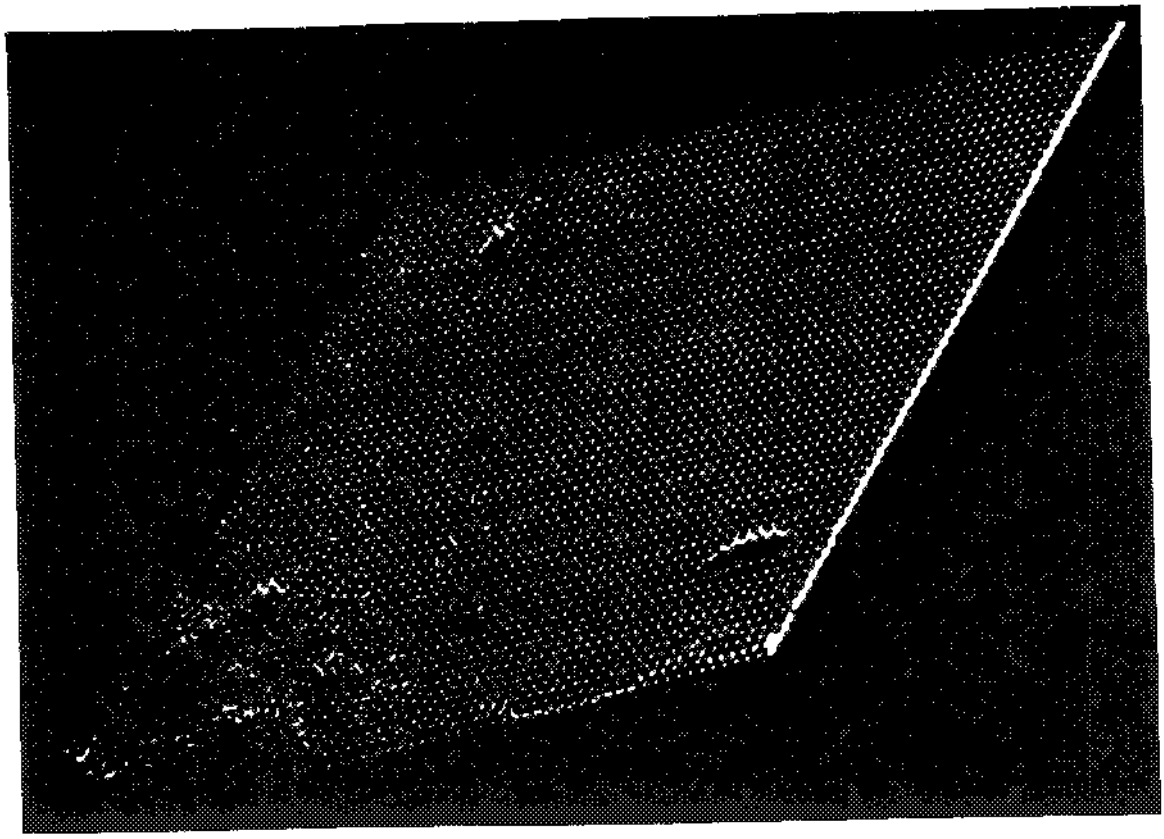

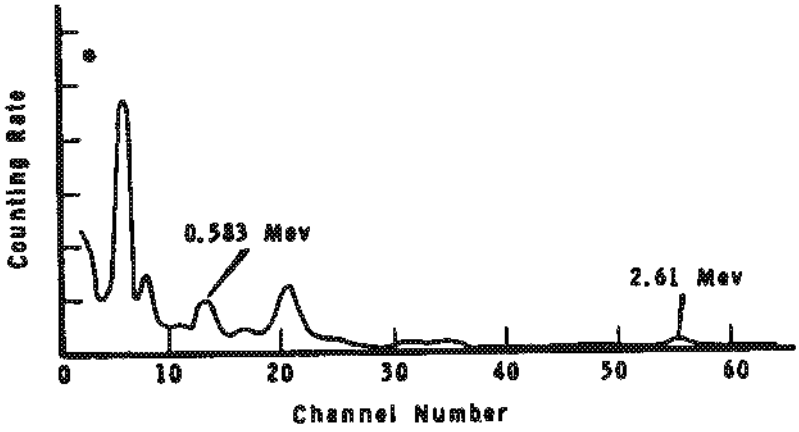

FIGURE 3.6

Thorium Chain Spectra

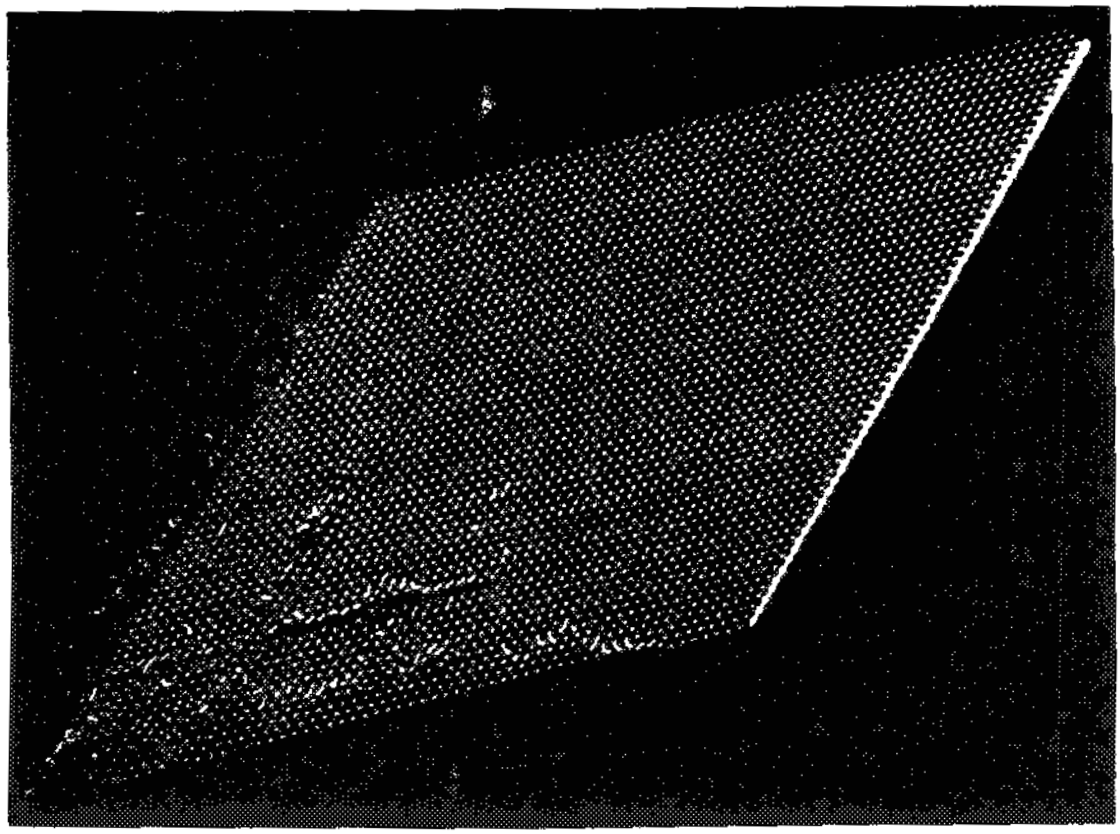

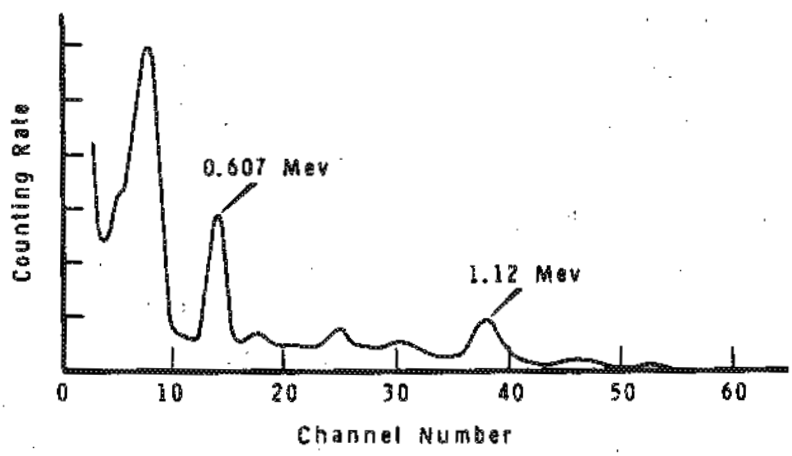

FIGURE 3.7
Uranium Ore Spectra

The measurement of fallout radionuclides is a very practical application of multidimensional spectrometry. In air filter samples containing fallout material collected during the past 2 yr it has been possible to make direct measurements of Na^{22}, Mn^{54}, Co^{60}, Y^{88}, Zr-Nb^{95}, Ru^{106}, Cs^{134}, Cs^{137}, and Ce^{144} from a single spectrum.* All of the radionuclides except Mn^{54}, Zr-Nb^{95}, and Cs^{137} are measured with little or no Compton interference by using the coincidence counting rate of the cascade photons. An additional very practical application is in the analysis of bioassay urine samples. The direct measurement of the short and long lived radionuclides has been made by this technique and is discussed in this report.** A problem in multidimensional measurements is that some of the single gamma rays which interact with one of the crystals are backscattered and absorbed in the second crystal thus producing a signal from each detector. These events are stored in the energy-energy plane of the memory as coincidence events and may interfere in the measurement of other radionuclides of interest. To minimize this interference, lead absorbers are used which cover all of the area between the crystals except where the sample is placed. In practice a 6 3/8 in. diameter by 1 in. thick lead absorber with a center hole the size of the sample (1 or 2 in. diameter) is used. This reduces back scatter from monogamma emitters such as Zn^{65} and K^{40} by 10 to 100 times in various regions and also reduces the background counting rate. With a point source sample in the 1 in. thick lead absorber and 1 in. center hole (beveled at 45° out to the flat surfaces from the middle of the center hole) the counting efficiency of Zn^{65} and Co^{60} are reduced to 0.7 and 0.5 (coincidence peak) relative to a geometry with no lead absorber and the crystals touching the source. The background reductions which are provided by various thicknesses of lead absorbers as well as by the anticoincidence shielding of the annulus are shown in Figures 3.8 and 3.9. Figure 3.8 presents backgrounds for a diagonal of the energy plane giving the coincidence background as a function of equal energies on each axis. Figure 3.9 presents the background for constant energy on one axis (0.5 Mev) but as a function of energy on the second axis.

---

* See "Fallout Studies," page 3.51.

** See "Bioassay Measurements by Multidimensional Gamma Ray Spectrometry, Page 3.12.

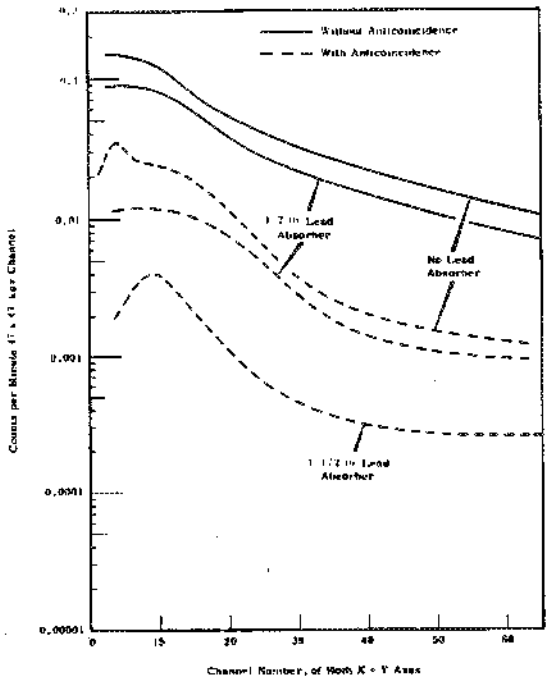

FIGURE 3.8

Background Measurements on a Diagonal from 0 to 3 Mev with Different Coincidence and Absorber Conditions

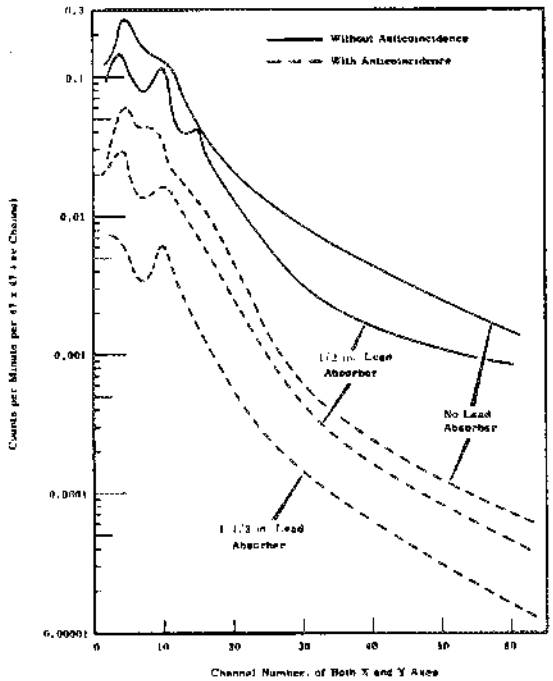

FIGURE 3.9

Background Measurements at 0.5 Mev on the Y Axis and 0 to 3 Mev on the X Axis

Although a main advantage of multidimensional analysis in gamma ray spectrometry is that it permits the direct measurement of many radionuclides which would otherwise require chemical separations, it also provides a generally greater sensitivity in the measurement of all radionuclide mixtures. As an example the increase in sensitivity provided for the measurement of the cascade gamma emitters Cu^{64} and Sc^{46} and the monogamma emitters Cs^{137} and Zn^{69m} in the presence of 10^5 disintegrations/min of Na^{24} has been calculated and are recorded in Table 3.1. The values compare sensitivities for measurements on a single 4 in. thick by 6 in. diameter crystal with that for the multidimensional system.

TABLE 3.1

SENSITIVITY IMPROVEMENT WITH MULTIDIMENSIONAL ANALYSIS FOR MEASUREMENTS IN THE PRESENCE OF 10^5 disintegrations/min of Na^{24}

Radionuclide	Sensitivity Improvement Factor
Cu^{64}	6
Sc^{46}	4
Cs^{137}	3
Zn^{69}	3

The present detector system, although excellent for multidimensional analysis, is not optimum for all sample types. If all sources to be analyzed were of near point source dimensions, a much lower Compton region on the X and Y axis and in the energy-energy plane could be obtained by extending the anticoincidence shield between the two principal detectors and by minimizing the internal crystal cladding.

Bioassay Measurements by Direct Counting on a Multidimensional Gamma Ray Spectrometer - R. W. Perkins

Bioassay measurements of urine samples from residents of Richland, Washington, by multidimensional gamma ray spectrometric counting techniques have shown the presence of several of the reactor effluent water and fallout radionuclides.

The direct measurement of natural or artificial radionuclides in either whole or ashed bioassay samples has had limited application because of both the relatively large amounts of natural K^{40} which are present and their overall low radioactivity levels. The normal presence of K^{40} with its characteristic high energy gamma radiation (1.47 Mev) drastically limits sensitivities for the direct gamma ray spectrometric measurement of other trace radionuclides. The decay of most radionuclides involves the emission of two or more photons in cascade, and the coincidence measurement of the characteristic photon energies of a given radionuclide provides a unique indication of its presence as well as a measure of its abundance. For the study of trace radionuclides in bioassay samples, an ultra low background multidimensional gamma ray spectrometer system has been devised.

This counting system is described in detail elsewhere in the report.*

Sample preparations involve evaporating the sample to dry salts and pressing them into a flat, standard geometric arrangement for counting. In preliminary studies it has been possible to measure the concentrations of Na^{22}, Na^{24}, Sc^{46}, Co^{60}, Cu^{64}, Zn^{65}, Cs^{134}, Cs^{137}, and Th^{232} (from the Tl^{208} daughter). The radionuclides Na^{24}, Sc^{46}, Co^{60}, Cu^{64}, and Zn^{65} are present in reactor effluent water and are directly available to people through drinking water and indirectly through foods irrigated with this water. The radionuclides Na^{22}, Cs^{134}, and Cs^{137} are present in fallout. Na^{22} is produced by cosmic ray spallation of argon as well as in nuclear detonations. Th^{232} is, of course, a natural radionuclide and is taken into the body in foods. Studies are presently underway which will relate observed levels of these radionuclides in bioassay samples to levels in various foods, water, and body burdens.

---

* See "Multidimensional Gamma Ray Spectrometry," page 3.1.

Background Reduction in Gamma Ray Spectrometry - R. W. Perkins

Background reduction of up to one order of magnitude has been obtained by a combination of anticoincidence shielding and light pipe shielding of the crystal from its phototubes.

The major obstacle in the measurement of trace amounts of radionuclides such as those found in environmental materials is the natural background counting rate of the detector. During the past year an elaborate three-crystal detector system was obtained for multidimensional gamma-ray spectrometry studies and this detector system was made available for these background studies. The normal background counting rate seen by a NaI(Tl) detector comes from

- Natural radioactivity in the crystal
- Radioactivity in its crystal cladding and its photomultiplier
- External gamma radiation and cosmic rays.

The three-detector system was obtained from the Harshaw Chemical Company and has been described in detail with illustrations.* Figure 3.10 shows four background measurements made with a 6 in. diameter and 4 in. thick NaI(Tl) detector. All of the measurements were made in a 4 in. thick lead shield. The top curve is the background from the normal crystal. The next curve down is the background obtained with the pure NaI light pipe between the crystal and its phototube and represents about a 20 to 50% background reduction. The bottom two curves are background measurements of this crystal placed inside the annulus and with a second 6 in. diameter by 4 in. thick crystal above it as shown in Figure 3.10. It is evident that the background is reduced simply by the NaI shielding in this arrangement. When the output pulses from the annulus and top crystal are connected in anticoincidence with the principal detector, a very substantial and desirabel reduction is obtained ranging from a factor of 5 to 10 except at the K^{40} peak. It should be pointed out that the background reduction of 20 to 50% obtained by use of the light pipe is extremely important if one is trying to

* See "Multidimensional Gamma Ray Spectrometry," page 3.1.

obtain maximum background reduction by anticoincidence shielding. This fraction of the original background is due to the phototube and is not effectively removed by anticoincidence.

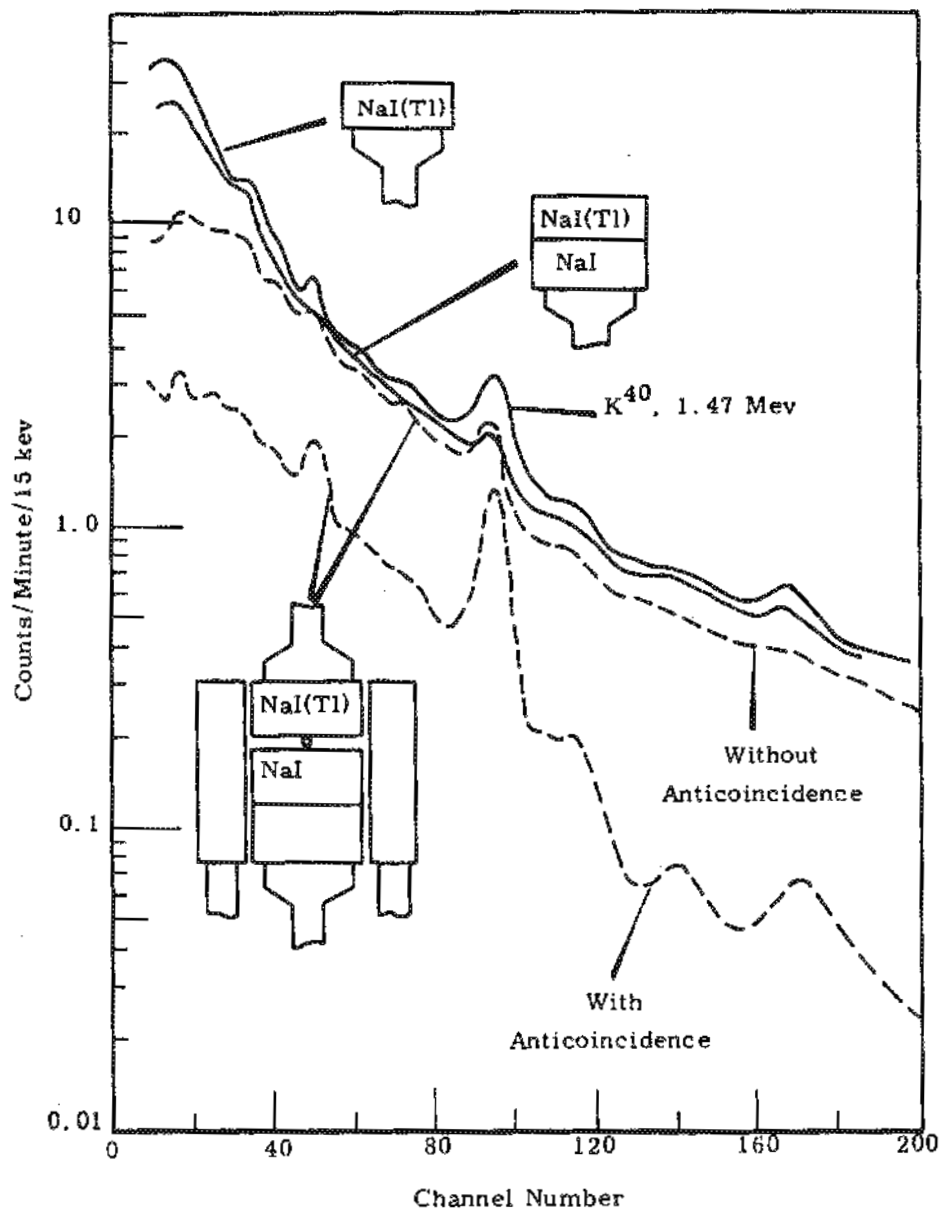

FIGURE 3.10

Background Measurements of a 4 in. Thick by 6 in. Diameter Crystal in a 4 in. Lead Shield

Uranium Ore Dust Inhalation Studies - T. M. Beasley

Sensitive radiochemical techniques have been developed for the determination of uranium and thorium in rat tissue following inhalation of uranium ore dust. Radiochemical yields from spiked samples show good recoveries (> 94%) for both uranium and thoriun with excellent decontamination from other uranium daughters. Preliminary results from exposed rats indicate a significant retention of thorium versus uranium in the rat lungs.

In conjunction with Hanford's Biology Laboratory, a study is being made of the tissue distribution of uranium and its daughter products following inhalation of uranium ore. Recent revisions in the recommended Maximum Permissible Concentration in air (MPC_{air}) for uranium ore have led to a value about 1/3 that of the former limit. The new value is due in large part to the assignment of a low MPC_{air} for Th^{230} (1×10^{-11} microcuries/cm^3), a daughter product of U^{238}. As an initial part of the study, thorium:uranium ratios were desired to determine which, if either, is preferentially solubilized and transported from the lung.

Direct determination of the uranium and thorium content of animal tissues using large area alpha ray spectrometers [3.3, 3.4] is complicated by the presence of Ra^{226} in the uranium decay series. Figure 3.11 shows an alpha energy spectrum of 300 micrograms of the uranium ore used for the inhalation study.[3.5] While uranium could be quantitatively determined from the 4.182 Mev alpha energy peak, no distinction between Th^{230} and Ra^{226} is possible from the spectrum. Radiochemical procedures are necessary, therefore, to separate uranium, radium, and thorium from one another and from other members of the uranium decay series.

A review of the radiochemistry of uranium and thorium [3.6, 3.7] suggested that the uranium could best be isolated from the thorium and radium by liquid-liquid extraction of the uranium by tertiary amines from an HCl media.[3.8] Uranium is quantitatively extracted into the amine (> 98%) while thorium and radium remain in the aqueous phase. Thorium is then isolated from the radium by a lanthanum fluoride precipitation and 2-thenoyltrifluroacetone extraction after the method of Perkins and

Kalkwarf.[3.9] Finally, radium can be determined by sensitive gamma-ray spectrometric measurements following attainment of secular equilibrium with its daughter products, the latter requiring about 38 days.

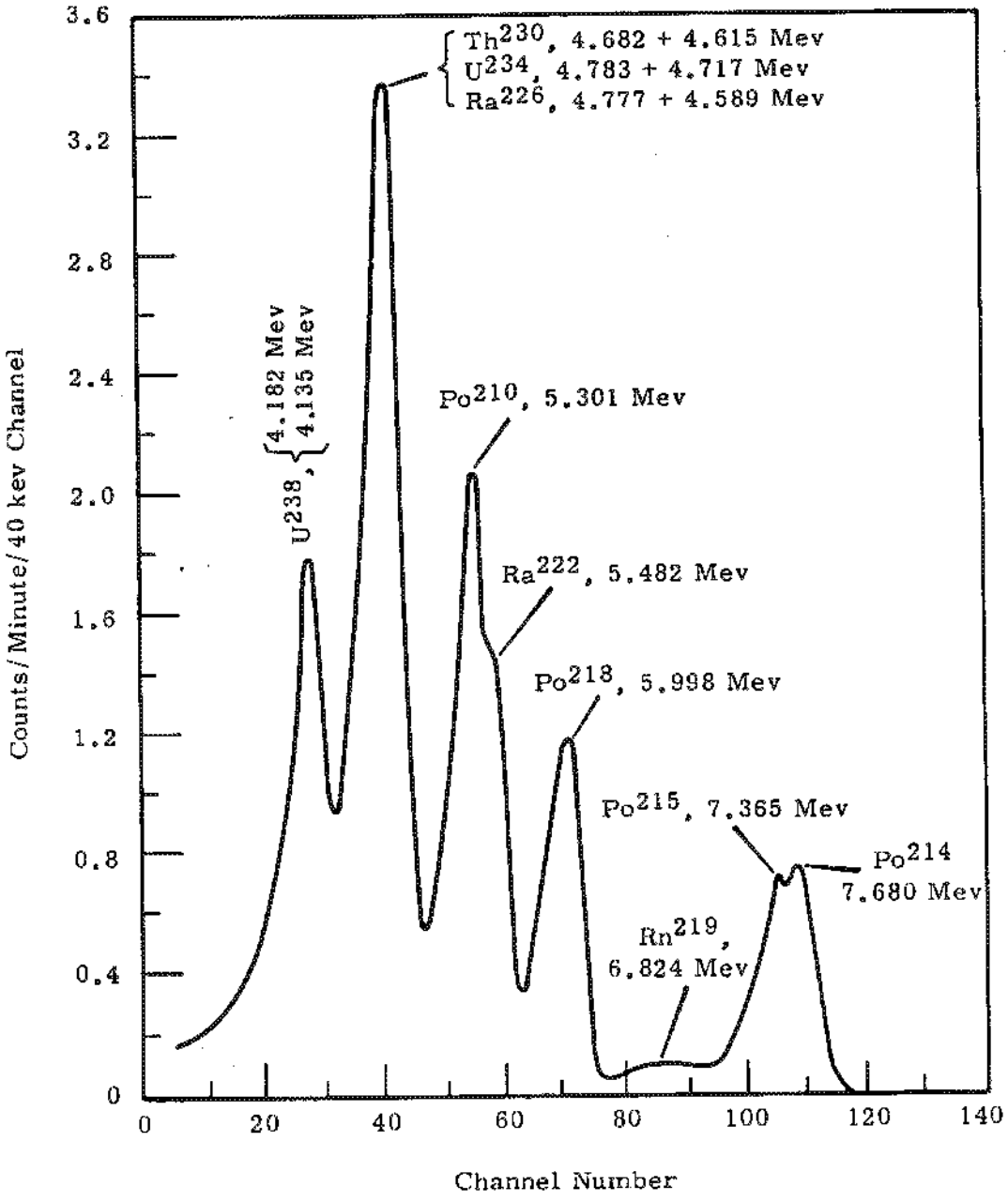

FIGURE 3.11

Alpha Energy Spectrum of 300 Micrograms of Finely Ground Uranium Ore as Measured in a Frisch Grid Chamber

Experimental

Ashing of the tissue samples is accomplished using a Tracerlab Low Temperature Asher (LTA-500). In the asher, ionized and atomic oxygen produced by a high frequency electromagnetic field is used as the oxidant. Sample temperatures during the ashing procedure are below 150 C, thus minimizing the formation of refractory compounds of uranium and thorium. Dissolution of the resulting ash is with 6M HNO_3.

Recovery and reproducibility of the procedures used for determining the uranium and thorium content of the tissues were tested using U^{233}, U^{235}, and Th-Pa^{234} tracers. Uranium is separated from the thorium and radium by liquid-liquid extraction using the long chain tertiary amine, "Alamine-336"* dissolved in xylene. The uranium is extracted from a 7M HCl solution with an equal volume portion of a 20% solution of amine and stripped from the organic solution with two equal volume portions of 0.1M HNO_3, and the back extractant is evaporated to dryness under a heat lamp. The residue is dissolved in a 20:1 glacial acetic acid-HNO_3 (conc.) solution and plated on a 1 1/2 in. stainless steel planchet for total alpha counting or for alpha energy analysis using Frisch Grid Chamber counting. Average uranium recoveries of 98.2% are obtained using the tracers mentioned above. Recoveries of macroquantities of uranium (9 to 44 mg) are also quantitative.

Thorium is recovered from the 7M HCl solution by coprecipitation on lanthanum fluoride. The fluoride precipitate is transferred to a small beaker and taken to dryness under a heat lamp in the presence of concentrated $HClO_4$. Thorium is purified by liquid-liquid extraction using 2-thenoyl-trifluroacetone in xylene by methods previously described.[3.9] Average thorium yields through the procedure are 94%, a value which is in good agreement with the findings of other investigators using a similiar thorium procedure.[3.10] Figures 3.12 and 3.13 show alpha energy spectra of the

* Tricaprylamine, General Mills Company, Kankakee, Illinois

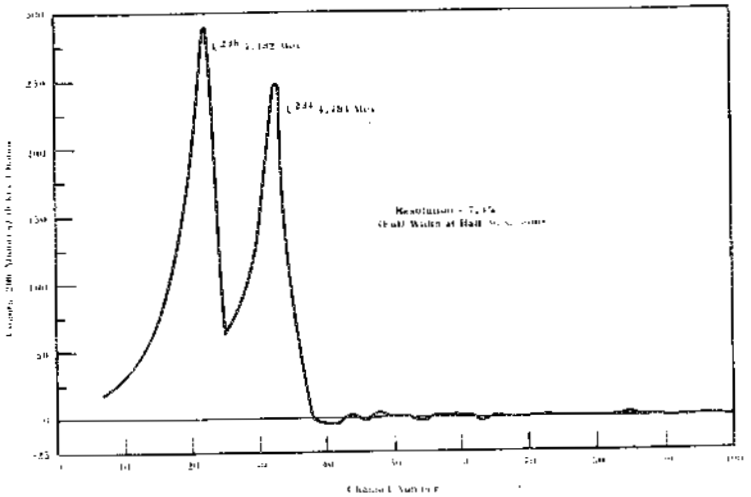

FIGURE 3.12

Alpha Energy Spectrum of Uranium Separated from Tissue as Measured in a Frisch Grid Chamber

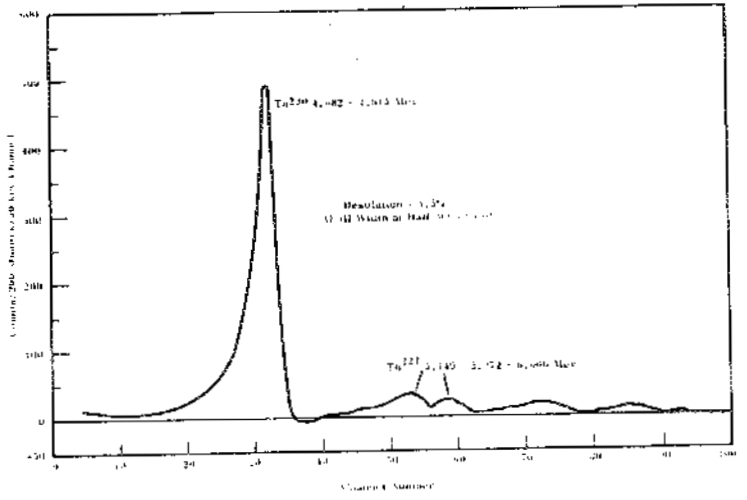

FIGURE 3.13

Alpha Energy Spectrum of Thorium Separated from Tissue as Measured in a Frisch Grid Chamber

uranium and thorium fractions which have been separated from the lungs of the experimental animals following inhalation of the uranium ore dust. The resolution obtained by direct plating of the isolated fractions is not comparable to that obtained from electrodeposited sources but is entirely adequate for total alpha counting. The alpha energy spectrum of the uranium fraction would indicate more U^{238} than U^{234} in the sample; however, this is due to energy degradation of the U^{234} alpha particles within the source, thus contributing to the U^{235} alpha energy peak. Uranium which has been separated from the ore and carefully plated for alpha energy analysis has shown the U^{238} and U^{234} to be very nearly in secular equilibrium.

The supernate from the lanthanum fluoride precipitation step and the aqueous phase of the 2-thenoyltrifluroacetone extraction are reserved for gamma-ray spectrometric determination of Ra^{226} following attainment of secular equilibrium with its daughter products.

Results

Preliminary results in measuring the thorium to uranium ratios indicate that thorium is preferentially retained in the lung. Rats exposed three times at weekly intervals and sacrificed 1 week following the last exposure showed thorium to uranium ratios of 1.5 (average of 5 exposed animals). Rats which were similiarly exposed and sacrificed 8 weeks following exposure showed thorium to uranium ratios of 2.7 (average of 5 exposed rats). Animals receiving a single exposure of the ore showed thorium to uranium ratios ranging from 1 to 17. The latter experiment could indicate a possible "mass effect" in which the majority of the material is removed rapidly from the lung by coughing and ciliary action. Analysis of the excreta of these animals showed relatively large amounts of uranium in the feces. The disequilibrium between thorium and uranium in rat lungs at various times following exposure is being studied, and the migration of thorium and uranium in the experimental animal is being traced.

Liquid Scintillation Counting of Pm^{147}; Bioassay Procedure for Pm^{147} - J. D. Ludwick

Techniques were developed for the introduction and quantitative determination of Pm^{147} in a liquid scintillator. Total energy absorption allowed absolute standardization of Pm^{147} and contributed to a sensitive bioassay procedure for analysis of this radioisotope. A minimum chemical separation and sample process time makes this technique most desirable for routine use.

Urine samples were treated to remove colored organic components and finally extracted into the scintillator with di-2-ethylhexyl phosphoric acid. The sensitivity of the method for a 10 min sample count is about 2×10^{-6} microcuries.

Significant quantities of the fission product, Pm^{147} have recently been chemically separated and made available for experimental use. This work was done to examine useful techniques for liquid scintillation counting of Pm^{147} and to provide an analytical procedure for monitoring individuals exposed to the nuclide. For people working with this isotope, it is necessary to minimize exposure and limit the body burden to 60 microcuries in bone.(3.11)

Pm^{147} presents several problems to efficient collection and detection, since it is a a low energy beta-emitting isotope (beta maximum is 0.23 Mev). Even small amounts of extraneous material adversely affect application of β-ray proportional counter techniques. Separation techniques for Pm^{147} usually result in radioactive contamination from other rare earth fission products. These problems are less important when Pm^{147} is introduced into a liquid scintillator where total energy absorption can take place. If uranium fuel irradiation times of several months to several years are considered together with about a 1 yr cooling interval, interference can be expected in the high energy beta ray region from the Ce^{144}-Pr^{144} decay chain. A considerable lesser interference can also be expected in the lower beta energy region from Sm^{151}.(3.12) Energy discrimination in the liquid scintillator can be used to allow determination of Pm^{147} without separation from these probable contaminants. Another advantage of liquid scintillation is that an absolute standard of Pm^{147} under these conditions can be obtained with little effort.

Experimental

Pm^{147} in the Liquid Scintillator

Previous work with liquid scintillator mixtures facilitated the proper choice of an efficient scintillator for Pm^{147}.[3.13] Standard samples of Pm^{147} were used in 1N HNO_3. The specific activity was known from half-life and mass spectrometric analysis data. A comparison of calibration techniques was made by preparing first, samples of the solution on plates for 4 $\pi\beta$ calibration in a polished aluminum prportional chamber, and second, by extraction of the Pm^{147} into an organic scintillator. Extraction was accomplished by diluting 10 microliters of the 1N HNO_3 solution with 2 ml of water and introducing 10 microliters of dibutyl phosphate along with 300 microliters of the scintillator. The mixture was shaken for 2 min, and centrifuged; the upper organic phase was drawn off with a micropipette and then transferred to a quartz vial for counting in apparatus presiously described.[3.14] This procedure was repeated twice to remove all the Pm^{147}. Favorable extraction took place at this acid concentration (pH 3). About 93% of the Pm^{147} was removed and counted after the first extraction and 99% after the second.

Pm^{147} Bioassay

Extraction of promethium from urine was accomplished by wet-ashing in HNO_3 followed by treatment with di-2-ethylhexyl phosphoric acid (HDEHP). In practice, a sample containing 250 ml of urine in an Erlenmeyer flask was treated with 20 ml of concentrated HNO_3 and the solution boiled to near dryness. Several more lesser additions of concentrated HNO_3 were necessary to decolorize the residue. The resultant wet-ash residue was completely dissolved with a minimum (about 15 ml) of dilute HNO_3 and transferred to a 25 ml volumetric flask. A dilute solution of NaOH was added to change the pH to 3.4. A 7% solution of HDEHP in the liquid scintillator was used for solvent extraction of the promethium. Three extractions, two of 150 microliters and one of 100 microliters, recovered at least 94% of the radio-isotope after the urine treatment. Each time the volumetric flask was shaken

for 2 min and then centrifuged. The upper organic phase was drawn off with a micropipette and transferred to a quartz sample vial, and subsequent extractions were combined in the vial. The vials were then cooled for 5 min in the dark and counted in a liquid scintillation spectrometer.

Discussion

Results of Pm^{147} extraction from varying HNO_3 concentrations are shown in Table 3.2. It is apparent that reasonably reliable pH control was necessary to accomplish consistently high solvent extraction performance. The effects on counting rate upon addition of HDEHP to the liquid scintillator demonstrated that up to 20% may be tolerated without significant loss in efficiency.

A comparison of the specific activity of the Pm^{147} solution calculated from mass spectrometric half-life data, $4\pi\beta$-proportional counting, and liquid scintillation counting are presented in Table 3.3. The agreement between the mass spectrometer and the liquid scintillation methods is excellent. The $4\pi\beta$-proportional counter results are low by about 5%, probably due to incomplete correction for sample self-absorption. The liquid scintillation technique provides a simple precise nuclide standardization.

Results were obtained concerning the accuracy and precision of the method for overall Pm^{147} extraction and counting efficiency for the bioassay procedure. Table 3.4 illustrates these results which were obtained from urine samples spiked with 25,500 disintegrations/min Pm^{147}.

The standard deviation was given for each 10 min count. Background samples of processed urine were counted for 60 min and are also shown. For a 10 min sample count, the sensitivity of the method was 2×10^{-6} microcuries at the 90% confidence level. In ease of sample preparation, short time for analysis, and very high counting efficiency, this technique compares favorably with other methods for Pm^{147} analysis.

TABLE 3.2

SINGLE EXTRACTION OF Pm^{147}
FROM HNO_3 SOLUTION BY HDEHP IN LIQUID SCINTILLATOR

pH	Pm^{147} counts/min	Extraction Coefficient
1.8	250	0.01
2.2	1350	0.06
2.5	2450	0.11
2.8	8100	0.50
3.2	15,800	1.6
3.4	19,300	3.1
4.5	21.000	4.7
5	--	Excessive Precipitation

TABLE 3.3

Pm^{147} STANDARDIZATION BY VARIOUS METHODS

Mass Spectrometry, disintegrations/min	Liquid Scintillator, disintegrations/min	$4\pi\rho$-Proportional Counter disintegrations/min
2.5×10^4	2.55×10^4	2.48×10^4
	2.53×10^4	2.43×10^4
	2.56×10^4	2.43×10^4

TABLE 3.4

EXPERIMENTAL COUNTING YIELD
AFTER PROCESSING URINE

Sample	Net Counts/min Pm^{147}	Overall Efficiency, %	Background Counts/min
1	24,500 ± 50	96	18.0 ± 0.6
2	24,200 ± 49	95	19.6 ± 0.6
3	24,700 ± 50	97	18.2 ± 0.6
4	25,000 ± 50	98	19.0 ± 0.6
5	24,100 ± 49	94	18.4 ± 0.6

Reactor Studies*

The Effect of Spokane River Salts on Hanford Reactor Effluent Radioactivity - W. B. Silker

The concentrations of various chemical elements in the Spokane River and the Columbia River at Hanford were measured during the first 6 mo of 1963. The salt contributions from the Spokane River were correlated with changes in the concentrations of their respective neutron activation products in Hanford reactor effluent water. Good agreements obtained with arsenic, manganese, lanthanum, uranium, and zinc indicated the Spokane River was a significant source of these radionuclides.

A previous study related the concentration of radioactive materials in the effluent water from the Hanford reactors with the concurrent Columbia River salt concentrations.(3.15) It was suggested that the Spring increase in the effluent concentration of several radionuclides resulted from introduction of water from the Spokane River to the Columbia River. This premise was based on the characteristic flow pattern of the Spokane River, which differed significantly from any other upstream tributary and also on the great similarity between the shapes of the Spokane River flow curve and the radioisotope concentration pattern. No data were available to quantitatively relate these observations, although analyses of scattered samples of Spokane River water did show much higher concentrations of certain materials than existed in the mainstream.

During the first 6 mo of 1963, samples were taken routinely from the Columbia River at Hanford and at Little Falls Dam which is located on the Spokane River about 25 mi from its mouth. This paper describes the results from analysis of these samples and the implications drawn from these data.

All samples were filtered through tared membrane filters with an effective pore size of 450 millimicrons, and the amount of filterable material

---

* Not funded by the Division of Biology and Medicine

was weighed. The solids were removed in this manner to simulate the treatment the water received before its use as reactor coolant. The reactor water treatment process is efficient in the removal of particulates of this size. Aliquots of the filtered samples were encapsulated in quartz ampules and along with ampules of standardized solutions of the elements of interest were placed in the thermal flux zone of one of the Hanford reactors. After a suitable residence time in the reactor, the samples were removed and analyzed radiochemically for sodium, copper, manganese, arsenic, uranium, lanthanum, iron, cobalt, zinc, and scandium. Quantitative measurement of the elemental concentrations was made by comparison of the counting ratio of the sample with an aliquot of the standardized solution that was separated by the same process as the sample.

All gamma spectral analyses were made with a 400 channel analyzer equipped with a 5 by 3 in. NaI(Tl) detector. A gamma-gamma coincidence counter with two 5 by 5 in. NaI(Tl) crystals was used for coincident gamma analysis of Cu^{64}, Sc^{46}, and Co^{60}.

The flow curve of the Spokane River in 1963 (Figure 3.14) shows the high degree of flow regulation by the various dams on the river. The regulation of Columbia River flow is evidenced in Figure 3.15 which represents the fraction of the flow past Grand Coulee Dam furnished by the Spokane River. The fractional flow curve shows little or no similarity to the change in radioarsenic concentration in the effluent from the KE Reactor, Figure 3.16, which showed a marked increase in late March, 1963. This lack of similarity was somewhat surprising as good correlation existed between these two measurements in previous years. One explanation is that the high flow period of the Spokane River extended over approximately 2 mo during 1963, while in previous years definite peaks occurred during which time the Spokane River furnished as much as 30% of the flow through Grand Coulee Dam. Any influence of the Spokane River on the concentration of reactor effluent radionulcides must result from the introduction of the radioisotope parent materials to the water of the Columbia River. A plot of the arsenic concentration of the Spokane River corrected for

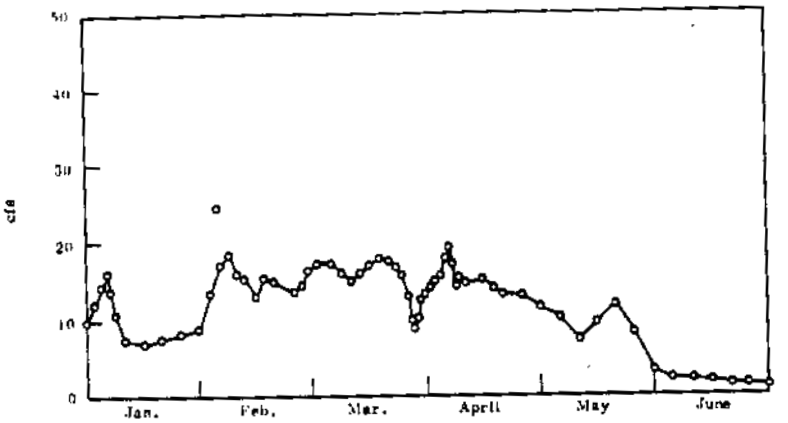

FIGURE 3.14

Flow Curve of the Spokane River, 1963

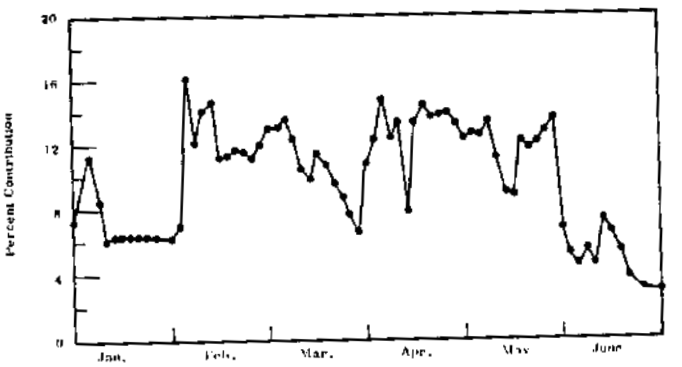

FIGURE 3.15

Coulee Dam Discharge Furnished by Spokane River, 1963

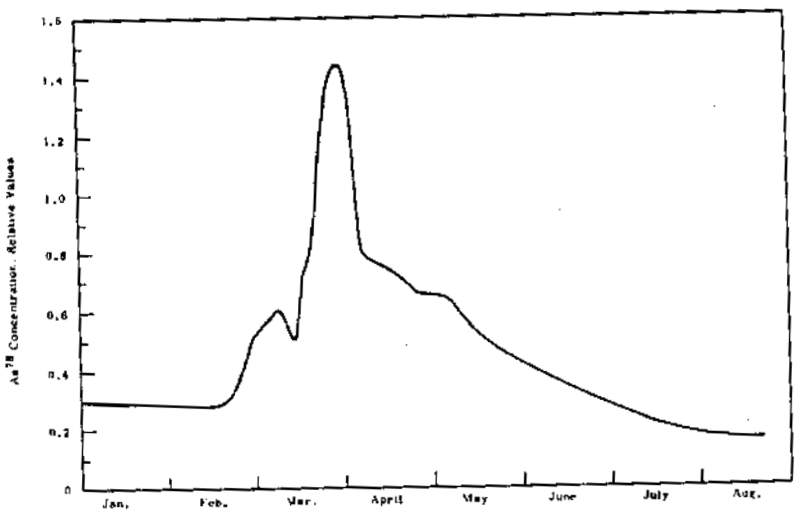

FIGURE 3.16

Radioarsenic Concentration in KE-Reactor Effluent Water, 1963

the dilution of this stream by the Columbia is presented in Figure 3.17. It can be seen that excellent correlation exists between this curve and the change in reactor effluent radioarsenic concentration. The highest contribution of arsenic from the Spokane occurred on March 17, and the corresponding peak radioarsenic value occurred approximately 12 days later. This time lag is considered to be representative of the transit time of water from the mouth of the Spokane River to Hanford. There is also an indication that an initial peak in the inert arsenic curve which occurred on February 10 resulted in an increase in radioarsenic on March 7. The difference in transit times is attributed to many factors, including river flow, relative water temperatures of the Spokane and Columbia Rivers, the regulation of river flow by the various dams, and the level of the reservoir from which water was taken from Lake Roosevelt for passage through Grand Coulee Dam.

The manganese, lanthanum, and uranium data revealed a corresponding similarity between the salt contribution from the Spokane River and the radioactive daughter concentration in reactor effluent. In addition, it appeared that a significant fraction of the radiozinc resulted from introduction of zinc by the Spokane River, which was not observed in previous years.

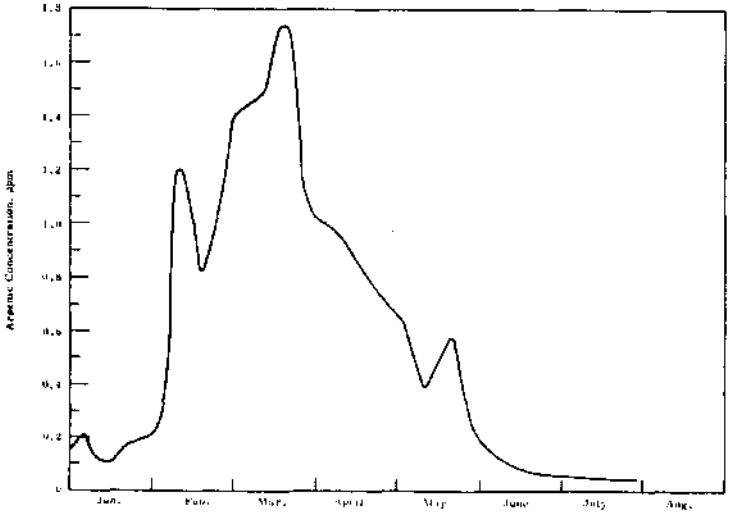

FIGURE 3.17

Columbia River Arsenic Concentration Furnished by the Spokane River

The Effect of Filter Flow Rate on Reactor Effluent Radioactivity - W. B. Silker and C. W. Thomas

During the initial period of operation of a Hanford water treatment pilot plant, the treated water was filtered at a rate of 4.8 gpm/ft^2 of filter area. Two months later a second filter was operated which permitted filtering at a rate of 8 gpm/ft^2. The filtered water was used to cool two reactor process tubes, one aluminum and the other zirconium, and allowed evaluation of the effect of filter flow rate on the concentration of radionuclides in the tube effluents.

A comparison of the concentrations of several radionuclides at the two flow rates is presented in Table 3.5.

TABLE 3.5

RATIOS OF RADIONUCLIDE CONCENTRATIONS AT HIGHER FILTER FLOW RATE TO THAT AT LOW FILTER FLOW RATE

	Zirconium Tube	Aluminum Tube	Average Ratio
Na^{24}	0.61	0.69	0.65
Mn^{56}	1.25	1.33	1.29
As^{76}	2.40	1.80	2.10
Np^{239}	1.71	3.20	2.45
Cr^{51}	0.61	0.80	0.70
Zn^{65}	1.33	1.20	1.26
La^{140}	1.71	1.00	1.35
Cu^{64}	2.33	2.00	2.16
P^{32}	1.50	2.50	2.00

With the exception of Na^{24} and Cr^{51}, the higher concentrations of all radioisotopes occurred at the higher flow rate. Treatment of the water before passage through the filter was the same during each measurement period. The increase in activity could therefore be attributed solely to the rate of flow through the filter. It was concluded that the

increased activity at higher filter flow resulted from mechanical fracture of the floc particles under increased hydrostatic pressure, which resulted in partial filter breakthrough. Operation of the filter at a flow rate of 4 gpm/ft^2 could provide a factor of two reduction in the concentration of As^{76} and P^{32}, both of which are isotopes of biological significance.

The Effect of Deionized Water on Reactor Effluent Activities - I. New Tubes and New Fuel Charges - W. B. Silker and C. W. Thomas

The relationship between reactor effluent activities and tube and fuel jacket surfaces was studied by measuring the concentration buildup of radioisotopes in the effluent from zirconium and aluminum process tubes cooled with deionized water. The experimental results, which were described mathematically, indicated that nearly all radioisotope production was associated with the corrosion product on the aluminum components. It was postulated that Na^{24} diffused from within the porous aluminum corrosion product, and the degree of porosity changed with tube age. Most isotopes were produced primarily on the fuel jacket surface, Zn^{65} was the most notable exception.

The buildup of radioisotope concentrations in the effluent from new zirconium and aluminum process tubes that were cooled with deionized water in a Hanford reactor was measured in studies on the mechanisms and kinetics of radionuclide production. It was determined that only small amounts of the radionuclides were produced on the surface of the zirconium tube, indicating that the aluminum tube and fuel element surfaces were responsible for the production of the radioactive materials found in the effluent water. This production, in general, resulted from a sorption-desorption reaction of coolant impurities on the aqueous aluminum corrosion product film and the resultant exposure to the reactor neutron flux during this residence period. Some sorption sites were available at the time of initial exposure of the aluminum surfaces to the coolant. The number of sites increases with time due to growth in the thickness and porosity of the corrosion product film. The buildup of the coolant concentration of radioisotopes could be described mathematically by the following equation:

$$C = a(1 - e^{-\lambda t}) + b(1 - e^{-\lambda t})(1 - e^{-\beta t});$$

where the first term is the radioactive buildup of the atoms sorbed on the initially available surface and the second term reflects the contribution resulting from the increased porosity with β being the porosity growth factor.

The constants a, b, and β were evaluated by least square fit of the Na^{24} data from the first fuel charge in the aluminum tube. A value of 0.00987 day^{-1} was determined for β, which corresponds to a reaction half-life of 70 days. The function β was determined to be characteristic of the system. By holding β constant and determining values of a and b for the other radioisotopes by least squares estimation, excellent agreement between calculated and observed concentrations was obtained for short half-life isotopes. A less precise fit was obtained for the longer-lived isotopes of P^{32} and Zn^{65}, which is probably due to the exclusion of certain controlling parameters from the mathematical model. Following each fuel recharge, the effluent Na^{24} concentration rather rapidly attained a new level which was significantly lower than had been attained during the previous charge. The constants a and b for the Na^{24} buildup during each fuel charge were evaluated by the method of least squares, and are presented in Table 3.6.

TABLE 3.6

SODIUM EQUILIBRIUM CONSTANTS

	Aluminum Tube		Zirconium Tube	
	a	b	a	b
First Charge	2.46	32.23	2.03	20.56
Second Charge	4.94	10.31	1.90	9.15
Third Charge	4.75	5.15		

For these calculations the time was assumed to start at zero following each recharge of the tubes. This assumption does not give constant values for "a" for successive fuel charges in the aluminum tube. This constant reflects the initial surface area from which the diffusion of Na^{24} could occur, and indicates that the film on the tube surface increased in its capacity to furnish Na^{24} to the effluent water by a factor of 2 during the period of operation with the first fuel charge. This increased capacity was immediately available for the production of Na^{24} during the second charge. The tube film surface apparently had attained maximum capacity during the first period of operation, as "a" remained relatively constant for the second and third fuel charges. The inertness of the zirconium tube was shown by the constancy of "a" for both fuel charges. The only aluminum surfaces available for Na^{24} production in this tube were the fuel element jackets, whose surface had been treated by autoclaving. The fact that "a" remained the same for both periods of operation showed that the same initial surface area was presented by both fuel charges, representing uniform preconditioning of the fuel elements.

The decreased Na^{24} concentrations in the effluent from successive fuel charges probably resulted from some factor which influenced the effective production capacity of the alumnium corrosion film. This may be due to a thinner film, a less porous film, or a film with less sorptive capacity and was manifested in a decreasing value of "b" in all subsequent fuel charges from both tubes.

Some changes in concentration of the other radioisotopes during subsequent fuel charges were observed; however, they were small when compared with the sodium behavior. The activation products in the zirconium tube effluent reverted to the levels measured during the initial fuel charge. From the data it was determined that production on the fuel element surface was responsible for most of the radioisotopes. The notable exception was Zn^{65} where about 90% was derived from the tube wall. This indicated a marked difference in either the source or deposition characteristic of zinc.

The Effect of Deionized Water on Reactor Effluent Activities - II. Zirconium and Aluminum Clad Fuel - W. B. Silker and C. W. Thomas

The relative importance of the aluminum tube and fuel jacket surfaces in the production of reactor effluent radionuclides was investigated. Zn^{65} was derived primarily from the tube; Mn^{36}, Np^{239}, and Ga^{72} were produced in equal amounts on the two surfaces; and Na^{24}, As^{76}, La^{140}, Cu^{64}, P^{32} and Ni^{65} production favored the fuel element surface.

Aluminum surfaces are the major production site for radionuclides in the Hanford reactor effluent water. To evaluate the relative contribution of the tube and fuel element surfaces in the production of radioactive species, two successive fuel charges were exposed in zirconium and aluminum tubes cooled with deionized water. The first charge, with zirconium clad fuel pieces and stainless steel dummy trains, eliminated all aluminum components from the charge string while the second was a standard charge with aluminum clad fuel and dummies.

Table 3.7 presents data as the fraction of the radionuclide concentration in the total reactor effluent that was observed in the individual tube effluent. Any time dependent variations in parent isotope concentrations and reactor operation are minimized in this presentation.

TABLE 3.7

COMPARISON OF RADIONUCLIDES IN EFFLUENT FROM TEST TUBES WITH THOSE IN TOTAL REACTOR EFFLUENT.

	Test Tube/Average			
	Tube 4963 (Aluminum) Fuel Cladding		Tube 5063 (Zirconium) Fuel Cladding	
	Zirconium	Aluminum	Zirconium	Aluminum
Na^{24}	0.26	0.70	0.01	0.50
Mn^{56}	0.06	0.08	0.01	0.08
As^{76}	0.21	0.50	0.06	0.40
Np^{239}	0.10	0.19	0.01	0.11
La^{140}	0.08	0.13	0.05	0.13
Cu^{64}	0.14	0.25	0.09	0.20
P^{32}	0.72	2.25	0.06	1.50
Ni^{65}	0.05	1.20	0.03	1.50
Ga^{72}	0.13	0.25	0.01	0.15
Zn^{65}	0.32	0.90	0.02	0.08

The concentrations of the various radionuclides in the effluent from the zirconium system dropped to very low values, showing the relative incapability of a zirconium surface of acting either as a site for retention and irradiation of parent isotopes or as a primary source of activated parent isotopes via corrosion or erosion. It was assumed thst the radioisotopes in the effluent from the zirconium system resulted from irradiation of coolant impurities and the contribution from this source would remain in all tube and fuel combinations tested. The contribution of the aluminum fuel cladding surface and the aluminum tube surface could then be evaluated from the respective effluent concentration from the zirconium tube with aluminum clad fuel and aluminum tube with zirconium clad fuel. These comparisons are presented in Table 3.8.

TABLE 3.8

PRODUCTION SITES OF RADIONUCLIDES

	Cooling Water	Aluminum Fuel Cladding	Aluminum Tube	Total	Aluminum Tube and Fuel Cladding
Na^{24}	0.01	0.49	0.25	0.75	0.70
As^{76}	0.06	0.35	0.15	0.56	0.50
La^{140}	0.05	0.08	0.03	0.16	0.13
Cu^{64}	0.09	0.11	0.05	0.25	0.25
P^{32}	0.06	1.44	0.66	2.16	2.25
Ni^{65}	0.03	1.47	0.03	1.52	1.20
Mn^{56}	0.01	0.07	0.05	0.13	0.08
Np^{239}	0.01	0.10	0.09	0.20	0.19
Ga^{72}	0.01	0.14	0.12	0.27	0.25
Zn^{65}	0.02	0.06	0.30	0.38	0.90

Good agreement is seen between the summation of the contribution of activity from the individual sources and that observed from the all aluminum system, which represents the integration of all individual sources reacting as a

single source. This would be expected if the aluminum surfaces provide the only sites available for the retention and production of radionuclides and if the tube and fuel element surfaces reacted independently of one another.

Of the isotopes measured, three were produced in equal amounts on the tube and fuel surfaces, one was derived from the tube, and six were predominantly formed on the fuel element surface. Zn^{65} was the only isotope measured that was contributed from the tube. Perkins (3.16) found that inert zinc concentrations were 2 to 10 times higher in samples of tube aluminum than in samples of fuel element jacket stock. Previous work by the authors * showed that radiozinc concentrations in the effluent from a new aluminum process tube remained at high levels after recharging the tube with new fuel elements indicative of a permanent source of radiozinc. It was concluded that the major portion of the radioactive zinc was formed by neutron activation of zinc impurities in the aluminum process tube. Its occurrence in the cooling water was either the result of corrosion or erosion of the tube surface or diffusion of the zinc through the aluminum corrosion film.

The three radioisotopes whose concentrations were contributed equally from the tube and fuel element surfaces were Mn^{56}, Ga^{72}, and Np^{239}. It was noted that only marginal amounts of these radionuclides were present in the effluent from the all zirconium system, indicating negligible concentration of their respective parents in the cooling water supply. Perkins' (3.17) measurements showed that the parent precursors of these three nuclides were present in approximately the same concentration in both the tube and fuel jacket material. It is believed that the aluminum components furnished the source of the parent isotopes which, after irradiation, were released to the coolant by one of the escape mechanisms previously mentioned. The only difference between these

---

* See "The Effect Deionized Water on Reactor Effluent Activities. I. New Tubes and New Fuel Charges," page 3.30.

three isotopes and the radiozinc is their contribution from the fuel surfaces as well as the tube aluminum.

The remaining isotopes showed a decided preference toward production on the fuel element; in fact, with the exception of Ni^{65}, all were present in a 2:1 ratio favoring the fuel element surface. Na^{24} and Ni^{65}, which will be discussed later, exhibited very low concentrations in the effluent from the zirconium system, thus minimizing the possibility of the cooling water as their source. The other four isotopes, As^{76}, P^{32}, Cu^{64}, and La^{140}, were present in significant concentrations in the effluent from the all zirconium system, hence the conclusion that the cooling water was the primary source of their precursors. The relative production of the radionuclides was interpreted to reflect a more favorable environment for parent isotope retention on the surfaces of the fuel element.

The production of Ni^{65} should obviously be weighted strongly in favor of the fuel element surface, as 1% nickel is added to the aluminum alloy from which the jackets are fabricated, while specifications limit the nickel content of the tube aluminum to less than 0.05%. The occurrence of Ni^{65} in the effluent water is interpreted as evidence of corrosion of the fuel jacket material, and the radionickel concentration provides a direct measure of the instantaneous corrosion rate of the jacket.

The effluent concentration of Na^{24} from the zirconium system attained only 1% of that observed in the total reactor effluent, but increased markedly upon introduction of aluminum components. The relative Na^{24} contribution was 2:1 in favor of the fuel element, which correlates well with the ratio of the fast neutron flux at the two surfaces.[3.17] These facts are resolved if the major production of Na^{24} is attributed to the Al^{27} (n, α) Na^{24} fast neutron reaction. The radiosodium, which probably diffuses through the film into the coolant, would vary in concentration with the thickness of the porous aluminum corrosion film. The observed contributions of Na^{24} from the tube and fuel element surfaces were proportional to the fast neutron flux at these points; therefore, the two corrosion product layers must be of approximately the same thickness.

Concentrations of Radionuclides in Reactor Film -

C. W. Thomas and W. B. Silker

Samples of film from downstream dummy fuel pieces were collected, separated into the outer surface layer containing the hydrous iron oxide and the subsurface aluminum oxide layer, and analyzed for the radioisotopes common to reactor effluent water. It was determined the hydrous iron oxide coating was codeposited within the aluminum oxide matrix and still retained colloidal characteristics. The sorbed cationic radionuclides were loosely held to the film and favored the iron oxide rich layer; conversely, anionic radionuclides were tightly bound and distributed throughout the film.

Excessive aluminum corrosion and higher than normal concentrations of reactor effluent radioisotopes have been observed when deionized water is used as a reactor coolant. Due to these observations, a test was made to study the radioisotope content of the corrosion film on aluminum surfaces. Initial investigations were made on fuel pieces downstream of the reactor neutron flux which meant that a resorption mechanism was responsible for any radioisotopes associated with the film. This film would not necessarily be comparable to that in the flux zone since the neutron flux had been known to affect it. (3.18)

One constituent of interest in the film was the iron oxide common to surfaces both in the flux and downstream zones. This iron oxide was considered to be the main sorption surface wherein the parent materials of effluent activities were held up, activated, and then released to the water. The source of iron was the coolant water and the carbon steel piping used to transport the water to the reactor.

During reactor outage on December 26, 1962 downstream dummies were obtained from tubes 4963, 5063, 4456 and 4355. Tubes 4963 and 5063 were aluminum and zirconium, respectively, and used deionized water as the coolant; also, tubes 4456 and 4355 were aluminum and zirconium, respectively, but used pilot plant process water as the coolant. The outer layer of film containing the hydrous iron oxide was removed by physically

scraping the surface and was analyzed by standard radiochemical methods for radioisotopes normally associated with the reactor effluent water. These results are presented in Table 3.9. On February 7, 1963, downstream dummies were obtained from an aluminum tube using process water and the iron-rich outer film was removed by brushing with a camel's hair brush and flushing off with water. The subsurface aluminum oxide layer was lost during analyses, consequently, only the iron-rich film and the water were analyzed. These results are presented in Table 3.10. On February 13, 1963, Tube 4963 was discharged and a downstream dummy was obtained for film study. To reduce possible translocations of radioisotopes from flushing off the outer layer of film with water, the film from this dummy was separated by first using a damp camel's hair brush to remove the iron-rich outer layer, then scraping off the underlying aluminum oxide film. These two fractions were analyzed and the results are presented in Table 3.11.

The iron oxide deposition in these three samples was not a coating over the surface but was codeposited within the aluminum oxide matrix. This was clearly indicated since in every case the film fraction containing iron was composed mainly of aluminum oxide. In addition, the iron oxide deposition, when suspended in water, was highly colloidal (zeta potention of +20 mv) indicating the existence of a colloidal condition on the film. (Colloidal iron oxide could account for an intense orange coloration observed on the film.) The absence of Na^{24} in samples from December 26, 1962, and February 7, 1962, was quite indicative of the mobility of this ion since these samples were not removed immediately after shutdown as was the sample on February 13, 1963. Even this latter sample showed Na^{24} concentrations which were a factor of 10 lower than expected. Comparing the concentrations of isotopes in the iron and aluminum oxide fractions from Table 3.11, certain conclusions were indicated. Fe^{59} was surface bound as was Zn^{65}, Sc^{46}, Ga^{72}, and Co^{60}. Na^{24} and P^{32} were evenly distributed between the two films, a condition which was expected for the mobile Na^{24} ion but not the P^{32}. An indication of how tightly bound the radioisotopes were to the film was suggested by comparing the aqueous phase and the iron film data from Table 3.10. These data showed

TABLE 3.9

COMPOSITION OF REACTOR DUMMY FILM

December 26, 1962 Samples

Tube Number	4456	4355	4963	5063
Tube Composition	Al	Zr	Al	Zr
Coolant Water	Process	Process	Deionized	Deionized
Film Weight/Unit Area, g/cm^2	8.0	4.7	2.6	2.9
Film Composition, %				
Aluminum Oxides	79	76	80	81
Iron Oxides	19	17	18	18
Film Radionuclide Concentration, nanocuries/mg				
As^{76}	66	65	68	33
Mn^{56}	41	91	16	4.9
Zn^{65}	6.1	23	46	0.35
La^{140}	5.7	5.5	7.1	0.034
Sc^{46}	3.8	7.5	3.2	0.38
Ga^{72}	2.5	1.8	3.3	0.09
Fe^{59}	1.3	1.1	0.8	0.49
Np^{239}	0.63	0.32	0.30	0.080

TABLE 3.10

LEACHING OF IRON-RICH FILM CAUSED BY USE OF WATER FOR FILM REMOVAL

February 7, 1963 Samples

(22.1 mg iron-rich film consisting of about 19% as iron oxides and 70% as aluminum oxides. 200 ml water used to wash)

Radionuclide	Amount in Iron-Rich Film, %	Amount in Wash Water, %
Na^{24}	None	None
P^{32}	93	7
Sc^{46}	87	13
Cr^{51}	87	13
Mn^{56}	87	13
Fe^{59}	89	11
Co^{60}	46	54
Cu^{64}	35	65
Zn^{65}	77	23
Ga^{72}	85	15
As^{76}	92	8
Np^{239}	54	46

TABLE 3.11

COMPOSITION OF REACTOR DUMMY FILM

February 13, 1963 Samples

(Tube Number 4963 (aluminum), deionized water coolant, 18.9 mg iron-rich film about 14% iron oxides 17.7 mg aluminum film over 98% aluminum oxides)

Radionuclide	Concentration in Film, nanocuries/mg	
	Iron-rich	Aluminum Oxide
Zn^{65}	200	20
Mn^{56}	100	17
P^{32}	98	67
As^{76}	88	32
Fe^{59}	36	0.42
Ga^{72}	6.7	4.8
Sc^{46}	4.6	0.68
Na^{24}	0.08	0.01
Np^{239}	0.58	0.27
Co^{60}	0.47	0.02
La^{140}	0.13	0.03

Co^{60}, Cu^{64}, and Np^{239} were loosely held to the film while As^{76} and P^{32} were tightly bound. The significant differences between Table 3.9 and Table 3.11 data on Tube 4963 are probably due to the differences in exposure times to water the dummies had after reactor shutdown. The data from Table 3.10 would tend to verify this conclusion. In general, the accumulated data indicated cationic species were loosely held and associated with the surface film while anionic species were tightly bound and distributed throughout the film.

Reduction of Radionuclides in Reactor Effluent Water: Final Report on the Effect of Chemical Additives and Coating Materials on the Adsorption of Radionuclide Parent Elements in Process Water on Aluminum Surfaces - D. E. Robertson and R. W. Perkins

The adsorption inhibiting effect of many types of corrosion inhibitors, standard surface pretreatment processes, and coatings were evaluated both in the laboratory and in in-reactor tests. The laboratory studies revealed a number of potential process water additives and coatings as adsorption inhibitors. Reactor tests showed the coatings to be satisfactory in regions downstream from the neutron flux, but they were decomposed and unsatisfactory in the neutron flux region.

A major portion of the reactor effluent water radionuclides is produced by the neutron activation of parent elements which have been adsorbed from process water onto the surface of the aluminum process tubes and fuel element jackets. Laboratory and in-reactor studies have been made with the aim of reducing effluent water radioactivity by minimizing this adsorption of parent material. It was found that several types of relatively nonadsorbent films could be formed on aluminum surfaces, either by the continuous addition of chemical additives to the process water, or by pretreatment of the aluminum surfaces with certain protective coatings. Laboratory and in-reactor tests have already demonstrated that sodium silicate is an effective adsorption inhibitor when added at 20 to 40 ppm as SiO_2 to process water.[3.19, 3.20] Laboratory studies have also shown that coatings

of organic inks on aluminum surfaces immersed in hot (95 C), stirred, process water significantly reduced adsorption of arsenic tracers added to the water.[3.19] The present study has extended the investigation and also includes the effect of many types of corrosion inhibitors, standard surface pretreatment processes, and coatings as adsorption inhibitors. The radionuclides As^{76} and P^{32}, which are of concern in reactor effluent water from a radiological health standpoint, were used as tracers in determining the adsorption inhibiting effect of a treatment or coating.

Process water additives were tested in the laboratory under simulated reactor conditions, except no effort was made to obtain a comparable flow rate or a radiation exposure. Of the additives tested, a class of proprietary corrosion inhibitors containing organic filming agents were the most successful and reduced arsenic tracer adsorption on aluminum turnings by factors of about 10 to 80 when used at concentrations of 100 ppm. Sodium vanadate reduced phosphorous tracer adsorption by about a factor of 3.5 when used at a concentration of 50 ppm.

The coatings and surface pretreatment processes were evaluated by exposing coated or pretreated aluminum coupons to hot, stirred, process water containing the radioactive tracer of interest. Of the coatings tested, a urea-formaldehyde resin, a fluorocarbon resin, a chlorinated polyether resin, a polyester resin, and a silicone resin were the most effective and reduced arsenic tracer adsorption by factors of about 190, 90, 7, 10 and 15, respectively. Aluminum surface treatments by anodizing, electropolishing, or chemical conversion coating were generally unsuccessful in that a more adsorbent surface to the arsenic tracers was formed.

An in-reactor study in which pretreated and coated aluminum coupons were exposed to reactor effluent water at a location downstream from the neutron flux zone, showed significant reductions in the adsorption rates for several radionuclides. Of the coatings tested, the black organic inks and the silicone resins were the most successful and reduced As^{76}, P^{32}, Cr^{51}, Zn^{65} and Np^{239} by factors of about 2 to 4. When these coated aluminum

coupons were tested in reactor tubes in the neutron flux region, no reduction in radionuclides adsorption was achieved. These coatings are, therefore, unsatisfactory as adsorption inhibitors in the neutron flux regions. However, these materials might be considered as coatings for downstream piping from a reactor or in recirculation loops where the adsorbed radionuclides produce local radiation problems. The process water additives have not been evaluated in in-reactor experiments, but laboratory studies indicate they would not be superior to silicate.

Substitution of Polyelectrolytes for Alum in Water Treatment - W. B. Silker

> Investigations were made to determine the possibility of substituting a positively charged polyelectrolyte for a portion of the alum flocculant used in water treatment. As much as half of the alum was replaced with a cationic polyelectrolyte with no decrease in process efficiency. It appeared mandatory to make alum and polyelectrolyte additions at the same location.

An effective water treatment process reduces the negative zeta potential of natural colloids and suspensoids to a degree which allows mutual coagulation. This is generally accomplished by the use of aluminum or iron salts, which upon hydrolysis furnish postively charged hydrous oxides to neutralize the surface charge of the colloids and enmesh them in the resulting flocculant precipitate. The Hanford treatment process produces a floc that not only removes solids, but also certain dissolved anionic materials. The zeta potential reduction could also be accomplished by addition of other agents, such as organic polymers containing functional groups that are positively charged upon hydrolysis. Possible cost advantages could be gained by the use of such a polyelectrolyte, and the gathering power of the high molecular weight polymer could produce a more dense floc which would settle and relieve the load on the filter, thus resulting in longer filter runs.

Beaker tests indicate that 0.5 ppm of Cat-Floc (a cationic polyelectrolyte produced by Black Laboratories, Inc., Gainesville, Florida) was effective in

reducing the zeta potential of river colloids from -17 mv to neutrality. No observable coagulation occurred. To accomplish the same zeta potential reduction with alum required the addition of 12 ppm. The possibility exists that small additions of the polyelectrolyte might successfully be substituted for some of the alum coagulant required in water treatment.

The feasibility of Cat-Floc addition was tested in a model water treatment plant under dynamic conditions. The processes were evaluated in their ability to remove radioactive phosphorous which had been added to the raw water supply. All experiments were carried out at pH 6.6 and alum addition was made at a level to provide a zeta potential of 0 mv. The results are presented in Table 3.12.

TABLE 3.12

THE EFFECTIVENESS OF CAT-FLOC IN WATER TREATMENT

Cat-Floc Addition	Addition, ppm		P^{32} Removal, %
	Cat-Floc	Alum	
With Alum	0.12	9	97
2 sec before Alum	0.2	5.5	96.5
20 sec before Alum	0.2	5.5	96-90*
----	0	12	96-97

* Very short filter run with rapid breakthrough. Very little floc observed.

It appears feasible to use this material in small concentrations as a control agent for reduction of the negative surface charge on colloids. Its addition must be made at the same location as the alum for beneficial effects, although a down-stream injection may be suitable.

The Estimation of Aluminum Corrosion from Reactor Coolant Activity Concentration - C. W. Thomas and W. B. Silker

Studies were conducted to determine the use of effluent concentrations of Ga^{72}, Ni^{65}, and Na^{24} as indices of the corrosion rate of aluminum reactor components. It was determined that Ga^{72} provided a direct measure of tube and fuel jacket corrosion, and Ni^{65} was directly correlated with fuel jacket corrosion. Na^{24} values indicated a much higher corrosion rate than did occur. It was hypothesized that the effluent concentration of Na^{24} provided a measure of the thickness of the aluminum corrosion product film.

An index of the corrosion of aluminum tubes and fuel element cladding was provided by the concentrations of Ni^{65}, Ga^{72}, and Na^{24} found in reactor cooling water. Ni^{65} was formed by thermal neutron activation of the nickel additive in the fuel jacket alloy, Ga^{72} from the gallium impurity inherent in aluminum, and Na^{24} was derived from a fast neutron reaction with aluminum. In conjunction with other studies, it was possible to relate the effluent concentrations of these isotopes with different parameters of the corrosion process and to provide a definitive correlation with the actual corrosion of the aluminum components.

For this test two process channels in a Hanford reactor were retubed; 4963 with aluminum and 5063 with zirconium. Both tubes were initially charged with aluminum clad fuel elements and subsequent fuel charges were either aluminum or zirconium clad. Throughout the test, both tubes were cooled with deionized water. The effluent water was periodically sampled and the concentrations of Na^{24}, Ga^{72}, and later Ni^{65} determined.

From these values, calculation of the corrosion rate was made by including appropriate factors for the surface neutron flux, the concentration of parent material in tube and fuel cladding stock, and the coolant flow rate. It was assumed that the effluent concentration of these isotopes and the aluminum corrosion product was in the same proportion as the parent material in the film. The calculated corrosion rate from Tube 5063 represented that occurring on the fuel cladding and by subtracting this value from that measured in Tube 4963, it was

possible to estimate the corrosion rate of the aluminum tube. For these calculations it was assumed the aluminum fuel cladding was corroding at the same rate in both tubes. This assumption would seem justified since both systems were using a common source for coolant water and operating at the same thermal conditions.

The corrosion rates of the tube and fuel jackets calculated on the basis of the three radioisotopes are presented in Figures 3.18, 3.19, and 3.20. Comparison with results from reactor coupon corrosion tests showed the corrosion estimates were valid only for Ga^{72} and Ni^{65}. It was surmised that Na^{24} estimates reflected some conditions which were characteristic of the corrosion film, not necessarily the corrosion rate, and that the abnormally high corrosion rate calculated on the basis of this mobile ion was related to an increasing porosity of the corrosion film providing a greater surface area from which Na^{24} could diffuse. The influence of film porosity on the Na^{24} concentration is developed in another report.*

At the start of the test, the corrosion products originated primarily from the fuel element jacket; however, within a few days the contribution from the tube had increased to a degree that equal amounts were furnished from both surfaces. This would be expected since, initially, the only significant film surface in the system was on the autoclaved fuel jackets; however, exposure to the coolant rapidly created a corrosion film on the new aluminum tube surface. The difference in tube corrosion as noted between Ga^{72} and Na^{24} indicated the corrosion rate was governed by the loss of oxide film from the apparent water film surface area and changes in film depth and porosity had little influence in the corrosion mechanism.

A reduction in corrosion rate was calculated following replacement of the original fuel elements. Each successive recharge provided an additional reduction in the corrosion rate of aluminum surfaces in both the aluminum and zirconium tubes. The only significant change during these time

---

* See "The Effect of Deionized Water on Reactor Effluent Activities. I. New Tubes and New Fuel Charges," page 3.30.

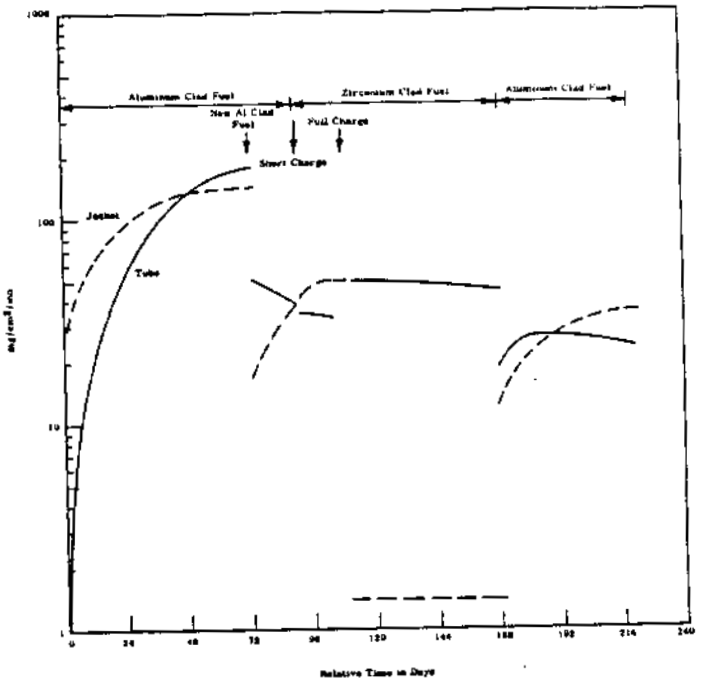

FIGURE 3.18

Tube and Jacket Corrosion Rates Based on Na^{24}

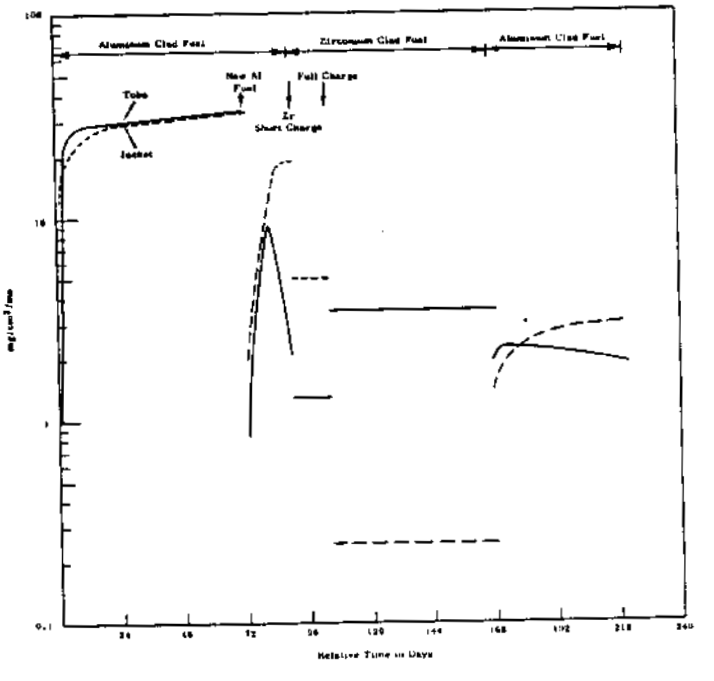

FIGURE 3.19

Tube and Jacket Corrosion Rates Based on Ga^{72}

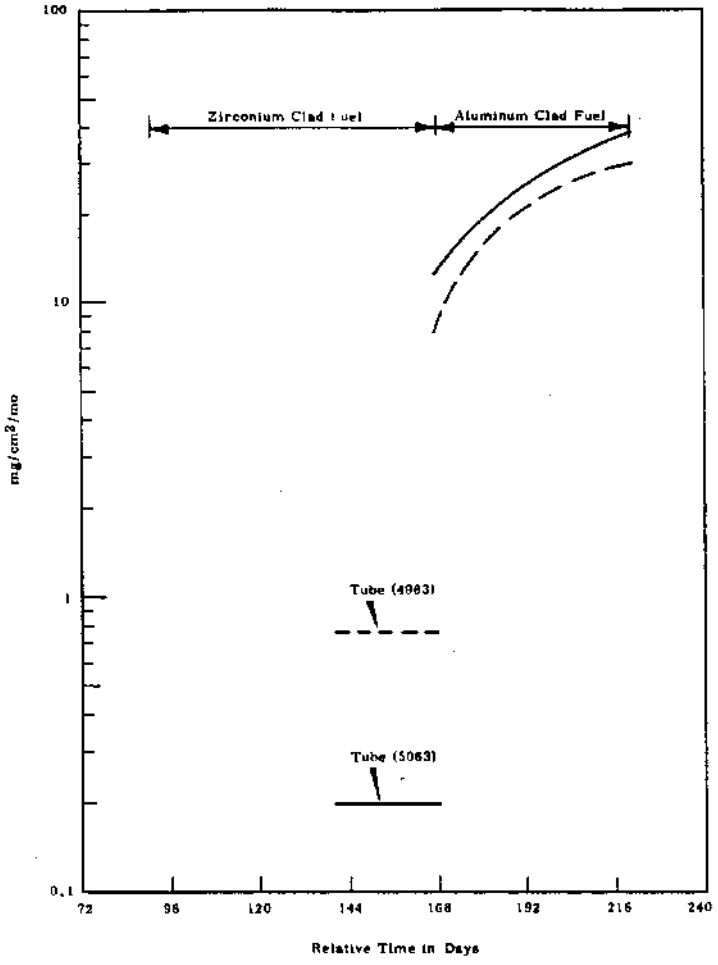

FIGURE 3.20

Jacket Corrosion Rates Based on Ni^{65}

intervals was the conditioning of the tube surface. It was therefore concluded that some factor concerning the age of the tube was instrumental in controlling the corrosion rate. The most apparent change with tube age was the buildup of the aluminum corrosion film and the surface deposition of hydrous iron oxide. This apparent interdependence of the two metal surfaces suggested an electrochemical reaction was possibly responsible for the corrosion rate change. If such was the case, instances of severe localized corrosion might be attributed to the film loss of localized electroactive areas.

During operation with a zirconium clad fuel charge it was determined that Ga^{72} and Na^{24} were derived from the aluminum components and not impurities in the water. The corrosion rate of the aluminum tube by this time had decreased by an order of magnitude from that observed from the start of the test.

To determine whether the Ga^{72} and Na^{24} were released to the water by dissolution or erosion, samples were analyzed before and after filtering through a 100 millimicron filter which was capable of removing particulates in the colloidal region. From these results presented in Table 3.13, it was quite apparent the release of Na^{24} was dissolution controlled since essentially no sodium was associated with particles. This was not the case for gallium where 60 to 70% of the isotope was associated with particles; thus indicating an erosion controlled mechanism. These data further confined the association of sodium activity with porosity and the gallium activity with the surface film. Due to the chemical similarity of gallium and aluminum, and the dissimilarity of sodium, it was concluded that the aluminum loss was also mainly from erosion and that estimations of corrosion rate using gallium should provide a direct corrosion measurement, but the corrosion estimates using Na^{24} should reflect the degree of porosity or thickness of the aluminum corrosion product film.

TABLE 3.13

ASSOCIATION OF Ga^{72} AND Na^{24} WITH PARTICULATES

	Tube 4963, % Filtered	Tube 5063, % Filtered
Ga^{72}	70	62
Na^{24}	< 2	< 2

During operation with the zirconium clad charge and subsequently with the aluminum clad charge, Ni^{65} concentrations were obtained to determine the merits of using this isotope in measuring jacket corrosion. The data (Figure 3.20) from the zirconium clad fuel indicated the concentration of Ni^{65} from the water

was about equal to the contribution from the aluminum tube and both concentrations were low enough to measure any significant jacket corrosion. After recharge of aluminum clad fuel the corrosion estimates based on Ni^{65} compared favorably with those based on Ga^{72} in Tubes 4963 and 5063. The use of Ni^{65} for estimating jacket corrosion was unique in that tube corrosion did not interfere as was the case for Ga^{72} and Na^{24}. As mentioned previously, the corrosion estimates, from Ga^{72} concentrations, for tube and jacket material, were only possible because of the dissimilarity of the two tubes used in the test but now with the association of Ni^{65} with only the jacket cladding it was possible to make these estimations in a single tube.

The Effects of High Alum and Low pH on the Corrosion of Aluminum Reactor Surfaces - C. W. Thomas and W. B. Silker

The corrosive effects from either varying the alum feed in the process water treatment plant or the pH of the reactor cooling water were studied under separate half-reactor tests. Alum feeds varying from 6 to 18 ppm did not noticeably affect the aluminum corrosion but varying the coolant pH from 6.6 to 7.0 significantly increased the corrosion and was most pronounced on the fuel jacket cladding.

The relative corrosion rates of tubes and fuel element jackets were estimated in two half-reactor tests designed to determine the effects of

- high and low alum feed in the water treatment plant and
- high and low pH reactor coolant.[3.21, 3.22]

In one test, the coolant for one side of a reactor was treated with 18 ppm alum feed while the other side used 6 ppm at pH 6.6. A second test used 6.6 pH coolant for one side of a production reactor and 7.0 pH coolant for the other side. Comparisons of the Na^{24}, Ga^{72}, and Ni^{65} concentrations from each side of the reactor were used as indicators of the relative corrosion and erosion of the aluminum surfaces. Although conditions such as reactor power level, ion reabsorption, water composition, and flow rate also influenced the effluent concentration of these isotopes, the effects should be the same in each half of the reactor and any difference noted should result from the test conditions.

The results from the test comparing high and low alum feed in the water treatment facilities indicated these conditions did not significantly change the corrosion or erosion of the aluminum reactor tubes and fuel element jackets.

The results from the test comparing different pH coolants (Figure 3.21) indicated that reduction of the pH of the reactor coolant from 7.0 to 6.6 reduced the capacity of the film to furnish Na^{24} to the effluent water. The Ga^{72} results indicated an immediate reduction in surface film dissolution and erosion with pH 6.6 coolant. The Ni^{65} values were obtained only during the latter part of the test but if it is assumed that Ni^{65} concentrations of the control and test side coolants were similar at the beginning of the test period (as were Ga^{72} and Na^{24}) these data indicated a very pronounced effect of the pH 6.6 coolant in reducing the corrosion of the fuel jacket material.

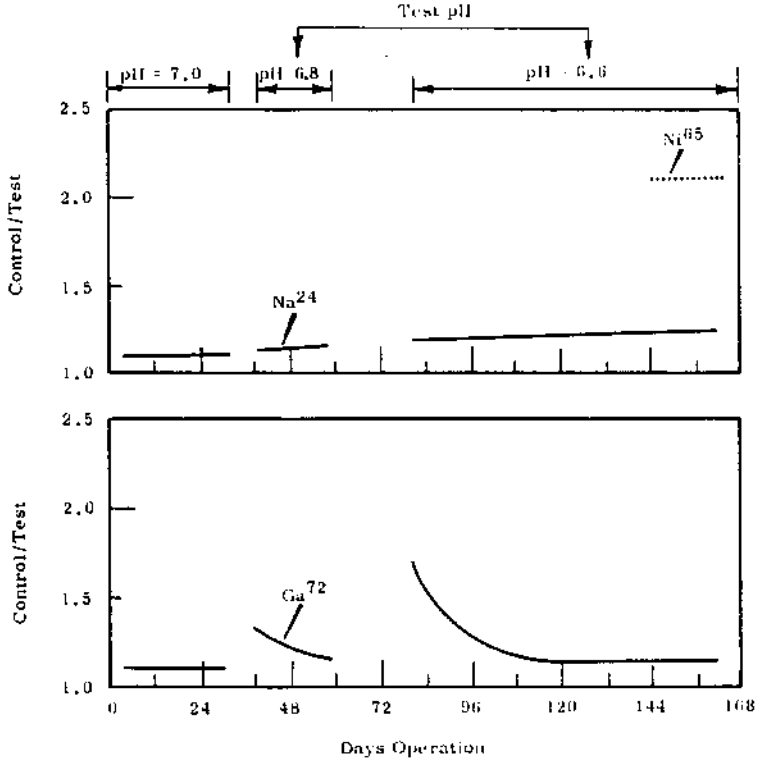

FIGURE 3.21

Ratios of Control/Test Concentrations of Na^{24}, Ga^{72}, Ni^{65}

Environmental Studies

Fallout Studies - R. W. Perkins

By use of newly developed multidimensional gamma-ray spectrometric counting techniques it has been possible to make direct measurements of eleven fallout radionuclides on air filters. The observed concentrations of Na^{22}, Mn^{54}, Co^{60}, Y^{88}, Zr^{95}-Nb^{95}, Ru^{106}, Sb^{124}, Sb^{125}, Cs^{134}, Cs^{137}, and Ce^{144} are reported and the significance of their relative concentrations is discussed.

The radionuclide content of the atmosphere has been measured on a continuing basis for the past 2 yr as part of a comprehensive study of fallout materials. The absolute and relative concentrations are of interest in determining the fallout rate and origin of the radionuclides as well as determining their availability for uptake by man. The tracing of some of the minor radionuclides in fallout as well as more precise measurement of the major radionuclides has been made possible by use of multidimensional gamma-ray spectrometric counting methods.*

Air sampling (3.23) is performed on a continuous basis by use of a 100 cfm vacuum pump which pulls air through a 5 micron pore size membrane filter that is backed up by a charcoal bed for collection of gaseous I^{131}. The membrane filters have been shown to be essentially absolute for fallout radionuclides.(3.23) After about 10^6 ft^3 have been drawn through the filters, they are counted in an anticoincidence shielded low background counter to determine their approximate activity levels. They are then composited on a monthly or semimonthly basis, pressed into a standard geometry of 1/2 in. thick by 1 in. diameter and counted on the multidimensional gamma ray spectrometer.* The air sampling location is on the roof of a building (approximately 15 ft high) 6 mi north of Richland, Washington. The observed activities of Na^{22}, Mn^{54}, Co^{60}, Y^{88}, Zr^{95}-Nb^{95}, Ru^{106}, Sb^{124}, Sb^{125}, Cs^{134}, Cs^{137}, and Ce^{144} are recorded in Figure 3.22. The radionuclide Y^{88} (3.24) was recently reported to be present on samples of grass near the Euratom Nuclear Center at Ispra, Italy.

---

* See "Application of Multidimensional Gamma Ray Spectrometry," page 3.1.

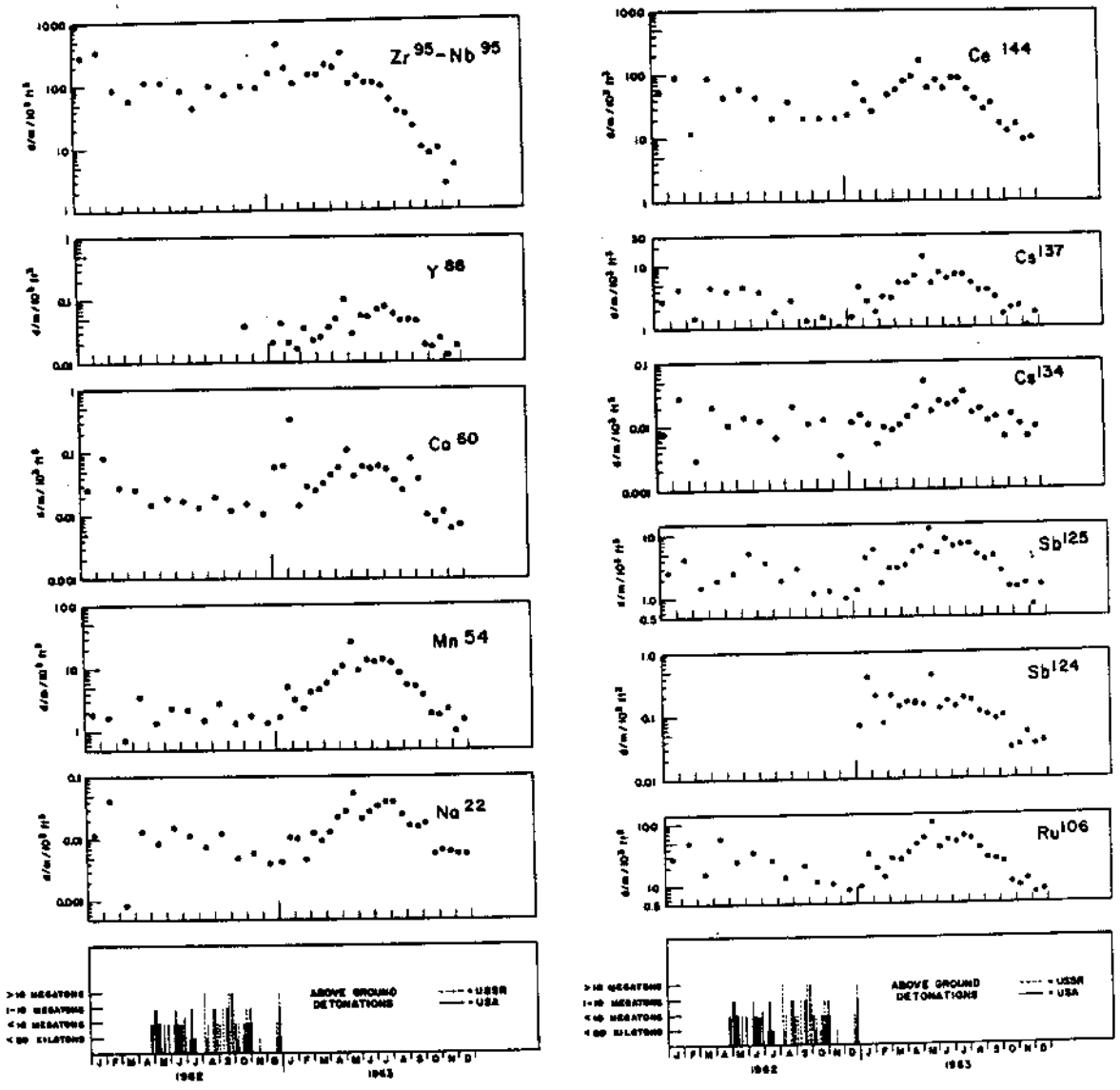

FIGURE 3.22

Observed Fallout Radionuclide Concentrations
at Richland, Washington,
During 1962-1963

AEC-GE RICHLAND, WASH.

It was in the form of insoluble particles containing much larger amounts of Zr^{95}-Nb^{95} and although its source was not known it did not come from the Nuclear Center and presumably came from either nuclear bombs or an uncontrolled release from a nuclear establishment.

Because of smaller air sampling volumes during 1962, Y^{88} could not be detected except during the month of November; however, it was easily detectable during 1963 and was measured on samples collected during the full calendar year. It is interesting and significant that although Y^{88} did show a peak concentration in May through August, its concentration at the end of the year was comparable with that at the beginning. Y^{88} is presumably formed during nuclear testing by an n, 2n reaction on Y^{89} and since there were no above ground detonations during 1963[3.25] it must have been injected into the atmosphere during 1962 or before. Although the Y^{88} (105 d) reservoir in the atmosphere decreased by a factor of 12 due to radioactive decay during the year, its concentration in air followed a pattern similar to Cs^{137} (30 yr).

The radionuclide Na^{22} was first reported to be present in the atmosphere by Marquez[3.26] in 1957 who found it in rain water at Rio de Janeiro in a concentration of 0.017 distintegrations/min/liter. It is produced naturally by cosmic-ray spallation of argon in the atmosphere but may also result from the reaction Na^{23} (n, 2n) Na^{22} during nuclear weapons testing. Its potential value as a tracer of atmospheric circulation has been recognized and recently reported measurements for this purpose by Bhandari and Rama[3.27] have shown air concentrations ranging from 1 disintegration/min/10^6ft^3 below the tropopause to 460 disintegrations/min/10^6ft^3 above the tropopause. Figure 3.22 shows that the Na^{22} concentrations in air were about a factor of two higher during 1963 than in 1962. Also the 1963 values are about an order of magnitude higher than those reported for troposphere measurements before the 1961 atomic tests.[3.27]

The Cs^{134} appears to be produced in nuclear detonations mainly by an n, γ reaction on Cs^{133} but is also produced directly by fission.[3.28] The

ratio of Cs^{134} to Cs^{137} is of particular interest in tracing the Cs^{134} and this ratio is presented in Table 3.14. The Cs^{134} to Cs^{137} ratio has been about 0.003 during the past year. During late 1962 and early 1963 cesium radionuclide analyses were performed on the dust collected by the large fiber glass filters which filter the air inlet to a laboratory building at Hanford. The observed Cs^{134} to Cs^{137} ratio on these filters was 0.016 to 0.017. [3.28, 3.29] It is very significant that the Cs^{134} to Cs^{137} ratios observed on these fiber glass filters were 2 to 4 times higher than those found on membrane air filters collected during the same period.

TABLE 3.14

Cs^{134} TO Cs^{137} RATIO DURING 1962-1963

1962		1963	
Month	$\frac{Cs^{134}}{Cs^{137}} \times 100$	Month	$\frac{Cs^{134}}{Cs^{137}} \times 100$
1/62*	0.29	1-A**	0.75
2/62*	0.66	1-B	0.56
3/62*	0.20	2-A	0.40
4/62	0.46	2-B	0.31
5/62	0.27	3-A	0.30
6/62	0.29	3-B	0.29
7/62	0.33	4-A	0.20
8/62	0.36	4-B	0.27
9/62	0.71	5-A	0.30
10/62	0.83	5-B	0.37
11/62	0.83	6-A	0.33
12/62	0.32	6-B	0.32
		7-A	0.36
		7-B	0.34
		8-A	0.48
		8-B	0.31
		9-A	0.46
		9-B	0.30
		10-A	0.44
		10-B	0.41
		11-A	1.19
		11-B	0.47
		12-A	0.64
		12-B	0.54

* Only small samples were available. Cs^{134} values give only the order of magnitude.

** A and B signify approximately the first and second half of each month, respectively.

The Cs^{134} is in a greater isotopic abundance on large atmospheric dust particles which are preferentially held by the fiberglass filters than on small particles which are all removed by the membrane filters. (3.23) This observation is in accord with the methods of formation of the cesium isotopes. Cs^{137} is a daughter of the rare gas Xe^{137} (3.8 min), while Cs^{134} is formed directly either by the reaction Cs^{133} (n, γ) Cs^{134} or as a direct fission product.

The radionuclides Mn^{54}, Co^{60} and Sb^{124} and apparently most of Sb^{125} are formed by neutron activations of the cladding or other inert material of bombs. Because of their long half-lives all these radionuclides except Sb^{124} (60 d) will be useful atmospheric tracers for several years. The radionuclides in fallout which are concentrated by biological processes are being studied as they move through the food chain to man.

Physical and Chemical Forms of I^{131} from Fallout and Chemical Processing Plants - R. W. Perkins

> Studies have continued on the form of I^{131} from fallout and from chemical separations plant stacks. It was observed at Hanford that less than 10% of the fallout I^{131} in the gaseous state is present as the elemental iodine or as HI. Greater than 50% of the stack gas I^{131} is in the form of organic iodides and does not attach itself significantly to particulate material at distances of several miles from its point of release.

A knowledge of the physical and chemical forms of I^{131} in the atmosphere is important in understanding its transport and in assessing the potential hazard due to its presence. A recently published study of I^{131} (3.23) in fallout summarizes much of the work at Hanford through mid 1963 and points out that the fraction of I^{131} in the gaseous phase during 1962 varied from 10 to 90%. Also, the I^{131} associated with particulate material was mainly in the reduced state as iodides or possibly I_2 with a small fraction in the IO_3^- form and little or none as IO_4^-. Studies of gaseous I^{131} in the atmosphere showed that less than 10% was present as elemental iodine or HI and suggested that most of the gaseous I^{131} was in the form of organic iodides. It was recently reported that some of the I^{131} in fallout is present in the form

of alkyl iodides [3.30] the major component being methyl iodide. During 1963 no above-ground atomic detonations were reported [3.25] and the levels of I^{131} relative to other fission products in the air were very low.* The major source of I^{131} in the atmosphere at Hanford is presumably from the chemical separations facilities; however, some may have been vented from the numerous underground atomic tests in Nevada. The absence of large amounts of I^{131} from atomic tests this past year has allowed a more careful observation of the physical and chemical form of the I^{131} which is normally released in small amounts from the chemical separations plants at Hanford.

Measurements of the stack gases from the Hanford separations plants have shown that the I^{131} being released is at least 99.9% in the gaseous state. This was established by filtering the stack gases through membrane filters (Gelman AM-7, 0.3 microns) followed by charcoal traps and measuring their respective I^{131} contents.

To determine the nature of the gaseous I^{131}, several trapping systems were used. Laboratory studies had shown that carrier-free elemental I^{131} or HI could be completely removed from an air stream by passing it at 0.2 cfm through a 2 ft long by 2 in. diameter Berl saddle packed column of 0.2N NaOH. In experiments with this column the air leaving it was diluted 1:2 with room air (to reduce the humidity) and the gases were passed through a 6 in. long by 2 in. diameter charcoal bed (6 to 14 mesh) to remove any remaining I^{131}. In studies of the separations plant effluents it was observed that the caustic scrubber collected between 30 and 50% of the I^{131}, the remainder being held by the charcoal. In experiments where the charcoal trap was placed upstream from the caustic scrubber all of the I^{131} was held on the charcoal trap. It was thus evident that most of the I^{131} was in a form other than I_2 or HI and was presumably present as an organic iodide. In a second experiment designed to further examine the effluent gases, a trap was used which consisted of a 4 in. long by 2 in. diameter silver mesh bed (1 x 20 mil mesh) followed by a 4 in. long by 2 in. diameter charcoal trap. Laboratory studies with this trap had shown that carrier-free I_2^{131}, and HI^{131} (at about 100 micrograms/m^3) were collected with 90 and 99% efficiencies at linear flow rates of 200 to 400 ft/m

* See "Fallout Studies," page 3.51

When these traps were used on separations plant effluents at the above flow rates, approximately 30% of the I^{131} was held by the silver mesh, again indicating that the I^{131} was in a form other than I_2 or HI.

Small amounts of the organic iodides have been collected in a gas train consisting of a magnesium perchlorate drying column followed by a toluene (or diethyl ether) scrubber held at -70 C (dry ice in acetone). Scrubbing the organic solutions with dilute NaOH did not remove the I^{131} activity and thus confirmed the assumption that I^{131} was present as organic iodides. This method of collection did not provide a high specific activity solution of the organic iodides and attempts to concentrate the organic species on a fractionating column met with limited success. Gas chromatographic studies were not completely definitive because of the very low specific activities studied. These studies used either silicon or carbowax columns and the gases from the columns were collected on charcoal cartridges that were changed periodically during the run. The I^{131} activity on these cartridges was very low but did indicate the possible presence of several different organic iodides. Compared with the rate of movement of butyl iodide on these columns, about half of the activity preceded it and half followed. The thermal conductivity output of the chromatograph did show the presence of at least 8 organic species that may or may not be associated with the radioiodine species. Gas chromatographic analyses starting with higher specific activity material is planned to obtain definite identifications of the major organic iodides present.

During a period of above normal I^{131} emission from a separations plant stack, air samples were collected to determine if rapid changes did occur as the material moved away from its point of release. Sampling was performed from an airplane by pulling air through a membrane filter (pore size 5 micron) followed by a charcoal trap.[3.23] Samples were collected at 200 to 500 ft by multiple penetrations of the stack plume at distances of 1, 3, 5, 10 and 25 mi from the source. The I^{131} on the filter and the charcoal was measured by taking long counts on highly sensitive gamma ray spectrometric equipment.[3.1] The fraction in the gaseous state is shown in Table 3.15. It

is interesting that very little change in physical form occurs over the distances measured. The observed activities at 25 mi on 9/4/63 and 10 mi on 9/3/63 were low and may not represent any change in physical form. The major change occurs between the stack and the first mile.

TABLE 3.15

PHYSICAL FORM OF I^{131} AT VARIOUS DISTANCES FROM THE SOURCE

(Sampled from aircraft 9/4/63)

Distance, mi	Percent Present as a Gas
0	> 99
1	73
3	90
5	92
10	92
25	96 ±10% (a)
(9/3/63)	
0	> 99
1	82
3	82
5	81
10	58 ±20% (a)

(a) Standard deviation of measurements

Investigation of the Nature of I^{131} in the Atmosphere -

J. D. Ludwick

The physical and chemical forms of iodine were investigated through air and vegetation sampling downwind from three I^{131} radioisotope releases. Mass sampling was conducted when iodine was dispersed during two separate tests having controlled emissions. Air sampling was also conducted subsequent to a Purex release. Significant changes in the form of iodine were noted over the distance sampled. The iodine released from the controlled tests did not indicate chemical or physical adsorption similarity with that from Purex.

National Reactor Testing Station (NRTS) Iodine Test

In the early summer of 1963 about 1 curie of I^{131} was released under controlled conditions over a prepared course near the NRTS, Idaho Falls, Idaho. Samples of air and vegetation were taken downwind in rows from five chemical generators. In the generators, radioactive iodine and carrier were oxidized from iodide to free iodine and flushed out of a weak acid solution with nitrogen at a controlled rate.

Air samplers were compartmentized to collect first, particulate on molecular filters, then reactive iodine species on 2 in. of silver mesh, and the remaining iodine in a 0.5 in. depth of activated charcoal. Some selected samplers also had a 6 in. backup charcoal bed to trap further iodine and to estimate the efficiency of the 0.5 in. bed. Vegetation samples were collected directly in front of the air samplers. From 0.75 to 2.0 ft^2 of vegetation were taken. This amounted to between 75 qnd 250 g of total crested cheat grass per sample. Each grass sample in the field was sectioned into 3 parts containing the approximate fraction, 0.35, 0.31 and 0.34 respectively, from top to bottom. The average grass height over the course was 10 to 12 in.

Tables 3.16 and 3.17 illustrate the air iodine concentrations and vegetation deposition observed during this test. Vegetation results indicated that 50% of the total activity of iodine deposited on grass could be found in the upper section (H) (by weight) and 30% in the middle section (M), while 20% was found in the lowest grass section (L). After making observations on the eating habits of cows over identical grass plots, it was concluded that only the upper and middle grass sections were being eaten and this should be considered in making any estimate of their intake. The backup charcoal sections were used to estimate iodine corrections to be applied to those samplers which did not have them. The samplers were positioned at 4 distances from generation point. Samples 1 through 4 were located 164 ft downwind; 5 through 8, 329 ft; and Samples 9 and 10 were located 565 ft and 964 ft downwind, respectively. An estimate of 25% grass cover was made from

TABLE 3.16

VEGETATION SAMPLE DATA FROM NRTS IODINE TEST

Sample	I^{131}, microcuries	Grass Weight, g
1-L	220	71.1
1-M	260	63.1
1-H	650	79.1
2-L	280	30.8
2-M	310	24.0
2-H	620	32.2
3-L	230	32.5
3-M	260	25.3
3-H	410	25.0
4-L	280	55.1
4-M	360	49.3
4-H	730	40.6
5-L	110	72.8
5-M	120	58.5
5-H	250	63.6
6-L	110	44.8
6-M	97	34.8
6-H	240	54.5
7-L	110	63.5
7-M	120	54.7
7-H	240	82.4
8-L	130	53.6
8-M	180	54.3
8-H	350	56.2
9-L	75	68.7
9-M	110	60.2
9-H	200	68.6
10-L	47	72.5
10-M	54	60.6
10-H	230	61.5

TABLE 3.17

AIR SAMPLE DATA FROM NRTS IODINE TEST

Sample	I^{131}, microcuries	% of Total	Flow Rate and Height
1 Filter	35	33.8	
1 Silver	52	50.7	1 cfm
1 Charcoal	14	13.5	1 ft high
1 Estimated Loss	2	2.2	
2 Filter	47	25.7	
2 Silver	110	58.3	1 cfm
2 Charcoal	25	13.8	3 ft high
2 Estimated Loss	4	2.2	
4 Filter	40	20.3	
4 Silver	90	54.5	1 cfm
4 Charcoal	23	14.0	3 ft high
4 Backup Charcoal	4	2.2	
5 Filter	19	17.1	
5 Silver	71	62.2	2 cfm
5 Charcoal	21	18.5	3 ft high
5 Estimated Loss	3	2.2	
6 Filter	24	23.6	
6 Silver	59	57.1	2 cfm
6 Charcoal	18	16.9	1 ft high
6 Estimated Loss	3	2.2	
7 Filter	37	33.4	
7 Silver	50	44.3	2 cfm
7 Charcoal	23	20.1	3 ft high
7 Backup Charcoal	2	2.2	
8 Filter	36	26.2	
8 Silver	76	55.9	2 cfm
8 Charcoal	22	16.2	5 ft high
8 Estimated Loss	3	2.2	
9 Filter	8	7.4	
9 Silver	66	63.6	4 cfm
9 Charcoal	23	22.2	3 ft high
9 Backup Charcoal	7	6.8	
10 Filter	20	22.0	
10 Silver	39	46.7	4 cfm
10 Charcoal	21	24.5	3 ft high
10 Estimated Loss	5	6.8	

AEC-GE RICHLAND, WASH.

observations of the plot. Between Rows 1 and 2, 12 microcuries of iodine was calculated to be present with 13 microcuries between 2 and 3, and 9 microcuries between 3 and 4. A restriction to free flow was found on Sample 3, Arc 1, and results from this sampler were omitted.

The generation technique was tested in the laboratory and found to produce elemental iodine gas which was not collected by membrane filters. The air samples showed that there was 20 to 30% of the activity present as particles. This amount did not change significantly with distance from the source. Explanation of this may be that only a certain amount of the generated iodine is in a very reactive form to attach to particles, or there was a local dust source between the generators and the first sampler row which added a definite amount of particles to the air stream with which the iodine could react.

About 75% of the gaseous iodine which passed through the membrane filters was collected as an active species in the silver mesh section while the remaining was collected on the charcoal. At low rates, the 0.5 in. charcoal proved quite effective in trapping iodine with only 2 to 3% escaping this narrow region. No significant change in the chemical or physical form was noted for the iodine as it traversed the grid. This was indicated by no significant variation between iodine sampler component ratios through the grid.

Hanford Controlled I^{131} Release

About 0.15 curie of I^{131} was released on a controlled course within the large meteorological grid at Hanford. The iodine was generated by heating elemental iodine. Seven grass plots were cultivated in an arc at 200 m from dispersal point. Samples of this grass and other natural vegetation were collected as well as air samples at ground level and on selected towers above the ground. A special materials test was also conducted for comparison purposes of iodine adsorption.

Polyethylene air samplers were manufactured to collect the iodine as it traveled downwind from generation point. These allowed collection of

particles on a membrane filter, followed by a gap to prevent cross-contamination and a 4 in. silver mesh cartridge for reactive iodine species. The silver compartment was separated from the 2 in. activated charcoal section with a charcoal filter paper sandwiched between two glass filters to prevent contamination. The charcoal filter paper will collect most remaining forms of iodine except such species as gaseous organic compounds.

Table 3.18 is a summary of data obtained from I^{131} assay of grass samples taken from the seven 20 x 7 ft plots. These plots were numbered from left to right as one looks out upon the course from generation point. The most northerly of the plots were about 098 degrees. The peak I^{131} was found on air samples to be about 085 degrees; consequently, all plots missed this peak. The data were averaged and it was found that exactly 2/3 of the activity was on the upper half of the grass and 1/3 on the lower half. This is in agreement with the Idaho Falls data which indicated a spread of 50-30-20 for approximately 1/3 section. The grass was very similar to that in Idaho Falls except for the clump nature of that at Idaho Falls. In almost all cases the grass from front sections contained more I^{131} than center or rear grass (up to twice as much). The left side of any individual grass plot was more toward the high activity region accounting for some left-back increased activity. The left-back samples of 5-6-7 are more northerly than the left-center samples, probably accounting for unusually high activity.

Results of ground and vegetation sampling from downwind of I^{131} dispersal are included in Table 3.19. The iodine was found predominantly on green-type vegetation such as green sagebrush leaves and green live Russian thistles. Very little, if any, was observed on the ground and where it was found or suspected to have been present, it was obscured by other radio-isotopes which have been accumulating for some time. The quantity of iodine adsorbed by sagebrush and Russian thistle was quite comparable; however, the interfering isotopes, which have been collecting on the sagebrush, are almost entirely absent on the Russian thistle samples, allowing much greater sensitivity for I^{131} analysis. This is due to the transient nature of the Russian

TABLE 3.18

IODINE ACTIVITY ON GRASS PLOTS AT 200 m

Relative Plot Position	Grass Fraction	Grass Weight, g	I^{131} Total Activity, disintegrations/min	I^{131} Specific Activity, disintegrations/min/g	% on Phase
1-Front	Top	68	48,400	710	68
1-Front	Bottom	48	15,900	340	32
1-Center	Top	Unweighed	38,800	-	-
1-Center	Bottom	70	31,300	450	-
2-Front	Top	60	63,500	1050	59
2-Front	Bottom	41	29,900	730	41
2-Center	Top	54	32,000	600	63
2-Center	Bottom	55	19,400	350	37
3-Front	Top	48	38,600	800	66
3-Front	Bottom	32	13,300	410	34
3-Center	Top	91	34,000	370	68
3-Center	Bottom	93	16,100	170	32
4-Front	Top	66	13,100	200	72
4-Front	Bottom	61	4,800	80	28
4-Center	Top	44	12,100	280	73
4-Center	Bottom	44	4,600	100	27
5-Left-Back	Top	55	6,500	120	71
5-Left-Back	Bottom	50	2,460	50	29
5-Left-Center	Top	87	3,700	40	76
5-Left-Center	Bottom	65	800	13	24
5-Right-Center	Top	53	11,800	220	60
5-Right-Center	Bottom	59	8,700	150	40
5-Right-Front	Top	52	9,100	180	65
5-Right-Front	Bottom	57	5,300	90	35
6-Left-Back	Top	46	8,200	130	66
6-Left-Back	Bottom	34	2,300	70	34
6-Left-Center	Top	51	3,250	64	67
6-Left-Center	Bottom	32	1,000	30	33
6-Right-Center	Top	85	2,730	30	67
6-Right-Center	Bottom	68	1,100	15	33
6-Right-Front	Top	80	10,800	135	69
6-Right-Front	Bottom	72	4,300	60	31
7-Left-Back	Top	69	1,700	25	68
7-Left-Back	Bottom	45	540	12	32
7-Left-Center	Top	37	1,150	30	-
7-Left-Center	Bottom	-	900	-	-
7-Right-Center	Top	71	1,400	20	56
7-Right-Center	Bottom	100	1,500	15	44
7-Right-Front	Top	54	1,000	20	-

thistle and their relatively rapid growth. The results indicate that sensitivity to 3200 m can be anticipated even with this small activity release.

TABLE 3.19

IODINE ADSORPTION ON NATURAL DESERT VEGETATION

Arc-Azimuth Position	Vegetation	Ground Area, ft^2	Disintegrations/min/ft^2	Arc-Azimuth Position	Vegetation	Ground Area, ft^2	Disintegrations/min/ft^2
2-078	Soil	1	0	3-082	Soil	1	0
2-078	Cheat	1	660	3-082	Cheat	1	0
2-078	Sage	1.5	2510	3-082	Sage	1.5	1140
2-080	Soil	1	0	3-083	Soil	1	0
2-080	Cheat	1	310	3-083	Cheat	1	Trace
2-080	Sage	2	4490	3-083	Sage	2	0
2-082	Soil	1	360	4-081	Soil	1	0
2-082	Cheat	1	2200	4-081	Cheat	1	0
2-082	Sage	2	5890	4-081	Thistle	1	0
2-084	Soil	1	0	4-082	Soil	1.5	0
2-084	Cheat	1.5	2440	4-082	Cheat	2	Trace
2-084	Thistle	1	3490	4-082	Thistle	1	74
2-086	Soil	1	530	4-083	Soil	1	0
2-086	Cheat	1	4820	4-083	Cheat	1	0
2-086	Thistle	1	4730	4-083	Thistle	3	0
2-081	Soil	0.7	Trace				
2-081	Cheat	1	200				
2-081	Sage	1.5	1030				

NOTE: Arcs 1, 2, 3 and 4 are 200, 400, 1600 and 3200 m, respectively from the source

The bulk of air sampling data near ground level is illustrated in Table 3.20. Only samples with significant activity were included which were located in the prevailing downwind direction. The angular location and number of analyses is given and the average percent of I^{131} on each phase is included next to the accumulated phase disintegration rate for the arc. Two types of samples were utilized on Arc 4 and the last row may not be comparable with the rest of the data since the charcoal filters were included.

It is apparent that the particles accumulate iodine as they traverse downwind from dispersal point. This can be attributed to the association of iodine with more particle species as it progresses. Evidently, this process of

iodine adsorption or reaction with particles is not a very fast one or only a certain amount of the iodine was available for this action in the first place. The amount that is available may react more quickly initially with no subsequent reaction such as was observed during the early summer run.

TABLE 3.20

I^{131} IN AIR SAMPLER SECTIONS TAKEN 1.5 m ABOVE GROUND

Sample Location (Azimuth)	Samplers (Number)	Filter (Particulate) disintegrations/min	%	Silver (Reactive) disintegrations/min	%	Filter Charcoal disintegrations/min	%	Backup Charcoal disintegrations/min	%
Arc-1 068-114°	22	18,400	(9.7)	139,300	(73.8)	15,000	(8.0)	16,100	(8.5)
Arc-2 072-118°	23	2,200	(12)	11,800	(65)	1,300	(7.4)	2,800	(15.6)
Arc-3 086-110°	24	1,300	(22.5)	3,000	(51)	600	(10.5)	900	(16)
Arc-4 080-106°	15	900	(30)	1,000	(34)	200	(6.0)	800	(28)
Arc-4 071-079° 109-115°	14	330	(37)	430	(48)	None present		140	(16)

Another interesting point is that the total reactive iodine, adsorbing on particles plus that found on silver mesh, changes only slowly with distance even though the particle species is rapidly increasing. The backup charcoal data indicate a slow decrease of reactive iodine with distance. It may possibly be that reactive iodine is being converted to organic forms not collected by charcoal paper. There may be two forms of iodine: that which is collected and remains constant with distance in the charcoal filter and that which reacts either with atmospheric chemicals or adsorbs to particles. It

appears that at longer distances the reactive iodine which appears on the silver mesh will eventually change to some other form and this reactive fraction will become insignificant. Results from air samples which were collected on towers to determine vertical iodine distributions did not lend themselves to any systematic conclusions and, in fact, were occasionally contradictory. There was some evidence that differences in the samplers due to some losses of iodine on an additional glass filter pad present directly behind the front face filter may have contributed to the conflicting results.

The data presented in Table 3.21 illustrate the results of analyses carried out for I^{131} deposited on the artificially prepared surfaces.

TABLE 3.21

I^{131} ADSORPTION ON SELECTED MATERIALS

Material	Plant A Disintegrations/min/ft^2	Plant B Disintegrations/min/ft^2	Area Tested, in.^{2}
Silver Mesh	1,274,800	771,600	20
Charcoal Paper	73,580	81,620	5.52 (A) 2.76 (B)
Silver Metal	58,860	57.080	16.62
Brass Metal	32,480	31,150	12.0
Copper Metal	22,410	28.080	11.08
Charcoal Plant Base	18,040	13,180	17.3
Charcoal Sheet	25,360		84

Because of the manner in which this experiment was conducted, only the metals data can be considered intercomparable. Silver picked up 1.8 times as much I^{131} as brass and 2.3 times that of copper; brass picked up 1.3 times that of copper. The charcoal paper picked up considerably more I^{131} than the silver metal; however, the sections of charcoal were relatively small and were higher than the metals. Consequently, more data are necessary and further experiments are needed to provide definitive information for the charcoal.

Much activity was adsorbed by the silver mesh. It was estimated that about 20 in.^{2} of area was encompassed by the mesh as seen from the wind vector; however, no estimate has been made on the actual area of thin metal foil in the mesh itself.

Purex Iodine Release

Iodine samplers identical to those utilized in the previous discussion were positioned at 15 ft intervals on a 200 ft meteorological tower located 3 mi from the Purex stack and also at a point about 1.5 mi and in a different direction from the stack near ground level. Samples were collected for 3 days and each set was run from 8 to 16 hr at a flow rate of 1 ft^3/min. The tower iodine distribution showed that at some time during one of the runs, the stack plume had hit the tower below 170 ft with the peak activity at 50 ft. The observed activity distribution along the tower (as well as the fact that this occurred during an 8 hr sampling and the activity level was much greater than preceding and following runs) led to the conclusion that the iodine sampled came directly from the stack.

Samples taken at the other station remained sensibly constant in their activity levels and are believed to represent the general iodine concentration and form present in the vicinity of Purex at that time. The important point here is that this iodine can be assumed to have had prolonged contact with the atmosphere and is not directly from the stack. Results of these sampling stations are shown in Table 3.22.

TABLE 3.22

PUREX IODINE DISTRIBUTION IN FIELD SAMPLERS

	Front Filter	Silver or Copper	Charcoal Filter	Activated Charcoal
Plume Tower Samples (Direct Iodine)	5%	46%	3%	46%
Ground Samples (General Iodine)	12%	15%	19%	54%

The differences in these samplers probably reflect some real differences in physical-chemical forms of the iodine. The ground samplers collect iodine which has travelled through the atmosphere for considerably longer times and distances than the tower iodine. In correlating the amount

of iodine found on the various phases here with that observed during controlled field generated iodine, we find much higher amounts in the activated charcoal section, indicating a great deal of nonreactive iodine species. Perkins* has demonstrated that the stack iodine, in contrast to the I_2 dispersed under field conditions, comes out with at least 50% in a nonreactive form; probably as organic iodine compounds. This would explain the very large amount of this species collected, even in the direct plume samplers. The increase in particle form from 5 to 12% is also readily understandable since the iodine collects more and more on particles as it associates with dust for a greater time. The drop in the reactive iodine species was also observed in controlled field testing; however, part of this species was converted into a form collected by the charcoal filter paper, a fact not observed during controlled iodine emission. Evidently, the iodine, which was in contact with the atmosphere for a considerably longer period than in controlled experiments, encountered other reactable species or reacted more slowly with certain atmospheric species whose kinetics precluded significant obserable effects in a short controlled experiment.

Dual Tracers Utilizing the Fluorescence of Fluorescein and Calcium Acetylsalicylate - J. D. Ludwick

A procedure was developed for the detection of fluorescent materials in a study of their possible use as atmospheric tracers. New instrumentation, which allowed differentiation of excitation and emission spectra, was used. This resulted in an analytical method for simultaneous analysis of the fluorescent materials, fluorescein and the calcium salt of aspirin. Cross-tracer interference was reduced to a minimum and as little as 5×10^{-11} g of fluorescein and 3×10^{-9} g of Ca-aspirin was measured.

Introduction

Detection of microgram quantities of material is usually a necessary analysis requirement when tracers are used to study atmospheric diffusion phenomena. Chemically and radiochemically inactive materials, with known

---

* See "Physical and Chemical Forms of I^{131} from Fallout and Chemical Processing Plants," page 3.55

size distribution and acceptable atmospheric characteristics, which can be detected with a sensitivity of less than 1×10^{-8} g per analysis are rare. Dilution factors of about 1×10^{12} must be tolerated from tracer dispersal point to sample collection. Simultaneous distribution of two such tracers in an effort to study other effects on wind diffusion compound the analytical problem and require two such described materials being compatible with each other and capable of being separately analyzed in mixtures. In addition to these requirements, there must also be a short simple analytical method for the many field samples that are necessary for definitive results.

A few fluorescent and phosphorescent materials satisfy many of the above requirements and have been investigated for their ability to simulate atmospheric diffusion.[3.31] Analytical techniques have been developed in this work for emission, collection, and sampling of two fluorescent tracers simultaneously dispersed to the environment. The sodium salt of fluorescein which has been used in the past was used with a new tracer, the calcium salt of acetylsalicylic acid (Ca-aspirin). These materials have been tested in a field experiment. The analytical distinction between these two fluorescent tracers was based upon their differences in the excitation and emission spectra.

The field dispersal technique of these materials calls for dissolution of a considerable amount of the tracer in water and generation of a fine spray through a nozzle. Although acetylsalicylic acid has good fluorescence properties, it is only slightly soluble in water. It was necessary to obtain a soluble form of the ester and test its fluorescence characteristics. Tests showed that the specific fluorescence of the calcium salt corrected for calcium and water of hydration was identical to the aspirin. After dispersal, the tracers were collected on molecular filters; consequently, the analytical system was developed to tolerate their presence. As little as 5×10^{-11} g of fluorescein may be detected in the presence of all normally anticipated Ca-aspirin concentrations. Although no significant cross tracer interference

that no adverse chemical reaction takes place between these organic compounds. Standard solutions of each tracer were prepared, and the fluorescence was measured under the other tracer's excitation-emission-optical filter-chemical addition settings. The amount of correction, if any, for the presence of cross-tracer could then be made. Table 3.24 illustrates the results in the range of concern for the tracers.

TABLE 3.24

CROSS TRACER FLUORESCENCE INTERFERENCE

Concentration of Ca-Aspirin, g/ml	Fluoroscein, Units	Concentration of Fluorescein, g/ml	Ca-Aspirin, Units
3×10^{-5}	120	1×10^{-7}	63
9×10^{-6}	25	1×10^{-8}	51
3×10^{-6}	22	1×10^{-9}	48

It can be seen that Ca-aspirin will not interfere with analysis of fluorescein since 3×10^{-5} g/ml shows a fluorescence comparable to only 1×10^{-10} g/ml under these conditions. A small correction may be necessary, in a few cases, for the presence of fluorescein when analyzing for aspirin since 1×10^{-7} g/ml exhibits about 3×10^{-9} g/ml comparable Ca-aspirin fluorescence.

Discussion

The most critical analytical criteria involved in the use of more than one fluorescence tracer are the spectral absorption and emission exhibited by the chemicals. Although complete separation of the individual spectra is not absolutely necessary, it is desirable and affords a much more sensitive analysis system. Differences in the absorption spectra of the tracers are the most ideal methods of differentiation. Obviously, if one does not excite the second tracers, no fluorescence will be observed.

Figure 3.23 illustrates the fluorescence absorption spectra of fluorescein (1×10^{-8} g) and Ca-aspirin (1×10^{-6} g). The Ca-aspirin spectrum has two fluorescence absorption peaks, the one at 300 millimicrons being the most

efficient. The observed peak at 410 millimicrons is simply the scattered excitation light observable, since the emission monochrometer was set at 410 millimicrons. Fluorescein excites several excitation maxima with the one near 490 millimicrons being the most useful. No significant scatter peak was observed since the tracer is effective in absorbing light near the emission setting of 530 millimicrons. After consideration of these spectra it is apparent that excitation of fluorescein at 490 millimicrons will not induce fluorescence in Ca-aspirin, and excitation of Ca-aspirin at 300 millimicrons will induce fluorescein fluorescence to a small extent.

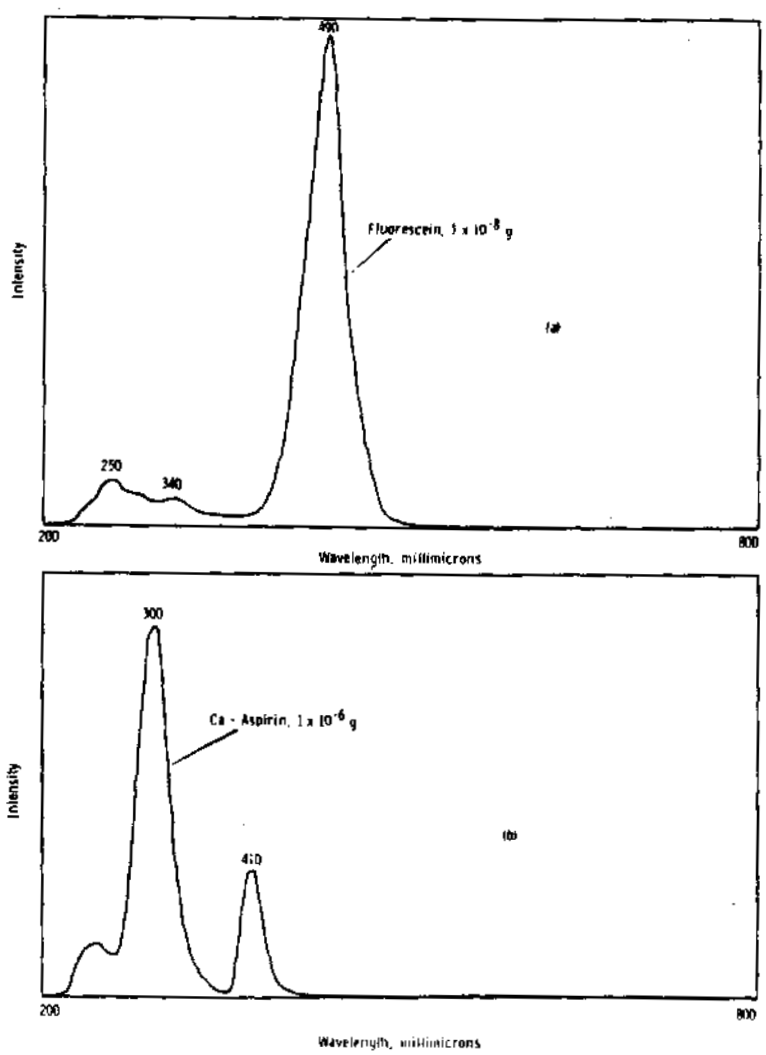

FIGURE 3.23
Fluorescence Absorption

The fluorescence emission of fluorescein is illustrated in Figure 3.24. Note the close proximity of the excitation scattered light and the fluorescence. When higher concentrations of fluorescein are measured, the scatter peak disappears, since more complete absorption of the 490 millimicron light takes place.

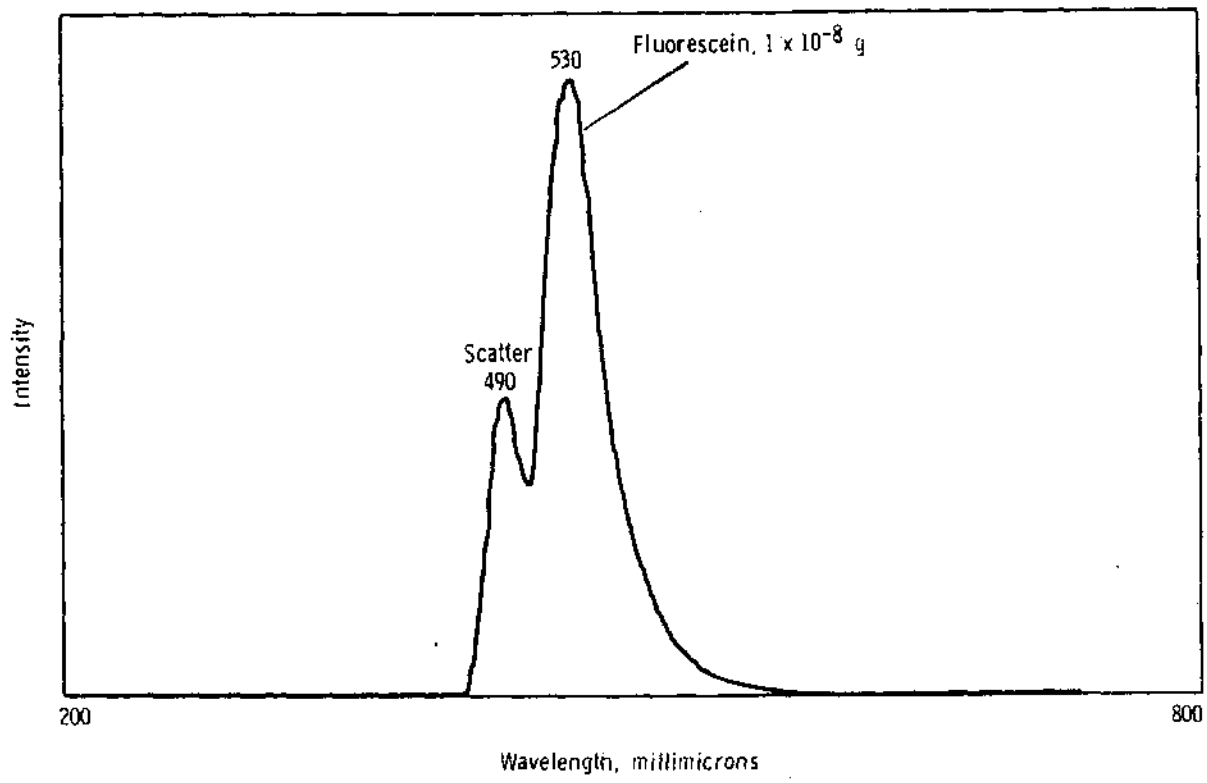

FIGURE 3.24
Fluorescein Emission

The two sections of Figure 3.25 illustrate the emission of these tracers and the cross interference of the other under typical analysis conditions and for identical quantities of trace materials. Note the interference of fluorescein in the Ca-aspirin spectrum when excited with 300 millimicron light and the lack of interference of Ca-aspirin in the fluorescein spectrum when exciting the 490 millimicron light. Transmission-type interference filters were used to reduce

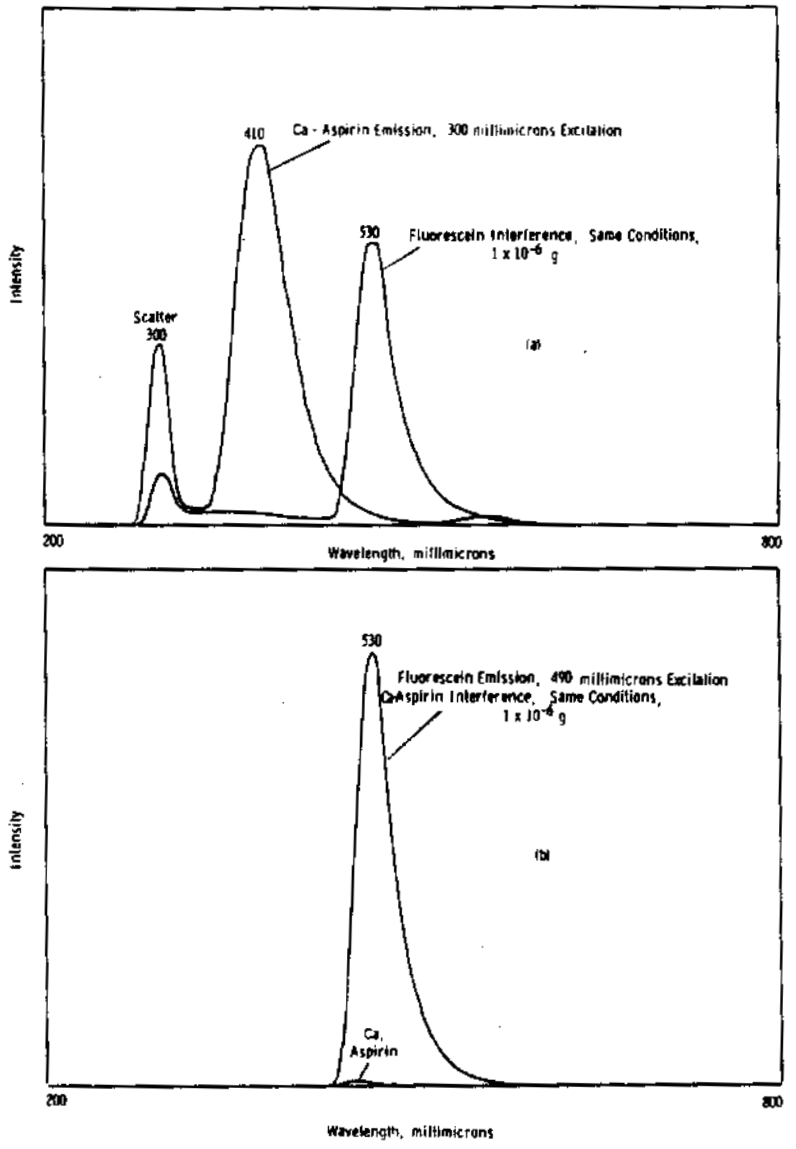

FIGURE 3.25
Cross Tracer Interference

the fluorescein interference in the Ca-aspirin spectrum by narrowing the detection band. In addition, an interference filter was also used when analyzing fluorescein to eliminate scattered excitation light and minimize certain background light. This latter, random light becomes important when smaller amounts of tracers are being measured. Figure 3.26

illustrates the effectiveness of these filters in eliminating cross-interference. The result is essentially no cross-interference between these two fluorescent materials. This makes the Ca-aspirin-fluorescein tracer system an ideal system from the analytical standpoint. Quite recently, these tracers were dispersed to the atmosphere by pressure generation of their respective aqueous solutions in order to determine their air transport characteristics.

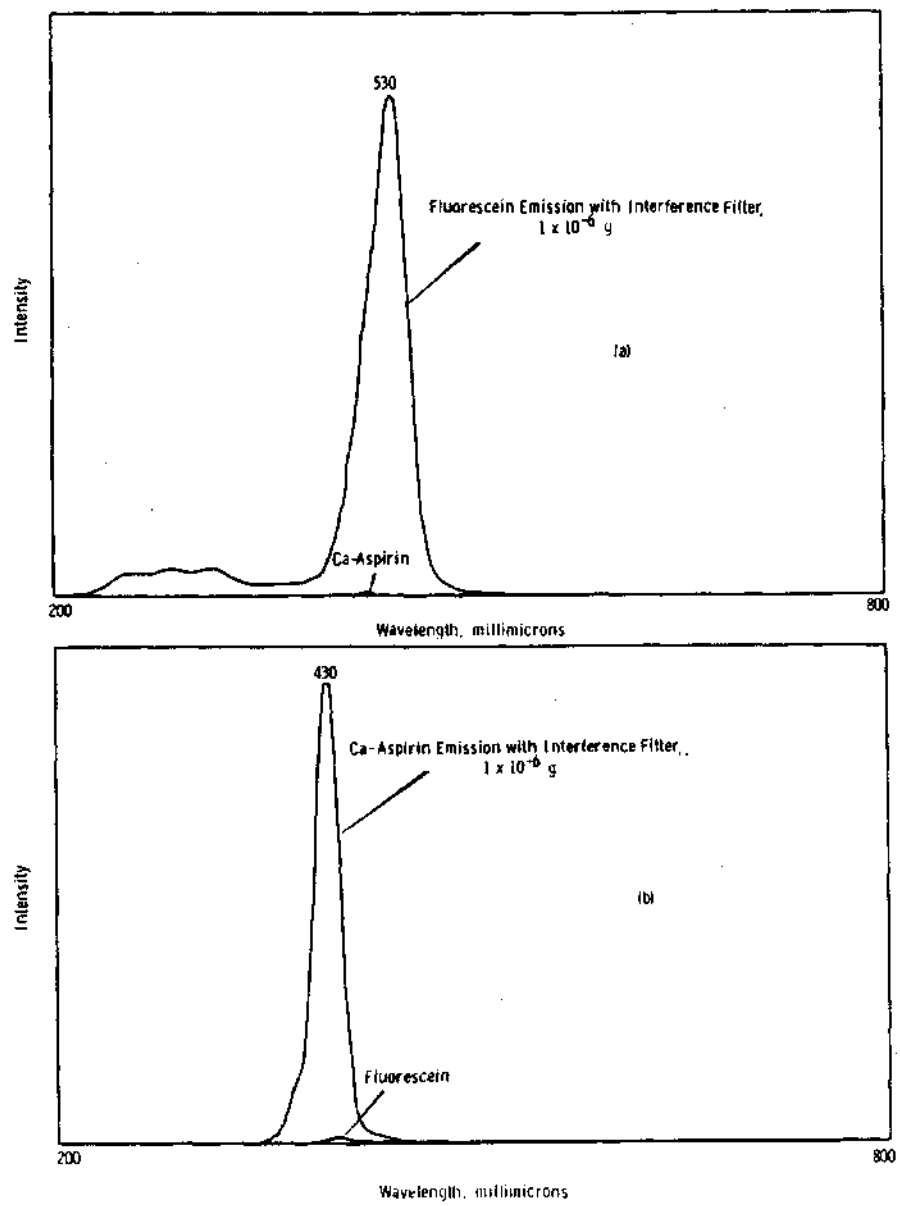

FIGURE 3.26

Cross Tracer Interference

Evaluation of Field Gamma Ray Spectrometric Measurements -
R. W. Perkins and H. G. Rieck, Jr.

The feasibility and value of the direct gamma ray spectrometric analysis of the Columbia River and of the atmosphere have been investigated. These measurements have shown that several radionuclides can be measured directly in the river and in the atmosphere by use of portable gamma ray spectrometric equipment.

General environmental studies of radionuclide movement in gaseous effluent discharged to the atmosphere and in reactor coolants discharged to the Columbia River require numerous samples for measurement. Most of the measurements are made by collecting the samples at the points of interest and returning them to the laboratory for study. The availability of readily portable gamma ray spectrometric counting equipment prompted a short feasibility study of the value of direct field measurements.

The equipment used in this survey consisted of a 9 3/8 in. diameter by 4 in. thick NaI(Tl) detector and a portable 400 channel transistorized analyzer.

River Studies

Gamma ray spectra were measured through about a 1 in. thick fiber glass and wood boat bottom with the detector positioned face down 1/2 in. above the bottom. In this position the face of the crystal was about 2 in. below the surface of the river. The crystal was large enough that it approached a total absorption spectrometer and the gamma ray spectrum obtained nearly represents the actual photon energies interacting with it. Measurements were made near midstream at locations a few miles upstream from the Hanford reactors; in individual reactor effluent plumes in the river; at Pasco, Washington, and in the McNary Dam reservoir. The measurement upstream from the project served as background for downstream observations. In Table 3.25 the response of the detector at a point 2 mi upstream from the first reactor is compared with the normal background of the detector in a 4 in. thick lead shield.

TABLE 3.25

GAMMA RADIATION FROM THE COLUMBIA RIVER UPSTREAM FROM THE HANFORD REACTORS

Energy, Mev	Relative Counting Rate[(a)]
0.1	25
0.2	10
0.3	10
0.4	7
0.5	10
0.6	9
0.7	13
0.8	18
0.9	8
1.0	5
1.5	4
2.0	4
3.0	2

(a) Observed background on the river divided by that obtained in a 4 in. thick lead shield

The photopeaks which were most easily discernible were those due to $Ru^{103-106}$, Zr^{95}-Nb^{95}, and radon daughter radioactivity.

At locations a few hundred yards below the reactor coolant discharge points in the river the activity level was, of course, high and the most easily discernible photopeaks were due to Cl^{38} (37.3 min) at 2.15 Mev, Mn^{56} (2.6 hr) at 0.84 and 1.8 Mev and Na^{24} (15 hr) at its 2.76 Mev peak. Table 3.26 presents the energy response of the detector relative to background as measured at Pasco and at McNary Dam (39 mi and 76 mi respectively downstream from the Hanford reactors).

TABLE 3.26

GAMMA RADIATION FROM THE COLUMBIA RIVER AT PASCO AND McNARY COMPARED WITH THAT ABOVE THE HANFORD PROJECT, 7/10/63

Energy, Mev	Counting Rate at Pasco[(a)]	Counting Rate at McNary[(a)]
0.12	10	2
0.25	10	2
0.5	8	2
0.75	4	1.3
1.0	8	2
1.5	10	2
2.0	23	4
2.5	48	8

(a) Counting rates at Pasco or McNary divided by those upstream from the Hanford Project

The photopeaks most easily discernible at McNary Dam were those due to Na^{24} (at 2.76 Mev) and Zn^{65} (1.11 Mev). At Pasco the prominent peaks were due to Na^{24} and Cu^{64} (0.51 Mev). The counting rate of the 2.76 Mev Na^{24} photopeak at McNary Dam was 400 counts/min (8 times background) while that due to Zn^{65} at its 1.11 Mev photopeak was about 100 counts/min. From these measurements it was evident that the counting rate of the 2.76 Mev Na^{24} peak provided the largest signal to background counting rate and could easily be used in field studies of flow time and depletion rates or of dispersion. Subsequent measurements from an airplane showed that Na^{24} (2.76 Mev peak) could be measured reasonably well in the river at elevations of 100 or 300 ft. The short (2 min) counts which were made did not permit the identification of other radionuclide photopeaks.

Airplane Measurements

The aircraft measurements were more difficult to interpret because it was not possible to determine the fraction of the counting rate which was due to

the airplane. Twenty minute measurements were taken at 3000, 6000, 9000 and 12,000 ft and the relative counting rates at these levels as a function of energy are recorded in Table 3.27.

TABLE 3.27

RELATIVE COUNTING RATES
AS SEEN BY A 9 3/8 in. BY 4 in. THICK γ NaI(Tl)
CRYSTAL AS A FUNCTION OF ENERGY AND ALTITUDE, 7/9/63

	Relative Counting Rates (c/m per 20 kev Channel			
Energy	3,000 ft	6,000 ft	9000 ft	12,000 ft
0.1	1430	1080	1340	1600
0.2	750	540	680	860
0.5	220	190	230	300
0.75	150	120	150	180
1.00	55.0	45	56	80
2.00	13.0	12	16	27
3.00 (a)	2.8	5.3	8.9	13.3
4.00 (a)	2.4	3.7	6.9	10.0

(a) Radiation at these energies would result mainly from cosmic rays

The most prominent photopeaks were those due $Ru^{103-106}$ (0.5 and 1.1 Mev), Zr^{95}-Nb^{95} (0.75 Mev) and the radon daughter Bi^{214} (1.78 Mev). For these measurements the crystal was located in the rear baggage compartment of the aircraft. It was positioned face down, 1/2 in. above the floor and was shielded on it sides only with 2 in. of lead. At these elevations the contribution from the ground would be negligible; however, the contribution from the airplane would possibly be responsible for a significant portion of the counting rate. These measurements indicate that it would be possible to make direct measurements of radionuclides at the "natural" fallout levels. It would require a considerable amount of calibration work (collecting samples and making measurements at the same time) but could be a very valuable tool in permitting a direct study of the fallout concentration and composition under various meteorological conditions.

Preliminary Measurements of the Adsorption of Reactor Effluent Water Radionuclides by Columbia River Water Particles *

L. L. Humphreys and R. W. Perkins

Experiments were conducted to measure the overall rates of absorption of reactor effluent water radionuclides (Mn^{56}, Na^{24}, Np^{239}, Cr^{51}, Cu^{64}, Sc^{46}, Zn^{65}, and La^{140}) by Columbia River water particles. Conditions were controlled to simulate as nearly as possible actual river conditions (constant temperature, rate of mixing, age of reactor effluent water, etc.). The reactor effluent water was filtered through a membrane filter to remove radionuclides already associated with particles. These ranged from 0.25% for Na^{24} to 42% for La^{140}.

Initial absorption of soluble reactor effluent water radionuclides onto Columbia River water particles is rapid. In the first minute of contact, absorption ranged from 0.2% for Na^{24} to 14% for La^{140}. This absorption is 25 to 40% of that occurring in 1500 min. The changes which occur after the first minute show a general increase with time but are much slower and probably more complex, being affected by river temperature, microorganism content, etc.

Sediment Studies: Particle Size Separation of Bottom Sediments from the McNary Reservoir of the Columbia River * - J. L. Nelson and L. L. Humphreys

A wet sieving particle sizing technique was used to size bottom sediments from the McNary Dam reservoir. The radionuclide contents of the size fractions are reported.

The quantity of radionuclides sorbed from reactor effluent on Columbia River sediments has been shown to vary as a function of particle size.(3.32) However, previously used procedures employing elutriation and sedimentation did not give sharp separation of the particle sizes. A wet sieving technique was found (by microscope examination) to give a much cleaner particle size

* Not funded by the Division of Biology and Medicine

separation than the former methods. The sieve sizes used were 74, 62, 44, 38, and 20 microns. Screen sizes of 10 and 5 ± 2 microns were also obtained but difficulties were encountered in trying to flow water through them, even using a vacuum. The sieves were used individually rather than as a nest for more effective separation, as reported by other investigators.(3.33)

Other improvements were also made in the particle size separation procedure. Washing was done mostly with 95% methyl alcohol to avoid elution and hydrolysis of nuclides by the wash water. An efficient electric mixer was used to attempt to separate soil agglomerates. Also, since a separation of the < 10 micron fraction was desired, a repeated centrifuging-decantation method was used for the finer particle sizes.

These particle size separation techniques were used for sediment samples taken from the McNary Reservoir in December, 1963. The fractions were analyzed with a gamma spectrometer and 5 in. well crystal for Co^{60}, Zn^{65}, Sc^{46}, and Cr^{51}. The data are given in Table 3.28.

TABLE 3.28

PARTICLE SIZE DISTRIBUTION
OF RADIONUCLIDE CONCENTRATION IN COLUMBIA RIVER SEDIMENT

Sample Size Range, microns	Fraction	Weight %	Radioactivity, distintegrations/min/g			
			Co^{60}	Sc^{46}	Zn^{65}	Cr^{51}
> 62	Sand (& Organic)	3.6	240	231	7534	3374
38 - 62	Coarse silt	10.8	157	135	3263	1487
20 - 38	Medium silt	28.9	140	104	3138	2130
5 - 20	Fine silt	41.0	118	194	3018	3257
1 - 5	Coarse silt	10.3	221	1000	6324	16,600
0.2 - 1	Fine clay	5.4	198	1300	7125	20,720

These results are averages of data from two slices of the top 3 in. of bottom sediment core. In addition to relatively higher radionuclide concentration in the finer particle sizes it can be seen that the larger particle sizes also contain higher nuclide concentrations than the intermediate sizes. This is

probably due to sorption by the organic material which would be found primarily in the coarsest fraction. Organic material was not separated from the samples before particle size separation. An attempt was made to separate the organic fraction with the density gradient technique using bromoethanol but it was found that, even with repeated extractions, only a small part of the organic could be separated due to its partially decomposed condition in deposited sediments.

Even though the largest particle size contains a relatively large concentration of nuclides, the total quantity in this fraction is low due to the low weight of the fraction. This can be seen in Table 3.29 where the percent of the total of each radionuclide is shown for each particle size.

TABLE 3.29

PERCENT OF RADIONUCLIDES IN EACH TOTAL PARTICLE SIZE FRACTION, COLUMBIA RIVER SEDIMENT

Particle Size, microns	Fraction	Co^{60}	Sc^{46}	Zn^{65}	Cr^{51}
> 62	Sand (& Organic)	5.9	2.8	7.1	2.4
38 - 62	Coarse silt	11.6	4.9	9.4	3.3
20 - 38	Medium silt	27.5	10.1	24.2	12.5
5 - 20	Fine silt	32.9	26.6	32.9	27.1
1 - 5	Coarse clay	15.6	34.8	17.4	34.8
0.2 - 1	Fine clay	6.5	20.7	9.1	19.9

The total content of radionuclides is low in the two coarsest size fractions and spread over the finer fractions with a relatively greater fine particle concentration in the cases of Cr^{51} and Sc^{46}.

Sediment Studies: Isolation of Organic Material from Suspended Columbia River Particles* - L. L. Humphreys

A density-gradient method has been applied to the separation of organic material from suspended Columbia River particles. Extent of separation is determined by "chlorophyll A" extractions, and differences in the adsorption of Co^{60}, Zn^{65}, Sc^{46}, and Cr^{51} onto inorganic and organic material were determined by gamma ray spectroscopy.

Previous studies (3.32, 3.34) have indicated a difference in the radionuclide spectrum on organic and inorganic portions of the river sediments. To provide better separation of the fractions for analysis, a density gradient technique (3.35) was applied for the isolation of organic material held in suspension in the McNary Reservoir.

Summary

Chlorophyll "A" extractions (3.36) indicate separation of 75% of the living organisms from the matrix. The organic portion separated is 6 to 10% (by weight) of the suspended sediments sampled in the fall of the year. The specific activity of Co^{60} in the organic material was higher than that in the inorganic fraction. The other radioisotopes measured (Zn^{65}, Sc^{46}, and Cr^{51}), however, were more concentrated in the inorganic fraction. Application of the density gradient technique to samples taken with a plankton net (greater than 50 microns) indicate these samples are essentially all organic.

The method employed for these separations is an application of the gradient-density technique developed by Lammers.(3.35) The two liquids used are water and 2-bromoethanol (reagent grade; density is 1.77 g/cm^3). The columns are prepared by pouring 20 ml of the heavier liquid into a 50 ml conical centrifuge tube. The sample is then stirred in 20 ml of water and carefully layered over the bromoethanol. This forms a sharp density gradient at the junction, with the upper layer containing the sample. The tube is then centrifuged for 30 min. After centrifuging, the four zones referred to by Lammers are observed; that is, in the bottom of the tube are particles heavier

---

* Not funded by the Division of Biology and Medicine

than 1.77 g/cm^3 then a clear liquid layer; then the junction of the two layers, which has those particles of density greater than 1.0 but less than 1.77 g/cm^3; and finally, the clear water layer. The best separation was obtained by decanting the top three zones from the heavy soil. The supernate is then diluted with water to decrease the density and the sample centrifuged to isolate the lighter (organic) portion of the sample. Samples taken with a plankton net remained at the interface (density less than 1.77 g/cm^3) and were thus organic. This is reasonable, since inorganic particles of that size have a high settling rate in water and would be part of the "bed load" except in high current.

Samples thus far separated by this technique are suspended sediments obtained from the river water by pressure filtering [3.37] through a membrane filter (pore size is 300 millimicrons). The samples were collected from surface water in the McNary Reservoir. It was felt that organic material which stayed with the inorganic fraction (centrifuged down through the bromoethanol layer) could be of two types: organic material entrained in or attached to inorganic material, so that the combined density is greater than 1.77 g/cm^3; or diatoms which have a large silica shell and thus a density greater than the bromoethanol. To estimate the amount of organic material in each fraction an extraction was made for "chlorophyll A". [3.36] In this procedure, the samples which have been kept cool and dark and are used as soon as possible after sampling are contacted with 90% acetone and 10% water. After sufficient time has elapsed for complete extraction, spectrophotometric analysis of the acetone solution (absorbance at 665 Å) is applied to measure the "chlorophyll A" content which is proportional to the live organic content. Results from this analysis are given in Table 3.29.

TABLE 3.29

SPECTROPHOTOMETRIC ANALYSIS

	Unseparated Sample	Separated Samples	
	Aliquot	Inorganic	Organic
Sample Weight, mg	9.3	72.1	8.2
Absorbance, 665 Å	0.034	0.073	0.226

These data show that 75% of the "chlorophyll A" containing material is isolated by one separation step. Since diatoms have silica shells, it is quite reasonable to expect some of this material to have a density greater than bromoethanol. Other organic materials (detritus, etc,) would be expected to separate more completely. The samples were analyzed on a high-sensitivity gamma ray spectrometer [3.1] for four different radionuclides. The results are given in Table 3.30 as disintegrations per minute per gram of sample.

TABLE 3.30

DISTRIBUTION OF RADIONUCLIDES FROM COLUMBIA RIVER SUSPENDED SEDIMENT BETWEEN ORGANIC AND INORGANIC FRACTIONS

	Activity, disintegrations/min/g			
	Co^{60}	Sc^{46}	Zn^{65}	Cr^{51}
Inorganic Fraction	250	2370	2510	57,100
Organic Fraction	410	900	660	22,600
Original Sample	320	2220	3140	56,100

The specific activity of the Co^{60} is higher in the organic fraction than the inorganic. [3.34] The other radionuclides measured have a higher activity in the fine inorganic particles.

Columbia River Sediment and Transport Studies* - R. W. Perkins

The fate of radionuclides which are introduced into the Columbia River in reactor effluent water is of continuing interest. A project is presently underway in cooperation with the U.S. Geological Survey to study the Columbia River transport of these radionuclides, including their adsorption, sedimentation, translocation and uptake by inorganic and organic detritus. This section includes a brief description of the more general observations of the study whereas the work on sediment particle size analysis and the initial changes which occur on introducing reactor effluent water to the Columbia River are covered separately.

* Not funded by the Division of Biology and Medicine

The reactor effluent water which is returned to the Columbia River after having passed once through a reactor contains many different radionuclides. Most of these are produced by (n, γ) reactions on the parent materials in the water and are rather short-lived. The fission products are normally present in much lower concentrations than the (n,γ) products. The more abundant long-lived radionuclides are Zn^{65} (243 days) and Cr^{51} (27 days) and are the most easily traced in river water and on suspended sediments. The radionuclides Sc^{46}, Co^{60}, Mn^{54} and the fission products Zr^{95}-Nb^{95}, $Ru^{103-106}$, Ce^{141} are present in lesser amounts.

The fission products in the river are due to both fallout and reactor operation. During the past year the fission products Zr^{95}-Nb^{95} have been measured in Columbia River water from above the Hanford reactors (near Priest Rapids Dam), in Snake River water just before it enters the Columbia River (near Ice Harbor Dam), and in Columbia River water below both the reactors and the Snake River influent (at McNary Dam). These data are summarized in Table 3.31 and indicate a comparable level of these radionuclides at the three locations. The Columbia River water above the reactor area is lower in Zr^{95}-Nb^{95} than at McNary Dam; however, the Snake River is at about the same level as the Columbia at McNary Dam. It would therefore appear that during this period of time a large portion of the fission products in the Columbia came from fallout. The concentrations of the long-lived (n, γ) - produced radionuclides which are introduced by reactor operations have not been precisely measured above the reactors and in the Snake River; however, indications are that by comparison they are negligible.

TABLE 3.31

Zr^{95}-Nb^{95} PRESENT IN SOLUTION OR AS PARTICULATES IN THE SNAKE AND COLUMBIA RIVERS.

Concentration disintegrations/min/liter

	McNary Dam			Priest Rapids Dam			Ice Harbor Dam	
Date	Particulate	Solution	Date	Particulate	Solution	Date	Particulate	Solution
12/6/62	13.3	12.2						
1/25/63	6.3	16.6	1/15/63	2.1	2.8	1/21/63	6.7	10.0
2/27/63	7.9	14.9	2/20/63	4.3	3.8	3/6/63	6.4	21.5
4/1/63	13.0	25.0	3/20/63	5.1	7.2	4/1/63	6.1	19.9
			5/17/63	7.6	3.2			
8/2/63	3.0		7/16/63	2.9	4.3	7/24/63	3.6	1.8
9/11/63	4.1	3.2	9/4/63	1.1	2.4	9/6/63	0.6	1.2

(a) Filtered through a 0.5 micron filter

During the course of the Columbia River study the U.S.G.S. has provided water samples from sampling locations at the highway bridges at Pasco, Washington, Hood River, Oregon, and Portland-Vancouver. These samples are filtered immediately on collection through 0.3 micron membrane filters and both the filter and water are analyzed. These studies which included measurements of variations in cross sectional and vertical radionuclide concentration, and detailed studies of the bottom material radionuclide content will be published later. Some of the general observations from these measurements are included here. In Figure 3.27 the transport rates of Zn^{65} and Cr^{51} for the latter part of 1962 and 1963 at Pasco and Vancouver are presented.* Although there is some lack in definition because of the long intervals between some samples it is evident that a large portion of the radioactivity which passes Pasco does not reach Vancouver. Some of the Cr^{51} loss is due to decay (up to about 30%); however, the Zn^{65} decay during this river's travel time is negligible. It is apparent that the Vancouver radioactivity reaches a maximum which is actually higher than that at Pasco during late May when the river is approaching its peak flow and the maximum scouring of deposited sediments would be expected to occur. In Figure 3.28 the fraction of Zn^{65} and Cr^{51} associated with suspended particulate material is presented. These data show that for most of the year a much larger fraction of the Zn^{65} is associated with particulate material at Vancouver than at Pasco. Since Zn^{65} is readily adsorbed by particulates and presumably by river bottom materials it would be expected that considerable losses could occur during its transport to Vancouver. The fraction of Cr^{51} associated with particulate material is relatively small but higher at Vancouver than at Pasco. The change in the physical form of Zn^{65} relative to Cr^{51} is perhaps best illustrated in Figure 3.29. In this graph the ratio of Zn^{65} to Cr^{51} in filter river water at Pasco and Vancouver are compared for a year period. For most periods of the year the Zn^{65} to Cr^{51} ratio is a factor of 5 to 10 lower at Vancouver than at Portland. Figure 3.30 provides a similar comparison of the Zn^{65} to Cr^{51} ratio for raw (unfiltered river water) and compares these ratios with

---

* Values are calculated from observed concentrations with no correction for concentration changes produced by diurnal flow variation produced by Priest Rapids Dam operation

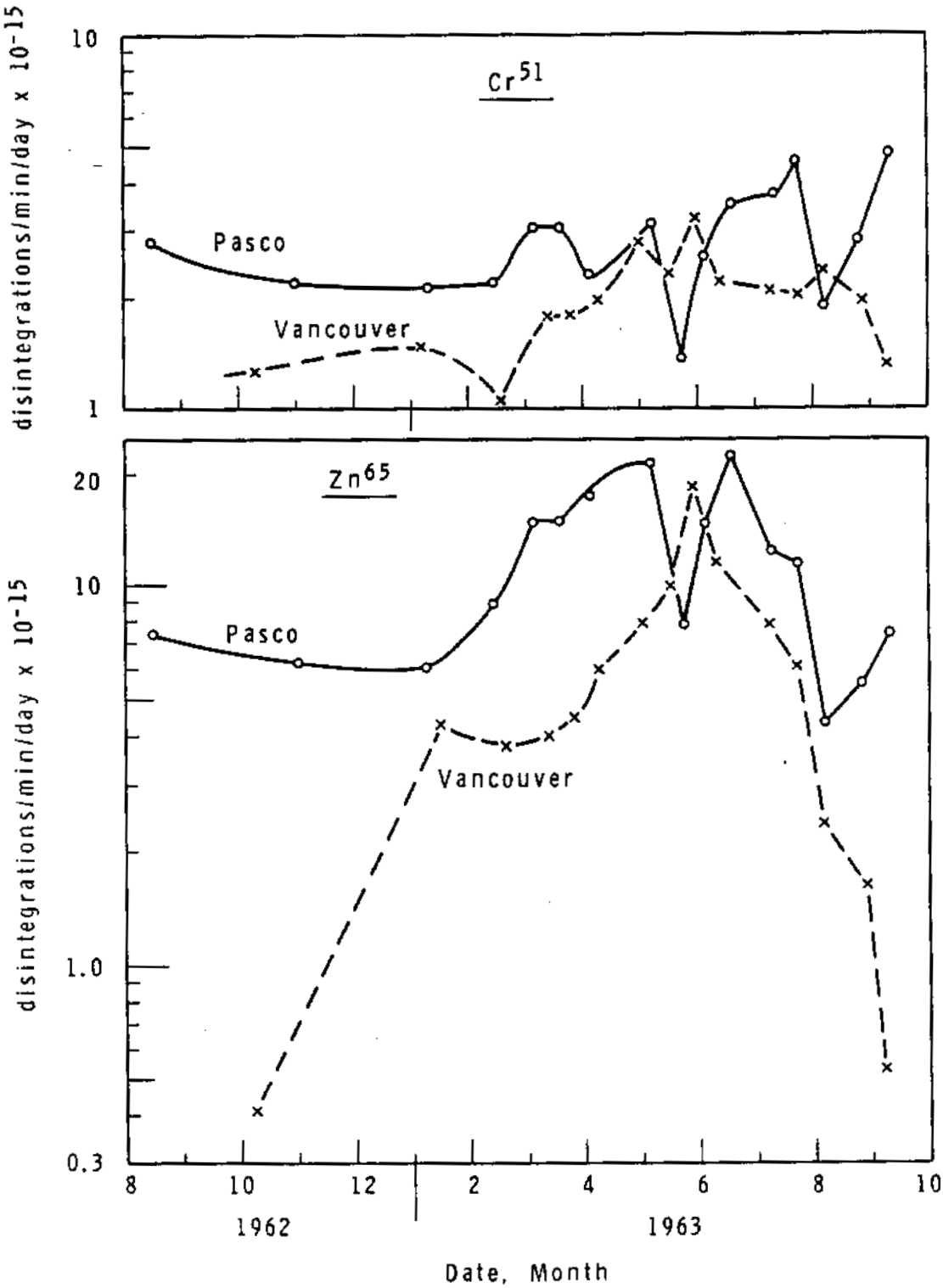

FIGURE 3.27

Zn^{65} and Cr^{51} Transport at Pasco and Vancouver

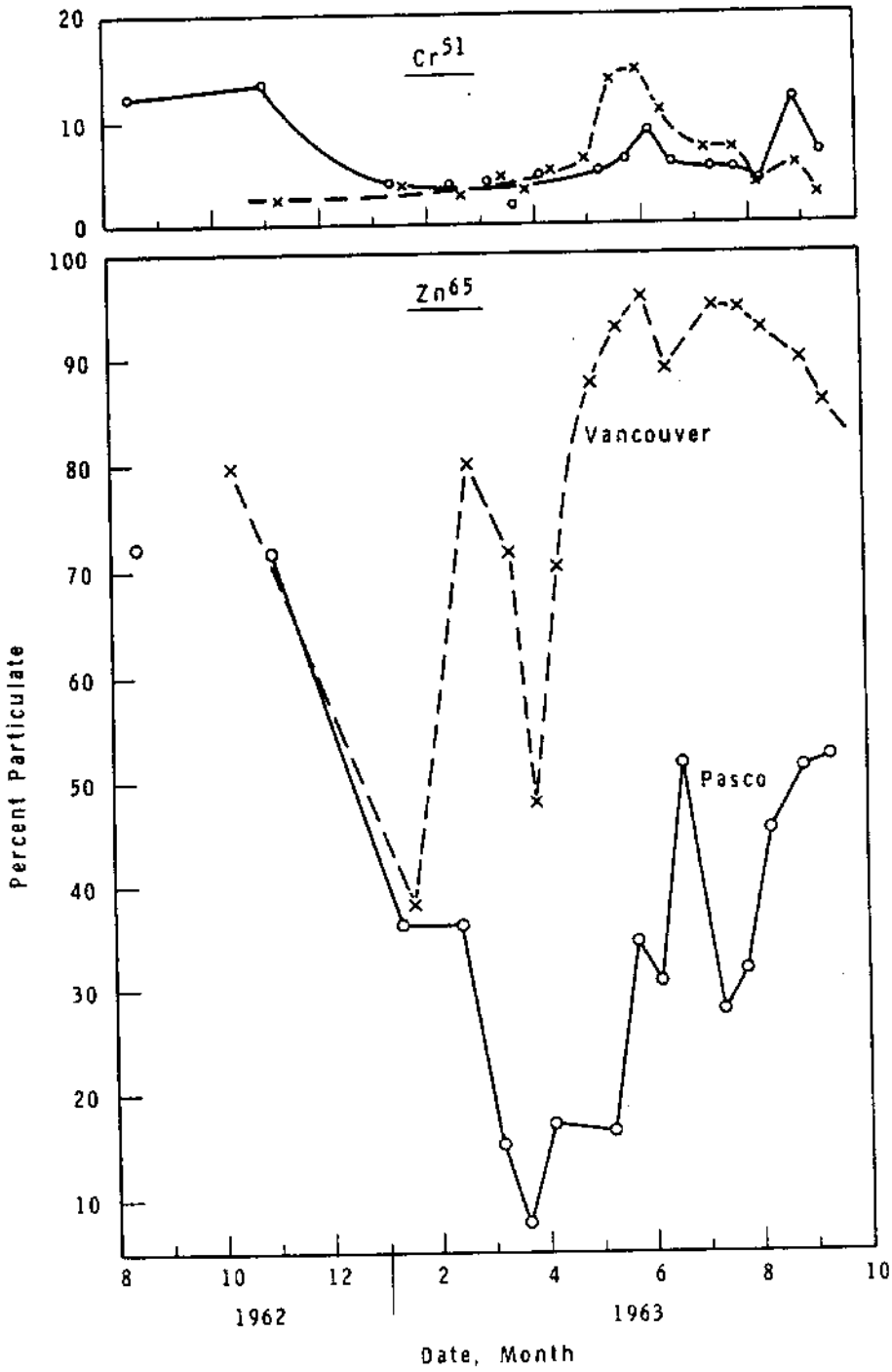

FIGURE 3.28

Fraction of Zn^{65} and Cr^{51} Associated with Particulate Material at Pasco, Washington, and Vancouver, Washington

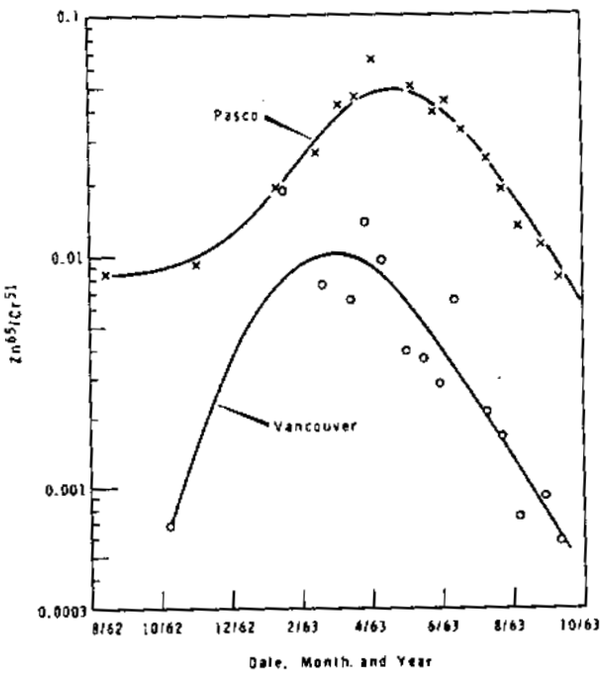

FIGURE 3.29

Zn^{65} to Cr^{51} Ratio in Filtered Columbia River Water

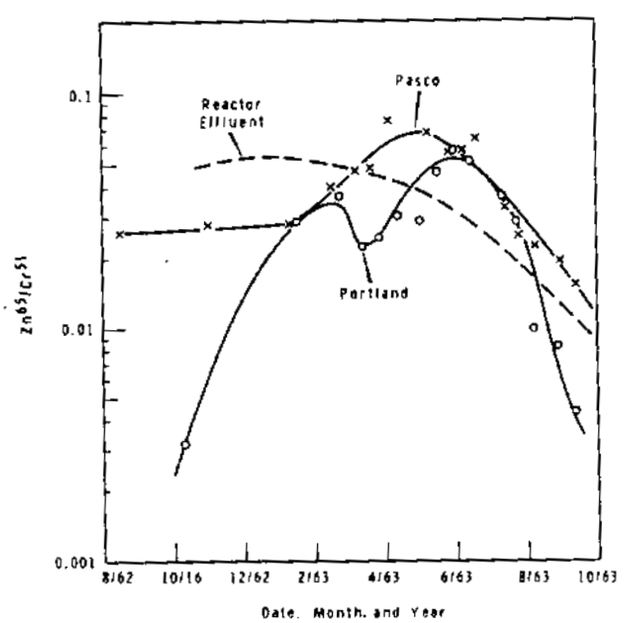

FIGURE 3.30

Zn^{65} to Cr^{51} Ratio in Reactor Effluent Water and Raw Columbia River Water

those reported for the reactor effluent water when it enters the river. During most of the year the ratio is much lower at Vancouver indicating a substantial loss of Zn^{65} in transit.

Analyses of river bottom materials have not been sufficiently extensive to define the complete picture of the radionuclide sedimentation areas in the river; however, the measurements which have been made indicate that extensive "permanent" sedimentation occurs only in the reservoir of the McNary Dam and in the estuary. The sedimentation in the McNary Reservoir is very fine material and of relatively high specific activity. Those stretches of the river (which we have observed) where the flow is not controlled by reservoirs have rock or coarse sand bottom material with low specific activity. The river bottom area immediately above Bonneville Dam is also mainly rock and coarse sand. The relatively new Dalles Dam has not yet been investigated for radioactive sediment buildup. The radionuclide content of typical Columbia River bottom material from McNary Dam; Hood River, Oregon; Vancouver, Washington; and the estuary are presented in Table 3.32. The relatively high radionuclide concentrations at McNary Dam plus the fact that these deposits are known to be deep (a few feet) indicate that this is the major deposition area. The estuary has a rather high specific activity particularly in Cr^{51} and is probably second in total activity inventory.

TABLE 3.32

RADIOCHEMICAL ANALYSIS OF TYPICAL BOTTOM MATERIALS FROM THE COLUMBIA RIVER,

disintegrations/min/g

Location	Sc^{46}	Cr^{51}	Co^{60}	Zn^{65}
McNary Dam	90	3000	200	4000
Hood River	1-10	400	1-10	100
Vancouver	0.5	50	0.5	25
Estuary	5	1000	4	75

Core sampling equipment has been designed and used for sediment buildup studies at the McNary Dam Reservoir. For this work a 6 in. diameter by 2 ft (or interchangeable 3 ft) long coring device is used (see Figure 3.31). The coring tube contains a 6 in. lucite pipe in which the core is collected. The core is obtained by dropping the device from about 20 ft above the bottom of the reservoir, pulling a 2 lb vacuum at the fitting between the ball valve and the core and holding this vacuum while the core is raised into the boat. The cores are quick frozen, and taken to the laboratory where they are sectioned (in 1/2 in. lengths) by cutting them with a radial arm saw which uses a jet of hot water. The outer 1 in. annulus of each core section is discarded, and the remainder is measured for radioactivity by gamma ray spectrometric techniques. In Figure 3.32, the Sc^{46},

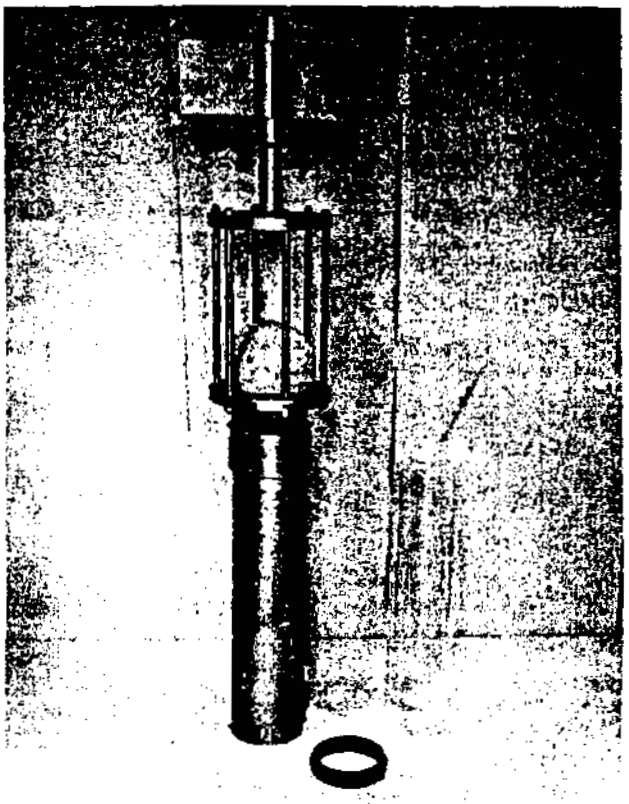

FIGURE 3.31
Core Sampler

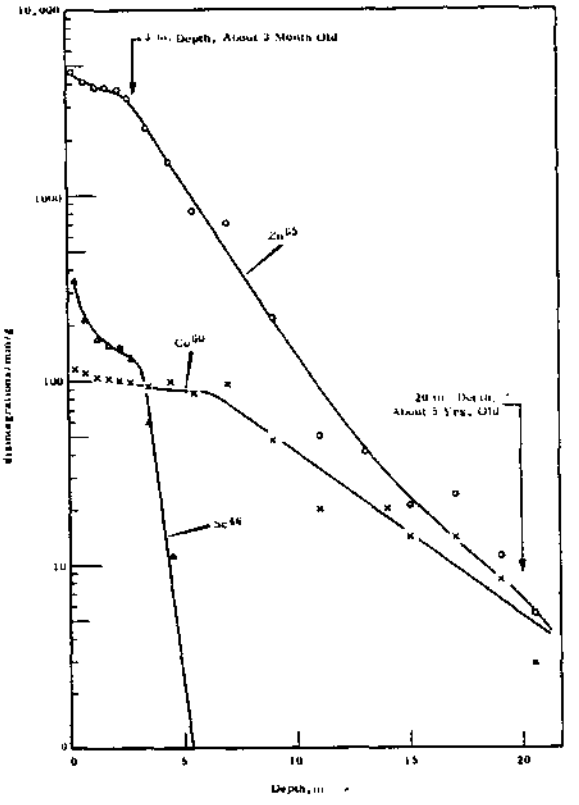

FIGURE 3.32

Sc^{46}, Zn^{65}, and Co^{60} Contents of Core as a Function of Sediment Depth

Zn^{65}, and Co^{60} contents of a core which was collected during December 1963, are plotted as a function of sediment depth. By use of the radionuclide ratios (and knowing the ratio in which the radionuclides were released to the river during the past years) it is possible to calculate the age of the sediment at various depths. The 3 mo age and the 5 yr age are noted on the graph. It is evident that the deposition rate for the last 4 mo is about 10 times that during the 5 yr period of the core formation suggesting that a large fraction of the top surface sediments are washed out during Spring high flow period. Periodic core measurements at this location during the coming year will establish if this is the case.

Measurement of Uranium Ore Particle Inhalation by Radon Daughter Counting - R. W. Perkins, H. E. Palmer*, and B. O. Stuart**

Preliminary studies have shown that the deposition of uranium ore dust in the respiratory system can be traced by whole body counting of radon daughters that attach themselves to these particles. Measurements at a uranium crushing mill showed about 30% retention of inhaled particles with approximately equal amounts of activity in the head and chest region.

The inhalation of dust particles in mine atmospheres is a major contributor to respiratory disorder in mine workers.[3.38, 3.39] In studying exposures resulting from the inhalation of uranium ore dust it is important to know the relationship between air dust concentration and particle sizes, and the location of deposition in the respiratory system. This is of interest in estimating exposures to the various regions of the respiratory system and also in comparing deposition rates in experimental animals with those in humans. External measurement of the very small amounts of ore dust actually deposited in the respiratory systems of uranium mine workers cannot be made because of the very low specific activity of uranium ore. However, in uranium mines and mills the short-lived radon daughter (half life 26.8 min and less) concentrations are high and these newly formed atoms immediately attach themselves to suspended dust particles and can serve as a tracer for the dust. Experimental measurements have shown that when radon daughters in normal atmospheric air and in membrane filtered air are breathed into the human respiratory system that 25 and 75% respectively are retained.[3.40] The point of deposition and the fraction retained would certainly be a function of particle size and concentration.

To determine the feasibility of tracing ore dust by measurement of the radon daughters the concentrations of ore dust (Ra^{226}), Rn^{222} and radon daughters (Bi^{214}, 1.76 Mev) were measured in the atmosphere of the uranium

---

* Radiological Physics

** Biology Laboratory

ore crushing mill. For convenience in this initial study the mill of the Dawn Mining Company at Ford, Washington was selected and measurements were made at a location near the bottom of the plant where ventilation was a minimum. This mill handles low grade ore of about 0.2% uranium. All of the measurements were made by gamma counting of the collected samples. The ore dust and radon daughters were collected on membrane filters (2.0 μ pore size*) while the radon was collected on a charcoal bed at -70 C. The observed results are shown in Table 3.33 and indicate that the radon daughter content of the air might be high enough to measure internal deposition in the respiratory system.

TABLE 3.33

RADIOACTIVITY AT A POINT OF MINIMUM VENTILATION IN A URANIUM CRUSHING MILL ATMOSPHERE

Radionuclide	disintegrations/min/liter
Rn^{222}	107
Bi^{214}	52
Ra^{226} (ore dust)	0.024

A second set of measurements was taken at the mill 1 mo later and at this time whole body measurements were made (using the Hanford Whole Body Counter) of individuals who had spent about 30 min at the locations where the air sampling was being performed. The exposed individuals showered to remove external contamination and were in position for a whole body count 10 min after leaving the mill. Although the radon concentration of the mill air was similar to that previously observed, the radon daughter content was about 1/5 of the former value and whole body counting at these low levels was difficult. It was possible, however, to establish that, based on a breathing rate of 8 liters/min, about 30% of the inhaled particles are retained in the respiratory system at least for the period of these measurements. Crude collimation

* The AM-3 (2 μ) filters appear to collect radon daughters quantitatively. When outside air is filtered through an AM-3 filter followed by an AM-7 (0.3 μ) less than 1% of the radon daughter material is collected on the AM-7 filter.

measurements indicated that the radioactivity content was distributed in approximately equal amounts between the head and the chest region. Particle size analysis of atmospheric dust by electron microscopy showed a count median diameter of 0.6 μ and mass median diameter of 9.7 μ for the particle range that could be seen (greater than 0.01 μ). Assuming that the dust retained on inhalation was of the same particle size as that in the air, approximately 0.8 mg of dust would be deposited in the body during the 30 min exposure.

Plans have been made to make a careful study of uranium ore inhalation rates in a mine in the southwestern part of Colorado. In these areas the radon concentrations are orders of magnitude higher and the relationship between dust concentrations, particle size, and deposition location in the body can be measured much more precisely.

Determination of Subterranean Water Flow Rates by Measurement of the I^{133} to I^{131} Ratio - D. E. Robertson and R. W. Perkins

Radioactive tracers are a useful tool in hydrological studies. The usefulness of the radioiodine I^{131} and I^{133} have been demonstrated in underground water flow rate measurements.

Normal reactor effluent water disposal at Hanford involves holding the effluent water in retention basins for 1 to 4 hr before its discharge to the river. In addition to the normal basins, other large secondary basins are available for use where the radioactivity level of the effluent exceeds established limits. These secondary basins are simply large pits and it is intended that their water will reach the river by seepage through several hundred feet of earth. In estimating the decontamination which seepage from these basins to the river would provide it is essential to know the underground flow rates from these locations.

The feasibility of measuring these flow times by use of the normal concentrations of I^{131} and I^{133} in effluent water has been demonstrated. Radiodine is a particularly useful tracer since it is not significantly adsorbed on percolating through the soil [3.41] and its arrival represents the leading

edge of the radioactivity. Some of the normal effluent water basins through which water is passed before discharge in the river leak sufficiently that springs have formed along the bank of the river. A comparison of the I^{131} (8.05d) to the I^{133} (21 hr) ratio at the retention basin and at these springs has provided a measure of the flow time. The normal concentration of I^{133} in effluent water is about eight times that of I^{131} and both are of sufficient concentration so that standard low level radiochemical plus gamma spectrometric techniques provide an accurate measurement of the I^{133} at concentrations to less than 1% of its original concentration. These levels cover the time intervals of concern (up to 1 wk) and are very useful.

The radioiodine is separated from the samples by a standard CCl_4 extraction and AgI precipitation followed by gamma ray spectrometric measurement of the I^{131} and I^{133}. From the disintegration rates thus determined, the flow time is taken directly from a curve of I^{133}:I^{131} ratio versus time (Figure 3.33). The travel time is the time difference between the radioiodine ratios at the basin and in the springs.

This technique might also be applicable in other hydrological studies such as ground water movement from wells, river flow rates or water diffusion rates.

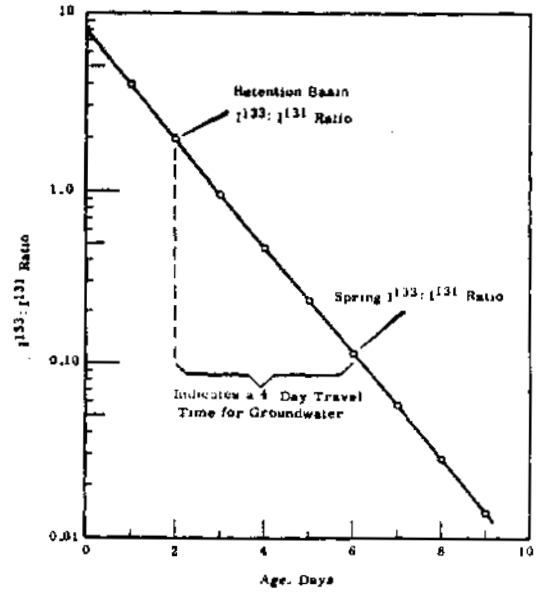

FIGURE 3.33

A Typical Groundwater Travel Time Determination by Use of the I^{133}:I^{131} Ratios

Spectroscopic Determination of Equilibrium Constants -

W. D. Felix

A method for the calculation of equilibrium constants and specific absorptivities from spectrophotometric data is presented for a general complex ion system, $D^+ + A^- = DA$. Calculations are made from experimentally determined absorbances of solutions at a number of different concentrations of the nonabsorbing ion, D^+.

Equilibrium constants for dissociation reactions of the type

$$DC \rightleftharpoons D^+ + C^-;\ K = \frac{[D^+]\quad[C^-]}{[DC]} \tag{1}$$

are often determined spectrophotometrically when DC and C^- exhibit absorption spectra in an accessible region. The absorbance at any given wavelength is simply given as the linear combination of the absorbances of the individual species present

$$A = \epsilon_c\,(C^-) + \epsilon_{dc}\,(DC) \tag{2}$$

where the spectrophotometric cell is assumed to be 1 cm. To determine the equilibrium constant from spectrophotometric data, it has heretofore been necessary to know at least one of the absorptivities, ϵ_i. It is difficult to determine the absorptivities if the individual spectra of the contributing species overlap and if it is impossible to isolate at least one of the absorbing species from the other. This is normally the case when considering the absorption spectra of the equilibrium states of a general polyvalent system:

$$\begin{aligned} D_nA &\rightleftharpoons D^+ + D_{n-1}\,A^- \\ D_{n-1}\,A^- &\rightleftharpoons D^+ + D_{n-2}\,A^{-2} \\ DA^{-(n-1)} &\rightleftharpoons D^+ + A^{-n} \end{aligned} \tag{3}$$

However, calculation of absorptivities for both absorbing species and the equilibrium constant system present may readily be made by computer

techniques from the knowledge of the absorbances of the solution at a number of different D^+ concentrations (assuming D^+ does absorb in the same spectral region as $D_{n-1}\ A^-$ and D_nA).

Consider a common case, that of an acid-base indicator system,

$$H^+ + A^- \rightleftharpoons HA$$

where A^- may be a polyvalent anion. The presence of two and only two absorbing species is guaranteed by the presence of an isosbestic point in the spectra.[3.42] Then at any wave length close to the isosbestic point, a set of equations may be written for a series of pH's:

$$A_i = \epsilon_A (A^-)_i + \epsilon_{HA} (HA)_i \quad (i = 1, 2, \cdots n). \tag{4}$$

The following relationships are necessary

$$C_o = HA + A^- \tag{5}$$

$$K = \frac{(H^+)\ (A^-)}{HA} = \frac{(h)\ (A^-)}{(C_o - A^-)} \tag{6}$$

when

$$A^- = \frac{KC_o}{h+K}; \quad (HA) = \frac{hC_o}{h+K} \tag{7}$$

Substituting Equation (7) into Equation (4) and rearranging, we have

$$A_ih_i = \epsilon_A - KC_o + \epsilon_{HA} h_i C_o - A_iK\ . \tag{8}$$

Let $W = \epsilon_A - K$, then

$$A_ih_i = W C_o + \epsilon_{HA} h_iC_o - AK_i\ . \tag{9}$$

The three unknowns W, ϵ_{HA}, and K, may be found from this set of n equations by the method of least squares in three dimensional space. The method was programmed for the IBM 7090 computer.

Application to Methyl Red

The method, as outlined above, was applied to the data of Ramette, et al.[3.43] and the results were compared with the results from other standard techniques of determining equilibrium constants. Species present in solutions of methyl red are related by two equilibrium constants, Q_1 and Q_2,

$$Q_1 = \frac{[H_3O^+] \quad [HM]}{[H_2M^+]}$$

$$Q_2 = \frac{[H_3O^+]\ [M^-]}{[HM]}$$

Results are compared as follows,

	Q_2	Method
(Calculated at λ = 510)	(Ramette)	
4.31×10^{-3}	4.0×10^{-3}	Spectrophotometric
	3.9	Solubility
	5.0	Solvent Extraction

Absorbance values were not reported close enough to the isosbestic point to allow calculation of the equilibrium constant of the Q_1 system.

Application of the Method to Tropeolin-O

Tropeolin-O is expected to undergo the following sequence of reactions

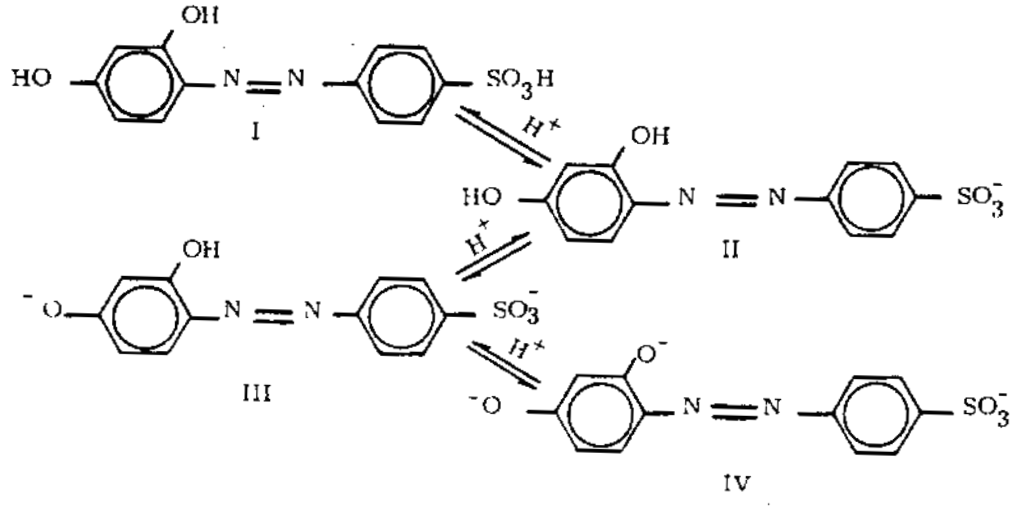

The order of ionization of the ortho and para phenolic groups has not been determined. Using the following notation

$$IV + H^+ \rightleftharpoons III \quad K_3 \text{ pH:10 to 14}$$

$$III + H^+ \rightleftharpoons II \quad K_2 \text{ pH:4 to 6}$$

$$II + H^+ \rightleftharpoons I \quad K_1 \text{ pH:0 to 1.8}$$

the results for tropeolin-O are reported for a range of wavelengths which brackets the isosbestic point for each equilibrium system.

	K_1			K_2			K_3		
λ	pK_1	ε_A ($\times 10^{-4}$)	ε_B	pK	ε_A ($\times 10^{-4}$)	ε_B	pK	ε_A ($\times 10^{-4}$)	ε_B
380	- 0.13	1.149	2.332	5.68	2.449	1.826	--	--	--
415	--	--	--	5.83	1.811	4.016	12.06	4.058	1.679
425	- 0.15	3.330	1.487	--	--	--	--	--	--
429	--	--	--	5.85	1.490	4.507	12.08	4.569	1.75
435	--	--	--	--	--	--	12.11	4.438	1.788
450	- 0.61	7.536	0.988	--	--	--	12.06	3.584	2.125
475	- 0.62	6.780	0.629	--	--	--	12.08	1.412	2.831
488	--	--	--	--	--	--	12.10	0.694	3.104
500	--	--	--	--	--	--	12.10	0.258	3.038

As may be seen from the column of pK values under K_3, over the relatively wide range of wavelengths used, the variation of the pK's about the mean pK value appears to be random. Thus, over the wavelength range used, the determination of the equilibrium constant does not appear to be dependent on wavelength used.

Results for K_2 and K_3 with respect to deviation from the mean pK values are good. Results for K_1 are not as good as for K_2 and K_3, due in part, perhaps, to ionic strength differences. It is known that the absorbance of a solution is dependent on the ionic strength as well as on the pH. Control of the pH over the range for which K_1 equilibrium conditions held required high acid concentrations, such that the ideal conditions of an ionic strength of 0.1 could not be met. Also the effect of association of HCl under low pH conditions was not considered.

This method has thus been shown to be an effective, convenient, and rapid approach to the determination of equilibrium constants and absorptivities.

Adding to the attractiveness of the method is the general availability of digital computers with which the tedious calculations of determinants in which eight significant figures must be retained is circumvented.

Radiation Chemistry

Evidence for the Reaction of Atomic Chlorine Radicals in Neutral Irradiated Solutions - D. R. Kalkwarf

The presence of chloride ion during the irradiation of several neutral aqueous solutions altered the course of the reactions induced. This alteration could not be attributed to a change in ionic strength of the solutions and was considered to be an indication of the chlorine atoms.

Chloride ions can react with hydroxyl radicals produced by the radiolysis of water to form chloride atoms via the reaction:

$$OH^{\cdot} + Cl^{-} \rightarrow OH^{-} + Cl^{\cdot} \qquad (1)$$

In acid solutions, this reaction proceeds to such an extent as to significantly alter the radiation chemistry of the system,[3.44, 3.45, 3.46] however, in neutral and basic solutions, no evidence has been reported to indicate that Reaction (1) occurs.[3.47, 3.48] In many biological systems, chloride ion is present in substantial amounts; for example, in human plasma it appears at a concentration of 0.10M. It is thus of considerable concern to determine whether Reaction (1) proceeds to a large extent during irradiation of neutral, aqueous, chloride solutions, and, if so, how the replacement of hydroxyl radicals by chlorine alters the amount and type of damage.

In the present work, the effect of Reaction (1) during the irradiation of neutral solutions was observed in the following manner. Various solutes were allowed to compete with the dye, erioglaucine, for the radicals formed in irradiated aqueous solution, and the relative rate constants for the competing reactions were evaluated by the method described previously.[3.49] Ethanol, thiourea, and nitrite ion were chosen as representative solutes to compete with the dye, and each solution irradiated contained one of these test solutes at a concentration of 5×10^{-5}M and erioglaucine at a concentration of

6×10^{-6}M. In some of the solutions, the ionic strength was left at $\sim 6 \times 10^{-5}$M, while in others it was adjusted to 0.15M with either NaCl or Na_2SO_4. In all cases, the solutions were in equilibrium with air.

Table 3.34 shows the "relative rate constants" obtained assuming that the test solute and dye compete only for hydroxyl radicals. In the presence of sodium sulfate, which would not be expected to interpose a new radical species into the system, the relative rate constants are experimentally indistinguishable from those obtained at very low ionic strength. This absence of an ionic salt effect indicates that one of the reactants in the competition is uncharged, [3.50] and since the dye certainly is charged, the radiation-produced reactant must be uncharged—evidence, again, that hydroxyl radical is this reactive species. In the presence of 0.15M NaCl, however, the apparent relative rate constants are only from one-half to three-quarters as large. Some reaction is obviously causing a redistribution of products, and Reaction (1) is the logical possibility.

TABLE 3.34

"RELATIVE RATE CONSTANTS" OF SOLUTES WITH HYDROXYL RADICALS AS A FUNCTION OF TEMPERATURE AND IONIC STRENGTH

Solute	Temperature, C	$\frac{k(OH + Solute)}{k(OH + Erioglaucine)}$ I ~ 6×10^{-5}M	I = 0.15M in Na_2SO_4	I = 0.15M in NaCl
Sodium Nitrite	4.5	0.62 ± 0.03	0.61 ± 0.03	0.45 ± 0.04
	25	0.53 ± 0.01	0.55 ± 0.03	0.32 ± 0.02
	45	0.44 ± 0.01	0.45 ± 0.02	0.28 ± 0.02
	65	0.40 ● 0.01	0.42 ± 0.02	0.25 ± 0.02
Ethanol	4.5	0.17 ± 0.01	0.20 ± 0.01	0.13 ± 0.02
	25	0.14 ± 0.01	0.16 ± 0.01	0.10 ± 0.01
	45	0.12 ± 0.01	0.12 ± 0.01	0.06 ± 0.01
	65	-----	0.096 ±0.005	0.044± 0.008
Thiourea	4.5	0.72 ± 0.04	0.67 ± 0.02	0.53 ± 0.05
	25	0.70 ± 0.03	0.62 ± 0.02	0.46 ± 0.04
	45	0.63 ± 0.03	0.57 ± 0.02	0.40 ± 0.03
	65	0.59 ± 0.03	0.49 ± 0.01	0.38 ± 0.03

If chlorine atoms are indeed reactants, the values shown in Table 3.34 for solutions in 0.15M NaCl are really a composite of the rate constants for reactions of the dye and test solute with both hydroxyl and atomic chlorine radicals. Although the exact relationship between the reaction-rate constants involved may be quite complicated, it appears that, since the effect of chloride ions is to allow more dye to decompose for a given amount of irradiation, chlorine atoms show more preference in reacting with the dye than do hydroxyl radicals. This selectiveness of the chlorine atom could, of course, be of great importance in determining the major reaction routes in irradiated biological systems.

The Effect of Temperature on Radical-Capturing Reactions in Irradiated Aqueous Solutions - D. R. Kalkwarf

A variety of ionic and neutral solutes were found to compete more effectively with erioglaucine for the hydroxyl radicals formed in irradiated aqueous solutions as the temperature was decreased. Viewed in terms of differences in activation energies for competing reactions, these differences fell within a 3.5 kcal $mole^{-1}$ range.

As reported previously,[3.51] the relative rate constants,

$$\frac{k(OH^{\cdot} + \text{solute})}{k(OH^{\cdot} + \text{erioglaucine})}$$

for small molecules such as glycine, alanine, ethanol, and tyrosine increase with decreasing temperature. This behavior has now been found to be shown by a wider variety of solutes. Relative rate constants were again measured by the dye-competition method,[3.49] and the data are collected in Figure 3.34. As can be seen from this figure, the relationship,

$$\frac{k_2}{k_1} = (\text{constant})\ e^{-(E_2 - E_1)/RT}$$

where $k_2 = k(OH^{\cdot} + \text{solute})$

$k_1 = k(OH^{\cdot} + \text{erioglaucine})$

E_1, E_2 = corresponding activation energies

is supported although other interpretations of the data are possible;[3.51] and activation energy differences could be calculated to the nearest 0.5 kcal $mole^{-1}$. In all cases, the activation energy, E_1, for reaction between erioglaucine and hydroxyl radicals is larger, and the values for the other reactions are compared in Table 3.35 together with those obtained from previous data.[3.51]

These results illustrate the extent to which control of irradiation temperature can be used to manipulate reactions in aqueous systems. If the

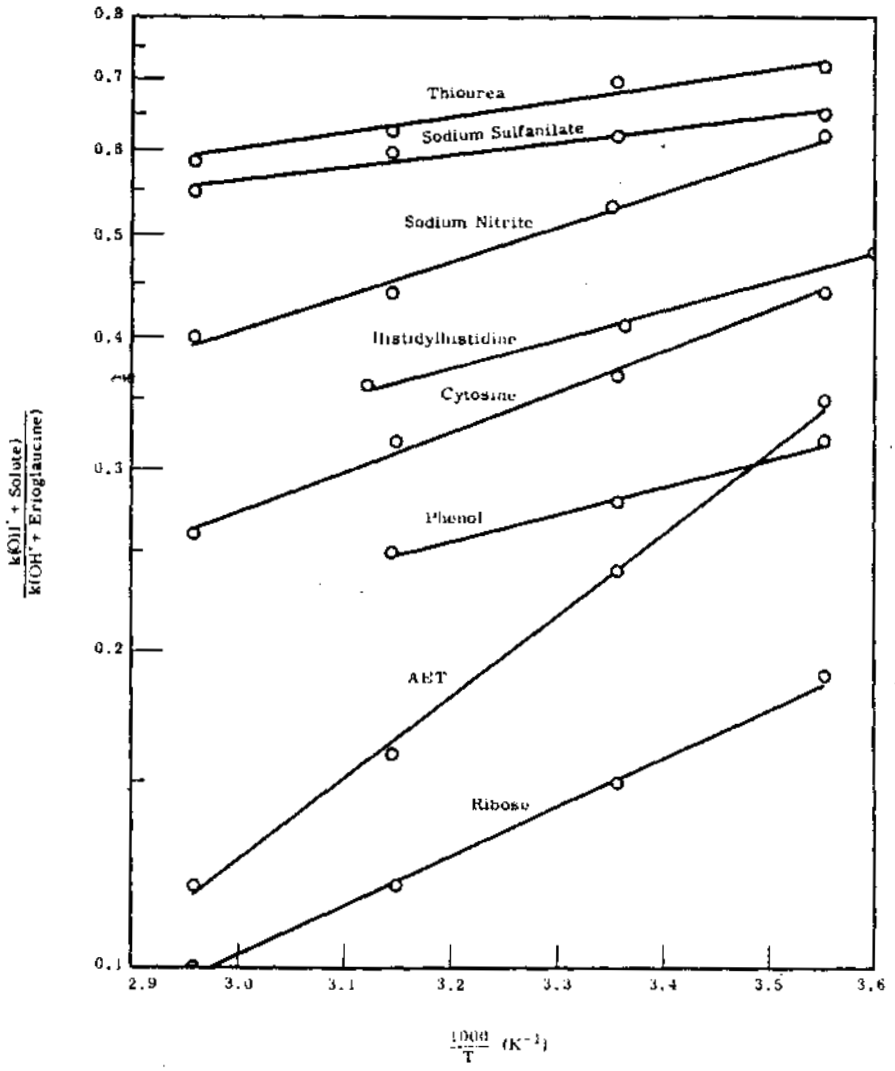

FIGURE 3.34
Relative Rate Constants for Several Solutes

TABLE 3.35

ACTIVATION ENERGIES FOR REACTIONS OF THE TYPE:
SOLUTE + $OH^{\cdot}$ →

Solute	E, kcal $mole^{-1}$
Erioglaucine	E_1
Sulfanilate	E_1 - 0.5
Thiourea	E_1 - 0.5
Phenol	E_1 - 1.0
Tyrosine	E_1 - 1.0
Glycine	E_1 - 1.0
Alanine	E_1 - 1.0
Histidylhistidine	E_1 - 1.0
Cytosine	E_1 - 1.5
Nitrite	E_1 - 1.5
Ribose	E_1 - 2.0
Ethanol	E_1 - 2.0
AET (2-aminoethyl-isothiuronium bromide)	E_1 - 3.5

activation energies of the two competing reactions differ by 3.5 kcal $mole^{-1}$, a change in temperature of 10 C^{o} will alter the ratio of their rate constants by about 20%. Temperature variation does not offer as great a control over the course of radiation-induced reactions as does, for example, addition of other radical-capturing reagents to the system; however, it provides a further degree of flexibility to this control which can be put to beneficial use.

Postirradiation Effects in Aqueous Dye Solutions -

W. D. Felix and D. R. Kalkwarf

Evaluation of the reaction-rate constants of tropeolin-O and erioglaucine with hydrogen peroxide showed that these reactions are too slow to account for the postirradiation bleaching of these dye in aqueous solution. This post-irradiation effect is thus attributed to the reaction of relatively long-lived organic radicals in the solution.

Following irradiation, aqueous solutions of either tropeolin-O or erioglaucine continue to bleach slowly for as long as several weeks. The

extent of these postirradiation effects is very slight as can be seen from Figure 3.35; however, it is measurable and provides information on the reactivities of intermediates formed during the irradiation process. While the free radicals formed by the radiolysis of water have lifetimes of less than 10^{-4} sec, free-radical products resulting from reactions of these primary radicals with solute molecules, such as the dyes, could have much longer lifetimes. Postirradiation bleaching could result from the dimerization, disproportionation, or hydrolysis of these organic radicals; however, another possible cause could be the slow reaction of the dyes with hydrogen peroxide generated during the radiolysis of water. The purpose of these experiments was to decide between these possibilities.

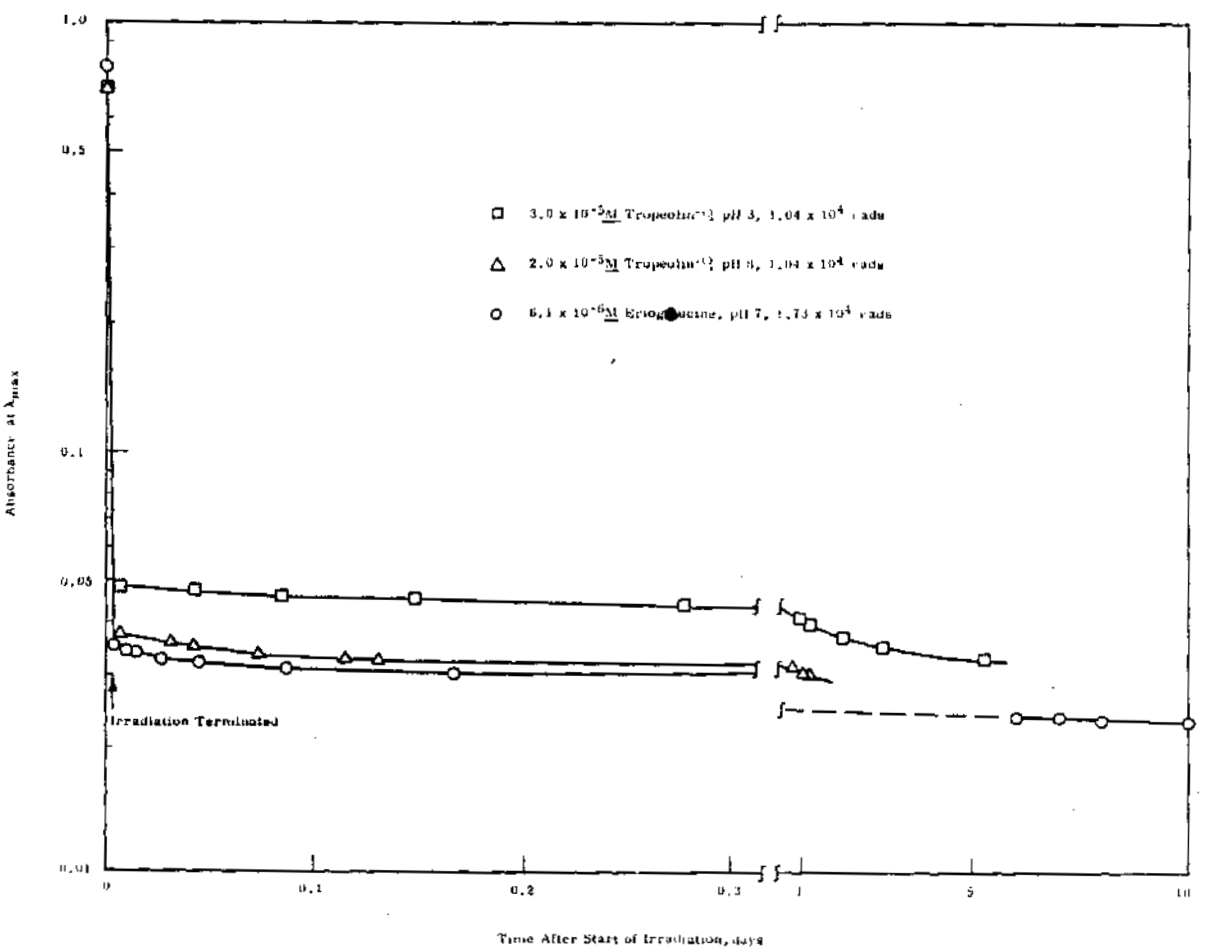

FIGURE 3.35
Postirradiation Bleaching of Tropeolin-O and Erioglaucine

The reactions of hydrogen peroxide with erioglaucine and tropeolin-O were followed colorimetrically by allowing the dyes to bleach in the presence of excess hydrogen peroxide of analytical grade. Under these conditions, the reactions are pseudo first order as shown in Figure 3.36. By varying the initial concentration of reactants, the reaction rates were found to be first order in dye and in hydrogen peroxide concentrations with a second order rate constant of 1×10^{-4} liters $mole^{-1}$ sec^{-1} at 25 C and pH = 7 for erioglaucine and 2×10^{-3} liters $mole^{-1}$ sec^{-1} at 60 C and pH = 12 for tropeolin-O.

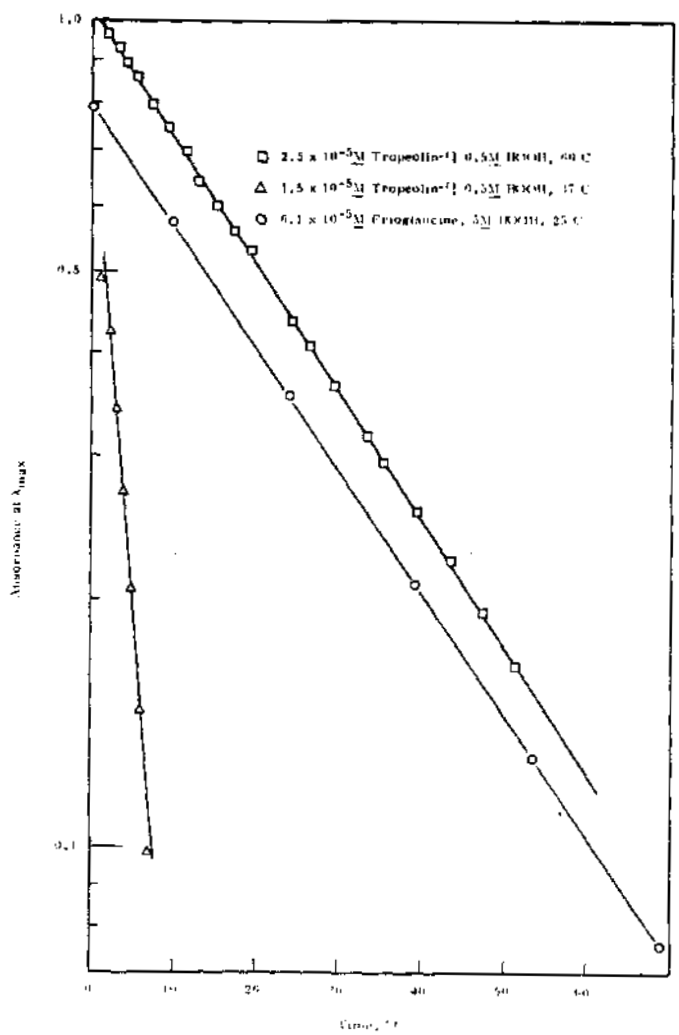

FIGURE 3.36

Dye Bleaching in Excess Hydrogen Peroxide

During the irradiation of aqueous solutions of organic solutes, hydrogen peroxide is formed with a yield of 3.54 molecules per 100 ev. Using this yield, upper limits for the concentration of hydrogen peroxide in the dye solutions immediately after irradiation were calculated and theoretical curves, shown in Figure 3.37, were prepared to describe the amount of dye bleaching which could be attributed to reaction with hydrogen peroxide. As can be seen from this figure, the actual postirradiation bleaching is preceeding much more rapidly. The necessary conclusion reached is that the reaction of radiation generated hydrogen peroxide with erioglaucine or tropeolin-O cannot be the primary reaction leading to the bleaching of the dyes. Mechanisms proposed to account for the postirradiation bleaching effect must therefore include chains of events in which a hydrogen peroxide-dye reaction does not become the rate controlling step. Such reaction steps may include the dimerization and disproportionation of dye radicals, the reaction of organic peroxides spawned from the dye molecules, or the reaction of dye molecules with radical products of the dye decomposition.

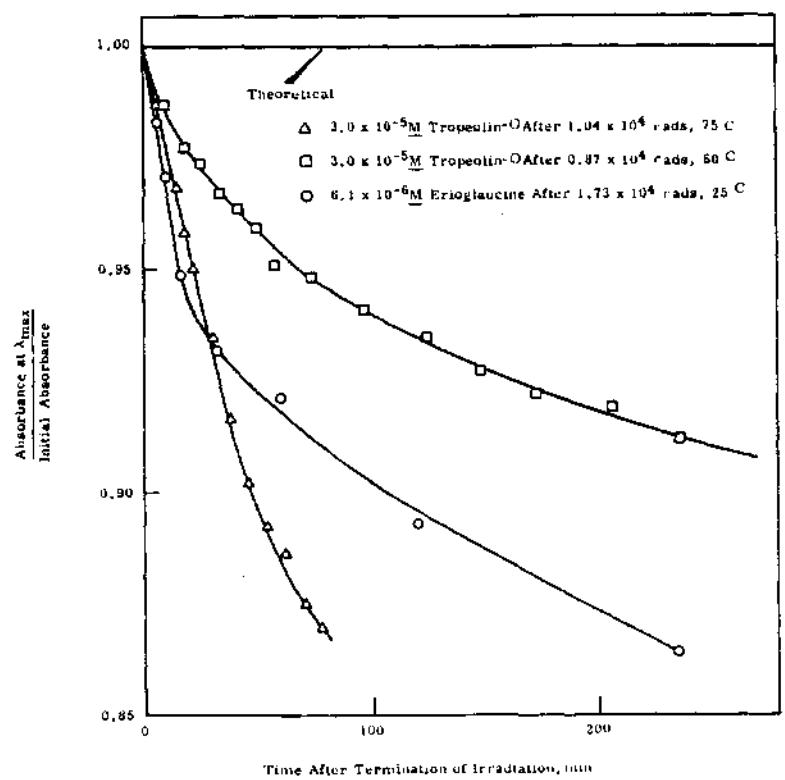

FIGURE 3.37

Postirradiation Bleaching of Tropeolin-O and Erioglaucine

Attempted Chemical Protection of Radish Seeds from Radiation Damage - D. R. Kalkwarf

Erioglaucine, which reacts rapidly with hydroxyl radicals, was tested as a protective agent in radish seeds subjected to radiation damage. No protective effect was observed in seed germination trials, although factors which may have masked such an observation were noted.

Since discovery of the mutagenic effect of ionizing radiation, optimistic expectations have arisen that improved varieties of vegetables and grains could be obtained by irradiation of currently available seeds. One impediment to progress in testing for such improvements has been the loss in germination ability of seeds as the radiation dose is increased to enhance the probability for mutations. It is conceivable that seeds could be chemically protected from the former type of radiation damage while still being subjected to the mutagenic effects of irradiation. Testing such a possibility is not only of practical importance but also of more general interest since seeds are convenient laboratory models in which to test protective measures under conditions which must be considered in many other biological systems.

Seeds of the radish plant, Raphanus sativus, germinate easily and rapidly under laboratory conditions and were used to test the effectiveness of the potent, hydroxyl radical scavenger, erioglaucine,[3.49] as a chemical protective agent. Samples were soaked in either distilled water or an aqueous 1% solution of erioglaucine for 18 hr, and then the water content of the seeds was adjusted to either 1.4 or 20.1% by storing them at room temperature in atmospheres controlled to maintain water vapor pressures of either 0.5 or 17.5 mm Hg at a total pressure of 760 mm Hg. Co^{60} gamma radiation was used to irradiate the seeds. After irradiation, the seeds were placed in groups of ten on blotter paper soaked with 10^{-3} M potassium gibberellate[3.52] and stored in covered, plastic petri dishes. The number of seeds that germinated after 7 days was recorded, it having been established that seed which did not germinate in 4 days were not likely to ever germinate under the above conditions. The results expressed as the variation of the fraction germinated as a function of dose are shown in Figure 3.38.

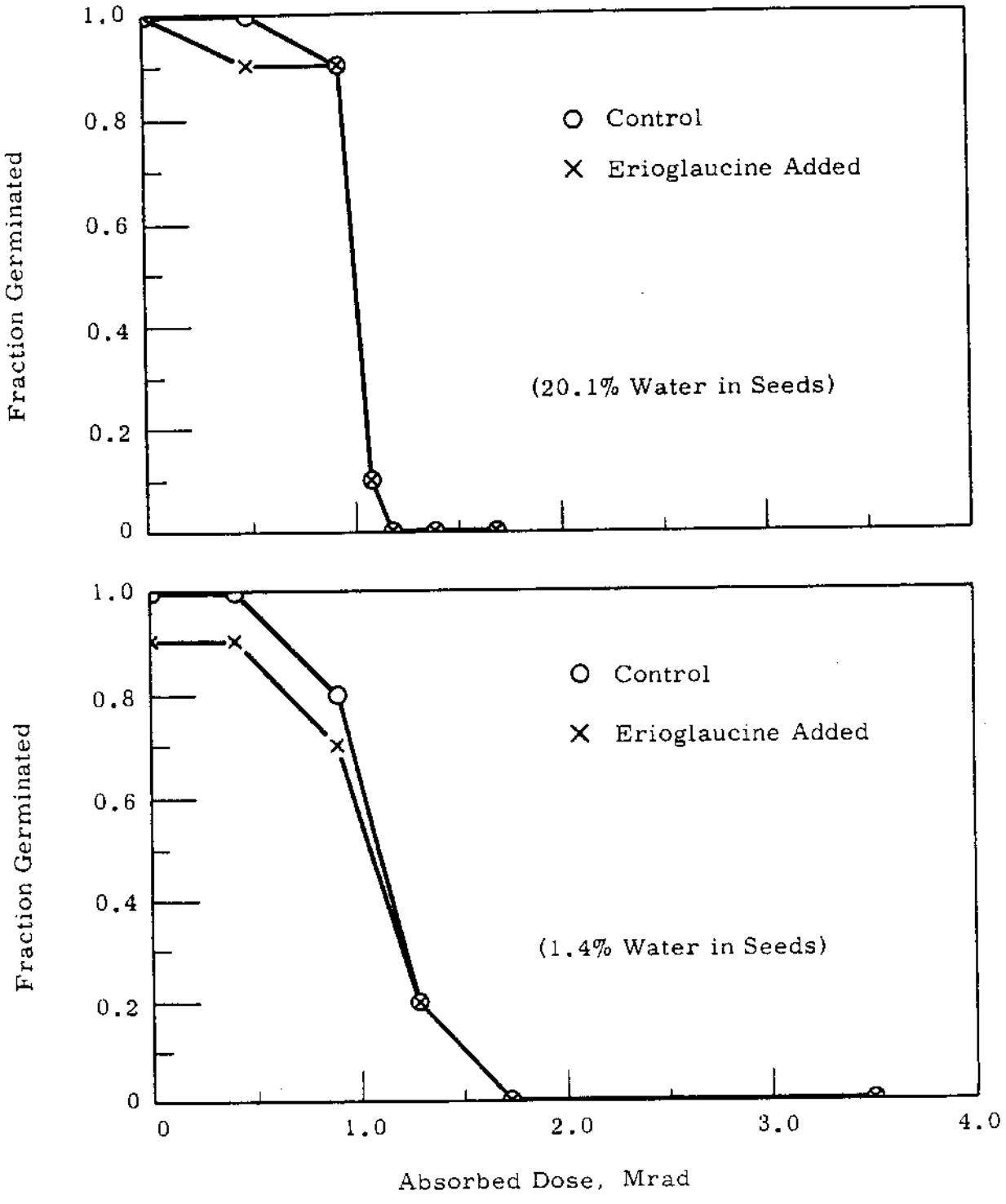

FIGURE 3.38

Variation in Germination Ability of Radish Seeds with Radiation Dose

ASC GE RICHLAND WASH

The lack of demonstrable chemical protection in this test prompted auxiliary observations on the seeds and consideration of whether protection might not be masked by other factors. Distribution of the additive within the seed plays a critical role in such tests since a protective agent must obviously be present at the site where protection is needed. The distribution of erioglaucine is particularly easy to determine because of its intense blue color; and although its average concentration in the test seeds was 10^{-4}M, variation in its microscopic concentration was considerable. Evidence for a slight toxic effect of erioglaucine on seed germination can also be noted in Figure 3.38, and removal of the compound before germination may reveal a protective effect now masked by this toxicity to normal metabolism. There thus appears the possibility that an altered procedure for introducing the compound may prove beneficial.

Kinetic Studies of Organic Radicals Formed in Irradiated Aqueous Solution - R. N. Diebel and D. R. Kalkwarf

Organic free radicals, formed by gamma irradiation of aqueous solutions, were studied in a continuous flow system which was monitored by an electron spin resonance spectrometer. Radicals formed from p-nitroaniline were found to have half-lives of 15 sec even at room temperature.

The free radicals formed in irradiated aqueous solutions are commonly considered to be very reactive and to have disappeared from the solution in a few thousandths of a second after the termination of irradiation. This is certainly true for the primary radicals formed from the decomposition of water, but the reaction of these radicals with solutes usually results in the formation of secondary radicals which may or may not be reactive. Long-lived radicals in aqueous solution are well known, e.g., peroxylamine disulfonate ion (often used for magnetic field calibration in electron spin resonance spectrometry), Wursters salts (the oxidation products of the N-substituted phenylenediamines), and several semiquinones. It is reasonable to suspect that irradiation would produce many other radicals, stable for seconds to days, which were not attainable by other chemical methods. This

possibility is of keen interest in examining methods for modifying the effects of ionizing radiation. If chemical additives capable of forming such stable radicals were compatible with living tissue they could serve to slow down, if not terminate, the rate that damage was done in the irradiated system. Alternatively, if naturally occurring substances themselves form such radicals, there is the prospect of chemically treating the system after irradiation to modify the eventual amount of damage.

To explore the production of long-lived free radicals in aqueous solution, the apparatus shown in Figure 3.39 was constructed. Essentially, it consists of a closed, flow system in which a solution can be irradiated with Co^{60} gamma radiation and rapidly transferred to an aqueous sample cell of an electron spin resonance spectrometer. An adjustable volume reservoir in the line allows one to alter the time interval before the solution is reirradiated and to add or remove chemicals in the system without stopping the flow. The flow rate through the system can be varied to 125 ml sec^{-1} allowing a delay to 0.4 sec between the exit of the irradiator and the electron spin resonance cell.

To test the apparatus, a solution of p-nitroaniline in alkaline, aqueous solution was examined since this compound has been reported to yield a free radical stable for several seconds in a variety of solvents after electrolytic reduction.[3.53] In an irradiated aqueous solution, reducing species such as hydrogen atoms and solvated electrons are accompanied by oxidizing species such as hydroxyl radicals which might oxidize the organic radical back to the original nitro compound. Some net production of organic radicals was expected since the yield of hydrogen atoms and solvated electrons exceeds that of hydroxyl radicals in irradiated water by 20%; and substances could be added which selectively scavenge hydroxyl radicals, thus increasing the organic radical yield.

A 4×10^{-3} M solution of p-nitroaniline, adjusted to pH 13.0 with NaOH and purged of dissolved oxygen with helium gas, was passed through the apparatus and found to exhibit the electron spin resonance spectrum shown in Figure 3.40A. This spectrum was not attained immediately but increased in intensity over a period of 15 min. The concentration of radicals finally attained

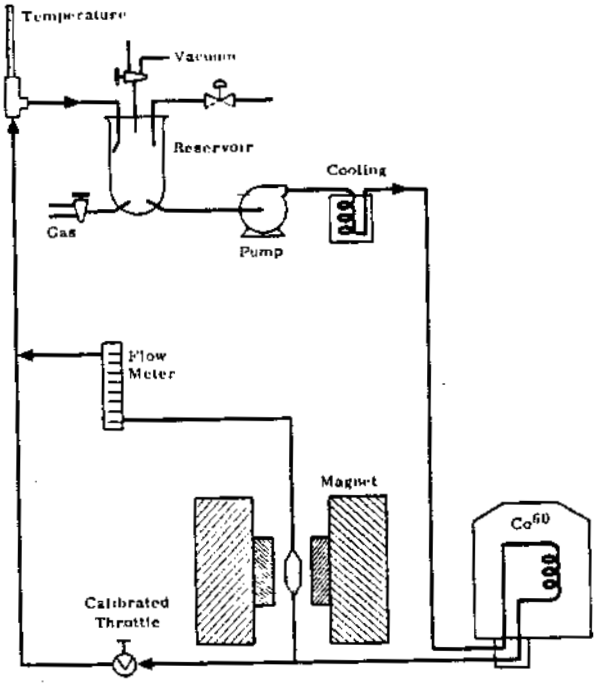

FIGURE 3.39

Flow System for Gamma Irradiation and Observation of Free Radicals by Electron Spin Resonance

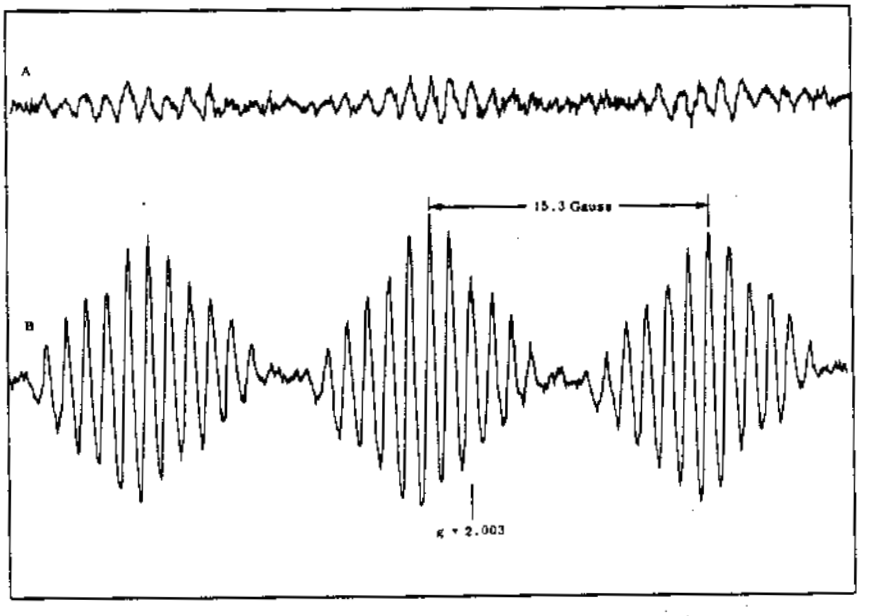

FIGURE 3.40

ESR Spectra of Product Formed During Irradiation of p-nitroaniline in 0.1M NaOH

A. Nothing else Added B. Ethanol Added

AEC-GE RICHLAND, WASH.

was estimated to be 1.5×10^{-6} M by comparison with a standard solution of the free radical, diphenylpicrylhydrazyl, in benzene. No electron spin resonance signal was obtained from the solution at pH 12.0 nor was any signal obtained in the presence of dissolved oxygen. Ethanol reacts with hydroxyl radical about fifty times as fast as with hydrogen atoms; and as predicted, its presence at a concentration of 1.4×10^{-2} M increased the stationary-state concentration of p-nitroaniline radical to 6.2×10^{-6} M.

From the spectrum shown in Figure 3.40, one can gain some idea of the structure of the radical. The dominant feature is the set of triplets separated by 15.3 gauss indicating that the unpaired electron is closely associated with a nucleus of spin I = 1 which would split the absorption line into 2I + 1 = 3 lines. This nucleus seems to be the nitrogen atom in the nitro group since an unpaired electron on the amino nitrogen would also show strong coupling with the amino hydrogens which is not evident in the spectrum. The free radical generated by electrolytic reduction of p-nitroaniline gives a very similar spectrum which was identified both by polarographic analysis and by theoretical synthesis of the hyperfine, electron spin resonance spectrum as:

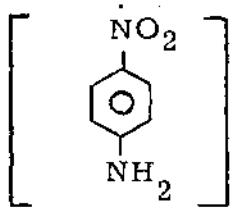

As the temperature of the flowing solution was lowered, the concentration of radicals measured in the electron spin resonance cell increased as shown in Figure 3.41. If the flow was stopped suddenly and the magnetic field was kept constant at an electron spin resonance absorption peak, the decrease in radical concentration could be followed as a function of time; e.g., see Figure 3.42. At present, the aqueous sample cavity is not thermostatic so that curves at temperatures other than near room temperature are only of qualitative interest. At 20 C, however, the data shown in Figure 3.43 were obtained, indicating that the radicals were disappearing via a reaction that

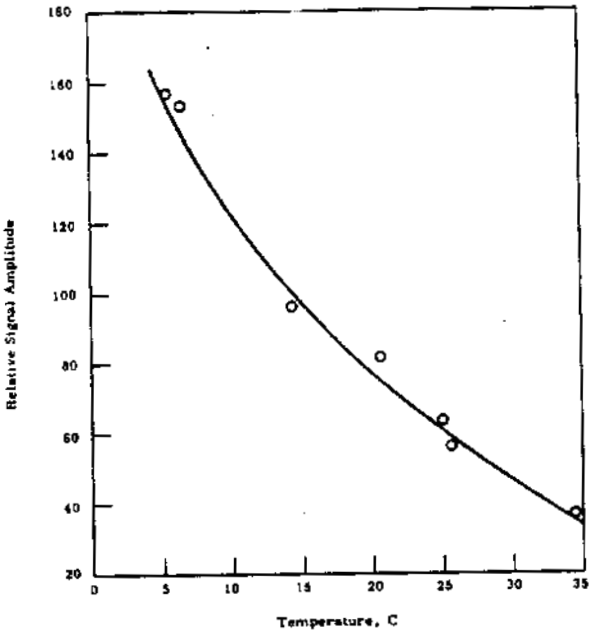

FIGURE 3.41

Variation in the Steady-State ESR Signal Amplitude from 3×10^{-3} M p-nitroaniline as a Function of Temperature

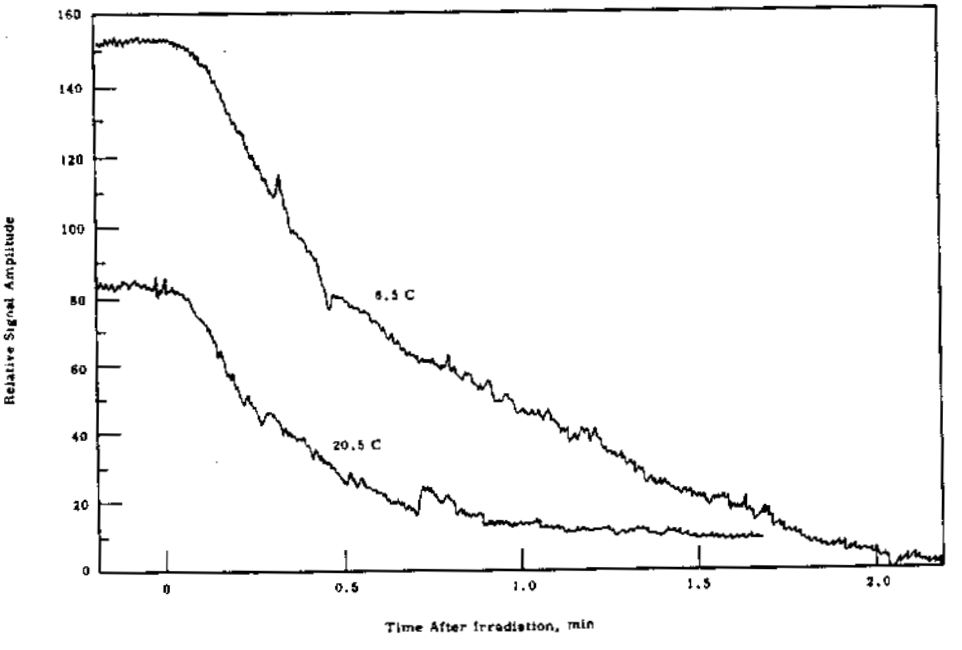

FIGURE 3.42

Decay of ESR Signal Amplitude from Steady-State Value in Irradiated p-nitroaniline Solution

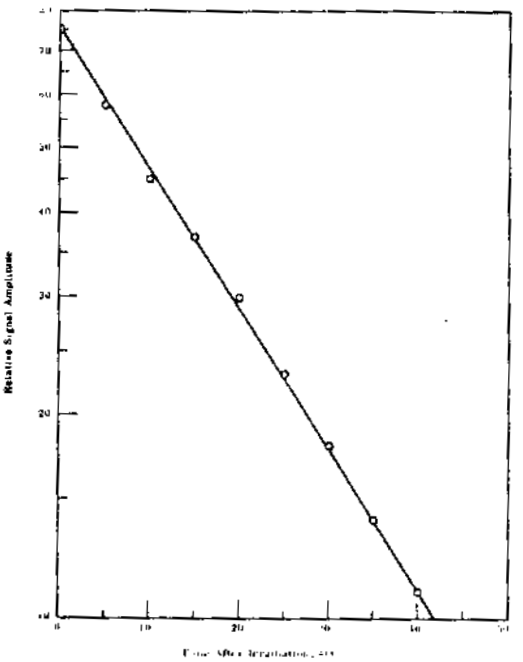

FIGURE 3.43

Decay of ESR Signal Amplitude After Irradiation of 3×10^{-3} M p-nitroaniline Solution at 25 C

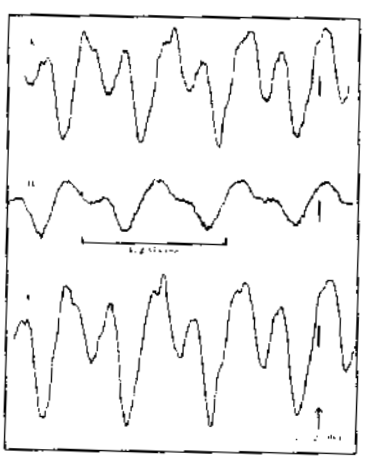

FIGURE 3.44

ESR Spectra of 10^{-3} M. N, N dimethyl p-phenylene diamine hydrochloride

A. Initial spectrum due to air oxidation after air has been purged with helium
B. After bubbling air for 3 minutes. Further exposure to air will completely eliminate the ESR signal
C. Solution from B after thorough purge with helium

is first order in radical concentration rather than second order. Thus, rather than dimerization of radicals, a pseudo first order reaction with some ubiquitous solute appears to remove radicals from the solution. The identity of this solute is undecided; dissolved oxygen cannot be excluded from consideration until a more gas-tight system is constructed.

In addition to p-nitroaniline, aqueous solutions of N, N-dimethyl-phenylene-diamine were irradiated in the flow system. Free radical products from the electrolytic oxidation of this compound have been reported in the literature,[3.54] and even air oxidation is sufficient to form a pink-colored solution of the radical cation in acid solution, e.g.

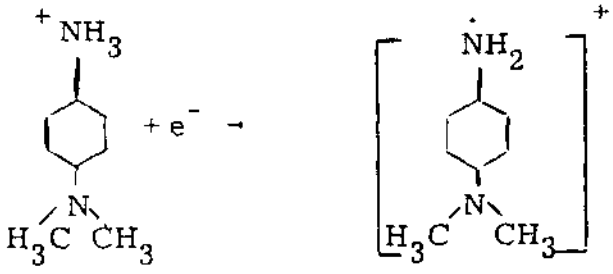

(DMPPD) (DMPPD·)

During irradiation of a 10^{-3}M solution of DMPPD·HCl, no signal was obtained. Presumably the reducing activity of the hydrogen atoms more than counterbalanced the oxidizing activity of the hydroxyl radicals. It was suspected that addition of oxygen to the irradiated solution would remove hydrogen atoms by the reaction:

$$H^{\cdot} + O_2 \rightarrow HO_2^{\cdot}$$

so that a net oxidation to DMPPD· could take place. Such a possibility is complicated, however, by the behavior of the DMPPD· radical with oxygen. Figure 3.44 shows that this radical, prepared by air oxidation, combines in some way with dissolved oxygen to give a structure whose electron spin resonance signal is much more flattened out. Thus, while oxygen may prevent reduction of DMPPD· radicals during irradiation, it rapidly reacts with these radicals to give a new type of radical whose electron spin resonance signal is difficult to distinguish from the noise. Compounds, other than oxygen, which react selectively with hydrogen atoms are thus being sought as additives to test these ideas.

Electron Paramagnetic Resonance Line Shape - W. D. Felix

A linear approximation which combines Gaussian and Lorentzian forms is applied to the calculation of electron paramagnetic resonance (EPR) line shape. The approximation is applied to an EPR signal generated by DPPH.

A difficult problem that the EPR spectroscopist must meet is that of obtaining absolute values of the integrated line intensities. The general problem has been outlined elsewhere.[3.55] The specific problem of interest is that of determining the EPR line shape.

The shape of the EPR line yields information on the types of interactions of the various resonance centers. A Lorentzian shape, for example, is indicative of an homogeneously broadened resonance line whose width is inversely proportional to the spin-spin relaxation time, T_2. Hyde[3.55] determines if a line is Lorentzian by comparing relative line positions of the experimental line against the ideal shape at selected intervals. Generally, however, the line shape is neither truly Lorentzian nor Gaussian.

The Gaussian form may be written

$$\varepsilon = \varepsilon_o \exp\left[(\sigma - \sigma_o)^2 / B^2\right] \tag{1}$$

where ε_o is the peak height at σ_o, the midpoint of a symmetrical peak. B is an experimentally determined parameter, unique to the system. The derivative curve

$$\frac{d\varepsilon}{d\sigma} = \varepsilon_o \exp\left[-(\sigma-\sigma_o)^2 / B^2\right]\left[-2\frac{(\sigma-\sigma_o)}{B^2}\right]$$

exhibits symmetric maxima and minima, thus,

$$\frac{d^2\varepsilon}{d\sigma^2} = 0 = \varepsilon_o \left\{\exp\left[-(\sigma-\sigma_o)^2 / B^2\right]\frac{2}{B^2}\right\}\left[1 - 2\frac{\sigma-\sigma_o}{B}^2\right]$$

whence

$$B = \pm\sqrt{2}\,(\sigma_{max} - \sigma_o) \tag{2}$$

where σ_{max} is the value of σ at the maximum or minimum.

For the Lorentzian form

$$\varepsilon = \varepsilon_o \left[\frac{1}{1 + \left(\frac{\sigma - \sigma_o}{C} \right)^2} \right] \tag{3}$$

where C is a constant. Then

$$\frac{d\varepsilon}{d\sigma} = -\varepsilon_o \left[\frac{1}{1 + \left(\frac{\sigma - \sigma_o}{C} \right)^2} \right]^2 2 \left[\frac{(\sigma - \sigma_o)}{C^2} \right].$$

By setting $\frac{d^2\varepsilon}{d\sigma^2} = o$ we have

$$o = \frac{2}{C^2} \left\{ 1 + \left[\frac{(\sigma - \sigma_o)}{C} \right]^2 \right\} \left\{ 1 - 3 \left[\frac{(\sigma - \sigma_o)}{C} \right]^2 \right\}.$$

Solving for C and discarding the imaginary case,

$$C = \pm \sqrt{3} \, (\sigma_{max} - \sigma_o) \tag{4}$$

For convenience, the notation is now simplified. Let $f'(x) = 1.000$ at σ_{max}, $(\sigma - \sigma_o) = x$ and $a = \sigma_{max} - \sigma_o$. Hence,

$$\varepsilon = g(x) = 1.65 \, a \, e^{-x^2/2a^2} \tag{5}$$

for the Gaussian and

$$\varepsilon = 1(x) = \left(\frac{8a}{3}\right) / \left(1 - \frac{x^2}{3a^2}\right) \tag{6}$$

for the Lorentzian forms. Now the derivative curve is written as a linear combination of the Gaussian and Lorentzian forms,

$$f'(x) = r \, g'(x) + s \, 1'(x) \tag{7}$$

where r and s are the degree of Gaussianess or Lorentzianess, respectively.

An experimental curve and the fitted Gaussian, Lorentzian, and combination curves are shown in Figure 3.45 for DPPH absorbed on radish

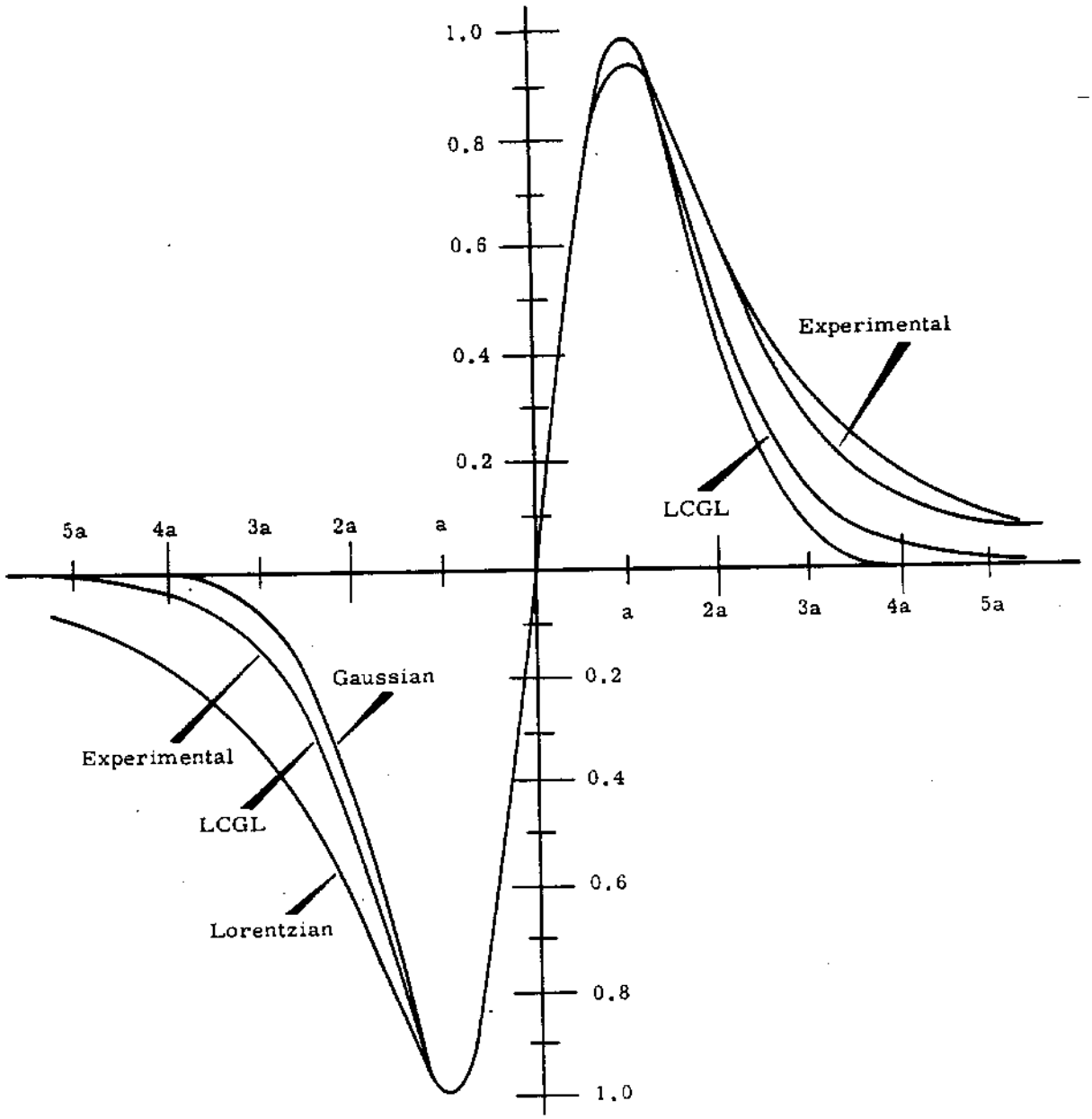

FIGURE 3.45

First Derivative EPR Curve of DPPH Saturated Radish Seeds Compared with Gaussian and Lorentzian Derivative Curves and a Linear Combination of Gaussian and Lorentzian (LCGL).

AEC-GE RICHLAND, WASH.

seeds. The corresponding tabular array, Table 3.36, presents a comparison of the calculated curve with the experimental curve at selected points along the curves. As may be seen, the experimental curve is fitted exactly by the linear combination of the Gaussian and the Lorentzian forms on the left leg of the derivative EPR curve. The experimental curve is not symmetrical, hence the fit on the right side is poor. Thus one must add half of the moment calculated by fitting the curve to the left leg to half of the moment calculated by fitting the combination curve to the right leg. One may also derive a non-symmetrical form for the entire curve. The latter method would mean introducing correction terms such that the Gaussian form becomes [3.56]

$$\epsilon = b\sigma e^{-B(\sigma - \sigma_o)^2} \qquad (8)$$

that is, the maximum no longer occurs at σ_o, but is displaced to

$$\sigma_o + \delta^2/(\sigma_o 2\ln 2).$$

The Lorentzian form need also be similarly corrected. In practice it is easier to add the moments of each individual leg.

The significance of the method may now be considered. Let $f'(x)$ be the experimentally determined signal, i.e., the first derivative signal. The number of spins which give rise to this signal is proportional to $f'(x)dx^2$. Andrew [3.55, 3.57] has pointed out that a graphical determination of the first moment of the experimental resonance signal is equal to the double integral

$$\int\int f'(x)dx^2 = \int xf'(x)dx .$$

The experimental first moment thus obtained graphically, by a moment balance or by integration of Equation (7) is compared to the first moment of a standard to obtain the spin concentration.

TABLE 3.36

LORENTZIAN AND GAUSSIAN CURVES APPLIED TO EPR SPECTRA

Height, % of Maximum	Relative Position			
	Lorentzian	Gaussian	Combination, G + L	Experimental
100	1	1	1	1
80	1.55	1.5	1.545	1.51
60 (Est. Point)	2.1	1.8	1.84	1.84
40	2.75	2.1	2.13	2.32
20 (Est. Point)	1.80	2.5	2.17	2.17
10	5.0	2.8	3.28	3.27

An Effect of Polyelectrolytes on Hemolysis of Irradiated Alligator Red Blood Cells - W. B. Silker

An inhibition of hemolysis of alligator red blood cells following irradiation was observed in solutions containing an anionic polyelectrolyte.

Alligator red blood cells, which undergo hemolysis after absorbing a sufficient dose of ionizing radiation, possess a negative electrokinetic surface potential. Kalkwarf has examined the degree of protection afforded human red cells against radiation-induced hemolysis by various agents and concluded that the best protective agents were the efficient free radical scavengers. The resistance of red cells against radiation damage may also be influenced by the surface potential of the cell. An attempt to measure this influence was made by adjustment of the cell wall potential by addition of polyelectrolytes.

Three samples of alligator blood, selected because of its stability against hemolysis, were diluted 1:1000 in isotonic saline solution. To one sample was added 1 ppm of a cationic polyelectrolyte; to the second was added 10 ppm of an anionic polyelectrolyte; and the third sample was untreated. The samples were divided, one-half being irradiated in a Co^{60} facility to a total absorbed dose of about 2×10^5 rads, while the remainder was used as a control to determine the degree of hemolysis in unirradiated samples. The electrophoretic mobility of the red cells in both fractions was measured about 10 min after the exposure to the cobalt source, and the results are presented in Table 3.37.

TABLE 3.37

ELECTROPHORETIC MOBILITY OF RED BLOOD CELLS

Sample	Untreated Blood	Blood plus Cationic Polyelectrolyte	Blood plus Anionic Polyelectrolyte
	Mobility, $\mu sec^{-1} v^{-1} cm^{-1}$		
Unirradiated	-1.20	-1.08	-1.90
Irradiated	0.0	-0.28	-1.60

Red cell hemolysis was measured visually in a hemocytometer cell, and the degree of hemolysis was measured by comparison of the irradiated and unirradiated samples. Less than 5% of the red cells in the unirradiated samples were hemolyzed after sitting for 6 hr at room temperature, the degree of hemolysis of the irradiated samples is presented in Figure 3.46. It is evident that the sample containing the anionic polyelectrolyte was protected against radiation-induced hemolysis of the red cells. This experiment did not define whether this protection was due to maintenance of the surface potential of the red cells, or if the anionic polyelectrolyte itself acted as a free radical scavenger thus providing protection of the red cells by competition for the radiation-induced free radicals. The sample containing cationic polyelectrolyte was hemolyzed to a lesser degree than the untreated sample and may reflect a degree of protection afforded by this agent.

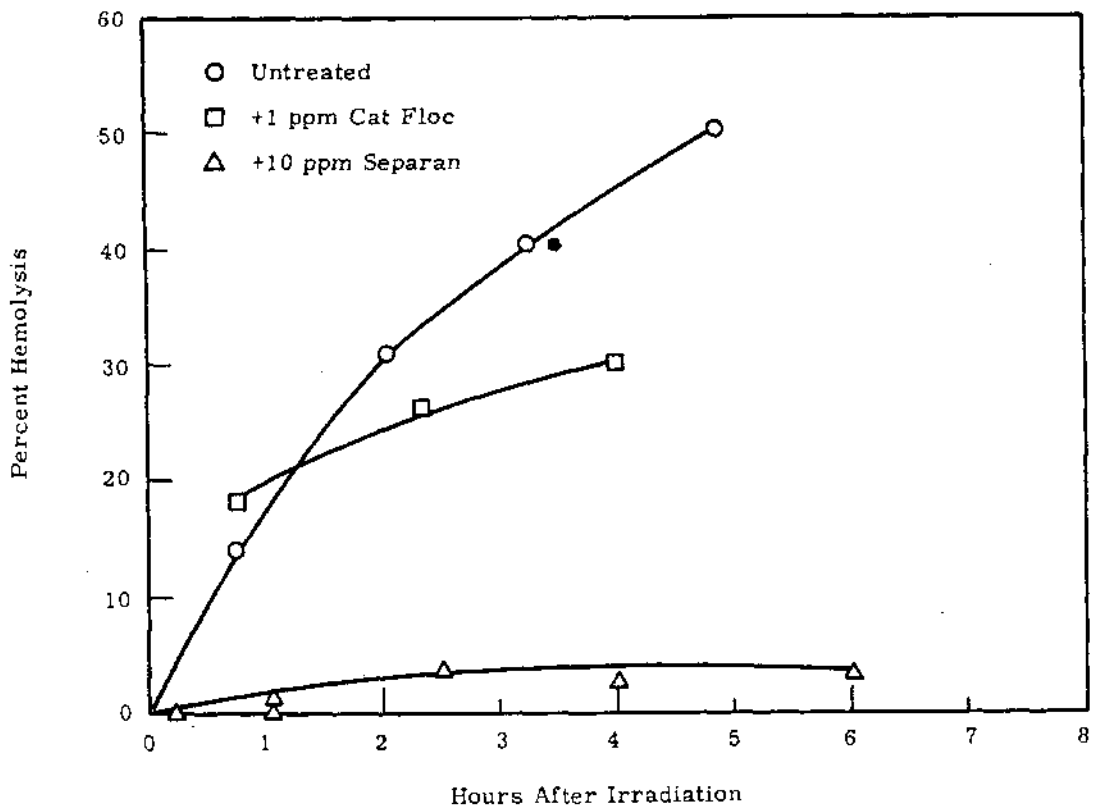

FIGURE 3.46

The Effect of Polyelectrolyte Addition on the Hemolysis of Red Blood Cells

REFERENCES

3.1 R. W. Perkins, J. M. Nielsen, and R. N. Diebel. "Total-Absorption Gamma-Ray Spectrometers Utilizing Anticoincidence Shielding," Rev. Sci. Instr., vol. 31, pp. 1344-1349. 1960.

3.2 R. W. Perkins. "Gamma-Ray Spectrometric Systems of Analysis," Proceedings of the Second United Nations International Conference on the Peaceful Uses of Atomic Energy, Geneva, vol. 28, pp. 445-461. New York: United Nations, 1958.

3.3 C. R. Hill. "A Method of Alpha Particle Spectroscopy for Materials of Very Low Specific Activity," Nuclear Instruments and Methods, vol. 12, pp. 299-306. 1961.

3.4 C. R. Hill. "Identification of α-Emitters in Normal Biological Materials," Health Physics, vol. 8, pp. 17-25. 1962.

3.5 R. W. Perkins. "Uranium Ore Dust Inhalation Studies," Hanford Radiological Sciences Research and Development Annual Report for 1962, HW-77609, pp. 3.55-3.60. 1962.

3.6 J. E. Grindler. The Radiochemistry of Uranium, NAS-NS-3050. March 1962.

3.7 E. K. Hyde. The Radiochemistry of Thorium, NAS-NS-3004. January 1960.

3.8 F. L. Moore. "Liquid-Liquid Extraction of Uranium and Plutonium from Hydrochloric Acid Solution with Tri(iso-octyl) amine," Anal. Chem., vol. 30, pp. 908-911. 1958.

3.9 R. W. Perkins and D. R. Kalkwarf. "Determination of Thorium in Urine," Anal. Chem., vol. 28, pp. 1989-1993. 1956.

3.10 A. H. Helman. The Determination of Thorium in Urine, PGR-178S, pp. 1-10. 1961.

3.11 K. Z. Morgan (ed.) "Report of Committee II on Permissible Dose for Internal Radiation(1959)," Health Physics, vol 3, p. 65. 1960.

REFERENCES (Contd.)

3.12 J. W. Healy, G. E. Pilcher and C. E. Thompson. Computed Fission Product Decay, HW-33414. December 1, 1954.

3.13 J. D. Ludwick. "Liquid Scintillation Tritium Counting Improvements," Hanford Radiological Sciences Research and Development Annual Report for 1962, p. 3.23, HW-77609. January 1963.

3.14 J. D. Ludwick. "Liquid Scintillation Spectrometry for the Analysis of Zirconium-95—Niobium-95 Mixtures and Coincidence Standardization of These Isotopes, Anal. Chem., vol. 32, pp. 607-610. 1960.

3.15 W. B. Silker. Variations in Elemental Concentrations in the Columbia River, HW-SA-3147. July 22, 1963.

3.16 R. W. Perkins. Source of Reactor Effluent Water Radioisotopes, HW-69969. May 1961.

3.17 R. W. Perkins. Thermal and Fission Neutron Flux Measurements in Process Tubing and in Neutron Activation Test Locations, HW-68377. February 2, 1961.

3.18 R. B. Richman. Radiation Effects on Aluminum Filming and Corrosion, HW-76642. February 20, 1963.

3.19 R. W. Perkins and D. E. Robertson. The Effect of Chemical Additives and Coating Materials on the Adsorption of Radionuclide Parent Elements on Aluminum Surfaces, HW-75976. December 26, 1963.

3.20 D. E. Robertson and R. W. Perkins. Reduction of the Effluent Water Radionuclides by the Addition of Sodium Silicate to Process Water, HW-75782. December 10, 1962.

3.21 C. W. Thomas and W. B. Silker. Concentration of Corrosion Isotopes in Half-Plant Low Alum Feed Water Treatment at F Reactor, HW-78431. July 19, 1963.

3.22 C. W. Thomas and W. B. Silker. Concentration of Corrosion Isotopes in Half-Plant Low pH Coolant at D Reactor, HW-78964. September 3, 1963.

REFERENCES (Contd.)

3.23 R. W. Perkins. "Physical and Chemical Form of I^{131} in Fallout," Health Physics, vol. 9, pp. 1113-1122. 1963.

3.24 A. Malvicini, M. De Bortoli, P. Gaglione, E. Van der Stricht. "Yttrium-88 on High-Activity Zirconium-95 Fallout Particles," Science, vol. 139, pp. 1287-1288. March 29, 1963.

3.25 Radiological Health Data for 1963. Volume 4.

3.26 L. Marquez, N. L. Costa and I. G. Almeida. " The Formation of ^{22}Na from Atmospheric Argon by Cosmic Rays," Nuovo Cimento (10), vol. 6, pp. 1292-5. 1957. (NSA-2:6022)

3.27 N. Bhandari and Rama. "Atmospheric Circulation from Observations of Sodium-22 and Other Short-Lived Natural Radioactivities, J. Geophys. Research, vol. 68, pp. 1959-66. 1963.

3.28 H. E. Palmer and R. W. Perkins. "Cesium-134 in Alaskan Eskimos and in Fallout," Science, vol. 142, pp. 66-67. October 4, 1963.

3.29 R. W. Perkins. "Cesium-134 from Fallout," Hanford Radiological Sciences Research and Development Annual Report for 1962, p. 3.49. HW-77609. January 1963.

3.30 D. H. F. Atkins and A. E. J. Eggleton. Iodine Compounds Found on Release of Carrier-Free Iodine-131. AERE-M-1211.

3.31 J. D. Ludwick. Dual Atmospheric Tracer Techniques for Diffusion Studies Using Phosphorescence-Fluorescence Analysis, HW-70892. March 1961.

3.32 L. L. Humphreys. "The Columbia River Sediment Studies," Hanford Radiological Sciences Research and Development Annual Report for 1962, HW-77609, p. 3.61. January 1963.

REFERENCES (Contd.)

3.33 J. J. Sabo and R. H. Bedrosian (eds). "Studies of the Fate of Certain Radionuclides in Estuarine and Other Aquatic Environments," Public Health Service Publication Number 999-R-3. 1963. (U.S. Dept. of Health, Education, and Welfare., Washington, D. C.)

3.34 R. J. Morton. Status Report Number 1 on Clinch River Study, ORNL-3119. 1961.

3.35 W. T. Lammers. "Density-Gradient Separation of Organic and Inorganic Particles by Centrifugation, Science, vol. 139, p. 1298-1299. 1963.

3.36 F. A. Richards and T. G. Thompson. "The Estimation and Characterization of Plankton Populations by Pigment Analysis," Part 2, "A Spectrophotometric Method for the Estimation of Plankton Pigments," J. Marine Res., vol. 11, pp. 156-172. 1952.

3.37 L. L. Humphreys and R. W. Perkins. Preliminary Measurements of the Adsorption of Reactor Effluent Water Radionuclides by Columbia River Particulate Material, HW-79279. 1963.

3.38 Ludwig Teleky. "Occupational Cancer of the Lung," J. Ind. Hyg. and Toxicology, vol. 19, pp. 73-85. 1937.

3.39 Egon Lorenz. "Radioactivity and Lung Cancer; A Critical Review of Lung Cancer in the Mines of Schneeberg and Joachimsthal., J. Nat. Cancer Inst., vol. 5, pp. 1-15. 1944.

3.40 D. A. Holaday, Sanitary Engineer Director. "Control of Radon and Daughters in Uranium Mines and Calculations on Biological Effects," Public Health Services Publication Number 494. 1957. (U.S. Dept of Health, Education and Welfare., Washington, D.C.)

3.41 R. Hours. Application de la radioactivite' a' hydraulique souterraine, CEA-2096. 1961.

REFERENCES (Cont.)

3.42 J. R. Morrey. "Fused Salt Spectrophotometry, III. Isosbestic Points Generated by Variation in Temperature," J. Phys. Chem., vol. 66, pp. 2169-2173. 1962.

3.43 R. W. Ramette, E. A. Dratz and P. W. Kelly. "Acid-Base Equilibria of Methyl Red," J. Phys. Chem., vol. 66, pp. 527-532. 1962.

3.44 H. A. Dewhurst. "Effect of Aliphatic Alcohols on the γ-Ray Oxidation of Aerated Aqueous Ferrous Sulfate," Trans. Faraday Soc., vol. 48, pp. 905-911. 1952.

3.45 T. J. Sworski. "Yields of Hydrogen Peroxide in the Decomposition of Water by Cobalt γ-Radiation," J. Am. Chem. Soc., vol. 76, pp. 4687-4692. 1954.

3.46 W. A. Armstrong and D. W. Grant. "The Co^{60} γ-Radiolysis of Aqueous Cystine Solutions," Canadian J. Chem., vol. 41, pp. 1882-1887. 1963.

3.47 A. O. Allen. The Radiation Chemistry of Water and Aqueous Solutions: p. 63. Princeton, N.J. D. Van Nostrand. 1961.

3.48 J. F. Ward. Effects of Inorganic Anions on Some Radiation Chemical Yields in Aqueous Solution, UCLA-515. June 1962.

3.49 D. R. Kalkwarf. "Radiation Sensitivity and Chemical Structure," Proceedings of the Second United Nations International Conference on the Peaceful Uses of Atomic Energy, Geneva, vol. 29, pp. 379-384. New York: United Nations, 1958.

3.50 A. A. Frost and R. G. Pearson. Kinetics and Mechanism, Second Edition. p. 150. New York: John Wiley and Sons. 1961.

3.51 D. R. Kalkwarf. "The Effect of Temperature on Radical-Capturing Reactions in Irradiated Aqueous Solutions," Hanford Radiological Sciences Research and Development Annual Report for 1962, HW-77609, pp. 3.75-3.79. 1963.

REFERENCES (Contd.)

3.52 A. H. Haber and H. J. Luippold. "Dormancy Resulting from Gamma-Irradiation of Lettuce Seed," Int. J. Radiation Biol., vol. 1, pp. 317-327. 1959.

3.53 L. H. Piette, P. Ludwig, and R. N. Adams. "Electron Paramagnetic Resonance of Aromatic and Aliphatic Nitro Anions in Aqueous Solution," J. Am. Chem. Soc., vol. 84. p. 4212. 1962.

3.54 H. Y. Lee and R. N. Adams. "Anodic Voltammetry and EPR Studies of Isomeric Phenylenediamines," Anal. Chem., vol. 34, pp. 1587-1590. 1962.

3.55 J. S. Hyde. "Experimental Techniques in EPR," Sixth Annual NMR-EPR Workshop, Varian Associates. November 5-9, 1962.

3.56 C. K. Jorgensen. Adsorption Spectra and Chemical Bonding in Complexes, p. 85 ff. New York: Pergamon Press, 1962.

3.57 E. R. Andrew. "Nuclear Magnetic Resonance Modulation Correction," Phys. Rev., vol. 91, p. 425. 1953.

CHEMICAL EFFLUENTS TECHNOLOGY

Soil Chemistry, Geochemistry

Synthesis of a Clinoptilolite-Like Zeolite* [4.1] - L. L. Ames, Jr.

Portions of the high-silica, zeolitic or relatively low temperature region of several base cation systems were investigated. During the study, a clinoptilolite-like phase was synthesized. The data pertinent to the synthesis of the clinoptilolite-like phase are presented.

Starting materials used in the hydrothermal syntheses included Davison Silica Gel, silicic acid, LiOh, NaOH, KOH, dried $Al(OH)_3$, and silica and alumina gels coprecipitated from mixed solutions of sodium metasilicate and sodium aluminate. The Davison Silica Gel, hereafter referred to as silica gel, was supplied for use as a drying agent in 14 to 40 mesh size. Consequently, the 14 to 40 mesh gel was ball-milled to pass through a - 325 mesh sieve before use.

The constituents were added in the desired mole ratios and thoroughly mixed in a blender. The mixed starting material was placed in a 20 ml, silver-lined, Morey-type reactor and raised to the desired temperature in a furnace. The reactor was immediately quenched in cold water upon removal from the furnace. The pH of the remaining water soluble contents was determined at 25 C. Readings higher than pH 10 were of little interest and were recorded as merely greater than 10. Insoluble final products were washed with distilled water, air-dried, and examined by X-ray diffraction and with the petrographic microscope. Table 4.1 summarizes the hydrothermal experiments used to define the conditions of formation of the clinoptilolite-like phase in the system lithia-alumina-silica-water. Three starting mixtures were used with similar results, although reaction rates were not comparable. The silica gel-dried $Al(OH)_3$-LiOH mixture was the slowest to react. Compositions containing

---

* Supported in part by the Division of Biology and Medicine

silica-to-alumina ratios as high as 18 yielded the clinoptilolite-like phase with the silica gel-dried $Al(OH)_3$-LiOH starting mixture. Note in Table 4.1 that the final pH of the water soluble contents of the reactor is generally indicative of the degree of the reaction that has occurred; i.e., if the LiOH has reacted, lithium cations are removed from the equilibrium solution and the pH is lowered.

TABLE 4.1

HYDROTHERMAL DATA

FOR THE HIGH-SILICA PORTION OF THE LITHIA-ALUMINA-SILICA WATER SYSTEM

	Composition of Starting Materials	Temperature, C	Pressure, psi	Duration, days	Final Products	Final pH, 25 C
Silica Gel, Dried $Al(OH)_3$, $LiOH \cdot H_2O$ ($SiO_2/Al_2O_3/Li_2O/H_2O$)	6/1/0.5/8.5	293	1150	3	Little crystallization	> 10
	8/1/0.6/8.5	293	1150	2	Clinoptilolite-like phase	7.6
	8/1/1/8.5	285	1000	5	Clinoptilolite-like phase	7.1
	8/1/1.5/8.5	270	800	3	Clinoptilolite-like phase	8.6
	8/1/2/8.5	254	625	3	Clinoptilolite-like phase	7.5
	8/1/3/8.5	254	625	2	"Species A" plus quartz	10.0
	10/1/1/8.5	285	1000	5	Clinoptilolite-like phase	8.7
	10/1/1/8.5	304	1350	3	Clinoptilolite-like phase	8.2
	10/1/1/8.5	357	2500	2	Some petalite	10.0
	14/1/1/8.5	298	1200	2	Little crystallization	> 10
	14/1/1.5/8.5	298	1200	2	Clinoptilolite-like phase plus quartz	8.4
	18/1/1/8.5	298	1200	2	Little crystallization	> 10
	18/1/1.5/8.5	298	1200	2	Clinoptilolite-like phase plus quartz	7.7
Ethyl Orthosilicate, Calcined Nitrates ($SiO_2/Al_2O_3/Li_2O/H_2O$)	8/1/1/8.5	295	1160	3	Clinoptilolite-like phase	7.4
Silicic Acid, Dried $Al(OH)_3$, $LiOH \cdot H_2O$ ($SiO_2/Al_2O_3/Li_2O/H_2O$)	8/1/1/8.5	300	1250	4	Clinoptilolite phase	7.5
	8/1/1/8.5	260	700	3	Little crystallization	9.0

Other experiments with various starting mixtures and compositions are listed in Table 4.2. Starting with sodium or potassium-containing systems, no clinoptilolite-like phases were synthesized. Products included mordenite, analcime, quartz, and chabazite. Figure 4.1 shows mordenite and analcime crystals synthesized from the silica gel-dried $Al(OH)_3$-LiOH starting mixture. Several hydrothermal experiments with mixed-base starting materials consisting of silica gel, dried $Al(OH)_3$, LiOH, and NaOH yielded only mordenite. The clinoptilolite-like phase was not stable in a system containing both lithium and sodium. The mordenite crystals synthesized in the above lithium and sodium-containing system exhibited an unusual growth habit of radial clusters as shown in Figure 4.2. The clinoptilolite-like phase is shown in Figure 4.3.

TABLE 4.2

HYDROTHERMAL DATA FOR THE HIGH-SILICA PORTION OF SEVERAL RELATED SYSTEMS

	Composition of Starting Materials	Temperature, C	Estimated Pressure, psi	Duration, days	Final Products	Final pH, 25 C
Coprecipitated Gels, NaOH	8/1/0.5/8.5	245	520	2	Little crystallization	> 10
$(SiO_2/Al_2O_3/Na_2O/H_2O)$	8/1/1/8.5	254	625	2	Mordenite plus analcime	8.8
	8/1/1.5/8.5	293	1150	2	Analcime	> 10
Silica Gel, Dried $Al(OH)_3$,	8/1/0.5/8.5	245	560	2	Little crystallization	> 10
NaOH $(SiO_2/Al_2O_3/Na_2O/H_2O)$	8/1/1/8.5	293	1150	2	Mordenite plus analcime	7.8
	8/1/1.5/8.5	293	1150	2	Analcime	> 10
	10/1/1/8.5	293	1150	2	Mordenite	8.5
Silica Gel, Dried $Al(OH)_3$,	10/1/0.5/0.5/8.5	295	1160	3	Little crystallization	9.5
NaOH, LiOH·H_2O	10/1/1/1/8.5	295	1160	3	Mordenite	7.7
$(SiO_2/Al_2O_3/Na_2O/Li_2O/H_2O)$						
Silica Gel, Dried $Al(OH)_3$ KOH	8/1/1/8.5	293	1150	3	Quartz plus chabazite	8.7
$(SiO_2/Al_2O_3/K_2O/H_2O)$	10/1/1/8.5	227	400	3	Little crystallization	> 10

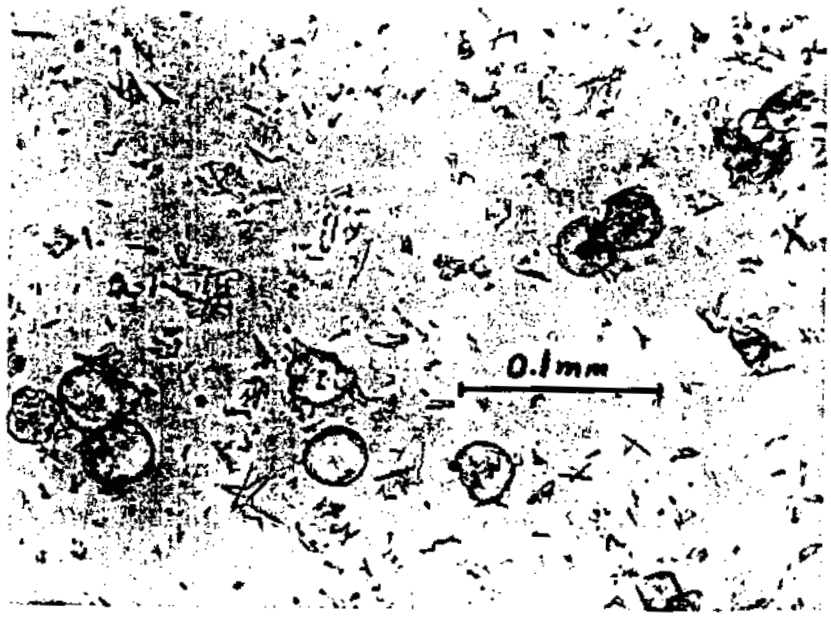

FIGURE 4.1

Mordenite (bladed crystals) and Analcime (spheroids)
(Grown from the starting composition 8 $SiO_2 \cdot Al_2O_3 \cdot Na_2O \cdot 8.5H_2O$; silica gel, dried $Al(OH)_3$, and NaOH were used as starting materials at 293 C for 2 days; final pH of the equilibrium solution was 7.8 at 25 C)

FIGURE 4.2

Mordenite in an unusual crystal habit (radiating groups)
(Grown from the starting composition $10SiO_2 \cdot Al_2O_3$. $Na_2O \cdot Li_2O \cdot 8.5H_2O$; coprecipitated alumina and silica gels, $LiOH \cdot H_2O$, and NaOH were used as starting materials at 254 C for 2 days; final pH was 8.5 at 25 C)

AEC-GE RICHLAND, WASH.

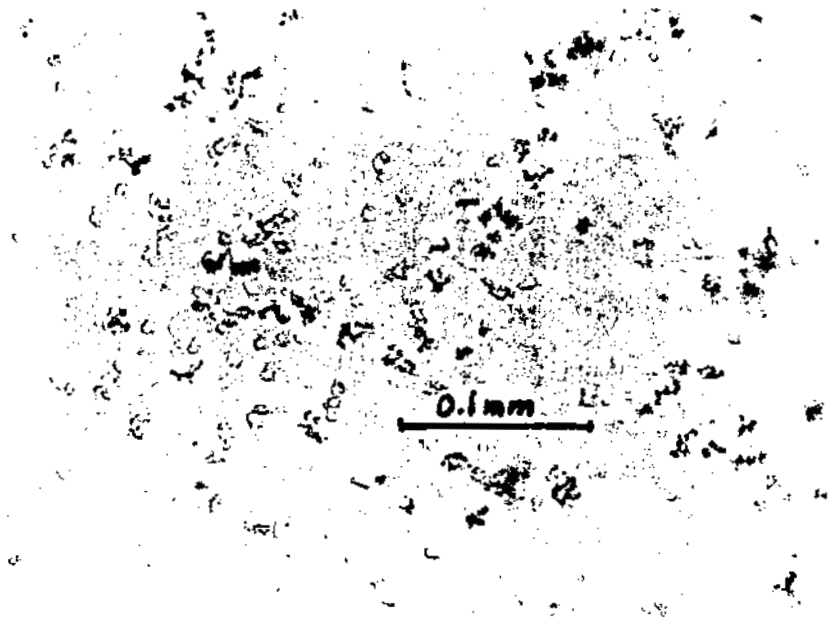

FIGURE 4.3

Synthetic, Clinoptilolite-like Phase

(Grown from the starting composition $8\,SiO_2 \cdot Al_2O_3 \cdot Li_2O \cdot 8.5H_2O$; Silica gel, dried $Al(OH)_3$, and $LiOH \cdot H_2O$ were used as starting materials at 285 C for 5 days. Final pH of the equilibrium solution was 7.1 at 25 C)

Some Zeolite Equilibria with Alkali Metal Cations* - L. L. Ames, Jr.

Cation exchange equilibria for natural zeolites (erionite, clinoptilolite, and phillipsite) and the synthetic zeolites (Linde AW-300, AW-400, AW-500, 13X, 4A and Norton Zeolon) in the systems sodium-cesium, potassium-sodium and potassium-cesium are presented along with derived thermodynamic data. Gibbs free-energies and enthalpies for the various exchange reactions were relatively small. Reaction enthalpies diminished as the sizes of the two exchanging cations approached one another. Thermodynamic data proved to be useful in several cases for interpretation of zeolite equilibria but proved to be most valuable when used in correlation with other properties of the zeolite exchange systems.

---

* Supported in part by the Division of Biology and Medicine

The clinoptilolite used in this study was obtained from two different locations: Hector, California, and John Day, Oregon. Impurities included quartz, feldspar, unaltered glass, secondary halite, and small amounts of montmorillonite and calcite (0 to 3 wt% calcite in selected material). Consequently, the Hector clinoptilolite was contacted for 1 hr with 10% HNO_3 to remove calcite and other acid-soluble contaminants before normal cation-basing procedure.

The other clinoptilolite was obtained from the Deep Creek Tuff of the John Day Formation,[4.2] Oregon. The Oregon clinoptilolite was relatively free of impurities except for minor amounts of plagioclase and unaltered glass. The average Oregon clinoptilolite purity was 95% or greater, as shown by the 2.0 meq/g capacity in Table 4.3. Part of the Oregon clinoptilolite was contacted with 10% HNO_3 to determine the effect of acid treatment on cation exchange properties.

TABLE 4.3

ZEOLITE PROPERTIES

Zeolite	SiO_2:Al_2O_3	Wt% Binder	Wt% H_2O 25 C	Structural Type	Capacity meq/g
Hector Clinoptilolite	8-10	5-15	12	Clinoptilolite	1.7
Oregon Clinoptilolite	8-10	5	11	Clinoptilolite	2.0
Nevada Erionite	6	5-10	13	Erionite	2.2
Nevada Phillipsite	4	5-15	14	Phillipsite (Monoclinic)	2.3
4AXW	2	10	30	A	3.9
13X	2.4	20	25	Faujasite	3.9
AW-300	9-10	25	9	Mordenite	1.6
AW-400	6-7	25	12	Erionite	2.0
AW-500	4-5	25	15	Chabazite	2.2
Zeolon	10	--	12	Mordenite	1.9

The erionite and phillipsite used in this study were from Pine Valley, Nevada, and averaged 90% or greater in purity.

Several synthetic zeolites were obtained as 1/16 in. diameter, sodium-based pellets from the Linde Company of Tonawanda, New York. Included were 13X, 4AXW, AW-300, AW-400, and AW-500. The Norton Company of Worcester, Massachusetts, supplied 1/8 in., sodium-based Zeolon pellets. Table 4.3 gives some of the pertinent properties of the zeolites used in this study.

Zeolites used in the equilibrium experiments were based with saturated, reagent-grade chloride solutions of the desired cations. Zeolites already based with sodium were rebased with NaCl solution in several contacting steps (Ames, 1963). The zeolites were thoroughly washed with distilled water which was tested for chloride ion with $AgNO_3$ solution. A final test for chloride ion was conducted on the distilled water after 2 days of contact with the zeolite. A negative chloride test was indicative of minimum NaCl inclusion.

Cation exchange capacities were determined by a double tracing technique. Weighed, sodium-based zeolite samples in polyethylene bottles were contacted with a solution containing 0.1N CsCl plus 0.1N NaCl plus Cs^{134} tracer to determine cesium removal. Cesium-based zeolites, corrected for the sodium-cesium weight differential, were then contacted with a solution containing 0.1N CsCl plus 0.1N NaCl plus Na^{22} to determine sodium removal onto the same zeolites. Total zeolite capacity pertinent to the study of cesium, sodium, or potassium equilibrium systems was assumed to be the sum of cesium plus sodium loading. A higher capacity could have been obtained in some instances if capacities were determined with smaller size or different valence cations.(4.3)

At least 2 days of contact in a controlled-temperature shaking bath were allowed to assure equilibrium between zeolite and solution. High specific activity Na^{22} and Cs^{134} were used to trace the equilibrium solution. Solution-

to-zeolite ratios were adjusted to yield statistically reliable Cs^{134} and Na^{22} counting rates in the equilibriun solution. Zeolites were originally based with the untraced cation in the system. For example, in the system potassium-sodium-Na^{22}, the zeolites were originally potassium-based.

The amount of traced cation removed from the equilibrium solution was assumed to represent the amount of traced cation on the zeolite. Eight to twelve points were determined on each isotherm by varying the ratios of contacting cations. The equilibrium solution was held constant at 1N. Errors introduced by zeolitic salt inclusion probably were less than 1%.[4.4] A determination of equilibrium relationships in the sodium-cesium system at a total solution normality of 0.1 resulted in essentially the same equilibria after solution activity corrections, confirming that salt inclusion was not a major problem.

Because the equilibrium solution was 1N, it was necessary to determine mean activities of the two salts. Only the ratios of cations were varied so that Glueckauf's equation[4.5] could be used to determine mean activities. Figure 4.4 is a graph of the mean activity coefficients of NaCl, KCl, and CsCl used in this study. Note that concentration is expressed in molality rather than normality. An error of between 2 and 3% was introduced in the worst possible case at a molality of one-for-one of the salts (CsCl) by direct application of molal activity coefficients. Consequently, the molal activity coefficients were directly applied to equilibrium solution concentrations. The use of mean activity coefficients to correct equilibrium solution cation concentrations is a first step in the determination of a rational thermodynamic equilibrium constant for the reaction. It is also necessary to determine activity coefficients for the cations on the zeolite.[4.6] For example, given the reaction for the zeolite phillipsite for which the equilibrium data are shown in Figure 4.5, $K_{zeolite} + Na_{solution} \rightarrow Na_{zeolite} + K_{solution}$, the mass action quotient uncorrected for solution activities is $(Na_z)(K_s)/(K_z)(Na_s)$. The fraction of potassium on the zeolite (K_z) is equal to one minus the fraction of

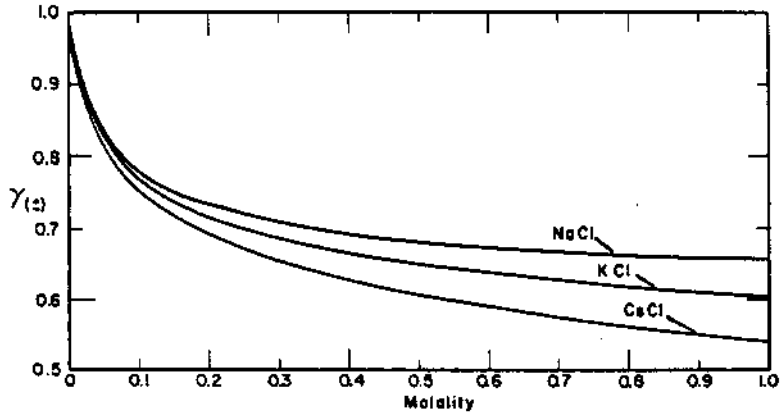

FIGURE 4.4

Mean Activity Coefficients
for NaCl, KCl and CsCl up to 1 Molal in Concentration

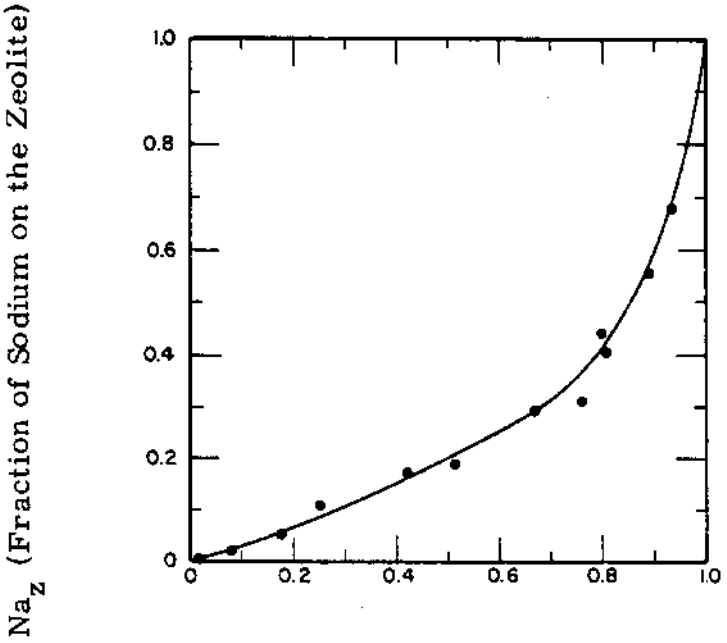

FIGURE 4.5

25 C Isotherm for the Reaction $K_z + Na_s \rightarrow Na_z + K_s$ with Monoclinic Phillipsite (Total equilibrium solution normality was constant at one)

Na_z = fraction of sodium on the zeolite
Na_s = fraction of sodium in the equilibrium solution

ARC-GE RICHLAND, WASH.

sodium on the zeolite (Na_z). The normality of potassium in the equilibrium solution (K_s) equals one minus the normality of sodium in the equilibrium (Na_s), because the total normality of the equilibrium solution is a constant one.

Figure 4.6 is a graph of sodium and potassium activity coefficients on the zeolite computed from Figure 4.5. The activity coefficients may be used to compute an average rational thermodynamic equilibrium constant, K.. The zeolite was treated as a solid solution of sodium-zeolite and potassium-zeolite; and the monoionic end-members, pure sodium-zeolite and potassium-zeolite, were assumed to have activity coefficients equal to unity.

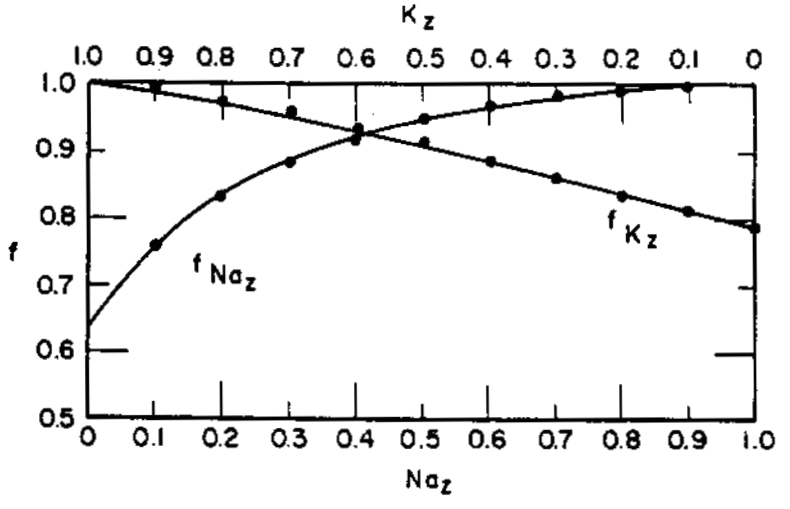

FIGURE 4.6

Activities of Sodium on the Zeolite (f_{Na_z}) and Potassium on the Zeolite (f_{K_z}) versus Sodium on the Zeolite (Na_z) and Potassium on the Zeolite (K_z) for Phillipsite

The equilibrium constant data are summarized on Table 4.4. The exchange reaction is identified along with the temperature. Table 4.5 gives the derived thermodynamic data.

TABLE 4.4

ZEOLITE EQUILIBRIUM DATA

(The notation $K_z \rightarrow Cs_z$ means the exchange of potassium on the zeolite to cesium on the zeolite, $K_z \rightarrow Na_z$ means the exchange of potassium on the zeolite to sodium on the zeolite, and $Na_z \rightarrow Cs_z$ means the exchange of sodium on the zeolite to cesium on the zeolite.)

	Thermodynamic Equilibrium Constant, K				
Zeolite	$K_z \rightarrow Cs_z$, 25 C	$K_z \rightarrow Na_z$, 25 C	$Na_z \rightarrow Cs_z$, 25 C	$K_z \rightarrow Cs_z$, 70 C	$Na_z \rightarrow Cs_z$, 70 C
13X	0.235	0.674	0.355	--	0.374
4AXW	0.236	0.747	0.323	--	0.346
AW-300	0.566	0.050	1.814	--	2.78
AW-400	3.20	0.083	39.0	--	20.8
AW-500	4.45	0.138	29.7	4.45	13.3
Zeolon	4.57	0.143	29.2	4.09	18.3
Erionite	--	0.091	32.9	--	17.5
Phillipsite	5.29	0.191	26.4	5.02	13.3
Hector Clinoptilolite	3.68	0.079	51.9	--	18.9
Oregon Clinoptilolite	--	--	47.6	--	24.8

TABLE 4.5

ZEOLITE THERMODYNAMIC DATA

(ΔG° is the standard Gibbs Free-Energy in cal/mole. ΔH° is the standard reaction enthalpy in cal/mole. The reactions are identified as in Table 4.4)

	$Na_z \rightarrow Cs_z$	$Na_z \rightarrow Cs_z$	$K_z \rightarrow Cs_z$	$K_z \rightarrow Cs_z$	$K_z \rightarrow Na_z$
Zeolite	ΔH°, 25 C, 70 C	ΔG°, 25 C	ΔH°, 25 C, 70 C	ΔG°, 25 C	ΔG°, 25 C
13X	+ 200	+ 600	--	+ 900	+ 200
4AXW	+ 300	+ 700	--	+ 800	+ 200
AW-300	--	--	--	--	+ 1800
AW-400	- 2800	- 2200	--	- 700	+ 1500
AW-500	- 3600	- 2000	0	- 900	+ 1200
Zeolon	- 2100	- 2000	- 500	- 900	+ 1100
Erionite	- 2800	- 2100	--	--	+ 1400
Phillipsite	- 3100	- 1900	- 200	- 1000	+ 1000
Hector Clinoptilolite	- 4600	- 2300	--	- 800	+ 1500
Oregon Clinoptilolite	- 2900	- 2300	--	-	--

Kinetics of a Replacement Reaction - L. L. Ames, Jr.

The kinetics of the replacement type of chemical reaction were studied in a "shallow bed" apparatus. A proposed kinetic model agreed quite well with the experimental kinetic results. Replacement type reactions are apparently diffusion controlled. The replacement of gypsum to form barite by a $BaCl_2$-bearing solution, or the reaction $CaSO_4 \cdot 2H_2O + BaCl_2 \rightarrow BaSO_4 + CaCl_2 + 2H_2O$ was chosen for study as typical of the replacement type reaction taking place in the soil.

An idealized model of the various processes during the alteration of a spherical particle of gypsum crystal to barite by $BaCl_2$ solution is shown in Figure 4.7. The gypsum is soluble to some extent in the altering solution and contributes Ca^{2+} and SO_4^{2-} ions. Ba^{2+} and Cl^- ions diffuse into the gypsum-barite interfacial area between the forward-growing barite crystals. The Ba^{2+} and SO_4^{2-} in solution exceed the activity product for barite at the ends of the growing barite crystals and barite is precipitated. The Ca^{2+} ions diffuse through the solution between the barite crystals and out into the contacting solution. Electrostatic neutrality is maintained during Ca^{2+} diffusion by Cl^- ions.

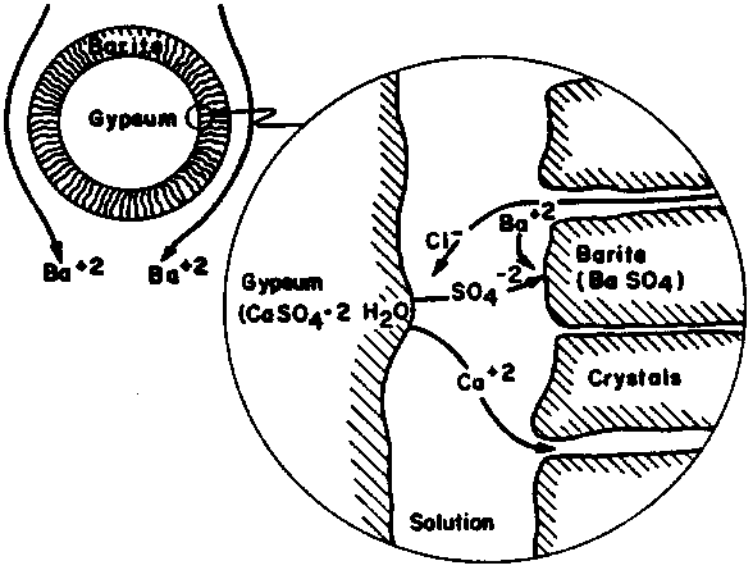

FIGURE 4.7
An Idealized Model for the Replacement of Gypsum by Barite

Thus the replacement reaction essentially consists of a very rapid, "irreversible" chemical reaction that is diffusion controlled, assuming that the model for the reaction is correct. An interface moves through the gypsum particle, separating a region consisting of all $BaSO_4$ from a region consisting of all $CaSO_4 \cdot 2H_2O$. A search of the literature showed that Crank[4.7] has solved this type of problem with a "steady-state approximation." If the gypsum particle is spherical and immersed in a $BaCl_2$ solution of constant composition, then

$$\frac{Dt}{a^2} = \frac{S}{6C_B}\left[1 - 3(r_o/a)^2 + 2(r_o/a)^3\right], \qquad (1)$$

where D = a Ba^{2+} diffusion coefficient in cm^2/sec

t = time since diffusion began in sec

a = the gypsum sphere radius in cm

S = the number of Ca^{2+} sites per unit volume of gypsum in meq/cm^3

C_B = the number of Ba^{2+} cations per unit volume of solution in meq/cm^3

r_o = the radius of the remaining sphere of gypsum after reaction time t.

The apparatus shown in Figure 4.8 was used to determine D in Equation (1) and to obtain the actual kinetics of replacement of gypsum by barite. The gypsum sample was kept in a $BaCl_2$ solution of constant composition by assuring that the Ba^{133} tracer count was the same before and after contacting the sample. As the Ba^{133} tracer count slowly increased on the altering gypsum bed, the bed activity was continuously monitored and recorded. The resulting recording was a smooth curve, except for 2 to 5% background fluctuation that eventually leveled off, indicating complete replacement of gypsum by barite. Many gypsum spheres (100 mg) were used to attain a reasonable Ba^{133} counting rate.

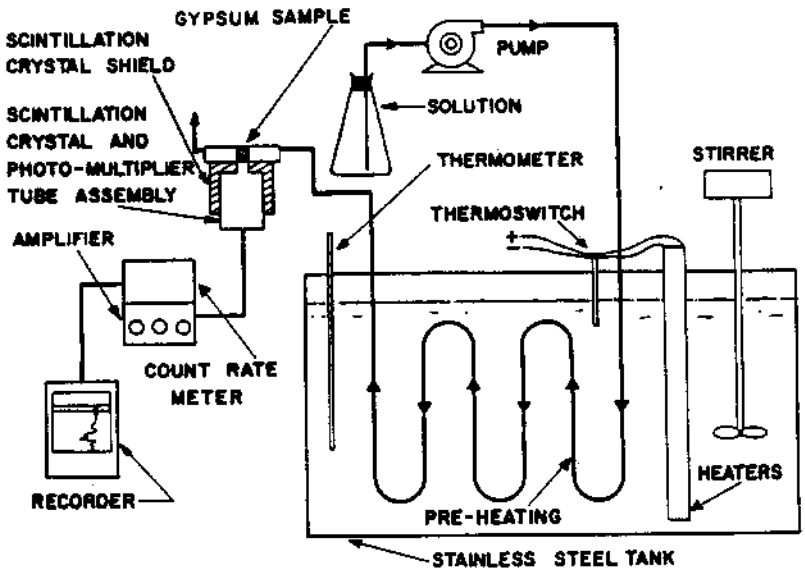

FIGURE 4.8

Experimental Apparatus Used to Obtain the Kinetics of the Replacement of Gypsum by Barite and the Time Required for Complete Replacement of Gypsum by Barite

Figure 4.9 shows the rate of replacement of 0.70 to 1.00 mm gypsum spheres by barite. The experimental replacement rate is initially faster than the model, perhaps because the crushing necessary to produce the gypsum spheres leads to fracturing and increased gypsum surface area. In any case, the agreement between experimental and model curves is good. It is assumed, therefore, that the model is essentially correct.

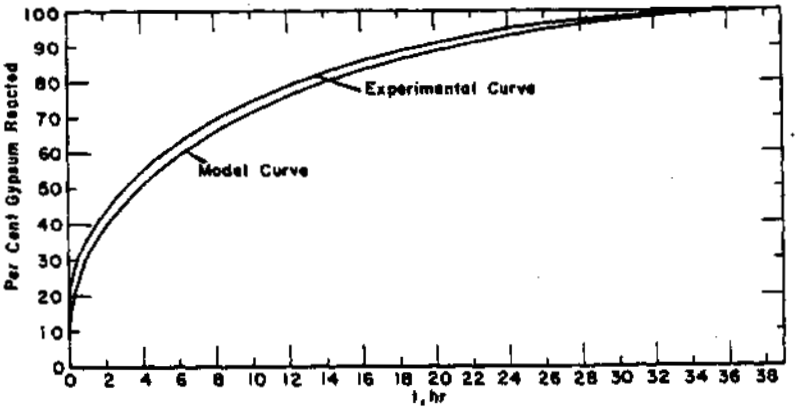

FIGURE 4.9

Experimental and Model Kinetics
for the Replacement of Gypsum by Barite

(Bed, 100 mg of 0.70 to 1.00 mm gypsum; D, 1.5×10^{-6} cm^2/sec temperature, 35 C; solution, 0.01M $BaCl_2$; a, 0.0425 cm; 13.47 meq Ca^{2+}/cm^3 of gypsum; total t, 140,000 sec (38.9 hr); C_B, 0.02 meq Ba^{2+}/cm^3)

Some Zeolite Equilibria with Alkaline Earth Metal Cations - L. L. Ames, Jr.

Isotherms for the zeolites Linde Type A, natural erionite, phillipsite, and clinoptilolite in the systems sodium-strontium, sodium-calcium, and strontium-calcium are presented. Thermodynamic data derived from the above isotherms indicated that reaction enthalpies are very small from 25 C to 70 C. An inverse relationship was noted between SiO_2/Al_2O_3 ratios and divalent cation selectivities. The above data plotted as log Kc versus cation B on the zeolite were adequately described by Barrer and Meier's case where $\frac{d\log Kc}{dB_z}$ does not equal a constant.

The clinoptilolite used in this study was obtained from Hector, California, and averaged 80 to 90% clinoptilolite. Impurities included quartz, feldspar, unaltered glass, secondary halite, and small amounts of montmorillonite and calcite (0 to 3% calcite). The Hector clinoptilolite was

pretreated by contacting for 1 hr with 10% by volume HNO_3 to remove calcite and acid-soluble contaminants before normal cation-basing procedure.

The erionite and phillipsite used in this study were from Pine Valley, Nevada, and averaged 90% or greater in purity as estimated from thin-section examinations and X-ray diffraction patterns. The erionite and phillipsite were not, of course, acid treated.

Several synthetic zeolites were obtained as 1/16 in. diameter, sodium-based pellets from the Linde Company of Tonawanda, New York. Included were 4AXW (Type A), 13X, AW-400, and AW-500. The Norton Company of Worcester, Massachusetts, supplied 1/8 in. sodium-based Zeolon pellets. Table 4.6 gives some of the pertinent properties of the zeolites used in this study.

TABLE 4.6

ZEOLITE PROPERTIES

Zeolite	SiO_2:Al_2O_3	Wt% Binder	Wt% H_2O, 25 C	Structural Type	Capacity, meq/g
Hector Clinoptilolite	8-10	5-15	12	Clinoptilolite	1.7
Nevada Erionite	6	5-10	13	Erionite	2.2
Nevada Phillipsite	4	5-15	14	Phillipsite (Monoclinic)	2.3
4AXW	2	10	30	A	3.9
13X	2.4	20	25	Faujasite	3.6
AW-400	6-7	25	12	Erionite	2.0
AW-500	4-5	25	15	Chabazite	2.2
Zeolon	10	--	12	Mordenite	1.9

Zeolites used in the equilibrium experiments were based with saturated, reagent-grade chloride solutions of the desired cations. Zeolites already based with sodium were rebased with NaCl solution in several contacting steps. $SrCl_2$ and $CaCl_2$ solutions were used to base the zeolites when required. The zeolites

were thoroughly washed with distilled water which was tested for chloride ion with $AgNO_3$ solution. A final test for chloride ion was conducted on the distilled water after 2 days of contact with the zeolite.

Cation exchange capacities were originally determined by a double tracing technique.[4.8] Weighed, sodium-based zeolite samples in polyethylene bottles were contacted with a solution containing 0.1N CsCl plus 0.1N NaCl plus Cs^{134} tracer to determine cesium removal. Cesium-based zeolites, corrected for the sodium-cesium weight differential, were then contacted with a solution containing 0.1N CsCl plus 0.1N NaCl plus Na^{22} to determine sodium removal onto the same zeolites. By tracing the sodium-strontium exchange reaction from both directions ($2Na^{22}_{solution} + Sr_{zeolite} \rightleftharpoons 2Na^{22}_{zeolite} + Sr_{solution}$ and $Sr^{85}_{solution} + 2NA_{zeolite} \rightleftharpoons Sr^{85}_{zeolite} + 2Na_{solution}$), it was shown that the above capacity determinations, using sodium and cesium, also were valid for the sodium-strontium reactions, and that equilibrium was attained. The thirteenth anionic site of Type A[4.4] was ignored because no exchange could be expected on the above site by divalent cations.

At least 2 days of contact time in an oscillating, controlled-temperature bath were allowed to assure equilibrium between zeolite and solution. High specific activity Na^{22} and Sr^{85} were used to trace the equilibrium solution. Solution-to-zeolite ratios were adjusted to yield statistically reliable Sr^{85} and Na^{22} counting rates in the equilibrium solution. Zeolites originally were based with the untraced cation in the system. For example, in the system calcium-sodium-Na^{22}, the zeolites were originally calcium-based. The amount of traced cation removed from the equilibrium solution was assumed to represent the amount of traced cation on the zeolite. Eight to twelve points were determined on each isotherm by varying the ratios of contacting cations. The equilibrium solution was held at a constant given total normality. A determination of equilibrium relationships in the sodium-strontium system at a total solution normality of 0.1 and 1.0 resulted in essentially the same mass action relationships, confirming that salt inclusion was not a major problem.

Figure 4.10 shows the mean activity coefficients of NaCl, $CaCl_2$, and $SrCl_2$ used in this study. Concentration is expressed in normality rather than molality. An acceptably-small error was introduced by direct application of molal activity coefficients.[4.5]

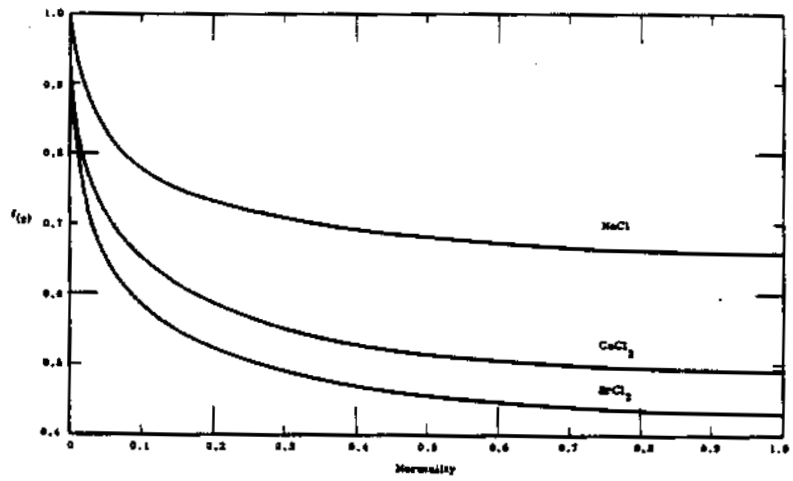

FIGURE 4.10
Mean Activity Coefficients Used in the Computations of This Paper

The use of mean activity coefficients to correct equilibrium solution cation concentrations is a second step in the determination of a rational thermodynamic equilibrium constant for the reaction. For example, given the exchange reaction, $2Na_{zeolite} + Sr_{solution} \rightleftharpoons Sr_{zeolite} + 2Na_{solution}$, the uncorrected mass action quotient is

$$\frac{(Sr_{zeolite})(Na_{solution})^2}{(Na_{zeolite})^2(Sr_{solution})}, \text{ or } \frac{(Sr_z)(Na_s)^2}{(Na_z)^2(Sr_s)}, \text{ and } K_c = \frac{(Sr_z)(Na_s)^2\ (^fNa_s)^2}{(Na_z)^2(Sr_s)\ (^fSr_s)}.$$

The general equation for the initial calculation from a given isotherm was

$$\text{Mass action quotient} = \frac{(A_z)^{n}A(B_N)^{nB}}{(B_z)^{n}B(A_N)^{n}A} \quad \text{where,}$$

A_N, B_N = concentration of cations A and B in equivalents per liter

A_z, B_z = equivalent fractions of cation A and B on the zeolite

n_A, n_B = the number of cations of A and B represented in the chemical equation for the exchange reaction of A and B.

Because the cation concentrations in the equilibrium solution were relatively high, it was necessary to determine mean activities of the two cations. Salts with a common anion were used so that a simplified Glueckauf's equation[4.5] could be employed to determine activity ratios in the mixed cation solutions. To show how Glueckauf's equation was used to compute activities in mixed solutions, the example of sodium-strontium will suffice.

Let us assume that $X_1 = Na^+$, $X_2 = Sr^{2+}$, and $Y = Cl^-$, a common anion. By definition, the mean activity coefficient is described by

$$f_{\pm} = \left(f^{+\,v^+} \cdot f^{-\,v^-}\right) \frac{1}{(v^+) + (v^-)}$$

where v^+ is the number of cations and v^- is the number of anions.

So $f^{X_1Y} = (fX_1 \cdot fY)^{1/2} = f\begin{pmatrix}X_1Y\\X_2Y\end{pmatrix}$ and $f^{X_2Y} = (fX_2 \cdot fY^2)^{1/3} = f\begin{pmatrix}X_2Y\\X_1Y\end{pmatrix}$.

Consolidating,

$$\frac{f\begin{pmatrix}X_1Y\\X_2Y\end{pmatrix}}{f\begin{pmatrix}X_2Y\\X_1Y\end{pmatrix}} = \frac{(fX_1 \cdot fY)^{1/2}}{(fX_2 \cdot fY^2)^{1/3}}, \text{ or } \frac{fX_1^{\,2}}{fX_2} = \frac{\left[f\begin{matrix}X_1Y\\X_2Y\end{matrix}\right]^4}{\left[f\begin{matrix}X_2Y\\X_1Y\end{matrix}\right]^3} \quad . \qquad (1)$$

Glueckauf's equation for two salts with a common anion is

$$\log_{10} f\begin{pmatrix} X_1Y \\ X_2Y \end{pmatrix} = \log_{10} f^{X_1Y} - \frac{X_2}{4I}\left(K_1 \log_{10} f^{X_1Y} - K_2 \log_{10} f^{X_2Y} - \frac{K_3}{(1+I^{-1/2})}\right) \quad (2)$$

where $f\begin{pmatrix} X_1Y \\ X_2Y \end{pmatrix}$ = a mean activity coefficient of NaCl in the presence of $SrCl_2$

$f\begin{pmatrix} X_2Y \\ X_1Y \end{pmatrix}$ = a mean activity coefficient of $SrCl_2$ in the presence of NaCl

f^{X_1Y} = a mean activity coefficient of NaCl

f^{X_2Y} = a mean activity coefficient of $SrCl_2$

I = the total ionic strength

X_1 = moles per liter of Na

X_2 = moles per liter of Sr

K_1 = $x_2(2X_2 - x_1 + y)$

K_2 = $x_1(x_2 + y)^2(x_1 + y)^{-1}$

K_3 = $1/2\, x_1 x_2 y(x_1 - x_2)^2(x_1 + y)^{-1}$ with

x_1 = the ionic charge of Na or 1,

x_2 = the ionic charge of Sr or 2, and

y = the ionic charge of Cl or 1.

Substituting Equation (1) into (2) we obtain

$$4 \log_{10} f\begin{pmatrix} X_1Y \\ X_2Y \end{pmatrix} - 3 \log_{10} f\begin{pmatrix} X_2Y \\ X_1Y \end{pmatrix}$$

$$= 4 \log_{10} f^{X_1Y} - \frac{4X_2}{4I}\left(K_1 \log_{10} f^{X_1Y} - K_2 \log_{10} f^{X_2Y} - \frac{K_3}{1+I^{-1/2}}\right)$$

$$- 3 \log_{10} f^{X_2Y} - \frac{3X_1}{4I}\left(K_1' \log_{10} f^{X_2Y} - K_2' \log_{10} f^{X_1Y} - \frac{K_3'}{1+I^{1/2}}\right)$$

with $K_1 = 8$, $K_2 = 9/2$, $K_3 = 1/2$, $K_1' = 1$, $K_2' = 8/3$, $K_3' = 1/3$ and $I = X_1 + 3X_2$.

Consolidating,

$$\frac{fX_1^2}{fX_2} = \left(4 - \frac{8X_2}{I} - \frac{2X_1}{I}\right)\log_{10} {}^{f}X_1 Y - \left(3 - \frac{9/2X_2}{I} - \frac{3/4X_1}{I}\right)\log_{10} {}^{f}X_2 Y - \frac{1/4X_1 - 1/2X_2}{I(1 + I^{-1/2})}.$$

Letting $r = X_1/X_2$, we obtain

$$\frac{fX_1^2}{fX_2} = \frac{r + 2}{r + 3}\left(2 \log_{10} {}^{f}X_1 Y - 9/4 \log_{10} {}^{f}X_2 Y\right) - \frac{1/4\,(r - 2)}{I(1 + I^{-1/2})}\,(X_2). \qquad (3)$$

The thermodynamic data derived from the experimental isotherms are given in Table 4.7. Computed Na-Sr results were obtained by multiplying the $2Na_z \rightarrow Ca_zK$ by the $Ca_z \rightarrow Sr_zK$. All other K values were derived from experimental data. Agreement between experimental and computed K values is good.

TABLE 4.7

THERMODYNAMIC DATA

(K is a rational thermodynamic equilibrium constant and ΔG^o is a standard Gibbs Free-Energy expressed to the nearest 100 cal/mole.)

	K				ΔG^o		
				Computed			
Zeolite	$2Na_z \rightarrow Ca_z$	$Ca_z \rightarrow Sr_z$	$2Na_z \rightarrow Sr_z$	$2Na_z \rightarrow Sr_z$	$2Na_z \rightarrow Ca_z$	$Ca_z \rightarrow Sr_z$	$2Na_z \rightarrow Sr_z$
4AXW	17.0	5.31	83.2	90.3	- 1700	- 1000	- 2600
13X	5.13	3.16	19.9	16.2	- 1000	- 700	- 1800
AW-400	0.708	0.603	0.363	0.427	+ 200	+ 300	+ 600
AW-500	0.724	0.371	0.288	0.269	+ 200	+ 600	+ 700
Zeolon	0.691	0.316	0.235	0.218	+ 200	+ 700	+ 900
Clinoptilolite	0.851	1.12	1.29	0.953	+ 100	- 100	- 100
Phillipsite	0.163	0.588	0.107	0.096	+ 1100	+ 300	+ 1300
Erionite	1.05	0.758	0.794	0.796	0	+ 200	+ 100

Barrer and Meier [4.3] have proposed three cases of $\frac{d \log Kc}{dB_z}$, where Bz is the fraction of cation B on the zeolite in the exchange reaction, $A_z + B_s \rightleftharpoons B_z + A_s$. The condition of $\frac{d \log Kc}{dB_z}$ may be assessed from a plot of B_z versus log Kc. If $\frac{d \log Kc}{dB_z} = 0$, Curve Type 1 of Figure 4.11 is typical, and K = Kc. If $\frac{d \log Kc}{dB_z}$ is constant but not zero, Curve Type 2 is representative, and $\log K = 1/2(\log Kc_1 + \log Kc_0) = \log Kc + C(1 - 2B_z)$, where Kc_1 is the value of Kc when $B_z = 1.0$, Kc_0 is the value of Kc when $B_z = 0$, and C = a constant. If $\frac{d \log Kc}{dB_z}$ is not constant, Curve Type 3 of Figure 4.11 may result, and $\log K = \log Kc - \int_{Kc_0}^{Kc_1} B_z \, d \log Kc$.

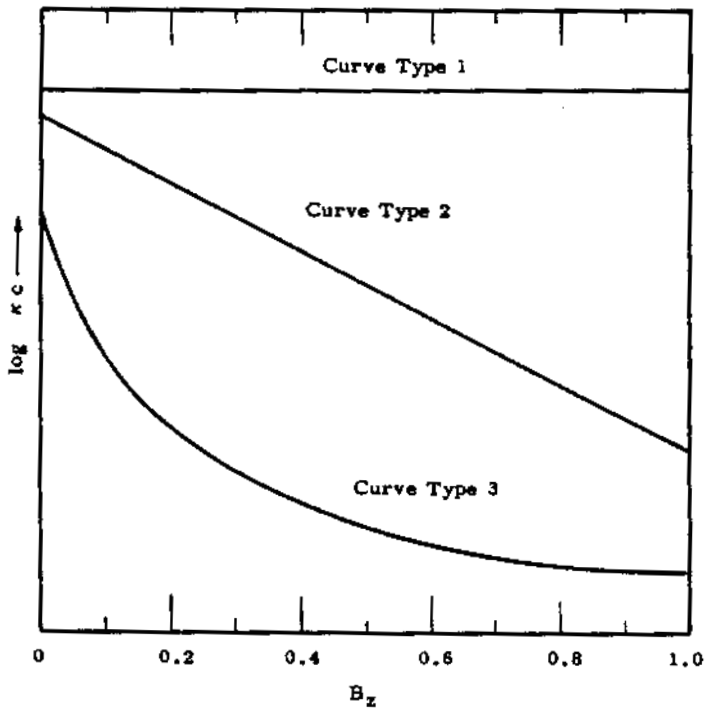

FIGURE 4.11

Some Typical Curves that may Result When log Kc is Plotted Versus Fraction of Cation B on the Zeolite (B_z)

None of the plots of log Kc versus B_z obtained during the present study yielded constant or zero values for $\frac{d \log Kc}{dB_z}$, with few exceptions. The thermodynamic equilibrium constants obtained from the isotherms given in this paper are listed in Table 4.8.

TABLE 4.8

A Comparison of the K Obtained from Barrer and Meier's Equation, $\log K = \log Kc_1 - \int_{Kc_0}^{Kc} B_z \, d\log Kc$, and an Average log K Obtained by Determining f_{B_z} and f_{A_z} Values at Several Points on the log Kc Versus B_z Curve (Log values are rounded to three places.)

Zeolite	$\int_{Kc_0}^{Kc_1} B_z \, d\log Kc$	Log Kc_1	Barrer's Log K	Average log K
		Na - Sr		
Clinoptilolite	- 0.809	- 0.720	+ 0.089	+ 0.110
Phillipsite	- 0.291	- 1.250	- 0.959	- 0.960
Erionite	- 0.777	- 0.880	- 0.103	- 0.100
		Ca - Sr		
Clinoptilolite	- 0.429	- 0.309	+ 0.039	+ 0.049
Phillipsite	C = - 0.690			
Erionite	C = - 0.567			
		Ca - Na		
Clinoptilolite	- 0.892	- 0.995	- 0.103	- 0.089
Phillipsite	- 0.405	- 1.186	- 0.781	- 0.788
Erionite	- 0.821	- 0.810	+ 0.011	+ 0.021

Soil Physics

Electrical Analog Simulation of the Hanford Ground-Water Flow System - J. R. Raymond

Equipment, techniques, and methods were tested to evaluate the feasibility of ground-water flow simulation by a large electrical analog model. Resistance test networks were constructed to evaluate assembly methods, components, and theoretical considerations and to compare analog digital techniques. Operational experience with the test models allowed evaluation of cost, component applicability, and assembly time involved in constructing a full scale project analog. Although design and construction of a large (10,000 to 14,000 node) project analog is feasible, numerical solution of the ground-water flow system by digital computer techniques appears more flexible and less costly.

A practical way to evaluate complex flow systems is by electrical analog simulation. Such methods, which utilize the similarity between saturated ground water flow and electrical current flow, are capable of simulating extreme complexities in both geometrical shape and conductance variation. Soil permeability is analogous to electrical conductivity and the fluid potential is a driving force equivalent to voltage in the electrical system. The electrical system that is the most convenient analog for general use consists of a resistor network with representative voltages applied at the various boundaries. Each network resistor represents the reciprocal permeability of the discrete soil volume occupying that position. The voltage at each resistor junction corresponds to the hydraulic head at that point in the soil.

Two test analog networks were constructed: 662 node, three-dimensional net with three rectangularly connected grid sizes; and an 81 node, three-dimensional, single grid size net. Numerical (digital computer) solutions for node voltages were obtained for comparison purposes. The large analog was fabricated to evaluate construction costs, assembly methods and techniques, hardware, and components. Information was also desired on electrical noise problems and accuracy and precision of analog simulation. The smaller model was designed to delineate mesh coupling errors encountered in the large model

and to evaluate errors associated with simulating a continuum with a discrete network.

One percent tolerance, 1/2 w precision, metal-film resistors were used in the networks. Values ranged from 10 kilohms to 787 kilohms. The resistors were in 20-hole taper-pin blocks (10 pins on a side with 8 common and 2 common), with each block representing a network node. The taper pin blocks were mounted on a steel frame by rods that passed through holes in each end of the blocks. Figure 4.12 shows block and resistor configuration of a portion of the network. The taper pin technique provided reliable, removable terminals.

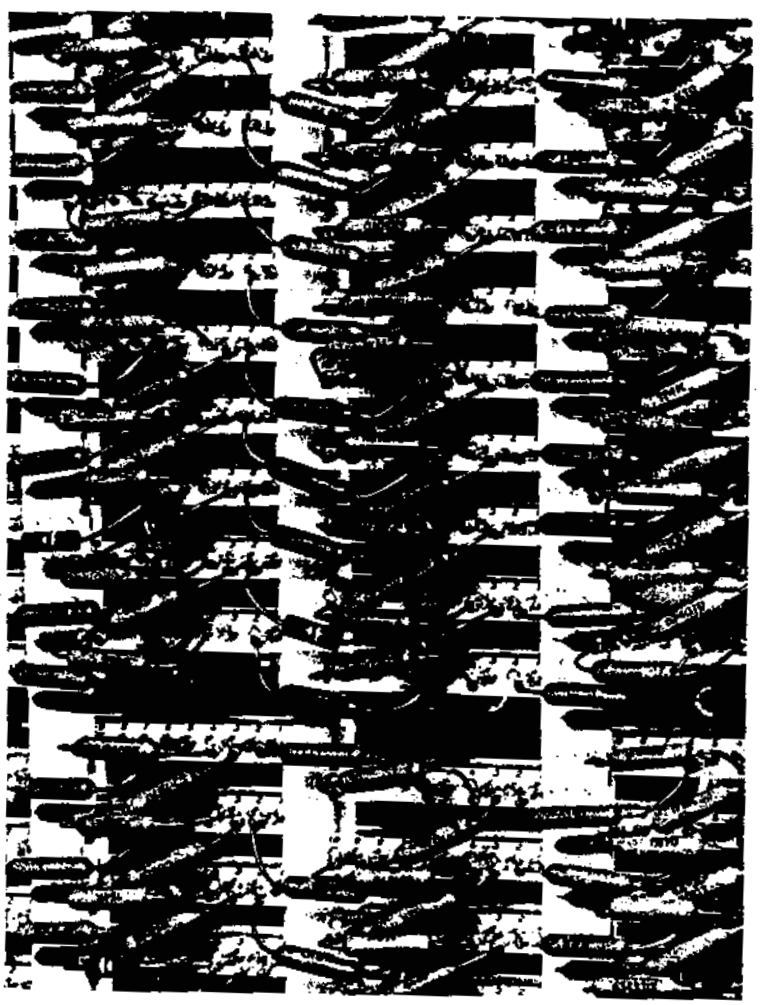

FIGURE 4.12
Taper Pin Blocks and Resistor Configuration

Node voltage readout equipment consisted of a digital voltmeter, 600-point crossbar scanner, digital printer, paper tape punch, and a storage and control unit. The system has the capability of reading voltage, voltage ratio, or resistance. Logging rate was three nodes per second. A precision constant voltage power supply was used to supply potential to the network. Figure 4.13 shows the readout equipment and the 662-node analog.

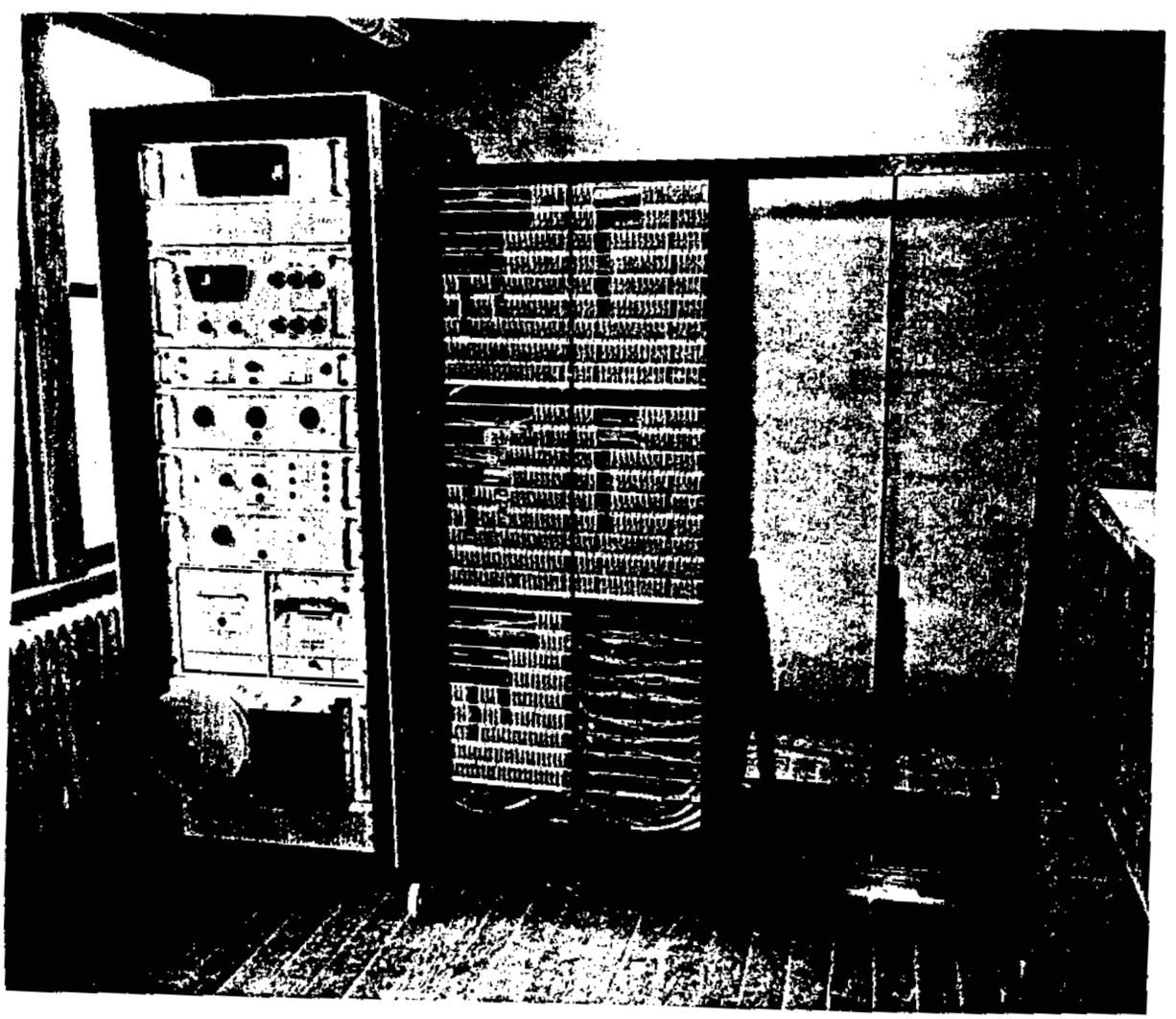

FIGURE 4.13
662-Node, Test Model Resistance Analog and Readout System

Network assembly was fairly straightforward though time consuming. Scanning and readout equipment functioned satisfactorily and all components appeared reliable and trouble free. However, use of smaller resistance grids adjacent to certain boundaries was desired to give increased detail and accuracy. Maximum potential errors of about 10% occurred at boundaries where different size resistance grids were rectangularly coupled. These errors can be reduced or eliminated by more sophisticated coupling methods (tetragonal coupling, etc.), but the network design and construction problems encountered with such techniques probably preclude their use in very large networks. Therefore, a single, compromise grid size should be selected to simplify the network. Voltage errors attributable to resistor variation and continuum simulation by a discrete network are negligible (on the order of 0.03%). An ac noise pickup, an expected problem with large networks, was about 5 mv peak to peak. This small alternating voltage presents no problem due to the large rejection capabilities of the readout system.

Node readout to scanner connections were made through seven 100-conductor cables and connectors. Cable connection makeup took too much time. Considering makeup time and the high cost of 100 conductor plugs and receptacles, hard wiring of node readout wires directly into the scanner is recommended.

The cost of the 662 node network, including components, readout system and construction time, was approximately $28,000 with the readout system accounting for $23,500. A 10,000 node expandable analog and associated readout and auxiliary equipment would cost about $100,000, based on test analog extrapolation. Flow system solution by digital computer methods is expected to provide the same information at less cost and with greater flexibility.

A Practicable Method for Measuring Fluid Potentials and Monitoring Ground Water Contamination in Various Aquifers - D. J. Brown

A Hanford-developed computer program was used to relate hydraulic potential distributions in sand-filled wells with those in wells which have cemented sections. The results showed that wells filled with sand yield measurements which more nearly duplicate the actual conditions in the field. Piezometer tubes installed in deep wells by the sand-pack method provide reliable structures for obtaining representative samples of the ground water with depth and for obtaining measurements of the ground water distribution in the various aquifers.

Over 400 cased, 8 in. wells have been drilled on the Hanford Project. Many of these wells penetrate aquifers having different hydraulic potentials. Some of the wells tap aquifers of sufficient head difference to create flow patterns which may result in erroneous or incomplete information on the status of contamination in the ground water. It was desirable, therefore, to modify these wells to permit representative sampling of the ground water and to obtain the potential measurements which are needed as input data in the program to construct a mathematical model of the Hanford flow regime. Such modification required that the hydraulic potential distribution within the casing be only slightly less than or equal to the potential naturally present in the corresponding formations outside the well. This potential distribution will insure that ground water entering and leaving the well at any point is representative of that in the adjacent formation regardless of the number of aquifers penetrated by the well.

The method initially used to equalize the hydraulic head within a deep well was to seal a number of piezometer tubes inside the casing at selected intervals. In that case, the casing was filled with sand in the zones where the piezometer tubes were perforated, and the casing sections between tubes were cement-filled. In this manner, access to the sealed-off aquifers was provided, and reliable samples and head measurements of the ground water were obtained, since the movement of ground water up or down the casing was restricted by the

cemented sections. One problem with this method was the relatively long installation time. It usually required from 6 to 14 days to complete installation in a well when the tubes were sealed in with cement. A faster and possibly more reliable method considered was one in which only sand is used to seal the piezometers in the well. The effectiveness of this method was evaluated by solving a series of three-dimensional cases simulating both a sand-filled well and one in which cemented sections were present.

The potential distribution in a well filled with sand was evaluated for two sets of boundary conditions selected as input to the computer program.[4.9] The first set of conditions was chosen as that most representative of the hydrological conditions encountered in wells drilled at Hanford. Three cases were run on the IBM 7090 computer, using the first set of boundary conditions. The first case determined the potential distribution in the model with no well present. These data provided a standard for comparison of the results from the sanded-well and the cemented-well cases. The second case solved for the potential distribution in a well filled entirely with sand. In the third case, the middle half of the casing was filled with cement and the upper and lower quarters were filled with sand. Figure 4.14 is a graphical representation of these cases showing the potential variance in the sanded and cemented wells from the calculated true potential pattern. The results show that the piezometric head distribution in sand-filled wells is within 0.007 ft of the true potential distribution existing in the formation outside the well. The potential distribution within the well containing the cemented section varied from the true value in the formation by 0.01 ft.

The second set of boundary conditions was chosen to duplicate some of the more extreme hydrological conditions encountered in a few of the deep wells at Hanford. Three cases were solved using these conditions. The first case was for the naturally-occurring potential distribution (no well present). The second and third cases were solved for the sand-filled well and the cemented well respectively. The variances determined for these boundary conditions are compared in Figure 4.15. The results again show that potential distributions in

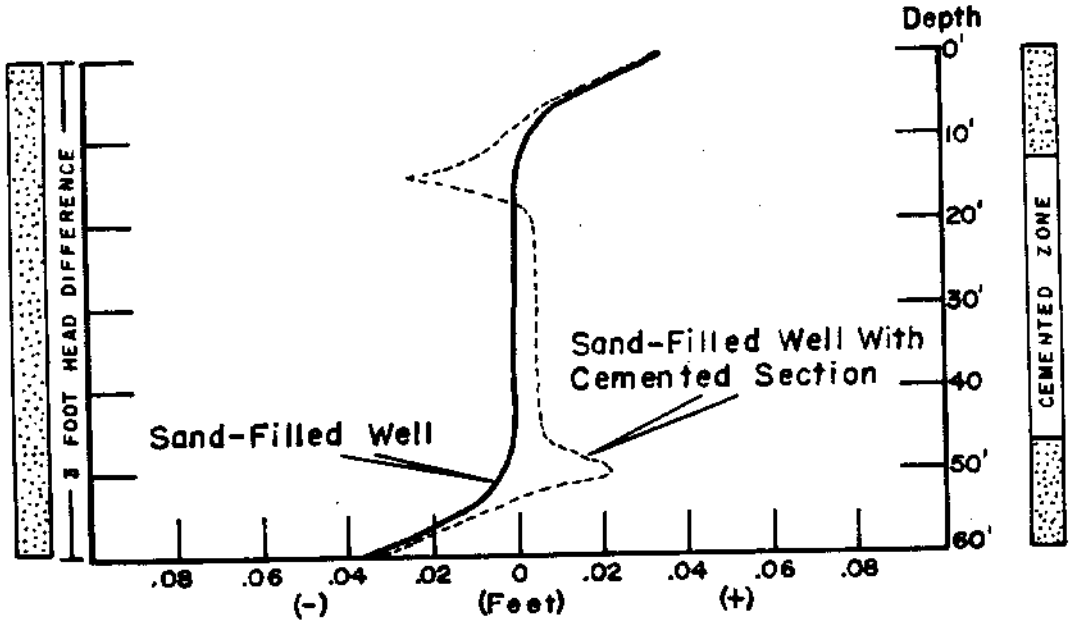

FIGURE 4.14

Variance of Potential in Well from True Potential in Formation
(φ Well - φ Formation) for a 3 ft Head Difference

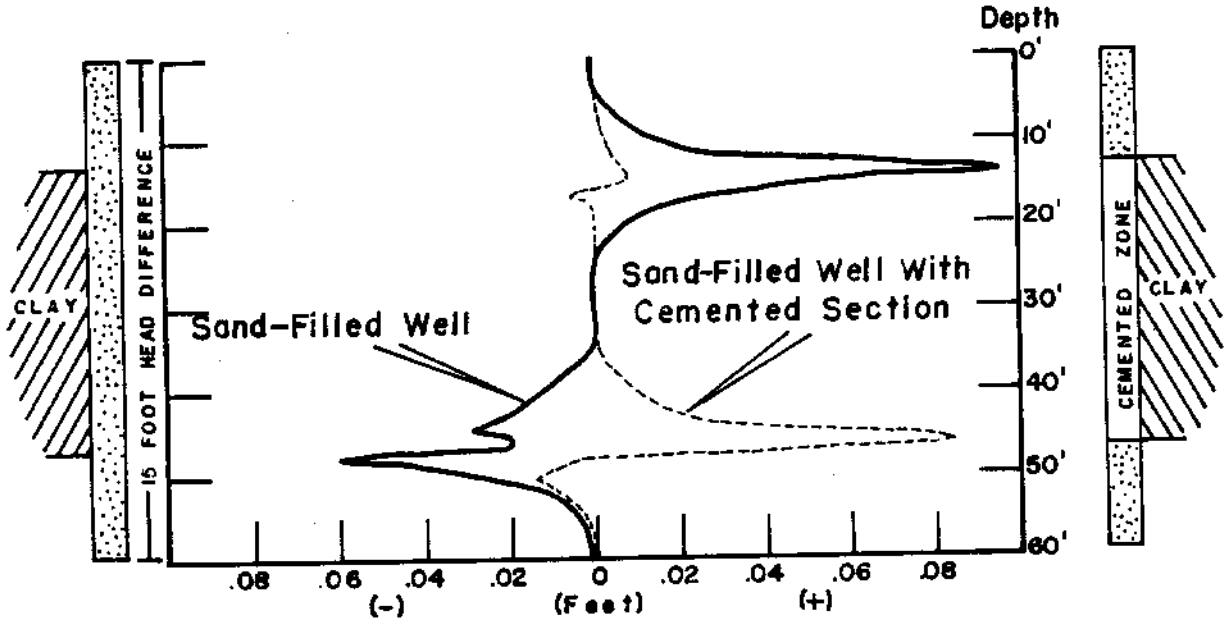

FIGURE 4.15

Variance of Potential in Well from True Potential in Formation
(φ Well - φ Formation) for a 15 ft Head Difference with a Clay Interbed

AEC GE RICHLAND, WASH.

wells filled with sand alone are as close to the true potential values in the formation as are those in the wells with the cemented sections. In this case, however, the variance from the true value was about 0.1 ft for both the sand and the cement at one point in the well. This large difference occurred in the zones where the upper and lower clay interfaces exist. The average variance in the second model is probably closer to 0.01 ft.

A calculation was made to determine the ratio of head loss in an unobstructed pipe to the head loss in a pipe filled with sand. Poiseuille's equation for head loss in open pipe and Darcy's equation for head loss in a pipe filled with sand were equated to obtain the ratios for head loss and velocity.

$$\frac{32\,\mu\,\ell\,V_1}{h_{L_1}\,\gamma\,d^2} = \frac{\mu\,\ell\,V_2}{h_{L_2}\,k\,\gamma} \qquad (1)$$

V_1 and h_{L_1} designate the velocity and head loss in the open pipe, and V_2 and h_{L_2} are the velocity and head loss in the sand-filled pipe. The diameter of the pipe is d, the intrinsic permeability k, the viscosity μ, the specific weight γ, and the length of the pipe ℓ. From Equation (1), if $V_1 = V_2$ then

$$\frac{h_{L_1}}{h_{L_2}} = \frac{32\,k}{d^2}, \text{ or if} \qquad (2)$$

$$h_{L_1} = h_{L_2}$$

then

$$\frac{V_2}{V_1} = \frac{32\,k}{d^2}. \qquad (3)$$

The head loss ratio in the case of the open pipe and the pipe filled with sand is 8.4×10^{-9}. A similar ratio for an open pipe and a pipe filled with cement is 8.4×10^{-13}. These ratios indicate that sand alone is extremely effective in dissipating most of the head differences in a well. Some flow of

water naturally takes place between the aquifers within a formation. Sand more nearly duplicates the actual conditions present in the formation because it does not restrict the flow as completely as does cement. Accordingly, sand in most cases gives more accurate results than does cement.

This study demonstrates that a bank of piezometer tubes installed in a well casing, using sand alone to dissipate the hydraulic head difference between aquifers, will provide a reliable structure for obtaining representative samples of the ground water and for obtaining accurate measurements of the potential distribution within the formations.(4.10)

Investigation of the Disposition and Migration of Gross Gamma Emitters Beneath Liquid Waste Disposal Sites - J. R. Raymond

Wells immediately adjacent to liquid waste disposal sites were logged with a gamma scintillation probe to determine the penetration depth of radionuclides. Information is presented to show contamination magnitude and migration changes at several "typical" sites. Well scintillation logs are shown to illustrate changed in waste penetration at three waste disposal facilities that have different operational histories.

Depth of penetration and extent of lateral spread of radionuclides beneath a waste disposal facility depend upon the volume and type of waste discharged and the physical and chemical characteristics of the earth material beneath the site. Each facility requires inidvidual study to evaluate the disposition of radionuclides in the subsoils. Gamma-scintillation logging of wells near disposal facilities is helpful in determining the degree of vertical and horizontal contaminant spread during disposal and in evaluating continued soil drainage and radioactive decay after disposal has terminated. Scintillation logging has only limiteduse, however, after the entire soil column has become highly contaminated.

Equipment and Techniques

Three different scintillation probe systems have been used for 10 yr for well logging. The present system is a third generation evolution from earlier-developed equipment. The system consists of a 4 in. diameter and 13.5 in. long

probe, armored wire line, and surface hoisting and electronic equipment. The present system has greater sensitivity and stability than the earlier equipment, and more refined hoisting and recording methods are used. The equipment has a lower detection limit of 2×10^{-6} microcuries/cm^3 in water (Ru^{106} - Rh^{106}) and about 0.002 mr/hr (Ra^{226}) in air; maximum detection limit is about 150 mr/hr (Ra^{226}).

Discussion

The vertical migration of radionuclides beneath Hanford waste disposal sites varies from thin zones directly under the facility to areas where the entire soil column is contaminated. Horizontal spread varies from a few feet from the edge of the crib, trench, or cavern to several hundred feet from the disposal site. The concentration of radioisotopes in the soil varies from barely detectable to beyond the maximum range of the scintillation probe. Adequate, monitoring-well coverage exists around the major disposal sites to delineate fairly accurately the vertical extent of subsurface contamination.

Three disposal sites were selected to illustrate "typical" findings for three different operational conditions. Figure 4.16 shows scintillation logs of Well W11-55 for 1953, 1958, and 1963. This well monitors a crib site which received 4.5×10^7 liters and 18,000 curies of mixed fission product wastes from August 1946 to July 1951. The 1953 log shows a narrow zone of gross contamination from about 15 to 35 ft below ground surface. The logs for 1958 and 1963 show almost exactly the same contaminated zone. The zone from 35 to 75 ft appears slightly contaminated. This log is typical of that for a disposal facility which received relatively low-activity density wastes and one which has been out of service for a long time. Very little downward migration of contamination occurred after the facility had been out of service for several years. This supports the belief that much of the flow beneath a crib is under unsaturated flow conditions where subsequent drainage would be slow.

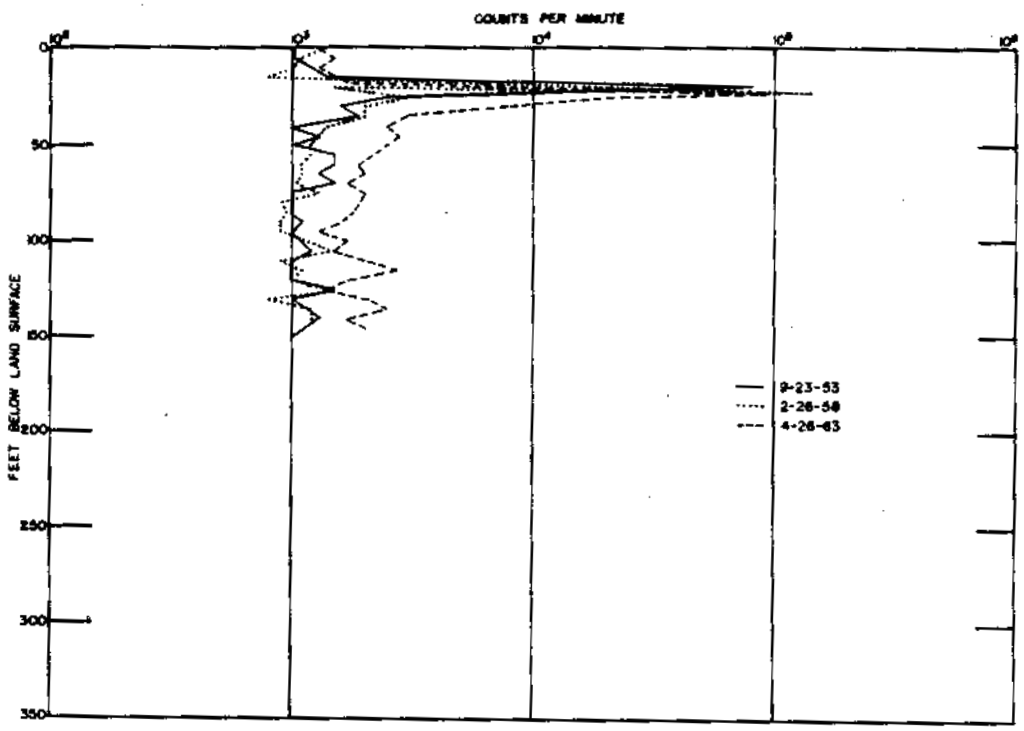

FIGURE 4.16
Probe Results in Well 299-W11-55

Figure 4.17 shows scintillation logs of Well E13-6 for 1956, 1958, 1959, and 1963. Well E13-6 monitors a site with six cribs that received 4×10^7 liters and 3.2×10^5 gross beta curies of waste from January 1956, to December 1957. Three months after the initial disposal, radionuclides had penetrated to a depth of about 80 ft. Four months after site use was discontinued, contamination had moved to 170 ft. Radionuclides migrated downward an additional 15 ft the following year. Four years later, in 1963, the contaminants had reached a total depth of about 210 ft. The effect of radioactive decay is apparent on the last trace. Data extrapolation indicates contamination migration to 225 ft beneath ground surface by 1966. This log is typical of that for a site which has been out of service for a moderate length of time and has received medium volumes of relatively high activity density, high-salt waste.

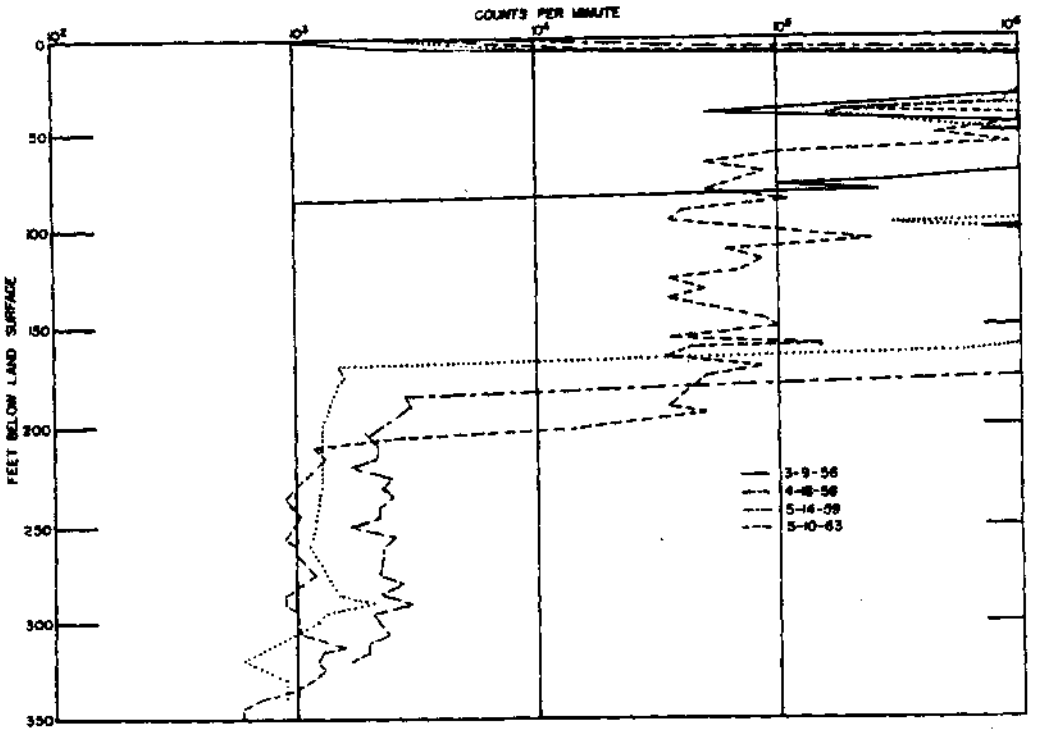

FIGURE 4.17
Probe Results in Well 299-E13-6

Figure 4.18 shows scintillation logs of Well E26-5 for 1958 (three logs) 1959 and 1963. This well monitors part of a crib that has received about 7.6×10^8 liters and about 4500 gross beta curies of tank farm condensate waste from May 1958, to present. The well was logged on April 1958, before site use for background information. On May 27, 1958, 1 wk after disposal started, contamination was present to a depth of 105 ft. Radioisotpoes (Ru) had migrated to about 130 ft by June 1958, and the entire soil column beneath the crib was contaminated by June 1959. Both the volume and quantity of radioactive material discharged to the crib were greatly reduced in late 1959, and the latest log (May 1963) reflects this reduction. These probe results are typical for a site that receives large volumes of low level waste and is still in service.

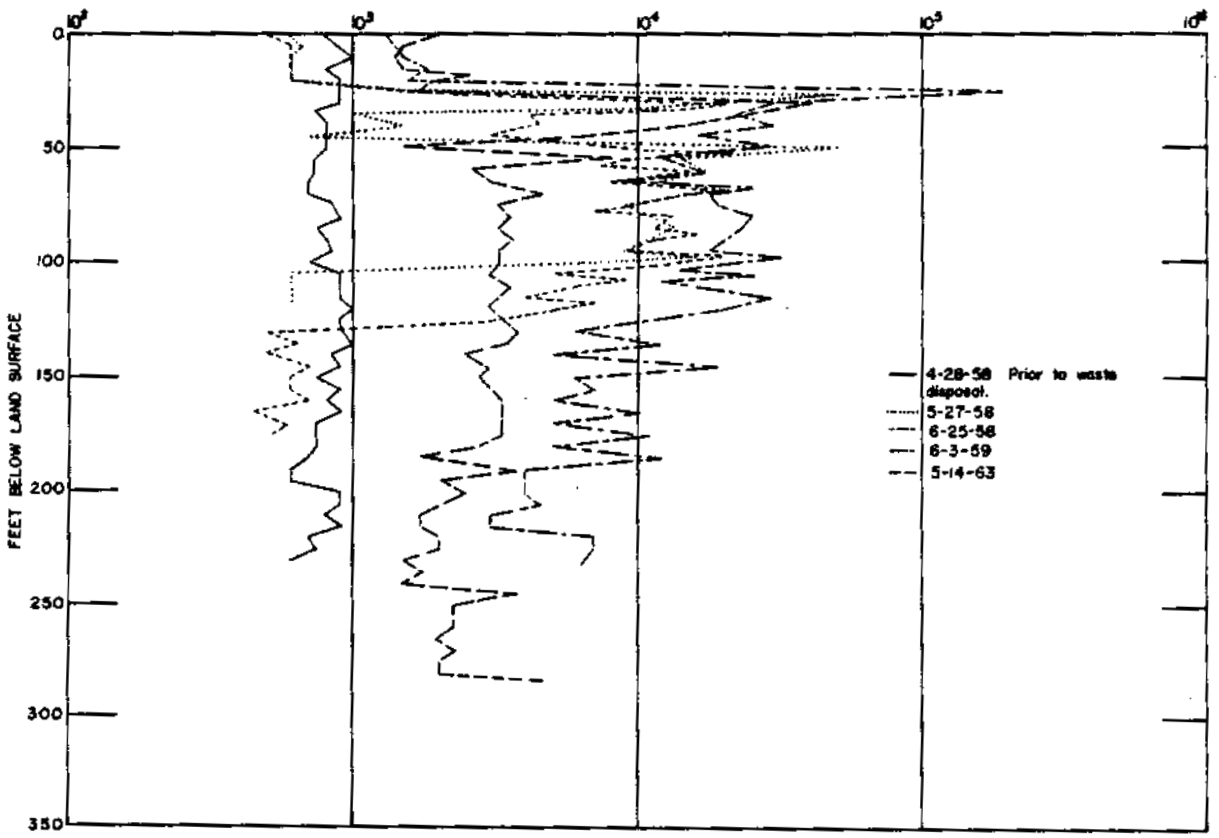

FIGURE 4.18
Probe Results in Well 299-E26-5

Future Investigation

Logging of project wells adjacent to disposal sites will be continued. Determination of isotopic composition of the contaminants will be attempted by use of a multichannel pulse height analyzer. Information gained from these field studies should be of considerable value in linking the results of laboratory tests, which use confined soil columns to evaluate the uptake of specific radionuclides, with the observed waste flow patterns typical of the true field situation.

Soil Parameters Necessary for Solution of Partially Saturated Flow Problems - L. G. King

The solution of problems involving flow through partially-saturated porous media requires a knowledge of the three interrelated soil parameters: permeability, capillary pressure, and mositure content. It is concluded that the relationships may be expressed as two curves: moisture content as a function of capillary pressure and premeability as a function of capillary pressure. These relationships are shown to arise from the basic equation describing the flow.

The general equation describing the flow of a liquid through a stable porous material which is partially saturated with the liquid is

$$\frac{\partial \theta}{\partial t} = \operatorname{div}\left(\frac{k}{\mu}\operatorname{grad}\,\phi\right), \tag{1}$$

where θ is the moisture content expressed on a bulk volume basis, t is time, k is the permeability * expressed in length-squared dimensions, μ is the viscosity of the liquid, and ϕ is the potential. The potential may be written **

$$\phi = p + \rho g z, \tag{2}$$

where p is the liquid pressure, ρ is the density of the liquid, g is the acceleration of gravity, and z is the vertical space coordinate.

It is assumed that the liquid wets the solid and that the nonwetting fluid occupying the remaining pore volume has a pressure which is constant and uniform throughout the system. It is convenient to introduce the capillary pressure, p_c, defined as the difference in pressures between the nonwetting fluid and the wetting fluid.

$$p_c = p_{nw} - p_w. \tag{3}$$

---

* Sometimes called intrinsic permeability

** The potential is sometimes written $p/\rho g + z$ which is an expression of energy per unit weight; whereas, Equation (2) expresses the potential as energy per unit volume. The only difference in the two expressions is in units involved; the potential is physically the same.

Thus, for an air-water-soil system the capillary pressure is equal to the negative of the water pressure. For soils partially saturated with water, the water pressure is actually a negative value (the air pressure taken as a datum), so that the capillary pressure has a positive value.

Introducing the capillary pressure into Equation (2) and writing Equation (1) in Cartesian coordinates gives

$$\frac{\partial \theta}{\partial t} = \frac{\partial}{\partial x}\left(-\frac{k}{\mu}\frac{\partial p_c}{\partial x}\right)+\frac{\partial}{\partial y}\left(-\frac{k}{\mu}\frac{\partial p_c}{\partial y}\right)+\frac{\partial}{\partial z}\left(-\frac{k}{\mu}\frac{\partial p_c}{\partial z}\right)+\frac{\rho g}{\mu}\frac{\partial k}{\partial z}. \qquad (4)$$

The three soil parameters, θ, k, and p_c, are related. For homogeneous media the relationships may be expressed as $\theta = \theta(p_c)$ and $k = (p_c)$ i. e., a curve of θ as a function of p_c and a curve of k as a function of p_c. These two relationships are needed for the solution of boundary value problems involving partially saturated porous media. It may appear that only one relationship, $k = k(p_c)$, is needed for steady flow since the left side of Eqaution (4) is then zero, and the solution of the resulting equation gives p_c as a function of space. However, the practical interest usually lies in the distribution of moisture content. Once the solution giving the distribution of p_c is obtained, the curve $\theta = \theta(p_c)$ is needed to obtain the distribution of θ.

For transient flow, either θ or p_c may be made the dependent variable in Equation (4).[4.11] For p_c the dependent variable, the left side of Equation (4) is written

$$\frac{\partial \theta}{\partial t} = \frac{d\theta}{dp_c}\frac{\partial p_c}{\partial t}. \qquad (5)$$

For θ the dependent variable,

$$\frac{\partial p_c}{\partial x} = \frac{dp_c}{d\theta}\frac{\partial \theta}{\partial x}, \quad \frac{\partial p_c}{\partial y} = \frac{dp_c}{d\theta}\frac{\partial \theta}{\partial y}, \quad \frac{\partial p_c}{\partial z} = \frac{dp_c}{d\theta}\frac{\partial \theta}{\partial z}, \qquad (6)$$

and Equation (4) becomes

$$\frac{\partial \theta}{\partial t} = \frac{\partial}{\partial x}\left(D \frac{\partial \theta}{\partial y}\right) + \frac{\partial}{\partial y}\left(D \frac{\partial \theta}{\partial y}\right) + \frac{\partial}{\partial x}\left(D \frac{\partial \theta}{\partial x}\right) + \frac{\rho g}{\mu} \frac{\partial k}{\partial x}, \tag{7}$$

where D is the diffusivity (a function of θ) given by

$$D = - \frac{k}{\mu} \frac{dpc}{d\theta}. \tag{8}$$

From Equations (4), (5), (7), and (8) it is apparent that both curves, $\theta = \theta(p_c)$ and $k = k(p_c)$, are needed for the solution of a transient flow problem regardless of the choice of dependent variable. Furthermore, the slope of the $\theta = \theta(p_c)$ curve must be determined.

The fact that hysteresis exists in the two functions, $\theta(p_c)$ and $k(p_c)$, is well known.[4.12, 4.13] The theory of Miller and Miller [4.13] shows that the functions depend upon the capillary pressure history but are invariant to monotonic time-scale distortions of that history. From this theory there are two histories which give unique functions. They are drainage of liquid from completely saturated material and imbibition of liquid by dry material. There are, of course, a multitude of possible scanning curves between these two unique curves.

Measurement of Soil Parameters for Partially Saturated Flow - L. G. King

A laboratory program is in progress to measure simultaneously the relationships between the three soil parameters: permeability, capillary pressure, and moisture content. Moisture content measurements utilize the excellent characteristics of soils having different degrees of wetness to attenuate the low-energy gamma rays from an Am^{241} source. Simultaneously, capillary pressure and permeability are measured by more conventional techniques. These data, collected for typical project soils, are used as inputs to the "steady-state" computer program which solved for the equilibrium waste-flow patterns beneath ground disposal facilities.

The relationships between the three partially-saturated flow soil parameters, permeability, capillary pressure, and moisture content, for both imbibition and drainage* are needed as input data to computer programs which will evaluate the flow-patterns beneath waste disposal facilities and leaking tanks (the transient-flow-program for the latter case has yet to be developed).

The basis for the discussed method of measurement is a phenomenon observed by Childs (4.14) and explained by Scott and Corey. (4.15) In 1945, Childs observed that as liquid flowed downward at a steady rate through a long vertical column of partially-saturated, uniformly packed porous material, the capillary pressure and moisture content were sensibly constant over a considerable length of the column. For this region of the column the potential gradient is due only to gravity and is constant. Hence, the permeability can be calculated if measurements of the outflow rate are made. If methods of measuring the capillary pressure and moisture content are available, then the relationships between the three parameters can be determined on the same sample.

The measurement of moisture content is made by a gamma-ray absorption technique (Figure 4.19). In this method, the soil sample is placed between the source of gamma radiation and the detector probe. The count rate received at the probe can be correlated to the moisture content of the sample (the drier the sample the higher the count rate). Ferguson and Gardner (4.16) and others have used Cs^{137} as a source of gamma radiation. In this case an Am^{241} source is used to obtain more accurate results for the desirable column size (about 2 in. ID). Also, the low gamma-ray energy (0.06 Mev) of Am^{241} permits the use of a relatively high flux with only minimum shielding.

The capillary pressure is measured with tensiometers (Figure 4.19) like those described by Scott and Corey(4.15) except that a rigid porous porcelain material is used instead of a flexible porous plastic.

---

* See "Soil Parameters Necessary for Solution of Partially Saturated Flow Problems," page 4.37.

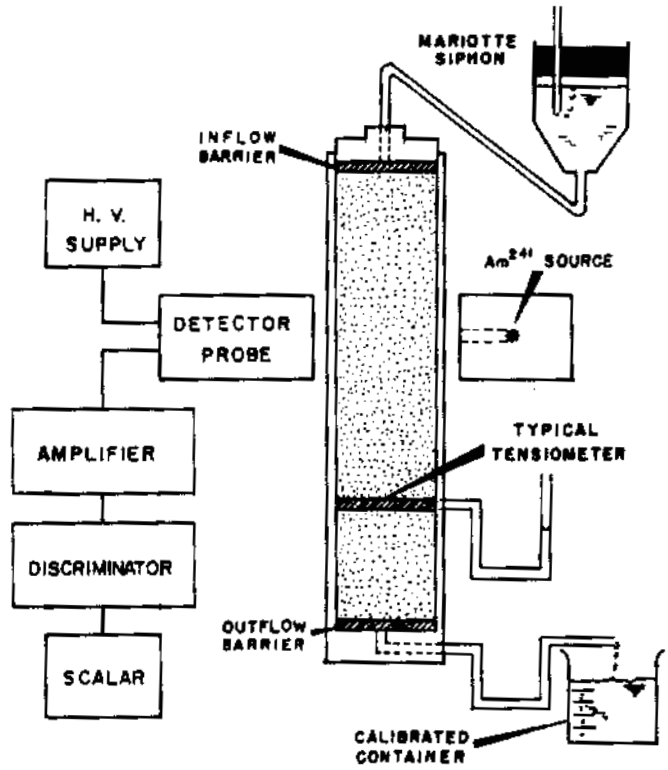

FIGURE 4.19

Schematic Drawing of Equipment for Measuring Soil Parameters for Partially Saturated Flow

A soil column packer, similar to the one described by Jackson, Reginato, and Reeves[4.17] was built to obtain uniform distribution of material within the column. The column, clamped into the packer, is continually vibrated while a motorized tremie lays down a helical pattern of soil as it rises from the bottom to the top of the column. The vibration causes rearrangement of soil particles only within 1/4 in. of the surface.

The measurement method may be outlined as follows: The column of dry material from the soil-column packer is allowed to fill with liquid until steady downward flow is established. Then the capillary pressure, moisture content, and permeability are determined. The capillary pressure at which the liquid is allowed to enter the column is reduced, steady flow is once again obtained, and the above measurements are made. Thus, the two curves,* $\theta = \theta(p_c)$ and $k = k(p_c)$, are determined for imbibition by a succession

* See "Soil Parameters Necessary for Solution of Partially Saturated Flow Problems," page 4.37.

of steady-state measurements at various values of p_c. The method for making drainage measurements is the same except the material is initially saturated under vacuum [4.15] and one steady state condition is produced from another by an increase, rather than a decrease, of the capillary pressure at which the liquid enters the column.

Analytical Description of Soil Parameters for Partially Saturated Flow - L. G. King and A. E. Reisenauer

Methods were derived for accurately fitting experimental data for soil permeability and moisture content as functions of capillary pressure by equations in closed form. The immediate utility of these equations is in the simplification of input data used to obtain accurate solutions to steady-state, partially-saturated flow problems. Future applications, such as those related to transient-state waste flow problems (leaking waste tank or pipeline), appear promising.

An analytical solution of any partially-saturated flow problem necessitates description of the relationships between the soil parameters by mathematical equations. Even with such equations, integration of the partial differential equation describing the flow may be virtually impossible; hence, numerical solution methods are usually used. Equations relating the soil parameters will greatly simplify the handling of input data and the programming for computer numerical solutions.

Schleusener and Corey [4.18] and Scott and Corey [4.15] approximated the curve* $k = k(p_c)$ by the equation

$$k_r = (p_d/p_c)^n, \quad p_c \geq p_d, \tag{1}$$

where p_d and n are constants for a given soil and capillary pressure history, p_c is the capillary pressure, and k_r is the relative permeability defined as the ratio of the permeability at the moisture content considered to the permeability at complete saturation. Gardner [4.19] used the equation

$$k = a/(p_c^n + b), \tag{2}$$

where a, b, and n are constants.

---

* See "Soil Parameters Necessary for Solution of Partially Saturated Flow Problems," page 4.37.

The data[4.15, 4.18] show that for drainage of some materials from complete saturation, there must exist a finite, and sometimes substantial, capillary pressure before any desaturation (and hence permeability reduction) takes place. Further increase of capillary pressure causes a gradual and then more rapid decrease of permeability, until the curve approaches a straight line on a logarithmic plot. The data of Figure 4.20 show that imbibition curves have a similar shape. The phenomenon of constant permeability for a range of capillary pressures will be described by saying that the curve has a "plateau".

Equation (1) is a straight line on a logarithmic plot and completely ignores the existence of a plateau. The data[4.15, 4.18] show considerable deviations from Equation (1) for values of relative permeability from 1.0 to 0.1. Recent results of Hanks and Bowers[4.20] show the above range to be quite important for transient partially-saturated flow problems during imbibition. Equation (2) does describe a plateau and approaches the straight line asymptotically for large capillary pressures.

The equation proposed here is

$$k_r = \sigma \left\{ \frac{\cosh \left[(p_c/p_r)^{\eta} \right] - 1}{\cosh \left[(p_c/p_r)^{\eta} \right] + 1} \right\} , \qquad (3)$$

where σ, η, and p_r are constants for a given soil and capillary pressure history.* The parameter p_r is some reference capillary pressure and is not given further significance here.

Figure 4.20 shows Equation (3) fit to experimental imbibition data. These data were measured by the long-column method.** The imbibition curves have a plateau for some materials. Since drainage curves have a similar shape, they can be fitted equally well. Figure 4.20 shows that,

---

* See "Soil Parameters Necessary for Solution of Partially Saturated Flow Problems," page 4.37.

** See "Measurement of Soil Parameters for Partially Saturated Flow," page 4.39.

although the fit is not too good where the slope is changing most rapidly, Equation (3) does describe the data for the complete range of capillary pressures measured. For sufficiently large capillary pressure, Equation (3) becomes very nearly a straight line with the slope equal to $2n$ on a logarithmic plot and thus approaches Equation (1) asymptotically. As the capillary pressure becomes infinite, the permeability approaches zero. When $p_c = 0$, $k_r = \sigma$. (Note that for drainage from complete saturation, $\sigma = 1$).

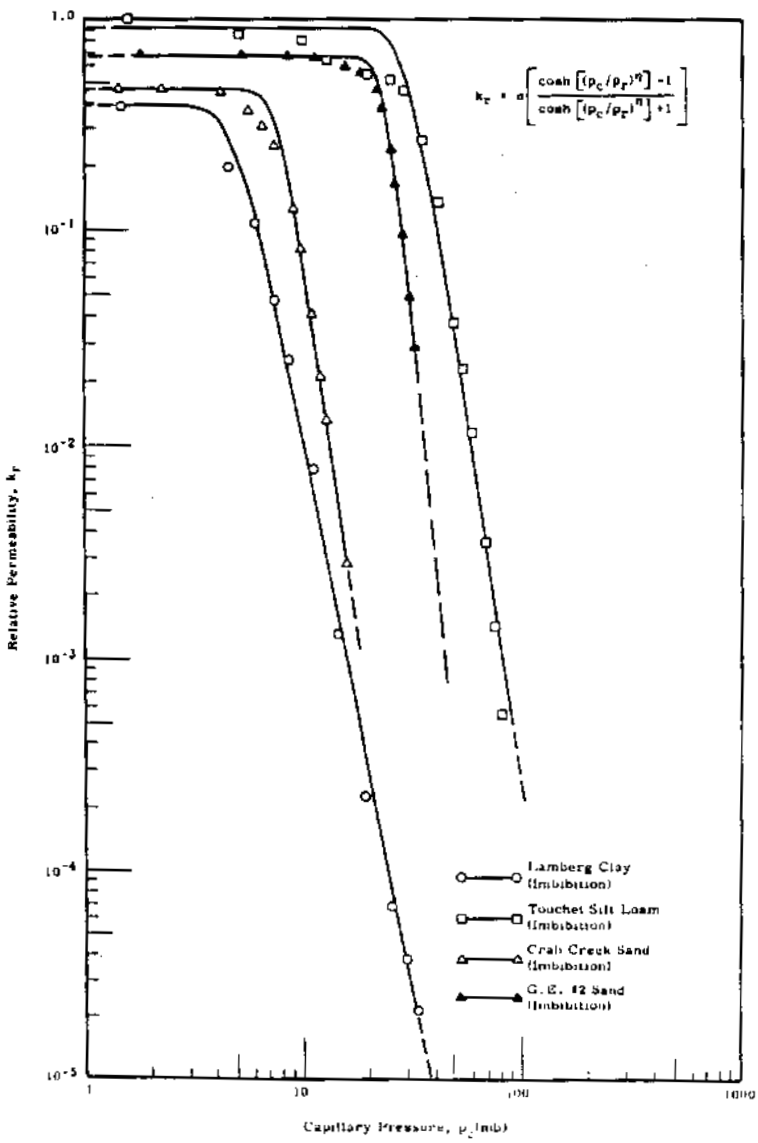

FIGURE 4.20

Experimental Data for Permeability as a Function of Capillary Pressure Fit by Equation (3)

It is convenient to replace the curve* $\theta = \theta(p_c)$ by the curve $S = S(p_c)$, where $S = \theta f$. The saturation, S, is the ratio of the pore volume filled with liquid to the total pore volume, and f is the porosity. The values of S range between 0 and 1.

Brooks and Corey (4.21) propose the equation

$$\frac{S - S_r}{1 - S_r} = \left(\frac{p_d}{p_c} \right)^{\lambda}, \; p_c \geq p_d, \tag{4}$$

where λ, p_d and S_r are constants. The residual saturation, S_r, is the saturation at which the permeability is assumed to approach zero. Brooks and Corey (4.21) approximate S_r as the vertical asymptote to the curve $S = S(p_c)$ at the large values of p_c.

The equation proposed here is

$$S = \delta \left[\frac{\cosh\left\{ \left[(p_c + \varepsilon) / p_o \right]^{\beta} \right\} - \gamma}{\cosh\left\{ \left[(p_c + \varepsilon) / p_o \right]^{\beta} \right\} + \gamma} \right], \tag{5}$$

where δ, γ, β, ε, and p_o are constants depending again on the soil and the capillary pressure history. Here, also, p_o is given as a reference capillary pressure with no attempt to attach any physical significance to it.

Figures 4.21 amd 4.22 show Equation (4) fitted to experimental data. Note that:

$$\lim_{p_c \to \infty} S = \delta \left[\frac{1 - \gamma}{1 - \gamma} \right]. \tag{6}$$

Equation (6) gives a rational way of determining the residual saturation, S_r. Figures 4.21 and 4.22 show that these curves also have a plateau for some materials. Equation (5) can fit data which either exhibit or lack a definite plateau. The deviations for G.E. Number 2 Sand between S = 0.9

---

* See "Soil Parameters Necessary for Solutions of Partially Saturated Flow Problems," page 4.37.

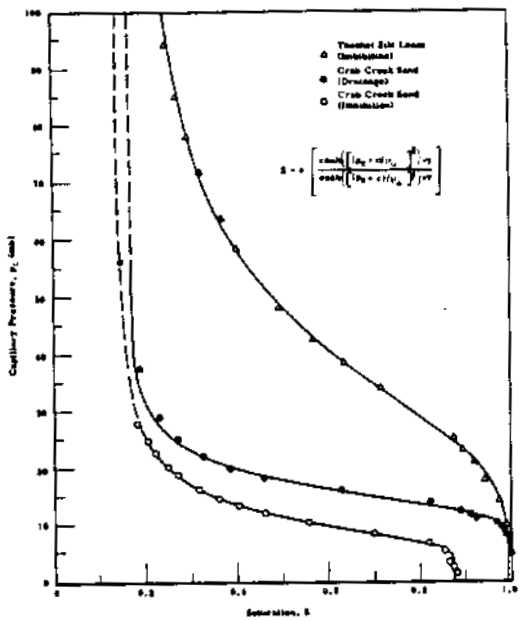

FIGURE 4.21

Experimental Data for Saturation
as a Function of Capillary Pressure Fit by Equation (5)

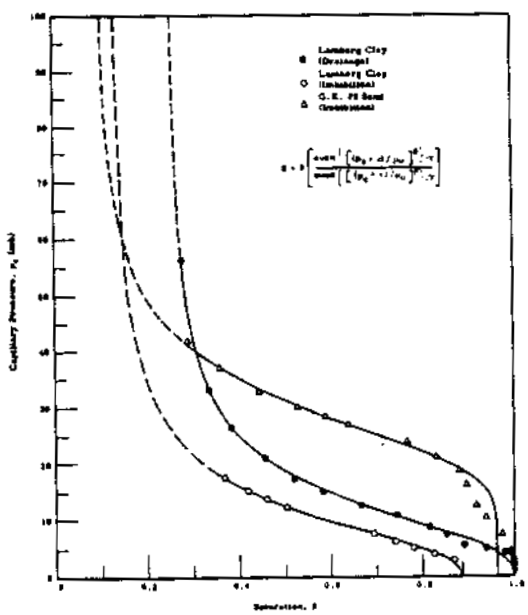

FIGURE 4.22

Experimental Data for Saturation
as a Function of Capillary Pressure Fit by Equation (5)

and S = 1 are not of too much concern since these data are not compatible with the permeability data shown in Figure 4.20. The saturation data were measured on a different sample, and the gamma ray technique* was not used. Equation (5) is easily differentiated to obtain the slope, dS/dp_c (or $d\theta/dp_c$), necessary for the solution of any transient, partially-saturated flow problem.** Thus, the laborious graphical differentiation often used for numerical data is avoided by use of Equation (5).

The parameters σ, n, p_r, δ, γ, β, ϵ, and p_o were chosen with the aid of a nonlinear data fitting program, "NELLY," developed at Hanford. This program employs a steepest descent method of minimizing the sum of the squares of the residuals.

In-Place Measurement of Permeability in Heterogeneous Soils - R. W. Nelson

An extended sequence of analysis is presented which overcomes the computation problems associated with the determination of soil permeability distributions in heterogeneous media. The potential function, obtained from orthogonal regression methods, provides the permeability through integration of appropriate functions along flow paths which are also found from the potential function.

The accurate evaluation of ground-water flow systems requires realistic in-place measurement of the permeability distribution throughout the region. A complete theory of measurement for steady flow is available from earlier work.[4.22, 4.23] The basic theory states that if the steady ground-water potentials are known throughout the region of interest, and permeabilities are known along one irregular surface which intersects every stream tube in the flow system, then a unique permeability distribution everywhere in the system can be obtained. Moderate progress has been made in overcoming the computation problem arising from the potential distribution being a tabular set of data rather than a

---

* See "Measurement of Soil Parameters for Partially Saturated Flow," page 4.39.

** See "Soil Parameters Necessary for Solution of Partially Saturated Flow Problems," page 4.37.

mathematical function. Such a function is needed since the paths of fluid flow must be found and appropriate integrals evaluated along those paths to obtain the permeability distribution.

The functional fitting and permeability determination steps are illustrated in Figure 4.23. In the upper left corner, are shown the field data which include the location, x, y, and z coordinates; time, t; and a potential observation, φ, for each location. These data are used as input to the generalized orthogonal regression program (GENORO) to obtain the fitted function. The logic and methods used in GENORO are adaptations of methods used by the Upper Atmospheric and Plasma Physics Unit of the Bureau of Standards in connection with numerical mapping of the ionosphere. The method of fitting generates a set of ortho-normal fitting functions (orthogonal with respect to the irregular locations of potential measurement). This special class of functions uncouples the unknown coefficient matrix

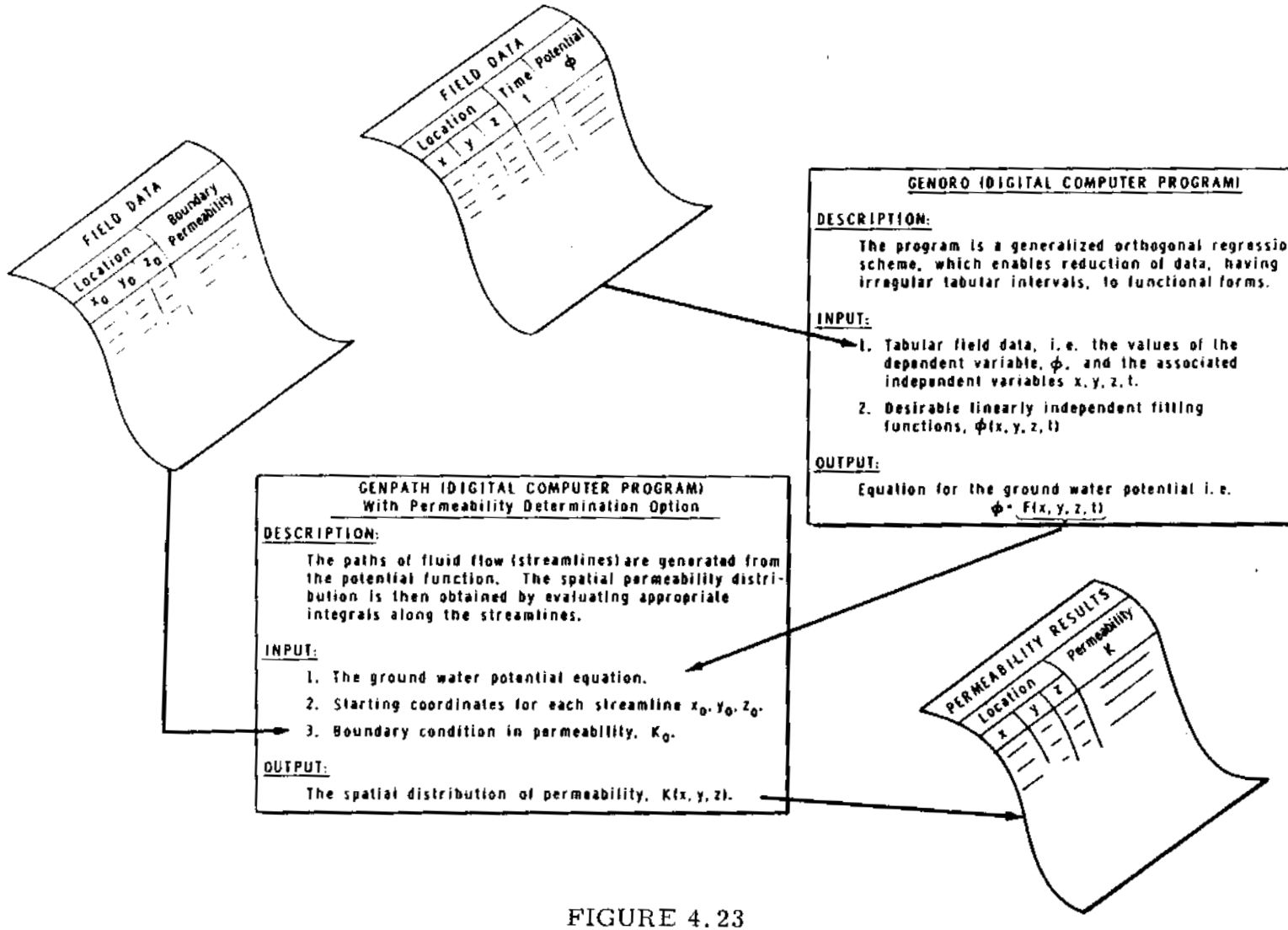

FIGURE 4.23

Data and Computer Operations
Required for Determining the In-Place Permeability Distribution for Heterogeneous Soils

Extension and Simplification of Stream Functions for Flow in Heterogeneous Porous Media - R. W. Nelson

The stream functions derived previously[4.26] for heterogeneous media are extended to give simplified equations for the velocity, in terms of the stream function pair, and for the flux distribution. In this new form the flux equations are directly integrable and are therefore simple to use.

Stream functions are a particularly useful tool in the analysis of waste flow in ground water, since they describe the individual paths of fluid flow. Integration along these paths defines the travel time which is one of the parameters needed for accurately assessing the potential radiological hazard.

Summary of Background Equations

Potential Equations:

$$\text{div } (K \text{ grad } \varpi) = 0 \qquad (1)$$

$$K \text{ div } (\text{grad } \varphi) + \text{grad } K \cdot \text{grad } \varphi = 0, \qquad (2)$$

where,

K is the hydraulic conductivity or spatial distribution of permeability

$\varpi = \frac{p}{\gamma} + z$ is the hydraulic potential or potential function

$\frac{p}{\gamma}$ is the pressure head

z is the elevation head.

Flow Paths:

Along the path of a fluid particle the convectivity derivative of the path function, Ψ, is zero,. i. e.:

$$\frac{D\Psi}{Dt} = K \text{ grad } \varphi \cdot \text{grad } \Psi = 0. \qquad (3)$$

Solution of Equation (3) reduces to finding the integrals of the pair of differential equations

$$\frac{dx}{K\frac{\partial\varphi}{\partial x}} = \frac{dy}{K\frac{\partial\varphi}{\partial y}} = \frac{dz}{K\frac{\partial\varphi}{\partial z}} \tag{4}$$

having the solutions

$$f(x, y, z) = a \tag{5}$$

$$g(x, y, z) = b. \tag{6}$$

Equations (5) and (6) make up the adjunct stream function pair with the intersections of the f and g surfaces being precisely the streamlines, as illustrated in Figure 4.24.

Definition of the velocity vector, $\underline{v}$ is

$$\underline{v} = K\Lambda(\text{grad } f \times \text{grad } g) \tag{7}$$

where Λ is a scalar parameter of space, yet to be obtained.

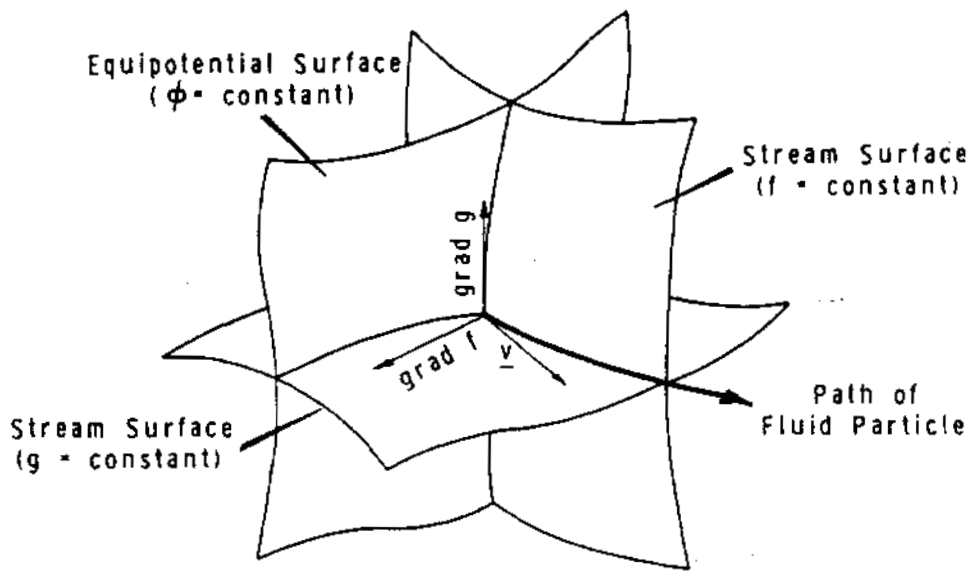

FIGURE 4.24

Geometrical Interpretation of Stream Surfaces as Defined by the Function Pair f and g.

New Description of Velocity and Results

Equation (7) expresses the velocity components as a function of the adjunct pair and $K\Lambda$; however, it is shown through use of the theory for postmultipliers and integrating factors that $\underline{v}$ can be expressed in a more compact functional form. By direct calculation or by Theorem 1, page 32 of Golubev,[4.27] the equation is identically zero.

$$\text{div}\left(\frac{1}{\Lambda}\ \text{grad}\ \varphi\right) = 0 \tag{8}$$

Equation (8) is the defining relationship for Λ to be a postmultiplier (see Equation (14) page 34, Golubev)[4.27] With Λ shown to be a multiplier, a new alternative appears. Rather than using the independent functions f and g followed by meeting boundary conditions with Λ, the boundary conditions can be included by judiciously selecting Λ and using one of the independent integrals, say f = a, to specify a new second integral, G. Upon comparing Equations (1) and (8), a judicious selection of Λ is the reciprocal of the permeability distribution, K; therefore,

$$\Lambda = \frac{1}{K} \tag{9}$$

and the function defining the new secons integral, G, must be (see pages 25-41, Golubev)[4.27]

$$dG = \frac{1}{\frac{\partial f}{\partial z}}\left(\frac{\partial \varphi}{\partial y}\ dx - \frac{\partial \varphi}{\partial x}\ dy\right). \tag{10}$$

The substitution of K from Equation (9) into (7) gives as the velocity, from Equation (10),

$$\underline{v} = (\text{grad}\ f) \times (\text{grad}\ G)\ . \tag{11}$$

Using Equation (11) the flux, Q, is

$$Q = \int_{f_1}^{f_1} \int_{G_1}^{G_2} df\ dG$$

or

$$Q = (f_2 - f_1)(G_2 - G_1), \tag{12}$$

as contrasted to the earlier result -

$$Q = \int_{f_1}^{f_2} \int_{g_1}^{g_2} \frac{\partial^2 F(\Gamma)}{\partial f \, \partial g} \, df \, fg \, .$$

Geology

River Water Bank Storage and Exchange at Hanford -

J. R. Raymond and D. J. Brown

Information is presented on water behavior adjacent to fluctuating rivers concerning bank storage and river water penetration into ground water aquifers. Methods of investigation are discussed. Evaluation of storage and exchange was carried out for the Hanford side of the Columbia River. Total bank storage for a typical year was 2.0×10^9 ft^3 of which 36% was river water. Total river water in the aquifer was 2.9×10^9 ft^3. This volume is equivalent to only about 8 hr river flow, based on an average flow rate of 1×10^5 ft^3/sec.

Behavior of ground water adjacent to fluctuating rivers, lakes, or reservoirs is of interest to the hydrologist for any of several reasons. A surface water body may derive most of its flow from ground water sources in some instances. In others, the ground water can be almost totally composed of water from the surface body. These two conditions (or a variety of modifications) may exist in the same region at different times, depending on the stage of the surface and ground waters. The changing elevation of the surface water may cause changes in ground water quality and quantity available for use due to inflow or outflow. Or, conversely, the fluctuations may cause similar changes in the surface water characteristics from ground water discharge.

Knowledge of ground water exchange with varying stage surface water can lead to better and more efficient use, conservation, and control of both ground and surface waters.

Figure 4.25 shows a vertical cross section of an aquifer and adjacent river; b is the aquifer thickness. The base flow is ground water that flows to the river at initial water table and river stage. If the river level rises by a distance h_o, the water table rises due to the inflow of river water and at time t rises by a height of h at x distance back from the river. Therefore, we see that a stream fluctuation may produce large variations in magnitude and direction of ground water flow.

Bank storage, the general term used for the river water stored in the aquifer during flood stage, is defined as water, both river and ground, that is stored in the zone above base flow stage. This is depicted at flood stage by the crosshatched zone in Figure 4.25. At low stage, this water is contributed to the river in addition to the "exchanged" river water in the base flow zone.

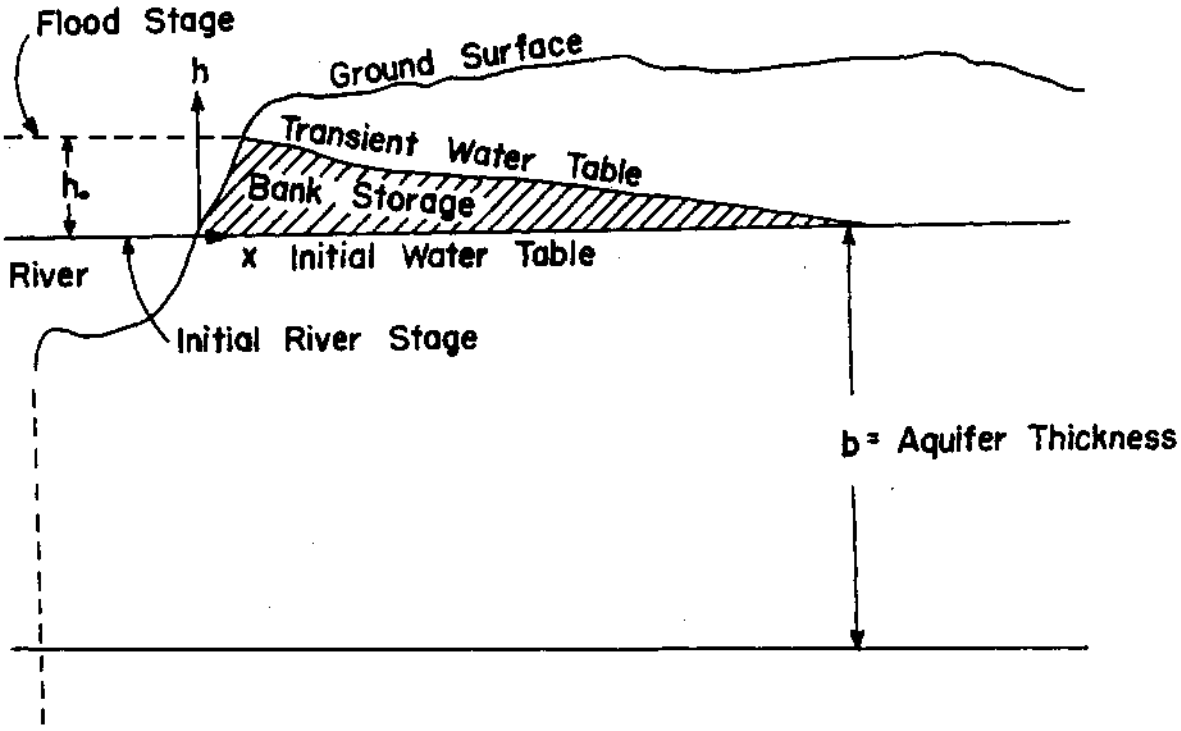

FIGURE 4.25
Aquifer and River Cross Section

Bank storage and ground and river-water exchange may be evaluated semiempirically from well and river hydrographs where sufficient control exists. Distance of river water penetration into the aquifer can sometimes be determined by well water temperature studies when river and ground water temperatures differ significantly. Bank storage may also be evaluated by use of the following equations.

$$h/h_o = 1 - P(x) \qquad (1)$$

where h = water table rise at distance x from river at time t since river stage was raised a distance h_o

$P(x)$ is the error function erf $(x/\sqrt{4\alpha t})$ sometimes called the probability integral, given by:

$$P(x) = 2\sqrt{\pi}\int_o^{x/\sqrt{4\alpha t}} e^{-u^2} du$$

$\alpha = Kb/S = T/S$

K = Coefficient of permeability

b = Aquifer thickness

S = Coefficient of storage

$T = Kb$

$$V = \frac{2Kh_ob}{\sqrt{\pi\alpha}}\sqrt{t} \qquad (2)$$

where V = Total volume of river water in the aquifer at time t.

The aquifer coefficients of transmissibility (or permeability and aquifer thickness) and storage must be known. Aquifer transmissibility, the ability of the porous media to transmit water, can be determined by pumping tests, tracer tests, and well-water fluctuation observation. The

latter method is particularly adapted for use near fluctuating streams. Methods developed by Werner and Noren,[4.28] Ferris,[4.29] or Rowe[4.30] may be used. The water occupies only the pore space in the aquifer. The volume available for water transmission is called effective porosity or, for water table conditions, the numerically equivalent storage coefficient. The coefficient of storage is defined as the volume of water released from storage from 1 ft^2 of aquifer when the hydraulic head is reduced 1 ft. The storage coefficient can be determined from pumping tests. Effective porosity can also be determined from the relationship $S = f(\frac{Q}{AV})$ where S is the effective porosity (or storage coefficient) V the average ground water velocity, Q the total quantity of flow through cross section A, and f is a temperature correction factor used when the water temperature varies from 60 F. In use at Hanford, V was obtained from tracer tests using radioactive isotopes, Q was a measured amount of cooling water discharged to the ground, and A was determined by temperature measurements. S can vary from about 0.05 to 0.3 under water table conditions.

To evaluate the bank storage and river water exchange throughout the entire Hanford Project it is first necessary to consider the geo-hydrologic changes which occur along this section of the river. Studies have shown that there are four distinct regions which differ significantly in aquifer characteristics and should, therefore, be evaluated individually. Figure 4.26 shows the reach of the Columbia River from Richland to Priest Rapids, with cross sections depicting the major geologic changes in the zone where bank storage occurs. This figure shows the two relative positions of the river stage which defines the bank storage zone. The lower stage (represented by a solid line) is based on an average minimum flow rate of 50,000 ft^3/sec while the upper stage (represented by the dashed line) is based on an average maximum flow rate of 500,000 ft^3/sec. The geology of particular interest in this discussion is limited to the rocks through which the ground water percolates at these two extreme stages. The subdivision into regions is indirectly based on the geologic changes which are shown in

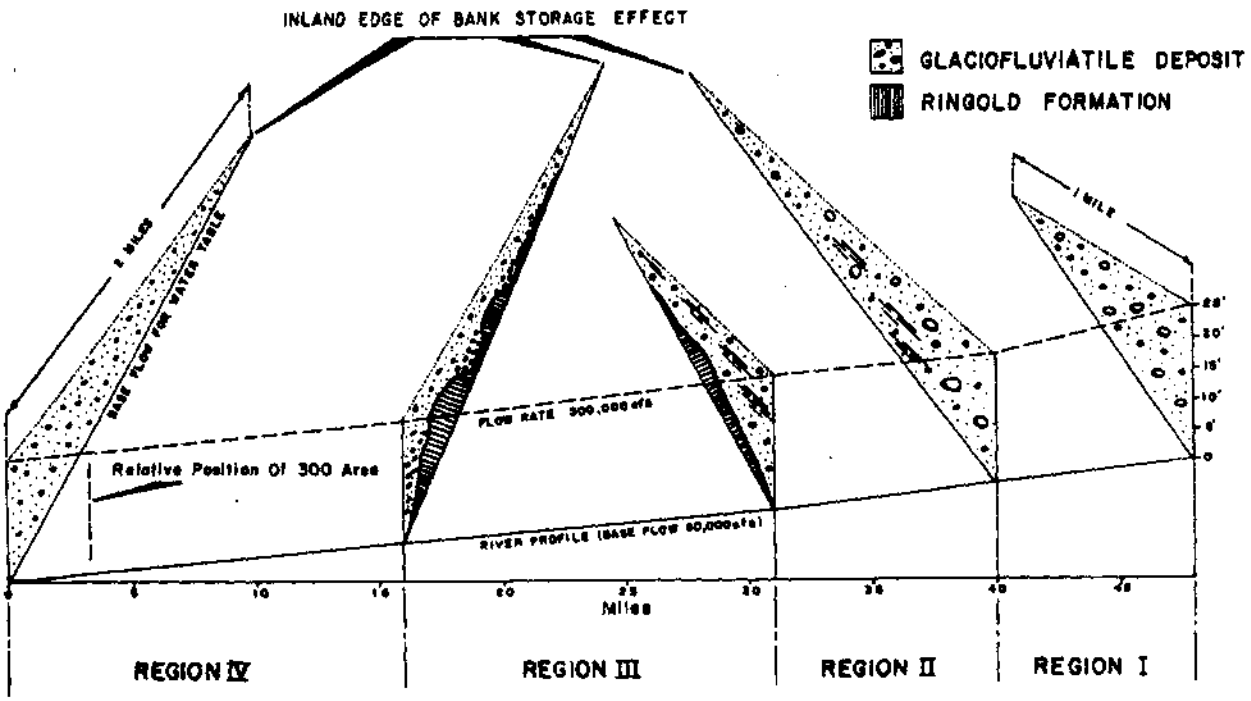

FIGURE 4.26

Regional Geologic Changes in Bank Storage Zone

this diagram. Within Region I the rocks are predominantly sands and gravels of the glaciofluviatile deposit. These rather coarse materials range in size from boulders, several feet in diameter, to fine sand, only a few thousandths of an inch in diameter. A gradual facies change occurs between Region I and Region II within the glaciofluviatile deposit. The amount of silt gradually increases from Region I to Region II. In addition to the increased amount of silt in the glaciofluviatile deposit, sediments of the Ringold Formation are present in the lower portion of this zone. These materials are predominantly made up of cemented sand and gravel. A change also occurs between Regions II and III. The Ringold beds underlying the glaciofluviatile deposit in Region III are silt and clay size sediments rather than the cemented material found in Region II. The amount of silt

in the glaciofluviatile deposit diminishes in Region III to that more like Region I; however, the sands and gravels show more evidence of sorting. Region IV, being the farthest downstream, shows the greatest amount of sorting. All of the sediments in Region IV are glaciofluviatile in origin.

The bank storage and river water exchange was determined in each of these four regions. For example, Figure 4.27 shows the river and well hydrographs which were used to calculate the transmissibility for Region I. These hydrographs dramatically point out the degree to which the ground water table fluctuates in response to the change in river stage. Sufficient information was obtained from these data to calculate the transmissibility for this region by the Rowe method, and by the time lag and stage-ratio methods of Ferris. Similar data are available and were used for all of the four regions.

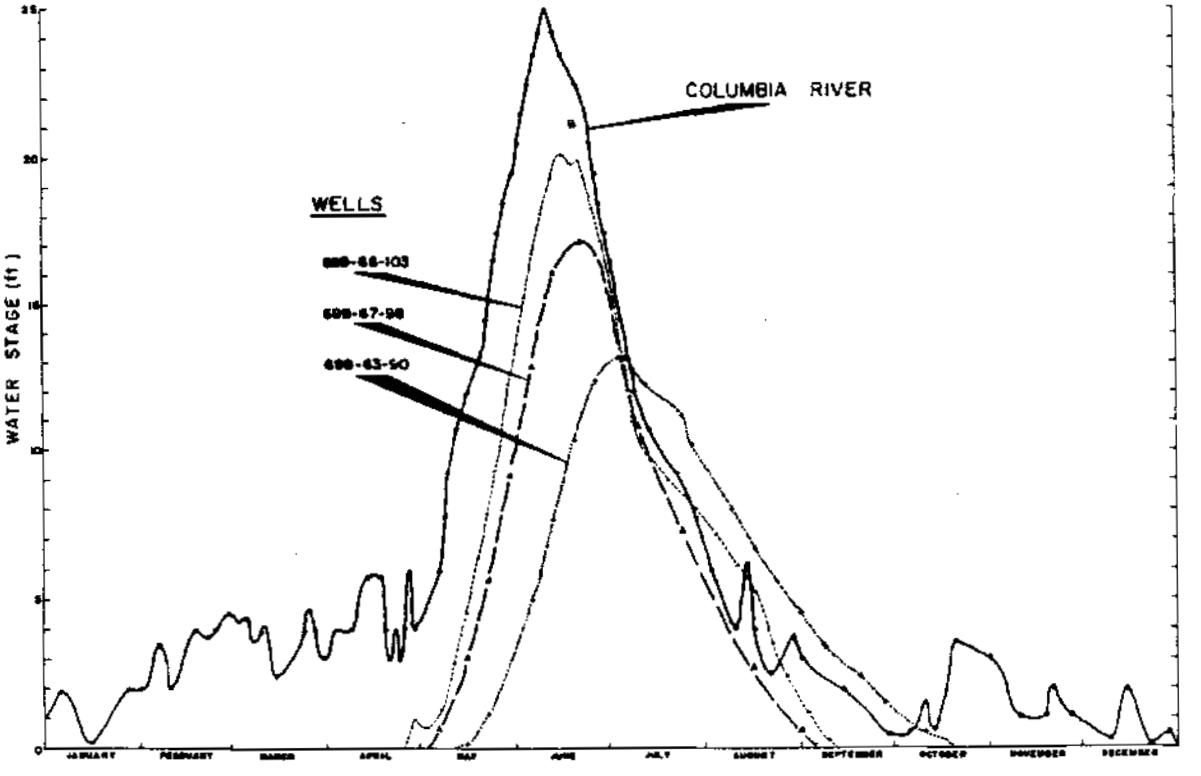

FIGURE 4.27
Region I River and Well Hydrographs

Figure 4.28 is a map of the Hanford Project showing the inland boundary of the ground water fluctuation and the portion of the zone, delineated by temperature survey, believed to be direct river water recharge. Beyond the limit of the hachured line running roughly parallel to the river, there is no evidence of water table fluctuation that can be attributed to the stage changes of the Columbia River. The enclosed table in Figure 4.28 shows the aquifer characteristics of each of the four regions and those values used to determine the total bank storage.

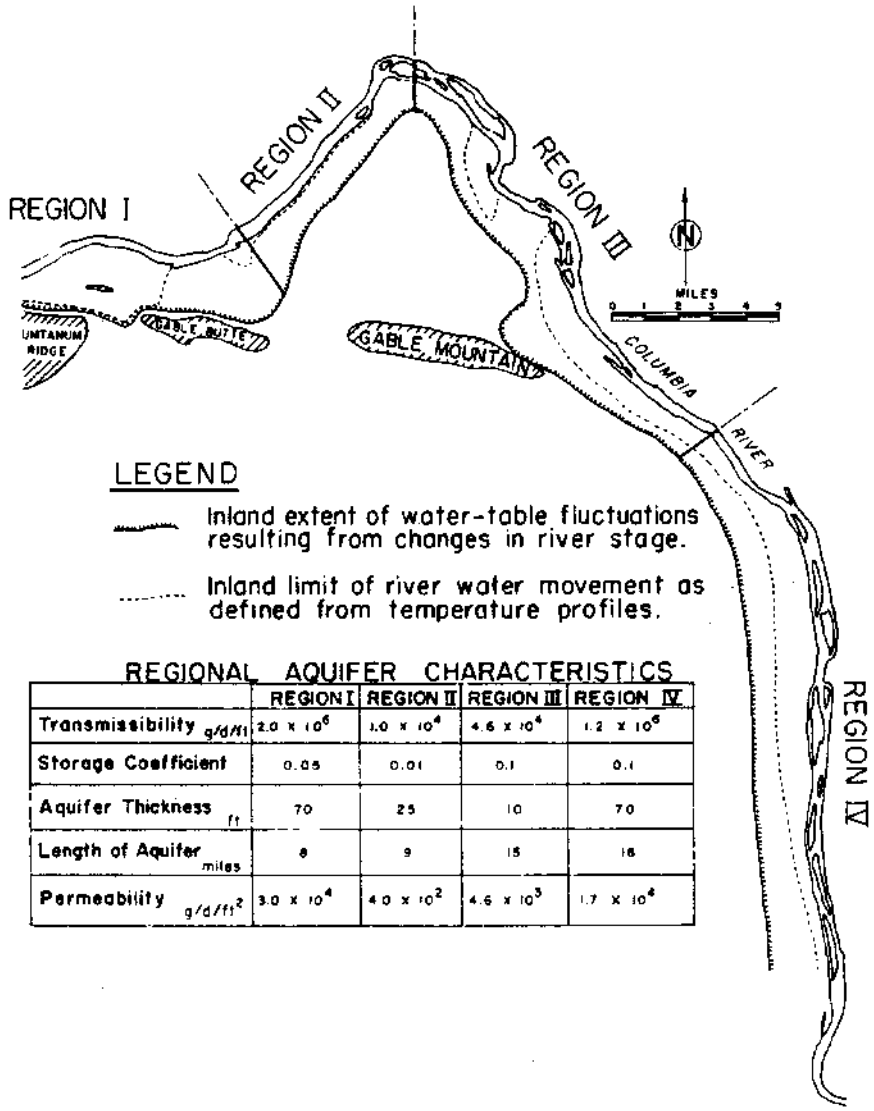

REGIONAL AQUIFER CHARACTERISTICS

	REGION I	REGION II	REGION III	REGION IV
Transmissibility $_{g/d/ft}$	2.0×10^6	1.0×10^4	4.6×10^4	1.2×10^6
Storage Coefficient	0.05	0.01	0.1	0.1
Aquifer Thickness $_{ft}$	70	25	10	70
Length of Aquifer $_{miles}$	8	9	15	16
Permeability $_{g/d/ft^2}$	3.0×10^4	4.0×10^2	4.6×10^3	1.7×10^4

FIGURE 4.28

Inland Boundary of Ground Water Fluctuation and River Water Penetration

A breakdown of this total bank storage for the Hanford Project appears in Table 4.9 by regions. It appears significant that of the total 2.0×10^9 ft^3 of water in bank storage on the Hanford side of the river, only 36% is river water. In 1961 the U.S. Geological Survey made a reconnaissance evaluation of bank storage along this same reach of the Columbia River for the Atomic Energy Commission.[4.31] They determined the total bank storage to be 3.4×10^9 ft^3, which is in good agreement with that determined in this study; however, they concluded that approximately 99% of the recharge was by river water. It should be pointed out that the bank storage calculated for the Hanford side of the Columbia River cannot be used as an estimate for storage along the opposite bank of the river because of the completely different geohydrologic conditions present there.

TABLE 4.9

REGIONAL SUMMARY OF BANK STORAGE BENEATH THE HANFORD PROJECT

	Region I	Region II	Region III	Region IV	Total
Bank Storage, ft^3	3.6×10^8	2.8×10^7	6.9×10^8	9.1×10^8	2.0×10^9
Ground Water in Bank Storage, ft^3	1.3×10^8	2.3×10^7	5.0×10^8	6.1×10^8	1.3×10^9
% Regional Bank Storage	36	08	72	67	64
River Water in Bank Storage, ft^3	2.3×10^7	5×10^6	1.9×10^8	3×10^8	7.3×10^8
% of Regional Bank Storage	64	2	28	33	36
Total River Water in Aquifer, ft^3	9.27×10^8	1.1×10^8	3.8×10^8	1.5×10^9	2.9×10^9

BIBLIOGRAPHY

Abstracts of Papers, International Association of Scientific Hydrology, vol. VIII, 226 pp. August 1963.

D. K. Todd. "Ground-Water Flow in Relation to a Flooding Stream," Proc. Am. Soc. Civil Engin., vol. 81, Separate No. 628. February 1955.

D. K. Todd. Ground Water Hydrology, John Wiley & Sons, New York, N.Y. 1959.

BIBLIOGRAPHY (Contd.)

P. Ya. Polubarinova-Kochina. Theory of Ground-Water Movement, Translated from the Russian by J. M. DeWiest, Princeton University Press. 1962.

Tables of Probability Functions, Vol. I. Federal Works Agency, New York. 1941.

Geophysical Seismic Survey Study - R. E. Brown and J. R. Raymond

A test program demonstrated the applicability and advantages in the use of geophysical seismic methods in procurement of geological data important in defining ground-water flow paths. Characteristics of the post-basalt sediments were readily determinable and significant units were traceable. Features below the topmost basalt flow were not identifiable or traceable with techniques tested. Refraction seismic methods (using surface shooting with fertilizer-grade ammonium nitrate), rotary drilling, and inhole logging of wells for geologic control present a fast, definitive and economical combination of shallow exploration techniques.

A geophysical seismic evaluation study was completed and final results are being evaluated to determine the applicability of seismic methods at Hanford to determine the geological and geohydrological conditions pertinent to the disposal of radioactive wastes. Usable techniques, data obtainable, accuracy of the data, and the cost and speed of the optimum, production-type survey were desired.

The study differed from normal seismic evaluation studies in that the depths to features of interest ranged from about 100 to 1000 ft. That range lies between depths normally explored in engineering seismic studies and those involved in petroleum exploration. Moreover, considerable geological data were available to which the seismic data could be related. Hence, the survey also sought to determine if seismic methods could extend and supplement existing geological information obtained from wells. Geophysical Service, Inc. of Dallas, Texas, was chosen to perform the 1 mo field study because of their research orientation and advanced data processing and evaluation methods.

Three principal sites were selected where the combinations of geological conditions differed appreciably, where locally detailed geological information was available, and where the confirmation and extension of that detail by new methods were highly desirable.

In reflection shooting, continuous profiling provided accurate depths to basalt when coupled with advanced computer techniques. Work proceeded rapidly with predrilled shot holes, although considerable drilling was required. The depth to basalt was difficult to determine when it was less than 600 ft. No basalt flows beneath the uppermost flow were identifiable with techniques that could be tried in the time available, because of the thin nature of the flows and the numerous interbeds that provided a highly complex layering problem.

Refraction methods accurately determined the depth to the surface of the Ringold Formation and the basalt. Computer processing of data was not necessary. Surface shooting with fertilizer-grade ammonium nitrate proved fully adequate and it eliminated the need of much drilling and the use of more expensive explosives. Separate beds within the Ringold Formation were noted in the drilling of "tie" holes, and their properties were determined by inwell logging and by uphole shooting. They could not be differentiated by refraction shooting, however, because of their lack of adequate extent and often thin nature. Variations in basalt velocities from site-to-site appeared to correlate well with the different flows which form the basalt surface.

Excellent performance and data were obtained by rotary drilling methods. Inwell logging combined with grab samples permitted excellent determinations of strata boundaries and indicated the practicability and desirability of use of rotary drilling in place of cable-tool drilling in some instances.

No single method of exploration appears adequately definitive and economical, however, for obtaining the geohydrological information that Hanford's experience has indicated to be desirable. A combined program of

rotary drilling, with inwell logging, for "tie" holes, and refraction seismic profiling appears to be the best combination of techniques.

The seismic results permitted the identification of materials that evidently are reworked Ringold Formation sediments intermediate in properties between the in-place Ringold sediments and the later glacio-fluviatile sediments. That identification is important in resolving the recent geological history of the area and in delineating old Columbia River channels in the Ringold Formation surface that readily transmit ground waters. The lowest known point on the local basalt surface was detected. This structural identification has a bearing on the possible movement of waste products at depth in confined aquifers. The apparent differentiation of two basalt flows, on the basis of the seismic wave velocities, confirmed and validated previous interpretations. The differentiation is important in defining the possible path of movement of low-level wastes into the uppermost part of the basalt series and potentially beneath land adjoining the Hanford Works.

All aims of the seismic program were achieved and sufficient data obtained to permit the planning of a production-type survey if such is considered desirable. Also, the information obtained from this program should have direct application in planning and carrying out similar studies at existing or potential nuclear plant sites.

Radioisotopes as Particulates and Volatiles

Subisokinetic Sampling of Particles in an Air Stream - G. A. Sehmel

The errors associated with sampling at filter face velocities much below the carrying stream velocity (subisokinetic) were studied. Data were obtained for several subisokinetic flow rates for wind speeds between 2.7 and 9 miles/hr. Zinc sulfide particles in the range of 2 to 25 microns were used. For the collector geometry used and the flow conditions imposed, a 10 micron diameter particle would appear to be present at a concentration as high as 2.4 times the actual concentration. Corrections for various diameter particles, sampling velocities, and relative subisokinetic rates are presented.

A true sample of an aerosol-laden air stream will be obtained only if the sample is withdrawn parallel to the stream flow and only if the air velocity through the aerosol collector is identical to the air stream velocity at the sampling point. Sampling with these conditions satisfied is termed "isokinetic". Additionally, the collector must be highly efficient and create a minimum of aerodynamic disturbances to the approaching air. In practice these requirements are seldom, if ever, absolutely achieved.

Fluorescent ZnS has long been used as a tracer in diffusion studies and more recently for particles in rain washout research. Practical considerations have required air sampling rates for this airborne material less than isokinetic (subisokinetic); in some experiments, far less. It is the purpose of this study to establish correction factors for various particle sizes and subisokinetic sampling rates for the ZnS particles used. The identical membrane filters and the polyethylene holders used in the atmospheric diffusion studies were to be employed in these measurements.

When the sampling rate is subisokinetic, some air initially in the projected area of the filter collector will be deflected around the collector. Larger and heavier particles will not be able to follow the air path and will impact on the filter. A nonrepresentative number of larger particles will be collected. In the extreme case all large particles approaching the collector in a cylinder of air of diameter equal to the filter diameter would be caught on the filter regardless of the amount of air drawn through the filter. Very small particles will follow the air paths because of their very low inertia.

The experimental measurement of the sampling error involves introducing the particles into an air stream circulating in a closed loop duct at a given velocity. At a point downstream a filter in its support is held with its face normal to the stream. Sampling is started and the rate adjusted to the isokinetic rate. Adjacent to this sampler is another filter and holder through which is drawn a sample at a lower flow rate controlled by a calibrated

critical orifice in the vacuum line behind the filter. After the sampling is complete, the number of particles in size increments is determined microscopically for the two filters. The quantity, N/N_o, for a given particle size is determined. N_o is the number of particles collected for a given size range on the isokinetic sample; N is the number found of the same size on the subisokinetic sample. If there is no error in the sampling method, this ratio should be identical to the ratio of the air flows through the subisokinetic filter, U, and through the isokinetic filter, U. The factor by which

$$\frac{N}{N_o} \cdot \frac{U_o}{U}$$

exceeds one is the correction to be applied to the air concentration determined by the subisokinetic sample. The indicated concentration will appear to be high by this factor.

The isokinetic filter sampler was modified to assist obtaining a representative sample. The front surface of the filter retaining ring was rounded back from the inlet to promote smoother air flow around the filter and the backing was replaced with a screen support. At the higher wind speeds it is impossible to collect at isokinetic velocity through the filter area because of the high pressure drop. In these situations a tapered nozzle inlet was provided. Some deposition occurs on this inlet nozzle and must be taken into account.

Results of the measurements are presented in Table 4.10 in which is shown the product

$$\frac{N}{N_o} \cdot \frac{U_o}{U}$$

as defined above.

The values in Table 4.10 are those from smoothed curves passed through the actual experimental data points for the particle sizes corresponding to the globe and circle graticule used. Inconsistencies in the data

Particle Deposition and Retention in Vertical Conduits - G. A. Sehmel and L. C. Schwendiman

Available experimental data relating to particle deposition were evaluated in an effort to establish agreement with a theoretical model or to develop a correlation more accurately disclosing the relationship of the deposition constant to the several variables. The data lend support to a theoretical model proposed; however, the precision of the data is such that critical comparison cannot be made. A parameter grouping was found with which the deposition constant could be better correlated. The parameter group was dominated by the reduced stopping distance term, S^+, used in the theoretical model. The empirical factor by which S^+ is adjusted results in the better correlation. A possible trend to higher than predicted deposition is indicated for very low values of reduced stopping distance, S^+.

Representative samples from gaseous streams containing fine particles of radioactive materials are commonly required in plants which process nuclear materials. Since the sample delivery lines are usually unavoidably long, information on the impaction and deposition of these particles is required to interpret the sample results in terms of the concentration in the gaseous streams.

Identification of the parameters controlling deposition on surfaces will contribute also to a better understanding of deposition of airborne particles on terrain and vegetation. The retention of particles on surfaces is also of interest in evaluating contamination spread and the degree of hazard from unusual incidents releasing appreciable quantities of radioactive aerosols.

It is the purpose of this study to determine the quantitative relationships among the variables governing particle deposition in conduits and to establish deposition models which are supported by the data.

Particulate deposition during turbulent flow has been measured by Friedlander and Johnstone, [4.32] and by Postma and Schwendiman. [4.33] In both studies, the deposition velocity, K, cm/sec, was determined from the average concentration of particles in the gas stream and the number of

particles counted on the tube wall. Deposition was measured in an incremental tube length for tube diameters in the range of 0.54 to 2.64 cm.

In studies during the past year the data in References (4.32) and (4.33), and the data of Sehmel and Schwendiman [4.34] for total deposition of ZnS particles * in a 17.7 length of 9.68 cm diameter vertical tube were reevaluated to determine how well the data available agreed with the model proposed by Friedlander and Johnstone. A second objective was to establish whether an empirical modification to the equations presented by Friedlander and Johnstone would give a better correlation.

The data available are shown in Figure 4.29, with $\frac{K}{V}$, the particle mass transfer coefficient, plotted as a function of S^+, the reduced stopping distance. The deposition velocity, K, is the quotient of the number of particles deposited per unit area per unit time divided by the average concentration of particles per cm^3. The average air flow velocity is V. The reduced stopping distance, S^+, is defined by the expression,

$$\frac{d^2 \rho_p f Re^2}{40 \rho D^2},$$

in which

d = particle diameter
ρ_p = particle density
f = Fanning friction factor
Re = Reynolds number for the conduit, $\frac{DV\rho}{\mu}$
ρ = gas density
D = conduit diameter
μ = gas viscosity.

The solid line shown in Figure 4.29 is the K/V predicted from the equations of Friedlander and Johnstone. [4.32] The equations are, for

---

* U.S. Radium Corporation fluorescent zinc sulfide No. 2210; average particle size = 2 microns.

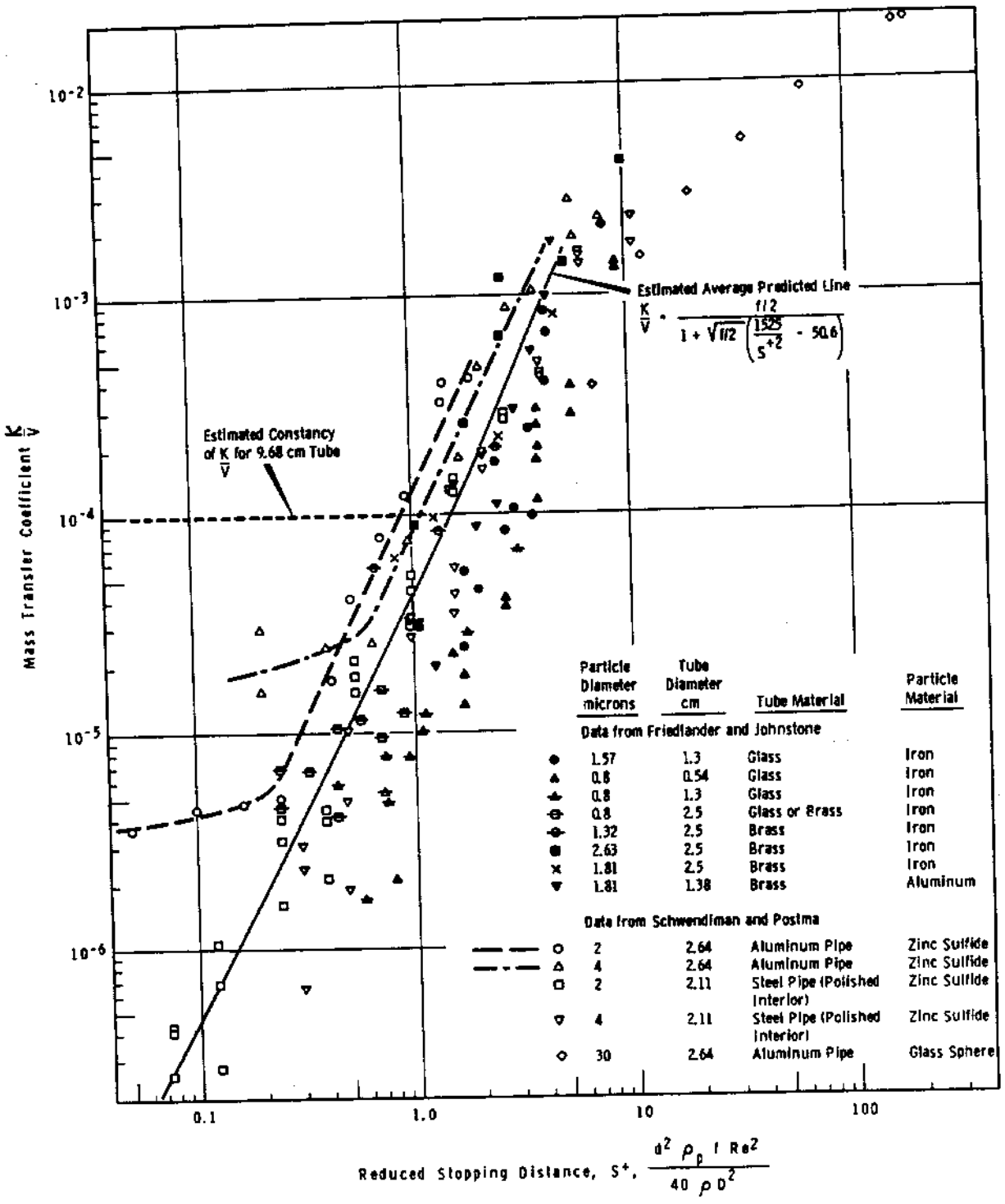

FIGURE 4.29

Mass Transfer Coefficient, K/V, as a Function of S^+

$S^+ \leq 5$,

$$\frac{K}{V} = \frac{f/2}{1 + \sqrt{f/2}\left(\frac{1525}{S^{+2}} - 50.6\right)}, \quad (1)$$

for $5 < S^+ < 30$,

$$\frac{K}{V} = \frac{f/2}{1 + \sqrt{f/2}\left[5 \ln\left(\frac{5.04}{S^+/5 - 0.959}\right) - 13.73\right]} \quad (2)$$

For S^+ between 5 and 30 the experimental K/V falls about a factor of two lower than the values predicted by Equation (2).

The data points as displayed in Figure 4.29 lend support to the equations proposed by Friedlander and Johnstone; however, the low precision of the bulk of the data does not permit critical comparison. The broken lines shown for two sets of data are drawn in to suggest that at low values of S^+ the actual deposition might be much higher than predicted by the equations. The deposition in the 9.68 cm diameter tube was such that a deposition constant well above the curve would be required to account for the deposition found in the tube. Since the tube diameter was much larger than for other tubes used, the relatively high deposition may be indicative of a dependence on diameter of greater effect than given by Friedlander and Johnstone's equations.

Others have shown [4.35, 4.36] that the deposition constant will decrease as particle size decreases until a minimum is reached, then increase. An observation of higher than predicted deposition or a trend toward constant deposition could be interpreted as an indication that the deposition had passed through or was approaching a minimum. Very small particles in laminar flow will deposit very significantly in conduits. Transition from turbulent to diffusional deposition will require that the deposition constant pass through a minimum.

An empirical modification to the stopping distance parameter resulted in an independent variable yielding a better correlation of the overall data. The least squares fit line and its equation are shown in Figure 4.30.

Considerable refinement in experimental methods is indicated before accurate prediction of deposition constants can be made.

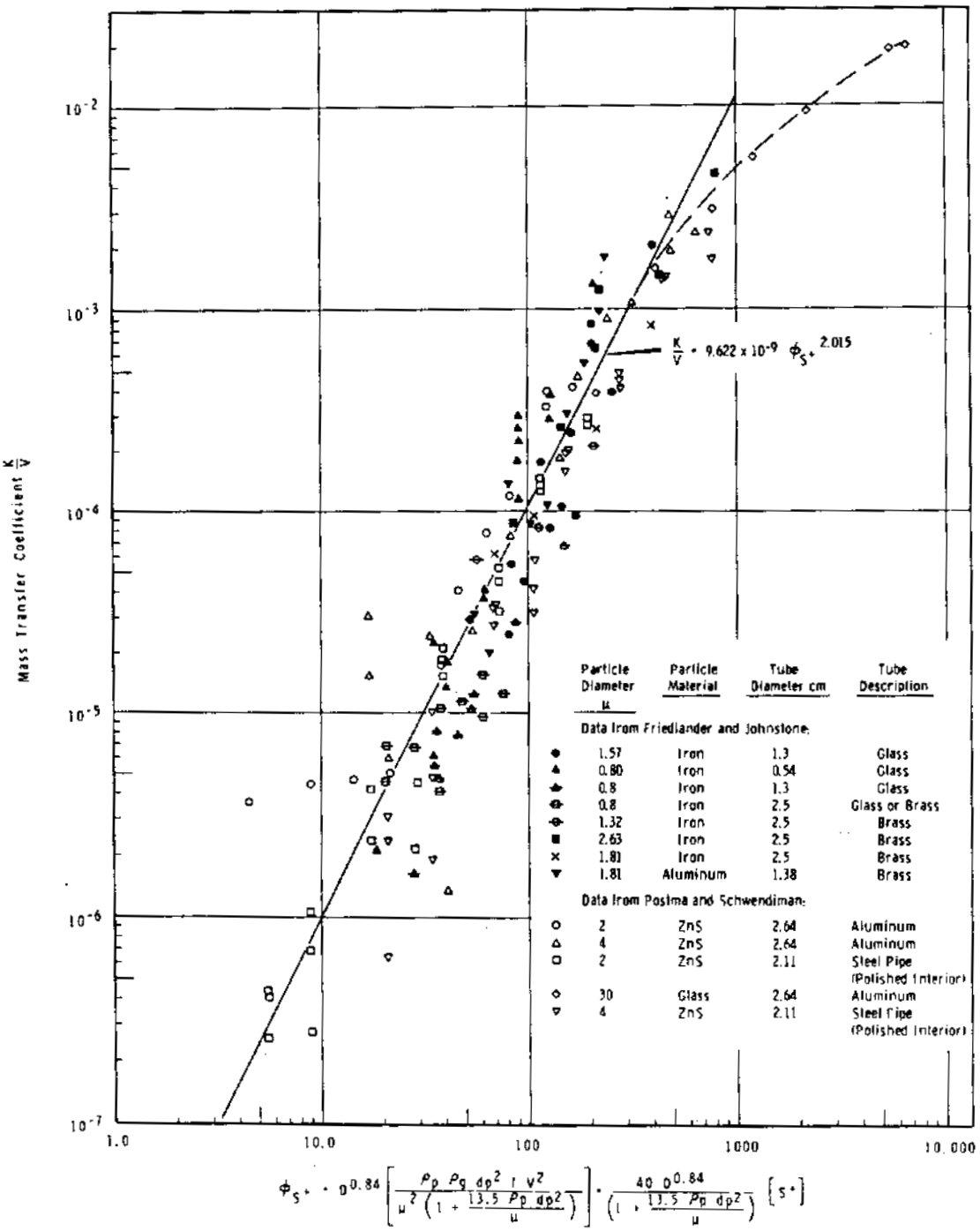

FIGURE 4.30

Mass Transfer Coefficient, K/V, as a Function of Φ_{S^+}

Efficiency of Charcoal for Radioiodine Absorption* - J. D. McCormack

The I^{131} retention of charcoal deteriorates materially over a period of 60 days when used on a separations plant gaseous stream. Studies on the stream and laboratory studies using tracer I^{131} showed: several organic constituents were present in the stream, hexone present didn't materially influence the elution of iodine, and methyl iodide at levels of 50 to 100 micrograms/g of charcoal is rather easily eluted by passing air through the charcoal. The need for carefully evaluating the efficiency of charcoal under the conditions to be imposed was emphasized by these studies.

Charcoal is used widely as an adsorbent for I^{131} in gaseous effluent streams because of its high efficiency for retaining molecular iodine under a rather wide range of humidities, temperatures, and iodine concentrations. Charcoal efficiencies, however, have been demonstrated almost exclusively using laboratory-generated iodine vapor with little consideration to the effects of actual chemical makeup of the carrying gas stream and the nature of iodine in these streams.

The observation that a newly installed charcoal bed in a plutonium extraction plant exhaust rather quickly became very inefficient for I^{131} removal, prompted studies to help identify the nature of I^{131} in the stream and to establish if possible the chemical constituents responsible for this lowered efficiency.

The exhaust stream was sampled in various ways to establish the reason for the lowered efficiency. Sampling with charcoal cartridges confirmed that the efficiency of charcoal, initially about 90% dropped gradually over a 2 mo exposure to about 30%. A caustic scrubber, efficient for removing molecular I^{131}, removed a variable quantity of iodine from the stream ranging frequently down to as little as 50%. Fresh charcoal proved much more efficient. This observation strongly suggested that compounds of iodine were present, likely organic iodides, although direct confirmation was not achieved.

---

* Charged in part to the Division of Biology and Medicine

Considerable refinement in experimental methods is indicated before accurate prediction of deposition constants can be made.

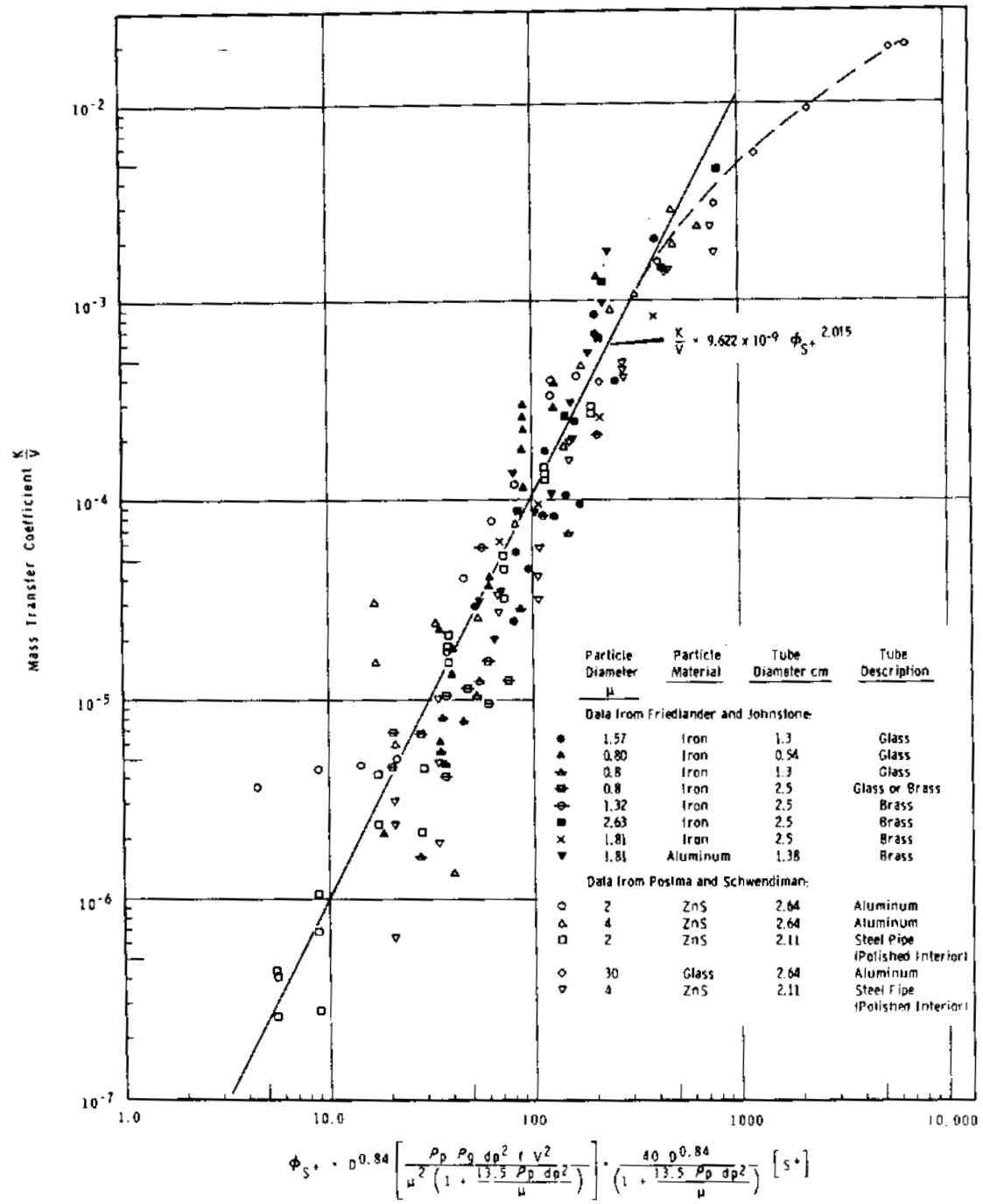

FIGURE 4.30

Mass Transfer Coefficient, K/V, as a Function of Φ_{S^+}

Some nine different organic constituents were collected on charcoal from the effluent as judged by chromatographic separation of the desorbed materials. Hexone was present to a significant degree, but was shown to not be interacting appreciably with I^{131} present on charcoal. Nearly all the hexone could be desorbed while removing less than 10% of the I^{131} on the charcoal. The other organic compounds have not been identified.

The transient retention of methyl iodide on charcoal was demonstrated using I^{131}-tagged CH_3I. Three grades of charcoal upon which small quantities (about 50 to 100 micrograms) of methyl iodide were adsorbed released the iodine rather quickly when air was passed through the bed. An elution half-time of 6 to 8 hr was found. These data discourage the use of charcoal for adsorbing iodine in forms other than molecular iodine, particularly in applications in which continued I^{131} releases are anticipated.

This study has shown clearly that satisfactory application of charcoal for removing iodine may not be achieved when the carrying gas contains traces of organic materials. The charcoal efficiency is further a marked function of the form of the iodine present. The stream examined had an unusually complex composition and definition of each compound present was not achieved.

Particle Deposition in 90° Tube Bends - A. K. Postma and L. C. Schwendiman

The turbulent deposition of particles in 90° tube bends was measured for several flow rates and particle sizes. The bends were formed to an inside radius of 3.8 or 11 cm, in 1.01 cm inside diameter aluminum tubing. Deposition was found to be highly significant (up to 75%) for 7 micron particles. Two-micron particles were not significantly deposited. Deposition increased about linearly with air flow. Effects of particle density were not determined. The spinning disc aerosol generator used proved of great value in this study.

Particles are carried to the wall in tube bends due to the centrifugal force acting on the particle moving in the curved path. In turbulent flow,

Figure 4.32 shows more clearly the influence of velocity and particle size on deposition in the 90° bend. Deposition varies approximately linearly with velocity. Deposition is significant for 4 micron particles, but of no consequence for 2 micron particles of density 1.1. Insufficient data were obtained to establish the influence of radius of bend on deposition.

This brief study emphasized the very significant wall losses which occur when relatively short radius bends are placed in lines. The parameter of bend radius was not investigated to any degree, neither were surface roughness or particle density effects evaluated.

The spinning disc generator proved to be an excellent device for preparing aerosols for this study.

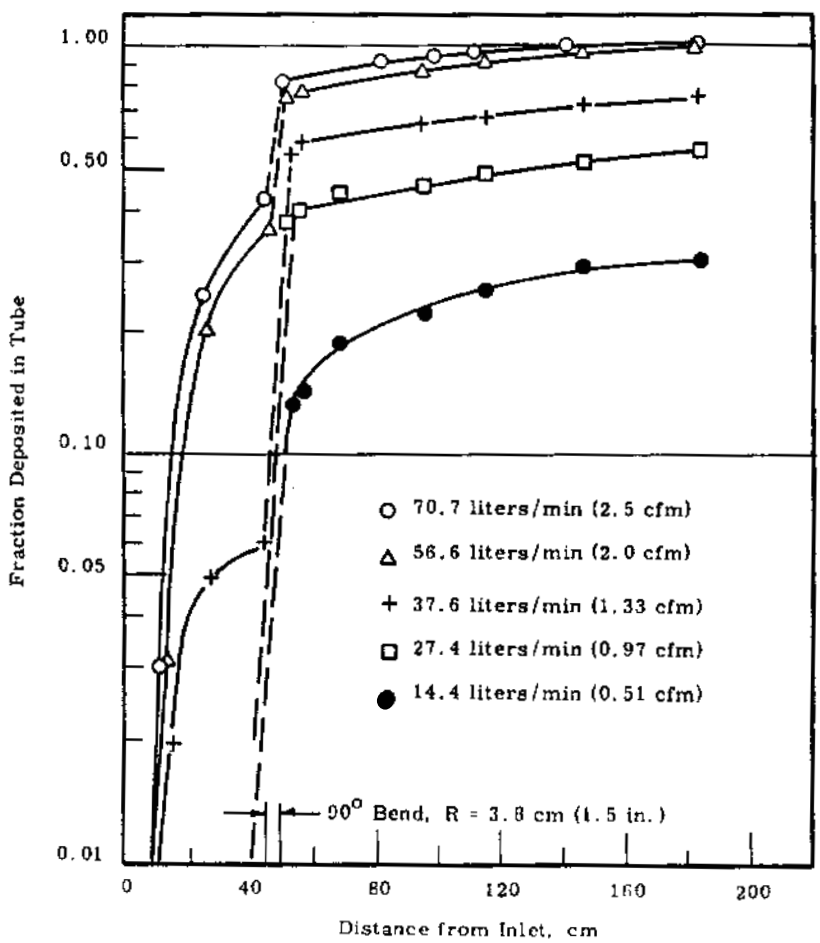

FIGURE 4.32

Deposition of 7.4 micron, Density 1.1 Particles in a 1.01 cm Inside Diameter Tube with a 90° Bend

REFERENCES

4.1 L. L. Ames, Jr. "Synthesis of a Clinoptilolite-like Zeolite," American Mineralogist, vol. 48, pp. 1374-1381. 1963

4.2 R. L. Hay. "Origin and Diagenetic Alteration of the Lower Part of the John Day Formation near Mitchell, Oregon. Petrological Studies," A volume in honor of A. F. Buddington. Geol. Soc. Am., pp. 191-216. 1962.

4.3 R. M. Barrer and W. M. Meier. "Exchange Equilibria in a Synthetic Crystalline Exchanger," Trans. Faraday Soc., vol. 55, pp. 130-141. 1959.

4.4 R. M. Barrer and W. M. Meier. "Structural and Ion Sieve Properties of a Synthetic Crystalline Exchanger," Trans. Faraday Soc., vol 54, pp. 1074-1085.

4.5 E. Glueckauf. "Activity Coefficient in Concentrated Solutions Containing Several Electrolytes," Nature, vol. 163, pp. 414-415. 1949.

4.6 E. Ekedahl, E. Hogfeldt and L. G. Sillen. "Activities of the Components in Ion Exchangers," Acta Chem Scand., vol. 4, pp. 556-558. 1950.

4.7 J. Crank. "Diffusion with Rapid Irreversible Immobilization," Trans. Faraday Soc., vol. 53, pp. 1083-1091. 1957.

4.8 L. L. Ames, Jr. "Some Zeolite Equilibria with Alkali Metal Cations," Am. Mineralogist., vol. 49. 1964. (HW-SA-3031) 4-16-63.

4.9 R. W. Nelson and A. E. Reisenauer. "Hanford Studies on Flow in Porous Media," Proceedings of the Second Ground Disposal of Radioactive Wastes Conference," Atomic Energy of Canada Ltd., September 26-29, 1961. TID-7628, pp. 130-144. (HW-SA-2251. 8-10-61.)

REFERENCES (Contd.)

4.10 D. J. Brown. "Piezometric Head Distribution in Sand-Filled Wells," J. Hydrol, vol. 2, No. 1. March 1964.

4.11 L. A. Richards. "Capillary Conduction of Liquids Through Porous Mediums," Physics, vol. 1, pp. 318-333. 1931.

4.12 W. B. Haines. "Studies in the Physical Properties of Soil. V. The Hysteresis Effect in Capillary Properties and the Modes of Moisture Distribtuion Associated Therewith," J. Agr. Sci., vol. 20, pp. 97-116. 1930.

4.13 E. E. Miller and R. D. Miller. "Physical Theory for Capillary Flow Phenomena," J. Appl. Phys., vol. 27, pp. 324-332. 1956.

4.14 E. C. Childs. "The Water Table, Equipotentials, and Streamlines in Drained Land," III. Soil Sci., vol. 59, pp. 405-415. 1945.

4.15 V. H. Scott and A. T. Corey. "Pressure Distribution During Steady Flow in Unsaturated Sands," Soil Sci. Soc. Am. Proc., vol. 25, pp. 270-274. 1961.

4.16 H. Ferguson and W. H. Gardner. "Water Content Measurement in Soil Columns by Gamma Ray Absorption," Soil Sci. Soc. Am. Proc., vol. 26, pp. 11-14. 1962

4.17 R. D. Jackson, R. J. Reginato, and W. E. Reeves. "A Mechanized Device for Packing Soil Columns," U. S. Dep. Agr. - ARS 41-52. 1962.

4.18 R. A. Schleusener and A. T. Corey. "The Role of Hysteresis in Reducing Evaporation from Soils in Contact with a Water Table," J. Geophys. Res., vol. 64, pp. 469-475. 1959.

4.19 W. R. Gardner. "Some Steady-State Solutions of the Unsaturated Moisture Flow Equation with Application to Evaporation from a Water Table," Soil Sci., vol. 85, pp. 228-232. 1958.

REFERENCES (Contd.)

4.20 R. J. Hanks and S. A. Bowers. "Influence of Variations in the Diffusivity-Water Content Relation on Infiltration," Soil Sci. Soc. Am. Proc., vol. 27, pp. 263-265. 1963.

4.21 R. H. Brooks and A. T. Corey. "Hydraulic Properties of Porous Media and Their Relation to Drainage Design," Paper No. 63 - 214, presented at the Annual Meeting of the Am. Soc. Agr. Eng., Miami Beach, Florida. June 1963.

4.22 R. W. Nelson. "In-Place Measurement of Permeability in Heterogeneous Media. I. Theory of a Proposed Method," J. Geophys. Research, vol. 65, no. 6, pp. 1753-1758. 1960.

4.23 R. W. Nelson. "In-Place Measurement of Permeability in Heterogeneous Media. II. Experimental and Computional Considerations," J. Geophys. Research, vol. 66, no. 8, pp. 2469-2478. 1961.

4.24 C. A. Oster. GENORO, A General Data Fitting and Linear Functional Evaluation Computer Code for the IBM 7090, HW-76692. May 1963.

4.25 R. W. Nelson. Stream Functions for Three-Dimensional Flow in Heterogeneous Porous Media, HW-SA-2772. March 15, 1963. Proceedings of the Thirteenth General Assembly Intern. Assoc. Geodesic and Geophysics. Berkeley, California. August 1963.

4.26 R. W. Nelson. "Stream Functions for Steady State Flow in Heterogeneous Porous Media," Hanford Radiological Sciences Research and Development Annual Report for 1962, HW-77609. pp. 4.25 - 4.28. January 1963.

4.27 F. F. Golubev. "Lectures on Integration of the Equations of Motion of a Rigid Body About a Fixed Point," State Publishing House of Theoretical Technical Literature, Moscow, p. 229. 1953. (U.S. National Science Foundation Translation, Office of Technical Publications., Dept. of Commerce. 1960)

REFERENCES (Contd.)

4.28 P. W. Werner and D. Noren. "Progressive Waves in Non-Artesian Aquifers," Am. Geophys. Union Trans., vol. 32, pp. 238-244. 1951.

4.29 J. G. Ferris. "Cyclic Fluctuations of Water Level as a Basis for Determining Aquifer Transmissibility," International Geod. Geophys. Union Association of Scientific Hydrology, General Assembly. Brussels, vol. 2, pp. 148 - 155. 1951.

4.30 P. P. Rowe. "An Equation for Estimating Transmissibility and Coefficient of Storage from River-Level Fluctuation," J. Geophys. Research., vol. 65, no. 10, pp. 3419-3424. 1960.

4.31 R. C. Newcomb and S. G. Brown. "Evaluation of Bank Storage Along the Columbia River Between Richland and China Bar, Washington," U.S. Geol. Survey Water-Supply Paper 1539-I. 1961. U.S. Goverment Printing Office, Washington, D.C.

4.32 S. K. Friedlander and H. F. Johnstone. "Deposition of Suspended Particles from Turbulent Gas Streams," Ind. Eng. Chem., vol. 49, pp. 1151-1156. 1957.

4.33 A. K. Postma and L. C. Schwendiman. Studies in Micromeritics, I. Particle Deposition in Conduits as a Source of Error in Aerosol Sampling, HW-65308. May 1960.

4.34 G. A. Sehmel and L. C. Schwendiman. "The Turbulent Transport and Deposition of Particles within Vertical Tubes," Eighth AEC Air Cleaning Conference, Oak Ridge, Tennessee, October 22-25, 1963, HW-SA-3183. 1963.

4.35 C. Wells. Unpublished Data. 1963. Atomic Energy Research Establishment, Harwell, England. (Personal Communication)

4.36 L. C. Schwendiman, G. A. Sehmel, A. K. Postma. "Radioactive Particle Retention in Aerosol Transport Systems," International Conference on the Radioactive Pollution of Gaseous Media, Saclay, France, November 12-16, 1963, HW-SA-3210. 1963.

INSTRUMENTATION

Automatic Monitoring and Recording Methods

Detection of Air Concentrations of Fluorescent Material for Atmospheric Physics Studies - M. O. Rankin and E. M. Sheen*

Atmospheric physics field diffusion experiments require measurement of airborne particulate concentrations. An instrument was developed to monitor a scintillating tracer material on a real time basis, and three monitors were assembled for use in the experiments. The data obtained will provide information about the time history of such airborne concentrations which contribute to the mean concentration. The developed instrument includes a sampler probe where the particles (2210 fluorescent pigment) are exposed to ultraviolet light, a viewing chamber where a phototube is used to detect the phosphorescent particles, and a recorder. The minimum detectable air concentration was determined, through a series of experiments, to be 4×10^{-7} g/m^3.

Discussion

An instrument[5.1] was developed to measure air concentrations of fluorescent particles on a real time basis during atmospheric physics diffusion studies. Within the technical limitations of the sampling instrument, parameters such as source height, meteorological conditions, terrain, vegetation, and distance from the source can be related to time-dependent variables such as arrival and departure of the contaminant, percent of time contaminant is detectable, or peak to mean air concentrations.

The sampler probe is shown schematically in Figure 5.1. Pigment enters a chamber where it is exposed to ultraviolet light from a 100 w mercury vapor lamp. The pigment then passes to the viewing chamber where the phosphorescence is observed with a multiplier phototube. Both the instantaneous and the integrated anode current of the phototube are presented on a

---

* In cooperation with P. W. Nickola and M. F. Scoggins of Atmospheric Physics

dual pen strip chart recorder. A light trap, formed by mating concentric circles, is placed between the multiplier phototube and the mercury lamp.

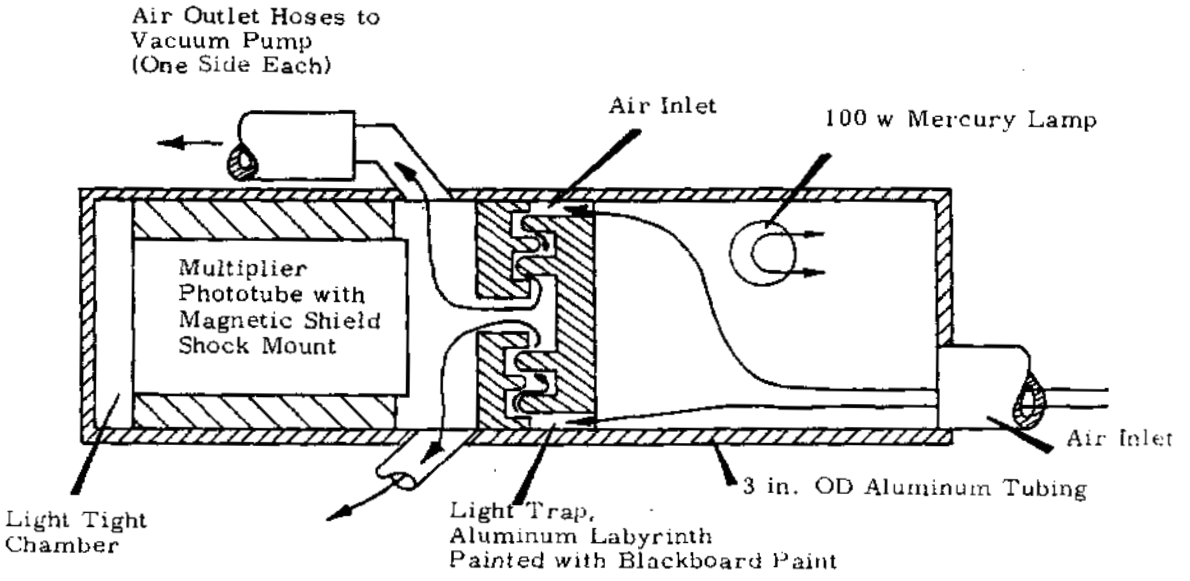

FIGURE 5.1

Probe of Airborne Fluorescent Particle Detection Instrument

The disassembled probe, Figure 5.2, shows the lamp, light trap, phototube and a holder for a light source. The light source (not shown) utilizes Pm^{147}-activated self-luminous paint on a retractable aluminum disc to field check the phototube gain. The phototube base wiring and current range resistors are shown in Figure 5.3. The anode current is converted to voltage by resistors R-12 through R-18, and the most sensitive range of the instrument is 3 namp/mv. Figure 5.4 shows the complete system as mounted in a light truck for field operational use. The instrument system uses a gasoline-

powered motor generator to supply 110 vac for the operation of the mercury-vapor lamp and the recorder. High voltage for the phototube, usually 500 to to 1200 vdc, is obtained from a battery-powered, corona-tube-regulated, miniature, high voltage supply.

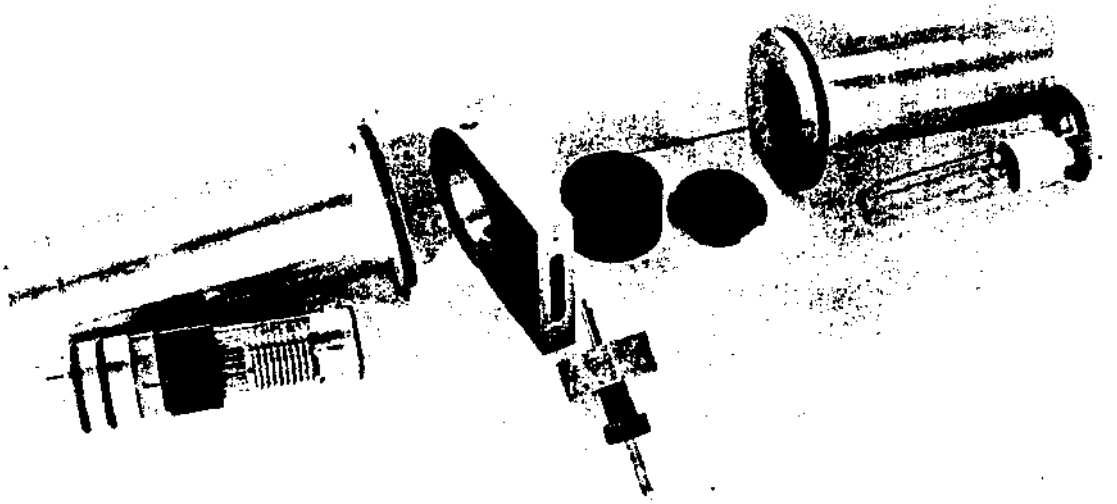

FIGURE 5.2
Disassembled Detection Probe

Calibration of the sampling instruments is accomplished primarily during their use in routine field experiments. A filter of a type normally used in Hanford atmospheric diffusion studies is exposed as close to the real time sampler as practical, i.e., within 6 in. These filters are removed and replaced after each "puff" of tracer passes, as is indicated by the real time record. A knowledge of the flow rate through the real time sampler and the adjacent routine filter, the interval over which the tracer was collected, and the mass of tracer passing through the real time sampler, as determined from the adjacent filter, permits a calibration of the real time sampler in terms of mass per unit volume. Since the mass of tracer passing through the real time device is the integral of the instantaneous concentration, the automatic integrating feature of the recorder has proven to be a valuable asset in the calibration.

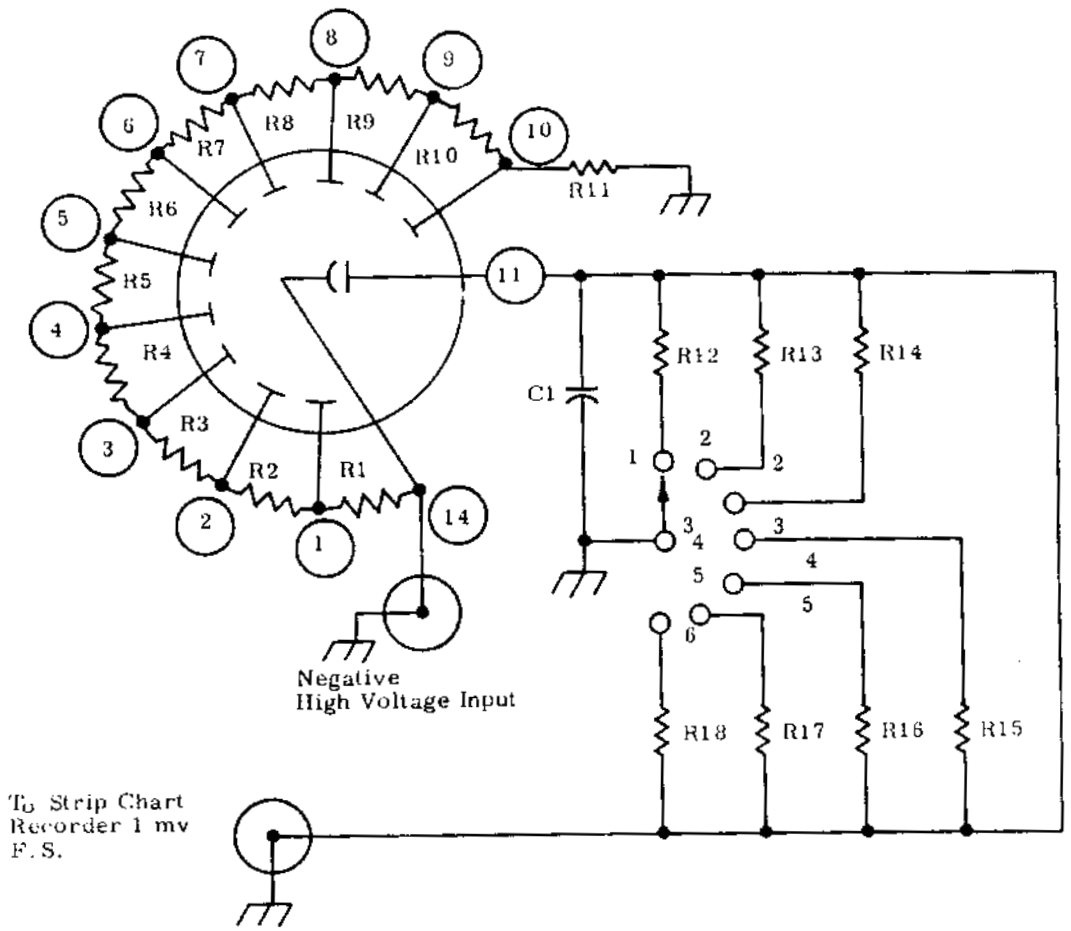

Note:

R1; 4.7MΩ, 1/2 w ± 10%
R2 through R11; 2.2 MΩ, 1/2 w ± 10%
R12; 332Ω, ± 1%, Position 1, 3 μamp/mv
R13; 1000Ω, ±1%, Position 2, 1 μamp/mv
R14; 332Ω, ±1%, Position 3, 300 namp/mv
R15; 10.0 kΩ, ± 1%, Position 4, 100 namp/mv
R16; 33.2 kΩ, ± 1%, Position 5, 30 namp/mv
R17; 100 kΩ, ± 1%, Position 6, 10 namp/mv
R18; 332 kΩ, ±1%, Position 7, 3 namp/mv
C1; 0.01 μf, 400 v dc, Mylar
Multiplier Phototube; EMI-US 9536 B

FIGURE 5.3

Multiplier Phototube Connections and Components
for Particle Detection Instrument

AEC GE RICHLAND, WASH.

FIGURE 5.4
Particle Detection System Assembled for Field Use

Experience to date suggests that the chart calibration for concentration is linear and is about 2×10^{-7} g/m^3 per chart unit. Full chart scale is 100 units (10 in.) A drift in recorded background voltage of about 4 units was observed over a period of 75 min; however, the drift was less than 2 units over a period of 1 min. If it is concluded that the minimum detectable concentration is equal to the short-period range in background, the detection limit of the device is 4×10^{-7} g/m^3. The three completed monitors are nearly ready for regular operational use during the planned diffusion experiments.

Automatic Data System for Atmospheric Physics Studies - E. M. Sheen and C. A. Ratcliffe

An automatic data collection and recording system was developed for use in atmospheric physics micrometeorological studies regarding air diffusion and particulate transport. Wind speed, wind direction, and temperature data are collected from six stations mounted on an 80 ft portable field tower. A 5 sec collection time interval is employed as this permits short term analysis and recording of the variables. The collected information is digitized and printed and is also presented on punched paper tape for use in computer reduction. Except for minor difficulties with a commercial digital voltmeter used in the system, general field tests, conducted over a period of several months, indicated that satisfactory operation could be achieved.

Discussion

Atmospheric physics air diffusion and particulate transport studies are conducted and detailed micrometeorological data are required. These data are concerned with changes in atmospheric temperature, wind speed, and wind direction gradients in the initial 80 to 100 ft of elevation. An automatic data system was developed for use in measuring and recording the desired parameters.

Figure 5.5 shows the major portion of the electronics system. Figure 5.6 is a photograph of an 80 ft portable field tower or mast that holds six anemometers, six wind vanes, and six thermocouples at various elevations as required for the specific experiments.

Figure 5.7 is a block diagram of the instrumentation system. In operation, the 20 point and 6 point sequencers direct the collection and printing of the data. In addition, a 15 point sequencer controls the serializing of the data to a form required by the incorporated paper tape punch.

Wind speed data, which arrives at the main instrument in pulse-rate form from the specially circuited high performance anemometers, are gated and stored in individual registers for 3.5 sec of the normal 5 sec collection time interval and then are printed in appropriate sequence. The storage time

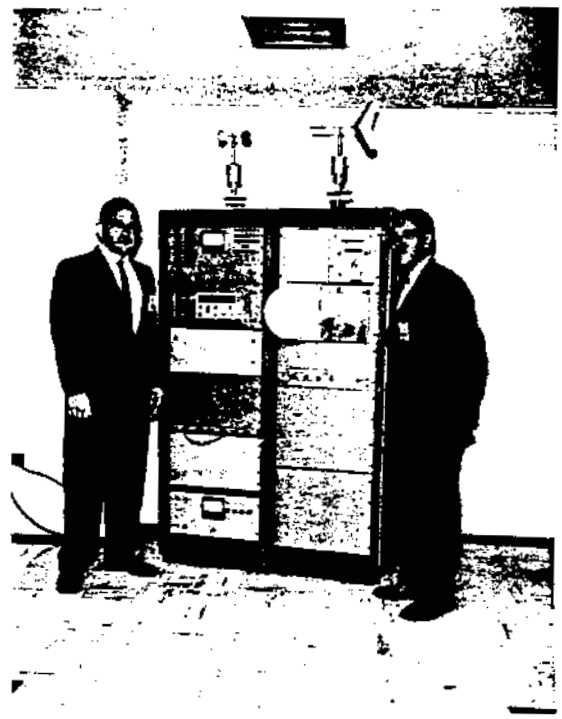

FIGURE 5.5
Automatic Data System Electronics Instrumentation

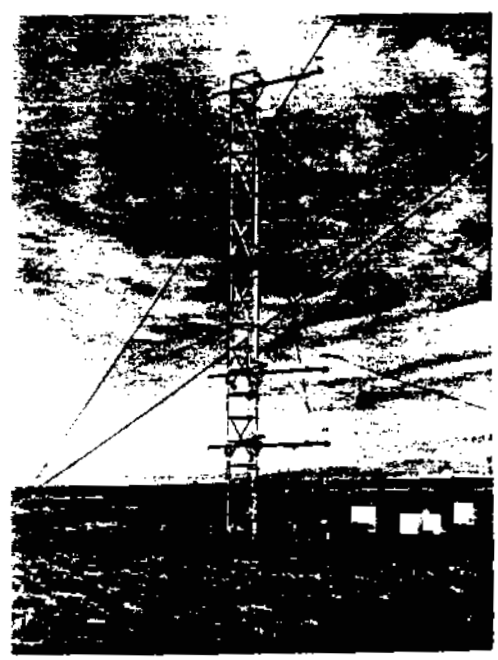

FIGURE 5.6
Portable Field Tower for Atmospheric Physics Studies

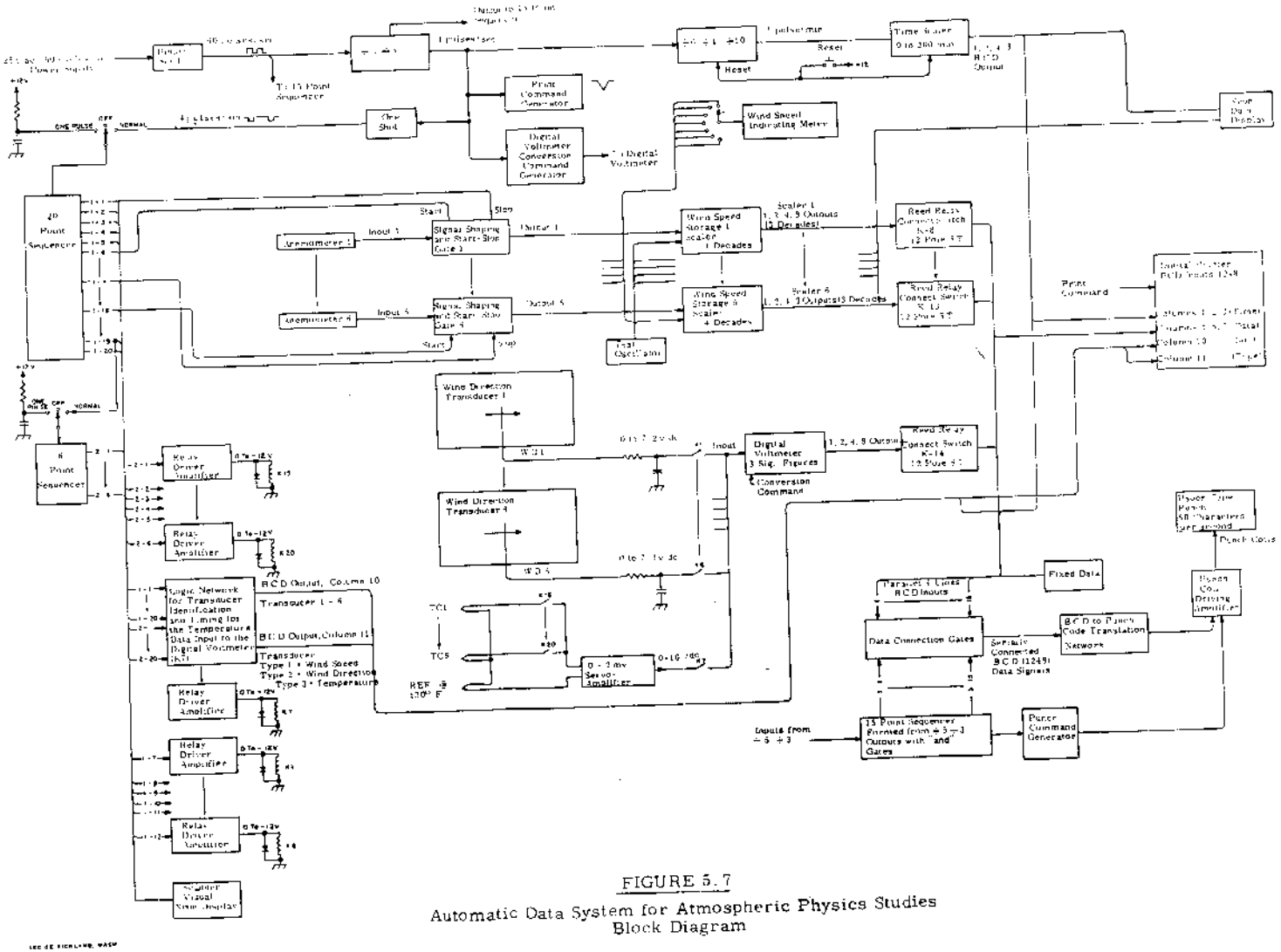

FIGURE 5.7
Automatic Data System for Atmospheric Physics Studies
Block Diagram

employed makes the calibration factor between true and indicated wind speeds very nearly equal to one. The wind direction data are obtained from potentiometers driven by the high performance wind vanes. These voltages are smoothed by RC networks and are switched in sequence to the digital voltmeter for appropriate digitizing. After being digitized, the information is printed. The temperatures are measured by thermocouples; the signals are compared to a reference and amplified and then are digitized and printed. The sequencers that control the digitizing and printing also create identification symbols to be printed with the data. Time information is also printed.

Simultaneously with printing, a "parallel-to-serial" converter changes the signals on the several wires to a sequential signal suitable for use by the paper tape punch. Included in the sequential signal are appropriate fixed signals needed in the data reduction process.

Since the portable field tower and the main electronic instrument system are separated by about 500 ft of cable, certain precautions were required to avoid degradation of the signal. For the temperature measuring portion, the required reference signal was supplied remotely at the base of the tower and the difference signal was brought to the main instrumentation in a separate, shielded, twisted pair cable. The reference signal is generated by a "bucking" thermocouple that is housed in a constant temperature oven and is sequentially switched into each of the measuring circuits. This method of connection permits use of copper leads to the main instrument since copper-constantan thermocouples were used. The switching relays used were carefully selected to be of a thermally-symmetrical type to avoid the introduction of spurious thermally-induced voltages.

The signals from the anemometers required careful processing to avoid loss due to cable capacitance and attenuation or contamination by adjacent cable pair "cross talk". A preamplifier was developed which preserved the sinusoidal character of the waveshape and was able to drive the cable as a terminated transmission line. Signal shaping gates were

developed and used at the receiving end to convert the signal to a form suitable for driving the decade scalers.

A sound-powered telephone was included for communication between the main instrumentation and the field tower.

Solid-state 200 kc/sec logic modules were used to perform the scaling and some of the sequencing and logic operations. Both diode and transistor "AND" and "OR" gates were used. The sequencers were obtained by appropriately connecting binaries and "AND" gates to provide a "ONE" output sequentially at the output terminals. Logic levels of 0 to -1 and -10 to -12 were used for all of the logic circuits. A single power supply was designed to provide regulated ± v dc to the card files and relay drivers respectively. Separate fused outputs were provided to each card file.

The completed system is presently undergoing extensive field tests and is being carefully examined for early component failures. Preliminary operational results indicate reliable, satisfactory operation.

Radiotelemetering System Improvements - C. A. Ratcliffe and E. M. Sheen

To achieve improved operational capabilities and reliability, considerable circuitry development was undertaken on the Meteorological Radiotelemetry System with the work supported by Atmospheric Physics funds. A thorough system study was conducted and specific circuits were than developed to replace those of marginal capability. Major problems were noted with the remote data stations (19) and the resultant development activities were concentrated in this area. One data station was, in essence, redesigned to incorporate the desired improvements. Following initial testing of this field prototype, a second data station was similarly converted to provide comparative data. The basic improvements incorporated included elimination of vacuum tube circuits, elimination of most of the original relays and other moving parts, development of a three range radiation monitoring portion, and incorporation of a simpler and more reliable wind direction measurement scheme. Preliminary testing of the field prototype data station has shown satisfactory performance over a wide range of ambient conditions, and plans were established for thorough in-field testing of both modified data stations. The completed system is slated to provide wind speed, wind direction, and radiation level data from various Hanford locations.

Discussion

Following careful study of the Meteorological Radiotelemetry System, planned developments were conducted to improve operational capabilities and general system reliability. It was determined from the study that general upgrading and modernization approaches would be required, especially for the many remote data stations employed in the system.

The initial development activity was devoted to improvement of the remote data stations; one modified station is shown in Figure 5.8. Because of generally unsatisfactory preformance of the original 6 v battery and wind charger scheme for supplying power to the data stations, a general conversion was made to permit use of 110 v ac line power for all necessary stations. A regulated power supply was designed and tested over the expected ambient conditions. This unit supplies all power for the incorporated circuit modules and for the transceiver. The supply is shown schematically in Figure 5.9.

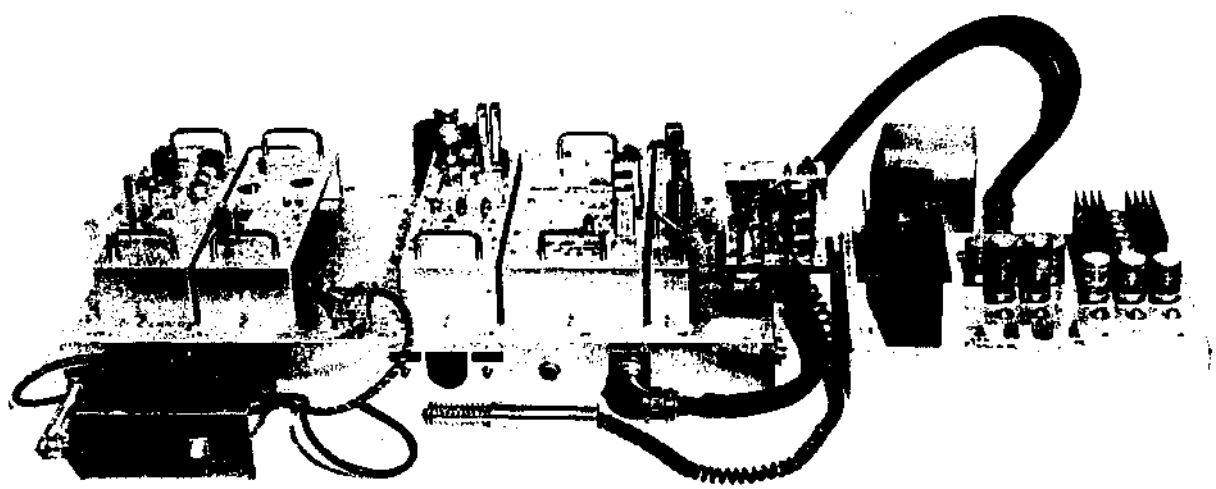

FIGURE 5.8
Remote Data Station of Radiotelemetering System

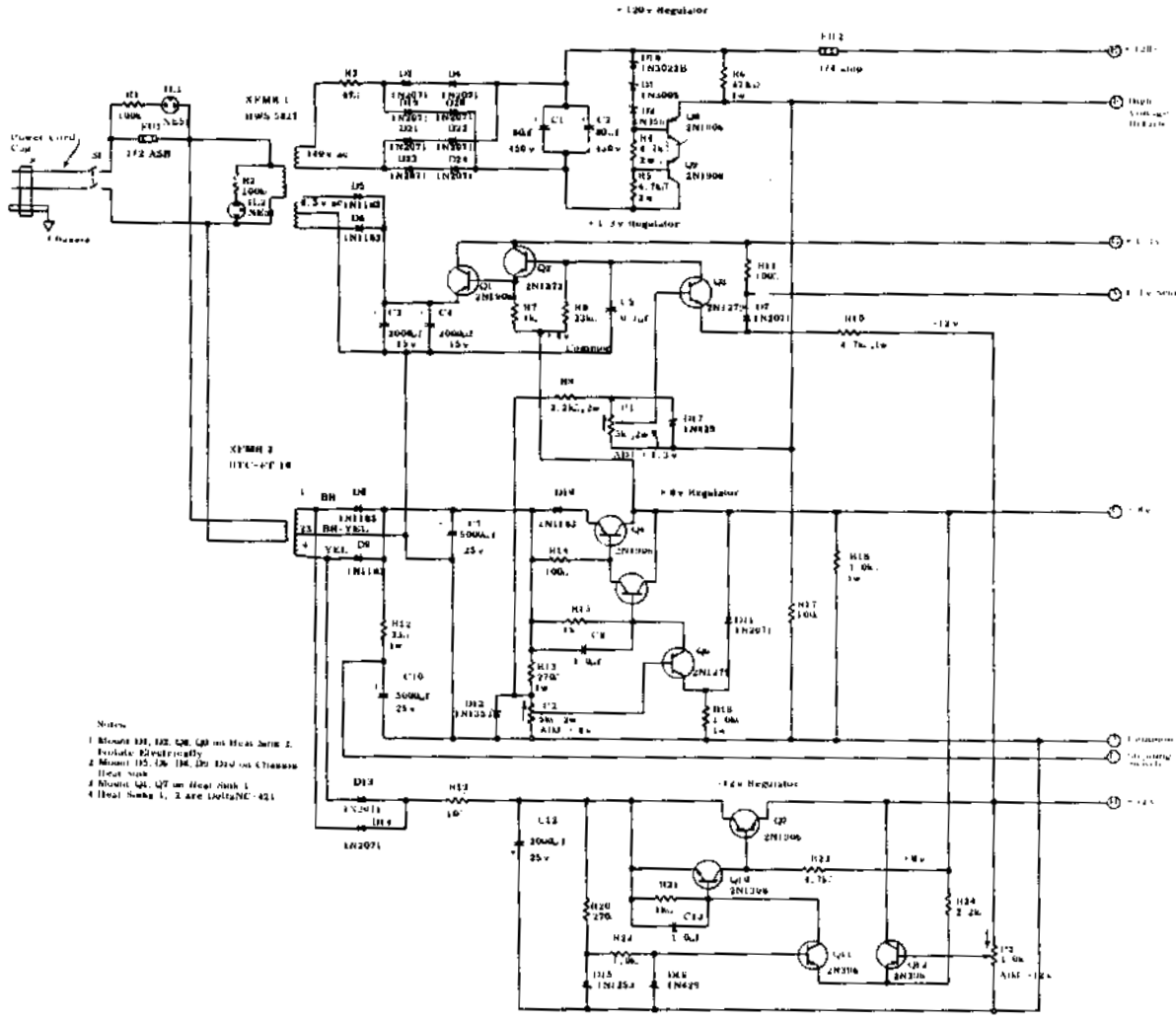

FIGURE 5.9

Power Supply Circuitry for Remote Data Station

AEC-GE-RICHLAND, WASH.

One of the chronic problems in the remote data stations concerned the voltage controlled oscillator. A solid state circuit was developed, using feedback control for stability, to replace the original chopper and vacuum tube circuitry. The voltage controlled oscillator that was developed (Figure 5.10) requires only 0.2 μamp of input current and this minor loading does not appreciably discharge the signal storing capacitors. Figure 5.10 also shows the driving amplifiers for the resonant reed relays.

The original method of reporting integrated wind direction, while having theoretical advantages, involved a servo-mechanism, several large relays, a power oscillator, and several other moving parts for performance. The data, in practice, were of low credibility. The new direction reporting system involves passive short term smoothing and sends back the sine and cosine components separately. The direction angle is determined by using a simple conversion chart. Longer term smoothing may be obtained by more frequent call-in, an existing feature. Nearly two subchassis of circuit components were eliminated by these changes.

The original beta-gamma radiation measurement system integrated the electric charge from window-type ion chambers and presented this as dose information. Two full scale dose ranges of 100 μrads and 1 rad were provided, assuming negligible charge leakage. To avoid the problems associated with the fragile low-leakage ion chamber system, a 3 channel, G.M. tube, count-rate circuit was developed to provide a relative indication of background radiation and possible contamination at the data station location. A single high voltage supply, G.M. tube, and an amplifier drive the 3-channel, count-rate circuit [5.2] which provides linear (±1%) voltage outputs from 0 to 5 v dc for each channel. Count-rates above full scale on any channel saturate the output at 5 v. The three channels are 0 to 10^3, 10^4, and 10^5 counts/min respectively. Figure 5.11 shows the circuit diagram for the G.M. tube radiation monitor.

Circuit tests were conducted with the original vacuum tube transceiver. However, a solid state unit has been ordered for evaluation and testing

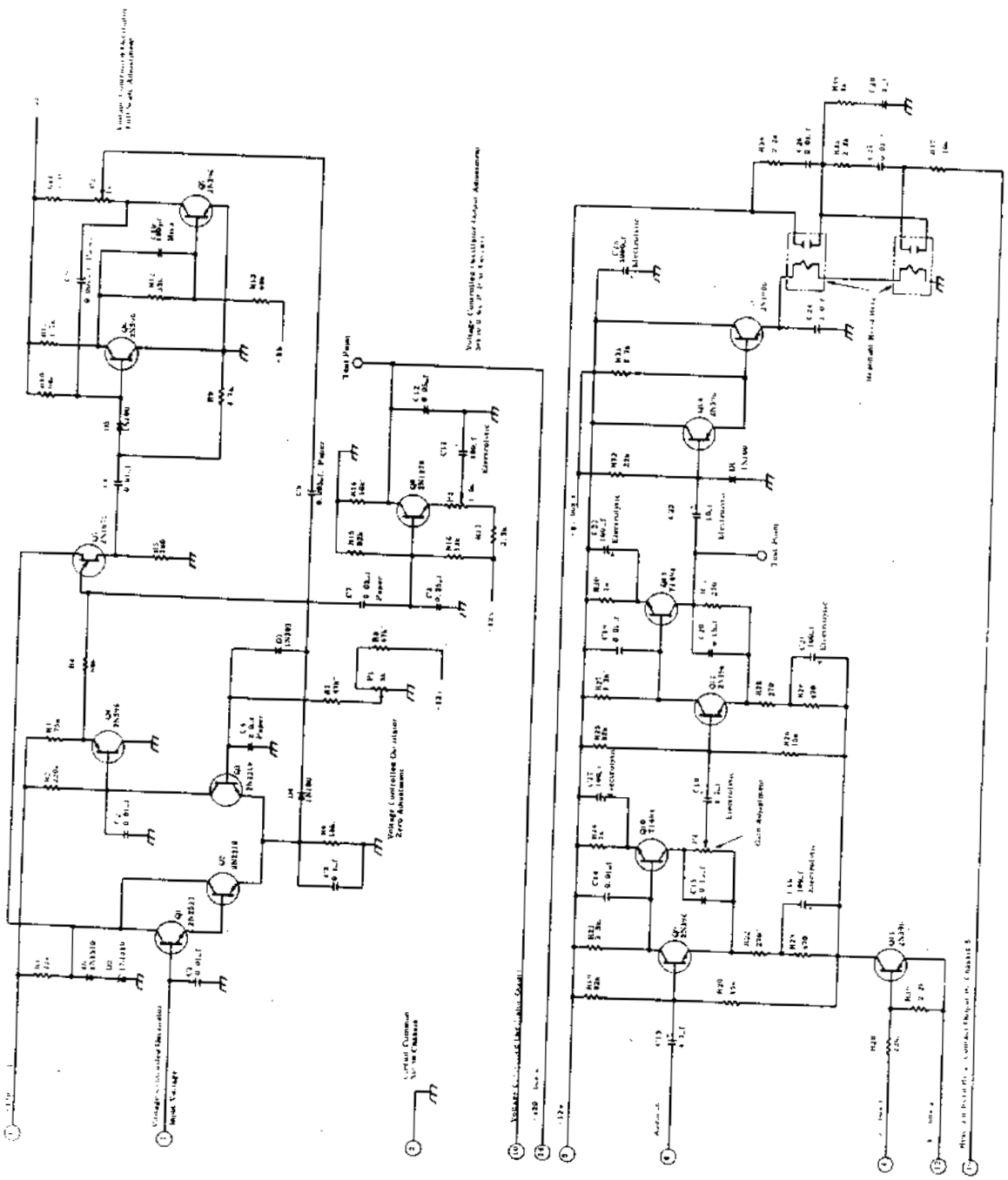

FIGURE 5.10
Voltage Controlled Oscillator Circuitry

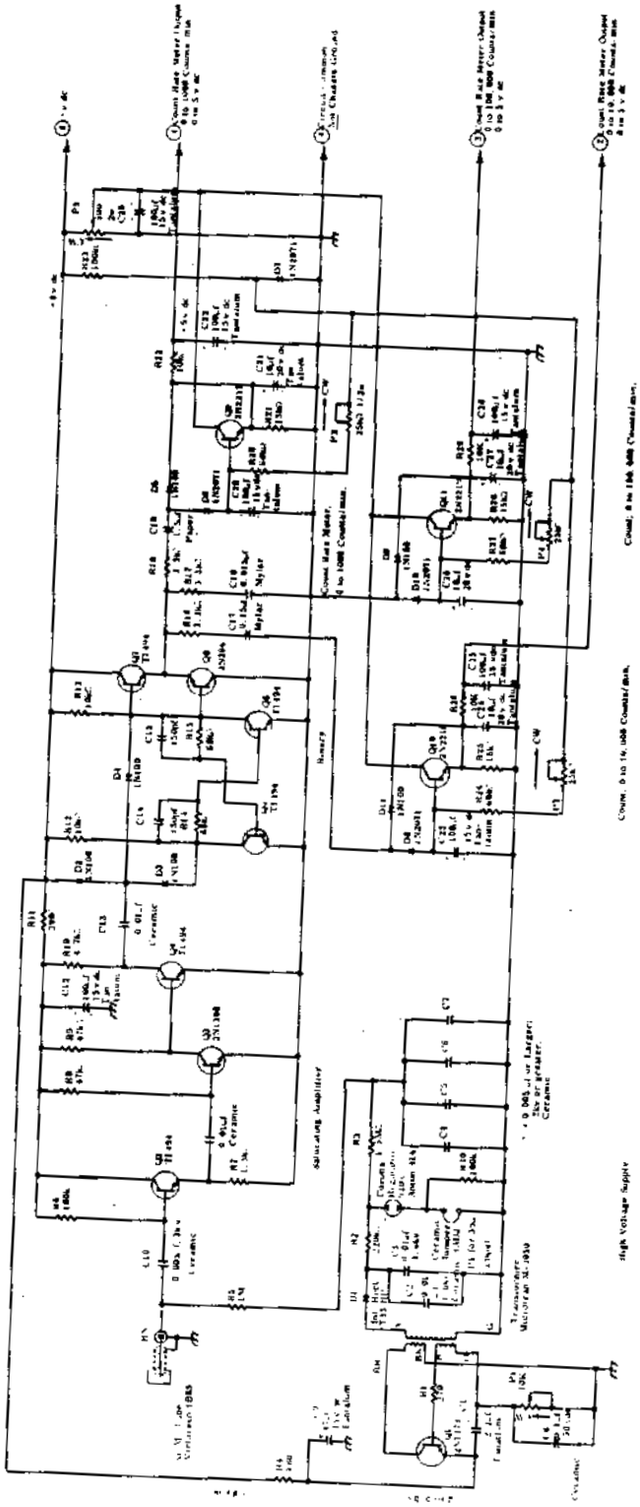

FIGURE 5.11
Radiation Monitoring Circuitry

AEC-66 RICHLAND, WASH.

with the modified data station. As a part of the modernization effort, solid state transceivers should be installed throughout the system.

A test circuit was designed and the base chassis rewired to facilitate environmental testing of each complete data station before field installation.

Biology Instrumentation

An Intrathoracic Pressure Monitor - N. S. Porter

Physiological pulmonary function studies are performed at the Biology Inhalation Toxicology Laboratory. During the studies, it is desirable to be able to measure the intrathoracic pressure of animal subjects. Measurements must be obtainable either in the esophagus or in the bronchia itself; typical pressures, in centimeters of water, vary from animal to animal and even vary with time in the same subject. A suitable pressure detection measuring and recording system was developed to permit satisfactory experiments to be carried out. The monitor measures thoracic pressure for indefinite periods during the investigative work. A small pressure transducer, which is attached to the end of an insulated cable, is inserted into the esophagus of the animal. Pressure changes are translated into frequency modulated signals that are transmitted through the cable to a control unit and discriminated by appropriate circuitry. The changing dc levels are calibrated in terms of pressure changes in centimeters of water and recorded with standard recording equipment. The transducer employs a single transistor in a circuit that requires 8.4 v dc at 2.5 mamp or 21 mw. The batteries employed can power the circuit continuously for about 900 hr.

Discussion

The intrathoracic pressure monitor was developed to aid in the physiological pulmonary function studies conducted with canine subjects at the Biology Inhalation Toxicology Laboratory.

Transducer

The pressure transducer is a basic Hartley oscillator with a variable inductance. A conical ferrite slug, which is attached to a rubber diaphragm, moves in and out of the inductor winding with variation of pressure. Figure 5.12 is a schematic diagram of the transducer. The changing inductance causes the oscillator frequency to change about its center frequency of 200 kc/sec. These

changes are sensed by the discriminator in the control unit that is cable-connected to the transducer. Figure 5.13 is a cutaway view, four times normal size, of the complete probe. The coil form for the winding is also conically shaped. As the core moves in and out, the inductance variation provides a linear frequency change over a narrow band width. Figure 5.14 shows the measured relationship of the measured air pressure versus the recorder reading deflection.

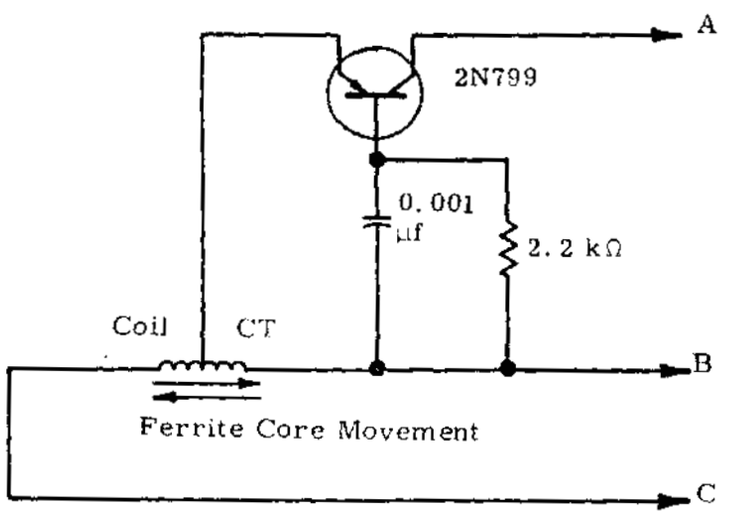

FIGURE 5.12
Hartley Oscillator Pressure Transducer

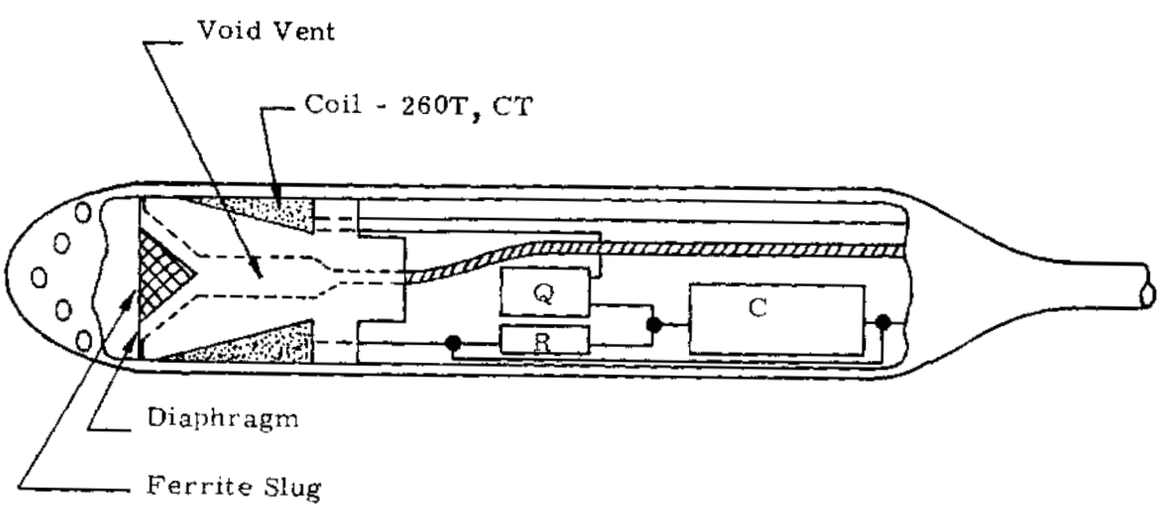

FIGURE 5.13
Sensor Probe (4X)

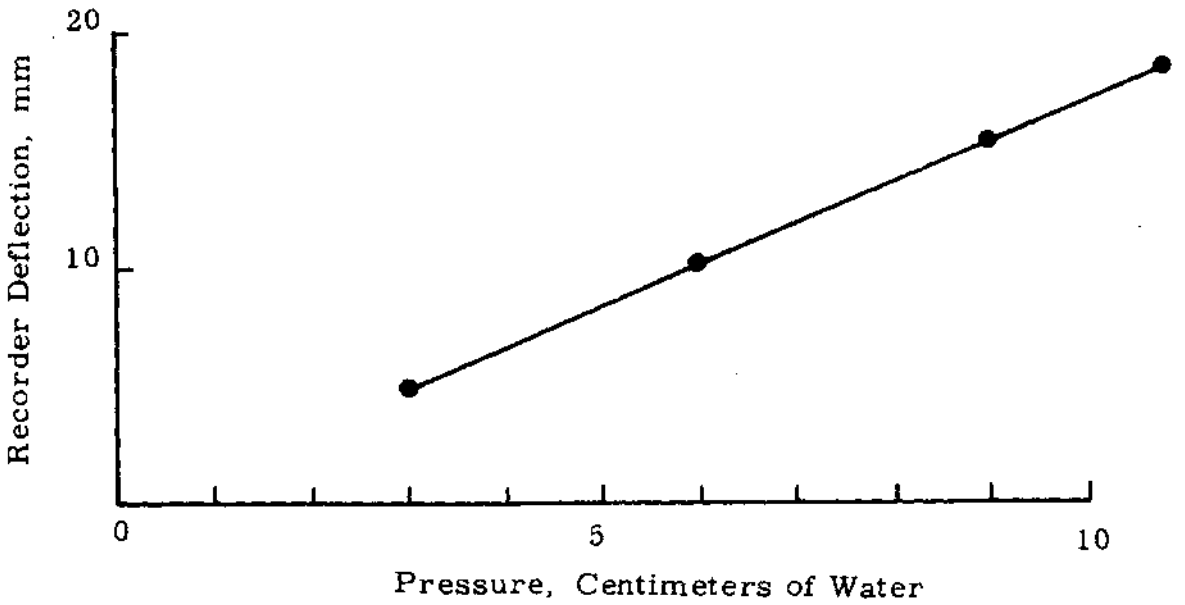

FIGURE 5.14
Air Pressure Versus Recorder Deflection

To keep the transducer as small as possible (approximately 5/16 in. in diameter) miniature components were used, and the power source as well as one capacitor were mounted in the control unit instead of in the transducer itself. The diaphragm was attached to the coil form with adhesive and a plastic torpedo-shaped cover was placed over that to provide smooth insertion. For greater temperature stability, the void inside the coil form is vented to the atmosphere through the cable tubing. The unit was potted with epoxy then coated with silver conducting paint to provide shielding. Miniature coaxial cable was used to provide greater stiffness to the assembly for easier insertion into the experimental animal.

Discriminator and Control Unit

A modified ratio detector was employed as the frequency modulation detector (Figure 5.15). The circuit output consists of the rectified differences between voltages produced across the two resonant tank circuits, one of which is tuned slightly above center frequency at 202 kc/sec and the other slightly below at 198 kc/sec. The dc voltage output is then proportional to the frequency changes

generated in the transducer. The only external controls needed are two switches, S-1 for on-off control and S-2 to insure prompt starting of the oscillator. Diodes D1 and D2 protect the transistor if the batteries are accidently inserted backwards. The 2N799 transistor circuit draws approximately 2.5 mamp during normal operation; hence, the two batteries are sufficient for some 900 hr of continuous use.

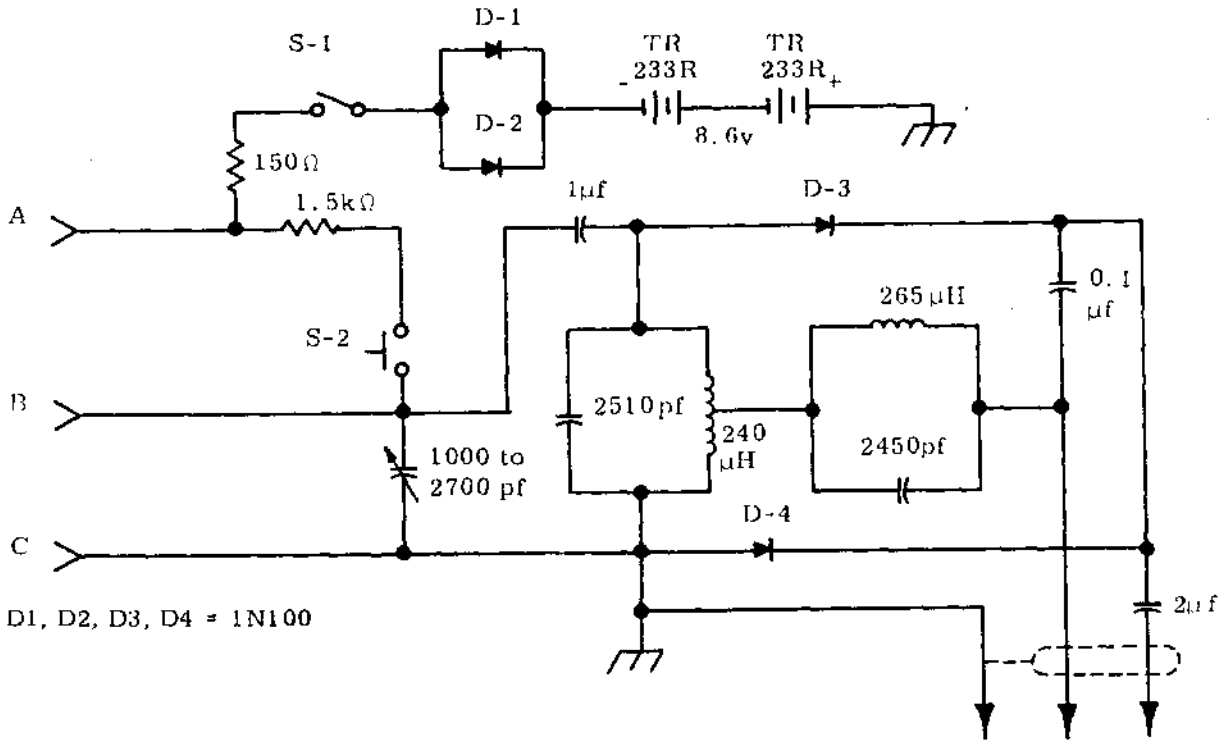

FIGURE 5.15
Frequency Discriminator and Controls

Operation

The completed monitor (Figure 5.16) was calibrated in the laboratory to provide 1 cm of deflection on a strip-chart recorder for a 6 cm change in pressure, water equivalent; thus, 1 cm of pressure change (water equivalent) equates to 1.67 mm deflections on the recorder.

Testing of the transducer was accomplished by inserting the probe into the esophagus of an anesthetized experimental animal and observing the recorder (Figure 5.17). The results were satisfactory and no apparent side effects were noticeable on the animal.

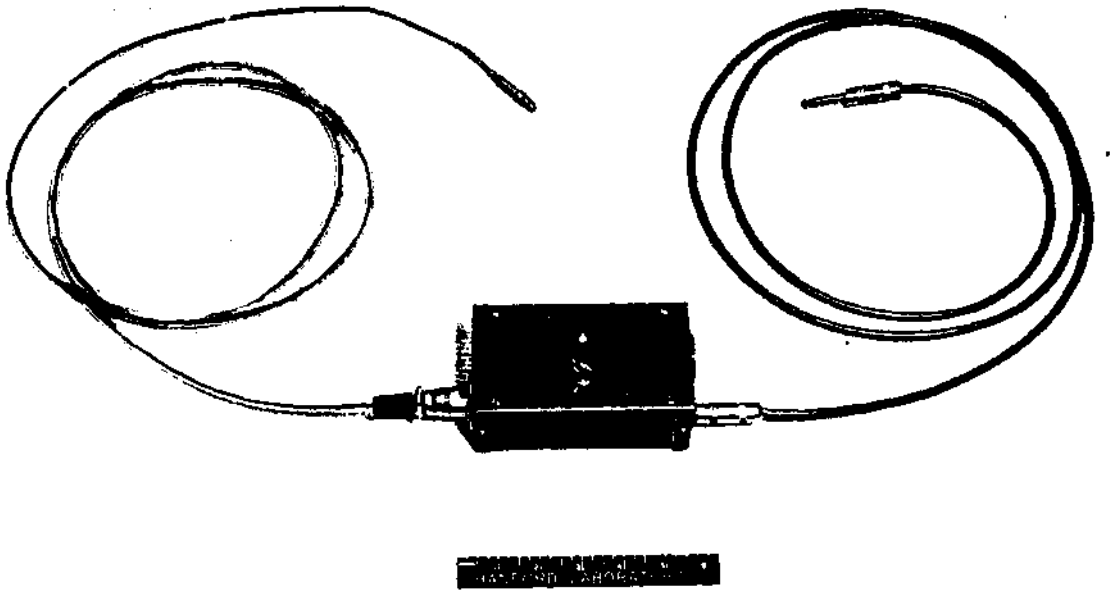

FIGURE 5.16
Intrathoracic Pressure Monitor

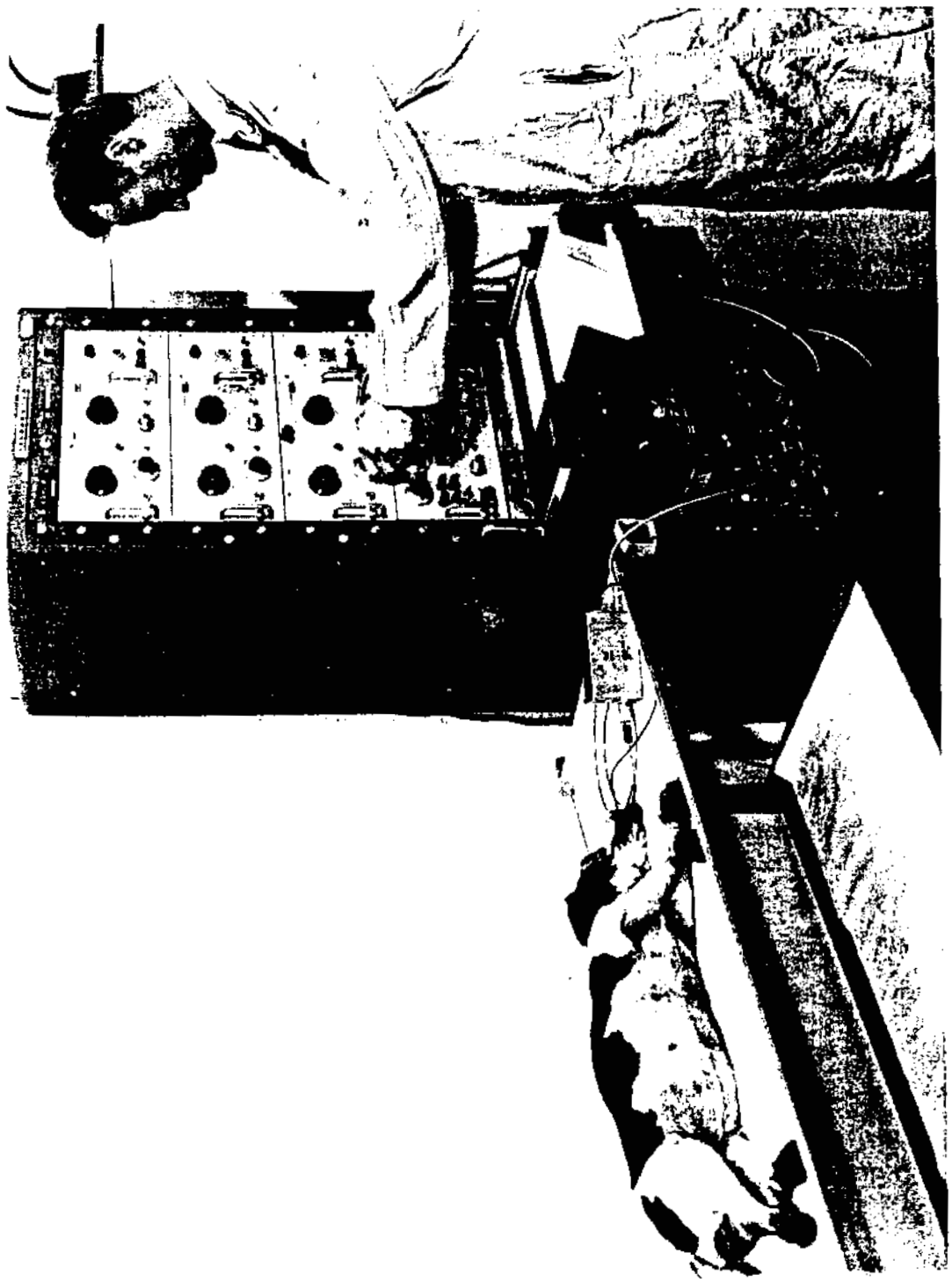

FIGURE 5.17
Operating the Intrathoracic Pressure Monitoring System

ABC-GS RICHLAND, WASH.

An Automatic Entomological Species Counter - N. S. Porter and E. M. Sheen

During the study of radiation effects on entomological species such as the tribolium casaneum and confusum, it is necessary periodically to count colony populations. By hand, such counts are tedious and time consuming; similarly, photographic methods require laborious techniques. An automatic counter for performing such tasks was developed for Radioecology, Biology Laboratory. The instrument counts whole colonies of the species being investigated.

Discussion

An automatic entomological species counter was developed to provide a simple and automatic means of counting experimental colonies of the common flour beetle.

The counter, a solid state device, comprises a control box, power supply, general electronics and an electromechanical register, and a probe head which holds the detector assembly. In the probe head a miniature focused light bulb directs light through a glass tube into a photocell. as insects pass from the funnel-type container (above) through the tube, they interrupt the light beam changing the current through R9. The resulting voltage change across R9 operates a voltage comparator circuit, consisting of Q2 and Q3, to drive Q1 and operate relay K-1. The closure of contacts K-1a advances the register one digit. After the insect passes, the increased illumination of the photocell results in K-1a deenergizing the register coil and restoring initial conditions. Thus, the register advances one digit for each interruption of the light beam and totals the insects passing through the counter.

The probe head is versatile in that the stoppers holding the glass tube can be changed to accommodate insects of varying sizes. The unit obtains its operating power from a 115 v, 60 cycle line. An included Zener-regulated dc supply furnishes B+ power for the electronics. For safety purposes, the five-decade electromechanical register is isolated from the supply source. The circuit diagram is shown in Figure 5.18, and Figure 5.19 shows the instrument being used to count a colony of the common flour beetle.

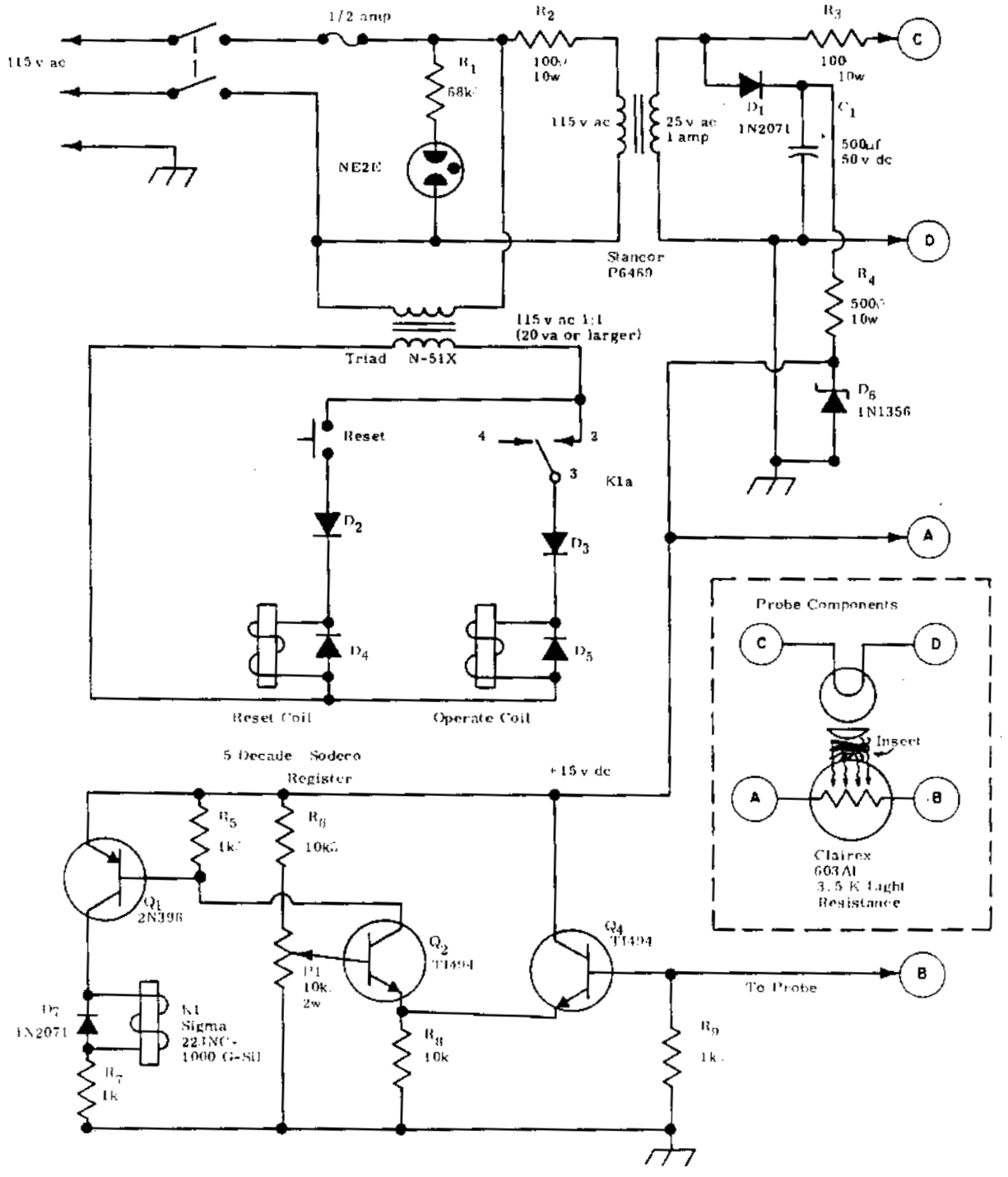

FIGURE 5.18

Automatic Entomological Species Counter

FIGURE 5.19
Entomological Species Counter in Operation

A Glove Box Air Balance Monitor - N. S. Porter

An instrument was developed for use at the Biology Inhalation Toxicology Laboratory to monitor the negative air differential across a glove box. A manometer is filled with black (dyed) ethylene glycol and is mounted on a chassis in a photocell light beam. Loss of air balance causes the fluid to interrupt the light beam which causes the alarm to operate. The photocell circuitry is powered by the same 110 v ac source that supplies the air balance fans; hence, loss of that power also operates the alarm. The alarm is a battery-operated variable frequency oscillator and amplifier driving a loudspeaker. There is no standby power consumption and maximum current drain during alarm is only 0.6 mamp. The two mercury cell batteries can provide over 3000 hr of alarm time at this rate. The manometer will energize the alarm circuit when the loss of air balance differential is as small as 0.1 in. of water equivalent.

Discussion

To conduct radioactive aersol experiments in a safe manner in glove boxes, a negative air pressure differential must be maintained in the box with respect to the outside atmosphere. Loss of the air balance could lead to the exposure of operating personnel to contaminated air. Consequently, it is desired to have an air balance monitor which will instantaneously alert glove box operators in the event of an air system failure.

The air balance differential between the glove box and room atmosphere is maintained by a suction fan. A glass manometer with a spill trap is connected to the inside of the glove box; the other end is open to room atmospheric pressure. Energizing the suction fans to the closed glove box causes the manometer fluid to rise towards the lesser air pressure. The manometer is adjustable and can be raised into the light beam path so loss of negative pressure will cause the fluid to return to gravity level thereby activating the alarm. The manometer is diagrammed in Figure 5.20.

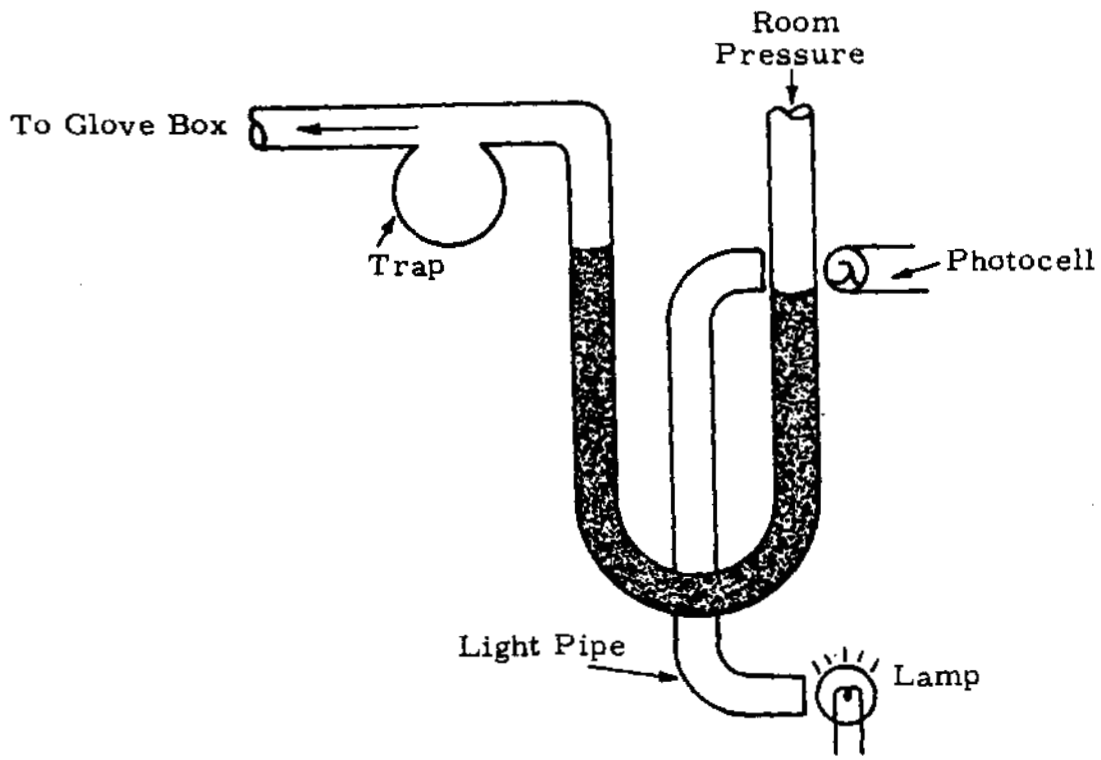

FIGURE 5.20

Manometer-Photocell Arrangement

The circuit diagram is shown in Figure 5.21. The energized photocell causes transistor Q-1, a solid state switch, to conduct thereby keeping relay K-1 in an energized state. An increase of photocell resistance, caused when light is removed from it when air balance is lost, cuts off Q-1 causing the alarm to operate. Sensitivity is adjustable with potentiometer P-2. Loss of 110 v ac power to the full-wave rectifier bridge also causes the alarm to energize.

The alarm is energized upon closure of relay contacts K-1B. This action applies 8.4 v dc to Q-2, an oscillator whose frequency is adjustable at the chassis face with potentiometer P-2. The output signal is coupled to Q-3, an amplifier stage which drives the loudspeaker. The volume is adequate under the normal background noise conditions. No standby current is used in this circuit and only 0.6 mamp is drawn from the batteries during normal alarming.

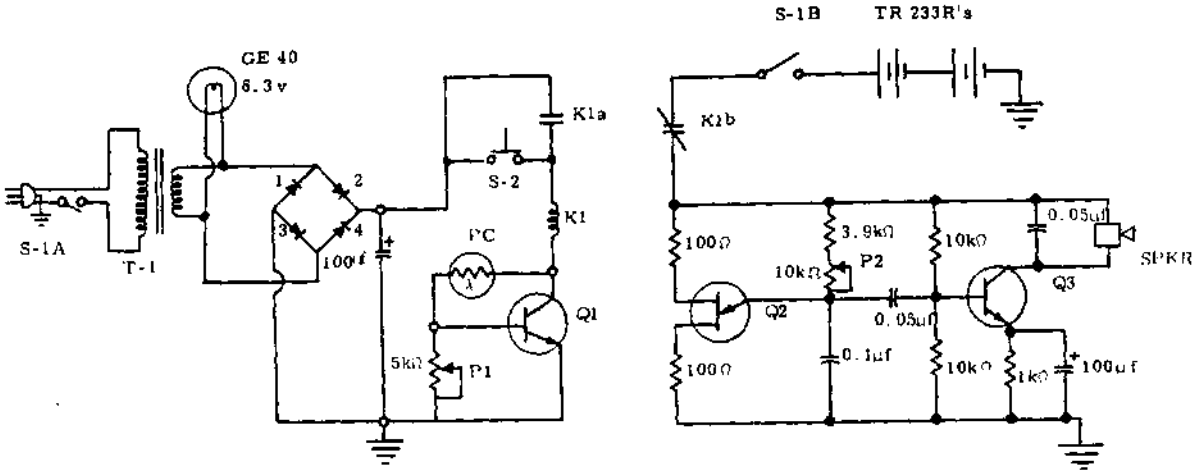

T-1 Filament Transformer, 6.3 v
D-1, 2, 3, 4 1N2701
PC Clairex 603AL
K-1 Sigma, 22RJCC-1000-GSPC
Q1, Q3 2N1279
Q2 2N1671
SPKR UA-1614-A, Rcvr, Sound Powered

FIGURE 5.21
Circuit Diagram of Air Balance Monitor

Once the alarm has been switched on, it can be stopped by turning off the power, switch S-1, or by resetting relay K-1. It will be noted that resetting is only possible when there is 110 v ac power applied and when the proper air balance is being maintained. When these two conditions are fulfilled and resetting still does not occur by pressing reset switch S-2, either vertical adjustment of the manometer is necessary or else the cut-off sensitivity potentiometer, P-1, should be adjusted.

A working model of this instrument, illustrated in Figure 5.22 is now in use at the Biology Inhalation Toxicology Laboratory. Careful adjustment during bench tests provided alarm energizing for a loss of air balance differential as small as 0.1 in. of water.

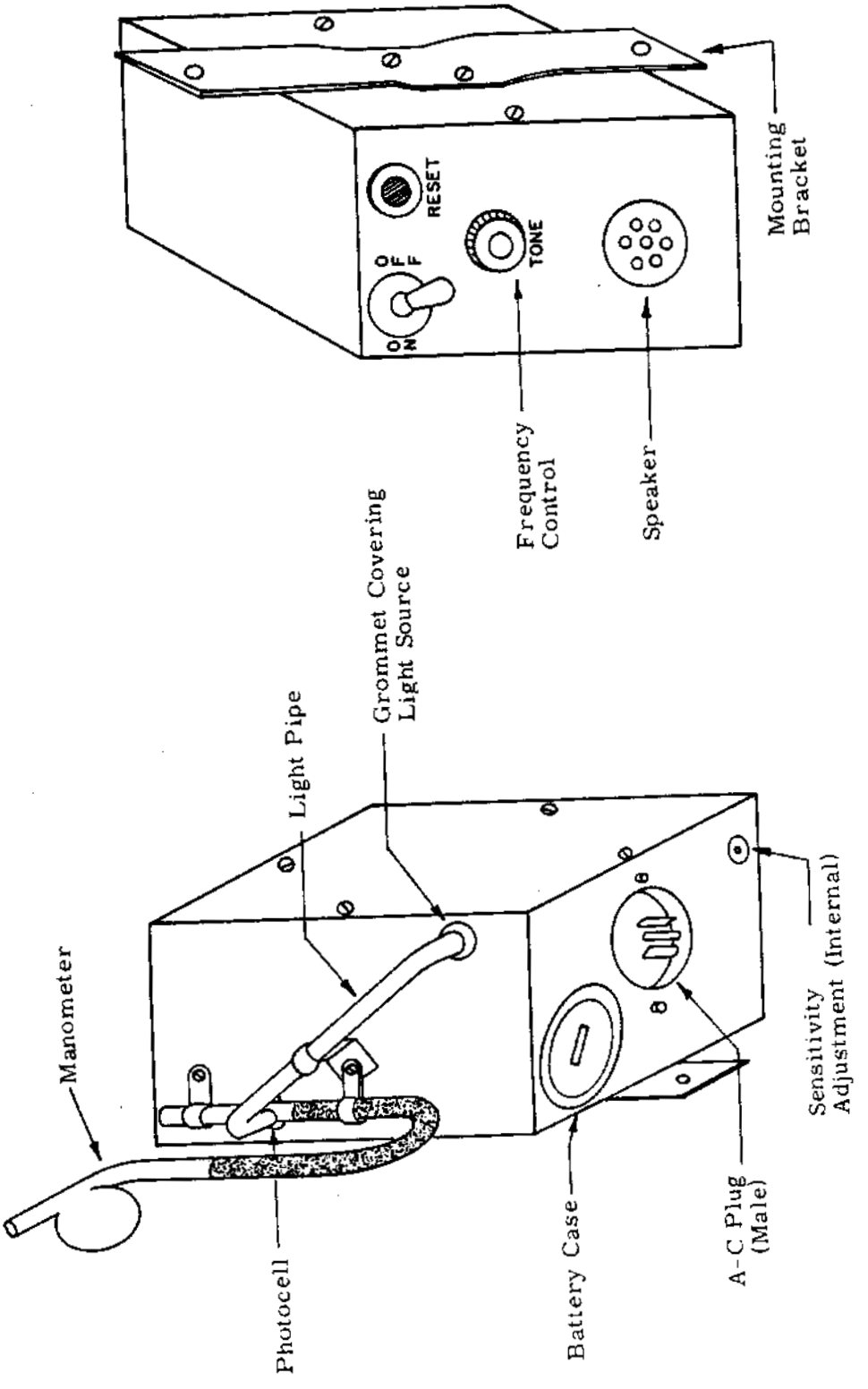

FIGURE 5.22

Glove Box Air Pressure Monitor-Alarm

Instrumentation for Toxicity Studies of Inhaled Radionuclides -

N. S. Porter

Specialized instrumentation is required to obtain physiological data during toxicity studies of inhaled radionuclides at the Biology Inhalation Toxicology Laboratory. Data taken during the inhalation experiments include tidal volume and respiration rates. These parameters are measured with a thermistor-controlled bridge that drives a chart recorder under properly calibrated conditions. Deposition to the respiration tract has to be measured indirectly. To provide accurate measurements, the instrumentation was developed to control the flow of inspired and expired aerosols through a sliding valve. Considerable experimental work has been accomplished to date and further refinements have been established for future incorporation.

Discussion

The Inhalation Toxicology Laboratory conducts an extensive program to determine toxicity effects of inhaled radionuclides in animals. Investigative procedures require considerable instrumentation to enable the scientists to obtain the parameters needed for accurate determination of actual deposition and retention. The parameters of interest include the amount of the radionuclide in the aerosol, respiration rate, tidal volume, the quantity of deposition in the respiratory tract, particle size, amount of retention by the animal over a long time period, and the toxic effects of the deposition. Techniques are available for obtaining these parameters but with varying degrees of success and time factors. The instrument development effort is directed towards finding more accurate and better ways of measuring these parameters. Work has been carried out to aid the biologists to more reliably determine inhaled tidal volume at the corresponding respiration rate and to compute the amount of total deposition in the experimental animal.

Respiration and Volume Measurement

Respiration and volume measurements can usually be made using standard pneumograph techniques, particularly if the test animal is anesthetized;

however, the experimental animals at Hanford are not anesthetized for inhalation studies. Instead, they are trained to use a face mask for extended periods of time. During the experiments, however, nervous and body movements or those made by animal attendants attempting to calm the dogs disrupt the pneumographic system. To circumvent this problem, a thermistor bridge, shown in Figure 5.23, was developed to measure inspiration volume through the cooling effect. The thermistor is operated near the upper limit of its self-heating characteristic. During inspiration, it is cooled in proportion to the passing air volume and the resulting signal difference across the bridge is recorded. Since thermistor cooling is also dependent upon flow rate, a family of calibration curves is made. Total tidal volume can then be calculated for the deposition computations. The bridge and transducer are shown in Figure 5.24.

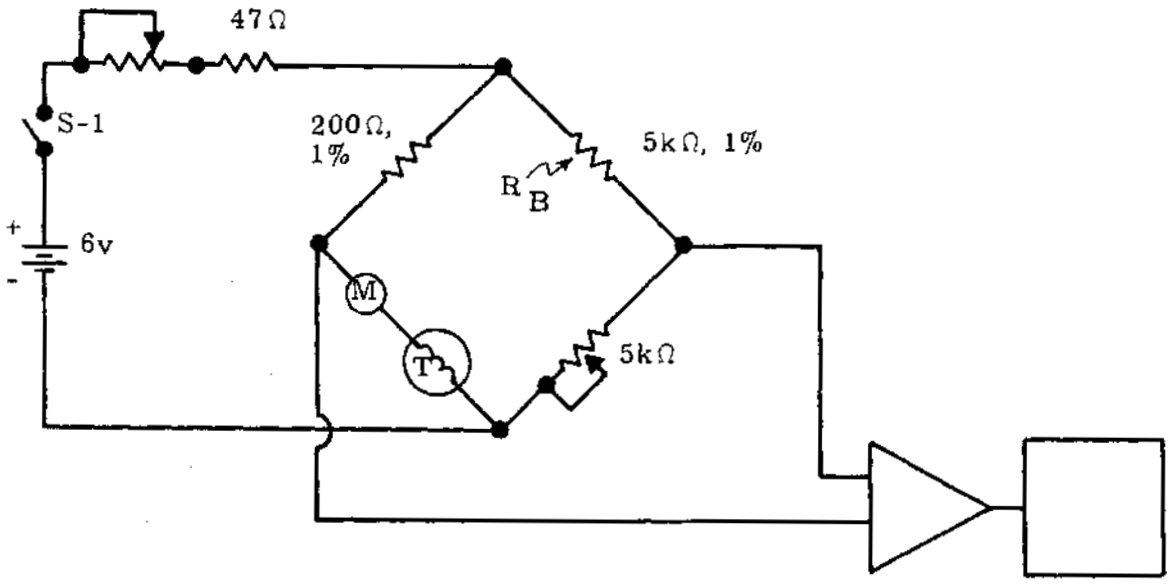

M = 20 Milliammeter
T = VECO 32A50

FIGURE 5.23
Thermistor Bridge

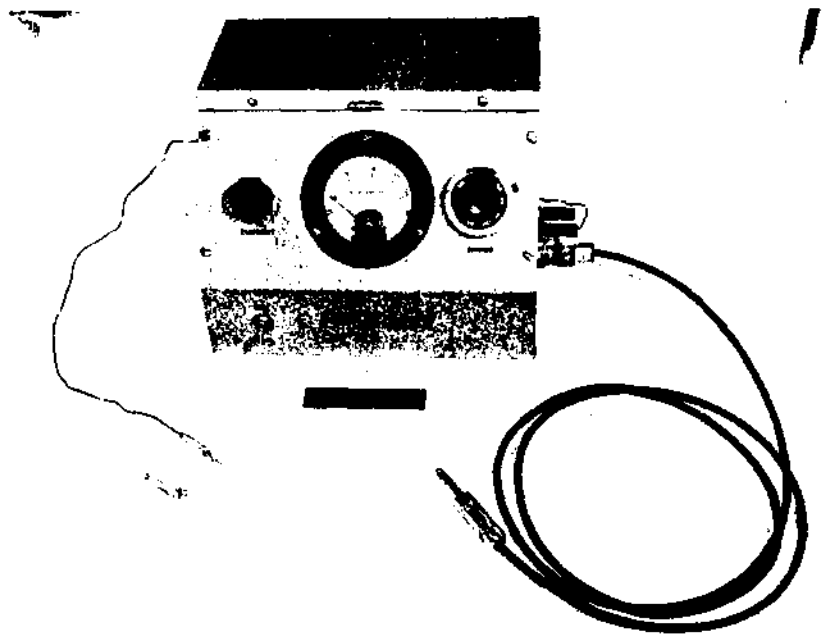

FIGURE 5.24
Bridge and Transducer Instrumentation

Inhalation-Exhalation Control Valve

The total deposition in an animal during the exposure experiment can be calculated. First, by recording the number and tidal volume of all inspirations which occurred during the exposure, the volume of aerosol the animal has inhaled can be determined. During exposure, samples are taken periodically using an electrostatic precipitator to determine the aerosol concentration. Second, by multiplying total volume inhaled by the aerosol concentration, the total exposure is obtained. All exhalant from the dog is collected and filtered to remove the remaining radionuclide material. The difference between the filtrate and the calculated amount to which the animal was exposed is the total deposition.

There are, however, several inherent sources of error in this method and the error magnitude is not known until after the animal is sacrificed or dies. These error sources include the volume calculations, concentration sampling. dead space in passageways, and incomplete separations of inhaled and exhaled aerosol. The volume problem has been

discussed and refinements are being made to obtain better sampling. An improved control valve system has been adapted to improve dead space and separation of inhaled from exhaled particles.

A sliding valve, similar to the one developed at the University of Rochester[5.3] for similar work, was designed for mounting nearer the animal than was possible with the flapper valves used previously. The new valve is a "break before make" type which greatly reduces the chance of inhalant and exhalant mixing. Operation control of the valve is electronic and solid state circuitry is used throughout as shown in Figure 5.25. System operation is described in the block diagram of Figure 5.26. As the dog, seated in the animal chamber with the mask strapped to his nose, breathes into the system, pressure changes are sensed by the transducer coupled to the mask. The transducer frequency modulates an oscillator whose output is discriminated, amplified, and used to trigger a circuit which in turn operates relay K-1 in the emitter circuit of Q-5. This electronic switch alternately supplies power to one of the two solenoids which operate the sliding valve in synchronism with the breathing pattern of the dog.

The experimental results to date have shown promise. By using the thermistor bridge, greater accuracies in determining aerosol deposition can be obtained by having a record of respiration rate and tidal volume. Calibration is easily accomplished by using a variable volume/speed respirator to obtain calibration curves similar to the one shown in Figure 5.27. Although the valve has not been used with actual animals in inhalation experiments as yet, the inhalation-exhalation control valve is expected to improve the reliability of total deposition calculations in future studies. The system, shown in Figure 5.28 in a training situation, has already demonstrated reliably that it can follow the respiration rates (up to 56 respirations per minute) encountered so far in training. Improvement and final detailed testing work will be conducted in 1964.

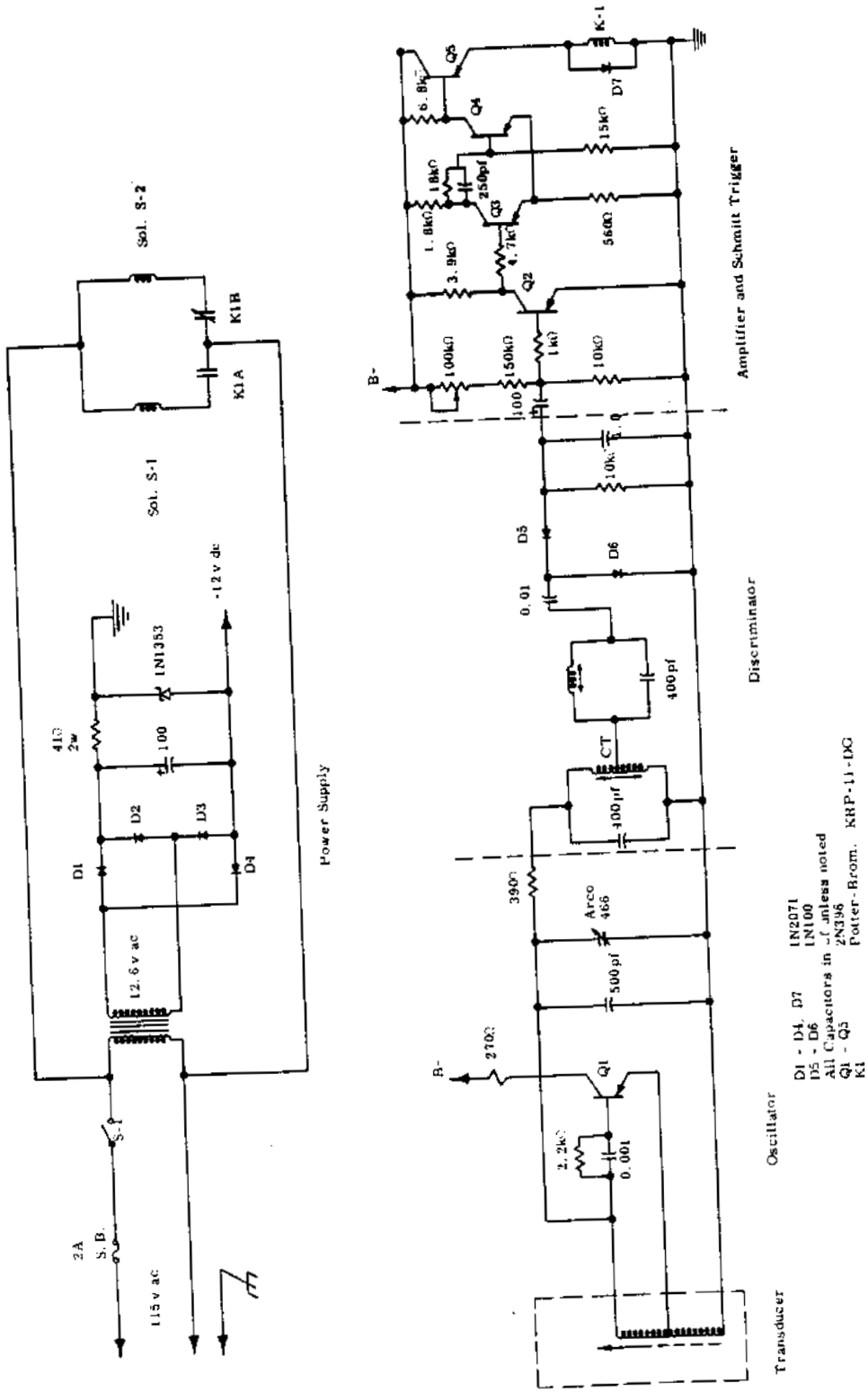

FIGURE 5.25

Electronic Switch and Controls

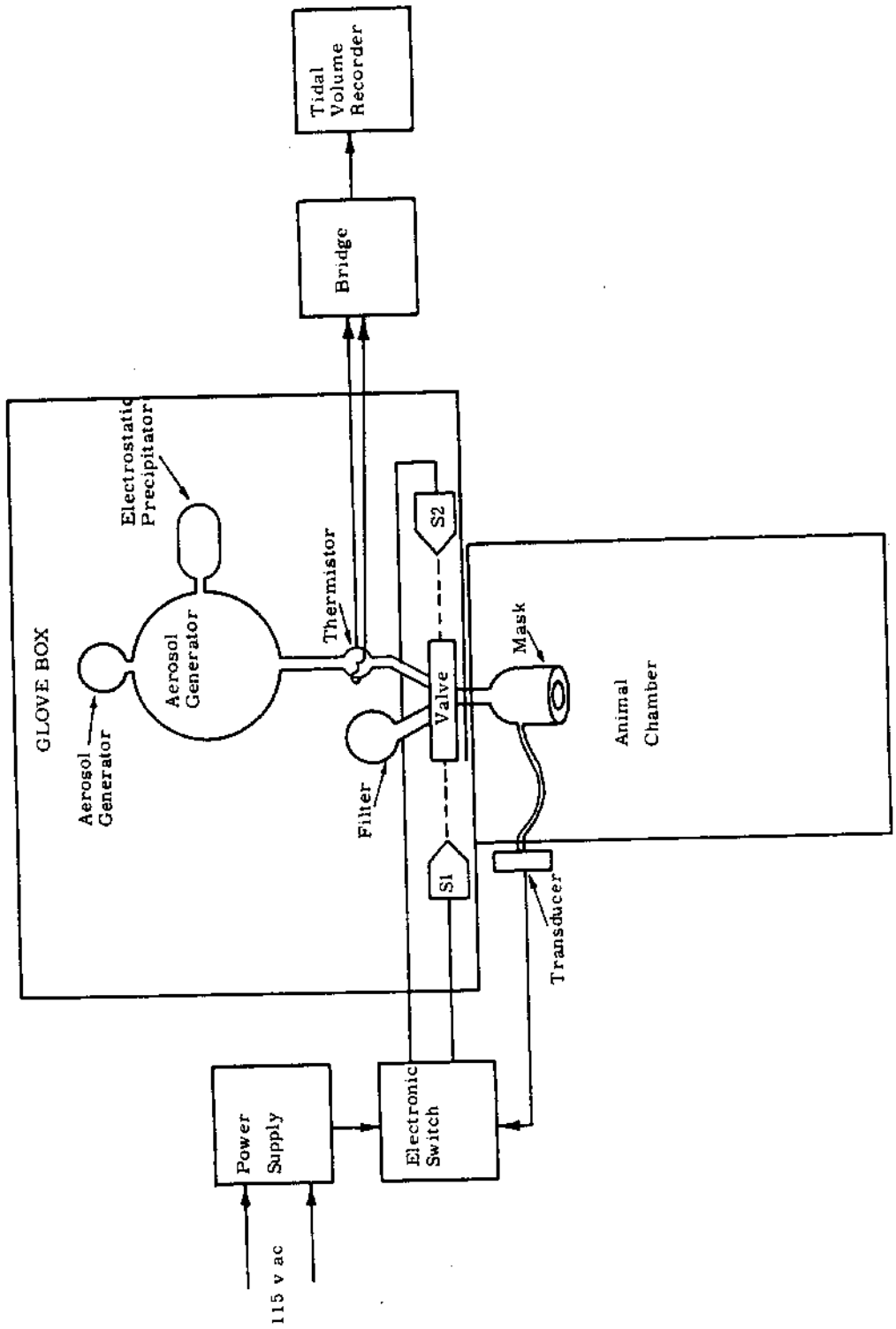

FIGURE 5.26
Inhalation Experiment

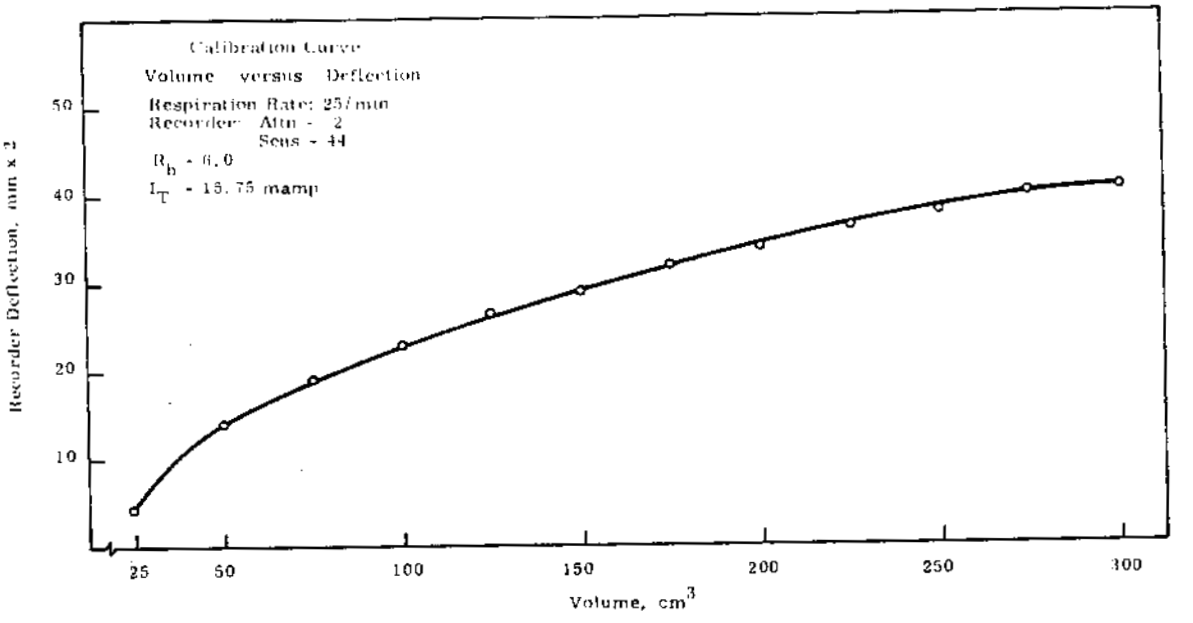

FIGURE 5.27

System Calibration Curve

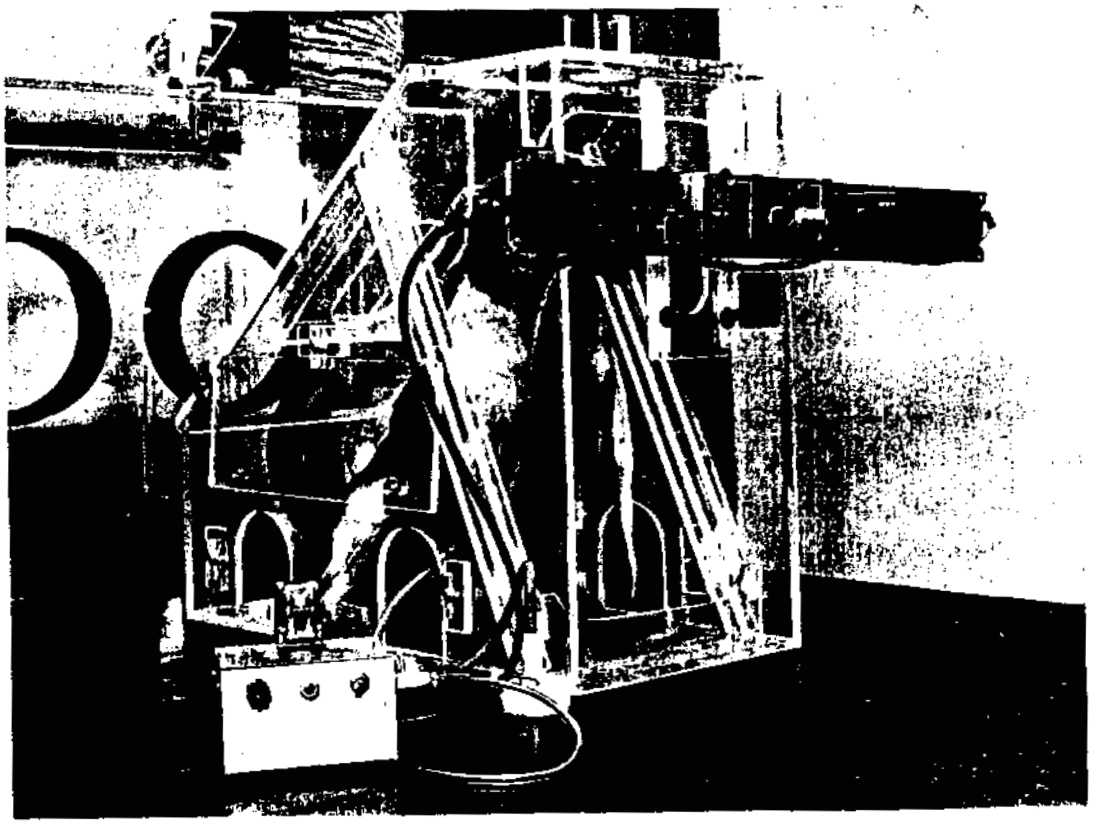

FIGURE 5.28

Operation of Instrumentation

AEC-GE RICHLAND, WASH.

Physiological Data Telemetry - D. P. Brown, N. C. Hoitink, N. S. Porter, and J. Ryden

During biological studies of radiation effects on sheep, swine, and dogs, it is generally necessary to monitor physiological functions such as temperature, respiration rate, and cardiac activity. Provisions must be made for continuous monitoring during periods when subjects are ambulatory, under direct observation during experimentation or surgery, and in terminal status. The physiological data telemetry system is being developed to provide the required information. Miniature solid state circuitry is employed to reduce transducer and transmitter size and to minimize animal discomfort. Initial experimental effort utilized both amplitude and frequency modulated signals at a transmission frequency of about 46 kc/sec. Later experiments employed considerably higher frequencies to secure more miniaturized instrumentation. To date, with the latter system approach, successful telemetry of body temperature has been achieved using sheep. Progress has been made in using transducers in the respiration rate and cardiac activity measurements. The experiments completed to date indicate that the system will be developed in 1964.

Discussion

Pathological studies of irradiated animals often require monitoring of physiological conditions such as body temperature, respiration rate, and cardiac activity. Many such studies are long term during which time the condition of the subject might vary from ambulatory to terminal. Further experimentation and surgery may also be conducted. At any specific time, it is desirable to be able to monitor any or all of the stated physiological conditions, typically, when the animal moves normally about its pen and during the final stages for the terminal case. In the latter event, monitoring can be used to provide a signal alarm in the event of death to alert laboratory personnel who will perform immediate postmortem tissue analysis. In the terminal case, the subject is generally incapacitated and transducer leads can extend directly to the readout instrumentation. A similar situation exists during operations or experiments while the subject is restrained or anesthetized. However, for the more typical case, varying degrees of telemetry are required from the ambulatory animals to a fixed receiver for monitoring and recording.

A portion of the development was directed toward satisfying the requirements for terminal cases and for direct telemetry for the larger animals. The required electronic circuits were developed and tested using simulated physiological transducers. For this work, the instrumentation used a solid state transmitter which operated on a carrier frequency of 46 kc/sec. Both frequency and amplitude modulation were used to convey the signal intelligence. The receiver consisted of amplifiers and demodulating circuits which separate the three information signals of respiration rate, heart rate, and temperature.

Later work was centered around higher frequency, 88 to 108 Mc/sec, transmission to miniaturize circuitry. In addition, one of the measurement parameters was changed from heart rate to blood pressure to satisfy biological study requirements. The smaller system was developed and successfully used with a sheep in the field to telemeter body temperature information. In addition, promising results were achieved with a respiration rate transducer.

Low Frequency Telemetry Development

This work entailed the use of a 46 kc/sec system for application when telemetry is needed while animals are either restrained or in terminal status. This system utilized inductive coupling between two coils to transfer information from the animal to the readout instruments. The first coil was excited by the transmitter and the second, a much larger coil, repsonded to the magnetic field produced in the first. Separation of coils up to 5 m was determined to be feasible while much closer coupling would be typical in the actual application. Each coil is tuned to resonance at the 46 kc/sec carrier frequency to achieve satisfactory response. The transmitter circuit, shown in Figure 5.29, uses an astable multivibrator to generate the carrier frequency. The output of the multivibrator is changed to a sinusoidal waveform by passing it through the low pass filter composed of L, C_2, and C_3.

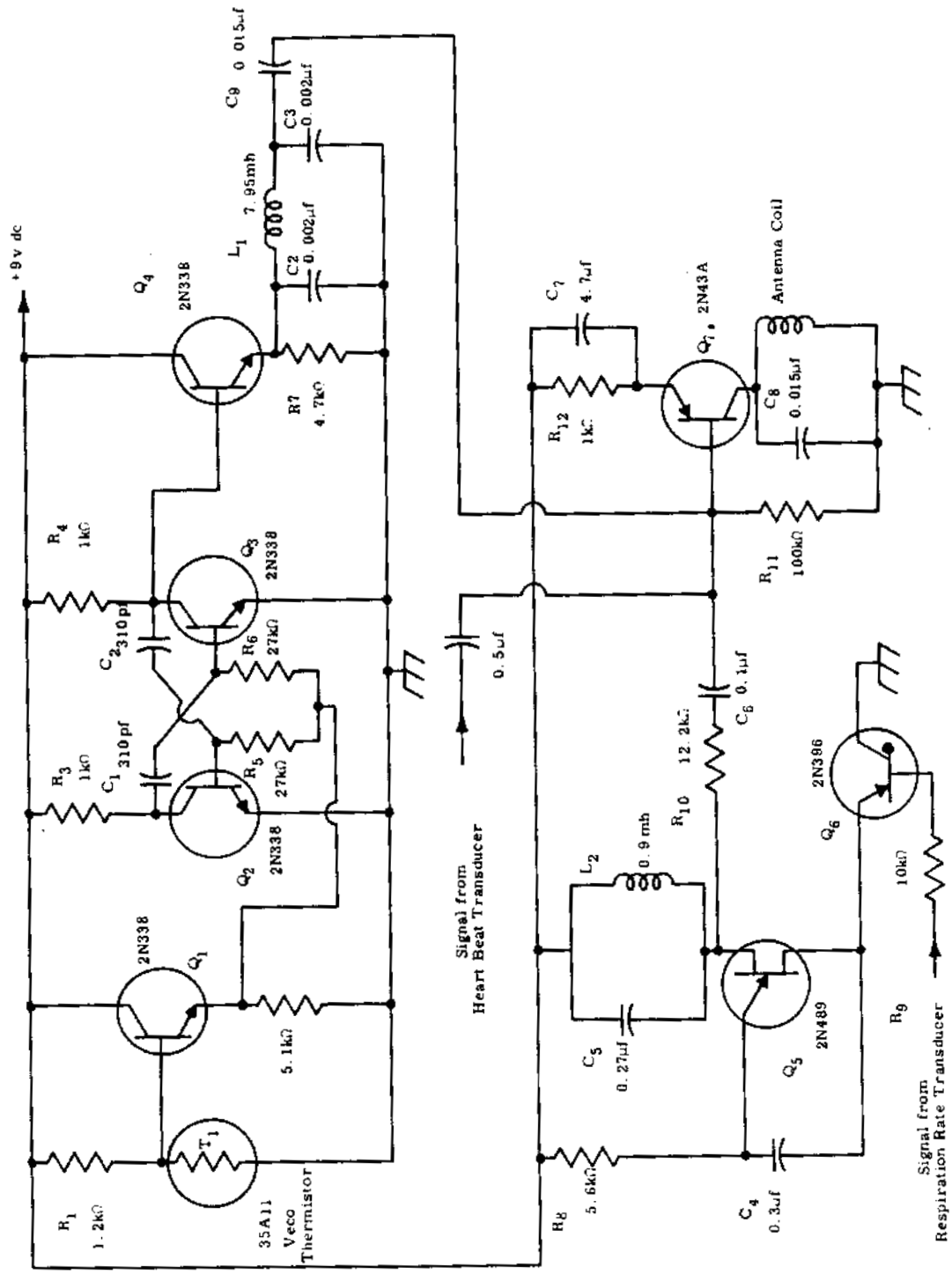

FIGURE 5.29
Transmitter Circuit

Thermistor T_1 is used as the temperature transducer. As the temperature varies, the resistance of the thermistor changes proportionally. The voltage change across the thermistor is coupled through Q_1, R_5, and R_6 to the multivibrator which translates it to a frequency change. In this manner, temperature changes cause frequency modulation of the carrier. For a temperature change of 10 F^o, it was determined that a 6 kc/sec change occurred in the carrier. The multivibrator temperature stability is such that its frequency does not change over 200 cycles for temperature variations from 75 to 110 F^o. This was adequate for the planned applications.

The signal from the heart beat transducer is in the form of pulses which directly amplitude-modulate the carrier frequency by changing the base bias of the output driver transistor, Q_7.

The respiration rate transducer signal is used to operate Q_6 which is a transistor switch used to start and stop a 1 kc/sec oscillator, Q_5. The generated tone is used to amplitude-modulate the carrier frequency at the respiration rate.

The receiver is composed of an amplifier section and three demodulating channels, one for each of the information signals. Temperature information is extracted using a diode pump frequency discriminator. With reference to Figure 5.30 and C_9, D_1, D_2, and R_{13}, the following equation applies:

$$e_o = \frac{E\,f\,T}{1 + f\,T} \qquad (1)$$

where

E is the ac voltage at the collector of Q_{16}
f is the frequency
T is the time constant of C_9 and R_{13}
e_o is the dc voltage across R_{13}.

By making $fT << 1$, the following approximation can be made:

$$e_o \cong E\,f\,T. \qquad (2)$$

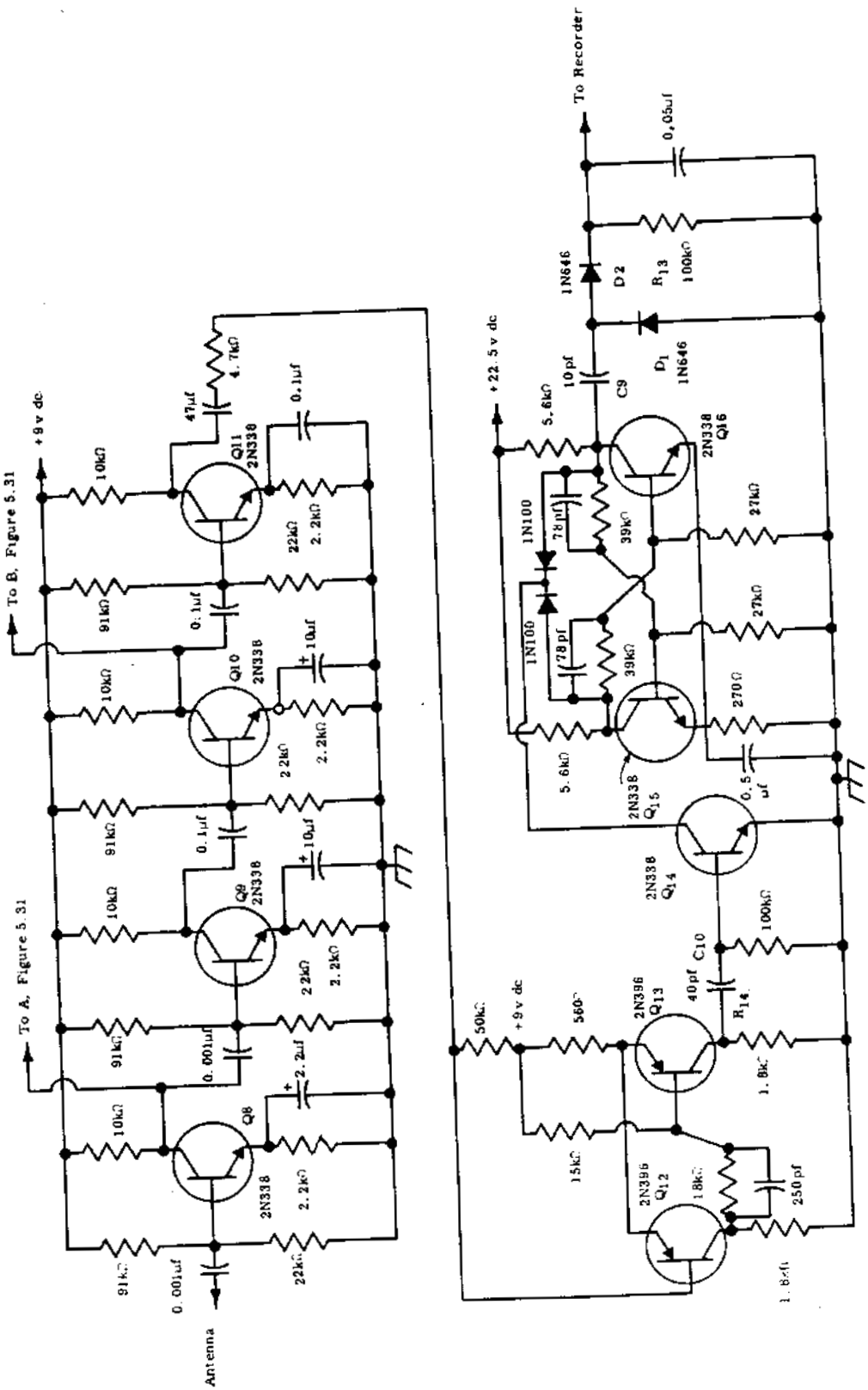

FIGURE 5.30

Amplifier Section and Temperature Demodulating Circuits of the Receiver

From this equation, it can be seen that E must be constant to insure a linear relation between e and f. The trigger circuit (Q_{12} and Q_{13}) provides a constant amplitude output for an input above 2.19 v rms. This output itself is not used as an input to the diode pump since the pulse width of the trigger circuit output varies with the amplitude of the input signal. With the proper value of T to make Equation (2) valid, the capacitor C_9 cannot charge fully when the pulse width of the trigger circuit decreases to a particular value. To remedy this, the output is differentiated and used to activate a bistable multivibrator (Q_{15} and Q_{16}). This multivibrator is operated at an E_{cc} of 22.5 v dc to provide a substantial e_o, which is in the mv range.

The respiration rate channel is coupled from the first amplifier Q_8 in Figure 5.30. The carrier frequency is eliminated from the respiration rate information by use of a parallel tuned circuit, C_{10} and L_3 of Figure 5.31, resonant at 1 kc/sec. However, the Q of this tuned circuit is such that the heart beat rate is not attenuated sufficiently; therefore, a diode pump circuit is used to obtain the respiration rate information with the heart beat being filtered out by C_{11}. The heart beat signal is coupled from the output of Q_{10} to a detector and two amplifiers. The output signals from all three channels drive chart recorders for recording the signal traces.

High Frequency Telemetry Development

The transmitter for this system, shown in Figure 5.32, operates in the 88 to 108 Mc/sec frequency band. The carrier frequency is produced by a tunnel diode oscillator; and using a 6 in. antenna whip, the transmitted signal can be received at 100 ft by a receiver with a sensitivity of 10 μv. Three information signals can frequency modulate the carrier frequency and the intelligence recovered at the receiver. A prototype was successfully tested using two simulated signal inputs: respiration rate and temperature.

Temperature information is obtained using a thermistor in the frequency determining network of a transistor oscillator. As the temperature changes the resistance of the thermistor, the frequency changes accordingly.

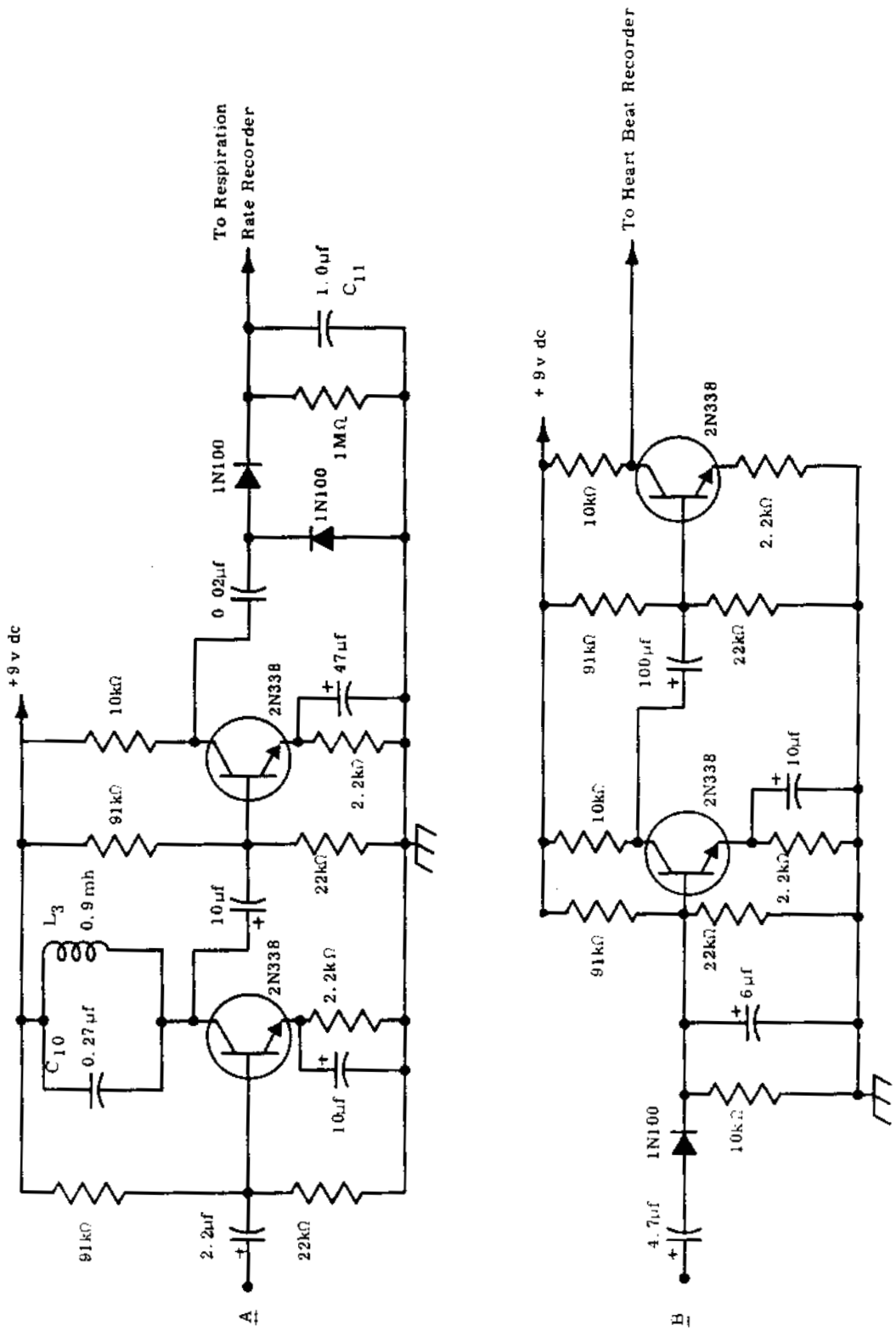

FIGURE 5.31
Respiration Rate and Heart Beat Demodulating Circuits

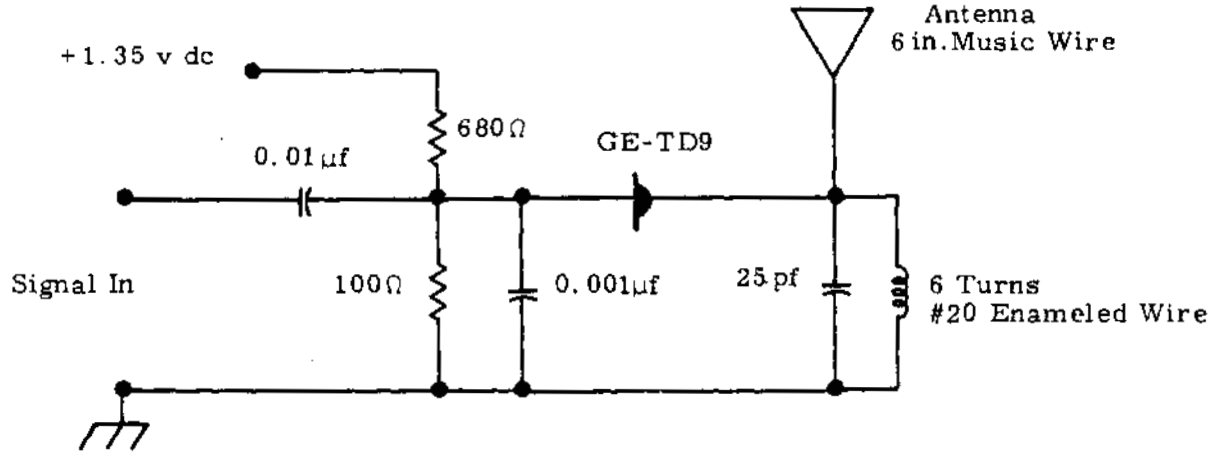

FIGURE 5.32
FM Transmitter

A transducer, Shown in Figure 5.33, which operates in this manner was assembled into a compact epoxy-potted module for direct implantation in animal subjects. The transducer output modulates the carrier frequency of the transmitter an audio rate.

For the initial studies, a commercial receiver was used to receive the temperature signal. The temperature value was displayed digitally on a commercial frequency counter with print-out capabilities. For field use, a miniaturized receiver is under development.

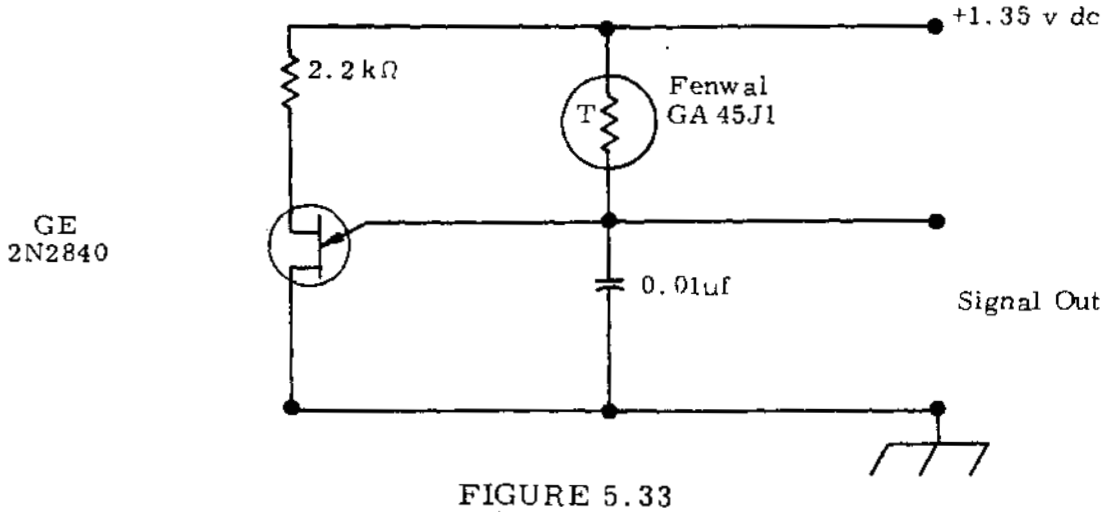

FIGURE 5.33
Temperature Transducer

A respiration rate transducer, shown in Figure 5.34, also employs a thermistor as a sensor. The thermistor operates in a self-heating condition at approximately 150 C. It is planned to implant the sensor in the nasal cavity of the animal. The cooling effects of inspiration on the thermistor will cause a varying voltage change across it. This changing voltage is used to switch a 10 kc/sec oscillator off and on, thus modulating the transmitter at the respiration rate. The receiver receives 10 kc/sec pulses each time the animal breathes. Laboratory tests have been quite encouraging.

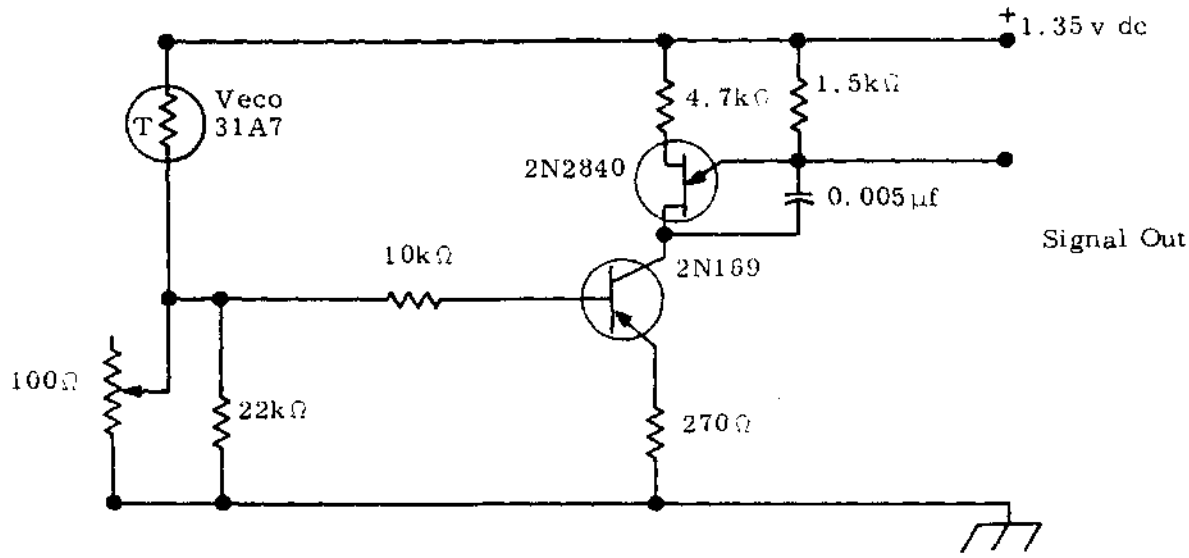

FIGURE 5.34
Respiration Rate Transducer

Field Tests

The field tests conducted to date have employed the miniature high frequency system. The temperature transducer was calibrated and two tests made using a sheep. The first test involved implanting the transducer under the back skin of the sheep. The system appeared to function properly. The animal had been shaved around the implant area, and as a consequence, environmental temperature changes affected the transducer response. In a second test, the transducer was used rectally. Comparison was made with a

standard thermometer and the results were within 0.25 F^{o} of each other. During the latter test, the animal was restrained in an aluminum cage which caused poor signal transmission. Future tests are designed to overcome this problem.

The entire transmitter and its polyethylene mounting weigh approximately 25 g and attachment to the animal has posed no problems. If necessary, the entire unit could be packaged to fit beneath the skin with only the antenna and a battery case projecting. Figure 5.35 shows the system as used in the field testing.

FIGURE 5.35
Telemetry System in Use

Dosimetry Instrumentation

Experimental Method for Measurement of Neutron Dose - G. F. Garlick

A technique was investigated for the measurement of neutron dose and dose rates over a wide energy range. The objective was to achieve a composite response corresponding to that established by the National Committee on Radiation Protection (NCRP). Further, it was desired that the developed instrument be compact for direct personal use and also be applicable for use in general area neutron monitoring. The experimental multiple-detector neutron dosemeter showed promise in providing a measurement of neutron dose and dose rates over an energy range from thermal to 10 Mev. A composite sensor system using three solid state junction diodes as thermal, intermediate, and fast neutron energy detectors was developed. Response over the thermal to low kev range is provided by a Li^6F cover over a diode plus a 3 in. diameter hydrogenous moderator. The intermediate range, from a low kev value to several hundred kev, is monitored by a Rh^{103} foil covered diode plus a cadmium cover and suitable moderation. The fast neutron portion of the spectrum is measured through the use of a U^{238} foil over the third diode. During the experimental tests, appropriate weighting functions were applied electronically by line-operated instrumentation to the signals from the three detectors.

The composite response curve was determined through measurements with neutron sources, a Van de Graaff

neutrons are counted, each 5 ev neutron should have its count weighted by 1.2; each 100 kev neutron by a factor of 8, and so on.

Neutron dosimetry investigations with moderated detectors were carried out at Hanford by DePangher and Roesch.[5.6, 5.7] In addition, Bramblett et al.[5.8] studied spherical moderators, and their techniques were employed by Hankins.[5.9] The Hanford work made use of moderated proportional (BF_3) counters, and Hankins used scintillation detectors (LiI) with various moderators. It was decided to pursue the dosimetry investigations using a family of solid state detectors with appropriate foil covers and moderators to attempt to achieve a useful dosemeter for use over the thermal through 10 Mev neutron energy range.

To analyze the effect of moderation, calculations and measurements were made; however, because of the considerable detail, this information will not be presented in this paper. It is planned to describe the experiments in detail in a formal report, and the report will describe the predictions of the flux spectrum within the moderator.

The moderated neutron flux is dependent both upon the scattering angle and the penetration depth. The theoretical prediction of the energy spectrum is an extremely difficult endeavor which would require following the spatial coordinates of each deflected neutron. This was done by Snyder at Oak Ridge National Laboratory for a semiinfinite slab of 30 cm thickness using a Monte Carlo program. However, since no analysis of this type has yet been carried out for the spherical geometry used, the effect of the moderator was predicted for the present investigations by use of empirical data and a simplified interpretation of the data to relate the amount of moderation needed to moderate high energy neutrons to a specific energy (such as the resonance cross section energy of rhodium).

Bramblett, Ewing, and Bonner[5.8] measured the relative counts for a uniform flux as a function of energy. The data were obtained with Li^6 scintillators for various diameters of spherical moderators. For the

present Hanford investigations, the referenced information was used to predict the response of the thermal detector. In applying the information to predict the response of the resonance detector, the referenced curves were moved up the energy scale by the amount from thermal to the resonance detection energy.

For the thermal to high ev range, a diode with a Li^6 foil cover and a polyethylene moderator was used. The moderator was chosen as a 3 in. diameter sphere. This size appears to provide the desired response. A commercial surface barrier solid state detector was used with the accompanying Li^6F coated cover. A cover using B^{10} may also be used.

In selecting the sensor for the resonance energy range, consideration was given to the energy of resonance; the resonance integral (the area under the resonance portion of the cross section versus energy curve compared to total area); the nature of the resulting radioactivity, i.e., half-life; and the energy of the charged particles emitted. Mn^{55}, Rh^{103}, Ag^{107}, In^{115}, and Au^{197} were considered, and Rh^{103} was chosen for use since it has a short half-life, a high energy beta, and a large resonance integral.

Using the resonance detector, the number of counts obtained in 1 sec can be multiplied electronically by an appropriate factor to obtain a gross number related to the desired value as determined by calibration. These counts can then be converted to a voltage and a capacitance can be charged with an appropriate RC time constant. After 1 sec, the voltage corresponding to the element activity can be sampled and compared with the capacitance voltage. The difference of these two voltages can again be interpreted as counts occurring during the monitoring time. In determining the thickness of the rhodium foil, the range of the beta particles must be considered. The maximum range of any beta from rhodium is calculated as [5.10]

$$1.19\ g/cm^2 \text{ where } E_{max} = 2.44 \text{ Mev.}$$

Since the detector is enclosed in a cadmium thermal neutron shield, and the rhodium foil is very thin, nearly all of the activation will occur due to the resonance cross section since the resonance cross section is several magnitudes greater than the epithermal cross section. For a thicker foil, all of the neutrons with the resonance energy will be captured within the first few mg/cm^2 of the foil and the resulting betas from this activation will undergo large self-absorption. The betas resulting from the epithermal capture further in the foil will have a higher probability of being counted. It is apparent that the choice of the foil thickness will affect the response of the detector.

To illustrate the dependence of the device response upon the foil cover thickness, Table 5.1 shows the percentage of neutrons captured within the given distance of penetration for the peak resonance cross section, for the cross section of 100 barns, and for the average cross section (6 barns) above resonance.

TABLE 5.1

RHODIUM FOIL THICKNESS FOR PERCENTAGE ABSORPTION OF NEUTRONS AT THREE ENERGIES OF INTEREST

(Thickness in mg/cm^2)

Neutron Flux Absorbed in Rh Foil, %	Resonance Energy, σ = 4500 barns	0.6 to 2.0 ev, σ = 100 barns	Average Epiresonance, σ = 6 barns
5	1.95	87.6	1,460
25	10.9	492	8,200
50	26.3	1184	19,743
75	52.58	2366	39,316
95	113.9	5125	85,470

Since the maximum energy beta from the rhodium decay is 2.44 Mev, the maximum foil thickness that would give an increase in counts would be 1.19 g/cm^2 which corresponds to 0.096 cm. It is seen that essentially all

of the neutrons at the resonance energy will be absorbed in the first fractional distance in the foil; whereas, approximately 50% of the neutrons at the 100 barn cross section and only 5% of the higher energy neutrons will be absorbed in the foil. For a sharper resonance measurement, a thin foil may be used; and for a diffused response, the thicker foil may be used.

Because of the relatively large penetrating distance of the resulting betas from the Rh^{103} foil, a surface barrier diode detector would be very inefficient. The maximum range of these betas is 1.19 g/cm^2 or 956.6 μ in silicon. For efficient counting, a 1000 μ depleted lithium ion drift detector was used for the investigations. Since this detector is used only to monitor the moderated flux at the resonance energy, a cadmium cover was used to eliminate the thermal flux.

For fast neutron energies, a detector is needed which has a relatively constant sensitivity in the region from 1 to 10 Mev. An element with a threshold fission cross section is needed. Am^{241}, Np^{237}, and U^{238} all have fission cross sections appropriate to this requirement. It is undesirable to use either Am^{241} or Np^{237} as the active element because of their radioactivity; hence, for the fast neutron detector, uranium with the isotope U^{235} depleted twenty-fold was used as a 13 mg/cm^2 foil cover.

From the fast neutron capture by U^{238}, the charged particles detected are fission fragments. Because of the high ionization and relatively short range, any surface barrier detector will adequately detect these particles. The area of the U^{238} foil and detecting junction should be as large as possible for maximum sensitivity; thus, a 4.5 cm^2 surface barrier detector was used.

Sensitivity

Due to both the respective cross sections and the relative numbers of neutrons per unit dose, the fast neutron detector is the limiting element for sensitivity. For the calculation, a foil thickness of 13 mg/cm^2 was used. This thickness corresponds to the maximum range of the resulting fission fragments.

From the National Bureau of Standards Handbook Number 63, the dose rate of 100 mrem per 40 hr corresponds to approximately 18 neutrons/cm^2-sec for the energy range from 1 to 10 Mev. Approximately 2.59×10^4 neutrons/cm^2 in this energy range are equivalent to 1 mrem dose. The flux corresponding to each count from the fast neutron detector can be calculated as,

$$1 \text{ count/sec} = K \sigma_f N \varphi .$$

In this equation, σ_f is the fission cross section of U^{238} which is taken as 0.6 barns, N is the number of uranium atoms in the assumed thickness of 13 mg/cm^2, and K is the probability of counting the fission fragments from a single fission event. Solving for the flux,

$$\varphi = (5.07 \times 10^4)/K \text{ neutrons/cm}^2$$

per one count for each cm^2 of detector surface. Hence, the dose corresponding to each count is,

$$\text{Dose} = \frac{5.07 \times 10^4 \text{ neutrons/cm}^2}{K\ 2.59 \times 10^4 \text{ neutrons/cm}^2\text{/mrem-cm}^2} = \frac{1.95}{K} \frac{\text{mrem/count}}{1 \text{ cm}^2 \text{ detector area}} .$$

The factor K will account for the diode detector counting fission fragments from only one side of the foil and the self-absorption within the foil. For the ideal case, K will be 0.5. The minimum dose sensitivity for the 4.5 cm^2 detector used can be calculated as,

$$\text{minimum dose} = \frac{1.95}{0.5} \frac{\text{mrem}}{\text{cm}^2} (4.5 \text{ cm}^2) = 0.865 \text{ mrem}.$$

The counts from each detector must be discriminated, electronically weighted, and summed to record dose and dose rate. For an experimental device to demonstrate the concept, these electronic processes were performed using 110 v ac operated instruments.

Experimental Evaluation

The multiple-detector unit was exposed to monoenergetic neutrons at the Hanford Van de Graaff facility. The detectors were placed in fluxes

where the neutron energy was at discrete values between the available limits of approximately 100 kev and 5 Mev; and at each chosen energy, the counts from each detector were recorded. Figure 5.36 shows the three assembled detectors as they appeared for the testing.

For the various tests carried out, the counts from each detector were recorded and compared to the flux as determined by the Van de Graaff instrumentation, and the necessary scale factors by which the counts from each detector should be weighted were calculated. The relative response curve for each detector was plotted and then graphically fitted to the desired response by multiplying each count by a suitable factor. In this manner, the weighting factors were determined as 1.0 for the thermal detector, 100 for the resonance detector, and 4000 for the fast neutron detector. With these weighting factors incorporated, the response of the integrated device is shown in Figure 5.37.

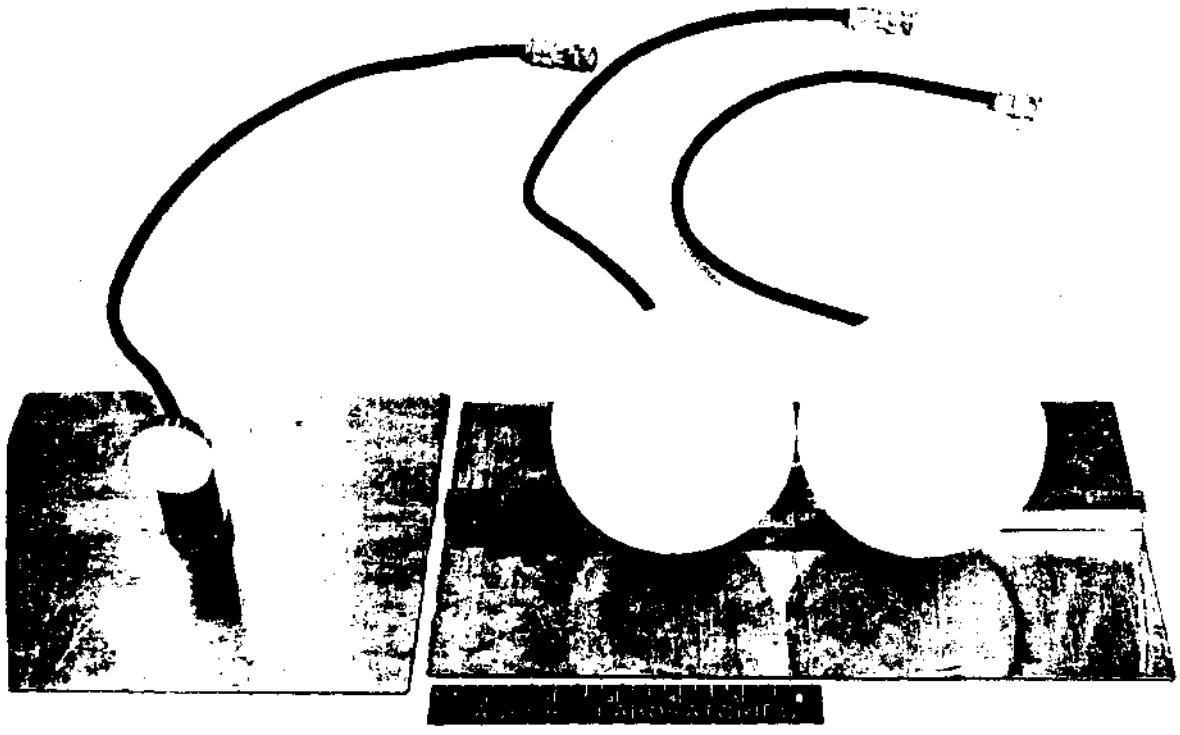

FIGURE 5.36
Assembled Detectors for Testing

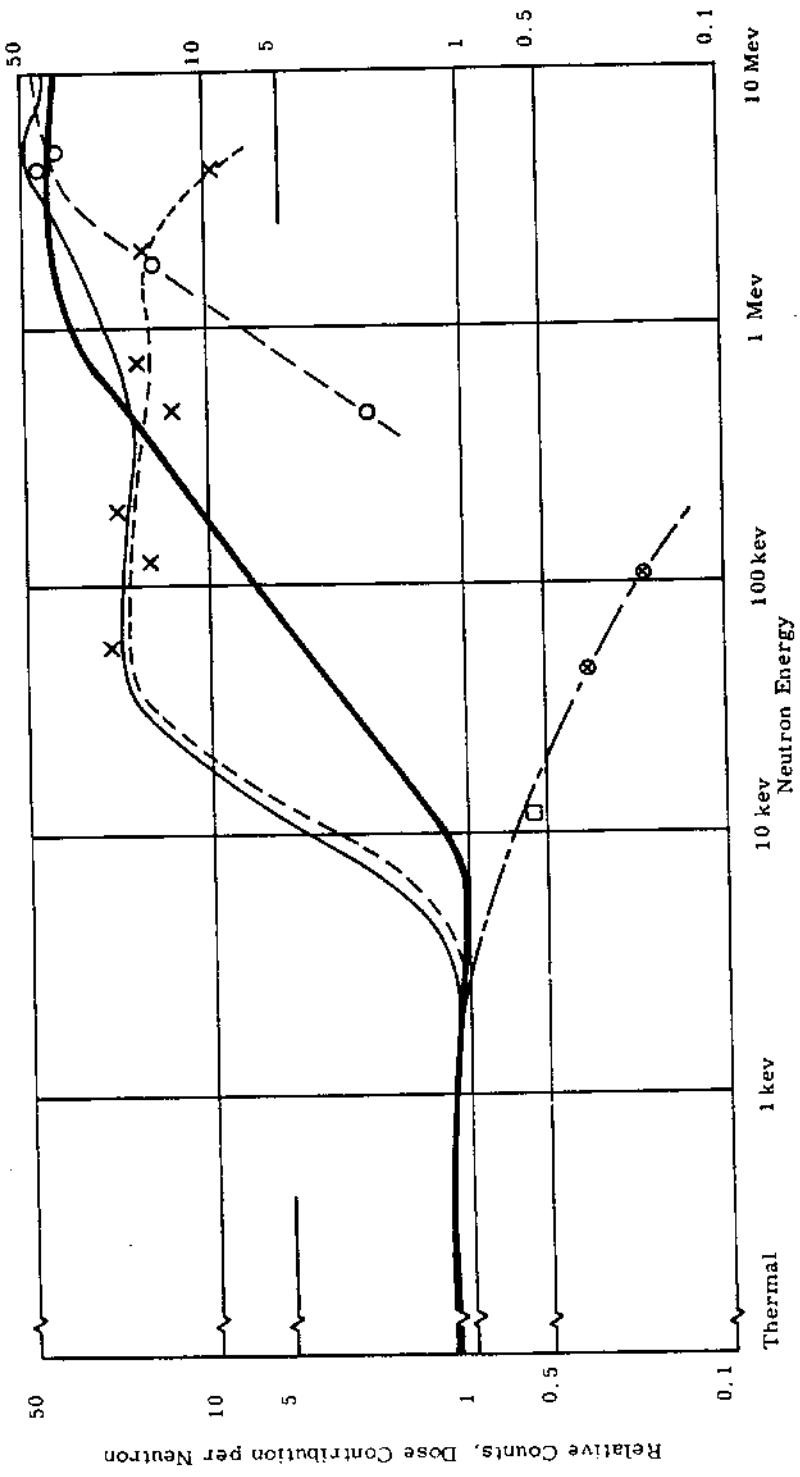

FIGURE 5.37

Relative Contribution to Dose Versus Neutron Energy

AEC-GE RICHLAND, WASH.

Signaling Radiation Dosemeters - D. P. Brown

The problem of measuring dose to personnel continued to receive attention. Development was accelerated on personally carried, miniature, signaling radiation dosemeters which employ a recharging type of ionization chamber as the sensor. The major effort concerned improving reliability and uniformity of response of the experimental dosemeters to provide a readily-apparent audible signal following accumulation of a predetermined dose. The effort centered around a single signal activation point, typically 50 or 100 mr. In addition, a number of solid state circuit refinements were incorporated along with a method of correctly charging the center rod of the "pencil" type ionization chamber before use. Other work was directed at improving the recharging fiber and center rod mechanical assembly to achieve reliable performance. Several experimental dosemeters were assembled and tested with promising results and a model was fabricated for use in possible offsite fabrication procurement of a representative number of dosemeters.

Discussion

Development work was accelerated regarding personally-carried, miniature radiation dosemeters which employ recharging-type "pencil" ionization chambers [5.11] as sensors, all solid state circuitry, and suitable audible signaling devices.

The ionization chamber, shown in Figure 5.38, employs a 2.5×10^{-4} in. diameter fiber to recharge the center rod of the chamber. Initially, the center rod is charged to the charging potential by a external, momentary switch. The rod and fiber will then reside at the same potential and the fiber will be positioned correctly. As the radiation-caused ionization within the chamber discharges the center rod, the difference in potential between the rod and the fiber causes the fiber to be attracted toward the rod by electrostatic attraction. When the fiber touches the rod, it recharges the rod to the charging voltage, where the charge is obtained from a storage capacitor.

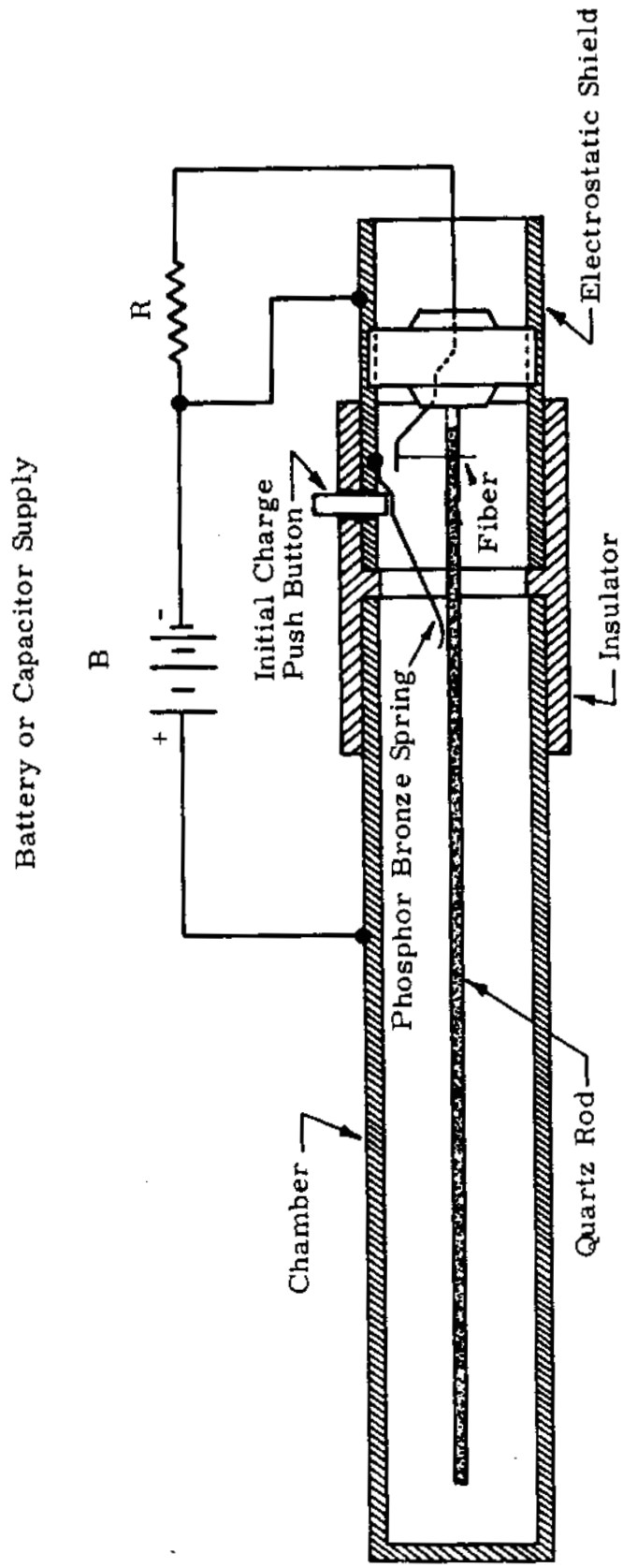

FIGURE 5.38
Recharging Ionization Chamber

During recharging, a pulse is developed which is used to trigger a bistable flip-flop circuit. This flip-flop then energizes the alarm circuitry consisting of an astable multivibrator audio oscillator and speaker drive circuit. The speaker is a miniature earphone coupled to an exponential horn. The input circuitry is a double emitter follower which provides high input impedance and reliable alarm triggering. The complete circuit is shown in Figure 5.39.

Alarm reset and alarm test functions are performed by magnetically operated glass switches. This eliminates the need for opening the case to achieve these functions. The charge storage capacitor is also charged through a glass switch to prevent accidental capacitor discharge and hence, disabling of the dosemeter.

Two experimental dosemeters were fabricated and thoroughly tested. One dosemeter was adjusted to cause alarm signal activation following a dose accumulation of about 50 mr and the second was adjusted for a 200 mr level. Testing indicated that alarm signal activation repeatability values of ±4 and ±3% were obtained for the 50 mr and 200 mr units, respectively. As stated, a simple mechanical adjustment within the chamber can provide dose value alarm trip points as desired. To alleviate minor angular dependence response problems, since the ionization chamber is close to the several circuit components (especially the battery), one unit was assembled with the pencil chamber mounted in a half-cylinder on the front of the dosemeter package. This method improved the situation; however, a comparatively bulky package resulted. Thus, the final model, shown in Figures 5.40 and 5.41, had the chamber mounted on the glass-fiber printed circuit board. The considerable testing accomplished indicated that general performance would be acceptable and it was tentatively planned to use the pictured model in offsite fabrication procurement of a representative number of dosemeters. Studies and experiments will be continued to effect improvements in methods of measuring dose to personnel. A report on the work to date will be published in 1964.

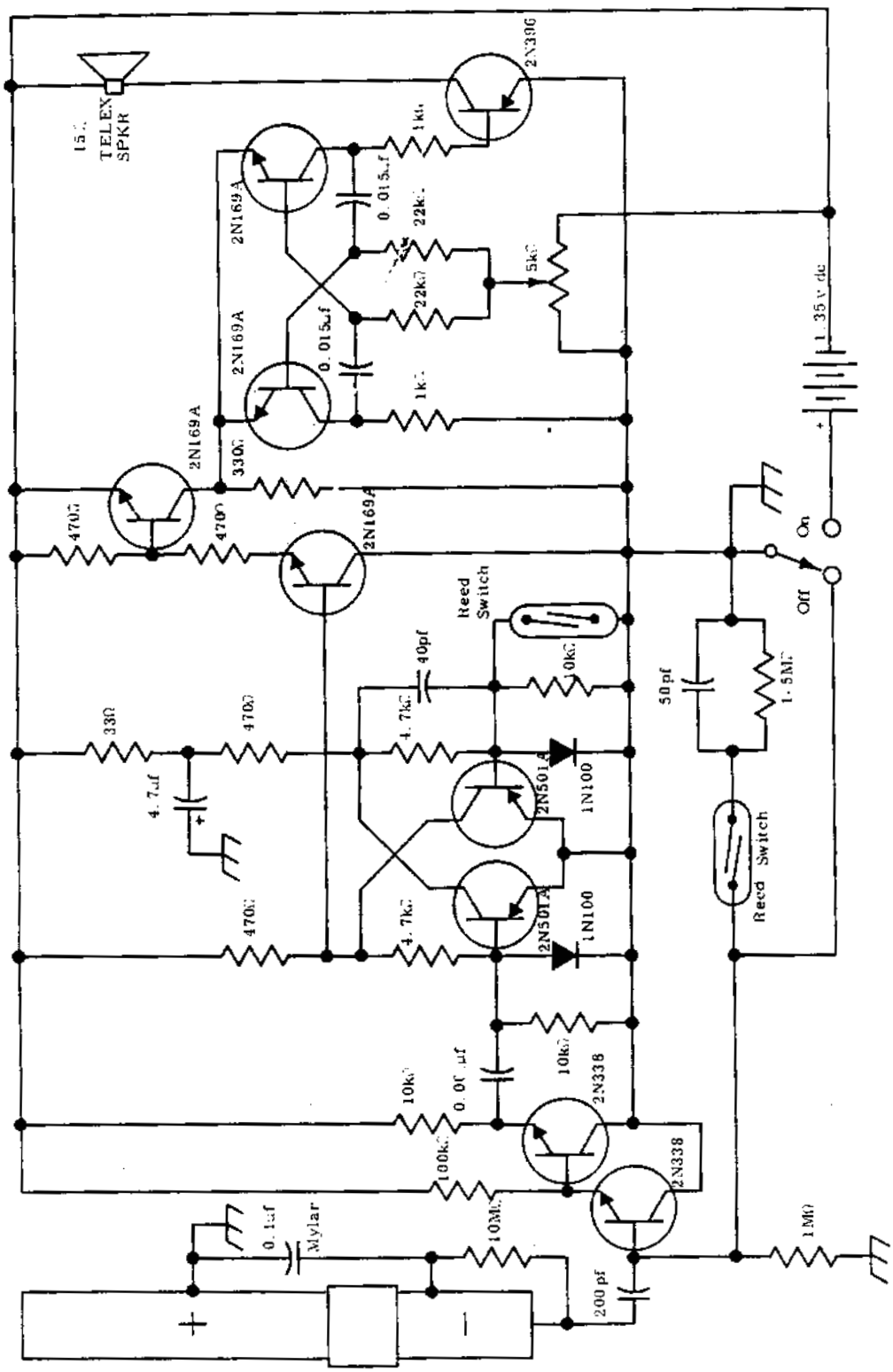

FIGURE 5.39
Recharging Dosemeter Circuit Diagram

FIGURE 5.40
Internal View of Completed Dosemeter

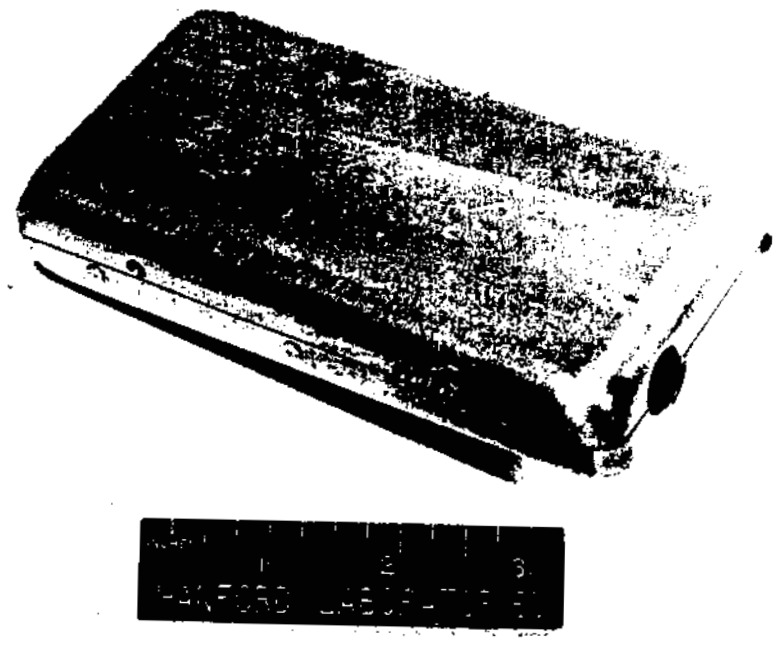

FIGURE 5.41
Complete Packaged Dosemeter

AEC-GE RICHLAND, WASH.

Contaminated Air Monitoring Techniques

Airborne Plutonium Detection - D. P. Brown

Development work was fulfilled on the investigation of alpha energy analysis techniques for the detection of airborne plutonium contamination. An experimental system was assembled and tested and work was initiated on a demonstration model to be used during biological inhalation studies. The original development work was started late in 1962. As a matter of review, detection of the Pu^{239} maximum permissible air concentration (MPC)(5.12, 5.13) of 2×10^{-12} μcuries/cm^3 is complicated by a varying background of natural alpha emitters. Since one MPC of airborne Pu^{239} is only 4.44×10^{-6} disintegrations/min/cm^3, it is necessary to integrate the activity on a filter to obtain adequate measurement sensitivity. Radon and thoron are also collected on the filter, and at times, their activity may accumulate to several hundred times the required detection level for Pu^{239}. Methods for the detection of low level plutonium air contamination were examined and a series of definitive experiments was carried out. A sensitivity of 40 MPC-hr was obtained using alpha energy analysis techniques where the contributions from higher energy radon and thoron which appear in the Pu^{239} channel were compensated using electronic balancing circuitry. This provided a considerable reduction in complexity compared to other air particulate monitors of similar sensitivities. Additional experiments showed that gamma background levels of 2 mr/hr and beta particle levels of 2.4×10^4 disintegrations/min will not adversely affect the sensitivity or general operation. An increase in air flow rate and/or an increase in detector and filter diameter will improve the basic sensitivity.

Discussion

Pu^{239} emits alpha particles with energies of 5.15, 5.13, and 5.10 Mev. Most of the daughters of radon and thoron also emit alpha particles ranging in energy from 5.3 to 8.95 Mev. Thus, with an adequate alpha energy analyzer, it would be possible to count only those alphas due to the plutonium on the filter. However, obtaining suitable energy resolution requires a vacuum and assumes all particles are emitted from the filter surface with no self-absorption. In a practical system with continuous air sampling, there is an air-filled gap between filter and detector. In addition,

there is also some energy loss from particles which had to pass through dust on the filter or through a portion of the filter itself. Thus, each emitter would exhibit a more or less continuous spectrum of alpha energies. Figure 5.42 shows a typical spectrum obtained with a multichannel analyzer with thin CsI crystal as a detector. Figure 5.42a is the spectrum for plutonium entrapped on a 2 in. diameter Millipore filter and Figure 5.42b is a spectrum of a typical radon-thoron background condition. Figure 5.43 shows these spectra superimposed. It is easily seen that pulses from plutonium are occurring at pulse heights where there is relatively little contribution from the background. A single channel analyzer properly adjusted to count the appropriate pulse heights will permit determination of the plutonium contribution. There will be some counts due to background counted; however, these can be compensated by counting those pulses with heights above the plutonium "cutoff" and using them to balance the contribution in the plutonium channel.

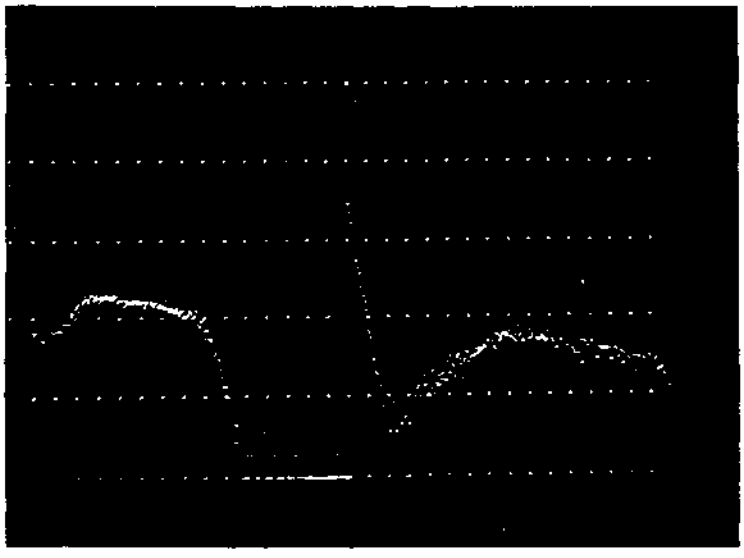

(a) Plutonium Spectrum (b) Background Spectrum

FIGURE 5.42
Typical Alpha Spectra

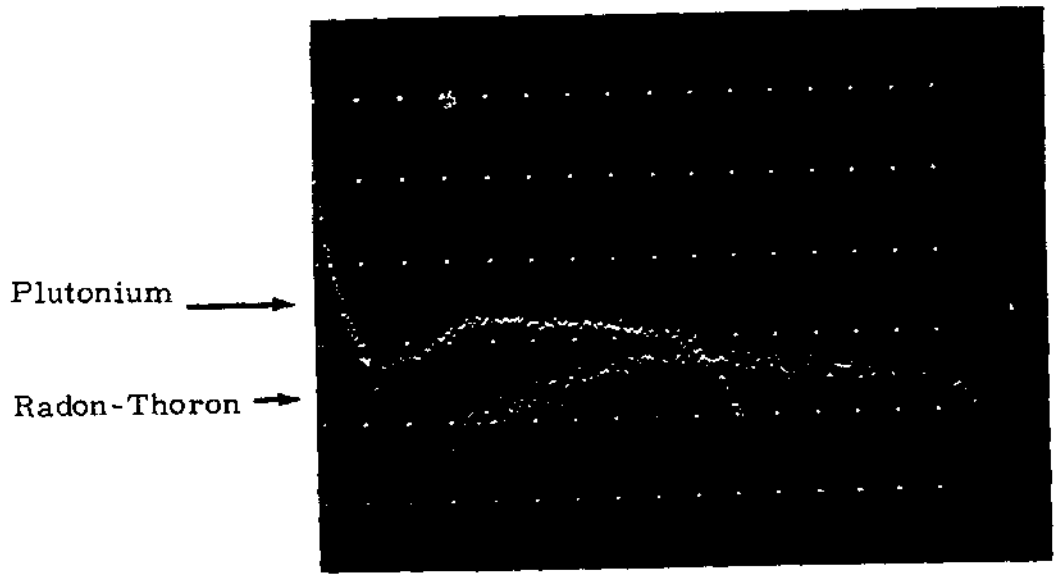

FIGURE 5.43
Spectra Superimposed

Figure 5.44 shows a block diagram of the general system used for the experiments. The detector is a thin (3 mil), 2 in. diameter CsI (Tl) crystal and a multiplier phototube. A 2 in. diameter Millipore filter was used with a 5 ft^3/min airflow. The construction of the Millipore filter tends to prevent the imbedding of alpha emitters in the filter; such imbedding considerably affects the energy resolution capabilities of the method. Standard commercial pulse amplifier, single channel pulse height analyzer, and count-rate-meter instruments were employed for the experiments.

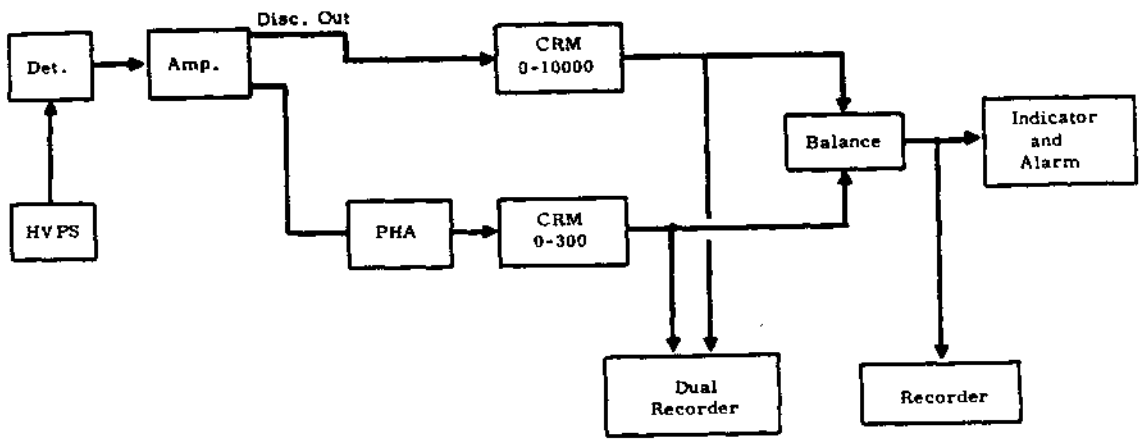

FIGURE 5.44
Block Diagram
Alpha Energy Analysis Air Monitor

It is also possible to employ solid state silicon alpha particle detectors in a similar manner as used for the CsI scintillation detector. Experiments were carried out in parallel using this alternate approach, and commercial surface barrier silicon units were employed. The solid state detectors provide a considerable improvement in energy resolution which slightly simplifies the balancing or compensation problem; however, the very small diameters available (3 to 4 cm) materially reduce the filter area coverage. A number of such solid state detectors could be used to view a large filter; however, because of detector container size and edge effects, the effective area covered would be only 30 to 40%. A second alternative would be to program one detector to physically traverse, via mechanical means, a large filter. This merely adds another item to fail in the system and additionally incorporates more complex switching and other circuitry. The comparative tests indicated that the scintillation approach was more satisfactory at this time.

For the scintillation energy analysis approach, which is less complex and less expensive than the solid state detector approach, the ideal system would employ a 5 in. diameter filter, a 15 ft^3/min air flow, and a 5 in. diameter (1 mil thick) CsI crystal detector. This would lead to a detection sensitivity of perhaps 15 MPC-hr which would correspond to the more expensive and more complicated dual-detector coincident-count method of continuous alpha air monitoring.

The system was assembled and operated for approximately 6 mo. Periodic testing with Pu^{239} samples during high radon-thoron level background conditions proved the ability of the technique to detect relatively small airborne concentrations of Pu^{239} as was desired. An equivalent sensitivity of better than 40 MPC-hr was achieved, and an increased airflow with a larger filter and detector could improve this if required.

Figure 5.45 shows typical recordings during a high radon-thoron buildup. The spike in the Pu^{239} channel was caused by a 1600 disintegrations/min Pu^{239} source placed on the filter. The system detection ability is clearly

demonstrated. Note that the overall up-scale deflection due to radon-thoron in both channels is quite small. The full scale deflection of the plutonium channel is 300 counts/min while that of the background is 10,000 counts/min. The difference in levels is corrected in the balance control portion of the system. The difference recording, thus compensated, is shown in Figure 5.46 where the spike again corresponds to the introduction of the Pu^{239} on the filter.

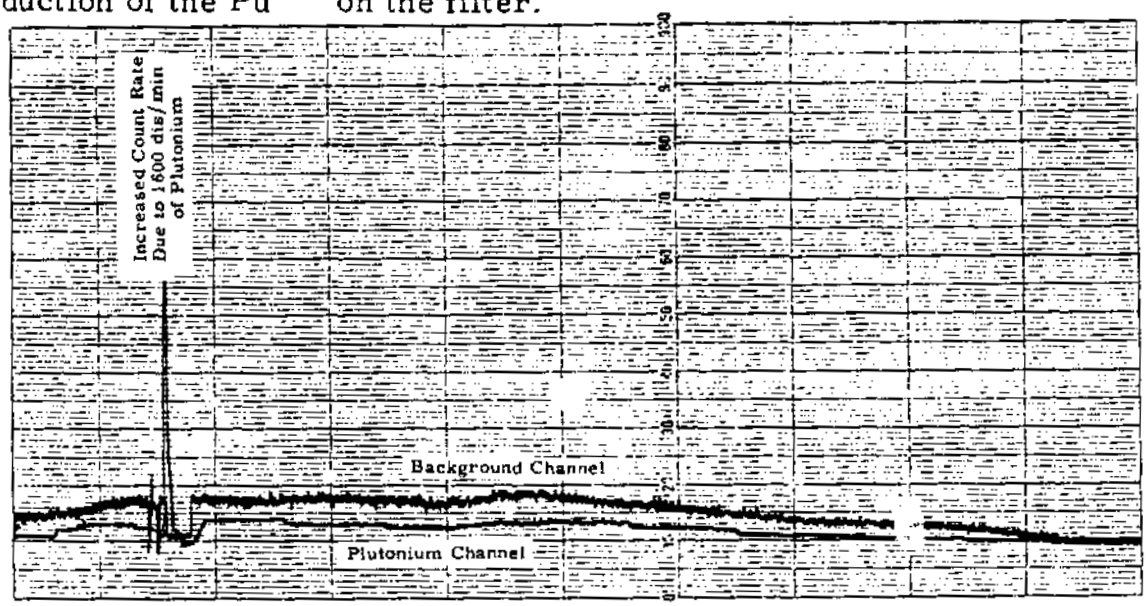

FIGURE 5.45

Dual Channel Recording During Radon-Thoron Buildup and Decay

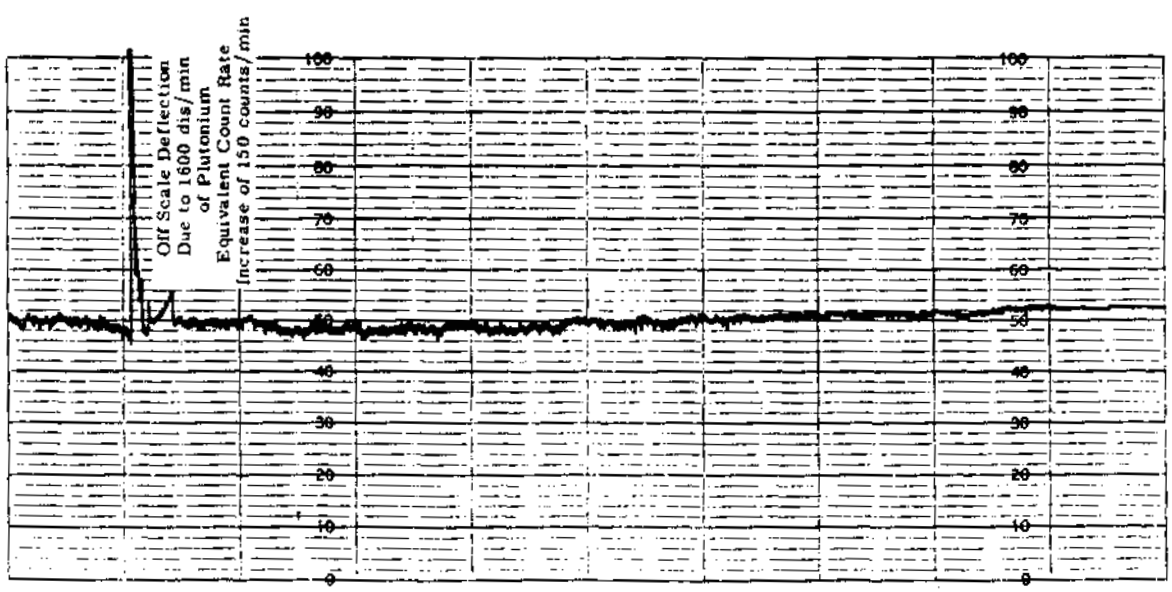

FIGURE 5.46

Difference Recording During Radon-Thoron Buildup and Decay

The thin CsI crystal detector is sensitive to beta particles and gamma rays as well as to alpha particles. Therefore for test purposes, the detector was subjected to a Co^{60} gamma field of 2 mr/hr and to a $Sr\text{-}Y^{90}$ source of 2.4×10^4 disintegrations/min. With the gamma field and beta source, there was no detectable increase of count rate in either channel. However, for Co^{60} gamma fields of 200 mr/hr, there was enough of an increase of count rate in the plutonium channel to cause the instrument to falsely indicate plutonium contamination. These and other experiments indicate that lead or steel shielding for the detector should be used where gamma background dose rate may exceed about 5 mr/hr if the stated sensitivity is to be achieved.

Although the obtained sensitivity was about 40 MPC-hr, a definite improvement can be achieved using higher air sample rates and/or by use of larger diameter detectors. Figure 5.47 illustrates the established sensitivities of several alpha air monitors developed at Hanford. The High Level Alpha Air Monitor [5.14] provides alarm energizing when the filter alpha activity reaches a predetermined level but it has no compensation for radon and thoron deposited on the filter. The Dual Alpha Air Monitor [5.15] uses two detectors which sample separate room air supplies with one supposedly free of contamination. The Medium Level Air Monitor [5.16] measures the rate of buildup of alpha activity, and the sensitivity is limited by the maximum expected filter buildup rate of radon and thoron. The Coincident-Count Air Monitor [5.17] provides the best sensitivity; however, it should be noted that while the alpha energy analysis method is not as sensitive, it is considerably less complex and less expensive. For many applications, the alpha energy analysis method provides an excellent combination of sensitivity, instrument simplicity, and moderate cost for continuous air monitoring.

If larger area solid state detectors of acceptable resolution become available at less cost, the use of such units should be reconsidered for alpha air monitoring. Consideration of all factors indicates that, at this time, the scintillation methods are superior.

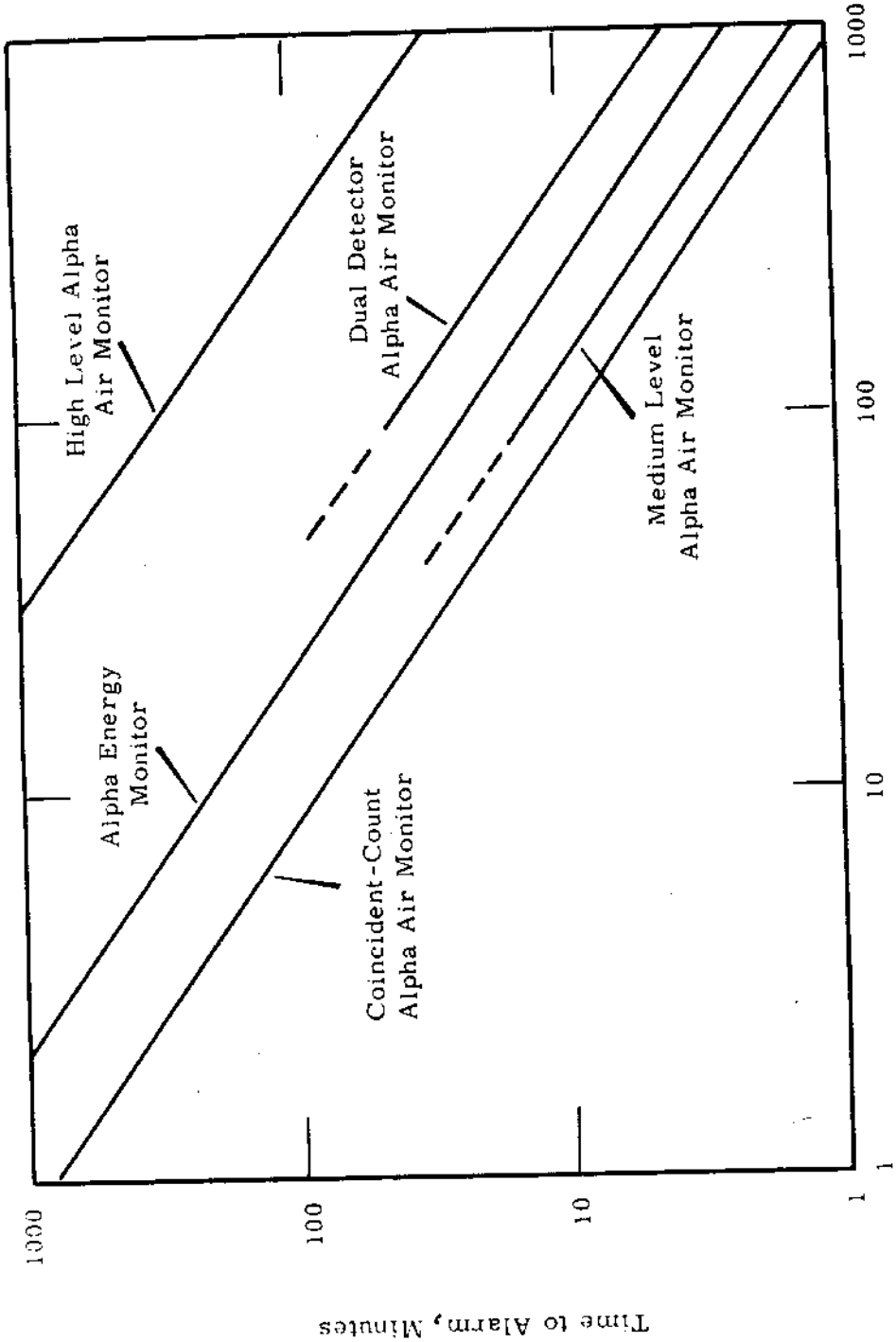

1 MPC = 2×10^{-12} μc/cc

Continuous Alpha Air Concentration Levels

FIGURE 5.47

Comparison of Response of Several Alpha Air Monitors

REFERENCES

5.1 M. O. Rankin. Detection of Airborne Zinc Sulfide, HWIR-1693. 1964. (HW-SA-3317)

5.2 E. M. Sheen. A Novel Count Rate Circuit, HWIR-1612. March 1963.

5.3 P. E. Morrow and L. J. Casarett. Experimental Approach to the Study of the Respiratory Deposition and Retention of Certain Alpha Emitters, UR-308, University of Rochester. March 1955.

5.4 G. F. Garlick. A Technique for Measurement of Neutron Dose, HWIR-1611. March 1963.

5.5 National Bureau of Standards, Handbook 63, Protection Against Neutron Radiation Up to 30 Million Electron Volts, U.S. Department of Commerce, Washington, D.C. November 1957.

5.6 J. DePangher and W. C. Roesch. "Neutron Dosimeter Having Uniform Sensitivity from 0.1 to 5.1 Mev," presented at American Physical Society Meeting, Los Angeles, December 28, 1955.

5.7 J. DePangher. Double Moderator Neutron Dosimeter, HW-57293. July 15, 1958.

5.8 R. L. Bramblett, R. I. Ewing and T. W. Bonner. "A New Type of Neutron Spectrometer," Nuclear Instruments and Methods, vol. 9, pp. 1-12. 1960.

5.9 D. E. Hankins. A Neutron Monitoring Instrument Having a Response Approximately Proportional to the Dose Rate from Thermal to 7.0 Mev, LA-2717, Los Alamos Scientific Laboratory. August 1962.

5.10 H. Etherington (ed.) Nuclear Engineering Handbook. McGraw-Hill Book Company., New York. 1958.

5.11 D. P. Brown and M. O. Rankin. Experimental Personnel Radiation Dosemeters, HW-SA-2590. May 21, 1962.

REFERENCES (Contd.)

5.12 National Bureau of Standards, Handbook 69, Maximum Permissible Body Burdens and Maximum Permissible Concentrations of Radionuclides in Air and in Water for Occupational Exposure, U.S. Department of Commerce, Washington, D.C. June 1959.

5.13 Hanford Laboratories, General Electric Company. Radiation Protection Standards, Hanford Atomic Products Operation, HW-25457 REV2. March 1960.

5.14 G. D. Linsey and R. A. Harvey. High Level Alpha Air Monitor, HW-49561. June 14, 1957.

5.15 R. A. Harvey and C. D. Boyne. Unpublished Data. January 1959. General Electric Company, Richland, Washington. (Personal Communication)

5.16 M. O. Rankin. "Medium-Level Continuous Alpha-Air Monitor," Health Physics, vol. 4, pp. 293-298. May 1961.

5.17 D. P. Brown, M. O. Rankin, C. D. Boyne, and W. G. Spear. A Coincidence Count Alpha Particulate Air Monitor, HW-75384. January 3, 1963.

INTERNAL DISTRIBUTION

Copy Number	
1	F. W. Albaugh
2	W. J. Bair
3	C. A. Bennett
4	O. E. Boston
5	L. K. Bustad
6	R. F. Foster
7	P. A. Fuqua
8 - 32	J. J. Fuquay
33	J. K. Green
34	W. A. Haney
35	F. P. Hungate
36	E. R. Irish
37	W. E. Johnson
38	R. L. Junkins
39	A. R. Keene
40	H. A. Kornberg
41	M. Lewis
42	C. E. Linderoth
43	R. E. Nakatani
44 - 93	J. M. Nielsen
94	W. D. Norwood
95	R. F. Palmer
96	H. M. Parker
97	R. S. Paul
98	W. C. Roesch
99	L. C. Schwendiman
100	R. K. Sharp
101 - 125	W. G. Spear
126	A. J. Stevens
127	F. Swanberg
128	R. C. Thompson
129	M. T. Walling
130	W. K. Woods
131	D. C. Worlton
132 - 133	Biology Library
134	300 File
135	Record Center
136	Technical Publications
137 - 141	Extra